UNIVERSITY OF SOUTHAMPTON

FACULTY OF ENGINEERING, SCIENCE AND MATHEMATICS

School of Civil Engineering and the Environment

Stresses in sprayed concrete tunnel junctions

by

Benoît David Jones MEng

Thesis for the degree of Engineering Doctorate

January 2007

UNIVERSITY OF SOUTHAMPTON

ABSTRACT

FACULTY OF ENGINEERING, SCIENCE AND MATHEMATICS
SCHOOL OF CIVIL ENGINEERING AND THE ENVIRONMENT

Engineering Doctorate

STRESSES IN SPRAYED CONCRETE TUNNEL JUNCTIONS

by Benoît David Jones

The low mobilisation cost and flexibility of geometry that sprayed concrete allows means that sprayed concrete linings (SCL) are now almost always used for short lengths of tunnel, tunnels of varying geometry and tunnel junctions. While considerable effort has been spent investigating the deformations of the ground during tunnelling of straight, constant diameter tunnels, comparatively little work has been done on the stresses in SCL tunnels or junctions. The structural behaviour of an SCL tunnel junction in terms of stresses is not well understood because design models are usually simplistic and field data are scarce. This research addressed these gaps in knowledge through literature review, field monitoring and a suite of numerical experiments.

Study of the behaviour of pressure cells revealed a new type of temperature sensitivity, the ground reaction temperature sensitivity, which constitutes a real radial stress as the SCL ring expands and contracts against the ground with changes in temperature. The field data showed that stresses on an SCL in soft ground were dependent on ring closure and if this occurred close to the face the stresses would approach a long-term maximum value well below hydrostatic overburden pressure once the face had advanced approximately two tunnel diameters away. The literature review indicated that if more ground deformation were allowed, the stresses would continue increasing over a long period of time, possibly approaching hydrostatic overburden pressure in the long-term.

The numerical experiments showed that the axial stress concentration factor at the junction was not dependent on nonlinearity, anisotropy, stiffness and plasticity of the ground, or its *in situ* stress distribution. However, the bending stress concentration factor was dependent on the ground stiffness and to a lesser extent the undrained shear strength of the ground.

Acknowledgements

This research was supported by the EPSRC and Mott MacDonald, to whom I am grateful hope I have been good value for money.

I would like to thank my supervisors, Professor Chris Clayton, Dr David Powell and Dr Alun Thomas for their advice and support during my research.

I would also like to thank those who helped me on site, Ken Henderson and John Corcoran of Morgan=Vinci JV, Ian Williams of BAA, and Alun Thomas, Matous Hilar and David Watson of Mott MacDonald.

In the laboratory I received considerable advice and assistance from Harvey Skinner and Ken Yeates.

Richard Harkness, Siavash Farhangi, Chris Pound and especially Yu Sheng Hsu helped with many questions about the mysterious workings of FLAC^{3D}.

I would also like to thank all those friends and colleagues who helped to keep me sane while writing this thesis.

Finally, and most importantly, thankyou Mum and thankyou Anna for your love and support.

Contents

Tables

Figures

1 INTRODUCTION

The objectives of the research were to improve the methods of stress prediction and stress measurement in sprayed concrete linings.

A short history of sprayed concrete linings is outlined in the following paragraphs, and then the case is made for the need for better predictions and measurements of stress.

Sprayed concrete linings (SCL) were first used for tunnel support in 1914 in the Bruceton Experimental Mine in the USA and by the 1920s had been used in several tunnels in Europe. By the 1950s, SCL had almost completely replaced timbering as the primary means of support and was used in rock tunnels and mines as a means of controlling rock pressures and deformations (Kovári, 2003a). The use of steel supports, rockbolts and sprayed concrete (also called 'shotcrete') removed the need for timber props and hence improved access to the face. Because the support could be applied much more quickly it better preserved the surface of the rock and reduced loosening and swelling. As such, thinner, more flexible linings could be used with rockbolts to aid the activation of a ground arch but prevent the build up of pressures associated with excessive loosening and swelling. This allowed faster, safer and more economical tunnelling compared to precursors such as the 'Belgian method' or the 'old Austrian method', which required much thicker brick or masonry linings (Golser, 1976).

Although developed simultaneously elsewhere, it was the seminal work of the Austrians and in particular Rabcewicz (1954a, 1954b, 1964a, 1964b, 1965, 1969a, 1969b, 1969c) and then Golser (Rabcewicz & Golser 1973, 1974a, 1974b; Golser, 1976, 1978) in the 1950s, 1960s and 1970s, coupled with the advances in sprayed concrete and rockbolt technology that really made this philosophy routinely applicable. Rabcewicz effectively rebranded these ideas as the 'New Austrian Tunnelling Method' (NATM).

The NATM philosophy stated that a certain amount of ground deformation should be allowed to take place to reduce the pressure acting on the tunnel and mobilise a ground arch ('mobilisation') while maintaining the integrity of the ground mass ('preservation'). This concept is usually illustrated by the 'ground-

reaction curve' (also known as the 'Fenner-Pacher' curve), shown in Figure 1-1. Fast installation of support, usually in the form of rockbolts and sprayed concrete, and fast closure of the invert, should help preserve the rock mass and prevent 'loosening pressures' from developing (Rabcewicz, 1964a). However, it is the 'mobilisation' of the ground arch that is more often remembered as a principle of the NATM, rather than the more important 'preservation' (Rokahr, 1995).

Rabcewicz wrote, "For the first time in tunnelling history systematic measurement of deformations and stresses enables the required lining thickness to be evaluated and controlled scientifically" (Rabcewicz, 1965). Due to the difficulties in predicting the stresses and deformations in a tunnel by calculation, the NATM was controlled by close observation. The lining was in essence dimensioned empirically. In fact, this empirical method was considered superior to any highly sophisticated mathematical treatment because all unknown factors were included implicitly in the observational method. Analysis methods at the time were considered promising, but due to "the usual complexity of geological conditions" and the inability to model the effect of time and construction stages, they were considered unreliable (Golser, 1976).

Today, the term 'NATM' is controversial (ICE, 1996), and some doubt whether it added anything to existing good tunnelling practice (Kovári, 2003b, Romero, 2002, ICE, 1996). The HSE report into the Heathrow collapse (HSE, 1996) recommended that the term 'NATM' should be used to mean a construction method involving an open face and the application of sprayed concrete, and its original meaning as a philosophy should be ignored. Brown (1981), however, said that NATM is a design philosophy, not a construction method, a sentiment reiterated by the ICE design and practice guide (1996). The Austrian national committee itself describes the NATM as a 'concept', "which makes the ground surrounding the cavity a load-bearing component of the construction by activation of a ground arch" (Rokahr, 1995). Since confusion would result from the use of the term NATM to describe a tunnelling method, the use of the term NATM will be restricted to references to NATM philosophy in this thesis.

Perhaps a more crucial question is whether the NATM philosophy, which was developed to deal with highly stressed rocks in alpine tunnels, can be applied to

soft ground. Many engineers refer to the 'successful application of the NATM' in soft ground situations, but since it is almost always unclear exactly what they mean by 'the NATM', these statements are meaningless. A better question may be whether 'mobilisation' and 'preservation' are principles that make sense in soft ground. To answer this, we need to know at what level of deformation 'loosening' occurs, i.e. at what level of deformation is the ground arch mobilised to take as great a share of the load as it can, before loosening occurs and the pressure acting on the tunnel begins to increase.

In his state-of-the-art report on "Deep excavations and tunnelling in soft ground" to the 7th ICSMFE, Peck wrote the following (Peck, 1969b):

> Long experience has demonstrated that, except possibly in certain swelling clays, no tunneling method has yet been developed in which the strains and deformations are so small that the strength of the soil is not largely mobilized. Therefore, it is quite properly considered good practice to keep the deformations as small as possible, in order to hold the avoidable loss of ground and consequent settlement to a minimum and to prevent deterioration of the soil due to excessive local distortions or remolding.

So the level of deformation required to mobilise the ground arch in soft ground was so small that it had never been found. Therefore, the concept of allowing a prescribed amount of deformation to occur is not applicable to soft ground open face tunnelling. In fact, Peck says that allowing deformation will only result in loosening and deterioration of the soil mass, and recommends keeping deformations as small as possible. To use the parlance of the NATM philosophy, this means that mobilisation will occur regardless, so preservation of the ability of the soil to support itself takes precedence in soft ground; soft ground tunnels enter the 'loosening' part of the ground-reaction curve almost immediately.

The principle that allowing deformation to occur in soft ground will result in higher loads on the lining is controversial, since it runs counter to the results of simple models. However, as will be explained in the literature review (Chapter 2) where previous stress measurements made in shallow soft ground tunnels are presented, the balance of evidence appears to be in favour of this principle. The detailed stress measurements made over 8 years at Heathrow Terminal 4 Concourse tunnel and over 9 months at the Heathrow Terminal 5 Stormwater Outfall tunnel presented in Chapter 4 provide further evidence and also show the mechanism by which this may occur in cohesive soft ground.

Design methods for sprayed concrete tunnels are based on assumptions and simplifications that make the design at best semi-empirical (HSE, 1996). Even if the material behaviour of the ground and the sprayed concrete are well known and a 3D analysis is performed, there are still uncertainties about the true ground mass behaviour and the variability of sprayed concrete to consider. This partially explains the reliance of the successful tunneller on observation (Muir Wood, 2003) but is equally because a geotechnical design cannot completely cover "every unfavourable situation that might be disclosed by the observations" (Peck, 1969a). Muir Wood (2003) puts great emphasis on "overall holistic surveillance": that a tunnel project should be approached as a system with a continuous risk management process through all phases of design and construction.

This risk management process was outlined by Powell & Beveridge (1998) and emphasises the interdependency of prediction and verification with observation and modification. Design must be managed through several phases, from conceptual and detailed design, through construction and into operation. During conceptual and detailed design, the emphasis is on prediction. At the same time, hazards are identified, risks are assessed and the management procedures to control risk during construction are formulated. During construction, the emphasis moves to verification of the design predictions and modification of the design based on observation (the observational method). Central to the direction of this process are the management procedures, which ensure that risks are controlled and new hazards identified. These management procedures will include quality assurance and regular design review meetings.

This holistic approach to SCL tunnel design, based on risk management, prediction and verification, observation and modification is fundamental to good tunnelling practice and is central to the NATM philosophy (Brown, 1981). The importance of prediction, observation and modification within a risk management framework is widely recognised, but the importance of verification may be lost if there is a general expectation in some quarters that designs should be accurate predictions.

There is an inconsistency between the way a tunnel is designed for ultimate limit state stresses and the way its safety is usually monitored during construction by

measuring displacements of the tunnel lining. Since design methods generally predict stresses more accurately than displacements, and the failure criterion defined by existing codes of practice is expressed in terms of stress, it would seem more appropriate to measure stresses in a tunnel lining to verify its performance (van der Berg *et al.*, 1998b). However, the simplest and most reliable measurements that can be made in a tunnel are measurements of lining displacements (Clayton *et al.*, 2000).

The interpretation of deformations has become an art in itself (Rokahr *et al.*, 2002), and fault zones ahead of the face can be predicted as well as the performance of the ground-lining system. Accumulated experience of typical deformation trends in different rock or soil types can be used to assess whether the system is achieving equilibrium (Müller-Salzburg, 1977). This empirical approach was seen as superior to static calculations with their associated assumptions of geological behaviour. It must be remembered that in the past the majority of NATM tunnels were constructed in mountainous terrain where investigation prior to tunnelling was difficult and expensive and the variability of ground conditions was high. Problems may be encountered with this almost entirely observational and empirical approach in soft ground, such as the stability of a temporary crown invert, or indeed any invert covered with backfill, which may be unknown due to the difficulties installing and reading monitoring points (Stärk *et al.*, 2002). The factor of safety of the structural lining is difficult to assess with any degree of confidence. Also, in soft ground, the time available to respond to observations is very limited, so it is considered good practice to fully design the excavation method and support measures in advance (ICE, 1996).

With the increased use of numerical models in design, good agreement between predicted and measured deformations is often taken to mean that the stress in the sprayed concrete lining has also been well predicted. Differences between calculated lining stresses and measured lining stresses are frequently attributed to unrepresentative or erroneous field measurements rather than inadequacy of the model (Negro & de Queiroz, 2000). Due to the complex behaviour of sprayed concrete, especially at early age, it is not clear that this is a reliable assumption.

Since the review of monitoring data represents the"umbilical cord that connects the growing construction with its design" (Clayton *et al.*, 2003), it would be

desirable to measure lining stresses directly if design assumptions are to be verified and design criteria refined for future tunnelling projects (Mair, 1998). The current dearth of stress measurements in sprayed concrete linings impacts negatively on design by introducing uncertainty. In order to estimate the factor of safety of a sprayed concrete lining it is necessary to determine stress, and in order to verify that the design predictions are reasonable it is necessary to determine stress.

The thesis has two main lines of attack. The first is the *measurement* of stress in sprayed concrete tunnel linings. The literature review in Chapter 2 describes the methods of stress measurement available, and comments on their fitness for purpose. Field measurements of stress using pressure cells and back-calculation methods are then described in Chapter 4.

The second line of attack is the *prediction* of stress in sprayed concrete lined (SCL) tunnel junctions. The literature review in Chapter 2 explains why junctions are of particular importance, and describes the various methods that have been employed in the past to estimate stress concentrations at junctions. Despite their apparent importance, the prediction of stresses in SCL tunnel junctions has been a much neglected subject. Therefore, Chapter 5 describes a suite of numerical experiments undertaken to investigate the effect of various parameters on the prediction of stresses at a junction, including ground parameters, sprayed concrete parameters, lining thickness and construction sequence.

Chapter 3 describes the tunnels that have been studied in Chapters 4 and 5. The thesis is ended by a set of conclusions and recommendations for future research in Chapter 6.

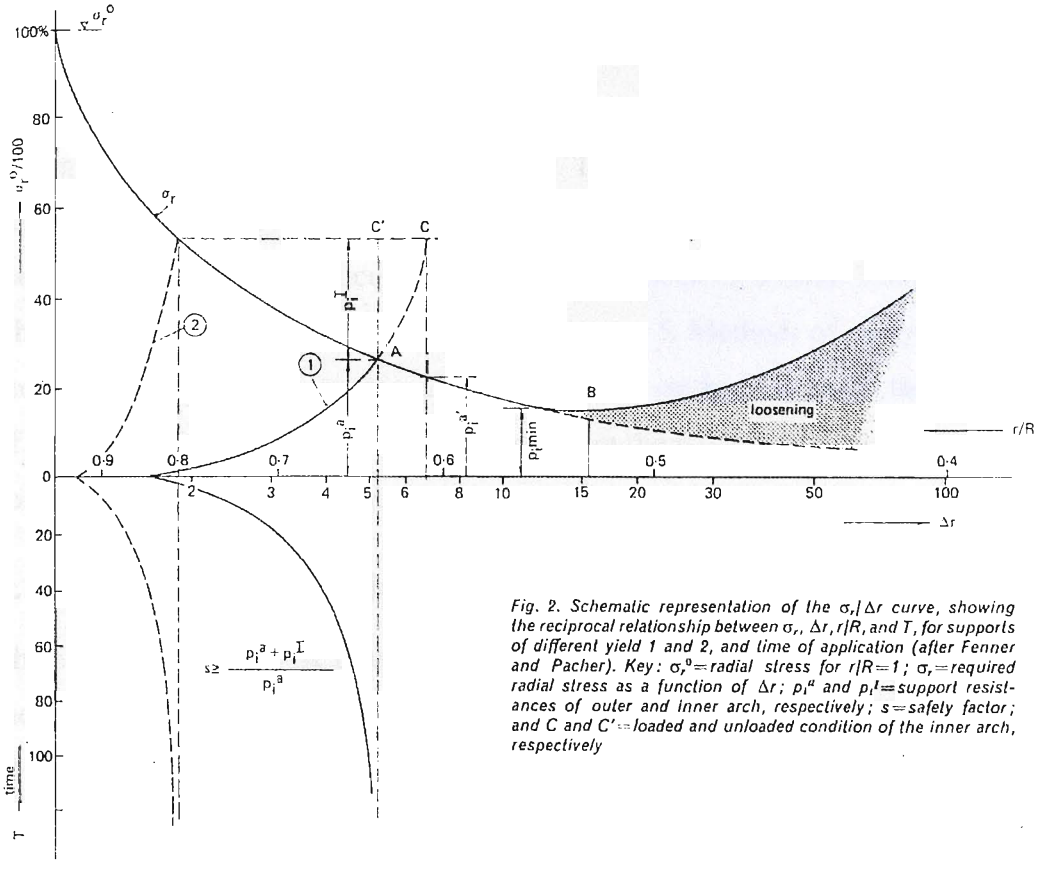

Fig. 2. Schematic representation of the $\sigma_r/\Delta r$ curve, showing the reciprocal relationship between σ_r, Δr, r/R, and T, for supports of different yield 1 and 2, and time of application (after Fenner and Pacher). Key: σ_r^0 = radial stress for $r/R = 1$; σ_r = required radial stress as a function of Δr; p_i^a and p_i^I = support resistances of outer and inner arch, respectively; s = safety factor; and C and C' = loaded and unloaded condition of the inner arch, respectively

Figure 1-1: The ground-reaction curve (from Rabcewicz & Golser, 1973)

2 LITERATURE REVIEW

The literature review will describe sprayed concrete tunnel junctions in terms of their geometry and methods of construction. The way in which the material behaviour of the sprayed concrete may be modelled is then described, both for the purposes of the back-calculation methods described in Section 2.5.3 and Chapter 4, and the numerical modelling in Chapter 5. Methods of analysis of tunnel junctions are then explored. Finally, several methods to verify the results of these analyses in the field, namely to measure the stresses in the sprayed concrete lining, are assessed for their practicality and accuracy.

2.1 Geometry of junctions

The economic case for SCL means it is frequently the preferred tunnelling method for short lengths of tunnel and for complex geometries and arrangements of tunnels.

SCL junctions can come in many shapes and sizes, depending on their purpose. Some basic types are:

- Shaft and tunnel.
- Crosspassage between two running tunnels.
- Chamber excavated downwards from a tunnel, e.g. for a sump.
- An adit[1] from a tunnel, e.g. for mechanical/electrical equipment rooms or a refuge.
- Tunnels linking running tunnels with shafts, e.g. for ventilation, access, emergency escape, water/sewage flows etc.

Usually there is a 'parent' or main tunnel, which is built first and generally has a larger diameter than the 'child' or subsidiary tunnel. The opening for the child tunnel is therefore broken out in the parent tunnel lining.

This research has focused on junctions where both the parent and child tunnel are sprayed concrete tunnels. Junctions involving at least one tunnel that is not

[1] An 'adit' is here defined according to convention as a dead-end tunnel. A 'tunnel' is open at both ends and is therefore technically an adit until it is finished. However, in this thesis an adit that will eventually be a tunnel is described as a tunnel to avoid confusion.

sprayed concrete lined, or other structures such as cut and cover structures, have not been considered. Other underground SCL structures of complex geometry such as caverns, enlargements, small radius bends, crossover tunnels, bifurcation tunnels and niches have not been considered either.

Many junctions are arranged such that the parent and child tunnel axes are perpendicular to each other and often the parent tunnel diameter is at least 1.5 times larger than the child tunnel. If the parent and child tunnel were of a similar diameter, then the size of the 'bite' taken out of the parent tunnel's cross-section could change the behaviour of the junction significantly. The typical shaft-tunnel junction chosen for the numerical experiments in this thesis was also perpendicular, and the shaft diameter was more than twice the tunnel diameter.

2.2 Construction methods

Junctions in sprayed concrete may be constructed in a variety of ways. Often, the flexibility of geometry afforded by sprayed concrete gives the opportunity during construction of the parent tunnel to make the future excavation of the child tunnel easier. This can be done by thickening or reinforcing the area around the future breakout in preparation for the additional loads.

A variant of this concept is to create a stub during construction of the parent tunnel, perhaps 1 m long and usually thicker and more heavily reinforced than the rest of the child tunnel will be. The advantage of the stub is continuity of reinforcement between the parent tunnel and the child tunnel, and it takes some of the existing hoop forces from the parent tunnel.

For the T5 SWOT frontshunt tunnel, only a top heading stub was created during excavation of the shaft. The shaft wall was locally thickened in an annulus around the eye, and reinforced with 3 layers of radial and circumferential reinforcement.

2.3 Sprayed concrete properties

In this section, the properties of sprayed concrete and its constituents will be described. Special emphasis will be placed on how sprayed concrete differs to normal concrete. Sprayed concrete has evolved to meet particular requirements driven by structural performance and the placement method.

2.3.1 Composition and placement

The differences between sprayed concrete and normal concrete are a response to the different performance requirements and the different method of placement. The performance requirements for sprayed concrete usually include the following:

1. Strength. Usually specified at 28 days.
2. Early age strength gain. Usually specified by the Austrian Guideline J2 curve (ÖBV, 1999) or similar.
3. Ductility in failure. Usually specified by ASTM energy absorption test method (ASTM, 1997) or EFNARC (1996) panel test method or similar.
4. Pumpability. The sprayed concrete should flow easily enough and not block the lines or the reducer.
5. Adhesion. The sprayed concrete must stay on the wall without falling off in lumps and rebound[2] should be minimised.
6. Homogeneity. The shotcrete should not segregate easily in the line, especially when it is pumped down a shaft.
7. Durability.
8. Fire resistance.
9. Permeability.

Thomas *et al.* (2001) compared a typical high-quality wet mix sprayed concrete to a typical cast *in situ* concrete. In general, the sprayed concrete has more sand, higher cement content, smaller sized aggregates and more additives.

Wet-mix sprayed concrete is usually mixed in a batching plant. A typical wet mix sprayed concrete could have the constituents per cubic metre (see for example Brooks, 1999 or Melbye & Dimmock, 2001) listed in Table 2-1.

[2] Rebound is the name given to the sprayed concrete that bounces off the wall or falls down. It is mostly made up of aggregate and steel fibres. An average value when using wet mix sprayed concrete is 5-10% (Melbye & Dimmock, 2001). Rebound will be highest when spraying the crown of the tunnel and could be 10-20% (Neville, 1995). It follows then that the sprayed concrete composition once sprayed may be different to the composition in the mixer.

Table 2-1: Typical sprayed concrete mix proportions

Aggregate (usually <6-8mm to aid pumpability)	315 kg/m^3
Sand, or rock dust	1255 kg/m^3
Cement	450 kg/m^3
Microsilica (also known as silica fume)	50 kg/m^3
Water	203 kg/m^3 (0.4 w/c)
Steel fibres	30 kg/m^3
Polypropylene fibres	1.5 kg/m^3
Superplasticiser	5.4 litres/m^3
Retarder[3]	1.1 litres/m^3
Accelerator	25 litres/m^3

Sprayed concrete is placed by spraying with compressed air. The impact drives out the air, such that the air content is similar to that of normal concrete (Kuwajima, 1999). There are two methods of placement, known as the 'wet mix process' and the 'dry mix process'. For the dry mix process, the water is added at the nozzle and is controlled by the nozzleman. This has logistical advantages when only small volumes are required intermittently, but the disadvantages are the lack of complete control of water content in the mix and increased dust (Melbye & Dimmock, 2001). For the wet mix process, dust is reduced and variability of quality is generally improved. In both cases, accelerator is included in the compressed air as a fine mist so that it is only added to the sprayed concrete in the nozzle. Once the accelerator is added, the sprayed concrete sets and hardens rapidly.

Selected parts of a sprayed concrete robot are identified in Figure 2-1. The reducer is approximately 300 mm long and reduces the diameter between the

[3] Retarder or 'hydration control admixture' is used to extend the pot-life of the sprayed concrete from 1-2 hours to 3-72 hours, depending on the dosage. The stabilising effect of the retarder is reversed by the accelerator, which disperses the retarder from the cement grains and immediately activates the hydration process (Melbye & Dimmock, 2001).

sprayed concrete line (approximately 60 mm diameter) and the back of the nozzle (approximately 40 mm diameter) where the compressed air is introduced.

The early-age strength gain is achieved using accelerator, superplasticiser and a high cement content (Melbye & Dimmock, 2001). The accelerator makes the sprayed concrete "go off" very quickly; it sets immediately and within minutes it is hard to the touch and cannot be indented with a thumbnail. The superplasticiser not only disperses the cement particles more evenly, but may also draw the water molecules into the cement, making the hydration process more efficient by reducing water diffusion paths (Melbye & Dimmock, 2001). More importantly, superplasticiser allows a reduction of the water/cement ratio without affecting pumpability; this increases the strength of the sprayed concrete without affecting its flowing properties. The high cement content also increases strength and the early-age strength gain.

The two most commonly-used accelerators today are known as 'alkaline' and 'alkali-free' accelerators respectively. Alkaline accelerators are composed of substances with strongly alkaline properties, such as aluminates, with a pH > 12 and often as high as 14. These have health risks to workers when spraying, such as burning of the skin, harmful effects on the respiratory system, irritation of the eyes and even etching of the cornea (Bürge, 2001). They also have an adverse effect on the properties of the sprayed concrete with a reduction of the final compressive strength, an increase in shrinkage and an increased risk of alkali-aggregate reaction. The strength may be reduced by 15-50 % in the long-term compared to an equivalent non-accelerated sprayed concrete (Bürge, 2001; Melbye & Dimmock, 2001).

Alkali-free accelerators, on the other hand, pose no known health and safety risks to the workers, and will not affect the long-term compressive strength at a normal dosage of < 5 % (Bürge, 2001). Therefore, they are superseding the alkaline accelerators.

Often, the ingredients necessary to achieve the required early age strength gain give the sprayed concrete a much higher 28 day strength than specified (e.g. Morgan=Tunnelling, 2002). Therefore 28 day strength is not normally a critical factor in sprayed concrete composition, and the composition is first of all driven

by the need for early age strength gain and ductility, but also for adequate pumpability and adhesion, good durability and low permeability.

Pumpability is mainly governed by water content and homogeneity. But since water content affects strength, water can be replaced in some part by superplasticiser[4], which acts like a detergent, dispersing the cement particles and making the concrete more fluid. If the sprayed concrete cannot be pumped, valuable time is wasted clearing the lines and ordering a new batch, which often costs much more than the materials wasted. Often a slump flow test according to BS1881, part 105 (1984) is performed before loading the hopper to make sure the sprayed concrete will pump. But for this purpose, sprayed concrete cannot be sampled according to BS1881, part 101 (1983), and the sample taken for the flow test will always be the first part out of the mixer truck. In addition, the quoted repeatability of this test is poor (BS1881 part105, 1984), and the reproducibility between different operators worsens the situation. Experience shows that sprayed concrete may pass the flow test but still not pump or *vice-versa* (Jones, 2003). Sometimes, water is added at the batching plant (within specified limits) until a certain workability is achieved, measured by the torque of the mixing paddles. This is not covered by any standard and the flow properties of the sprayed concrete still need to be checked by the flow test. Being able to vary the water content by adding more water to the mixer is helpful, so there is always a balance to be struck between strength and pumpability. In other words, there is a balance to be struck between the tightness of the specification required to achieve an economical design and the flexibility in the specification required to overcome problems on site (that could end up costing much more in delays and material wastage).

Large particles such as aggregate and steel fibres also affect pumpability (Melbye & Dimmock, 2001). Care must be taken to ensure steel fibres are well dispersed and do not clump together in 'hedgehogs'. This is done by introducing the fibres to the mix in strips lightly glued together. This prevents the formation of hedgehogs and the fibres are easily separated when compressed air is

[4] Superplasticisers are usually a combination of naphthalenes and melamines, and are chemically distinct from plasticisers or water-reducers which are lignosulphates and are not normally used for shotcrete applications (Melbye & Dimmock, 2001). New 'hyperplasticisers' are now available based on modified polycarboxylic ether such as MBT's Glenium™ product.

introduced in the nozzle. Aggregate size is normally limited to < 8-10mm (Melbye & Dimmock, 2001). The grading of the aggregates and inclusion of more fines such as microsilica and cement can prevent segregation. Microsilica has also been shown to improve pumpability and reduce wear on the pumping equipment by acting as a lubricant (Melbye & Dimmock, 2001).

Adhesion of the sprayed concrete to the substrate is due mainly to the presence of accelerator. The almost immediate setting of the sprayed concrete as it mixes with accelerator in the nozzle helps it to adhere. Experience and anecdotal evidence (Melbye & Dimmock, 2001), as well as fibre counts undertaken by Jeng *et al.* (2002) suggest that the presence of fines also makes the sprayed concrete adhere better and reduces rebound, especially the presence of microsilica, which greatly increases adhesion and is now nearly always included. Reducing the cement content, for example, is often a false economy because the cost savings will be outweighed by the increased loss of material due to rebound (Melbye & Dimmock, 2001). The Austrian Guideline (ÖBV, 1999) recommends that strength should achieve 0.1-0.2 MPa within 2 minutes to allow overhead placing.

The consistency of freshly sprayed wet mix sprayed concrete with a new generation alkali-free accelerator is almost spongy. The accelerator has an immediate 'gel effect' and then sets the shotcrete within 4 minutes[5]. Alkaline accelerators, on the other hand, make the sprayed concrete set immediately. Therefore, as alkali-free sprayed concrete is sprayed, it is embedded into the sprayed concrete already on the wall (Brooks, 1999). In this way, layers as thick as 500mm can be sprayed without excess rebound or lumps falling down, thereby reducing costs and improving quality and safety (Grøv, 2001).

When reinforcement such as lattice girders or steel mesh is used, rebound may be trapped in 'shadow zones' behind the bars. This can affect the strength and watertightness of the structure. This can be prevented up to a point by careful spraying and minimising the use of reinforcement. Laser or camera surveying of

[5] Alkaline accelerators (aluminates) are no longer used in the UK for health and safety reasons (they have pH>13 and can burn skin and eyes), and also because of their detrimental effect on long-term strength and alkali-aggregate reaction (Melbye & Dimmock, 2001). Alkali-free accelerators usually contain at least one water-soluble sulphate, usually aluminium sulphate, and other constituents (Bürge, 2001).

excavation and shotcrete thickness can avoid the need for lattice girders to control the shape and thickness of the lining. The use of steel fibres can remove the need for mesh to resist punching shear and light bending moments. However, at tunnel junctions the high bending moments and axial forces calculated in design often mean that several layers of reinforcement are required. If more sophisticated design methods could reduce the amount of reinforcement required, this would improve the quality and watertightness of the structure.

Spraying should always be done with the nozzle approximately 90 ° to the wall. This causes the sprayed concrete to be mildly anisotropic, with 10 to 25 % higher strengths in the plane perpendicular to the direction of spraying (Thomas *et al.*, 2001, reporting Ph.D. research by W. Aldrian at the Montanuniversität Leoben, 1991 and H.G. Huber at the University of Innsbruck, 1991).

The preferential drying direction (radial towards the intrados in the case of a tunnel) can also introduce anisotropy of initial stiffness of over 20 % less after 50 days (Burlion *et al.*, 2003). This means that cores taken from a tunnel lining will show an initial stiffness 20 % lower than in the plane of loading. Burlion *et al.* also found that preferential drying could increase permeability by an order of magnitude in the direction of drying over the first 2 years compared to the other two orthogonal directions. Both these phenomena are due to the formation of microcracks.

2.3.2 Reinforcement

Ductility in failure is mainly achieved by using mesh reinforcement or steel fibres. Without ductility, a failure would be brittle and sudden, therefore in order to have some warning of impending failure it is desirable (Vandewalle, 1998). In general, the higher the strength of concrete, the more brittle the failure, so if the sprayed concrete has a high strength, a larger quantity or higher strength of steel reinforcement is required to achieve ductility. This can substantially increase cost.

Panel tests by Ding & Kusterle (1999) found that steel fibre reinforcement provided better ductility, punching shear capacity and energy absorption at early ages, but the steel mesh gained ground with time and after 48 hours, steel fibres only performed better when there was three times the equivalent area of

reinforcement. However, since the early-age characteristics are often more critical and mesh requires installation time and makes spraying more difficult, the use of steel fibres is becoming much more widespread (Ortigao *et al.*, 1998). Steel fibres do have one problem – they can cause pumpability problems and can block the reducer, but normally only when hand-spraying, where lower pressures are used with a smaller diameter reducer and nozzle (Jones, 2003). The EFNARC specification (1996) recommends that fibre lengths should not exceed 0.7 times the smallest diameter of the pipes or hoses to prevent blockages.

There is evidence to suggest that increasing silica fume content and cement content improves ductility (Jeng *et al.*, 2002). However, these tests were on sprayed specimens, and fibre counts showed that the specimens with greater silica fume content or greater cement content had a lower steel fibre rebound rate. It is well known that the presence of fines decreases rebound (Melbye & Dimmock, 2001). Therefore, the increased ductility was probably due to the higher steel fibre content caused by the higher fines content reducing rebound of fibres, rather than the higher cement or silica fume content in the mix increasing the ductility directly.

Mesh or bar reinforcement in one plane will make the sprayed concrete behave in an anisotropic manner. Steel fibres also will be mostly aligned within the plane perpendicular to the direction of spraying (Ding & Kusterle, 2000). Ding and Kusterle (2000) assumed that in a cast specimen, the orientation of steel fibres would be random, but tests performed by Robins *et al.* (2003) showed that anisotropy of orientation is similar in both cast and sprayed specimens, with cast specimens having fibres mainly orientated in the plane normal to gravity and sprayed specimens having fibres mainly orientated in the plane normal to the direction of spraying.

2.3.3 Durability and permeability

Durability and permeability are the main reasons given in the past for not considering the sprayed concrete lining as part of the permanent works, or not using sprayed concrete for the secondary lining. The unknown long-term effects of the admixtures used or the high utilisation at early age being the most commonly voiced concerns for durability. High utilisation at early age is known

to damage concrete and reduce its long-term strength. Although for shallow soft ground tunnels the long-term strength is not so important because utilisation is usually very low in the long-term, stress concentrations around junctions may be much higher.

The effect of additives on durability of sprayed concrete has always been a problem. Lack of long-term evidence proving the effect of additives and the fast-changing nature of the additive products market make it difficult for designers to be sure of a sprayed concrete's durability. However, the improvements in sprayed concrete integrity and performance since the introduction of alkali-free accelerators have improved confidence in sprayed concrete as a permanent structural element (Grøv, 2001).

Cements containing alkaline accelerators can suffer from increased sulphate attack and ettringite formation, with tightly packed ettringite bundles causing cracking and spalling of the exposed surface (Paglia *et al.*, 2003). Alkali-free accelerators also increase susceptibility to sulphate attack, and suffer as much damage and softening, although with less cracking and spalling (Paglia *et al.*, 2003). Melbye & Dimmock (2001) reported that in independent tests the inclusion of microsilica with an alkali-free accelerator dosage below 5 % can produce a sprayed concrete with as good sulphate resistance as a mix with sulphate-resisting cement. Sulphate resisting cement is not used for sprayed concrete because of its slow strength development. Brooks (1999) also stated that new-generation alkali-free accelerators do not have worse durability characteristics than alkaline accelerators. It is generally considered good practice, regardless of the product used, to minimise the dosage of accelerator as much as possible.

The trend now is towards using sprayed concrete as a final lining instead of a cast-in-place secondary lining, and this is now common practice in countries such as Norway (Franzen *et al.*, 2001; Grøv, 2001). Sprayed concrete was first used as a final lining for the Washington Subway in 1970, in fractured rock with high water infiltration, and the first use of sprayed concrete as a final lining without a waterproof membrane was for the São Paulo metro in 1979 (Palermo & do Lago Helene, 1998). It has since been used in this way in many tunnels including the Heathrow Express (Annett *et* al., 1997) and Heathrow Baggage

Tunnel (Grose & Eddie, 1996) in London Clay. In recent years, the cost savings of spraying the secondary lining, coupled with improvements in permeability characteristics and increased confidence in sprayed concrete durability, have made it increasingly common (Golser & Brandl, 1996; Grøv, 2001).

Golser & Kienberger (1997) used the rate of flow method proposed by England & Illston (1965) to show that designing the secondary lining to take the load was illogical because the primary lining will always take the majority of the load and the secondary lining will only ever be loaded to a low utilisation. This has led to the increased interest in 'single-pass' or 'monocoque' linings, which have been used for the Terminal 5 sprayed concrete tunnels in London Clay and numerous applications in rock, for example the Gotthard Base and Vereina tunnels (Hagedorn & Wei, 2001). This can result in significant cost savings of up to 25 % compared to a double-shell lining (Hagedorn & Wei, 2001).

For permeability, not only the mass of the sprayed concrete, but also the joints need to be watertight. For the mass of the sprayed concrete, this means that cracking needs to be minimised. This can be done using reinforcement. Joints must be cleaned before spraying, and tapered to avoid trapping rebound. Joints in different layers should be staggered to prevent formation of higher permeability pathways. A well-constructed sprayed concrete lining can have good enough permeability characteristics that a waterproof membrane may be considered unnecessary (Grøv, 2001).

Fire resistance can be enhanced by using polypropylene fibres (Khoury, 2000). These fibres turn into a harmless gas at elevated temperatures, leaving voids in the sprayed concrete. Thus, when the adsorbed water evaporates, it can expand into these voids and does not cause the sprayed concrete to spall and split off compromising structural integrity.

2.3.4 Chemical reactions

Many of the properties of sprayed concrete are governed by hydration. Hydration occurs when water is added to a hydraulic binder such as cement, causing a chemical reaction to take place transforming the water and cement into hydrate crystals. As the quantity of hydrated cement increases, so do the strength and

stiffness of the shotcrete. Therefore it is an advantage to make the hydration of sprayed concrete occur rapidly and thus for it to gain strength more quickly.

Hydration occurs when water reacts with the clinkers in the cement. The main clinkers are calcium silicates (C_2S and C_3S) and calcium aluminates (C_3A and C_4AF)[6]. Hardening is due mainly to the hydration of tricalcium silicate (C_3S) and to a lesser degree dicalcium silicate (C_2S), forming calcium silicate hydrate (CSH) (Byfors, 1980). Gypsum (calcium sulphate) is usually added to cement to prevent the uncontrolled reaction of calcium aluminates, which would cause immediate setting. For most concrete applications, immediate setting would not be desirable.

For unaccelerated concrete, the hydration of calcium silicates takes several hours to even begin, during which time there is an initial rapid reaction creating crystalline calcium hydroxide $Ca(OH)_2$ and ettringite (period S_I in Figure 2-2). Ettringite is formed when gypsum (calcium sulphate) reacts with C_3A and C_4AF. Ettringite crystals form a shell around the C_3A and C_4AF particles, preventing their continued reactions. This causes a dormant period (S_{II} in Figure 2-2) where very few reactions take place (Byfors, 1980) until the calcium silicates begin to hydrate (see also Figure 2-3). When all the gypsum has been consumed in the formation of ettringite, the calcium aluminates begin to hydrate. This usually takes a few days to begin and is a slow reaction that contributes little to the strength.

In Austria and Germany, so-called 'shotcrete cements' have been developed that contain little or no gypsum and do not require an accelerator to be added (Melbye & Dimmock, 2001). This can only be done in a dry mix process, and causes an immediate setting as soon as water is added; the calcium aluminates react immediately to form calcium aluminate hydrates (CAH) with a plate-like microstructure (Hellmich *et al.*, 2001a). These provide a first skeleton and immediate strength. Later, the CAH is incorporated into the matrix of CSH (Hellmich *et al.*, 2001a). This is the reason for continued widespread usage of the dry mix process in Austria (Melbye & Dimmock, 2001), as well as continued

[6] C_3A, C_4AF, C_3S and C_2S are shorthand. The letters correspond to: C = CaO, S = SiO_2, A = Al_2O_3 and F = Fe_2O_3. C_3A is tricalcium aluminate and C_4AF is tetracalcium aluminate ferrite. Hellmich *et al.* (2001a) only refer to C_3A when discussing the role of calcium aluminate in hydration.

research in Austria and Germany into methods of dust reduction for the dry mix process (Kusterle & Pfeuffer, 2001) while most other countries now use only the wet mix process (Melbye & Dimmock, 2001).

Alkaline accelerators consist of sodium or potassium aluminates. These cause an immediate C_3A hydration, preventing ettringite formation around the cement grains (Prudêncio Jr., 1998).

The very fast setting of accelerated shotcrete using alkali-free accelerator is due mainly to the rapid formation of ettringite and calcium hydroxide (Bürge, 2001). A by-product of this reaction is aluminium hydroxide, which is also an accelerator. The dormant period characteristic of unaccelerated concrete is almost imperceptible and hydration of C_3S and C_2S begins soon after. Alkali-free accelerators allow overhead placement of layers up to 300mm thick and ultimate strengths are unaffected (Prudêncio Jr., 1998).

Hydration of clinkers is an exothermic reaction, i.e. there is a net production of heat. But the reaction requires heat to be put in before it can occur, known as the activation energy. Thus the heat produced by the first reactions will enable more reactions to take place, which explains the acceleration of heat liberation in Figure 2-2. The ambient temperature will therefore have an effect.

According to the law of Arrhenius (e.g. Laplante & Boulay, 1994; Hellmich *et al.*, 2001a), the higher the temperature is, the faster the reaction rate.

$$\dot{\xi} = A \exp\left(-\frac{E}{RT}\right) \qquad \textbf{Equation 1}$$

where ξ is the degree of hydration or 'reaction extent',

A is the affinity[7], which is the driving force of hydration,

T is the absolute temperature,

E is the activation energy and

R is the ideal gas constant.

[7] Affinity was first defined by Théophile De Donder (1872-1957), and allowed the incorporation of irreversibility into the Second Law of Thermodynamics by providing explicit expressions for the computation of entropy produced by irreversible processes (Kondepudi & Prigogine, 1998).

E/R has been found to be practically constant for calcium silicate clinkers at 4000°K by Laplante & Boulay (1994) and 4200°K by Hellmich *et al.*, 2001a.

Affinity is to chemical reactions as the Newtonian concept of force is to motion. For concrete it represents the thermodynamic imbalance between free water and water combined in the solid phase (Ulm & Coussy, 1995). In a closed system not initially in chemical equilibrium (such as fresh sprayed concrete), chemical reactions drive the system to a state of equilibrium in which the affinities of the reactions vanish (Kondepudi & Prigogine, 1998).

Therefore, the rate of hydration accelerates from a slow start point, then eventually slows as the quantity of unhydrated particles diminishes, reducing the rate of heat production. When the rate of heat production reduces to less than the rate of heat diffusion, the temperature will begin to drop (Figure 2-2). Note how the shape of the cumulative heat liberation curve in Figure 2-2 is similar to the shape of the strength development curve in Figure 2-4.

The degree of hydration is an extremely useful parameter, because the compressive strength development and development of porosity have an approximately linear relationship to it (Byfors, 1980) (Figure 2-5 and Figure 2-6). Degree of hydration can be found using several methods (Byfors, 1980): X-ray can be used to determine the quantity of unhydrated clinker, the quantity of bound water can be found by ignition or the quantity of heat developed can be measured (which is linearly proportional to the quantity of bound water). Hellmich *et al.* (2001a) defined it as:

$$\xi = \frac{m}{m_\infty} \qquad \textbf{Equation 2}$$

where m is the specific mass of water bound in the hydrates and m_∞ is the specific mass of bound water at complete hydration. m_∞ can be calculated from the clinker content per unit volume in the mix and the quantity of bound water per unit of clinker in Table 2-2.

Table 2-2: Bound water per unit of clinker component (after Byfors, 1980)

Clinker component	Bound water per unit of component
C_3S	0.24
C_2S	0.21
C_3A	0.40
C_4AF	0.37

This calculation can be greatly simplified since the C_3A and C_4AF clinkers contribute little to strength and the C_3S and C_2S clinkers bind a similar quantity of water. Hellmich *et al.* (2001a) modelled the calcium aluminate hydration explicitly for the Sieberg tunnel (using 'shotcrete cement' with no gypsum added) and found that the computed stresses were very similar to the model that only included the calcium silicate hydration.

Byfors (1980) proved that for a given concrete mix, the strength development as a function of degree of hydration will be the same regardless of the curing temperature. This function can therefore be used to predict the strength development with time of a given concrete mix for any temperature history. This is important because strength development with time is highly dependent on temperature. On the Heathrow Terminal 5 SWOT (Stormwater Outfall Tunnel) project, for instance, there were problems getting the sprayed concrete to set when the ambient temperature was below 5 °C in winter. This fact is largely ignored by codes of practice and specifications. At low ambient temperatures, the rate of strength gain may be significantly retarded at early age.

That ageing may be defined by a thermodynamic state variable is based on the hypothesis that stress and temperature variations do not affect the thermodynamic imbalance (the affinity). For this to hold true, the latent heat released to the exterior by deformation at constant temperature and constant degree of hydration, and the heat produced by chemical dissipation, must be negligible with respect to the latent heat of hydration (Ulm & Coussy, 1995; Coussy, 1995).

Hellmich *et al.* (2001a) have further exploited this concept by calculating the relationship of affinity to degree of hydration for different clinker components in adiabatic tests. Affinity A is the driving force of chemical reactions and in this case is a function of degree of hydration and temperature defined by:

$$A = -\frac{\partial \psi}{\partial \xi} \qquad \textbf{Equation 3}$$

where ψ is the free Helmholtz energy[8], which is the internal energy produced by irreversible processes, which also cause the increase in entropy of the exterior. Affinity is always positive, therefore free Helmholtz energy begins at a maximum and tends to zero (Kondepudi & Prigogine, 1998). Therefore, free energy can be interpreted as the chemical potential of the reaction, which can be found by adiabatic tests.

The rate of calcium silicate hydration at a macro level is related to the diffusion of free water through layers of hydrates already formed (Ulm & Coussy, 1995) (Figure 2-7). Thus the hydration process may be fully described using thermodynamic principles.

2.4 Methods of analysis of junctions

The economic case for SCL means it is frequently the preferred tunnelling method for short lengths of tunnel and for complex geometries and arrangements of tunnels. However, relatively little research on the subject of modelling of tunnel junctions has been published compared to the amount of research published on the modelling of straight tunnels. Similarly, there are many papers on the prediction of settlements due to the construction of straight SCL tunnels, but relatively few on the prediction of lining stresses. Therefore, there is a mismatch between the research into SCL technology and how it is designed and used in practice. The following section describes the previous work on the behaviour of SCL tunnel junctions and what factors have been found to be important. Finally, the areas that require further research will be identified.

[8] Free Helmholtz energy is equal to the 'Gibbs free energy' at constant volume (Kondepudi & Prigogine, 1998). Affinity is the negative of change in the Gibbs free energy when 1 mole of X and 1 mole of Y react to produce 2 moles of Z.

2.4.1 Rules of thumb

A rule of thumb commonly used in the design of tunnel junctions of any kind is that the stress present in the lining of the parent tunnel is redistributed equally on either side once the opening has been made. The distance over which this redistribution takes place is usually taken to be the designed width of the strengthened 'collar' or annulus around the opening. Implicit in this method is the assumption that the collar will attract the increase in load by virtue of its higher stiffness.

For example, for a junction between a parent tunnel or shaft and a 2.4 m radius tunnel, a 1 m strengthened annulus around the opening would take an additional load equal to 2.4 times the original axial load in the shaft lining. Therefore, the strengthened annulus would be designed for a stress 3.4 times higher than the rest of the parent tunnel lining.

This method would give no indication of the magnitude of the bending stresses caused by the opening, and nor does it take account of sequential excavation, curvature of the linings or soil-structure interaction.

2.4.2 Analysis with simplified geometry

The book 'Roark's formulas for stress and strain' (Young, 1989) gives an estimate of a stress concentration due to a circular hole in a flat infinite plate in Table 37, Case no.6, shown in Figure 2-8. The maximum and minimum stresses are given by:

$$\sigma_A = 3\sigma \qquad \textbf{Equation 4}$$

$$\sigma_B = -\sigma \qquad \textbf{Equation 5}$$

However, it is unknown how far the stress changes extend away from the hole. A similar solution attributed to Kirsch in 1898 was described by Hoek & Brown (1980), and it gives the same results. In addition, it provides the variation of stress concentration with distance away from the circular hole, given by:

$$\sigma_r = \frac{1}{2} p_z \left[(1+k)\left(1-\frac{a^2}{r^2}\right) + (1-k)\left(1-\frac{4a^2}{r^2}+\frac{3a^4}{r^4}\right)\cos 2\theta \right] \qquad \textbf{Equation 6}$$

$$\sigma_\theta = \frac{1}{2} p_z \left[(1+k)\left(1+\frac{a^2}{r^2}\right) - (1-k)\left(1+\frac{3a^4}{r^4}\right)\cos 2\theta \right] \qquad \textbf{Equation 7}$$

$$\tau_{r\theta} = \frac{1}{2} p_z \left[-(1-k)\left(1+\frac{2a^2}{r^2}-\frac{3a^4}{r^4}\right)\sin 2\theta \right] \qquad \textbf{Equation 8}$$

where σ_r, σ_θ, $\tau_{r\theta}$, r, a, θ, p_z and k are defined in Figure 2-9.

The variation of stress with distance away from the edge of the hole calculated using Kirsch's analytical solution is shown in Figure 2-10, for an example of an unwrapped shaft with a circular opening. Using the equations above, $p_z = 1$ is the hoop stress and $k = 0$ such that the vertical stress is zero. Within 1 radius distance of the edge of the opening, the hoop stress above the hole has reduced from a stress concentration of 3 to a stress concentration of 1.2. The reduction in hoop stress at the opening's axis level, however, is slower to return to the boundary stress from its zero value at the edge of the opening, with 47 % at 1 radius, 74 % at 2 radii and 85 % at 3 radii distance. The vertical stress concentration at axis level is -1, and it increases to the boundary value of zero within 1 radius distance from the edge of the opening.

The many assumptions made in this type of analysis, including the absence of soil-structure interaction and sequential excavation mean that it is usually assumed that they will provide an upper-bound solution. Again, estimates of bending stresses would not be possible using this method, which may actually make it unconservative overall.

2.4.3 2D numerical analysis

A 2D plane stress numerical analysis of an unwrapped (laid flat) lining with an opening may be performed (Biliris & Purwodihardjo, 2005). Soil-structure interaction, sequential excavation and bending moments in the lining are ignored. In terms of the assumptions made, this method is basically the same as the Kirsch solution, but details such as bolts and supporting beams, as well as more complex opening shapes may be modelled.

Biliris & Puwodihardjo (2005) used this analysis method to study rectangular openings in cast iron linings on the London Underground. The geometry of the model is shown in Figure 2-11[9]. Despite acknowledging the limitations of their method, they did not validate it with a 3D model or field measurements of stress. The hoop stress applied to the plate was obtained by the use of a 2D plane strain closed-form solution for a circular tunnel[10], which the authors said took account of the soil-structure interaction. However, the closed-form solution would not take account of the method of construction of the tunnel, which would have an effect on the hoop stress (e.g. Thomas, 2003). Nor would it take account of the 3D nature of the junction itself, and the soil-structure interaction during junction construction.

The increase in stress adjacent to the rectangular openings studied by Biliris & Puwodihardjo (2005) varied depending on the width of the opening. The tunnel was 6.46 m internal diameter, and the deviatoric stress (σ_1-σ_3) adjacent to the opening varied between 1.9 and 3.0 times the hoop stress applied at the boundaries as the opening width varied between 0.915 m (3') and 2.745 m (9'). It is not possible to compare these stress concentrations to the Kirsch solution, since the value of σ_3 was not given. The maximum stress was at the edge of the opening and decreased to the initial value a distance of approximately 1.5 times the opening width away from the edge.

Takino *et al.* (1985) proposed a simplified method of calculating ground movements at a junction using a 2D model[11] of a cross-section through the parent tunnel at the position of the child tunnel axis (Figure 2-12). By comparison with field measurements they showed that by varying the stiffness of the springs representing the ground, good predictions of ground movements at the crown of the parent tunnel could be obtained. But this is a purely inductive design and therefore of very limited application. In any case, as will be shown, the stresses in the lining are dependent on 3D effects (Geisler *et al.*, 1985, Hafez, 1995), and for design, it is the stress concentrations that are important. In addition, Fricker &

[9] It is not known whether the vertical side boundaries in Figure 2-11 were fixed in just the horizontal direction or both the horizontal and vertical directions as they were marked only as "fixed deformation".

[10] The closed-form solution used was not defined but several were cited including Morgan (1961), Muir Wood (1975), Curtis (1974) and Duddeck & Erdmann (1985).

[11] It is likely that this was a 2D plane strain model, but this was not specified by the authors.

Alder (2001) report that they have found bedded beam models of this type to be unreliable, possibly because of the inability of the springs, in the words of Tomlinson (1995, p.199) "to replicate the interaction, due to stress transfer within the soil mass, of settlements at separate points on the soil surface".

2.4.4 3D numerical analysis

Hafez (1995) created a 3D finite element model of a skewed tunnel junction of the Heathrow Baggage tunnel. The Heathrow Baggage tunnel was a shallow soft ground SCL tunnel in London Clay within Heathrow Airport. The SCL junction was modelled wished-in-place without any surrounding ground, and a pressure was applied to the lining. It was found that the highest stress concentrations were at axis level at the corners of the lining at the intersection of the parent and child tunnel. Two sprayed concrete models were used, an elastic and an elastoplastic model. There was very little discussion of the results, but the elastoplastic model appeared to result in lower loads in the lining[12], with the exception of the hoop bending moments, as shown in Table 2-3.

[12] This was contrary to what was reported by Thomas (2003), who wrote that the elastoplastic model resulted in higher loads – this may have been because of a misleading statement by Hafez in the discussion regarding higher "straining actions" for the elastoplastic case that Thomas took to mean stresses.

Table 2-3: Maximum and minimum forces around a skewed tunnel junction, from contour plots by Hafez (1995)

	Elastic model	Elastoplastic model
Nx max (tensile longitudinal force)	1600 kN	500 kN
Nx min (compressive longitudinal force)	-5000 kN	-4000 kN
Ny max (tensile hoop force)	500 kN	300 kN
Ny min (compressive hoop force)	-11000 kN	-9000 kN
Mx max (longitudinal moment)	500 kNm	400 kNm
Mx min (longitudinal moment)	-200 kNm	-200 kNm
My max (hoop moment)	250 kNm	300 kNm
My min (hoop moment)	-500 kNm	-550 kNm

The maximum (tensile) longitudinal force in the parent tunnel occurred above and below the child tunnel, and the minimum (compressive) longitudinal force occurred at the sides of the child tunnel. The much larger hoop force relative to the longitudinal force in the parent tunnel caused the child tunnel to squat and this created a concentration of compressive longitudinal stress at the sides of the intersection, and a concentration of tensile stress above and below the intersection. The tensile longitudinal force above and below the child tunnel was also caused by the hoop force being diverted around the opening; an effect predicted by the simple model of an infinite plate with a hole (Young, 1989).

The maximum (tensile) hoop force in the parent tunnel occurred above and below the child tunnel and the minimum (compressive) hoop force occurred at the sides of the child tunnel. Again, this was in keeping with the general pattern of behaviour of an infinite plate with a hole (Young, 1989).

The moments found by Hafez (1995) were not negligible. A moment of 550 kNm, assuming a linear elastic lining with a thickness of 0.5 m, would result in a stress due to bending at the extreme fibre of 13.2 MPa. A moment of 200 kNm would result in a stress of 4.8 MPa. Relative to a typical characteristic cube strength for a modern sprayed concrete of 40 MPa, these values are significant,

especially when factors of safety are included. These moments must be taken into account in design and therefore 3D numerical analysis is a necessity.

Lew (1976) and Thareja *et al.* (1985) investigated the effect of the surrounding ground on the stresses at a junction using a 3D finite element model.

Lew (1976) modelled a right-angle cross circular tunnel intersection. The tunnels were of equal diameter and the rock and lining were linear elastic. Lew found that the hoop thrust at the axis level adjacent to the intersection was about 1.5 times greater than in the tunnel far away from the junction for both a reinforced concrete lining and a steel lining. The reinforced concrete lining had the same stiffness as the rock and a radius to thickness ratio of 10, and the steel lining was 6 times stiffer than the rock and had a radius to thickness ratio of 32.

In Lew's (1976) model, the horizontal initial *in situ* stress was 0.5 times the vertical initial *in situ* stress. It was found that the bending moments in the tunnel lining at the junction were smaller than in the far field tunnel. Recommendations were therefore made that preliminary designs of junctions should use the bending moments calculated by closed-form solutions for a straight tunnel as a conservative estimate. Since Hafez (1995) applied a hydrostatic pressure to the lining (i.e. the horizontal and vertical stresses were equal), then the far-field bending moments should be expected to approach zero, in which case the bending moments were higher at the junction. It appears, therefore, that the importance of bending moments in a tunnel junction lining relative to a straight length of tunnel may vary depending on the initial *in situ* stress state. For a situation where the initial *in situ* stress state is hydrostatic, and possibly other states as well, the recommendations of Lew (1976) would be unconservative.

Brown & Hocking (1976) and Hocking (1978) investigated the effect of the *in situ* stress ratio (the ratio of horizontal total stress to vertical total stress) on the stress concentrations at the junction. The ground was modelled using a linear elastic boundary integral method, but the lining was not modelled. Therefore, the situation was as though the stiffness of the lining was equal to the stiffness of the ground. Only tangential stresses at the perimeter of the tunnel excavation were calculated. The highest tangential stress concentrations were found for the uniaxial initial *in situ* stress state (i.e. the stress ratio equal to zero), at tunnel axis

level at the inside corner of the junction. For a unit applied vertical stress, the stresses at the axis level of a cross-junction and a tee-junction, and for comparison a plane strain tunnel are listed in Table 2-4.

Table 2-4: Effect of *in situ* stress ratio on junction stress concentrations (from Hocking, 1978)

Stress ratio σ_h/σ_v	Cross-junction stress	T-junction stress	Plane strain tunnel stress
0.0	6.5	6.1	3.0
0.33	5.7	5.4	2.67
1.0	4.2	4.2	2.0
2.0	1.9	2.3	1.0

From Table 2-4, one can see that the tangential stress concentration at the junction was approximately 2 times the tangential stress for a plane strain tunnel, regardless of the value of stress ratio. This should be compared to Lew (1976), who found that this ratio was approximately 1.5 for a stress ratio of 0.5 when the lining had the same stiffness as the surrounding ground. The difference may have been due to the limitations of the analysis methods used in terms of mesh densities and element complexity, which at the time were severely limited by computer power. For instance, Lew's (1976) nodal coordinates were input using punched cards and it was not stated in the paper what kind of elements was used.

The focus of Thareja *et al.*'s (1985) work was hydroelectric pressure tunnels, and so the authors were primarily interested in the ability of junction structures to withstand internal pressures during service. However, since their models were linear elastic, the direction of the pressure is unimportant. The ground was modelled using a Winkler spring approach, for which the criticisms have already been mentioned. They found that the surrounding rock, even when of a low modulus, made a significant contribution to relieving stress concentrations. Therefore, designing a junction taking even a conservative estimate of rock modulus into account would greatly reduce the need for reinforcement. However,

the lowest value of rock modulus that they used was 1 GPa, which, relative to the stiffness of many soils, was a high value.

Thareja *et al.* (1985) found that the reduction in hoop stress concentration at the junction by modelling the ground was significant, and equal to or higher than the hoop stress reduction in a straight section of tunnel, which can be seen in the percentages deduced from Thareja *et al.*'s graphs in Table 2-5.

Table 2-5: Stress ratios of model including ground and model without ground at the junction and at the boundary (deduced from Thareja *et al.*, 1985)

Rock modulus (GPa)	σ_j/σ_{j0} *	σ_t/σ_{t0} *
0.98	59 %	77 %
4.91	22 %	36 %
14.72	8.5 %	22 %
29.43	4.2 %	10 %

*where σ_j was the hoop stress concentration at the junction for the model with the rock modulus indicated,

σ_{j0} was the stress concentration at the junction in the model without ground,

σ_t was the hoop stress in the parent tunnel at the boundary away from the junction for the model with the rock modulus indicated,

and σ_{t0} was the hoop stress in the parent tunnel at the boundary away from the junction in the model without ground.

If modelling the soil-structure interaction is of benefit to the designer of shallow soft ground tunnels (e.g. Muir Wood, 1975; Powell *et al.*, 1997; Fricker & Alder, 2001; Thomas, 2003), it should prove to be of even more benefit to the designer of shallow soft ground tunnel junctions. The elastic modulus of the concrete lining used by Thareja *et al.* (1985) was 19.62 GPa, and thus the relative stiffness of the ground and lining explains the very low ratios of stress at the higher values of rock elastic modulus in Table 2-5.

Full 3D numerical analysis of tunnel intersections including the ground-structure interaction is not commonplace, and the method described by Thareja *et al.* (1985) using springs to simulate the ground is usual practice according to Beer *et al.* (1997). Also, construction sequences are rarely modelled (Beer *et al.*, 1997).

A case study of a tunnel junction design that included construction sequences was given by Jäger (2002). This was the junction between a 6.6 m diameter SCL crosspassage and a 3.5 m diameter SCL sump in its invert, which was part of the Airside Road Tunnel (ART) at Heathrow Airport. Only one result was given: that the "maximum compressive stress resultant" at the junction was 4000 kN/m. Since the axis of the crosspassage was at approximately 20 m depth, assuming a constant soil density of 20 kN/m^3 makes the hoop force 1320 kN/m if full overburden pressure were applied to a plane strain tunnel. This makes the stress concentration factor equal to at least 3, or possibly up to around 4.5, since sequential excavation would have resulted in a reduced ground pressure acting on the tunnel and hence a lower normalising hoop force. A stress concentration factor of 3 is what would be expected from a simple analysis of an infinite plate with a hole. This result of greater than 3 appears to be an anomaly, since the work of Thareja *et al.* (1985) showed that modelling the ground-structure interaction should reduce stress concentrations, and Hocking (1978) and Lew (1976), who modelled the ground-structure interaction, calculated a stress concentration factor of 2 and 1.5 respectively. It may be that modelling the tunnel lining with relatively low ground stiffness resulted in a higher stress concentration factor. It is also unclear what Jäger (2002) meant by 'compressive stress resultant' and perhaps the effect of the bending moment to increase the maximum stress had already been taken into account.

Another answer to the apparently anomalous result of Jäger (2002) could be that modelling the junction as a wished-in-place structure and modelling the ground using Winkler springs may be wholly inappropriate to the problem that Jäger (2002) and Lew (1976) were attempting to solve. As an aside, the Winkler spring method *was* appropriate to the problem that Thareja *et al.* (1985) were tackling. For the construction of a junction modelled in this way, the Winkler springs cannot but help to reduce the applied loads on the tunnel linings compared to a similar model without the Winkler springs, as shown in Table 2-5. However, when an opening is made in a parent tunnel, the ground will arch around the opening applying additional load to the structure local to the opening. If this redistribution results in a net increase in the load applied to the parent tunnel, then it would be possible for the stress concentration factor to be greater than 3.0.

2.4.5 Summary

The economic case for SCL means it is frequently the preferred tunnelling method for short lengths of tunnel and for complex geometries and arrangements of tunnels that often include junctions.

Before the advent of 3D numerical modelling, the design of tunnel junctions involved gross assumptions about geometry and was really an educated guess. The most common, widely-accepted method of designing SCL tunnel junctions in 3D 10 to 20 years ago was by using shell or solid elements to model the lining and Winkler springs to model the ground (Beer *et al.*, 1997). Some researchers concentrated on the design of secondary linings (Thareja *et al.*, 1985; Geisler *et al.*, 1985), and on this subject the issue of the effect of construction sequence could be avoided. However, the improvements in computing power in the last few years have made explicit modelling of the ground and the modelling of construction sequences feasible (Fricker & Alder, 2001; Jäger, 2002).

Stress concentrations due to a junction have been found to be highest at axis level at the junction corner. Relative to the plane strain situation of a similar, but straight, length of tunnel, the stress concentration has been found to be 1.5 (Lew, 1976) and 2.0 (Hocking, 1978) for parent and child tunnels of equal diameter in various initial *in situ* stress conditions.

Modelling the ground-structure interaction has been found to have an even more favourable effect on the tangential stresses around a junction than it would for a single plane strain tunnel (Thareja *et al.*, 1985). However, this result may have been a product of the simplified analysis method used rather than a true reflection of reality. Jäger (2002) found axial stress concentrations at a junction that were higher than the plane stress Kirsch solution predicted (> 3.0), which implies that the ground-structure interaction was not favourable to the stress concentrations.

Bending moments in the tunnel lining may only be calculated explicitly using a 3D finite element (Hafez, 1995) or a coupled 3D finite element and boundary element method (Beer *et al.*, 1997). The pure boundary element method used by Hocking (1978) did not model the lining, and so could only be used for the case

of a tunnel lining with the same stiffness as the ground and it only calculated tangential stress at the internal boundary of the tunnel.

The bending moments calculated around a shallow soft ground tunnel junction by Hafez (1995) would make a significant contribution to maximum and minimum stresses and are therefore of significance to a designer. Therefore the use of a discretised 3D analysis method such as the finite element or finite difference method is necessary to predict the stresses in a tunnel junction.

Finally, the relatively small number of papers written on the subject of tunnel junctions in recent years, and their quality, must be commented on. It may be that junctions do not provide a neat case study, since field data are seldom available in any quantity (relative to field data for straight tunnels), the results are difficult to present, or lessons that can be universally applied are difficult to extract. Very little has been written by researchers in recent years. Beer *et al.* (1997) concentrated on the practical and theoretical aspects of implementation of a coupled finite element and boundary element model of caverns at the Large Hadron Collider project at CERN. Hafez (1995) concentrated on the implementation of plasticity models for the sprayed concrete lining in 3D finite element analysis.

Given the large advances in both computer power and analysis methods since Lew (1976), Hocking (1978) and Thareja *et al.* (1985), and the signs from the more advanced work of others since, such as Jäger (2002), that in their simplifying assumptions they missed important aspects such as bending moments, true soil-structure interaction and excavation sequences, the subject is in need of further research.

The idea of using stress concentration factors to present the results more clearly will be applied in Chapter 5. If Hafez (1995) or Jäger (2002) had presented their results in this way using graphs, rather than contour plots, their research would have been more instructive and more easily comparable to what had gone before.

2.5 Stress measurement methods

In this section, the various methods that could be used to measure stress in sprayed concrete tunnel linings are described. Their fitness for purpose is then discussed with the aim of making recommendations.

2.5.1 Slot-cutting

A 'slot-cutting' or 'flat jack' test involves cutting a slot transverse to the direction of the stress to be measured, all the while measuring strain adjacent and perpendicular to the slot. A flat jack is then inserted into the slot and the pressure in the jack is increased until the strain is restored to its original value before the slot was cut. This restoring pressure is related to the original stress state before cutting the slot. This method has numerous advantages, the main one being the minimal amount of interpretation required to arrive at the stress.

The 'large flat jack' test was first proposed for measuring the deformability of a rock mass by Rocha (1966) as an alternative to plate loading or water pressure tests applied to the walls of an adit. Similar methods had been in use at least as far back as 1951 in mines in Belgium and the Lorraine region of France (Li & Cornet, 2004). The principle was to cut up to 3 adjacent slots up to around 1-2m deep using a 600 mm diameter circular saw (Figure 2-13) and to apply an even pressure using flat jacks inserted in the slot while measuring the deformation of the slot and the surrounding rock using strain gauges (Figure 2-14 and Figure 2-15). The slot deformation measurements allowed the calculation of the rock mass stiffness to an accuracy previously unattainable by any other means, while the strain gauges in the surrounding rock allowed the measurement of the 'cancellation pressure' – the pressure at which the rock was returned to its original position before the slot was cut. The cancellation pressure was related to the *in situ* stress in the rock. The method was further developed and calibrated by laboratory tests for a single slot by Vogler *et al.* (1976).

A small flat jack test was developed by Rocha *et al.* (1966) specifically to measure *in situ* stress in rock. A single slot would be cut incrementally to a depth of 105, 170 then 240 mm by a 600 mm diameter circular saw, while deformations in the rock were being measured by strain gauges (Figure 2-16). The slot was therefore in the shape of a circular segment at each stage since the slot depth was always less than the saw radius. A flat jack of the same shape as the slot would be inserted at each stage and the pressure increased until the strains returned to their initial values before the slot was cut (Figure 2-17). The cancellation pressure would then be used to calculate the *in situ* stress. Using a load testing machine to calibrate the small flat jack, Rocha *et al.* (1966) found

that the product of the jack pressure and its surface area was not equal to the force applied but slightly larger (Figure 2-18). They attributed this to the pressure not being entirely transmitted in the vicinity of the welded edge of the flat jack; hence the effective area was slightly smaller than the area of the jack. It could also have been because the areas of rock around the edges of the slot would not have deformed as much as in the centre, being restrained by the uncut rock outside the slot, like a slab supported on 3 sides. They estimated the potential error due to this correction as ± 7, 8 and 9 % for the slot depths of 105, 170 and 240 mm respectively. The small flat jack method has not noticeably changed since Rocha *et al.* (1966) first proposed it and the latest ISRM Suggested Method was written by Kim & Franklin in 1987.

The slot-cutting method has been applied to masonry (e.g. Barla & Rossi, 1983, Hughes & Pritchard, 1997, Binda *et al.*, 2003, Schuller, 2003) and concrete structures (e.g. Kuwajima *et al.*, 1991). An overview of the method is given in BRE Digest 409 (1995). Compared to the small flat jack used for rock stress determination, the main difference is the size of the slot, which is usually limited in depth by the thickness of the structure. For this reason, it is sometimes referred to as the 'mini flat jack' test (Kuwajima *et al.*, 1991). A typical circular segment mini flat jack is shown in Figure 2-19.

Using 2 flat jacks in parallel can make the estimation of deformability parameters more reliable by effectively performing a large-scale uniaxial compression test (Figure 2-20), as performed by Barla & Rossi (1983) and Binda *et al.* (2003). Either way, assumptions of plane strain behaviour above and below the single jack or between the 2 jacks were always made to calculate the deformability parameters and this led to significant errors according to 2D and 3D numerical modelling by Li & Cornet (2004). However, this should not be an issue for stress determination.

There are two methods, distinguished by the shape of the slot and the flat jack. The slot can be made by a 300 mm or 350 mm diameter hand-held circular saw, in which case a 'D'-shaped flat jack can be used which fits the slot, as described by Kuwajima *et al.* (1991). Rectangular flat jacks are also common, and if a circular saw is used then a roughly triangular area is left open at the ends. Alternatively it is possible to stitch drill to make a rectangular slot, as done by

Hughes (1997) and Barla & Rossi (1983). In a masonry structure, it is usual to remove the mortar between 2 courses to create the slot (Barla & Rossi, 1983).

Barla & Rossi (1983) used the flat jack method in the 500 mm thick brick masonry lining of the San Pedrino tunnel in Italy. A rectangular slot was created by removing the mortar between the bricks. A 400 mm wide x 200 mm deep flat jack was then inserted and the pressure increased until the strains were reversed. Tangential stresses measured at four measurement cross-sections were 2.2 to 4.0 times full overburden pressure. Since the tunnel appears to be approximately 6 m diameter, this represented a radial rock pressure on the lining equivalent to 37 to 67 % of full overburden pressure. For a shallow tunnel at a depth of 10-25 m, these values are in line with other stress measurements of tunnel linings (e.g. Mair, 1998 or Powell *et al.*, 1997). The Young's modulus was also estimated by placing 2 flat jacks parallel to each other. The authors noted that the cross-section where the highest stress was obtained was also the cross-section with the lowest Young's modulus and they attributed this to poor quality brick lining. They did not mention the fact that the cross-section with the highest stress (67 % of full overburden) was at a depth of 10 m, while the other three cross-sections (37-43 % of full overburden) were at a depth of 20-25 m. It could be argued that the shallower depth resulted in a reduced arching action in the ground as described by Pöttler (1993), or a reduced ground stiffness, and hence a higher ground pressure on the lining.

Kuwajima *et al.* (1991) developed the mini flat jack test method for use in sprayed concrete linings during the construction of the São Paulo metro. They used a 14 " (356 mm) diameter circular saw to cut the slot and then inserted a flat jack in the shape of a circular segment ('D'-shaped). The size of the slot was limited by the undulating nature of the surface of the sprayed concrete between the lattice girders, shown illustratively in Figure 2-19. The slot was typically 100 mm deep with a radius of 178 mm and a chord length (width of the slot at the surface) of 310 mm. Two vibrating wire strain gauges with a gauge length of 165 mm were attached to the surface of the sprayed concrete 45 mm above the slot. The sprayed concrete lining was approximately 250 mm thick, so the depth of the slot was approximately 40 % of the lining thickness.

A rectangular mini flat jack slot-cutting method was used to measure stresses at 5 points on a cross-section of the Heathrow Express Terminal 4 station concourse tunnel approximately 1 month after construction (Hughes, 1997). Since this report was unpublished, and the data is pertinent to one of the tunnels studied in this thesis, the procedure is described below:

1. Bolt a rigid measuring frame and a slot router cutting frame to the tunnel lining.
2. Drill 30 mm deep holes for the measuring studs and fix with epoxy resin.
3. Attach a row of LVDT gauges on armatures between the measuring frame and the measuring studs.
4. Cut a rectangular slot by stitch-drilling approximately 230 mm wide and 110 mm deep 30 mm below the studs in increments of depth.
5. At each increment, take readings of the strain, but do not cut the reinforcement bars (these require a different cutting tool).
6. Once the full-depth slot is made, cut the reinforcement bars and take more readings.
7. Insert rectangular flat jack of size 228 x 117 mm.
8. Increase pressure in the jack in 0.1 MPa increments until the strain is back to zero, taking strain readings all the while.

The set up was the same as described for a masonry arch in Hughes & Pritchard (1997), shown in Figure 2-21. The results showed tensile or near-zero stresses at all the points on the cross-section. During cutting, the studs actually moved away from the slot, indicating that the lining had been in tension. Drying shrinkage of the intrados of the lining put the concrete in tension and the reinforcement into compression, so that when the slot was cut, the reinforcement pushed it open. When the reinforcement was cut, the slot would close again, although not enough to return to zero stress in most cases. Kim & Franklin (1987) stated that if the slot opens on cutting, the rock stress component at the test location is tensile and cannot be measured. Nevertheless an attempt was made by Hughes (1997) to measure the stiffness of the sprayed concrete by continuing to increase the pressure in the jack and hence extrapolate the *in situ* tensile stress. From the

stresses imposed and the strains measured, a value of stiffness could be calculated, and this was 2 GPa +/- 1 GPa. This was an order of magnitude lower than expected, but could be explained by the close proximity of the measuring studs to the surface, which in a sprayed concrete tunnel is often uneven, has a low density and a high porosity. It is also likely that the sprayed concrete above and below the slot was still in tension, restrained by shear forces around the reinforcement which was still in compression. Therefore there may still have been microcracks present that would be closed by expanding the slot. Negro *et al.* (1998) also found tensile stresses at the shoulder and crown level of the Brasilia South Wing tunnels using Kuwajima *et al.*'s (1991) mini flat jack method, but in this case it was explained by squatting of the tunnel, since the tests at axis level showed compressive stresses at the intrados.

The main drawback of the mini flat jack method at the concourse tunnel was the limited depth of the slot. The design thickness of the lining was 350 mm, and only the stress in the inner 117 mm could be measured. This part of the lining was placed last and in addition was also the most susceptible to drying shrinkage, so it was possible that the majority of the load was being carried by the rest of the section. The quality of the sprayed concrete at the surface or in the top 30 mm could also have been an issue since this was where the strains were measured. This problem was not reported by Kuwajima *et al.* (1991), whose measurements were also made approximately 30 days after installation of the lining; the same time delay as at the T4 concourse tunnel. Their average stress measurement was about 3 MPa, corresponding to approximately 25 % of the overburden pressure.

Kuwajima *et al.* (1991) calibrated the flat jack method in the laboratory by applying a known stress to a concrete slab. They found that the restoring pressure applied by the jack was 23 to 38 % higher than the applied stress and was on average 29 % higher. This was more than the pressure difference found by Rocha *et al.* (1966) for the small flat jack, but this is to be expected for the mini flat jack's smaller surface area. Usually there is a correction to be made to account for the difference between the jack-concrete contact area and the actual slot surface area. In the tunnel, Kuwajima *et al.* (1991) fixed graphite paper to the jack surface, such that the impression made on the graphite paper was taken to be

the actual contact area. There is also a correction to be made for the edge effect, as also found by Rocha *et al.* (1966) in rock and by Hughes & Pritchard (1997) for masonry arch structures, and so for the example results given the overall correction factor was taken as 0.75. Kuwajima *et al.* (1991) implied there were other reasons why the jack over-read stress, other than the difference between slot area and contact area, but did not elaborate. Hughes (1997) used only the ratio of the surface area of the jack to the area of the slot to correct the T4 data, and this correction factor was usually greater than 0.9.

A problem with the mini flat jack tests so far implemented in sprayed concrete linings are their inability to measure stresses deeper than about 120 mm from the surface. In order to measure stresses to a depth of up to 240 mm would require a larger diameter saw of 600 mm, of the kind commonly used in the small flat jack test for rock stress determination (Rocha *et al.*, 1966). For a relatively even surface of sprayed concrete, as built at the T4 concourse tunnel, this would have yielded more useful results.

Despite its failings, it could be argued that slot-cutting has been used successfully in sprayed concrete lined soft ground tunnels, as well as in rock and in brick masonry tunnels and arches. Although Hughes (1997) found that the slots made in the T4 concourse tunnel were not deep enough to draw conclusions about the stresses deeper in the section, the finding that very little stress existed close to the intrados of a sprayed concrete lining was an important result, though not the one they were looking for.

Kuwajima *et al.* (1991) identified a further drawback to the slot-cutting method, which was that it could only be used in fully hardened sprayed concrete with a linear response. The linear response became a necessary condition because the cancellation pressure required was approximately 3 times higher than the capacity of the flat jack they used so the cancellation pressure had to be extrapolated. A nonlinear response should usually be acceptable as long as it is reversible.

Since the slot-cutting method can only be used on mature sprayed concrete, no information is available about the more critical early-age stresses. Kuwajima *et al.* (1991) tried to reinterpret readings from pressure cells using the slot-cutting

results as the final stress, but since the pressure cell readings were an order of magnitude lower than the slot-cutting results, there must have been an error in the interpretation of the pressure cell data. Rokahr & Zachow (1999) claimed to have matched stresses from back-calculation of displacement monitoring to stresses measured using slot-cutting with good agreement. In fact, the correlation was far from 'good' with the average difference between the stresses provided by the two methods at over 80 % of the slot-cutting stress. The calibration method for the flat jack test was not given so no assessment of its accuracy could be made in this case.

In conclusion, the slot-cutting method requires careful calibration and execution, but has the potential to give reasonably accurate estimates of stress in a sprayed concrete tunnel lining, to within ± 10 %. A potential problem is that the depth of the measurement is limited by the choice of saw or drill and the size of the flat jack, and this has had a negative impact on results, in particular those of Hughes (1997). The other main disadvantage is that the slot-cutting method may only be used in mature concrete and cannot be used to measure the development of stress during the early-age of a sprayed concrete lining. Slot-cutting could be used as a check on pressure cells or a back-calculation method to improve confidence in their use, but this was not successful when attempted by Kuwajima *et al.* (1991) or Rokahr & Zachow (1999), perhaps because the results from the other methods were not reliable.

2.5.2 Over- and under-coring

Overcoring of a tunnel lining, like slot-cutting, is a stress-relief method of *in situ* stress determination adapted from an original application in rock mechanics. A strain gauge rosette is attached to the material to be tested, and a cylindrical core is drilled over the rosette, relieving the stress. The strains measured can then be used to estimate the stress before coring began. In rock mechanics overcoring is primarily a method of estimating the stress tensor at the base of a borehole (Sjöberg *et al.*, 2003) and is seldom used on a rock face exposed in an adit, because the borehole methods allow measurement in rock less disturbed by excavation, and because more accurate methods may be available for a rock face such as the small flat jack (de Mello Franco *et al.*, 2002). This is because many rock types are heterogeneous, with joints, bedding and other discontinuities, and

therefore the magnitude of the surface area tested will have an important effect on the variability of results and hence the number of tests required (Hudson *et al.*, 2003). Therefore, if overcoring were to be used to measure rock stress, it would be used in a borehole.

In the case of a concrete or sprayed concrete tunnel lining, which is relatively homogeneous and has a finite thickness, overcoring becomes a more attractive method due to its low cost and the fact that cores are in any case required for quality control of concrete strength. When the core is tested, the deformation modulus is estimated to derive the *in situ* stress.

Barla & Rossi (1983) described the overcoring method for tunnel linings. The procedure is shown in Figure 2-22. A metal pad with conical indents to form a 45° rosette is fixed to the lining surface. The stress is then relieved by coring over the rosette, such that no stress is considered to be present in the concrete core. The four strains across the rosette can then be measured by a mechanical strain gauge. This could also be done using types of electrical strain gauge, as long as they cannot be damaged during overcoring. To calculate stresses from these strains, it is necessary to perform unconfined compression tests in the laboratory to obtain values of Young's modulus and Poisson's ratio. To improve accuracy, the diameter of the core should be as large as is practical. Barla & Rossi (1983) also suggested an alternative method of inserting thin curved jacks symmetrically placed into the gap between the core and the concrete lining to estimate deformability (Figure 2-23). No comments on the accuracy of the overcoring method were made by Barla & Rossi (1983), and no attempts to calibrate the method in the laboratory were described.

Celestino *et al.* (1997) described the use of the undercoring technique. In this case, the strains *around* the core are measured. The authors first used this method for the São Paulo metro in 1990. Unlike the overcoring method, for which a direct relation using Hooke's law may be used, an elastic analytical solution for a hole in a plate was used to find the initial stress in the lining before coring.

Undercoring and overcoring have the same drawbacks as slot-cutting. They can only be used to measure the stress state at or near the surface of mature concrete, and only provide a one-off measurement. In the case of the Valsinni tunnel

(Barla & Rossi, 1983), they were only interested in the stress at the intrados in the crown, so the method was appropriate. However, if changes of stress with time, especially at early age, are required, or the stress away from the intrados is required, then other methods would need to be used.

Unlike the slot-cutting method, a back-calculation is required, although the stresses should be within the elastic range making this a simple calculation even for undercoring. However, the assumption of elasticity in both methods will introduce errors, since concrete is a nonlinear material that also creeps even at low levels of stress (Neville *et al.*, 1983). If the secant modulus in unloading to zero stress from a similar initial value of stress as found in the tunnel is used, this may minimise errors.

Sprayed concrete is not a perfectly homogeneous isotropic material. As mentioned in Section 2.3, sprayed concrete may have 10-25 % higher strengths in the plane perpendicular to spraying and may have anisotropy of initial stiffness 20 % lower in the direction of drying (radial direction). Therefore the stiffness measured by unconfined compression tests in the laboratory may be 20 % lower than the stiffness in the plane of the strain measurements during under- or overcoring. There is also the anisotropy introduced by reinforcement, whether it is steel mesh or steel fibres, which may restrain movement in the plane of the strains being measured.

Another point to consider is that sprayed concrete strength and stiffness will vary throughout the lining. The standard deviation of 28 day sprayed concrete core strengths on the Heathrow Express project at Terminal 4 was 15.3 MPa or 26 % of the mean strength (Annett *et al.*, 1997) and at the Terminal 5 works it was 17.5 MPa or 28 % of the mean strength. Since the stiffness is related to the strength, the stiffness should suffer at best a similar variability. To have a 95 % confidence in the accuracy of the results of a simple elastic back-calculation, the stiffness and hence also the calculated stress must only be considered to be accurate to within ± 55 % of the mean stiffness. The overcoring and undercoring methods have the advantage that the test results from the extracted core could be used, and this may eliminate the variability between batches of sprayed concrete. The standard deviation of the difference in strength between two cores taken from the same advance at Terminal 5 was 4 MPa, or 7.3 % of the mean strength

of the two cores. This would reduce the error in the calculated stress to ± 15 % if a 95 % confidence level were required.

In summary, stresses in a sprayed concrete lining measured using the under- or overcoring method may be underestimated by up to 20 % if the effects of anisotropy are not taken into account. Also, the variability of material properties will typically introduce an error of ± 55 %, or ± 15 % if batch-specific material properties are used.

2.5.3 Back-calculation

The "rate of flow method" was introduced by England & Illston (1965). This allowed the stepwise back-calculation of stress in concrete from a history of measured strain. Strain is broken down into:

1. instantaneous elastic strain
2. delayed elastic strain (recoverable creep ≈ primary creep)
3. flow (irrecoverable creep ≈ secondary creep)

Since for sprayed concrete loaded at an early age, shrinkage strains and also thermal strains during hydration are important; it is a simple matter to add terms to England & Illston's formulation to take account of these effects. This was done by researchers at the Montanuniversität Leoben and Geoconsult in Salzburg, Austria, initially by Schubert (1988) and further developed by Golser *et al.* (1989), Golser & Brandl (1996) and Golser & Kienberger (1997). In addition, Golser (1999) claimed that stresses could be recalculated from strain gauge measurements more accurately than they could be measured with pressure cells, although this was unsubstantiated.

The basic timestep formulation of the rate of flow method will include an elastic and delayed elastic part represented by a generalised Kelvin model with one or sometimes two Kelvin elements, a flow part often represented by a power law, and a shrinkage and thermal strain part as follows (Schubert, 1988):

$$\varepsilon_2 = \varepsilon_1 + \varepsilon_k + \varepsilon_f + \varepsilon_{sh} + \varepsilon_{th} \qquad \textbf{Equation 9}$$

where subscripts 1, 2, … represent timesteps,

ε_f is the flow strain between time 1 and 2,

ε_{sh} and ε_{th} are the shrinkage and thermal strains between time 1 and 2, and

ε_k is the strain in the generalised Kelvin element due to stress at time 2 and the delayed elastic strain between time 1 and time 2.

England & Illston (1965) used 2 Kelvin elements; representing a slow and a fast component. Schubert (1988) simplified their method and used only a single Kelvin element, given by:

$$\varepsilon_k = \sigma_2[1-\exp(-\Delta C_t/Q)] \qquad \textbf{Equation 10}$$

where $-\Delta C_t$ is the age dependent change of the specific yielding strain and

Q is a constant derived from the rate of the recoverable creep deformation as described by England & Illston (1969). In this equation, only the delayed elastic strain part is shown.

Thomas (2003) used a single Kelvin element in his creep model for numerical analysis of an SCL tunnel, which for the uniaxial case could be given by:

$$\varepsilon_k = \frac{\sigma_2}{9K} + \frac{\sigma_2}{3G} + \frac{\sigma_1}{3G_k}[1-\exp(-G_k t/\eta_k)] \qquad \textbf{Equation 11}$$

where K is the bulk modulus,

G is the shear modulus,

G_k is the Kelvin spring stiffness,

$t = t_2 - t_1$, and

η_k is the product of the relaxation time B and G_k, such that when $t = B$, $0.632 = (1 - e^{-t/B})$

The elastic stiffness parameters G and K are age-dependent.

The flow strain ε_f may be given by the 'Andrade one-third power law' as used by Schubert (1988):

$$C_t = At^{1/3} \qquad \textbf{Equation 12}$$

This relationship may be adapted to take the nonlinear increase of flow at stress levels above 50% utilisation into account (Schubert, 1988):

$$C_t = At^{1/3}e^{k\sigma}$$ **Equation 13**

Equally some other relationship such as that given by Acker & Ulm (2001) or by Bažant & Baweja (2000) could be used. The method should be calibrated to a creep test before being used to back-calculate stresses in a tunnel. This flow is sometimes known as the 'steady-state creep', because it continues at a rate dependent only on age and stress level.

As discussed by Acker & Ulm (2001), the irrecoverable creep is due to irreversible viscous slippage between layers of hydrates, which occurs under almost constant volume. The shorter-term (of the order of 10 days) delayed elastic strain mechanism is due to water movement in the pores, which occurs under increasing volume. Creep analysis methods often assume that creep only occurs under deviatoric stress, and hence under constant volume. Therefore, for short-term analysis where the majority of the creep deformation is due to water movements in the pore space, this may be an erroneous assumption.

Schubert (1988) included a term for shrinkage based on the hyperbolic relationship of ACI 209 (1978), which was exactly the same in the more recent revision ACI 209R-92 (1992) and is given by:

$$\varepsilon_{sh} = \frac{\varepsilon_{sh\infty}.t}{B+t}$$ **Equation 14**

where ε_{sh} is the shrinkage strain in microstrain [10^{-6} m/m],

$\varepsilon_{sh\infty}$ is the ultimate shrinkage strain in microstrain [10^{-6} m/m]; Schubert took this as 150 microstrain,

t is the age in days and

B is a constant; in this case Schubert took this as 2.77 days.

Schubert's (1988) formulation also included a term for thermal strain, given by:

$$\varepsilon_t = 30\left[1-\cos\left(0.25t^{0.25}\right)\right]$$ **Equation 15** [13]

where ε_t is the thermal strain in microstrain [10^{-6} m/m] and

t is the age in seconds.

[13] *This equation has been corrected from an assumed misprint in the paper, which was:* $\varepsilon_t = [-\cos(t^{0.25}\cdot 250)+1]\cdot 30$, and the units of t were not given.

The constants B and $\varepsilon_{sh\infty}$ for the shrinkage equation and the time relationship for thermal strains were derived by Schubert (1988) from laboratory tests. He acknowledged that there could be a significant deviation between the behaviour during a laboratory test and in a sprayed concrete tunnel lining due to the different shotcrete volumes and environmental parameters and that it should therefore be determined more accurately by field tests. It would be better, for instance, to estimate the development of the coefficient of thermal expansion with time from a laboratory test (e.g. using the method of Laplante & Boulay, 1994) and then to apply this to measurements of temperature across the section of the sprayed concrete lining to calculate the thermal strain component rather than using the equation proposed by Schubert (1988). Equally, the shrinkage parameter B, which controls the curvature of the hyperbolic shrinkage curve was very low, which results in a curve that approaches the ultimate shrinkage at a much faster rate than is usual. This was probably because of the size of the specimen. Schubert's method yielded good predictions when applied to laboratory slow loading tests beginning at an age of 1 day and 14 days and to a loading and relaxation test begun after 1 day, as shown in Figure 2-24 and Figure 2-25.

Golser *et al.* (1989) stated that thermal strains had proved to be insignificant and so they removed the thermal strain term from the formulation. Although the temperature changes in a sprayed concrete sample in a laboratory test may be small, the larger size of sprayed concrete elements in a tunnel should cause larger temperature changes to occur within the section due to the greater heat produced and retained in the exothermic hydration reaction. Conversely, the larger volume to surface area ratio should cause the shrinkage strain to be smaller in the tunnel due to the decreased influence of drying shrinkage, assuming the environmental conditions to be similar in both cases. A figure produced by Schubert (1988) comparing the effects of temperature and shrinkage in a simulation of sprayed concrete lining strains using the rate of flow method is reproduced in Figure 2-26. Using this figure it was demonstrated that thermal strains were at least as important as shrinkage strains when the relationships based on the laboratory tests were used. If more realistic relationships had been used, it should be expected that the thermal strains would be even more important. It is unclear,

therefore, how Golser *et al.* (1989) came to the conclusion that thermal strains were not important.

Schubert (1988) applied the rate of flow method, although it was calibrated to laboratory shrinkage and thermal strains, to strain gauges embedded in the sprayed concrete lining during construction of the Langen tunnel in the Arlberg pass. An example of a plot of the measured strain and the computed stress is shown in Figure 2-27. Although the absolute magnitudes of the back-calculated stresses were not reliable, the 'creeping out' of the bending moment was evident where a pair of strain gauges had been installed near the intrados and extrados of the sprayed concrete lining (Figure 2-28). This occurred because a higher stress on one side of a structural section will result in a larger creep deformation on that side (since creep is dependent on stress level), causing stress to be redistributed to the other side.

At the University of Hanover, Stärk *et al.* (2002) and Rokahr *et al.* (2002) came to the conclusion that despite the development of an 'art' of interpreting measurement results, monitoring of displacements of a sprayed concrete lining without any measurement or calculation of stress was not sufficient to guarantee safety. This was the rationale for their development of a method of back-calculation of displacement monitoring results obtained by optical surveying techniques, as described by Rokahr & Zachow (1997), Rokahr & Zachow (1999) and Stärk *et al.* (2001). The constitutive model used was from Rokahr & Lux (1987). It should be noted that previously the researchers at Montanuniversität Leoben had used strain gauges, not optical surveying, to measure deformations of the sprayed concrete lining.

The hidden assumption in the logic behind the development of back-calculation methods is that overstressing of a sprayed concrete lining may occur even though the displacement measurements show the tunnel is stable. Failure may be imminent or the sprayed concrete lining may have been damaged. The researchers at the University of Hanover, for example, repeatedly state in the introductions to their papers referred to above that they are interested in determining the factor of safety, since stability of the tunnel would only indicate that the factor of safety is greater than unity. Also, they are interested in determining the factor of safety at early age while the displacement

measurements are continually changing and an assessment of stability is only otherwise possible by empirical methods, or by comparing observed movements to predicted movements. They dismissed this kind of design verification as a method of ensuring safety of the tunnel since the variability of displacement measurements from section to section is usually very high.

This 'stress intensity' method had been used for monitoring 1300 cross-sections in 13 tunnels up to the year 2002 in Germany and Austria including the Egge, Römerberg, Irlahüll, Melk and Wachberg tunnels using a computer program called "STRESS" (Stärk *et al.*, 2002). The aforementioned papers indicated that the information required by the computer program was:

1. the actual as-built profile of the SCL
2. the actual absolute position of the measuring point relative to the tunnel axis and thus the deformation of the SCL at each point in time
3. nonlinear stress-strain behaviour of the sprayed concrete
4. the strength development of the sprayed concrete with time
5. the development of the ultimate strain of the sprayed concrete with time
6. the creep and relaxation behaviour as a function of stress, age and time

At the Egge tunnel (Rokahr & Zachow, 1999) flat jack stress measurements in circular segment slots with a 400 mm chord length and a depth of 120 mm were also made to check the back-calculation method, since stress levels indicated over 90 % utilisation in some areas. A comparison of the 2 methods is shown in Figure 2-29. Rokahr & Zachow (1999) described these results as "a good agreement", but the ratios marked on Figure 2-29 show that, relative to the magnitude of the stress measured, in some cases the stress found by the two methods were widely different, with the largest ratio at 4.33. In terms of absolute values in MPa, the differences in stress between the two methods are also marked on Figure 2-29, with the largest difference at 7.70 MPa and the average difference at 1.60 MPa. If the flat jack stress measurements were assumed to be the real stress, to have 95% confidence in the back-calculation results would require limits of ± 2.8 times the flat jack stress, amounting to no confidence at all. However, to avoid painting an overly critical picture of the method, there was

a definite correlation, which had an r^2 coefficient of 0.72. If the 6 best results of the 10 presented in Figure 2-29 were extracted and the 4 worst results ignored, the predictions would have all been in the range of ± 15 %. Due to the large errors in some of the predictions and the small data set, this method must be considered unproven. Since it is difficult to assess its accuracy by direct comparison, it may be possible to do it by looking at the variability of the parameters input to the method.

The advantages of using optical surveying as the basis of a back-calculation method are that monitoring targets are usually placed for displacement monitoring anyway, and the readings are not affected by temperature, creep or shrinkage in the same way as for embedded pressure cells or strain gauges. However, the disadvantages are the susceptibility of targets to damage, the delay before the first survey of the targets and the frequency that readings may be taken, and the repeatability of the measurements. Rokahr & Zachow (1999) do not provide any of this information, but inspection of a displacement-time graph in Stärk *et al.* (2001) from the Egge tunnel indicates that surveying frequency was once per day.

The delay before the first survey of the targets, though it appears to be a crucial issue, was never mentioned by these University of Hanover researchers in any of the papers referred to. Clayton *et al.* (2006) found at Terminal 4 station that targets were normally surveyed within 8 hours of finishing spraying the lining or within 12.5 hours of excavation. The frequency of surveying at Terminal 4 was approximately twice per day during construction. The delay to first reading and frequency observed at Terminal 5 were the same as at Terminal 4. Once installed, embedded strain gauges or pressure cells may be read remotely with no further disruption to construction activities at whatever frequency is required, and may also be read by a data logger. This was recognised as an advantage of the use of strain gauges for back-calculation rather than optical surveying by Schubert (1988).

Clayton *et al.* (2006) found that the survival rate for the top heading targets was 66 %, for the bench targets it was 50 %, and in the invert only 2 out of 16 targets survived.

Typical repeatability of optical surveying using a total station and prismatic targets is ± 2-3 mm according to Bock (2003) but with best practice methods could potentially be ± 1 mm according to Clayton *et al.* (2000). In a review of optical surveying measurements in the Heathrow Terminal 4 station tunnels, Clayton *et al.* (2006) found that repeatability was of the order of ± 1 mm over a distance of 20 m, but could be as poor as ± 3 mm as the distance from stable reference points increased.

The relationship between convergence c, diameter d and circumferential strain ε_c is given by:

$$\varepsilon_c = c / d \qquad \textbf{Equation 16}$$

So for best practice surveying giving a convergence of ± 2 mm the circumferential strain error would be ± 0.02 % for a 10 m diameter tunnel or ± 0.04 % for a 5 m diameter tunnel. Assuming a mature shotcrete stiffness of 20 GPa, the error would be ± 4 MPa for a 10 m diameter tunnel or ± 8 MPa for a 5 m diameter tunnel. At lower stiffnesses, this error is smaller. However, the strength of the sprayed concrete is also lower. If the stiffness to strength ratio were approximated to a constant value of say 500, then the error would be constant at 10 % of the strength for the 10 m diameter tunnel and 20 % of the strength for the 5 m diameter tunnel. This error would double if the stiffness to strength ratio were doubled to 1000.

For typical surveying repeatability of ± 2-3 mm rather than ± 1 mm, the error would be 2-3 times larger, that is, 20-30 % in a 10 m diameter tunnel or 40-60 % in a 5 m diameter tunnel, with a stiffness to strength ratio of 500. In the 5 m diameter tunnel, the circumferential strain error could therefore be up to 0.12 %. Furthermore, given that BS8110 (BS8110 Part 1, 1997) gives a limit of 0.35 % strain in reinforced concrete, accounting for the error would take up a large proportion of this allowance.

Errors introduced by assumptions made in the constitutive model are more difficult to estimate but are likely to be significant. Considering only the variability of strength, as mentioned in Section 2.5.2, the standard deviation of 28 day sprayed concrete core strengths on the Heathrow Express project at Terminal 4 was 15.3 MPa or 26 % of the mean strength (Annett *et al.*, 1997) and at the

Terminal 5 works it was 17.5 MPa or 28 % of the mean strength. Since the stiffness and creep parameters are related to the strength, they should suffer at best a similar variability. Thus to have a 95 % confidence in the accuracy of the results of a back-calculation, the calculated stress can only be considered to be accurate to within ± 55 %. If the test results from the same batch of sprayed concrete were used the standard deviation would be 4 MPa, or 7.3 % of the mean strength of the batch. This would reduce the error in the calculated stress to ± 15 % if a 95 % confidence level were required.

Clayton *et* al. (2006), on the basis of surveying accuracy alone, concluded that it was unlikely that displacement monitoring could be used to infer the stress state of a completed sprayed concrete shell. By consideration of the surveying accuracy and the variability of sprayed concrete strength, it appears impossible that displacement monitoring could be used to infer stress levels in the sprayed concrete to a degree of accuracy that would render the results useful. In the light of the sources of error described above, the correlation in Figure 2-29 was surprisingly good.

Errors will also be introduced if there is a delay between installation of the sprayed concrete lining and the first survey of the monitoring targets, during the time when most movement is occurring. Strictly speaking, if the soil is an undrained non-creeping continuum, the sprayed concrete lining will not be loaded until the next advance has begun to be excavated. However, load will be applied to the lining due to creep and time-dependent loosening of a fissured material. Also, heat produced by hydration of the sprayed concrete will cause it to expand. With state-of-the-art tunnelling methods, advance rates of 6 to 7 m per day are possible (Williams *et al.*, 2004). In this scenario, surveying targets once or twice per day will result in the loss of a considerable amount of information.

As identified in the literature review, much of the variation in the concrete strength gain will come from 3 sources:

1. Variation of the proportions of the constituent materials.
2. Variation of accelerator dosage.
3. Variation of ambient temperature.

The variation of the proportions of the constituent materials can be minimised by accurate weighing at the batching plant. However, it is generally not possible to accurately estimate the water content, since it will be affected by the moisture content of the aggregates which is difficult to control, evaporation governed by the ambient temperature, humidity and the time from batching to spraying, and the moistness of the mixing drum and the delivery method (e.g. concrete mixer lorry, pump and concrete delivery lines).

The accelerator dosage is usually adjusted by the pump man within specified limits, normally with more accelerator added when spraying the crown of the tunnel where adhesion and immediate setting is important.

The effects of temperature during hydration were explained by Ulm & Coussy (1995) of the LCPC in Paris by consideration of the 1st and 2nd laws of thermodynamics, the Arrhenius law and water diffusion processes and was explained in Section 2.3.4. This was based on Coussy's theoretical work on the mechanics of porous continua (Coussy, 1995). It accounts for hydration kinetics, chemomechanical couplings related to strength development, stiffness development, and autogeneous shrinkage (e.g. strength is not related to time, but to the formation of CSH gel). Short- and long-term creep was also modelled. The advantage of this material model is that the underlying material functions are intrinsic and independent of field and boundary conditions, and may be determined from standard tests. This led to a method of quantification of stress states in sprayed concrete linings developed by researchers at TU Vienna with assistance from Ulm (Hellmich *et al.*, 1999a; Hellmich *et al.*, 1999b; Hellmich *et al.*, 2001b; Hellmich *et al.*, 2003; Macht *et al.*, 2003).

The method outlined in Macht *et al.* (2003) was based on input data provided by 3D optical surveying of monitoring points measuring displacements of the sprayed concrete tunnel lining. The data were interpolated to provide continuous displacement fields in both time and space. Stresses were obtained either by 3D finite element analyses employing nonlinear elements or by a shell theory-based model.

The method for the interpolation of displacements was first described in Hellmich *et al.* (2001b) and further developed in Macht *et al.* (2003) to allow for

the possibility of monitoring target damage by changing the mode of interpolation from total displacements to displacement increments. Interpolation in time was achieved using the following formulation:

$$\Delta \mathbf{u}_{MPk}(t) = \frac{\mathbf{u}_{MPk}(t_{n+1}) - \mathbf{u}_{MPk}(t_n)}{t_{n+1} - t_n}(t - t_n) \quad for\ t \in [t_n; t_{n+1}] \qquad \textbf{Equation 17}$$

where $\mathbf{u}_{MPk}^T = [u_{x,MPk}, u_{y,MPk}, u_{z,MPk}]$ is the three-dimensional displacement vector of monitoring point (*MP*) number *k* at time instants t_n and t_{n+1}. This is simply a linear interpolation.

Interpolation in space was more complex. A smooth, continuous displacement field was assumed. As long as no hinge mechanisms are formed in the tunnel lining, this seems a reasonable assumption. Quadratic functions were used, so for the example top heading cross section with 5 MPs the coefficients were determined either by means of the incremental displacements of 3 MPs or by means of the incremental displacements of 2 MPs and the continuity of the gradient between 2 adjacent interpolation functions.

$$\Delta \overline{\mathbf{u}}^A(\varphi, t) = \begin{Bmatrix} \Delta \overline{\mathbf{u}}_x^A \\ \Delta \overline{\mathbf{u}}_y^A \\ \Delta \overline{\mathbf{u}}_z^A \end{Bmatrix} = a^A(t) + b^A(t)\varphi + c^A(t)\varphi^2 \quad for\ A = I, II, \ldots \qquad \textbf{Equation 18}$$

where *A* denotes the index of the quadratic function, i.e. the part of the sprayed concrete shell to which the interpolation refers, and φ is the angle around the circumference of the tunnel lining, as shown in Figure 2-30.

It is unclear how the functions would be made to fit if the cross section contained more MPs, or if the tunnel lining was a closed ring. This would probably require some consideration of the lowest energy state by minimising curvature. Macht *et al.*'s method would also encounter problems if the mode of deformation of the lining were of a higher order than the number of MPs.

The *z*-direction in Macht *et al.*'s (2003) interpolation method is the longitudinal direction. Immediately after the installation (when stresses and strains are zero) of the 'considered' monitoring cross-section (MCS), longitudinal displacement between the 'preceding' MCS and the considered MCS is assumed linear. As

soon as the 'succeeding' MCS is installed, the preceding, considered and succeeding MCSs are interpolated using a quadratic function (Figure 2-31).

In order to arrive at the stresses, a 3D finite element model consisting of a 1 m long ring of shell elements was used. Several assumptions were made, including perfect bond at the joints, no stress transfer to the rock at the footings of the top heading or benches and constant longitudinal curvature.

According to the assumption of constant longitudinal curvature, the increment of longitudinal strain is constant across the shell thickness. However, if longitudinal stresses are back-calculated from an interpolation between MCSs, which may be 5 to 20 m apart, the effect of circumferential joints, the effect of incremental advances of perhaps 1 m, should conspire to make this assumption of no bending in the longitudinal direction a gross simplification. Numerical modelling, even with perfectly continuous joints between advances, has shown that longitudinal stresses may vary greatly from the trailing edge to the leading edge of each advance (Thomas, 2003), particularly where a top heading, bench, invert sequence is used.

The interpolation method results in a distribution of strain in the 1 m length of tunnel lining in both space and time, which is put into the FE model to arrive at the stress, using the thermochemomechanical model. The change in utilisation with time may thus be calculated for any point in the tunnel lining.

The results from the Sieberg tunnel presented in Macht *et al.* (2003) show an unexpected pattern of stresses (Figure 2-32 and Figure 2-33). Hoop thrust (circumferential axial force) in the top heading begins with a relatively small compressive force which becomes tensile after about 350 days. It again becomes compressive after the bench is excavated. The computed stresses undergo large amplitude fluctuations throughout, and this may have been caused by errors in the displacement measurements, although this was not discussed in the paper. The strains in Figure 2-32 obtained by interpolation of displacement measurements achieved a maximum of 1500 microstrain (0.15 % strain). The Sieberg tunnel had an internal diameter of 12.1 m in the top heading, and a sprayed concrete lining 0.3 m thick. For this size of tunnel, a typical surveying repeatability of ± 2-3 mm would cause an error in the strain calculation of 320-

480 microstrain, a large proportion of the maximum strain and enough to cause large fluctuations. In a smaller tunnel the errors would be amplified.

Assuming the method can accurately calculate stress, the low compressive and tensile circumferential axial load calculated by Macht *et al.* (2003) in the Sieberg tunnel before the bench and invert were constructed (Figure 2-33) could have been caused by autogenous shrinkage strains and possibly thermal contraction strains that became larger than the compressive strains due to loading. So at times the lining of the top heading was calculated to be in tension and not contributing at all to the stability of the ground. This may be because the ground was very competent and effectively self-supporting. On the other hand, if the method were calculating erroneous stresses, the calculated low compressive and tensile axial load may have been caused by an overestimation of shrinkage and/or creep.

The thermochemomechanical model relies on deriving functions relating strength, autogenous shrinkage, elastic stiffness and creep compliance to the degree of hydration. The degree of hydration is in turn related to hydration kinetics (i.e. the thermally activated reaction rate) via the Arrhenius Law:

$$\dot{\xi} = \tilde{A}(\xi)\exp\left(\frac{-E_a}{RT}\right) \qquad \textbf{Equation 19}$$

Affinity $\tilde{A}(\xi)$ may be partly dependent on temperature but in this formulation it is decoupled from temperature and is assumed to be only dependent on degree of hydration ξ. Multisurface chemoplastic hardening rules are also applied, which relate the size of the yield surface in stress space not only to the hardening parameters but also to the degree of hydration. The state equation for an increment of stress is given by:

$$d\boldsymbol{\sigma} = \mathbf{C}(\xi) : \left[d\varepsilon - d\varepsilon^{p} - \mathbf{1}d\varepsilon^{s}(\xi) - \mathbf{1}\alpha_{T}dT - d\varepsilon^{v} - d\varepsilon^{f}\right] \qquad \textbf{Equation 20}$$

where $\mathbf{C}(\xi)$ is the elasticity tensor, dependent on Young's modulus $E(\xi)$ and a constant Poisson's ratio,

ξ is the degree of hydration as defined in Section 2.3.4,

ε is the strain tensor,

ε^p is the plastic strain tensor,

ε^s is the autogenous shrinkage strain,

ε^v is the short-term creep strain caused by stress-induced water movement in the capillary pores,

ε^f is the long-term creep strain caused by dislocation processes in the nanopores,

and **1** is the second order unit tensor, which converts the isotropic scalar parameter (coefficient of thermal expansion or autogenous shrinkage strain) into a second order tensor.

Both the coefficient of thermal expansion and Poisson's ratio are assumed to be constant with respect to degree of hydration, whereas in reality these vary significantly at early age (Laplante & Boulay, 1994; Byfors, 1980). The other material properties required for the model that are a function of the degree of hydration are:

1. affinity, $\tilde{A}$,
2. compressive strength, f_c,
3. Young's modulus, E,
4. autogenous shrinkage strain, ε^s,
5. characteristic time for short-term creep, τ_w, and
6. final viscous creep compliance, J_∞^v.

These material properties will be no more unreliable than material properties expressed as a function of time, as is usual practice. In fact, variability should be reduced because the effect of temperature on the degree of hydration, and hence on the development with time of all the other parameters will be accounted for. An example of the determination of chemical affinity as a function of degree of hydration is shown in Figure 2-34.

The method described by Macht *et al.* was set up to work with the information already available (i.e. conventional displacement monitoring of the tunnel lining), rather than questioning what information would be needed to make the method work. The errors due to surveying accuracy will in most cases be

significant and may render the method useless. For a sprayed concrete tunnel in soft ground where the invert is closed quickly and the lining loaded during the early age of the sprayed concrete, the accuracy of the constitutive model will become important. Also, the accuracy and frequency of the displacement monitoring will be of increasing importance as the speed that the load comes onto the lining increases and the magnitude of the displacements decreases.

Of all the back-calculation methods, the thermochemomechanical model shows the most promise. However, the intrinsic relationships quoted by Hellmich *et al.* (2003) are taken from a diverse range of laboratory tests on different sprayed concrete mixes. As for all the methods, site-specific data should be used to minimise errors. Also, the errors due to the surveying methods employed should be taken into account along with the likely magnitude of the displacements to assess whether the method will yield useful results.

The necessary interpolation of displacements across time should also be considered: will sufficient readings be taken to interpolate a realistic relationship between time and displacement at any given point? The first measurements should also be taken as early after spraying as possible so that the minimum information is lost.

For soft ground sprayed concrete tunnels, it is unlikely that 3D optical surveying of monitoring targets will yield sufficiently accurate and frequent results to be of use. Perhaps the promising field of optical fibre sensors for remotely measuring strains around a tunnel ring (Metje *et al.*, 2005) will provide the solution to this problem in soft ground.

2.5.4 Pressure cells

The various pressure cell designs adopted by different manufacturers work on the same principles, are constructed using the same materials and have similar dimensions and geometry. Pressure cells typically consist of two rectangular stainless steel plates, each 3 mm thick, separated by a 0.3 mm thick film of hydraulic oil (Figure 2-35). Previously mercury was sometimes used as the filling liquid (e.g. Clayton *et al.*, 1998), but lately this has become unacceptable for environmental reasons.

Two distinct types of pressure cell have been used in SCL tunnels. Radial pressure cells measure radial pressure at the interface between the extrados of the sprayed concrete lining and the ground and are typically 150 x 250 mm. Tangential pressure cells measure tangential stress or hoop stress within the sprayed concrete lining itself and are therefore installed perpendicular to the radial cells and usually have a larger pressure range. Tangential cells are typically 100 x 200mm. Usually a radial cell and a tangential cell are paired together and pairs of cells are arranged in an array so that the distribution of stress around the tunnel can be found at a particular section.

A commonly-held view is that pressure cells can only be used to measure changes in pressure and cannot reliably give absolute values (Aldrian & Kattinger, 1997; Bruzzi *et al.*, 1999). However, radial pressure cells at least have been shown to give reliable results (Clayton *et al.*, 2000).

The factors affecting recorded pressures were discussed by Clayton *et al.* (2002). These are:

1. Cell properties.
2. Installation effects such as positioning, cavities or rebound accidentally sprayed into the lining.
3. Temperature changes.
4. Crimping.

Crimping involves crushing the crimping tube using a specially-made crimping tool. This forces a fixed amount of fluid into the pressure cell cavity. This is done to ensure that the cell is properly embedded in the sprayed concrete and no loss of contact has occurred during hydration, since pressure cells can only sense positive pressure. If good crimping records are kept, the increase in pressure caused by crimping can easily be removed.

Cell action factor (CAF) is defined as the ratio of recorded pressure to actual stress in the medium normal to the cell (Clayton *et al.*, 1998). Pressure cells for use on and in sprayed concrete linings are designed so that the stresses in the medium are not significantly modified by their presence, such that the CAF should be close to unity. The cells are made wide and thin, with a low aspect

ratio, so that arching and end effects are negligible. It has been often stated that the ideal situation would be to design a pressure cell that has the same stiffness as the medium into which it is embedded (Clayton *et al.*, 1995; Bruzzi *et al.*, 1999). But for a medium with a nonlinear response, for example soil, or for a medium with a stiffness that varies with age, for example sprayed concrete, this would be impossible to achieve (Weiler & Kulhawy, 1982).

Since stress is not a directly measurable physical entity, pressure cells rely on "hard inclusion theory" to measure stress (Williams, 1974). This means that the ratio of pressure cell stiffness to medium stiffness is sufficiently high that variations in the medium stiffness become unimportant. Thus pressure cells are designed so that the CAF is insensitive to the stiffness of the medium. This was shown by Coutinho (1953), using an elastic solution for a cylindrical inclusion embedded in an infinite medium to show that as long as the pressure cell has an overall stiffness greater than or equal to the stiffness of the medium, the CAF should be tolerably close to unity. Clayton *et al.* (2002) used an axisymmetrical finite element model of a cylindrical pressure cell and then a conservation of volume calculation to take account of the filling liquid compressibility to show that values of CAF would be close to unity for typical values of concrete stiffness, soil stiffness and cell dimensions.

A comparison of CAF found in previous studies is shown in Table 2-6. According to Glötzl (1996), a typical oil-filled pressure cell with a 0.3 mm thickness of filling liquid will have an equivalent Young's modulus of 50 GPa. This is higher than the secant modulus of most concretes. For all the theoretical models quoted in Table 2-6, except the numerical analysis by Woodford & Skipp (1976), which was a parametric study, the Young's modulus of the concrete was taken as 30 GPa.

Table 2-6: Experimental and theoretical values of cell action factor

Experiment / Model		CAF
Load test of Glötzl radial cell at concrete-clay interface (Woodford & Skipp, 1976)		0.96
Air pressure calibration of Geokon radial cell (Clayton *et al.*, 1995)		1.0
Load test of 2 Geokon radial cells at sprayed concrete-clay interface (Clayton *et al.*, 1995)		>0.95
Load test of ready-mix concrete panel with 2 embedded Geokon tangential pressure cells (Clayton *et al.*, 1995)		0.87-0.99
Load test of sprayed concrete panel with 2 embedded Geokon tangential pressure cells (Clayton *et al.*, 2002)		1.08
Axisymmetric elastic FE analysis of Glötzl radial cell at concrete-clay interface (Woodford & Skipp, 1976)		0.78-1.18
Axisymmetric FE model of an embedded Geokon tangential cell (Clayton *et al.*, 2002)		0.95
Axisymmetric elastic solution (Coutinho, 1953)	Equivalent cell stiffness E_c = 50 GPa	1.01
	E_c = 20 GPa	0.99
	E_c = 10 GPa	0.95

The values of CAF in Table 2-6 suggest that the CAF of typical pressure cells are tolerably close to unity. The large range of CAF values Woodford & Skipp (1976) found in their numerical analysis was due to the unrealistic limiting values of Young's modulus they used for the parametric study.

Temperature sensitivity also has an effect on the recorded pressure. As well as the sensitivity of the vibrating wire transducer to temperature change, which can easily be removed using the manufacturer's calibration, there is also the temperature sensitivity of the cell-medium system to consider. Unless the coefficient of thermal expansion of the cell fluid, cell casing and medium are all

exactly the same, and the temperatures experienced by them are the same, pressure changes will be induced in the cell fluid by differential volume changes in the system. Most published work on the subject of pressure cells has ignored the effect of temperature sensitivity entirely.

Numerical modelling by Clayton *et al.* (2002) of an unrestrained sprayed concrete test panel has shown that temperature sensitivity of tangential cells is due to the concrete around the cell restraining the expansion of the stainless steel cell casing, and thus reducing the cavity volume and increasing the pressure of the cell fluid. The axisymmetric model with the same plan area of pressure cell as the rectangular pressure cells they used in the laboratory and on site (approximately 20000 mm^2, and mercury-filled) had a temperature sensitivity of 0.11 MPa/°C. Clayton *et al.* (2002) estimated from laboratory data of an unloaded test slab that the temperature sensitivity of tangential cells was about 0.1 MPa/°C, and from field data of a tangential pressure cell in a tunnel 0.08 MPa/°C. Therefore, for tangential pressure cells, this arching restraint appears to be the dominant mechanism that causes temperature sensitivity and this needs to be removed from the data in order to obtain meaningful results.

For a radial cell at the interface between the sprayed concrete and the ground, arching restraint around the cell is likely to be much less important when the ground is relatively much less stiff than the cell and therefore was ignored by Clayton *et al.* (2000). Since the calibration of the pressure cell is performed using fluid pressure with no shear stiffness, it follows that the ideal situation should be one where the medium has a very low stiffness relative to the cell. But the mechanism that has been ignored or unnoticed by all previous studies on pressure cells in tunnels is that as the temperature varies inside the tunnel and is likely to be relatively constant in the ground, the whole ring of sprayed concrete will expand and contract, increasing and decreasing the pressure measured by the radial cell at the sprayed concrete – soil interface and hence also increasing and decreasing the stress measured by the tangential pressure cells. No previous study has examined this mechanism or the relative importance of the two mechanisms – arching restraint and expansion/contraction of the tunnel ring – to the temperature sensitivity of tangential or radial pressure cells.

If arching restraint in the medium around the pressure cell can cause changes in recorded pressure due to temperature sensitivity, it follows that other strains in the medium such as creep and shrinkage should also cause changes in recorded pressure. However, the mechanism would be slightly less complex than temperature sensitivity since only the medium is experiencing a volume change in this case. Shrinkage or compressive creep of the sprayed concrete around a tangential cell should cause an increase in the recorded pressure. This is roughly equivalent to the opposite of what happens during crimping. Clayton *et al.* (2002) found that shrinkage pressures recorded by pressure cells in unloaded sprayed concrete test panels reached a stable maximum of about 1 MPa after 60 days.

Coutinho (1953) believed that because the pressure cell was insensitive to the stiffness of the medium, then creep of the medium would have a negligible effect. Pressure cells are after all designed to minimise arching and end effects by being wide and thin. This paradox may be explained by considering the hypothetical situation where there are no arching or end effects around the cell. If a test panel were constructed with the same cross-sectional dimensions as the plan area of the pressure cell, so that there was concrete above and below but not around the cell, then this would represent this situation. An increase in load applied to the top of the test panel would result in exactly the same load in the pressure cell. If the test panel were unrestrained, then shrinkage, creep and crimping would have no effect on the recorded pressure. This thought experiment demonstrates that increases in recorded pressure caused by shrinkage and creep must be due to arching effects, but it does not explain why they occur when the relative stiffnesses of the pressure cell and medium seem to be unimportant, and the strains caused by loading are of a similar magnitude to shrinkage and creep.

The difference between the response of a pressure cell to load and the response of a pressure cell to shrinkage or creep is that under load, the pressure cell also deforms. The reason the pressure cell appears to be affected more by strains not induced by loading such as shrinkage, creep and crimping is that there is no stress present in the medium except the stresses due to arching restraint around the cell.

2.6 Stress measurements in shallow soft ground tunnels

This section discusses previous measurements of stress in shallow soft ground tunnels, with particular emphasis on measurements made in London Clay. It describes current knowledge of the development of stresses onto tunnel linings. It includes stress measurements made in segmental tunnel linings as well as in sprayed concrete tunnels. Questions that require answers include:

- What is the maximum stress the lining will experience and when?
- How quickly does the stress increase in the short-term? Is this a function of time, the position of the face relative to the section in question, or both?
- Does the stress continue to increase into the long-term? If so, what drives these long-term stress changes?

The answers to these questions are critical to the design of sprayed concrete linings. In shallow ground, it is likely that the maximum hoop stress is much lower than the strength of the sprayed concrete lining in the long-term. However, at early age the sprayed concrete may experience a high utilisation if the stress increases more quickly than the strength gain of the sprayed concrete. Also, sprayed concrete junctions generally experience much higher stresses than straight sections of tunnel, and these stresses may be close to the design strength in the long-term as well as the short-term.

A comparison is made in Figure 2-36, Figure 2-37 and Figure 2-38 of previous stress measurements in London Clay by Skempton (1943), Ward & Thomas (1965), Muir Wood (1969), Barratt *et al.* (1994) and Bowers & Redgers (1996). These were all made using load cells or strain gauges in precast concrete and cast iron segmental linings. These data could have been presented in a single chart with log-time on the abscissa, but this would give a distorted perception of how the stresses change in the long-term.

2.6.1 Maximum load

The maximum load has always been found to occur in the long-term. Skempton (1943) found the maximum load to be approximately equal to that corresponding to the hydrostatic full overburden pressure (that is, the initial *in situ* stress with

K_0 = 1.0). Ward & Thomas (1965) found that one of the tunnels they studied reached full overburden pressure, while the second one did not but was continuing to increase when measurements ceased. They therefore arrived at the conclusion that hydrostatic full overburden pressure would eventually act on the lining in the long-term. Since then, measurements by Muir Wood (1969), Barratt *et al.* (1994) and Bowers & Redgers (1996) have all shown that load can stabilise at a value well below that corresponding to full overburden pressure acting hydrostatically. Values of maximum load as a percentage of hydrostatic full overburden pressure are shown in Table 2-7 below:

Table 2-7: Maximum stresses measured in tunnels in London Clay expressed as a percentage of hydrostatic full overburden pressure

Authors	**Tunnel**	**Maximum load (% hydrostatic overburden)**
Bowers & Redgers 1996	Jubilee Line Extension, St. James's Park	43-62 %
Barratt *et al.* 1994	Jubilee Line, Regent's Park	40-64 %
Muir Wood, 1969	Heathrow Cargo Tunnel, Heathrow	60-80 %
Ward & Thomas 1965	'Site V', Victoria Line	105 %
Ward & Thomas 1965	'Site O', London	71 % (not stabilised)
Cooling & Ward 1953	9' diameter water tunnel, London	53-64 %
Skempton 1943	Unknown, London.	102-108 %

It is possible that the amount of stress in the tunnel lining is related to the amount of ground deformation that was allowed to occur during construction, which may explain the higher loads in the older tunnels. The exception to this rule would be the Heathrow Cargo tunnel, which was constructed with an unusually high degree of face support at shallow cover and had a volume loss of only 0.2 %.

2.6.2 Stress increase in the short- and long-term

The load as a percentage of overburden in Figure 2-36 may be normalised to the maximum long-term load to show how quickly the maximum long-term load develops. This is shown in Figure 2-39. Figure 2-39 shows two distinct types of behaviour:

1. Tunnels which experience more than 80% of the maximum long-term radial pressure in fewer than 7 days (Cooling & Ward, 1953; Muir Wood, 1969; Bowers & Redgers, 1996).
2. Tunnels which experience less than 60% of the maximum long-term radial pressure in the first 7 days, and subsequently pressures continue to increase at a gradual rate for a long period (Ward & Thomas, 1965; Barratt *et al.*, 1994).

Mair & Taylor (1997) reported that in open face tunnelling, (which includes conventional sprayed concrete tunnelling without compressed air), where there is significant unloading of the ground, the magnitude and distribution of excess pore pressures depend on the degree of unloading and the strength and stress history of the clay. In the case of overconsolidated clays such as London Clay, excess pore pressures are nearly always negative, as exemplified by piezometer readings of pore pressures close to an advancing SCL tunnel side-drift in New & Bowers (1994), a pipe-jack in Marshall *et al.* (1996) and a top heading, bench, invert SCL tunnel in van der Berg (1999), which all show a relatively sudden decrease in pore pressure as the tunnel approaches, followed by a very slow rebound. An example from New & Bowers is shown in Figure 2-40. This effect appears to be independent of excavation method as long as the ground is unloaded. In this case, swelling rather than consolidation would be expected, resulting in no discernible post-construction surface settlements, according to Mair & Taylor (1997).

For tunnels at a similar depth in London Clay, the only factor affecting the magnitude and distribution of excess pore pressures that really changes from one tunnel to another is the degree of unloading during construction. This is governed mainly by the distance to ring closure. For a segmentally-lined tunnel, this can be a distance of a tunnel diameter or more, depending on how far back from the face

the rings are installed, and whether bolted rings are grouted immediately or grouted several metres further back. For an SCL tunnel, the degree of unloading depends on the construction sequence. For instance, the construction method employed at the T5 SWOT frontshunt tunnel of full-face excavation followed by installation of a complete circular ring should be expected to result in less unloading than the top heading, bench, invert sequence employed at the T4 concourse tunnel.

Thomas (2003) modelled the T4 concourse tunnel top heading, bench, invert construction in 3D. The unloading of mean total stress p is evident in Figure 2-41 and this would result in negative excess pore pressures as predicted by Mair & Taylor (1997). At crown and axis level, p rebounded to a certain extent as the face advanced further away and load was thrown back onto the rigid tunnel lining. At the invert, however, unloading was permanent. This unloading of mean total stress generates negative excess pore pressures that will dissipate over time causing swelling of the clay.

Swelling will gradually apply pressure to a tunnel over time as negative excess pore pressures are dissipated. Hence, the greater the degree of unloading, the larger the increase in load over time will be.

The main weakness in this argument is the fact that settlements almost always continue to increase above tunnels in London Clay long after construction has ceased. This could be explained by the fissured nature of London Clay. As the tunnel approaches and the soil is unloaded, the fissures open up, then once the tunnel has passed they close again. This movement along fissures may also explain why continuum models of tunnels in London Clay always predict surface settlement troughs that are wider and shallower than observed in the field (e.g. Franzius *et al.*, 2005).

2.7 Conclusions from literature review

Sprayed concrete linings (SCL) are frequently the preferred choice of support for short lengths of tunnel and for complex geometries and arrangements of tunnels. This means that junctions are not exceptions, but commonplace SCL structures.

The differences between sprayed concrete and normal concrete are a response to the different performance requirements and the different method of placement.

Modern alkali-free accelerators provide a durable and strong lining that does not necessarily require a secondary lining.

The chemical reactions within sprayed concrete are complex, but may be simplified since most of the strength gain results from calcium silicate hydration. Thermodynamic state equations may be used to describe the hydration reaction.

Very little has been published on the subject of SCL tunnel junctions. Simple methods may be used to estimate the concentration of hoop stress at the junction. However, the bending moments will also have a significant effect on the maximum and minimum stresses, and these may only be obtained from a 3D analysis. The soil-structure interaction and sequential excavation will also have an important effect on the stresses, and must be included in the model explicitly. Since 3D numerical modelling is relatively time-consuming, research is required to find which factors have a significant effect on the stresses calculated around a junction, and to find better ways of presenting the results.

Stress measurement is required for design verification as part of a holistic risk management process. Measurements of stress may be obtained using a variety of methods. Slot-cutting, overcoring and undercoring only provide a one-off measurement in mature concrete. Back-calculation of stresses from measured displacements introduces too many errors to provide worthwhile results. Pressure cells provide continuous measurement that if interpreted carefully will provide reasonably accurate measurements of stress. However, more research is required to estimate the effect of temperature, shrinkage and creep on tangential pressure cells.

Previous stress measurements in shallow tunnels in London Clay indicate that behaviour may be characterised by one of the two following categories:

1. Tunnels which experience more than 80 % of the maximum long-term radial pressure in fewer than 7 days.
2. Tunnels which experience less than 60 % of the maximum long-term radial pressure in the first 7 days, and subsequently pressures continue to increase at a gradual rate for a long period.

Tunnels with low volume losses tend to behave according to category 1, and tunnels with large volume losses tend to behave according to category 2. The

more unloading that occurs during construction, the higher the negative excess pore pressures. In the medium to long-term, as the negative excess pore pressures dissipate, swelling will increase the pressure acting on the tunnel lining in the same way that heave will apply pressure to base slabs or raft foundations.

More stress measurements are required to investigate the behaviour of shallow soft ground tunnels since the evidence suggests that the commonly-held view of how tunnels behave (allowing deformation to occur reduces the ground pressure) may not hold true.

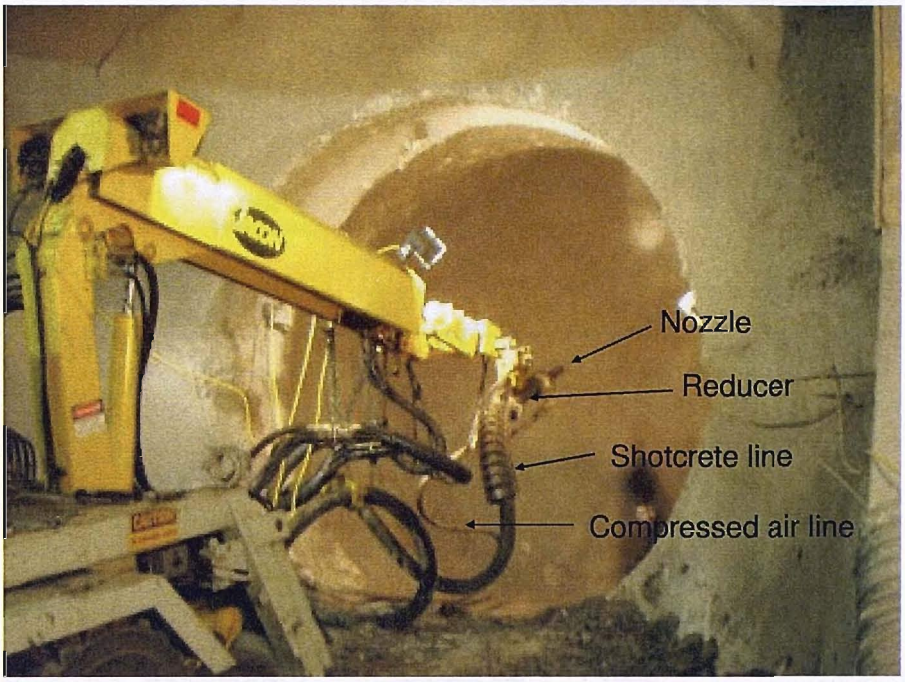

Figure 2-1: A sprayed concrete robot.

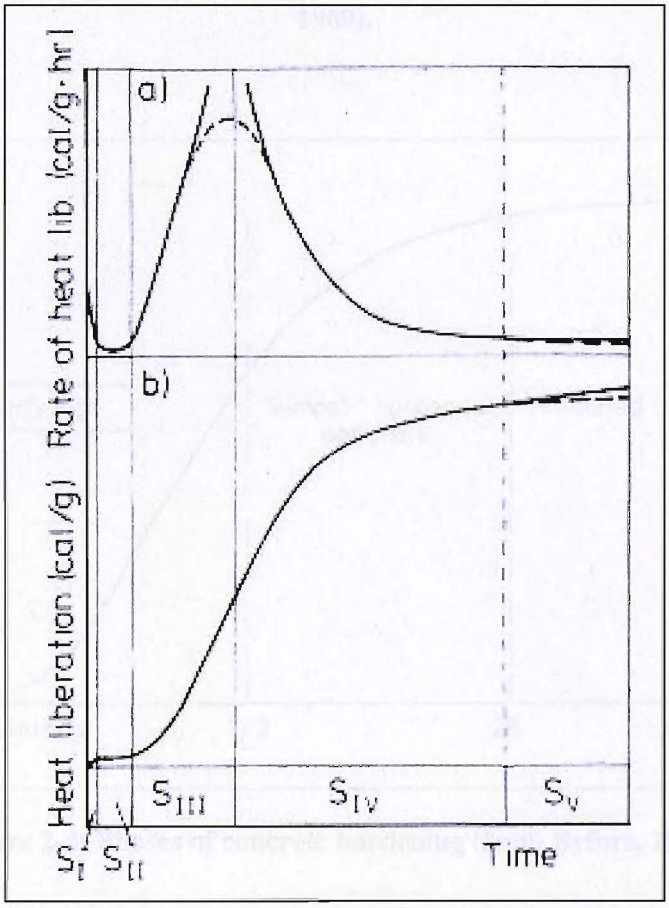

Figure 2-2: Heat liberation during hydration of cement (Byfors, 1980 after Kondo & Ueda, 1968)

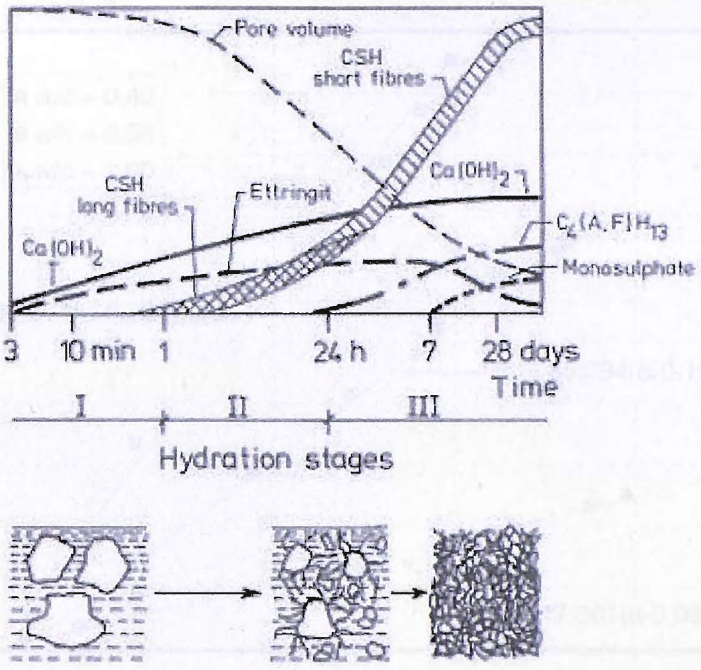

Figure 2-3: Formation of hydration products (from Byfors, 1980 after Richartz, 1969).

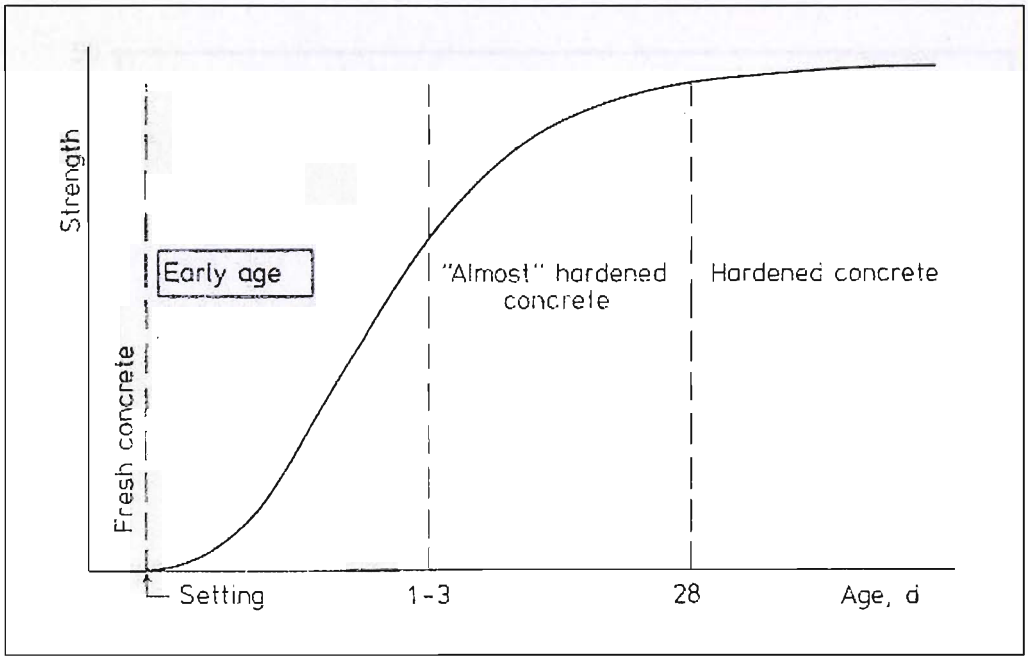

Figure 2-4: Phases of concrete hardening (from Byfors, 1980)

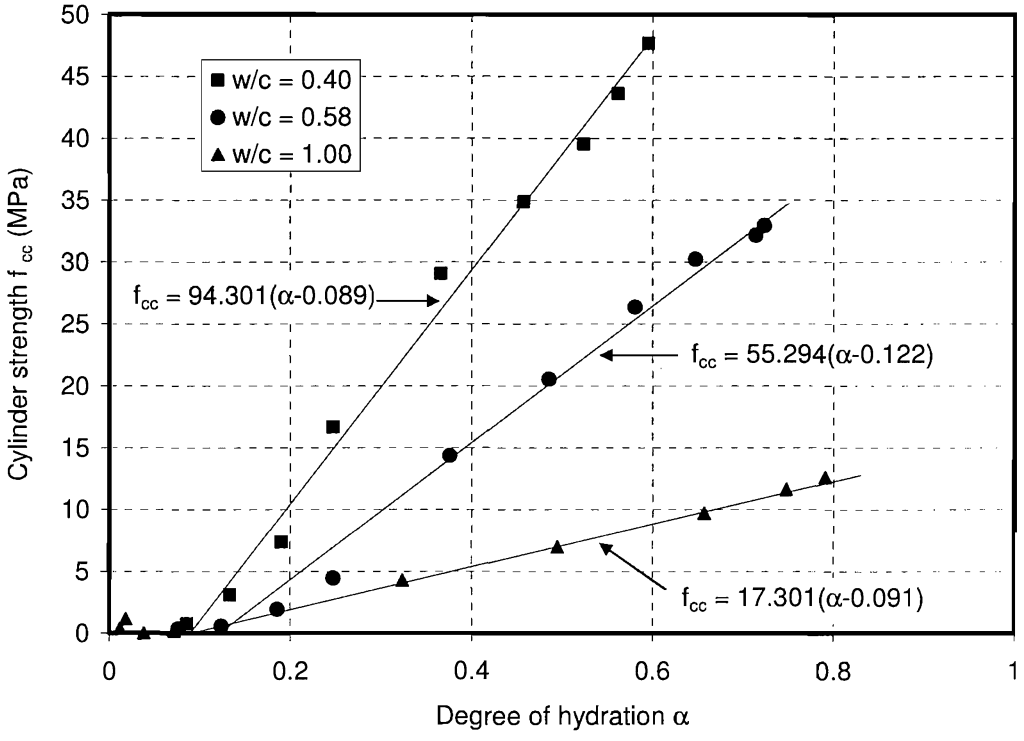

Figure 2-5: Relationship between compressive strength and degree of hydration of various concretes of different water:cement ratios (redrawn from Byfors, 1980)

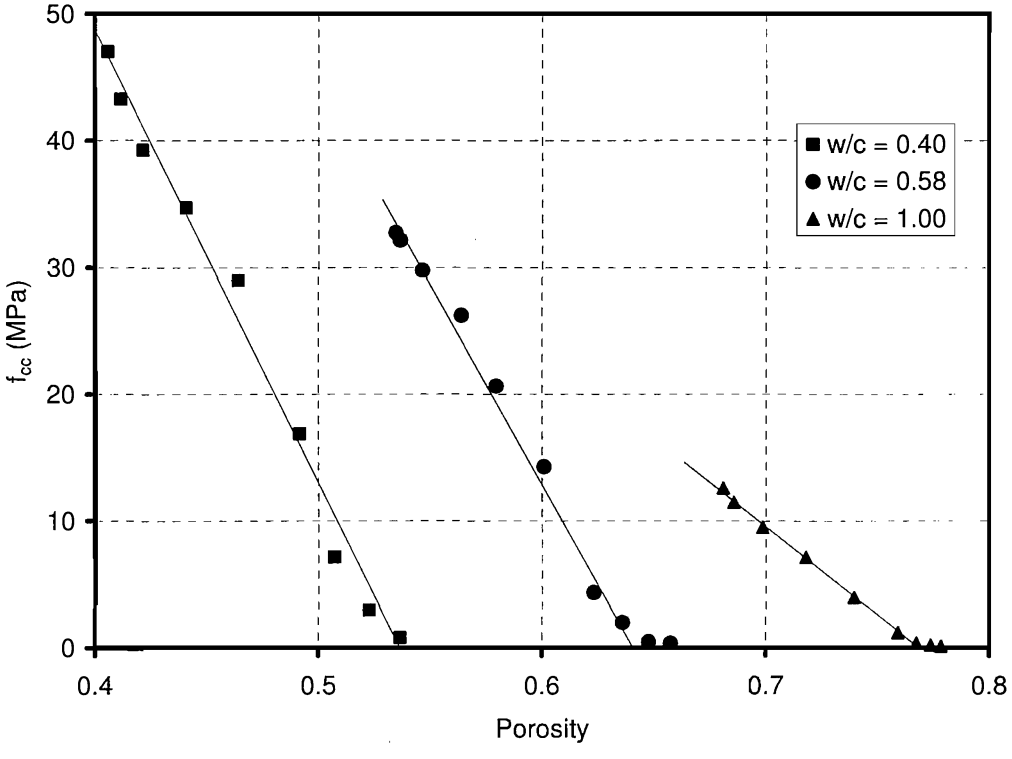

Figure 2-6: Relationship between compressive strength and degree of total porosity for concretes with different water:cement ratios (redrawn from Byfors, 1980)

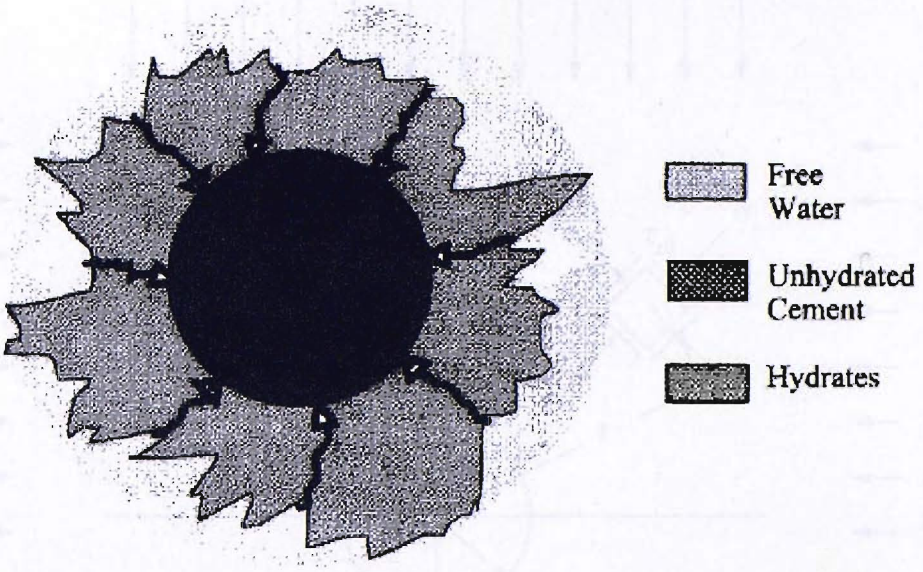

Figure 2-7: Diffusion of free water through layers of already formed hydrates towards unhydrated cement (from Ulm & Coussy, 1996).

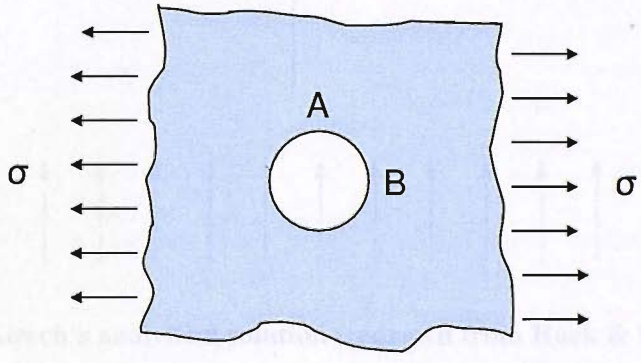

Figure 2-8: Infinite elastic plate with a hole

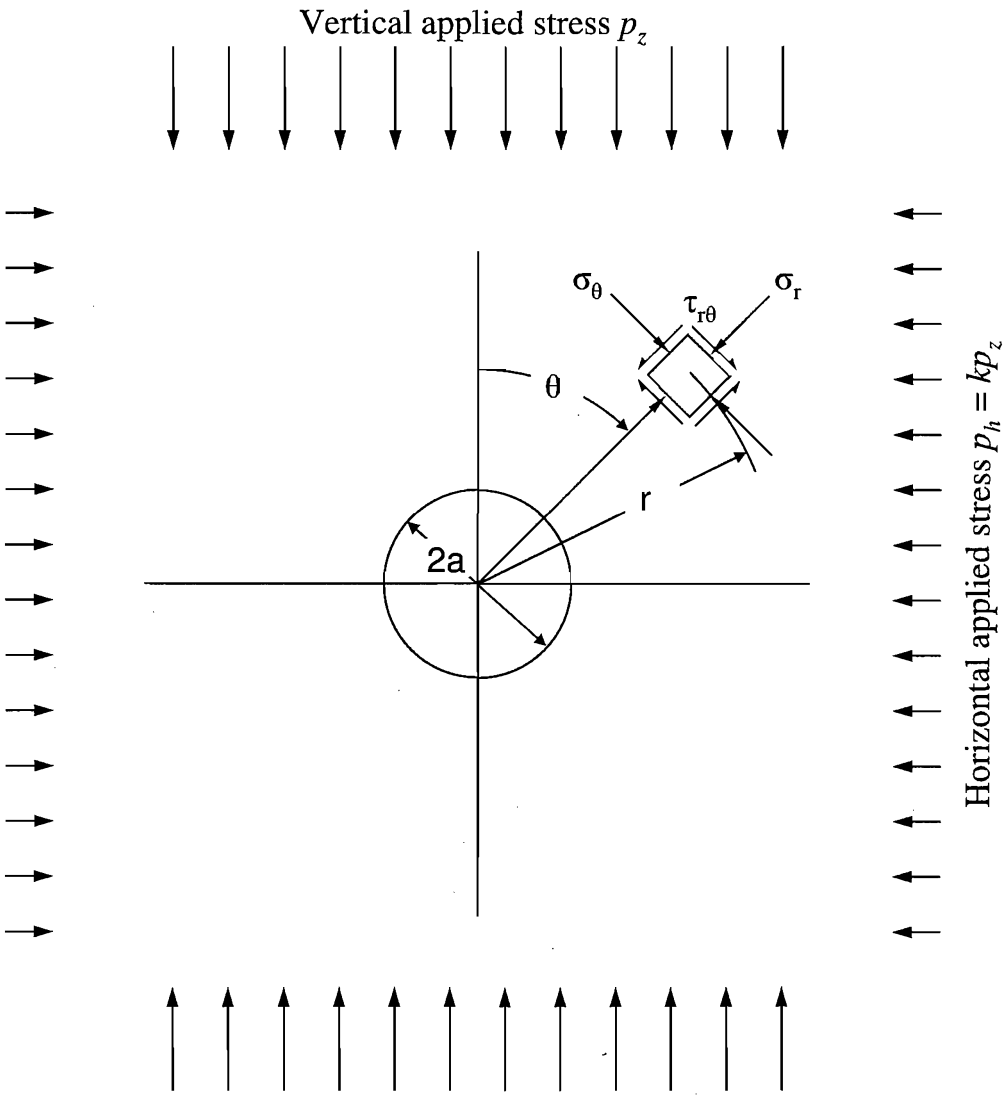

Figure 2-9: Kirsch's analytical solution (redrawn from Hoek & Brown, 1980)

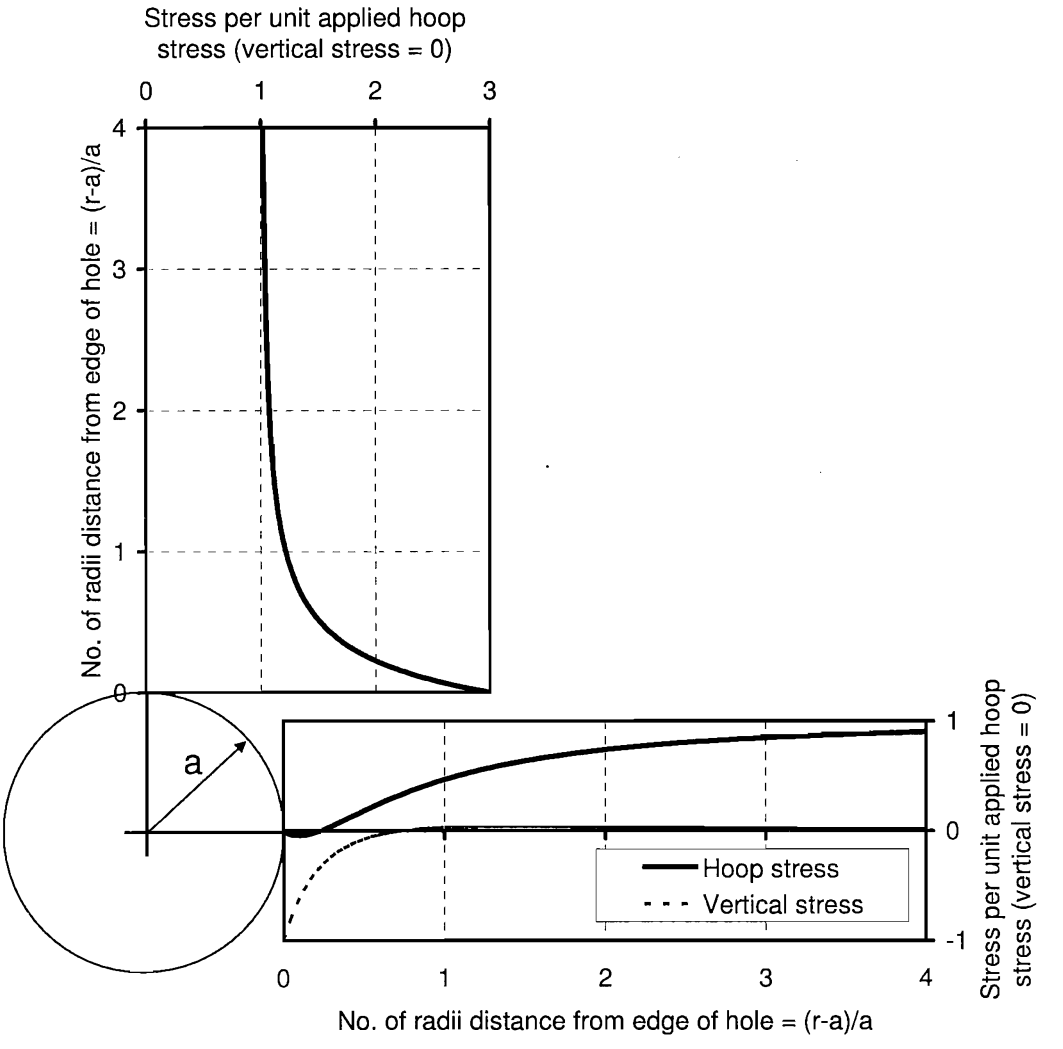

Figure 2-10: Variation of stress concentration with distance away from the edge of the hole, according to Kirsch's analytical solution (redrawn from Hoek & Brown, 1980)

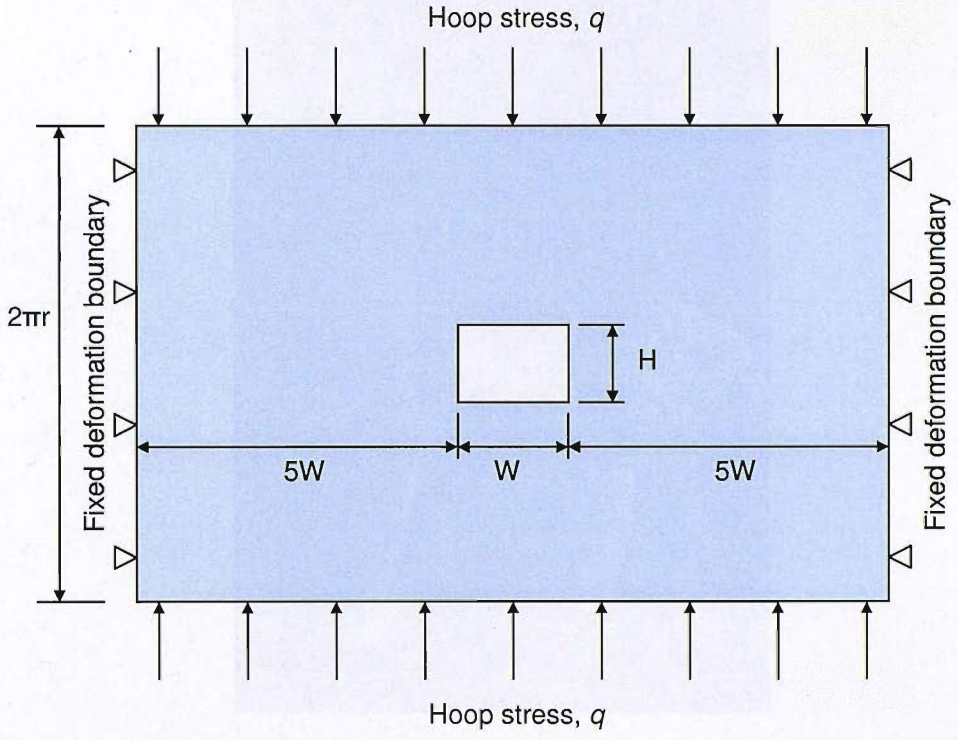

Figure 2-11: Model geometry and boundary conditions for plane stress analysis by Biliris & Purwodihardjo (2005)

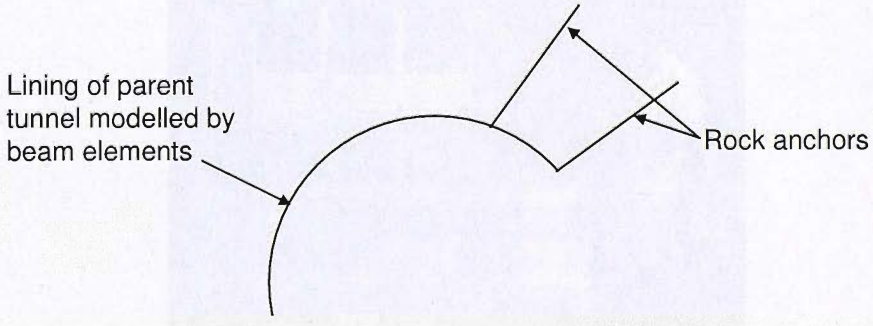

Figure 2-12: Model geometry for 2D analysis by Takino *et al.* (1985)

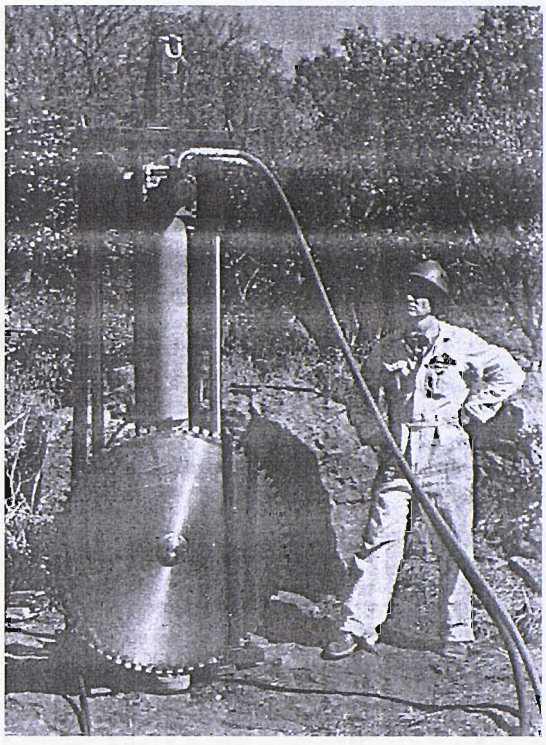

Figure 2-13: Drill and saw for creating slot for large flat jack (Vogler *et al.*, 1976)

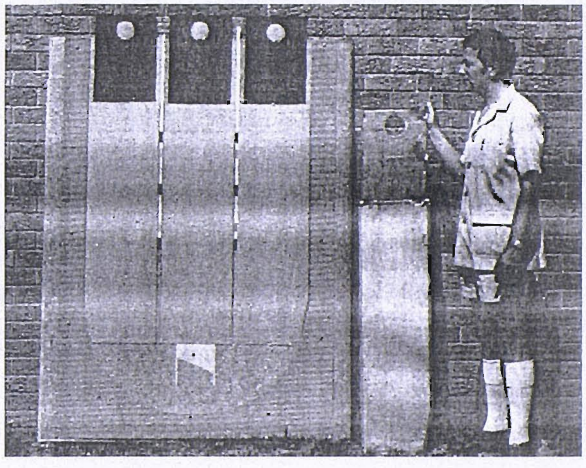

Figure 2-14: Full size model of large flat jack system (Vogler *et al.*, 1976)

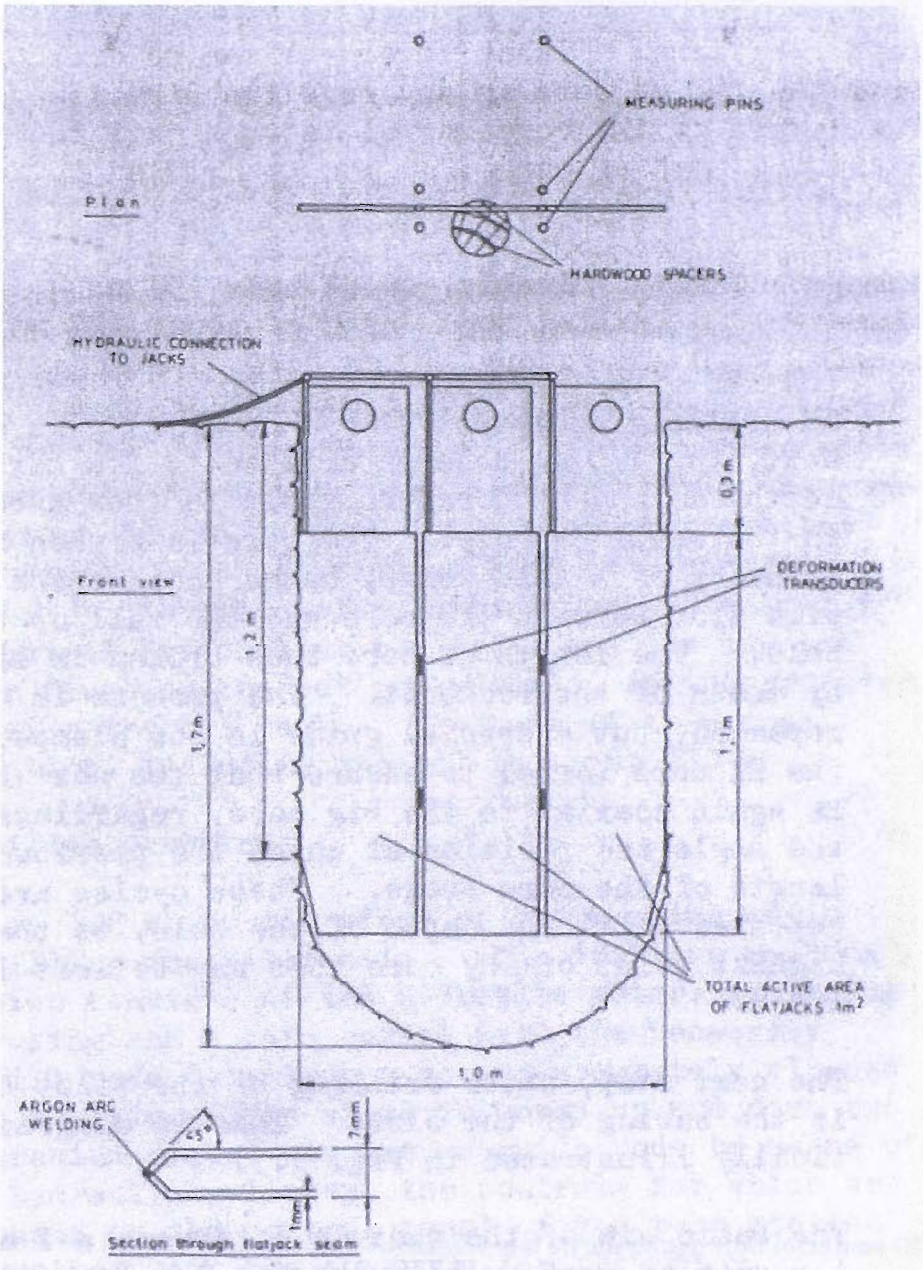

Figure 2-15: Large flat jacks (Vogler *et al.*, 1976)

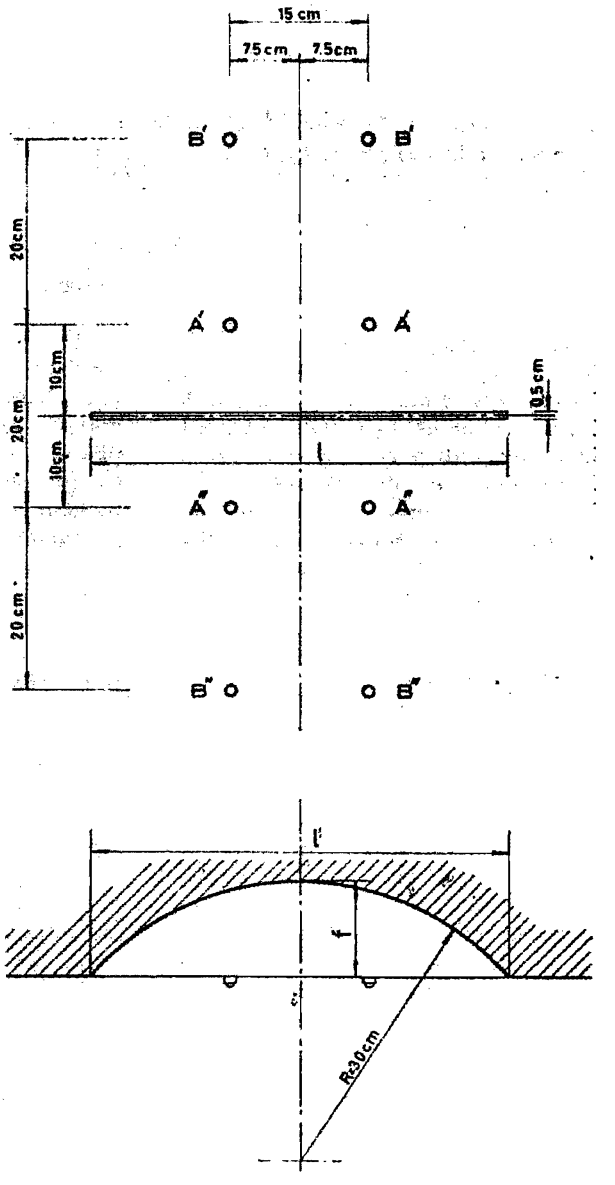

Figure 2-16: Small flat jack slot dimensions and strain gauge stud locations (Rocha *et al.*, 1966)

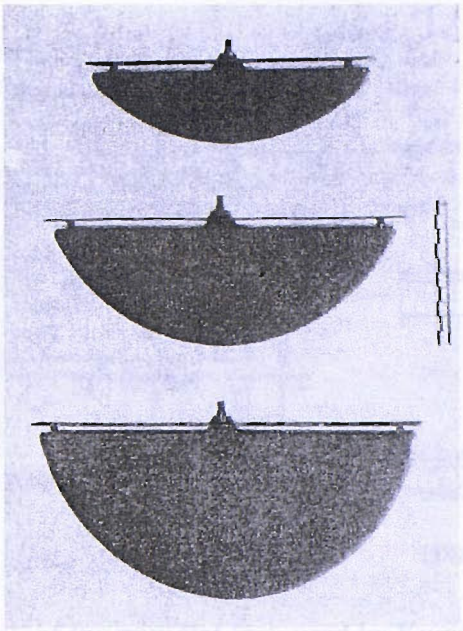

Figure 2-17: Circular segment small flat jacks as used by Rocha *et al.* (1966)

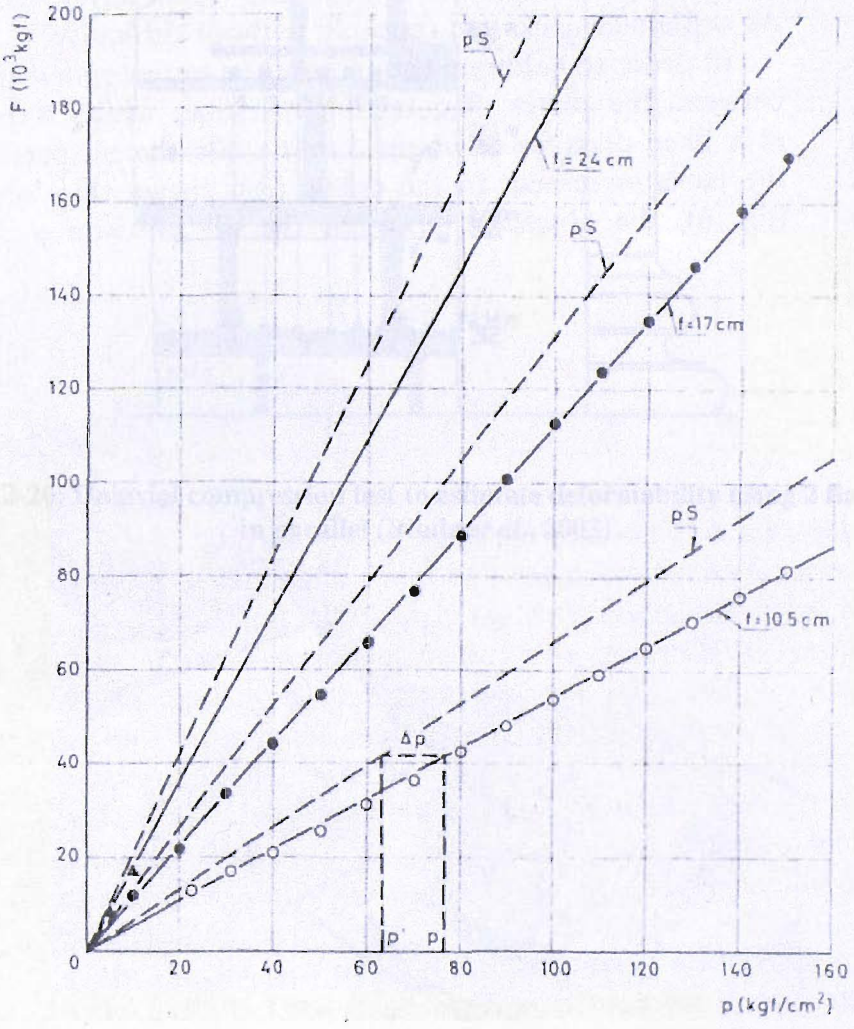

Figure 2-18: Laboratory calibration tests on small flat jacks by Rocha *et al.* (1966)

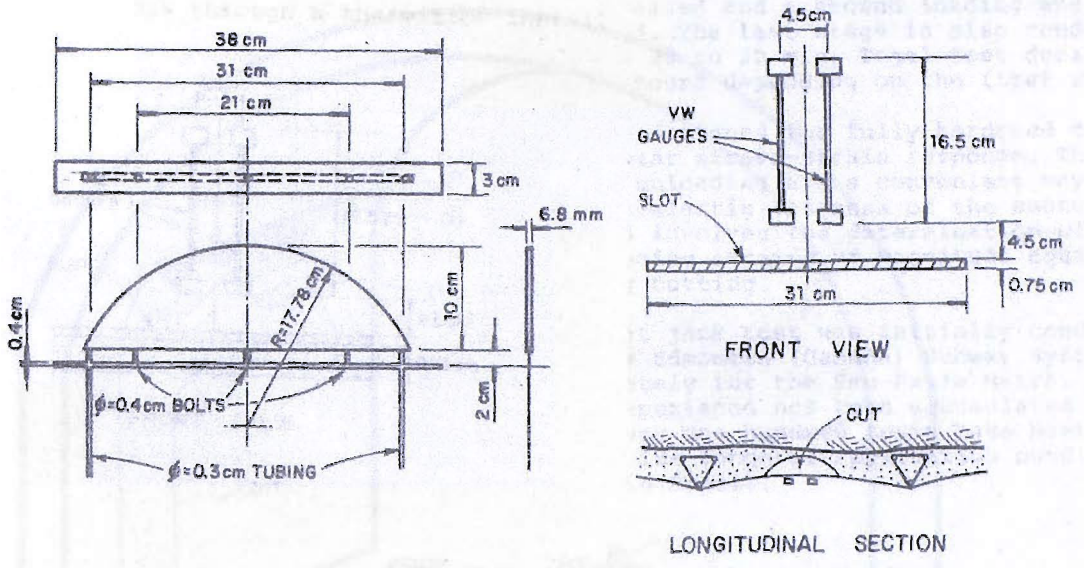

Figure 2-19: Details of the mini flat jack used by Kuwajima *et al.* (1991)

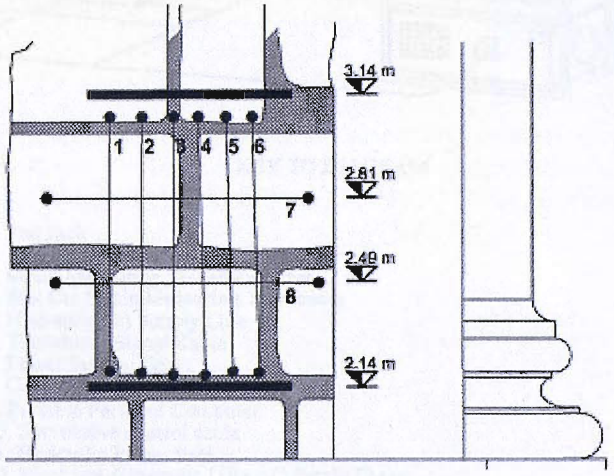

Figure 2-20: Uniaxial compression test to estimate deformability using 2 flat jacks in parallel (Binda *et al.*, 2003)

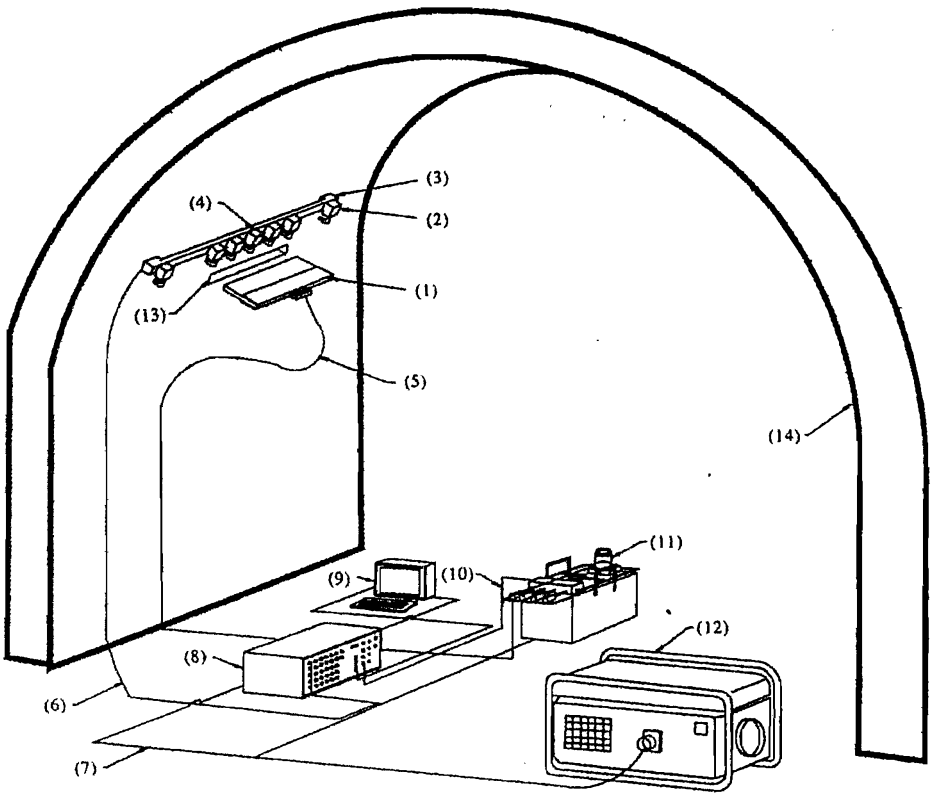

KEY TO DIAGRAM

1. Flat Jack
2. Remote Strain Measuring Transducer
3. Strain Measuring Transducer frame
4. Slot Cut Strain Measuring Transducer
5. Hydraulic Oil Supply Line
6. Transducer Signal Cable
7. Power Supply Cable
8. Computer Interface Unit
9. Portable Personal Computer
10. Servovalve control cable
11. Hydraulic Power Pack
12. Electrical Generator 110v AC Single Phase
13. Slot Cut in Masonry Bed Joint

Figure 2-21: Mini flat jack set-up used by Hughes & Pritchard (1997)

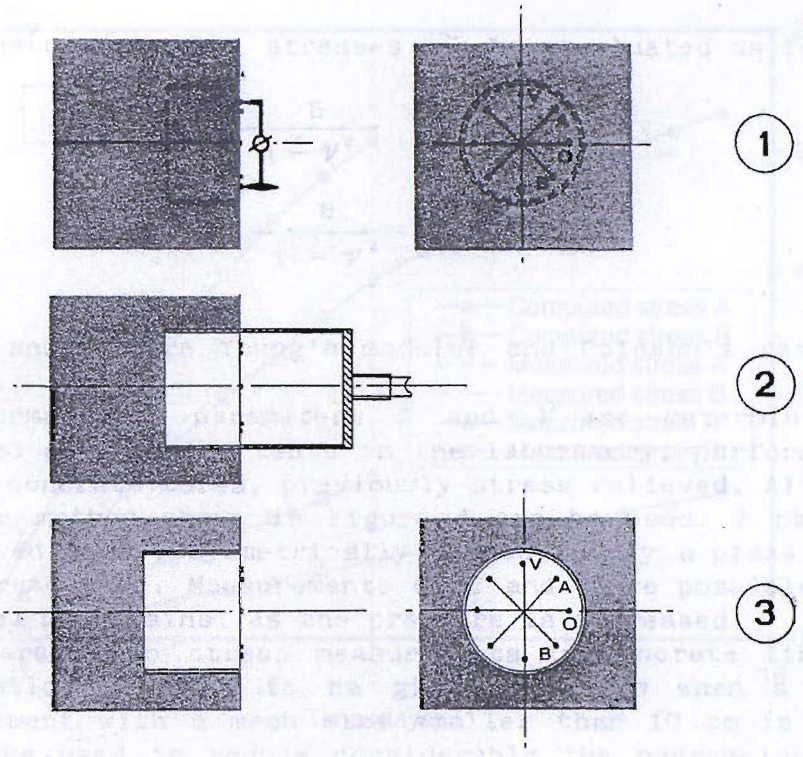

Figure 2-22: Schematic representation of the overcoring method in concrete linings (Barla & Rossi, 1983): (1) Measurement of distances across the diameters of the rosette. (2) Overcoring using a thin-walled bit. (3) Measurement of rosette displacements after overcoring.

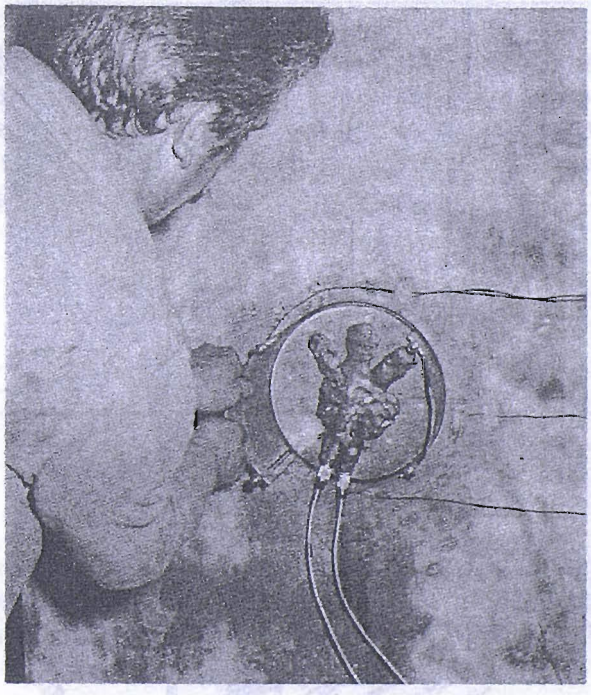

Figure 2-23: Use of thin curved jacks symmetrically placed to determine concrete deformability parameters (Barla & Rossi, 1983).

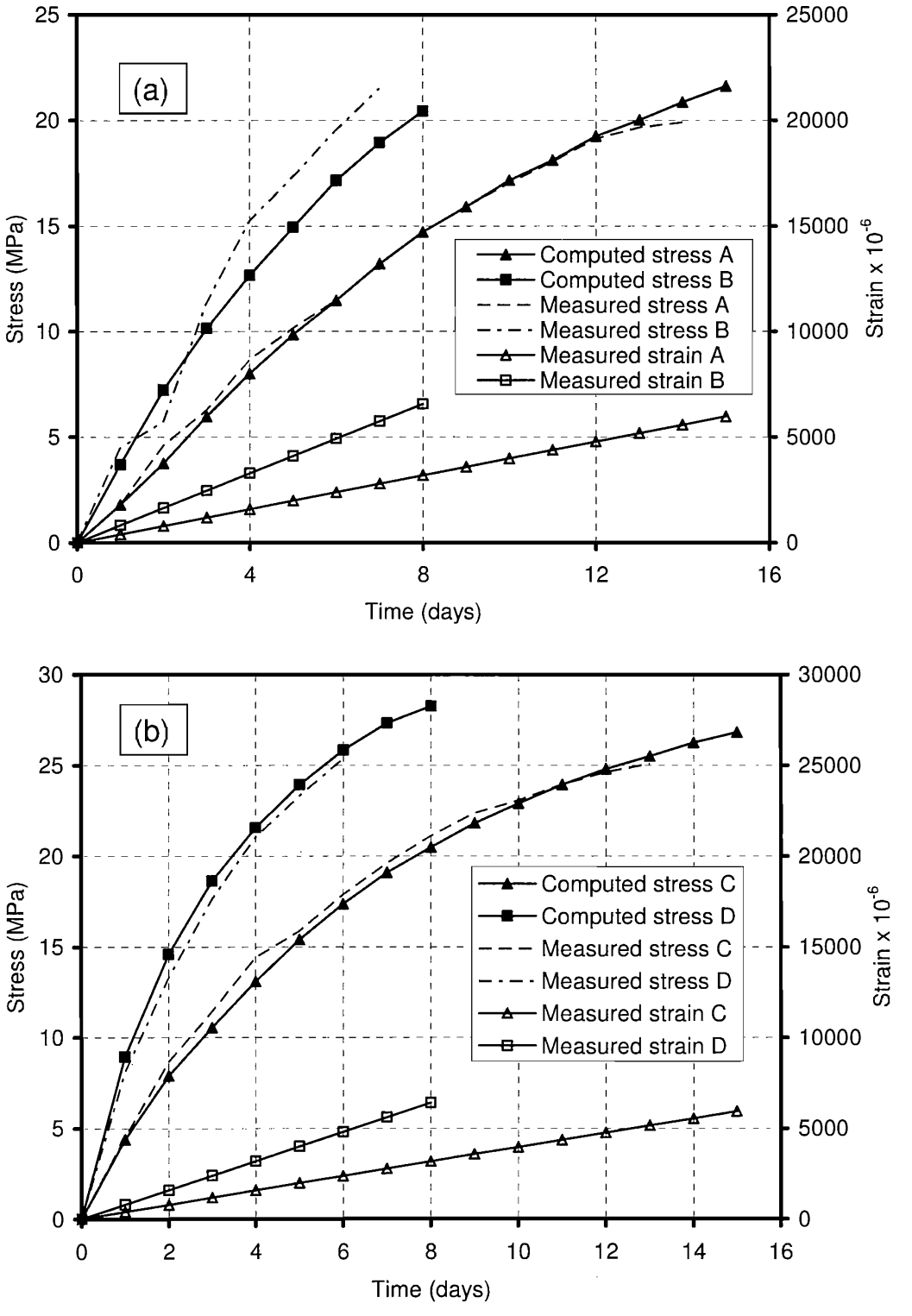

Figure 2-24: Comparison of a laboratory slow loading test on a sprayed concrete specimen and a computation using the rate of flow method, beginning at an age of (a) 1 day and (b) 14 days (redrawn from Schubert, 1988)

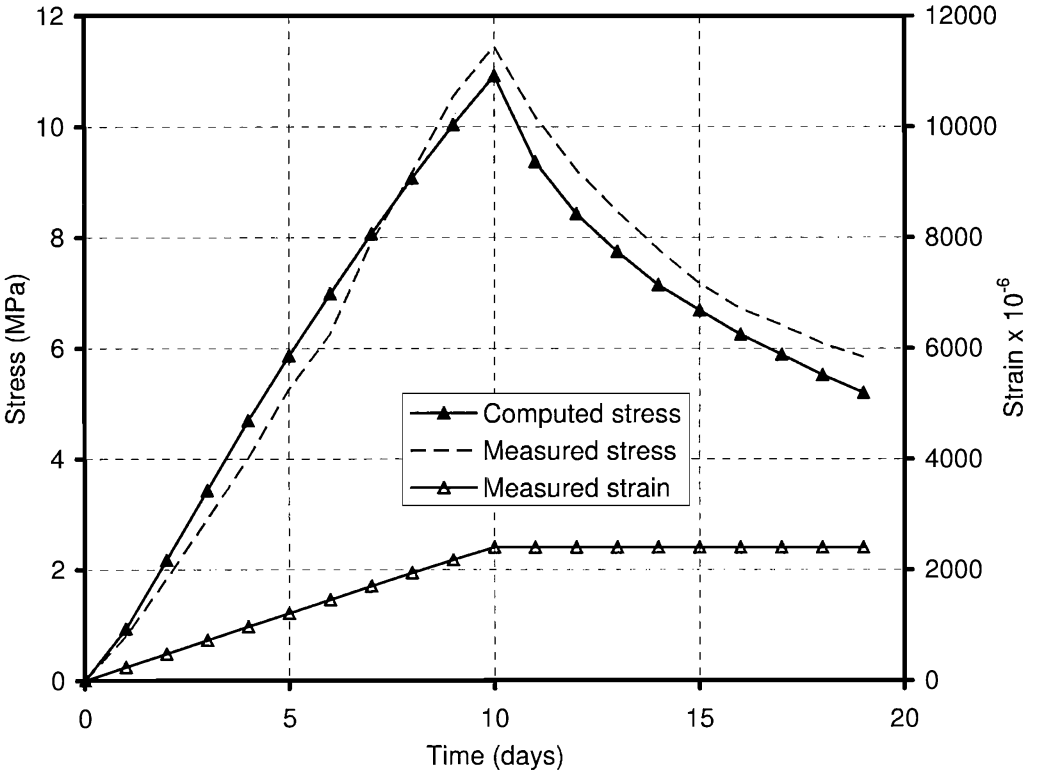

Figure 2-25: Comparison of a laboratory loading and relaxation test on a sprayed concrete specimen and a computation using the rate of flow method, beginning at an age of 1 day (redrawn from Schubert, 1988)

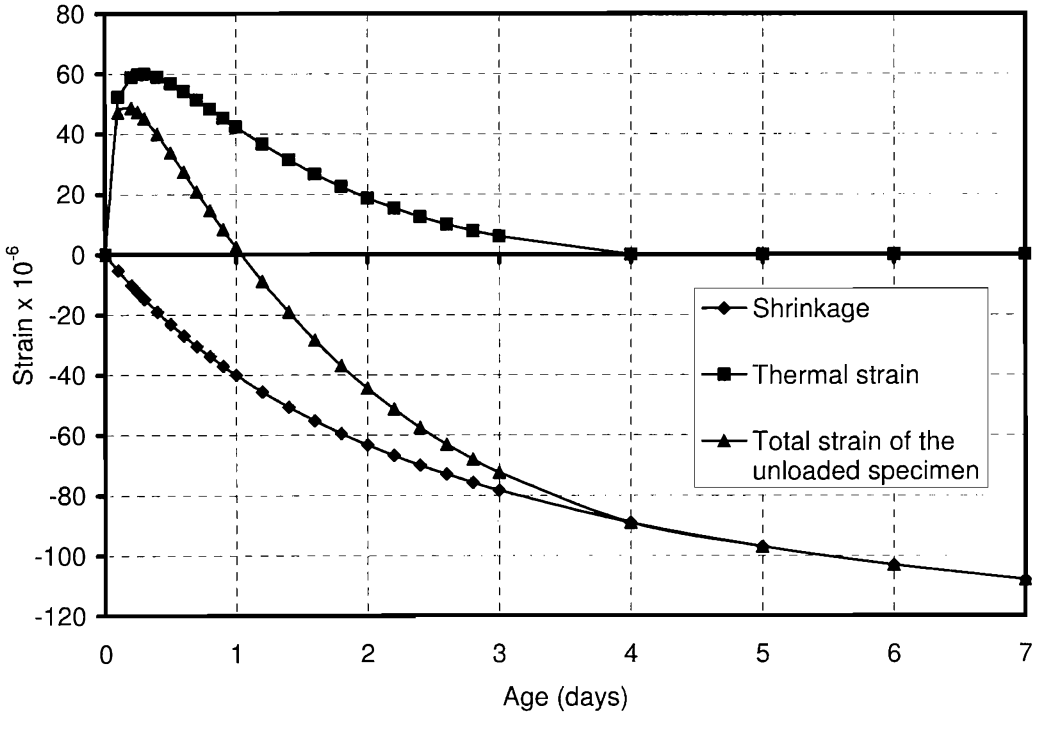

Figure 2-26: Simulation of shrinkage and temperature deformation using the rate of flow method (redrawn from Schubert, 1988)

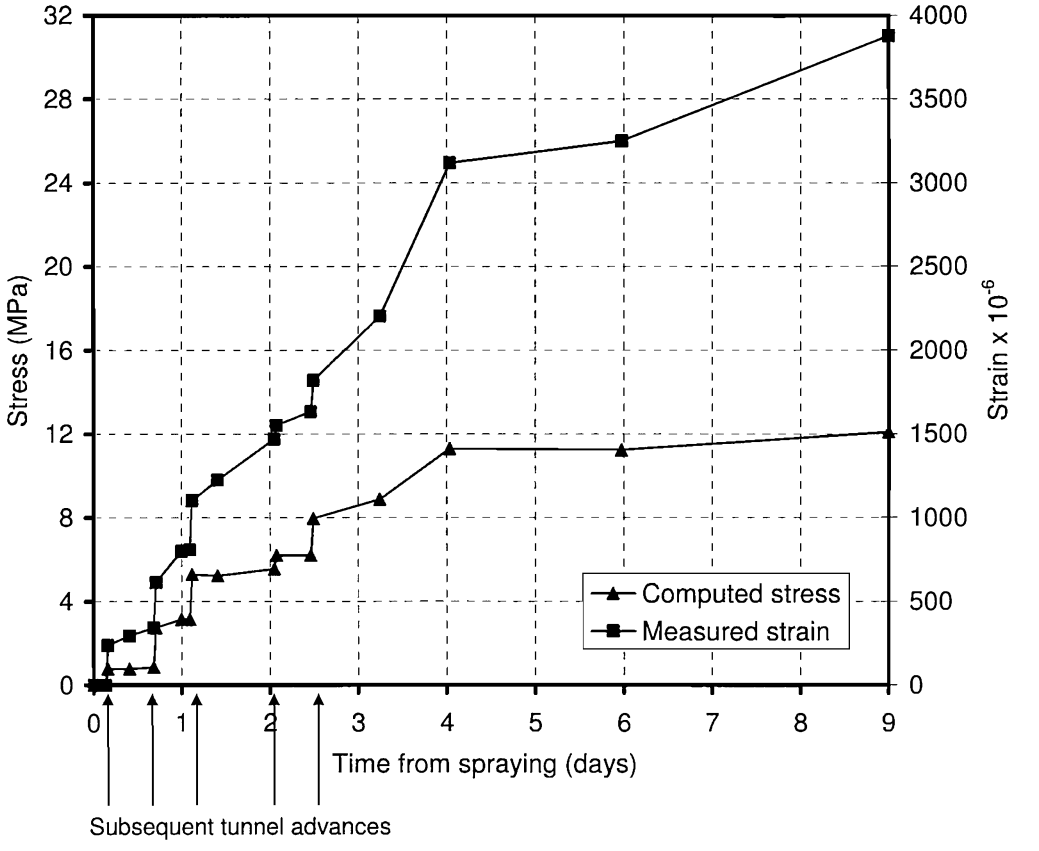

Figure 2-27: Computed stresses back-calculated from measured strain in the sprayed concrete lining of the Langen tunnel (redrawn from Schubert, 1988)

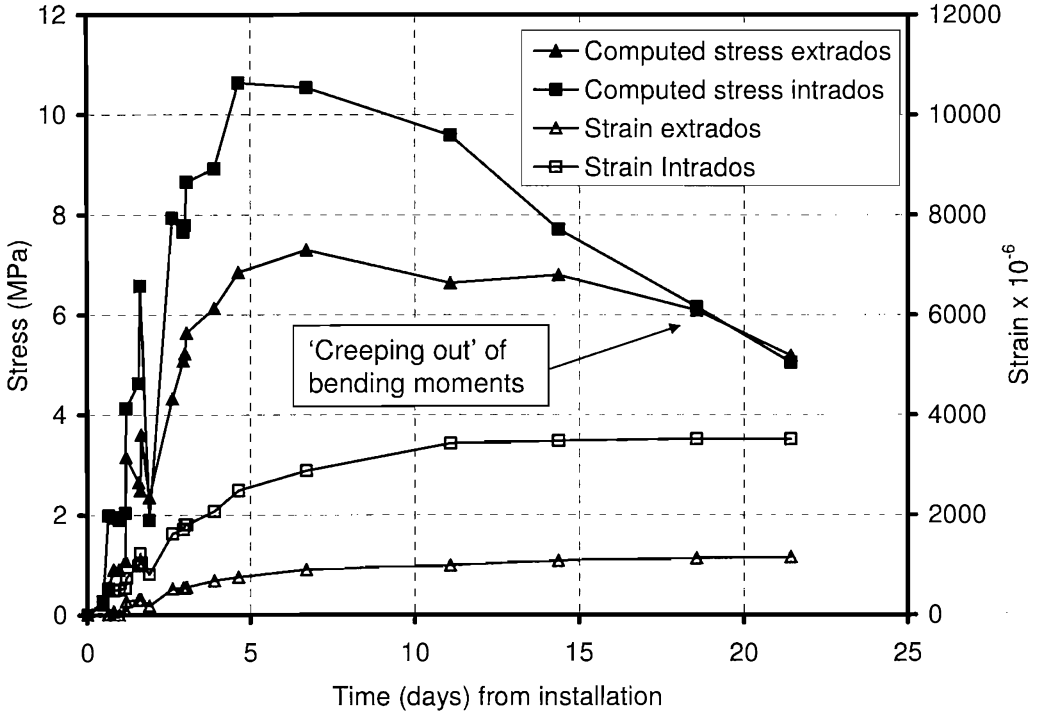

Figure 2-28: Stresses back-calculated from measured strain of a pair of strain gauges in the sprayed concrete lining of the Langen tunnel (redrawn from Schubert, 1988).

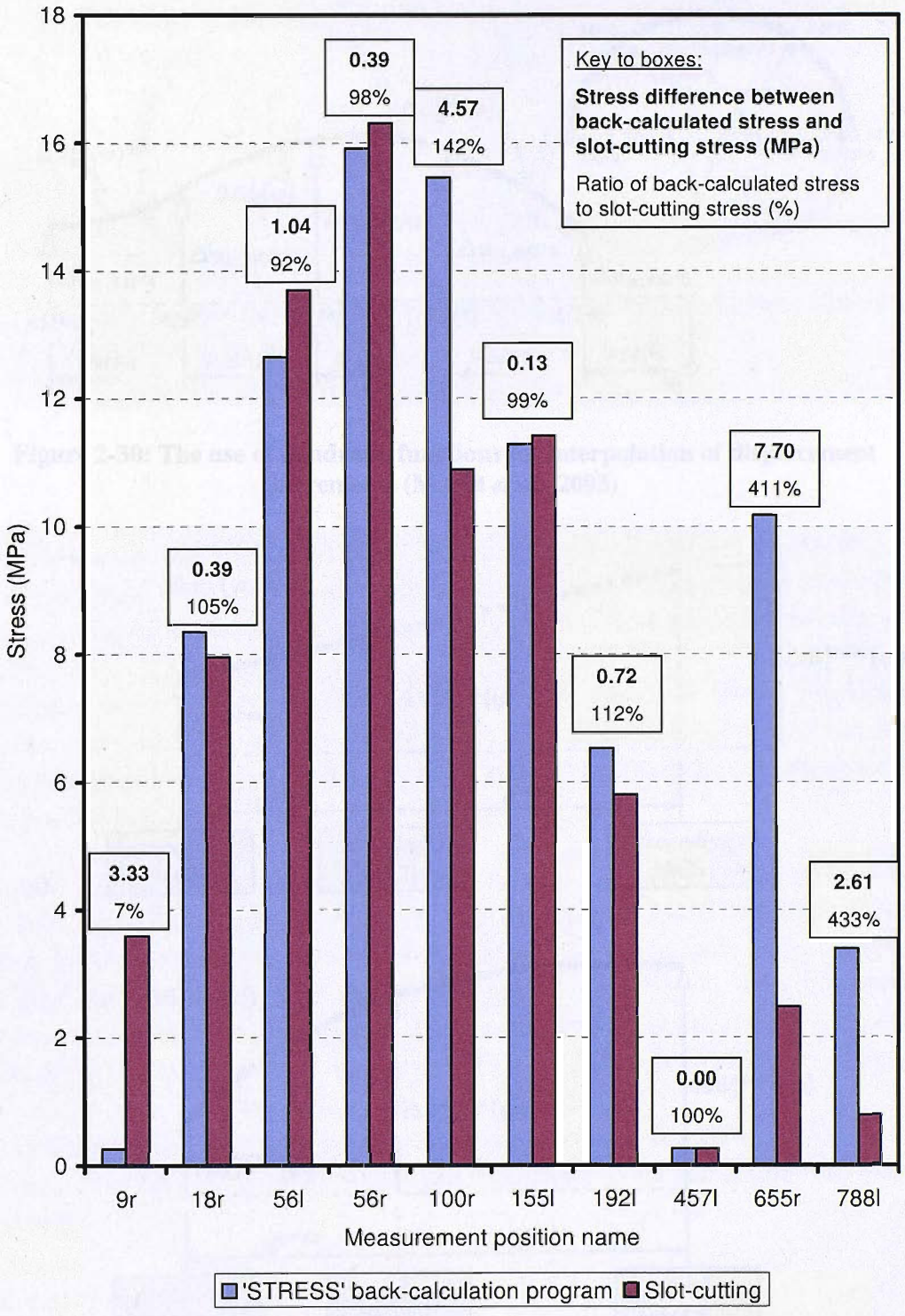

Figure 2-29: Comparison of stresses back-calculated from optical surveying by the University of Hanover 'STRESS' program and the average of flat jack stress measurements from 2 neighbouring slots; data from Rokahr & Zachow (1999).

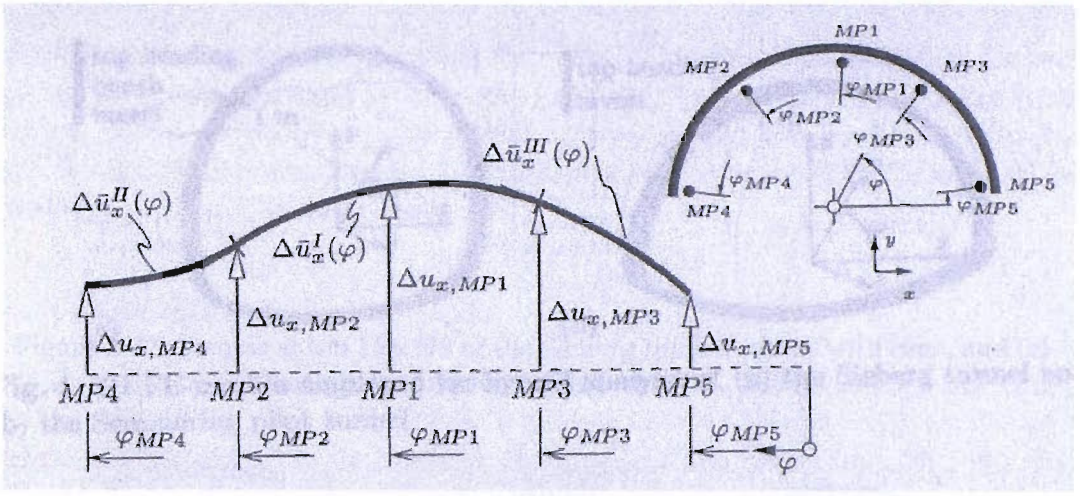

Figure 2-30: The use of quadratic functions for interpolation of displacement increments (Macht *et al.*, 2003)

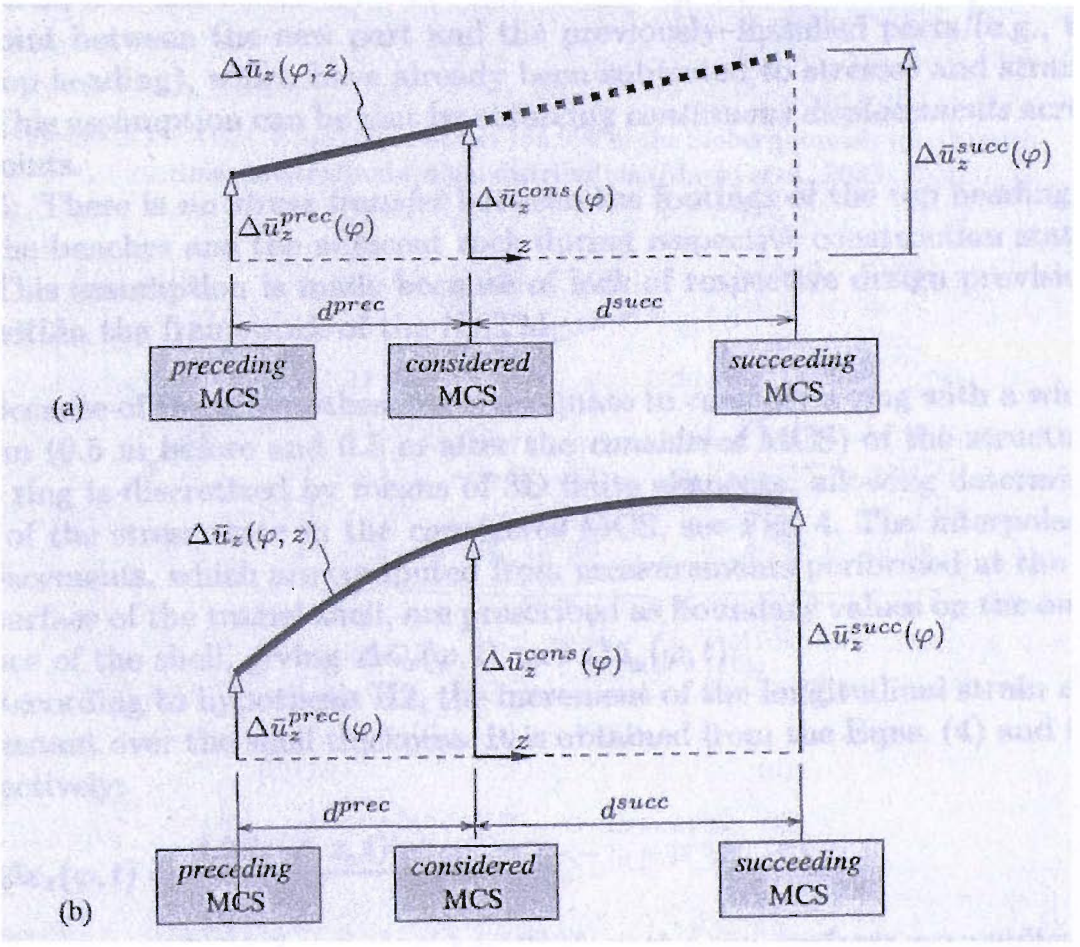

Figure 2-31: Evaluation of the incremental longitudinal displacement based on measured displacement increments at the *preceding*, the *considered* and the *succeeding* MCS (a) before installation of the *succeeding* MCS and (b) after installation of the *succeeding* MCS (Macht *et al.*, 2003)

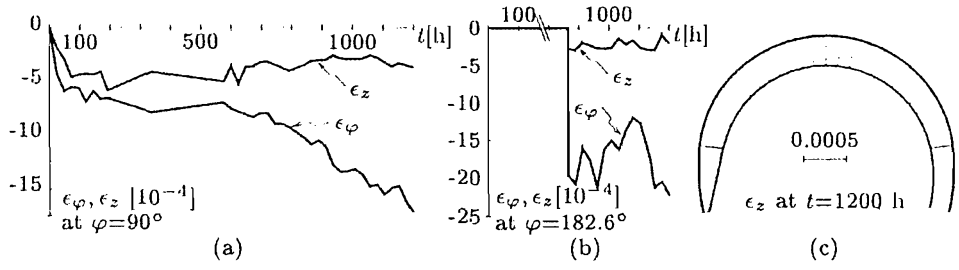

Figure 2-32: Strains at km 156.990 of the Sieberg tunnel: (a) (b) with time, and (c) final spatial distribution (Macht *et al.*, 2003)

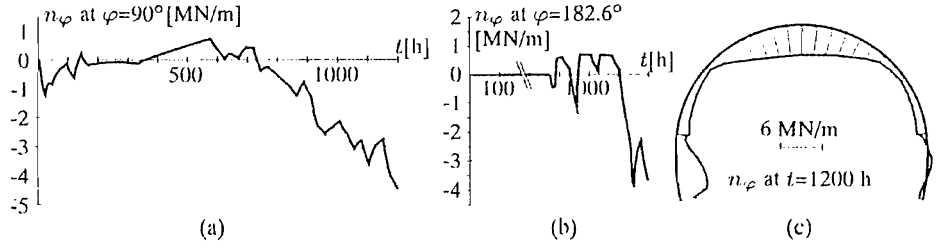

Figure 2-33: Axial (hoop) force at km 156.990 of the Sieberg tunnel: (a) (b) with time, and (c) final spatial distribution (Macht *et al.*, 2003)

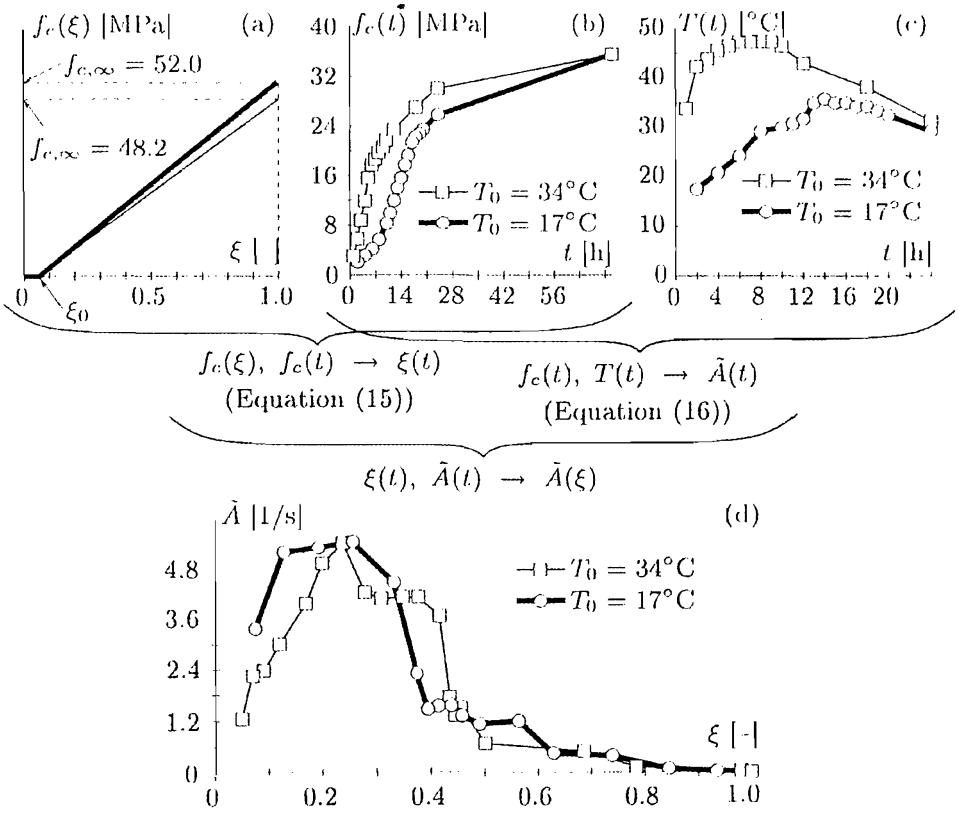

Figure 2-34: Determination of chemical affinity from strength evolution tests: (a) intrinsic material function for uniaxial compressive strength (b) compressive strength vs. time (c) temperature vs. time (d) intrinsic material function for chemical affinity (Macht *et al.*, 2003)

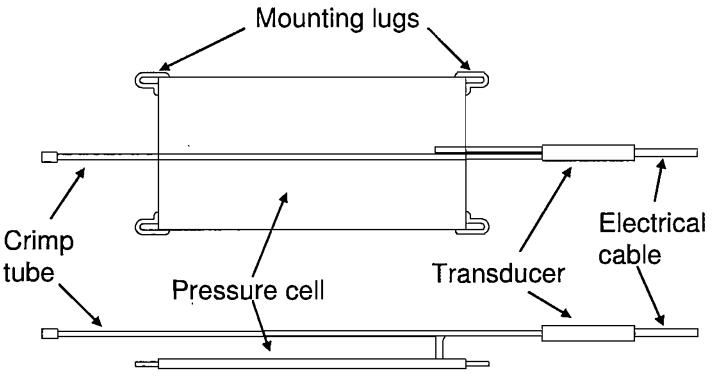

Figure 2-35: Geokon 4850 series pressure cell schematic

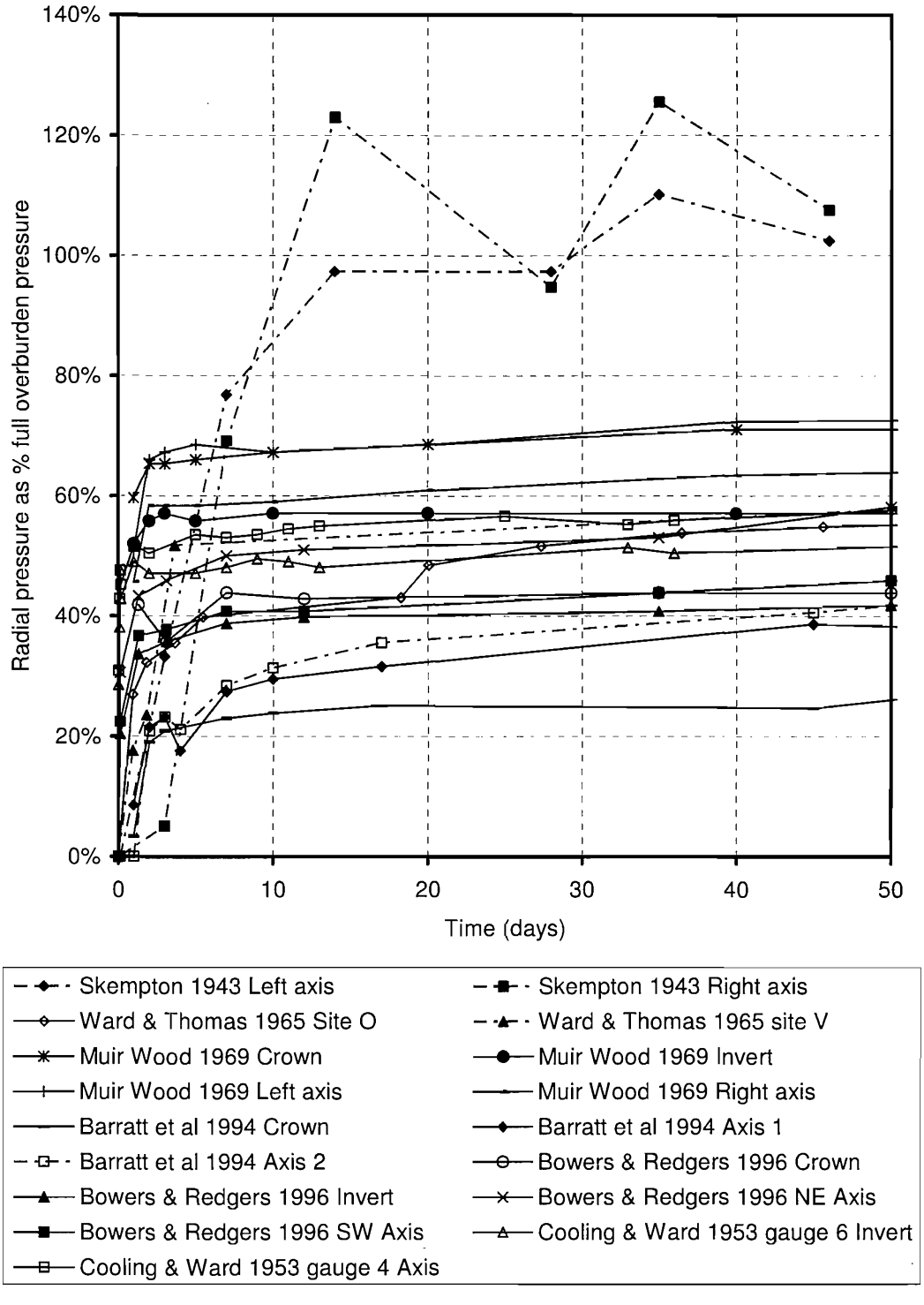

Figure 2-36: Stress measurements of tunnel linings in London Clay up to 50 days

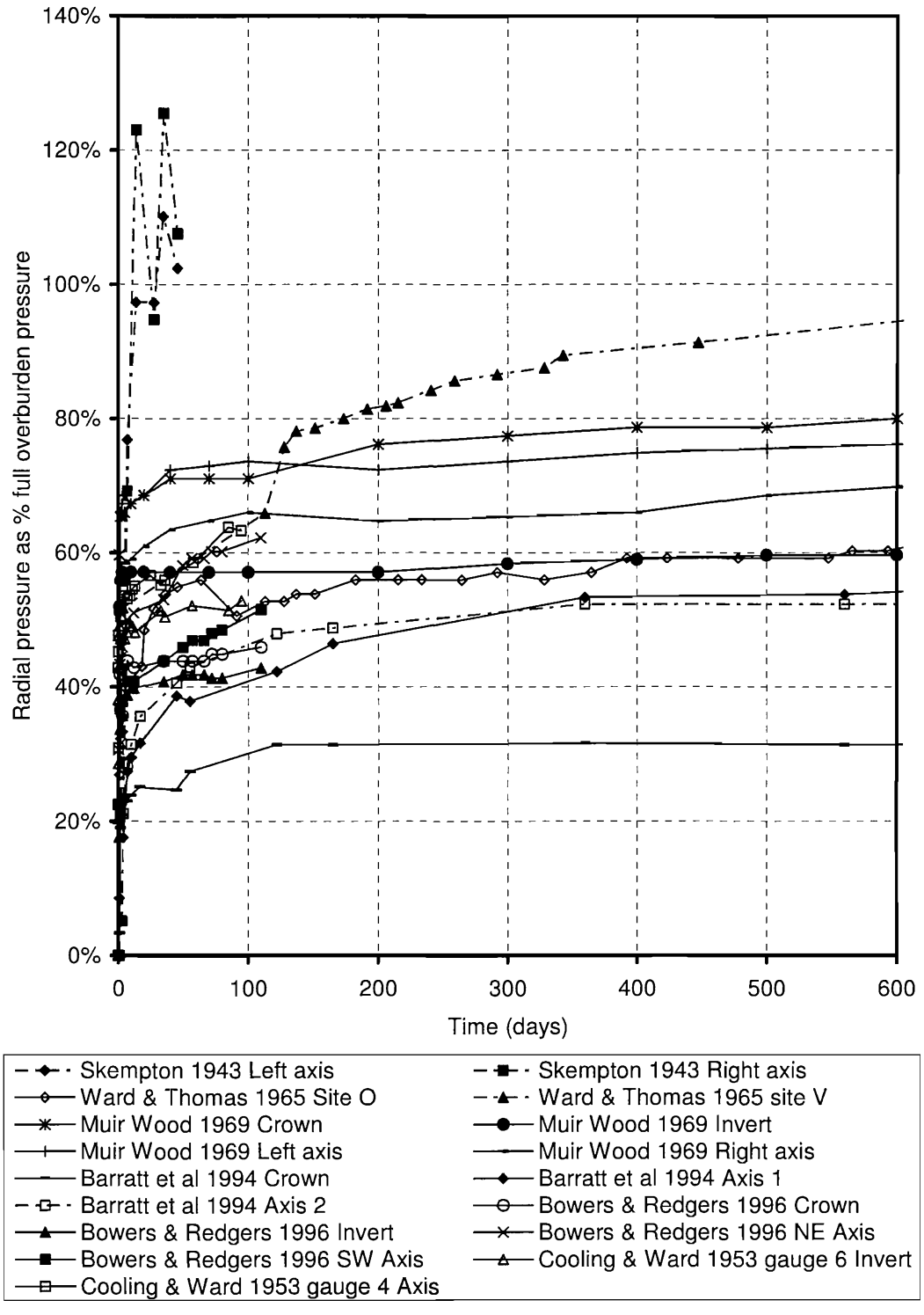

Figure 2-37: Stress measurements of tunnel linings in London Clay up to 600 days

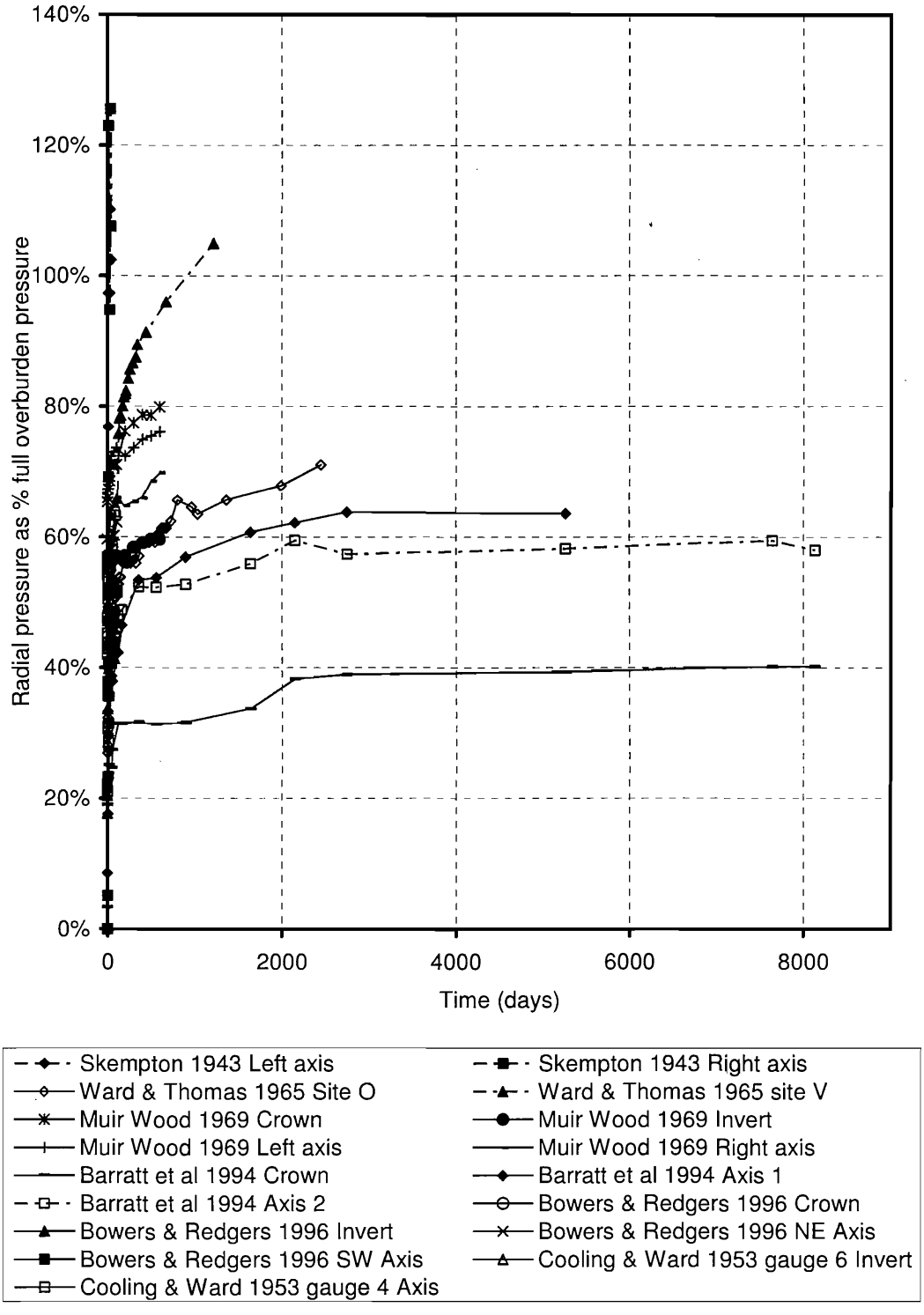

Figure 2-38: Stress measurements of tunnel linings in London Clay up to 19.5 years

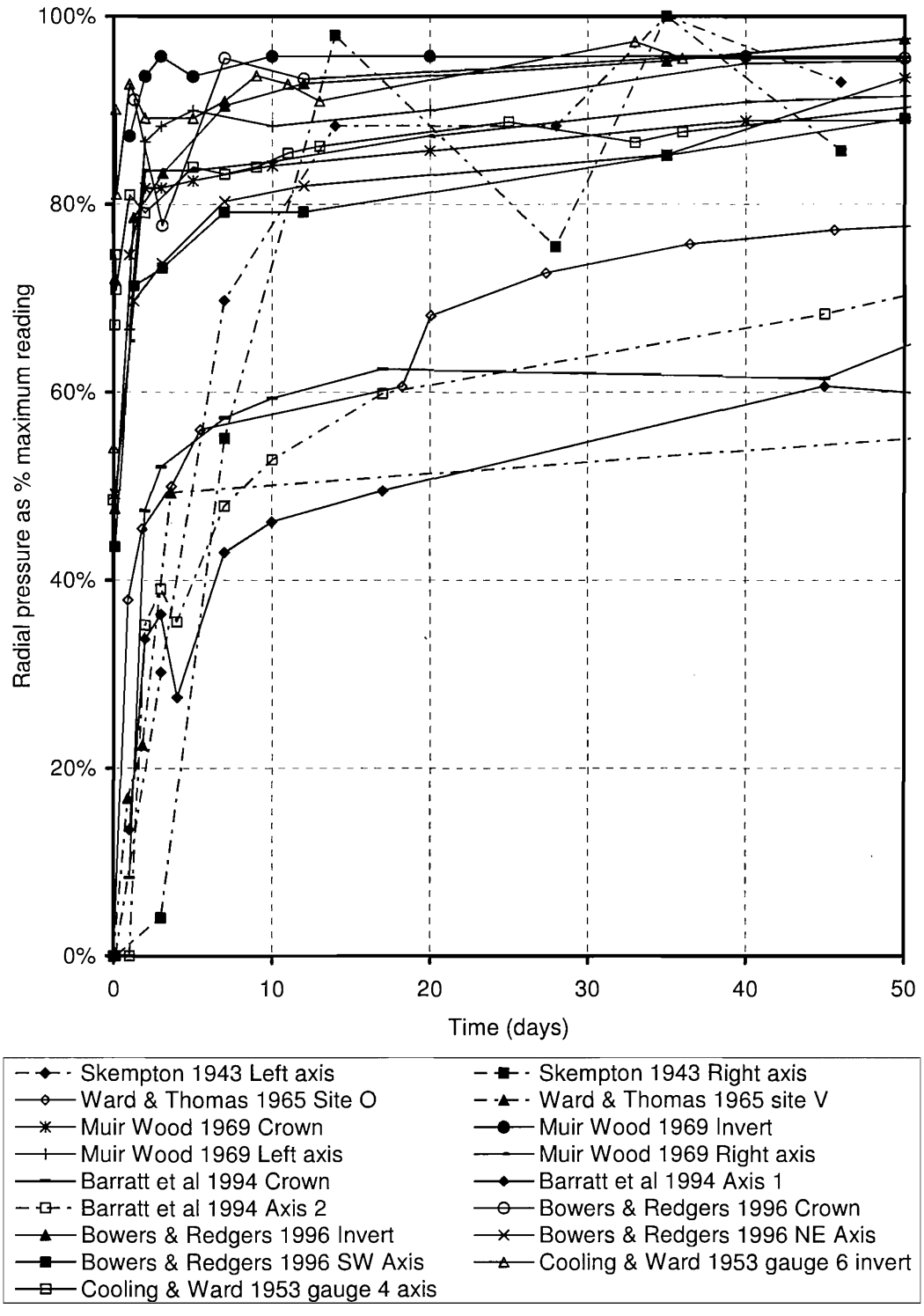

Figure 2-39: Radial pressure as a percentage of the long-term maximum radial pressure of tunnel linings in London Clay up to 50 days

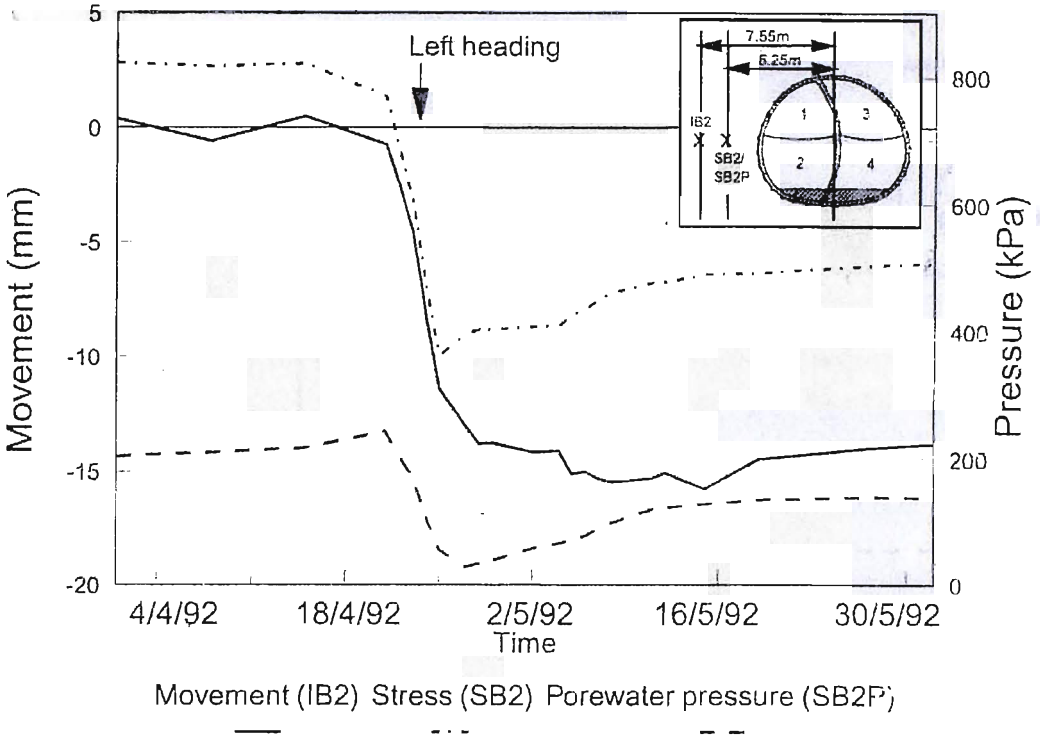

Figure 2-40: Movement, stress and pore pressure development with time as tunnel face passes (New & Bowers, 1994)

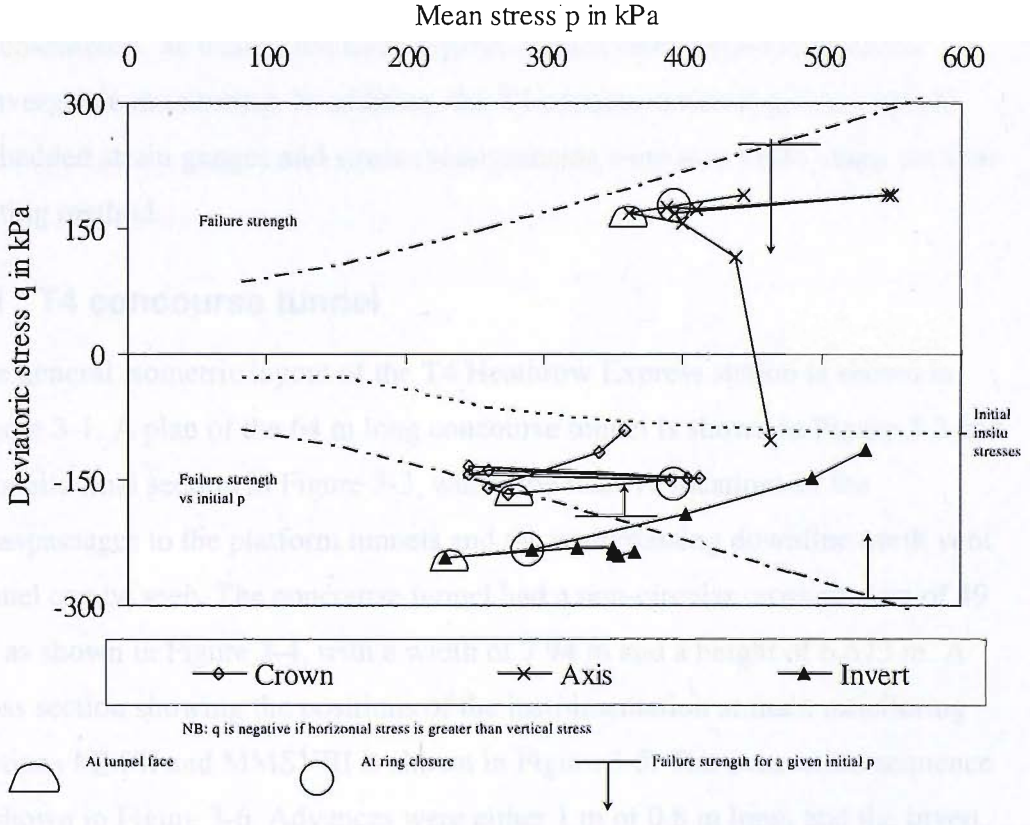

Figure 2-41: Total stress paths in the ground at crown, axis and invert of the T4 concourse tunnel (from Thomas, 2003)

3 DESCRIPTION OF THE HEATHROW TUNNELS

In this chapter the tunnels studied in this thesis are described. Their location, geometry and construction sequence are presented.

This thesis considers the behaviour of two SCL tunnels, both of which are within Heathrow Airport, London. The Heathrow Express Terminal 4 Station Concourse Tunnel (T4 concourse tunnel) was built between October and December 1996, and involved the installation of a considerable amount of instrumentation, which was described in detail by van der Berg (1999). The Terminal 5 Stormwater Outfall Tunnel (SWOT) Frontshunt Tunnel was built in February 2003 as a TBM launch chamber for the main drive. The SWOT frontshunt tunnel began from a shaft known as the 'SWOT inlet shaft' and the shaft-tunnel junction was chosen as the typical junction for the purpose of the numerical experiments in this thesis.

The field measurements from the SWOT have yet to be published, and so are included in this chapter.

Both tunnels were instrumented with pressure cells, inclinometers and extensometers, as well as the more typical surface settlement and in-tunnel convergence monitoring. In addition, the T4 concourse tunnel also contained embedded strain gauges and stress measurements were also made using the slot-cutting method.

3.1 T4 concourse tunnel

The general isometric layout of the T4 Heathrow Express station is shown in Figure 3-1. A plan of the 64 m long concourse tunnel is shown in Figure 3-2 and a longitudinal section in Figure 3-3, where the relative locations of the crosspassages to the platform tunnels and the underpassing downline north vent tunnel can be seen. The concourse tunnel had a non-circular cross-section of 49 m^2 as shown in Figure 3-4, with a width of 7.94 m and a height of 6.673 m. A cross section showing the positions of the instrumentation at main monitoring sections MMSI and MMSVIII is shown in Figure 3-5. The excavation sequence is shown in Figure 3-6. Advances were either 1 m or 0.8 m long, and the invert

was usually closed within 5 m of the face. The concourse tunnel axis was at a depth of 17.4 m below ground level.

The primary lining consisted of 350 mm thick sprayed concrete, with two layers of steel mesh reinforcement made up of 8 mm bars at 150 mm centres. The mesh had a minimum cover to the extrados of 30 mm and a minimum cover to the intrados of 60 mm. In between the two layers of mesh were full-section lattice girders of type Rom E3 at the leading edge of each advance along the tunnel. At each advance, the mesh was overlapped with the previous mesh by at least 300 mm. The primary lining was not considered the permanent support, which was provided by a cast *in situ* reinforced concrete secondary lining, therefore there were no durability concerns regarding the design of the primary lining.

The geology was similar to that at T5, with Made Ground and Terrace Gravels at the surface to a depth of approximately 2.5 m overlying London Clay to a depth of approximately 70 m.

3.2 T5 SWOT frontshunt tunnel

The 'T5 SWOT frontshunt tunnel' was a straight tunnel, 40 m long with a circular cross-section of 4.8 m external diameter. It was bored from a shaft known as the 'SWOT inlet shaft'. The structural sprayed concrete lining was 275 mm thick reinforced with 40 kg/m^3 of high carbon steel fibres, made up of a 75 mm initial layer and a 200 mm thick primary lining. To provide a smooth internal finish, this was supplemented by a 50 mm thick finishing layer of the same sprayed concrete mix, only with no steel fibres and less accelerator so that it could be trowel-finished.

A plan of the site layout is shown in Figure 3-7. The SWOT inlet shaft was constructed through the water bearing Terrace Gravels near to the surface using the caisson-sinking method and lined with segments with an internal diameter of 10.6 m until sealed into 2 m depth of London Clay. From then on, the shaft was excavated from within, and lined with a sprayed concrete primary lining 350 mm thick. A section through the lower part of the shaft showing the first stages of the SWOT frontshunt tunnel construction is shown in Figure 3-8. The sprayed concrete lining was locally thickened to up to 800 mm and layers of bar reinforcement added in the vicinity of the opening for the frontshunt tunnel.

The LaserShell method, described in detail in Williams *et al.* (2004), removed the need for lattice girders to control shape and mesh for reinforcement. This in turn removed the need for operatives to enter the face area of the tunnel, eliminating the risk of injuries from block falls. The face was also slanted at an angle of approximately 70° to the horizontal. This in effect provided a protective canopy over any operatives working close to the face, for example when cleaning the invert before spraying.

The tunnel excavation began at the SWOT inlet shaft at a depth of 11.8 m to the tunnel axis level. The locations of the surface settlement levelling points and the borehole inclinometers and extensometers are shown in Figure 3-7. The plan locations of the pressure cell arrays are shown in Figure 3-9.

3.2.1 Surface settlement levelling points

The grid pattern of settlement points for the tunnel was extensive; it included 97 points (Figure 3-7). Two arrays were installed adjacent to the shaft and ten arrays of points were installed across the tunnel axis. The spacing of the settlement points was generally 7 m in the longitudinal direction (spacing between each transverse array) and 5 m in the transverse direction (spacing between the points in a transverse array). Settlements at the end of shaft construction were subtracted from total observed settlements to show the effect of tunnel construction.

Surface settlements when the face was directly under each transverse array 1-6 are shown in Figure 3-10. With the exception of Array 1, these suggest a typically Gaussian settlement curve. As the tunnel moved further from the shaft settlements increased and by the time the face was under Array 3, about 15 m or 3 tunnel diameters from the shaft, the settlements, with the exception of certain outlying points, stopped increasing. This suggested that the presence of the shaft no longer had a significant influence on the settlements due to tunnel construction from Array 3 onwards.

The settlement trough for Array 3 had an unexpectedly large surface settlement 5 m to the left of the tunnel centreline, Array 4 had a larger settlement over the tunnel centreline than the other arrays and Array 5 had an unexpectedly large settlement 15 m to the right of the tunnel centreline. This phenomenon is also

evident in Figure 3-11, which shows the surface settlement at the same locations 2 weeks after construction of the frontshunt tunnel had finished. This suggests either a weaker zone of ground running obliquely over the tunnel from north to south to cross the centreline at Array 4, or a surcharge loading. No evidence of a tectonic shear zone in the London Clay was visible in the tunnel face during construction, so this effect could have been caused by either the collapse of buried services, poor surveying, or the traffic of cranes and muck lorries over these locations. The plan in Figure 3-7 shows that these points lay in the site road, so heavy traffic causing additional settlement would seem the most likely explanation.

The centreline settlements are shown in longitudinal section in Figure 3-12 and summarised in Table 3-1. The 'indicative settlement' marked on Figure 3-12 is a line drawn through the centreline settlements, ignoring the anomalous centreline settlement in Array 4. Figure 3-12 and Table 3-1 show that ahead of the face, even at 5 m distance from the face, very little surface settlement was observed. The 'steady-state' maximum settlement, ignoring the local effect that caused an anomalous reading at Array 4, was approximately 8 mm. The percentage of the maximum settlement 2 weeks after the end of construction occurring ahead of the face for Arrays 3 to 6 is shown in Table 3-1. Array 6 had the greatest value because the tunnel ended only 4 m beyond the array. The typical 'steady-state' value of settlement ahead of the face for continuous tunnelling was therefore around 45 % of the maximum settlement 2 weeks after the end of construction.

Table 3-1: Observed centreline settlements (in mm) over the frontshunt tunnel

	Observed surface settlement (mm)					
Array	1	2	3	4	5	6
Face at -5 m	N/A	-0.67	0.83	1.56	2.14	1.73
Face under array	-0.78	-	3.50	6.92	3.92	3.48
Face at +5 m	-	-	6.29	9.33	6.76	N/A
2 weeks after the end of construction	4.00	7.03	8.06	16.28	8.12	6.61
Settlement occurring ahead of the face (%)	-	-	43 %	43 %	48 %	53 %

The design prediction of surface settlements used the empirical method based on a Gaussian curve. The volume loss was assumed to be 1.1 % and a trough width parameter k of 0.45 was used. This value of volume loss was based on an upper bound of volume losses measured during the construction of previous SCL tunnels in London Clay at Heathrow, in particular the Heathrow Express tunnels, and is shown in Figure 3-13. The SWOT frontshunt tunnel had a considerably lower volume loss than this, and Figure 3-13 shows that a curve based on a volume loss of 0.63 % and a trough width parameter of 0.5 fits the data better, at least in terms of the maximum settlement over the centreline. However, the trough width appears to be wider than the Gaussian curve predicts. Indeed, the volume losses calculated by direct trapezoidal integration of the settlement data were 0.97 %, 1.09 % and 1.10 % for Arrays 3, 4 and 5 respectively. To match these volume losses with a maximum settlement of 8 mm would require a trough width parameter of between 0.8 and 0.9. The width of the trough may have been caused by ongoing local consolidation settlements; before construction began at least 1 m of fill was placed over the whole site.

3.2.2 Inclinometers and extensometers

2 inclinometer boreholes and 5 combined inclinometer and extensometer boreholes were installed in the positions shown in Figure 3-7. Interpretation of

the results implicitly assumed that the top of the instrument casing did not move horizontally, because the total station surveying of the top of the instrument casing was too inaccurate to be of use. In addition, translations and rotations of the whole inclinometer were not recorded because only relative movements could be measured. The extensometer data was adjusted according to the settlement of the top of the instrument casing measured by precise levelling.

Readings from inclinometer 48 are shown in Figure 3-14. Very little movement occurred until the tunnel face was less than 4 m from the inclinometer. The recorded movements before this were indicative of the accuracy of the inclinometer, and were generally within ± 2 mm of the baseline at the bottom of the borehole; similar to the accuracy reported by van der Berg *et al.* (2003). The maximum horizontal movement was 12 mm when the last reading was taken and the face was 0.9 m from the inclinometer.

Inclinometers 44 and 46, offset 6 m from the tunnel centreline, measured very little horizontal movement in the ground; less than the accuracy of the instrument. Similarly, the readings from extensometer 43 on the tunnel centreline showed very little movement while the tunnel approached the instrument, again, less than the accuracy of the instrument.

Figure 3-15 shows the vertical movements measured by extensometer 44, 6 m offset from the tunnel centreline. In this case, the extensometer could be continuously read as the tunnel passed and vertical movements were greater than those measured by extensometer 43. The deepest magnets A and B showed no discernible movement. Magnet C, located at about the same level as the tunnel axis, showed a downwards vertical movement, as did magnets D and E between the tunnel crown level and the surface. The repeatability of the extensometers measured when the tunnel face was too far away to influence the readings was of the order of ± 2 mm.

3.2.3 Convergence monitoring

Conventional monitoring of the lining was achieved using the 3D optical surveying technique to measure convergence of the lining. 7 arrays were installed approximately 5 m apart, each with 5 convergence targets (left knee, left shoulder, crown, right shoulder and right knee). Measurements made at Array 1,

5 m from the opening in the shaft, are shown in Figure 3-16. During the driving of the tunnel there were continual problems with the placing of the targets and many targets were damaged and had to be replaced. This resulted in a large amount of lost information. In general, measurements in the frontshunt tunnel showed noise of ± 3-4 mm. as can be seen in Figure 3-16. This is worse than is typical for this method of surveying under these conditions (Clayton *et al.*, 2006; Bock, 2003), which is ± 1 mm at best and typically ± 2-3 mm.

3.2.4 Summary

The SWOT frontshunt was constructed using an innovative SCL method. To provide assurance of the suitability of this method, it was investigated during construction by installing an extensive array of instrumentation in and around the tunnel to record the behaviour of the tunnel and the ground.

In general the pattern of behaviour of the ground was consistent with observations of other SCL tunnels in London Clay. The performance of the tunnelling method in controlling ground movements, with a volume loss of 0.63 %, was at the lower end of the range of previous experiences of SCL tunnelling in London Clay. For instance, the Heathrow Express T4 Station Platform tunnels brought about volume losses between 0.6 and 1.2 %, with an average of 0.9 % (Powell *et al.*, 1997). The deformations of both the ground and the lining were small and stabilised quickly. The tight control of deformations was mainly achieved by the relatively early ring closure in the full-face excavation.

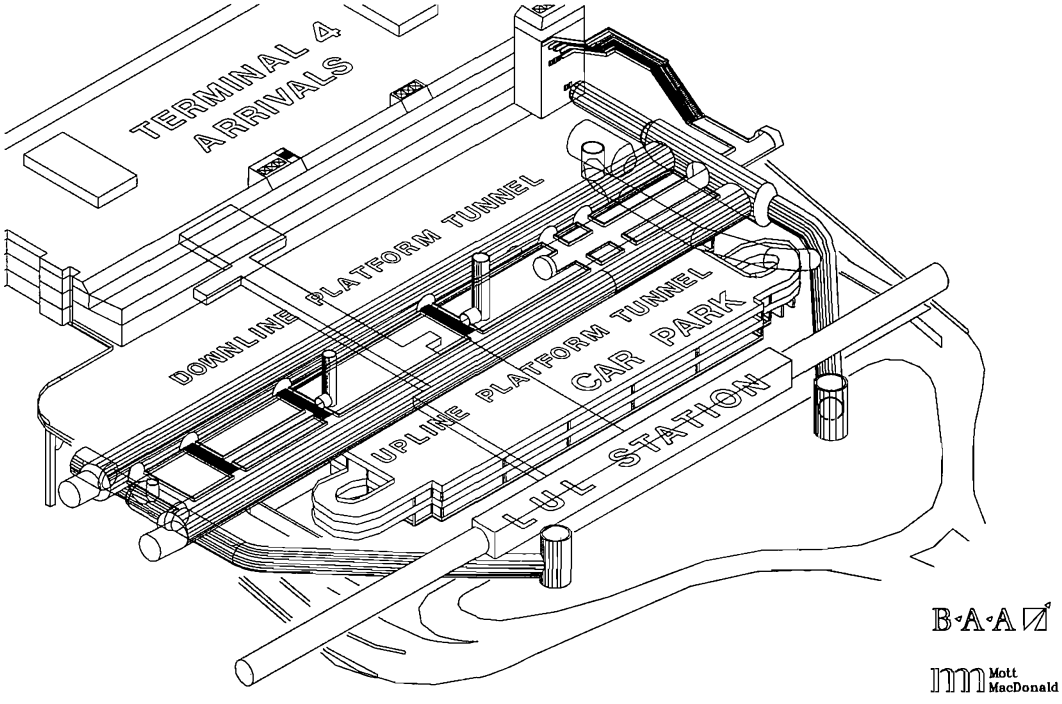

Figure 3-1: Isometric view of the Terminal 4 Station

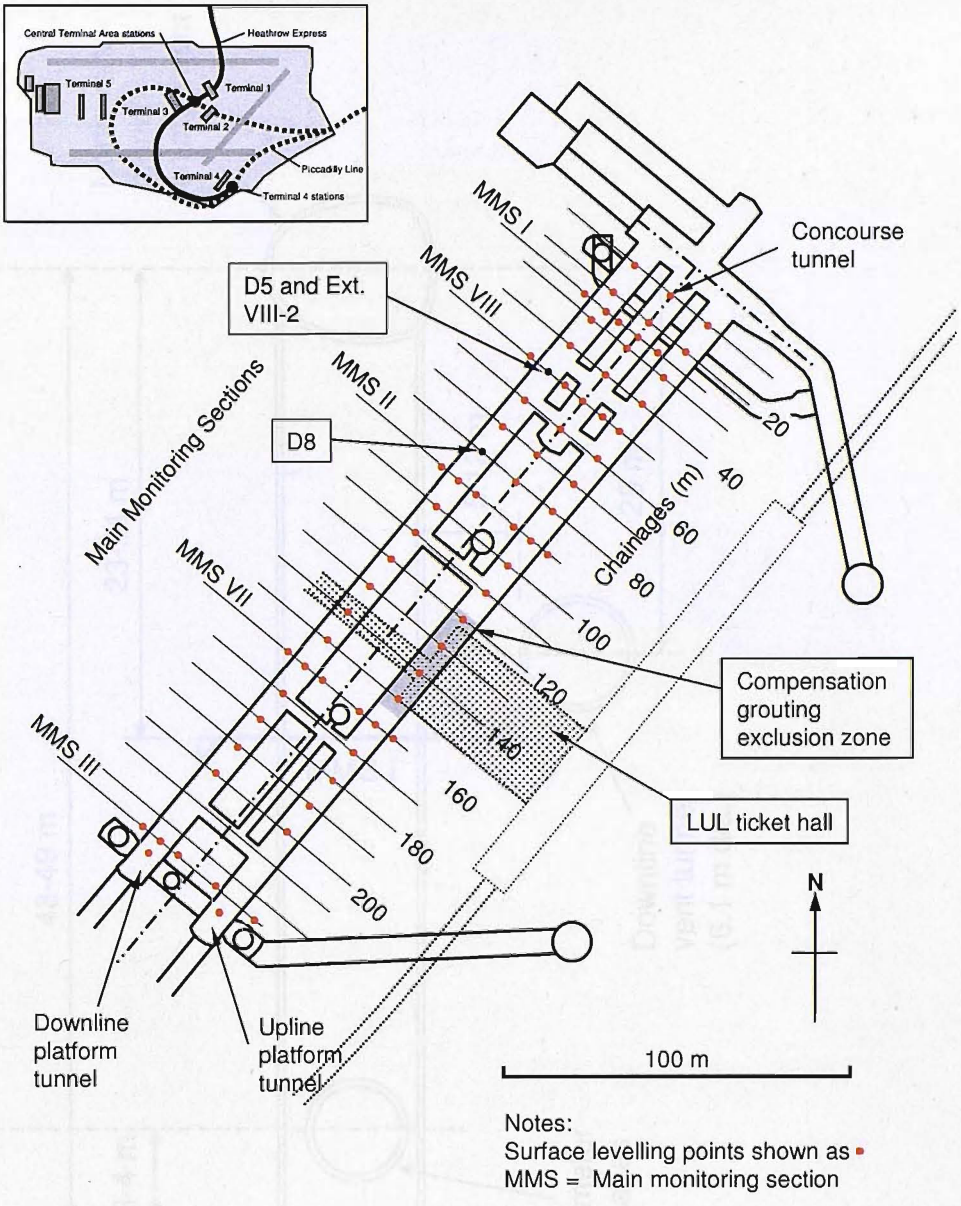

Figure 3-2: Plan view of T4 Concourse tunnel showing monitoring positions (from Clayton *et al.*, 2006)

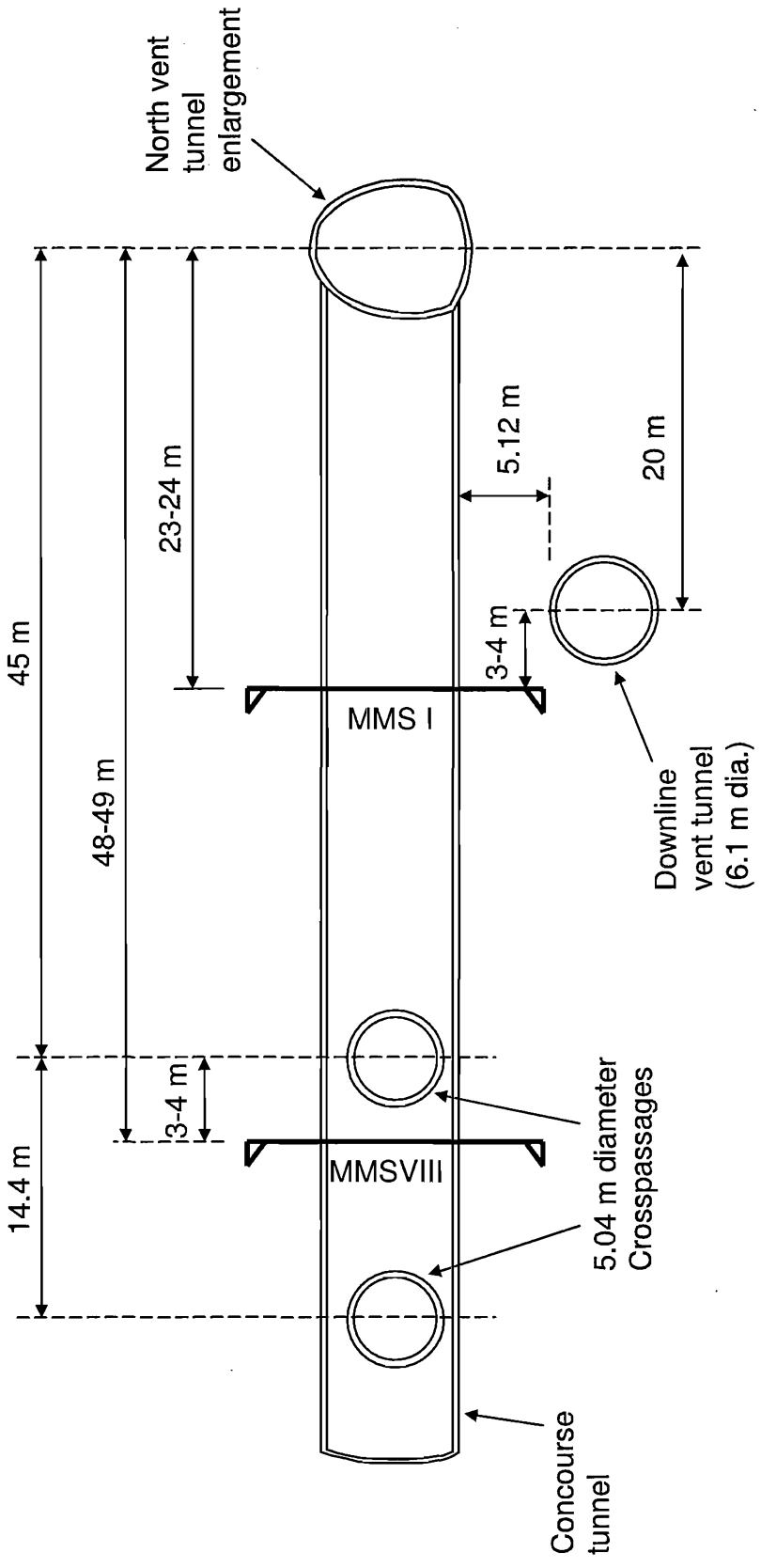

Figure 3-3: Long section of T4 concourse tunnel

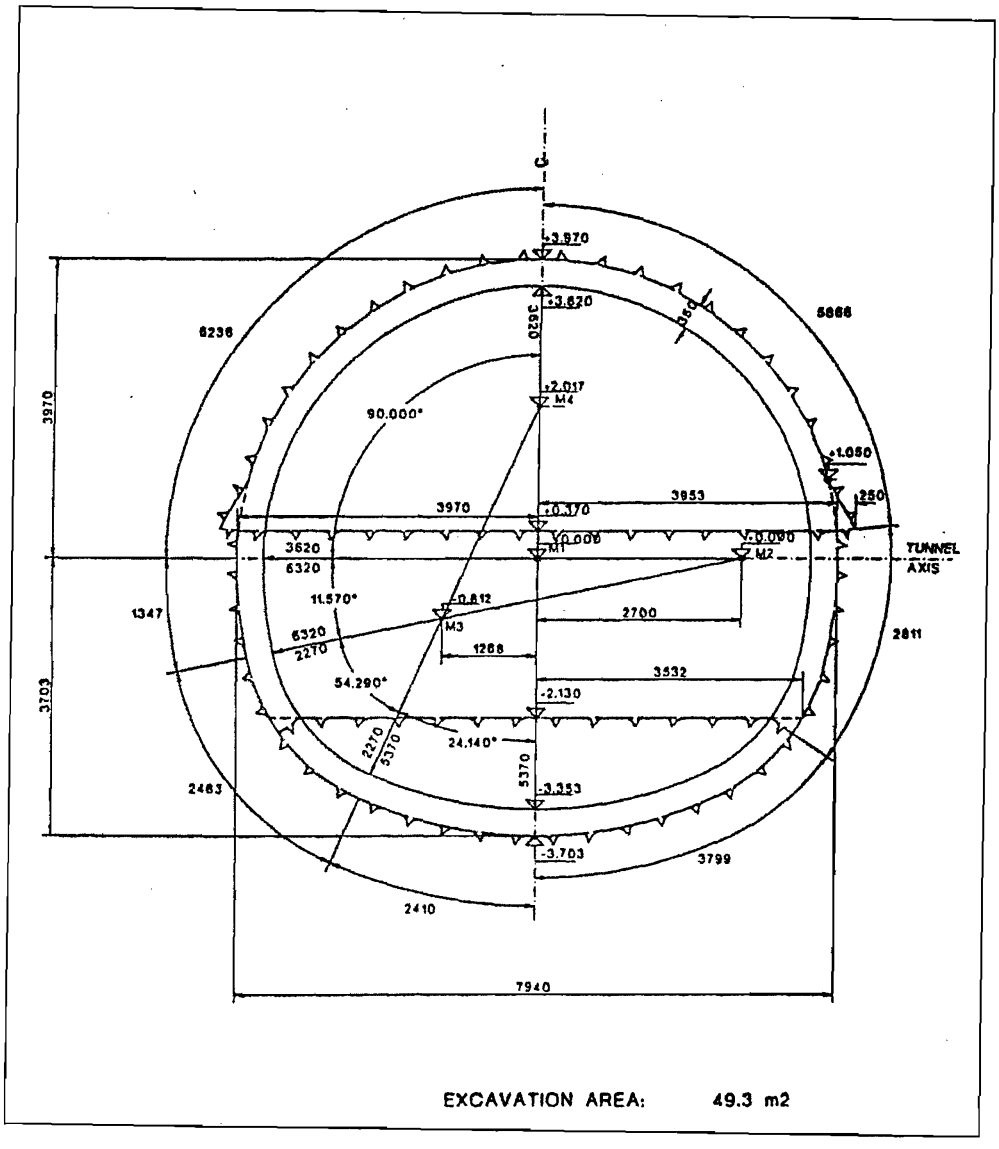

Figure 3-4: T4 concourse tunnel cross-section with dimensions

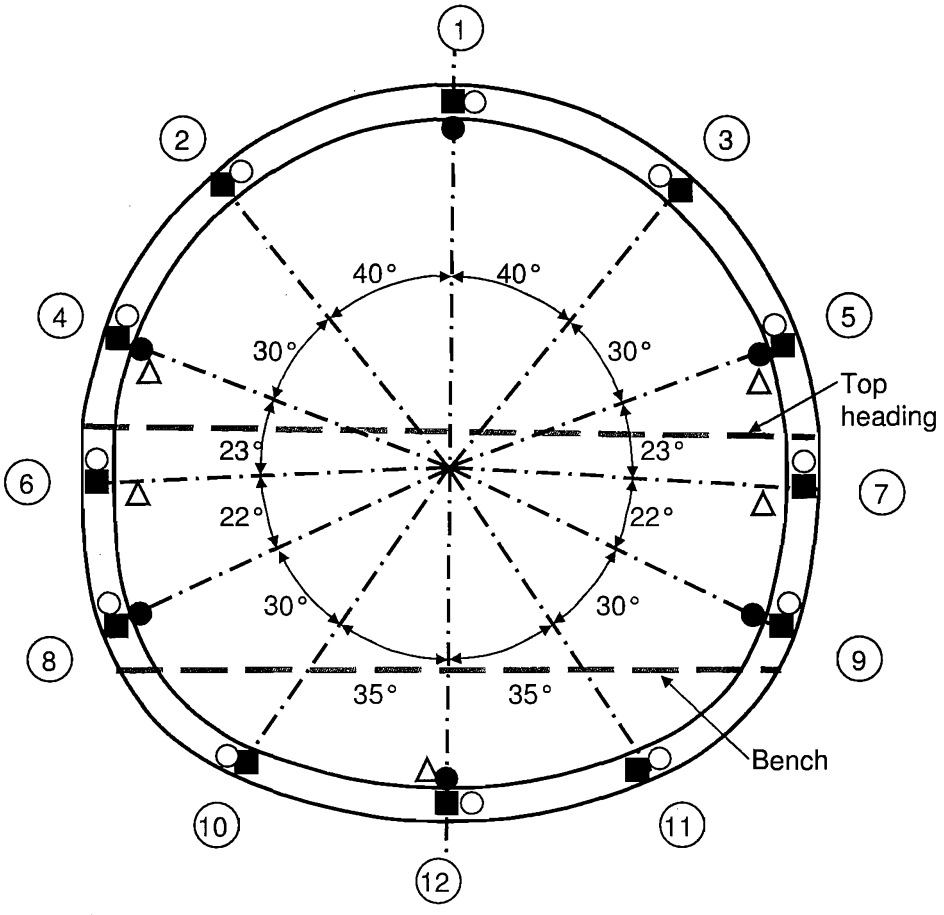

● Convergence bolt

○ Pair of embedded vibrating wire strain gauges

■ Tangential and radial pressure cells

△ Slot-cutting (displaced 1m longitudinally)

(#) Location reference no. (e.g. radial pressure cell = PCR#)

Figure 3-5: Section of T4 concourse tunnel at Main Monitoring Sections MMSI and MMSVIII showing locations of instrumentation

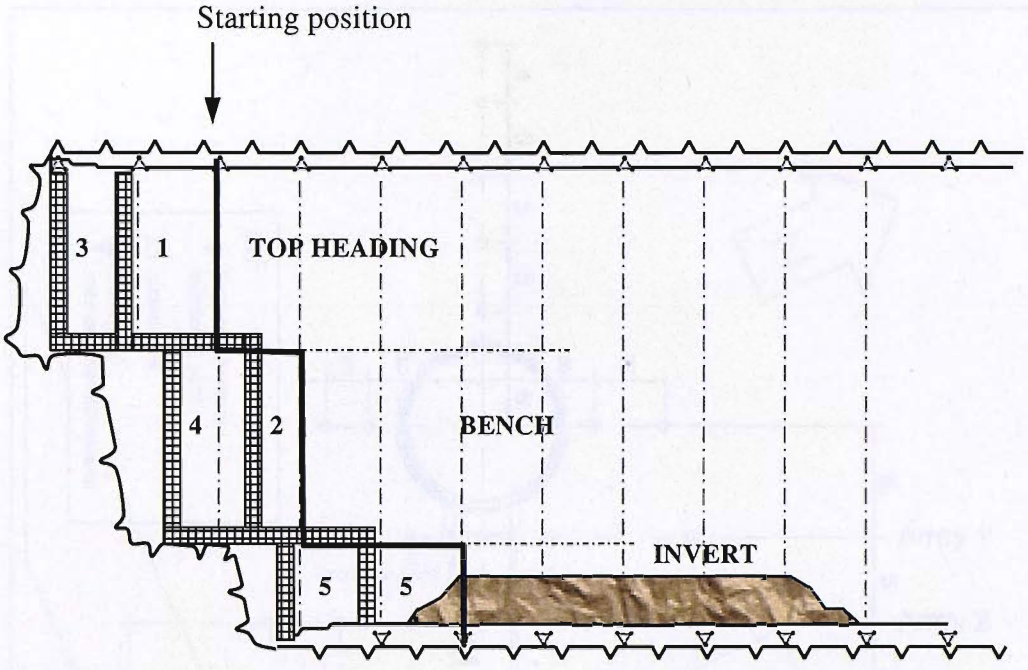

Figure 3-6: Excavation sequence for T4 concourse tunnel (from Thomas, 2003)

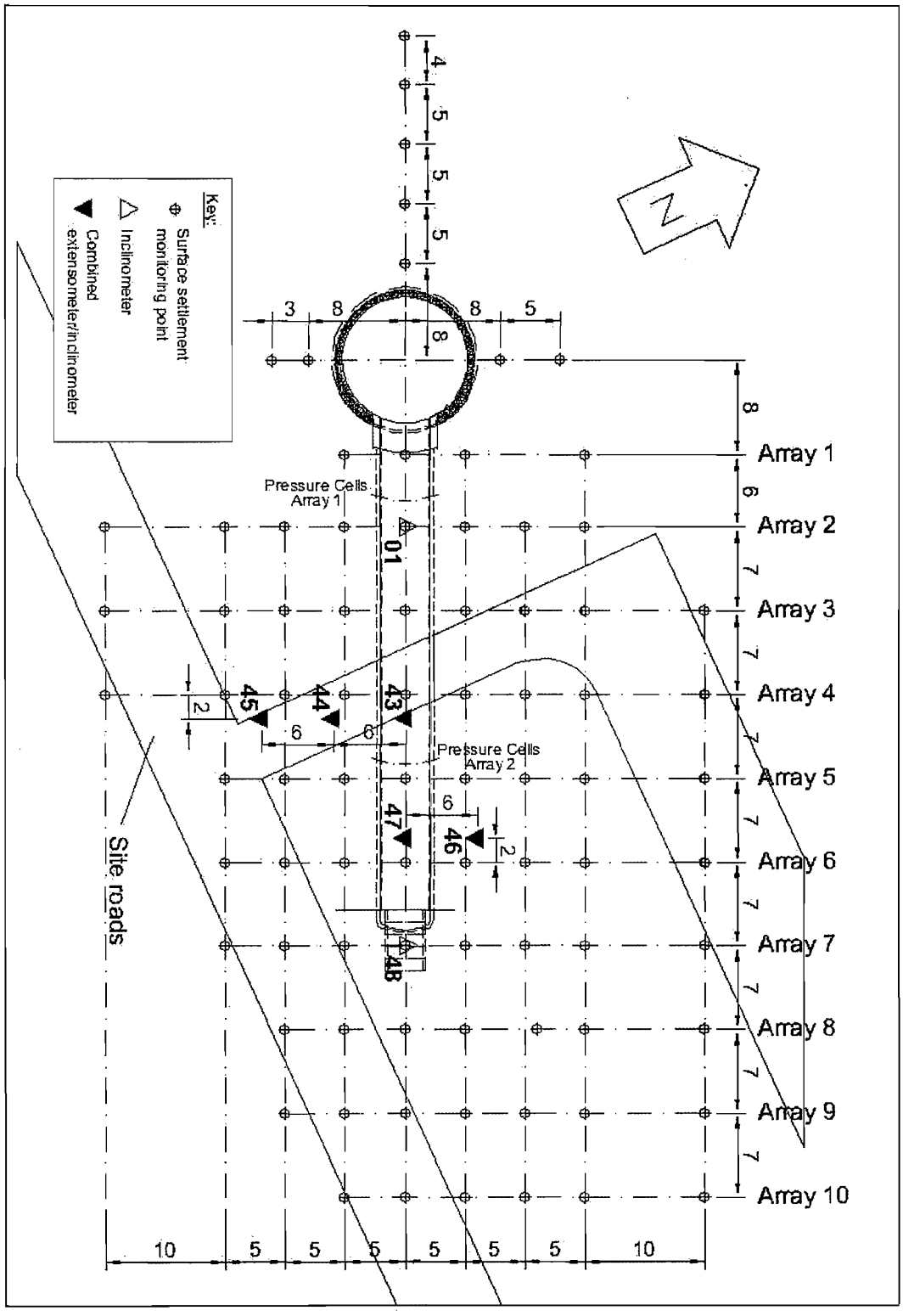

Figure 3-7: Plan of T5 SWOT frontshunt tunnel showing site layout and location of instrumentation

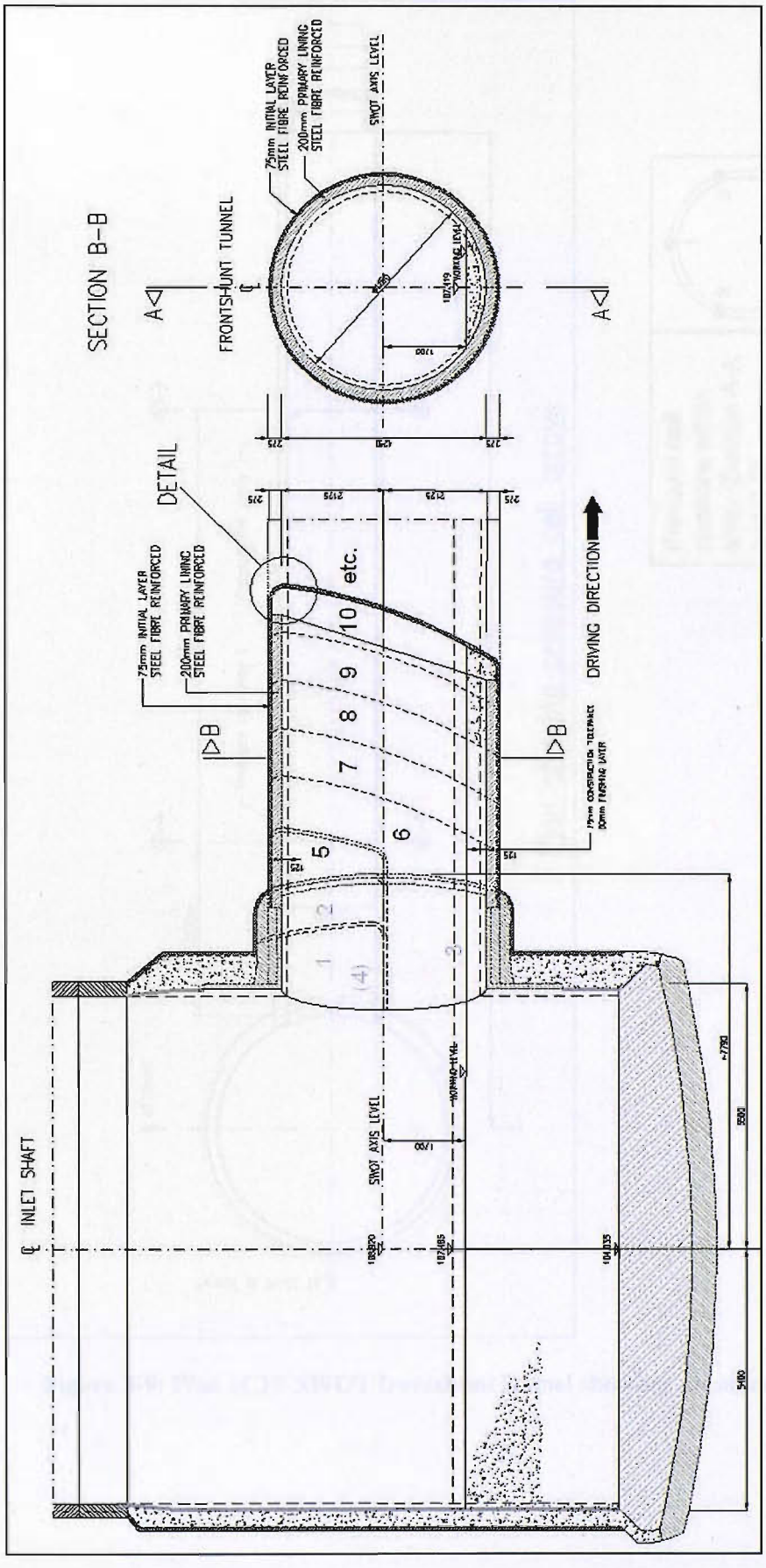

Figure 3-8: Section of T5 SWOT inlet shaft and frontshunt tunnel

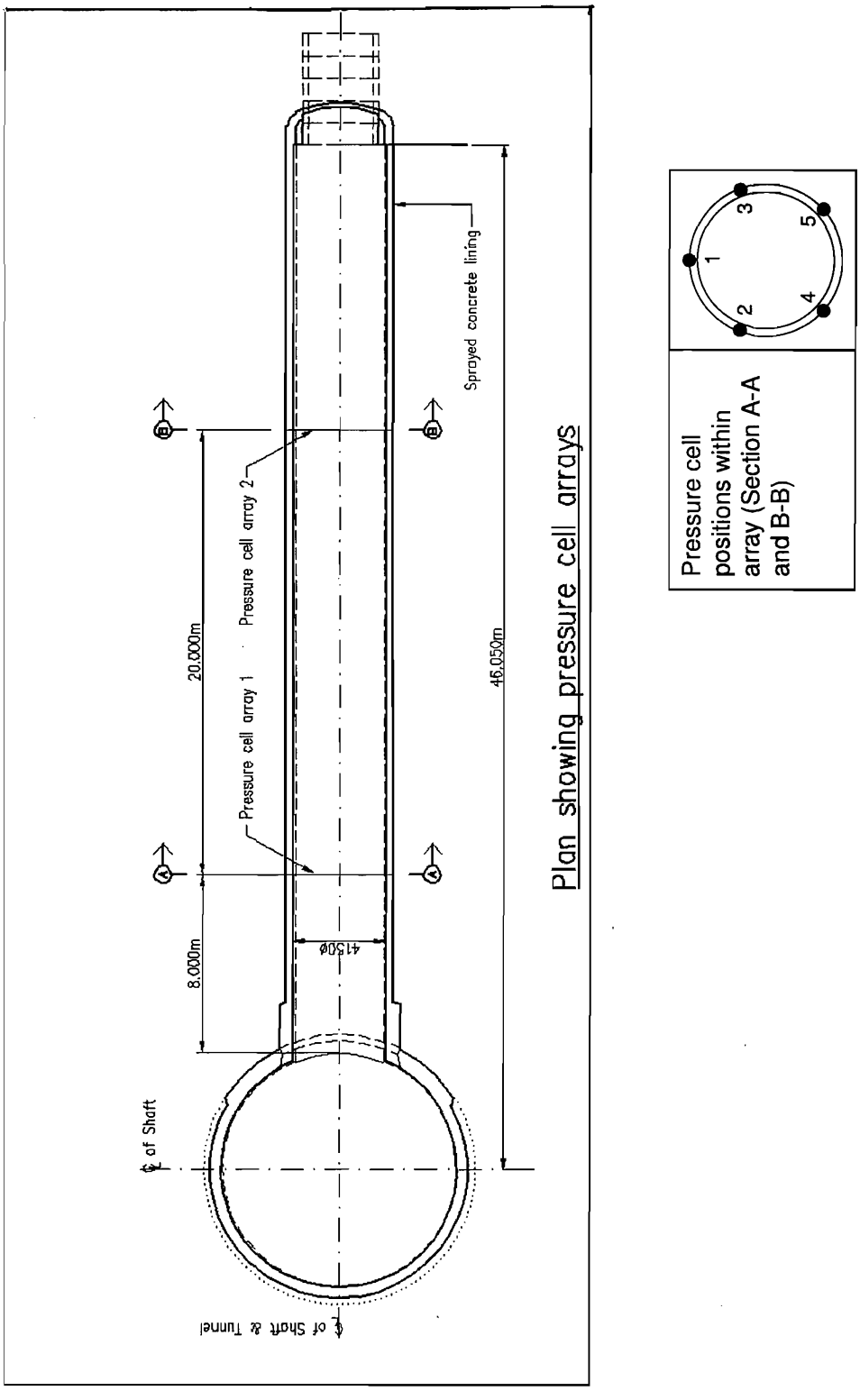

Figure 3-9: Plan of T5 SWOT frontshunt tunnel showing pressure cell arrays

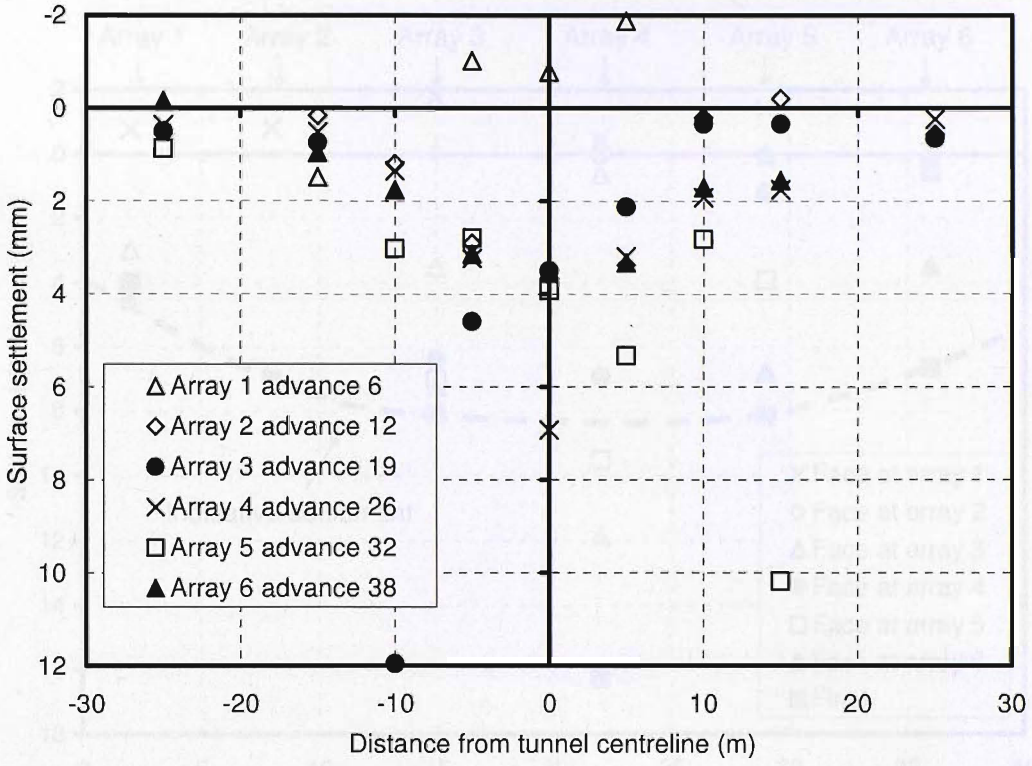

Figure 3-10: Transverse settlement profiles when the tunnel face was under the array

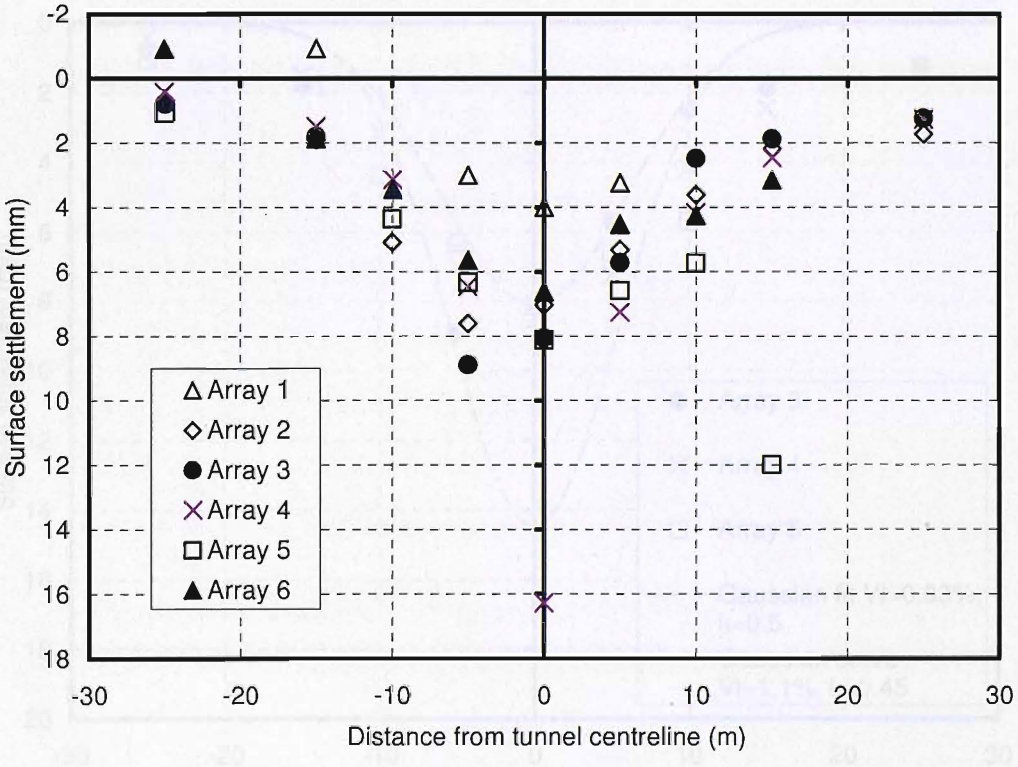

Figure 3-11: Transverse settlement profiles 2 weeks after construction

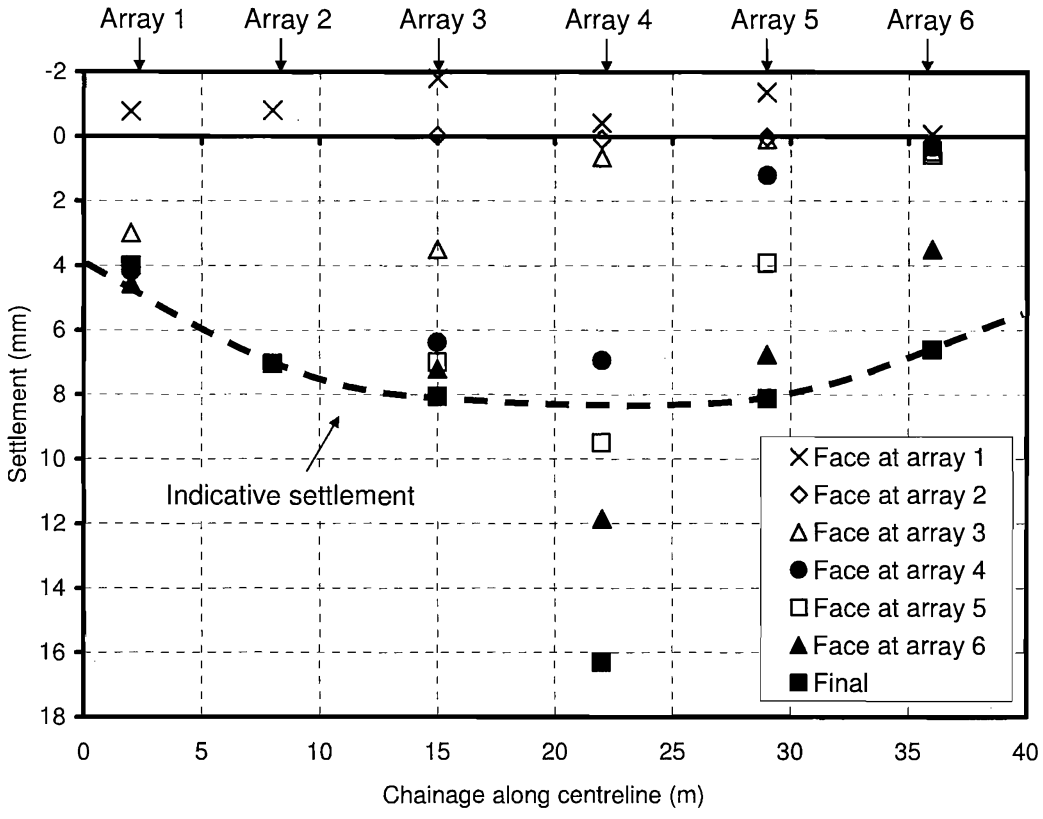

Figure 3-12: Longitudinal settlement above the tunnel centreline

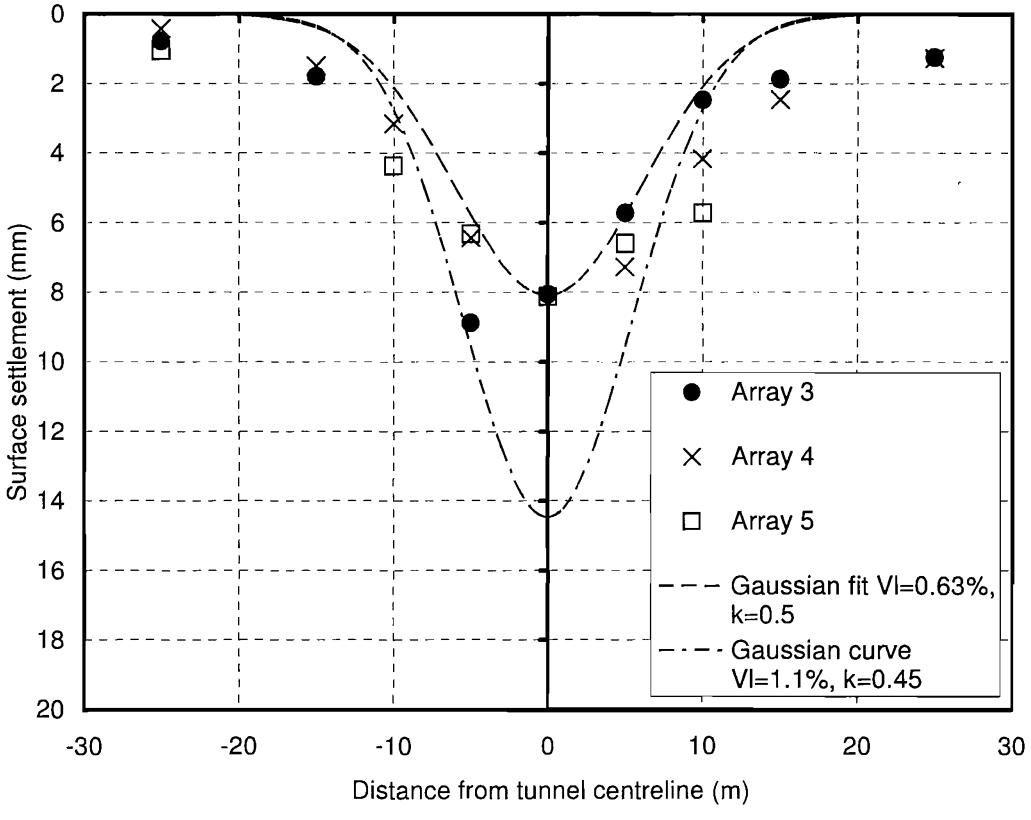

Figure 3-13: Comparison of surface settlements with empirical curves

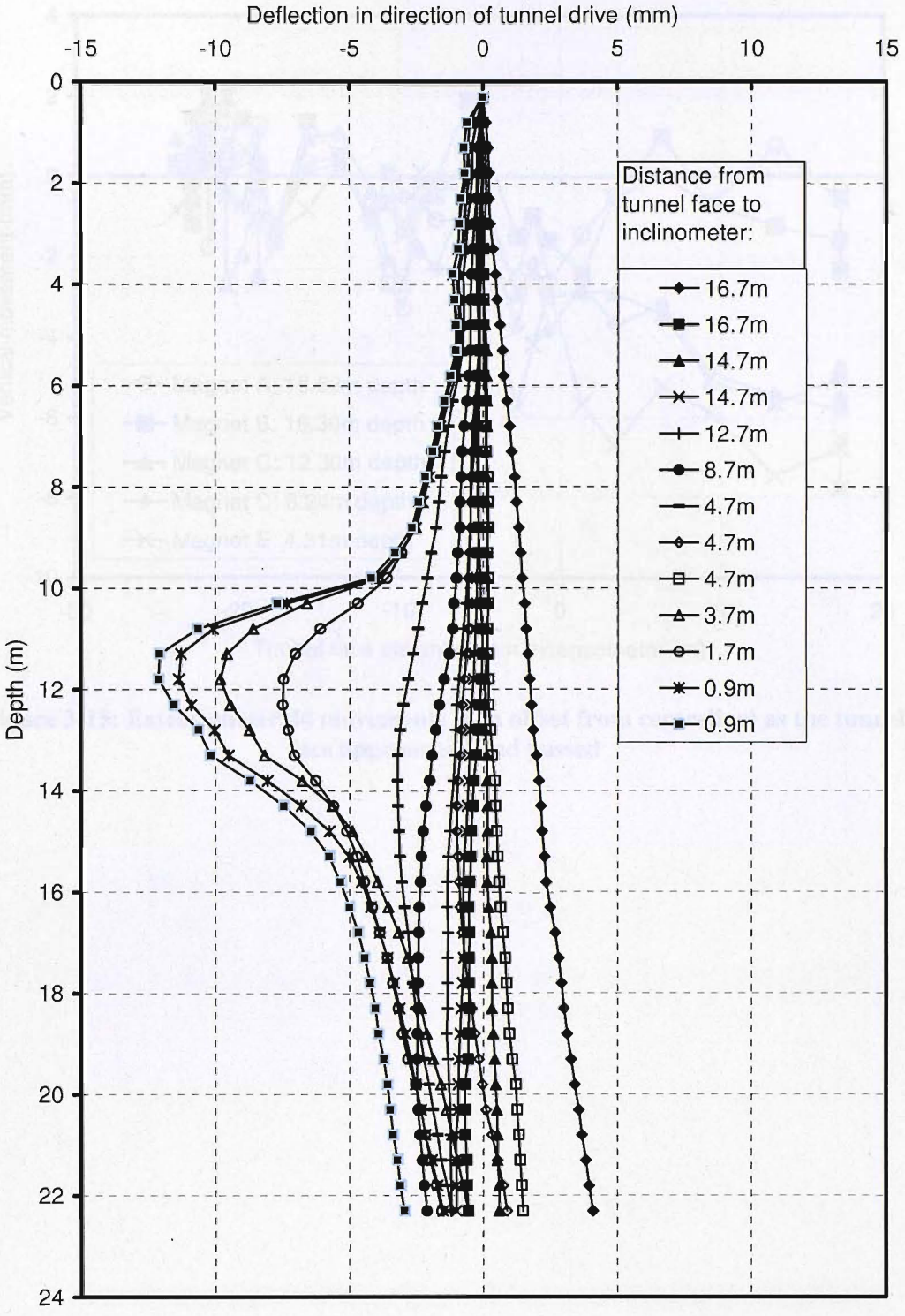

Figure 3-14: Readings from Inclinometer 48 on tunnel centreline

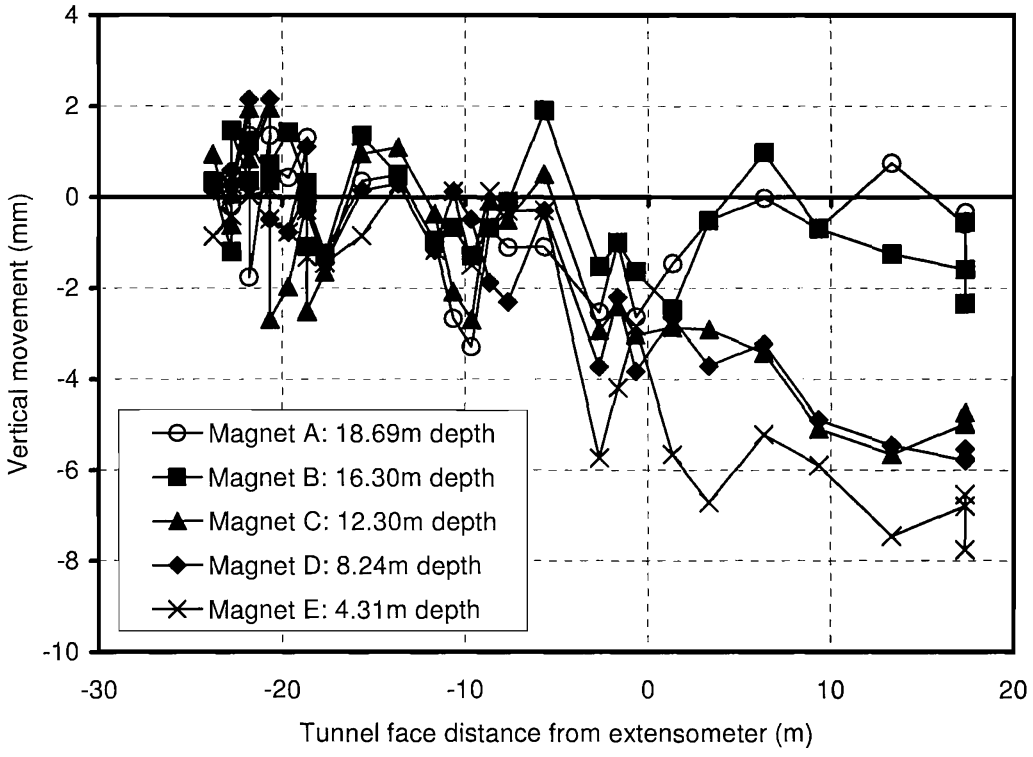

Figure 3-15: Extensometer 44 movements (6 m offset from centreline) as the tunnel face approached and passed

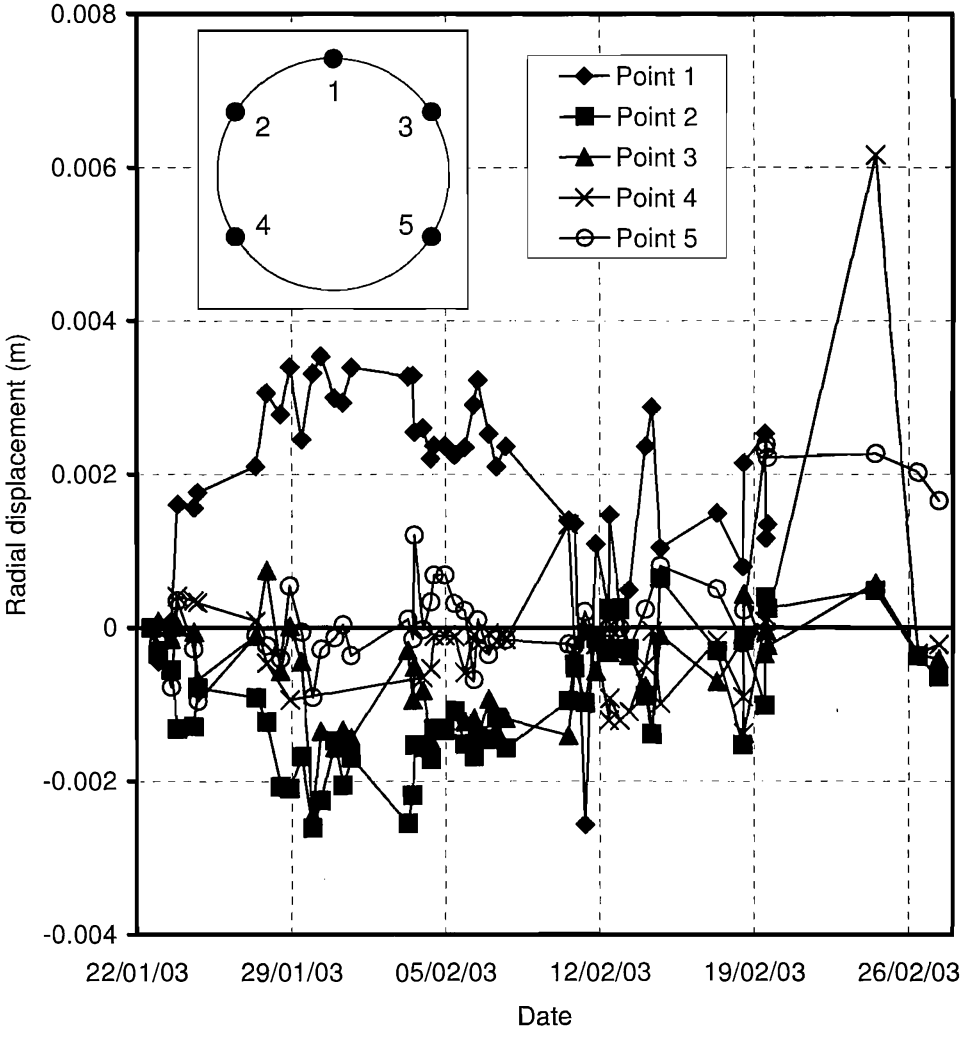

Figure 3-16: Radial displacements of the tunnel lining measured by optical surveying of targets at Array 1

4 STRESS MEASUREMENT IN THE FIELD

This chapter describes the measurement of stresses using various methods at the Heathrow Terminal 4 (T4) concourse tunnel and the Heathrow Terminal 5 (T5) Stormwater Outfall Tunnel (SWOT) frontshunt tunnel. The layout, geometry and construction sequences of the tunnels were described in Chapter 3.

Pressure cells were installed in two arrays in the T5 SWOT frontshunt tunnel (Figure 3-9), and two pressure cells were also sprayed into a test panel. A method of back-calculation based on the rate of flow method (England & Illston, 1965) was used to back-calculate stresses in strain rate controlled tests on early age sprayed concrete from the T5 works, and then applied to the tunnel displacement monitoring data obtained by optical surveying.

Two arrays of pressure cells were also installed in 1996 in the T4 concourse tunnel. Readings were taken over a period of 8 ½ years.

In addition, an assessment of the accuracy and reliability of the methods employed has been made and compared to other methods described in the literature review. The results are discussed with reference to previous tunnel lining stress measurements made in London Clay.

4.1 Interpretation of pressure cells

Pressure cell readings require adjustment for cell action factor (CAF), crimping offset, temperature sensitivity and strain sensitivity. Adjustments for CAF and crimping offset have been described in the literature review. In the following sub-sections, adjustments for temperature sensitivity and strain sensitivity will be described. In the last sub-section, an estimate of the accuracy of radial and tangential pressure cells has been made.

4.1.1 Cell action factor (CAF)

The cell action factor was assumed to be equal to unity at all times. The literature review in Chapter 2 identified laboratory and numerical studies of the CAF of an embedded pressure cell, which indicate that the potential variation from unity is of the order of ± 5 %.

4.1.2 Crimping offset

On the T5 site, the crimping tool provided by the instrumentation supplier was inadequate and did not crimp the crimping tube in a suitable manner. The tool supplied was a pair of bluntened bolt-cutters. The crimping of the test panel crimping tubes on site and in the laboratory can be seen in Figure 4-1. The crimping performed on site did not flatten the crimping tube properly such that it was not clear whether the tubing had been effectively crushed. Additionally, the tapered shape of the bites meant that the length of tubing that had been crushed could not be measured accurately.

In the laboratory a custom tool was made in the workshop and this produced better results. A pair of bolt-cutters was adapted by grinding down the tapered edge and fixing flat pieces of hardened steel to the jaws that were exactly 12.5 mm wide. This enabled the crimping tube to be properly flattened in 12.5 mm long sections. This allowed a fixed amount of oil to be pushed into the pressure cell cavity with each crimp; such that the increase in pressure experienced by the cell per unit crimped length would be a predictable, constant value for a pressure cell in good contact with the material surrounding it.

Keeping good crimping records meant that it was easy to remove the offset in pressure due to crimping from later readings. Anecdotal evidence suggests that this has not always been the case when pressure cells have been installed in sprayed concrete tunnels. An example of crimping of the test panel in the laboratory is shown in Figure 4-2. The gradient, at approximately 1 MPa per 40 mm crimped length was the same as Clayton *et al.* (2002) found for a well embedded tangential pressure cell in ready-mix concrete. The recorded pressure was allowed to stabilise between each 12.5 mm crimp, which occurred within 5 minutes, and this resulted in a very small amount of creep that is just visible in Figure 4-2.

Figure 4-2 shows that if crimping is done properly and good records are kept, the crimping offset may be removed from the data with negligible error.

4.1.3 Temperature sensitivity

The literature review identified temperature sensitivity as an area that required more attention in the interpretation of pressure cell data. Temperature sensitivity occurs due to three identifiable phenomena:

1. Temperature sensitivity of the vibrating wire and vibrating wire transducer.
2. Temperature sensitivity of the embedded cell due to differential thermal expansion of the filling liquid, cell casing and the surrounding material. This is dependent on arching restraint by the surrounding material and will be called 'cell restraint temperature sensitivity'.
3. Temperature sensitivity caused by thermal expansion and contraction of the ring of sprayed concrete against the ground. This will be called 'ground reaction temperature sensitivity'.

The temperature sensitivity of the vibrating wire and vibrating wire transducer can be easily removed using the manufacturer's calibration, which will be different for every cell produced.

Cell restraint temperature sensitivity can be estimated from data when it can be assumed that the changes in recorded pressure are caused solely by temperature changes. This could be in an unloaded test panel over a time period short enough to ignore the effect of shrinkage and creep, or in a tunnel when readings are taken over a time period short enough to assume that the stress is not changing.

Ground reaction temperature sensitivity of pressure cells has not previously been recognised in the literature, although the behaviour that causes it was seen by Brierley & Cording (1976) on the Washington Metro project when they observed a compression followed by a tension in strain gauges attached to steel ribs embedded in sprayed concrete. The compression and subsequent tension were caused by a rise and fall in temperature as the sprayed concrete hydrated. Similar effects have been noted in strutted excavations, with expansion of the struts causing wall movements against the ground and hence an increase in ground pressure on the wall (e.g. Niu *et al.*, 2005).

Since ground reaction temperature sensitivity represents a real stress experienced by the tunnel lining, it should not be removed from the data if absolute values of stress are required. However, if it is desired to know if the ground pressure acting on the lining is changing with time due to other phenomena, it may be necessary to remove this effect.

A test panel was produced during the T5 works, at the same time as Array 2 was installed. This was left in the SWOT inlet shaft for 1 month so that it would experience similar environmental conditions to the sprayed concrete lining in the SWOT frontshunt tunnel. The pressures recorded by the test panel pressure cells, adjusted only for the temperature sensitivity of the vibrating wire and vibrating wire transducer, are shown in Figure 4-3. Each pressure cell has a thermistor attached to it, and on the same graph the temperature readings are shown. The similarity between the fluctuations of temperature and pressure illustrates the marked dependence of tangential pressure cells on temperature, as well as the sensitivity of the pressure cells to small changes in pressure.

For the test panel, this temperature sensitivity could only be due to cell restraint since there was no ground reaction. It was hypothesised that cell restraint temperature sensitivity could be estimated by fitting a straight line to data over a time period during which changes in pressure due to external loads, shrinkage and creep could be ignored but changes in temperature were occurring. Unfortunately, this was not straightforward. Figure 4-4 shows the relationship between temperature and pressure in the test panel over 3 days. Since diurnal temperature variations did not have time to penetrate the full section, temperature gradients were set up leading to the looping shape of Figure 4-4.

Diurnal temperature variations do occur in tunnels that are ventilated, or tunnels that are close to a portal or access shaft and therefore exposed to the outside air. For example, the SWOT frontshunt tunnel was driven from the inlet shaft, and therefore was exposed to surface diurnal air temperature changes. The Heathrow Express tunnels, although at a greater depth and separated by both distance and separated from the outside by doors, are exposed to diurnal temperature variations because the tunnel is ventilated.

The looping shape of Figure 4-4 may be understood better if a thermodynamics equation commonly used in geophysics is used to estimate the penetration of temperature changes into the section (Carslaw & Jaeger, 1959). The equation is:

$$T = \Delta T_0 \exp\left(-z\sqrt{\frac{\omega}{2\kappa}}\right) \cdot \cos\left(\omega t - z\sqrt{\frac{\omega}{2\kappa}}\right) \qquad \textbf{Equation 21}$$

where ΔT_0 is the amplitude of the sinusoidal surface temperature variation in °C,

t is the time in seconds,

z is the depth into the section in metres,

ω is the angular velocity, given by $\omega = \frac{2\pi}{\tau} \quad [s^{-1}]$

where τ is the period, in this case 1 day or 86400 s,

κ is the thermal diffusivity, given by $\kappa = \frac{k}{\rho C_p} \quad [m^2/s]$

where k is the coefficient of thermal conductivity of the sprayed concrete = 2.6 J/m^{2}s°C/m,

ρ is the mass density of the sprayed concrete = 2400 kg/m^3,

and C_p is the specific heat capacity of the sprayed concrete = 1005 J/kg/°C.

The temperature variation at the surface and at depth is shown in Figure 4-5. The expansion and contraction of the test panel, and hence the pressure change due to temperature sensitivity read by the pressure cell, will be dependent on the average temperature across the section, which will be different to the temperature measured by the thermistor located close to the mid-section at a depth of approximately 0.15 m, and different to the temperature at the surface. There will also be a time-lag, as shown in Figure 4-5. For this reason, data points from the same time of day over several days were used to estimate the temperature sensitivity; an example is shown in Figure 4-6 for readings taken at midnight over a fortnight. The cell restraint temperature sensitivity of the test panel pressure cells was thus estimated from Figure 4-6 at 0.115 MPa/°C ± 0.005 MPa/°C. Clayton *et al.* (2002) estimated temperature sensitivity of a test panel tangential cell at 0.1 MPa/°C and of a tunnel tangential cell at 0.08 MPa/°C.

The temperature sensitivity adjustment was applied to the test panel data using the following formula:

$$P_{adj} = P_r - TS(T - T_0) \qquad \textbf{Equation 22}$$

where P_{adj} is the adjusted pressure in MPa,

TS is the temperature sensitivity, in this case 0.115 MPa/°C,

T is the temperature in °C,

T_0 is the base temperature for the adjustment in °C and

P_r is the read pressure in MPa.

The recorded pressures adjusted for this temperature sensitivity and the crimping offset are shown in Figure 4-7.

There is difficulty in ascertaining the value of the base temperature T_0. In the case of Figure 4-7 it has been assumed to be at the peak temperature of hydration, on the basis that what should be left once the adjustment has been made is a hyperbolic shrinkage stress curve that begins at zero, and this value of T_0 fulfilled this criterion. Setting T_0 at this value also resulted in the highest adjusted pressures, and was thus conservative. However, cell restraint temperature sensitivity will be shown below to be dependent on both the coefficient of thermal expansion of the surrounding medium and the stiffness of that medium, and neither of these is constant at early age.

The temperature sensitivities of the tangential and radial pressure cells at T5 were estimated at approximately 9 months. It was assumed, therefore, that pressure changes occurring 9 months after construction were only due to temperature over a time period of approximately 3 weeks when the readings were taken. These data are shown in Figure 4-8, Figure 4-9, Figure 4-10 and Figure 4-11. Several of the pressure cells did not show a sensitivity to temperature, especially in Array 1. This was probably because the cells did not have a good contact with the sprayed concrete. Cell 509 in Array 2 (Figure 4-10) shows clearly what happens when the pressure reading drops below zero; the pressure cell loses contact with the sprayed concrete and ceases to respond to further changes in pressure. If the pressure cells are not crimped enough to ensure the readings will always remain in the positive domain, this is what will happen.

The temperature sensitivity was approximately 160-170 kPa/°C for the tangential pressure cells. Cell 506 (Figure 4-10) had a low, but non-zero, temperature sensitivity. Given the insensitivity of the CAF of pressure cells to the stiffness of the material in which they are embedded, pressure cells should be expected to either function well or not at all (if they have lost contact). However, it will be shown that temperature sensitivity is dependent on the stiffness of the surrounding material. The behaviour of Cell 506 could be due to the presence of a void or rebound in the sprayed concrete close to the pressure cell's surface reducing the effective stiffness of the sprayed concrete.

If the difference between the temperature sensitivity of the tangential pressure cells in the tunnel lining and in the test panel was due to ground reaction temperature sensitivity, then this should correspond to the temperature sensitivity of the radial pressure cells. A comparison is made in Table 4-1 for the Array 2 pressure cells at T5. The overall tangential cell temperature sensitivity in column 2 was used to calculate the ground reaction temperature sensitivity in column 4 by subtracting the cell restraint temperature sensitivity of 115 kPa/°C estimated from the test panel tangential cells. The equivalent TS of a radial cell was calculated in column 5 by multiplying the TS of the tangential cell (column 4) by the thickness (column 3) and dividing by the radius of the tunnel (2.5 m). This may then be compared to the actual TS of the radial cells given in the last column.

Table 4-1: Comparison of ground reaction temperature sensitivity of tangential cells with temperature sensitivity of radial cells; T5 array 2

Cell location	TS (kPa/°C)	Thickness of lining (mm)	TS_{gr} (TS-115) (kPa/°C)	Equivalent TS of a radial cell	TS of radial cell (kPa/°C)
Left Knee	87.4	450	- *	- *	5.7
Left Shoulder	158.3	355	43.3	6.1	5.6
Crown	- †	-	-	-	5.7
Right Shoulder	169.2	435	54.2	9.4	7.1
Right Knee	168.6	320	53.6	6.9	14.9

* TS unexpectedly low so calculation not performed

† TS near zero so pressure cell has lost contact, calculation not performed

Table 4-1 shows that the separation of temperature sensitivity of tangential cells into components due to cell restraint temperature sensitivity and ground reaction sensitivity is reasonable. It explains the difference between the temperature sensitivity of the test panel tangential cells and the tangential cells in the tunnel, and the difference is of the same order of magnitude as the temperature sensitivity of the radial cells. Further evidence will be provided in the section on pressure cells at T4, where the temperature sensitivity of the radial cells was not apparent until the invert had been closed. Therefore, the lower cell restraint temperature sensitivity obtained from the test panel pressure cell data, should be used to correct the tangential pressure cell readings from the tunnel. The temperature sensitivity of the radial cells could also be used, and then a test panel would not be required for this purpose, but estimates of the thickness of the sprayed concrete lining would be required.

The estimates of lining thickness at the locations of the pressure cells in Table 4-1 were taken from the Tunnelbeamer™ data. This was a laser survey made during excavation and during spraying of the initial layer and the primary lining to direct the excavator and the nozzleman without the need for an operative to enter the face area. The accuracy of these estimates was probably within 50 mm,

the approximate size of the teeth of the excavator, yet they still show the extent of the overexcavation in this tunnel that led to a lining thickness that was usually at least 100 mm thicker than designed (the design thickness of the initial and primary layers together was 275 mm).

In order to investigate the mechanisms controlling temperature sensitivity, a 3D numerical model of a test panel 1000 x 1000 x 300 mm with a pressure cell at its centre was constructed in the finite element program LUSAS. A 3D model was used because previous studies had concentrated on plane strain or axisymmetric models (Clayton *et al.*, 2002) where the boundaries were relatively distant from the pressure cell. The 3D model allowed the effect of the closer boundaries in the direction of the thickness of the test panel or a sprayed concrete lining to be taken into account. 20-node hexahedral isoparametric elements were used. The sprayed concrete and the stainless steel cell casing were modelled by isotropic elastic materials with properties as listed in Table 4-2. The pressure cell modelled had the same dimensions as the tangential cells used at T5. The stainless steel plates were 3 mm thick and the oil-filled cavity between the plates was 0.3 mm thick. In plan, the cell casing was 100 x 200 mm and the cavity was 80 x 180 mm. The cell fluid was not modelled directly, and the method for finding the CAF by varying the cavity pressure, and finding the temperature sensitivity using a compatibility of volumetric strains equation, was applied as described in Clayton *et al.* (2002).

Table 4-2: Material properties used in numerical modelling of an embedded pressure cell

Material	E (MPa)	ν	α (m/m/°C)
Sprayed concrete	30000	0.25	10×10^{-6}
Stainless steel	210000	0.28	16×10^{-6}

The model as shown in Figure 4-12 was one-quarter of the full test panel with planes of symmetry on the X-Z and Y-Z planes. A further plane of symmetry through the pressure cell was exploited to make the model one-eighth of the full test panel. By placing a boundary at the centre of the cell, displacements and

strains of the cell casing were of a similar order of magnitude. A load of 1000 kPa was applied to the top face (surface in the plane of X-Y at Z = 0) and supports preventing movement in the Z-direction were applied to the bottom face (surface parallel to the plane of X-Y at Z = 1000mm). Displacement restraints were applied to the planes of symmetry in the normal direction.

To find the CAF, a pressure was applied to the internal surfaces of the pressure cell cavity. This was varied to find the relationship between volumetric cavity strain and the ratio of cavity pressure to applied pressure (CAF). The volumetric cavity strain was found by integrating the displacements of the nodes on the interior of the cell cavity. The displacement pattern was as would be expected of a plate in two-way bending. The relationship between the volumetric strain of the cell cavity and the CAF is shown in Figure 4-13. The volumetric strain in reality will be defined by the volumetric compressibility of the cell fluid, and this will determine the CAF. Volumetric compressibility is the inverse of bulk modulus. Clayton *et al.* (2002) used the bulk modulus in their diagram, but volumetric compressibility is used here since it has a linear relationship with the CAF.

The volumetric compressibility of the cell fluid $d\varepsilon_v^f/dp$, in this case for hydraulic oil, is shown. The point this crosses the line for the volumetric strain of the cell cavity corresponds to the CAF for this design of pressure cell, values for which are shown in Table 4-3. This process was repeated for different values of sprayed concrete stiffness.

The temperature sensitivity of the pressure cell was found by applying a uniform temperature change and again calculating the volumetric strain of the cavity. Then conservation of volume could be used in the following way to find the temperature sensitivity *dp/dt*, assuming cavity volume reduction to be positive (Clayton *et al.*, 2002):

$$\frac{dp}{dt} = \frac{\left(\frac{d\varepsilon_v^c}{dt} - \frac{d\varepsilon_v^f}{dt}\right)}{\left(\frac{d\varepsilon_v^f}{dp} - \frac{d\varepsilon_v^c}{dp}\right)} \qquad \textbf{Equation 23}$$

where $d\varepsilon_v^c/dt$ is the rate of change of volumetric strain of the cell cavity, as a function of temperature change; this value was obtained by varying the

temperature in the model and was found to be -0.000192 $°C^{-1}$ for the material parameters in Table 4-2,

$d\varepsilon_v^f/dt$ is the coefficient of volumetric thermal expansion of the cell fluid, which for hydraulic oil was taken to be -0.00072 $°C^{-1}$,

$d\varepsilon_v^f/dp$ is the volumetric compressibility of the cell fluid (the inverse of bulk modulus), which for hydraulic oil was taken to be 0.000625 MPa^{-1},

$d\varepsilon_v^c/dp$ is the volumetric cavity strain per unit of applied cavity pressure, this value was obtained by varying the applied cavity pressure in the model and was found to be -0.00624 MPa^{-1} for the material parameters in Table 4-2.

The sign convention used in this case was that a reduction in cavity volume was positive. Using this equation, values of temperature sensitivity were found for different values of sprayed concrete stiffness in Table 4-3.

Table 4-3: Values of CAF and temperature sensitivity for modelled tangential pressure cell at different values of medium stiffness

Sprayed concrete E (MPa)	CAF	Temperature sensitivity TS = dp/dt (MPa/°C)
30000	0.886	0.133
20000	0.907	0.099
10000	0.923	0.059
5000	0.925	0.036
1000	0.918	0.009

As found by Coutinho (1953), the CAF was relatively unaffected by the stiffness of the sprayed concrete. However, the temperature sensitivity was greatly affected by the stiffness of the sprayed concrete, and this was because temperature effects, along with crimping effects, creep and shrinkage, all rely on arching of the sprayed concrete around the pressure cell.

The effects of varying the coefficient of thermal expansion as well as the stiffness of the sprayed concrete were also investigated using the finite element

model. The results of analyses varying the coefficient of thermal expansion of the sprayed concrete are shown in Figure 4-14. Temperature sensitivity is significantly affected by the coefficient of thermal expansion of the sprayed concrete because the stainless steel casing of the pressure cell, which has a significantly higher coefficient of thermal expansion, attempts to expand against the sprayed concrete. The lower the coefficient of thermal expansion of the sprayed concrete, the more this expansion is prevented and the more the cell casing expands into the cell cavity, compressing the fluid. This mechanism is the cause of cell restraint temperature sensitivity and was identified by Clayton *et al.* (2002).

Figure 4-14 also shows that changing the elastic modulus of the sprayed concrete has an even greater effect on the temperature sensitivity. Low sprayed concrete stiffness will provide less restraint to cell expansion, and hence the temperature sensitivity will be lower. Figure 4-14 alerts us to the fact that the temperature sensitivity, unlike the CAF, will vary considerably depending on the age, specification and quality of the sprayed concrete around the pressure cell.

The broken line on Figure 4-14 shows an indicative path a sprayed concrete could take as it matures, beginning at a relatively high coefficient of thermal expansion and low stiffness. This was based on the relationship between concrete stiffness and coefficient of thermal expansion published by Laplante & Boulay (1994). This explains the low response of the pressure cells at T5 to temperature increases during the early stages of hydration: the low stiffness and high coefficient of thermal expansion of the sprayed concrete combined to make the temperature sensitivity much lower. Figure 4-14 could be used to estimate an adjustment for the cell restraint temperature sensitivity of tangential pressure cells during the early age of the sprayed concrete if the development of stiffness with time were known.

4.1.4 Strain sensitivity

'Strain sensitivity' is defined here as the sensitivity of a pressure cell to strains of the medium in which it is embedded, such as shrinkage and creep. For example, it is known that concrete shrinkage will cause a substantial increase in the pressure measured by a tangential cell (Clayton *et al.*, 2002).

Figure 4-7 shows that recorded pressures increased in the test panel tangential pressure cells in an approximately hyperbolic manner due to shrinkage of the sprayed concrete with time. The drop in pressure sometime between 250 and 350 days occurred when the test panel was disconnected from the datalogger and temporarily moved out of the laboratory. When it was in the process of being moved back inside, it was dropped from the trolley and the impact (the test panel had a mass of approximately 900 kg) may have caused cracking in the zones of stress concentration around the edges of the pressure cells, releasing the tensile stresses. As an aside, this indicates that pressure cells may be affected by blasting in a tunnel excavated by drill and blast methods. The increased rate of shrinkage stress from this point on may have been caused by removal of the formwork at this time, causing increased drying shrinkage.

It was possible to fit a hyperbolic shrinkage curve (shown on Figure 4-7) to the shrinkage pressures in the test panel over the 250 days before it was dropped, similar to the ACI 209R-92 (1992) formula for shrinkage strain:

$$p_{shr} = \frac{t}{B+t} \cdot p_{\infty} \qquad \textbf{Equation 24}$$

where p_{shr} is the cell pressure due to shrinkage in MPa,

t is time in days,

B is a constant that will adjust the curvature and

p_{∞} is the ultimate shrinkage pressure in MPa.

For both test panel cells, B = 55 days.

The finite element model of the test panel was used to investigate strain sensitivity. A strain was applied to the sprayed concrete only by setting the coefficient of thermal expansion of the pressure cell casing to zero. Then a temperature change was applied inducing a thermal strain in the medium to mimic a shrinkage or creep strain e [m/m]. Using the same notation from Clayton *et al.* (2002) as in Section 2.5.4, the strain sensitivity *dp/de* [MPa] is given by:

$$\frac{dp}{de} = \frac{d\varepsilon_v^c / de}{d\varepsilon_v^f / dp - d\varepsilon_v^c / dp}$$ **Equation 25**

where $d\varepsilon_v^c/de$ is the change of volumetric cavity strain with respect to strain in the medium,

$d\varepsilon_v^f/dp$ is the volumetric compressibility of the cell fluid, which in this case is 0.000625 MPa^{-1} for hydraulic oil and

$d\varepsilon_v^c/dp$ is the volumetric cavity strain per unit of applied cavity pressure [MPa^{-1}].

The strain sensitivity was found to be only dependent on the stiffness of the medium and was constant for a given value of stiffness. However, the relationship was complex. A polynomial equation was fitted to the results of the finite element modelling and this is shown in Figure 4-15. The graph shows that for a typical mature sprayed concrete stiffness between 20 and 30 GPa, the strain sensitivity is 4000-5000 MPa. This means that the increase in pressure due to shrinkage in the test panel tangential cells at 250 days of 4-5 MPa (Figure 4-7) corresponds to a shrinkage strain of the order of 1000 microstrain. This is a high but not implausible value of shrinkage strain.

Strain sensitivity is caused by arching effects around the edges of a pressure cell. This may be proven by thought experiment. If a test panel were constructed such that its dimensions in plan were the same as the dimensions of the pressure cell, i.e. there were only concrete above and below the pressure cell, the pressure cell would respond to a load applied to the ends of the test panel, but would not respond to temperature changes, shrinkage or creep since the test panel has no end restraint and so it can expand and contract freely. Therefore temperature sensitivity and strain sensitivity must be caused by arching around the edges of the pressure cell.

The simplest way to remove strain sensitivity from the tunnel tangential pressure cell data would be to subtract the shrinkage pressures measured in the test panel, as approximated by the hyperbolic shrinkage stress curve, from the recorded pressures in the tunnel.

4.1.5 Lost pressures

Lost pressures may occur if the pressure cell at any stage loses contact with the medium in which it is embedded, because pressure cells cannot read negative pressures. This may be prevented from occurring by ensuring that the cell is adequately crimped in good time.

If contact between the pressure cell and the medium is temporarily lost due to a decrease in temperature, an estimate of the lost pressure may be made using the temperature sensitivity because the thermistor attached to the cell will continue to record temperature changes. However, pressure changes due to other phenomena such as load, creep and shrinkage during the period of no contact will be permanently lost.

4.1.6 Interpretation overview

The interpretation of tangential pressure cell data should follow the following steps:

1. Make adjustment for temperature sensitivity of the vibrating wire and vibrating wire transducer (using manufacturer's calibration).
2. Remove any zero offset.
3. Remove any crimping offset.
4. Check for lost pressures, i.e. check if the pressure cell has at any time lost contact with the sprayed concrete (the read pressure is zero).
5. Estimate cell restraint temperature sensitivity from test panel data and estimate its variation with time during early age. Apply correction.
6. Estimate shrinkage pressure development with time from the test panel data and subtract from readings.

The interpretation of radial pressure cells should follow the following steps:

1. Make adjustment for temperature sensitivity of the vibrating wire and vibrating wire transducer (using manufacturer's calibration).
2. Remove any zero offset.
3. Remove any crimping offset.

4. Check for lost pressures if the pressure cell has at any time lost contact with the sprayed concrete or ground. This is unlikely in the case of radial cells.

Radial cells are therefore more reliable because there are fewer steps required in their interpretation. Furthermore, while steps 1-4 are fairly straightforward, steps 5 and 6 in the interpretation of tangential cells (not required for the interpretation of radial cells) are also the steps that introduce the largest errors.

4.2 Pressure cells at Heathrow Terminal 5

In the T5 SWOT frontshunt tunnel, 2 arrays of pressure cells were installed. In each array there were 5 tangential and 5 radial pressure cells. The results are presented below.

4.2.1 Array 1 tangential pressure cells

The left knee pressure cell 501 vibrating wire did not respond to excitation and had either been damaged or was malfunctioning.

Figure 4-17 shows the recorded pressures for the other 4 tangential pressure cells over the first 4 weeks. The pressure readings show no response whatsoever to temperature over the first 2-3 days, during which time there were significant changes of temperature, as shown in Figure 4-18. The peak temperature due to hydration was reached within approximately 12 hours. Since the sprayed concrete should be expected to have gained the major part of its long-term stiffness during this period, the lack of response to temperature can only be due to a lack of contact between the pressure cells and the sprayed concrete. The wild fluctuations of the Cell 505 data in Figure 4-17 were of unknown origin but may have been due to unstable readings caused by a weak signal or harmonics in the excitation of the vibrating wire. My experience suggests that automatic dataloggers such as the ones used for reading the test panel pressure cells give much more reliable readings than the hand-held vibrating wire readers used on site, although others are not always in agreement.

The pressure cells in Array 1 were crimped twice, on 27/1/03 at 11am (Phase 1) and on 12/2/03 at 11am (Phase 2). Figure 4-17 shows that although the first phase of crimping increased the recorded pressure in all the cells, no significant

changes in pressure were experienced by Cells 502 or 503 between the first phase and second phase of crimping. During this period, the temperature decreased by approximately 5 °C and this should have caused a decrease in pressure, as it did in Cell 504. It is possible that either the pressure decrease due to temperature was negated by a coincident increase in pressure due to increasing ground load, or that the pressure cells still had not gained contact with the sprayed concrete.

It should be possible to compare charts of pressure increase vs. crimped length and thus from the gradient of the curve find out if the pressure cell has achieved good contact or not. However, due to the substandard crimping tool used on site, it was not possible to do this with any degree of confidence (c.f. Figure 4-1). The creep effect shown in Figure 4-19, which did not occur to such a large degree in the laboratory (Figure 4-2), was further evidence of the poor quality of crimping on site.

An attempt to assess the efficacy of crimping and hence the quality of the installation is made in Figure 4-20. The measurements of crimped length were approximate, because the crimping tube was not properly squashed flat with every increment. Clayton *et al.* (2002) found that a well-performing tangential cell should experience an increase in read pressure of approximately 1 MPa for 40 mm of crimped length. An example of an under-reading cell from their paper experienced an increase of only 0.15 MPa for 80 mm of crimped length. These gradients were included in Figure 4-20 for comparison. None of the tangential pressure cells had a 'good' crimping gradient in Phase 1. In Phase 2, a dog-leg in the curve of Cell 505 can be seen, indicating that contact with the sprayed concrete was achieved during crimping. Cell 502 and 504 had a 'good' gradient. Cell 503 had a low gradient, but 7.5 cm of the total of 12.2 cm crimped was actually re-crimping of the section already crimped, albeit not very well, in Phase 1, so an assessment of the quality of the installation by inspection of the crimping gradient was not really possible.

All the available readings from the Array 1 tangential pressure cells were of little use because the pressure cells did not appear to have had a good contact with the sprayed concrete during the critical early-age period when most of the loading was applied to the lining by the ground. Phase 1 crimping was insufficient to

achieve contact and was undertaken too late. During Phase 2 crimping, contact was restored to Cells 502, 504 and 505, and possibly to 503, but this was already 3 weeks after installation.

Changes in pressure from Phase 2 crimping onwards are shown in Figure 4-21. It was not possible to take readings of the pressure cells between 26/2/03 and 11/9/03 since the junction box was behind the conveyor system for the main TBM tunnel drive and no provision was made for taking readings remotely.

Cell 502, although it responded well to crimping, exhibited a very low temperature sensitivity (c.f. Figure 4-8), and therefore the quality of the installation was questionable.

Cell 503 in the crown exhibited no change in pressure with time and no temperature sensitivity. This suggested that the quality of the contact it had with the sprayed concrete was questionable. This would normally have been indicated by the crimping gradient, but in the case of Cell 503 this was not possible, as explained above.

Cell 504 showed an increase in pressure with time with a noticeable temperature sensitivity in the most recent readings that suggested that all the changes in pressure from crimping Phase 2 onwards may be attributable to temperature changes. An estimate of the temperature sensitivity was made in Figure 4-8, and this was applied to the data to produce Figure 4-22. The initial decrease in pressure after crimping Phase 2 could be due to continuing creep of the crimping pressures.

Cell 505 in the right knee position showed a decrease in pressure to close to zero since crimping Phase 2 and no temperature sensitivity in the most recent readings. Therefore, the results from this cell are also questionable.

4.2.2 Array 2 tangential pressure cells

All 5 of the Array 2 tangential cells were functioning after installation.

Figure 4-23 shows the recorded pressures in the Array 2 tangential pressure cells over the first 4 weeks. All 5 of the pressure cells responded to the temperature rise due to hydration of the sprayed concrete, and its subsequent return to ambient. The varying degree to which they responded may be partly due to the

exact timing of spraying at each location, how much accelerator was added, how the layers were built up and the total thickness of the initial and primary linings. The fact that the pressure cells responded to temperature, whereas most of the Array 1 tangential cells did not, confirms the anecdotal evidence from site that the installation of Array 2 was much better than that of Array 1. Figure 4-24 shows a typical installation of pressure cells in a box-out in Array 2.

Unfortunately, Cells 506, 509 and 510 were allowed to reach zero pressure before they could be crimped. This meant that any pressure changes during the time that contact between the cell and the sprayed concrete was lost were not recorded. Crimping was performed only once at the same time as Phase 2 crimping of the Array 1 tangential cells; on 12/2/03 at around 11am.

An attempt was made to adjust the data for the cell restraint temperature sensitivity as outlined in Section 4.1.3. The strength gain of the sprayed concrete was used to estimate the development of stiffness, and the stiffness was used to estimate the coefficient of thermal expansion using the results of Laplante & Boulay (1994). The stiffness and coefficient of thermal expansion were used to estimate the temperature sensitivity using the results of the numerical modelling presented in Section 4.1.3 and in particular the linear relationships in Figure 4-14. Selected results of this calculation are shown in Table 4-4.

Table 4-4: Method for obtaining temperature sensitivity of a tangential pressure cell from Young's modulus of the sprayed concrete

Young's modulus E (GPa)	α ($^{\circ}C^{-1}$) interpolated from Laplante & Boulay (1994)	0.9α ($^{\circ}C^{-1}$)	TS from Figure 4-14 (MPa/°C)
1	21.5	19.35	0.003843
5	18.39	16.55	0.018611
10	15.13	13.62	0.043723
20	11.8	10.62	0.091471
30	11.8	10.62	0.12365

The linear coefficient of thermal expansion α in Table 4-4 found by interpolating from Laplante & Boulay's (1994) results was multiplied by 0.9 to take account of the different aggregates used at T5 and in Laplante & Boulay's study. The value of 0.9 was the ratio of the coefficients of thermal expansion that would be calculated for each concrete mix using the method in ACI209R-92 (1992).

A linear approximation for the relationship between temperature sensitivity and stiffness for the sprayed concrete mix employed at T5 was developed for the data in Table 4-4, based on Figure 4-25, and was given by:

$$TS = 0.00426E \qquad \textbf{Equation 26}$$

where TS was the temperature sensitivity in MPa/°C and

E was the Young's modulus of the sprayed concrete in GPa.

The Array 2 tangential pressure cell readings, adjusted for the crimping offset, and adjusted for temperature sensitivity using the equation above are shown in Figure 4-26. The temperature sensitivity was capped at a value of 0.115 MPa/°C, which was the long-term cell restraint temperature sensitivity estimated from the test panel tangential pressure cells. Lost pressures due to temporary loss of contact as the temperature fell to zero before crimping were estimated by consideration of temperature sensitivity as described in Section 4.1.5, for cells 506, 509 and 510 only.

Cell 508 in the crown of the tunnel was omitted from this interpretation because it showed no sensitivity whatsoever to temperature (c.f. Figure 4-10) so the quality of the installation was suspected to be poor.

Cell 506 shows a negative pressure. This is because it had very little contact before crimping and only responded to temperature changes when the temperature was above 35°C around the hydration peak, as shown in Figure 4-23. Therefore the adjustment for lost pressures due to loss of contact after the peak temperature of hydration led to an adjusted pressure that was negative. No adjustment could be made to account for the unrecorded changes in stress in the sprayed concrete lining during this period, or the increase in pressure due to temperature rise before the peak temperature of hydration was reached.

In the case of cells 509 and 510, contact was only lost as the temperature dropped below about 20°C after the peak temperature of hydration. It should be noted that this was 6 days before crimping was performed, and so changes in stress in the sprayed concrete lining during this period from 1.5 days to 7.5 days were not recorded by cells 509 and 510. This would explain the lower values of stress recorded by these cells compared to cell 507 in Figure 4-26.

The tangential cells still show a residual sensitivity to temperature in Figure 4-26, measuring higher stresses during hydration even though an adjustment has been made for temperature sensitivity due to cell restraint. This residual temperature sensitivity is due to ground reaction and should not be removed from the data.

The full range of adjusted pressures over 9 months is shown in Figure 4-27. The highest stress in the lining was at the peak temperature of hydration. This residual response to temperature changes may be explained by the ground reaction temperature sensitivity. Because the sprayed concrete ring was closed immediately, the lining pushed against the ground as the temperature rose and it expanded. The stress in the lining did not change significantly in the long-term and the stress never showed a trend towards hydrostatic full overburden pressure.

4.2.3 Array 1 radial pressure cells

The Array 1 radial pressure cells were all functioning after installation. However, 8 days after installation the connection with Cell 552 in the left shoulder position was lost when the cable was accidentally cut during routine coring for sprayed concrete quality control. The recorded pressures during the first 4 weeks are shown in Figure 4-28 and the temperatures measured by the thermistors attached to the pressure cells are shown in Figure 4-29.

The Array 1 radial pressure cells suffered a similar fate to the Array 1 tangential pressure cells. The readings were allowed to drop to zero before crimping was performed, and then the first crimping phase was in most cases insufficient to keep the readings above zero after further drops in temperature. The only exception was the right shoulder radial pressure Cell 554, which coincidentally was at the same location as tangential Cell 504, which also performed well. This indicated that the installation was probably better at this location.

It is not clear whether radial pressure cells should be crimped at all. If they are well installed, there is no reason why they should lose contact (Clayton *et al.*, 2000). Also, crimping will effectively jack the surface of the pressure cell against the London Clay. Since London Clay is a saturated porous medium, this will generate excess pore pressures, and in time, consolidation will occur. Along with the continuing temperature decrease, consolidation may partly explain the gradual drop in pressure with time after crimping in Figure 4-28.

Not only do Cells 552 and 555 drop to zero, but they also appeared to record significant negative pressures (Figure 4-28). This should not happen, because when the pressure cells lose contact they should cease to read any pressure. Pressure changes of this magnitude could not have been caused by poor calibration of the vibrating wire because the readings before installation were stable within ± 5 kPa for a temperature change of approximately 10-14 °C. One explanation is that suctions existed at the boundary caused by negative excess pore pressures in the ground due to unloading, and in the sprayed concrete lining due to hydration water demand. Another explanation is that the contraction of the sprayed concrete ring as a whole as temperature dropped either pulled the pressure cell plates apart through adhesion or negative fluid pressures in the pores.

The pressure cells in Array 1 were installed in a different manner to Array 2. Due to safety concerns, the initial layer, nominally 75 mm thick but often significantly thicker, was sprayed first. Then areas were jiggered out using a pecker mounted on the Schaeff excavator to expose the clay for installation of the pressure cells. This would have caused considerable disturbance to the clay. Also, the considerable time taken to achieve this meant that the initial layer had gained considerable strength by the time the pressure cells were sprayed over, which probably led to diversion of stresses around these locations. Many of the problems in the Array 1 pressure cells were caused by this installation method.

Only Cell 554 at the right shoulder was in good contact from Phase 2 crimping onwards and so an attempt was made to make an adjustment for the crimping offset in Figure 4-30. Figure 4-30 shows that the radial pressure was in fact negative if the crimping offsets are removed. However, since the cell was not in contact for most of the first 3 weeks since it was installed, the magnitude of the

pressure cannot be trusted. This was mainly caused by the installation method, and partly the crimping, since it would not usually be considered good practice to crimp soil cells as soil yield and consolidation would result.

What can be seen in Figure 4-30 is that in the long-term cell 554 was sensitive to temperature changes, and this was due to ground reaction as the ring of sprayed concrete expanded and contracted against the ground.

4.2.4 Array 2 radial pressure cells

The Array 2 pressure cells were installed differently to Array 1. Box-outs were used while spraying the initial layer, so the initial layer did not need to be chiselled out to expose the clay. Since less time was taken to install the pressure cells and there was much less disturbance of the clay, Array 2 had much better results.

The read pressures over the first 4 weeks are shown in Figure 4-31. Since the crown Cell 558 and the right knee Cell 560 both lost contact for significant periods during this time, even after crimping, the absolute values of pressure in the long-term cannot be trusted and have not been included in Figure 4-32, which shows the radial pressures over 9 months.

As discussed for Array 1, crimping should not have been performed on the radial pressure cells. It is not a coincidence that the radial cells that were reading zero pressure before crimping, Cells 558 and 560, dropped back to zero pressure again soon after crimping. Removing the crimping offset of the other radial cells by subtracting the increase in read pressure during crimping from subsequent readings may not be reasonable. Inspection of Figure 4-31 suggests that the read pressures 2 weeks after crimping were approximately the same as the read pressures prior to crimping. For this reason, the crimping offsets have not been removed from the read pressures shown in Figure 4-32.

Removing the crimping offset, the ground pressure acting on the sprayed concrete lining after 9 months at Array 2 was between 63 and 98 kPa at an average temperature of 15 °C, that is, between 26 and 41% of the hydrostatic full overburden pressure at tunnel axis level (240 kPa). If the increase of read pressure due to crimping were not subtracted from the data, as has been recommended, the ground pressure would have been between 126 and 155 kPa,

that is, between 53 and 65 % of the hydrostatic full overburden pressure at tunnel axis level.

The long-term pressures in September and October 2003 in Figure 4-32 were dependent on temperature as expansion and contraction of the sprayed concrete ring increased and decreased the radial pressure between the ground and the sprayed concrete lining, and the values of temperature sensitivity were shown in Figure 4-11.

From Figure 4-11 the temperature sensitivity of Cells 556, 557 and 559 was estimated at between 5.6 and 7.1 kPa/°C. This meant that at 0 °C the range of radial pressures would reduce to between 17 and 68 kPa. Conversely, at 35 °C, the read pressure would increase to between 245 and 264 kPa, in other words to between 102 and 110 % of hydrostatic full overburden pressure.

The highest radial stress, as with the tangential stress, occurred at the peak temperature of hydration. Since in general the design of sprayed concrete linings omits the effect of temperature, this phenomenon may need to be considered in future when the ring is closed immediately or very close to the face. The peak pressures during hydration and the long-term average pressures at 15 °C are listed in Table 4-5.

Table 4-5: Peak and long-term radial pressures at T5 array 2

Cell	Peak read pressure*	Long-term read pressure*
556 Left knee	54.4 %	53.7 %
557 Left shoulder	86.9 %	64.6 %
559 Right shoulder	78.1 %	52.7 %
560 Right knee	113.7 %	Lost contact

* % of hydrostatic full overburden pressure at tunnel axis level (239.9 kPa)

4.3 Back-calculation at Heathrow Terminal 5

An attempt was made to apply a back-calculation method in the T5 SWOT frontshunt tunnel; to calculate stresses from optical displacement measurements of the sprayed concrete tunnel lining. First the proposed method will be described, then the method will be evaluated by applying it to the early age sprayed concrete laboratory utilisation tests and then the attempts to apply the method to the field data will be described.

4.3.1 Description of the back-calculation method

The back-calculation method was based on the principles of the 'rate of flow method'. The following rheological model was used for the strain at timestep n:

$$\varepsilon_n = \varepsilon_{n-1} + \varepsilon_{(K)n} + \varepsilon_{(Flow)n} + \varepsilon_{(Shr)n} + \varepsilon_{(T)n} \qquad \textbf{Equation 27}$$

where $\varepsilon_{(K)n}$ is calculated by a Kelvin model representing elastic strain and delayed elastic strain taken from Thomas (2003),

$\varepsilon_{(Flow)n}$ is the flow strain, also known as secondary or steady-state creep, and is so called because its rate is only dependent on age and stress level,

$\varepsilon_{(T)n}$ is the strain due to temperature changes and

$\varepsilon_{(Shr)n}$ is the shrinkage strain.

Delayed elastic strain approximates the effect of primary (or recoverable) creep, which for concrete is due to water movement in the pores and occurs over a time period of the order of 10 days (Acker & Ulm, 2001) and is fully recoverable. Flow strain is caused by irreversible viscous slippage between layers of hydrates, occurs over a much longer time-scale than delayed elastic strain and is irrecoverable (Acker & Ulm, 2001). For the laboratory tests, which were over a short time period of between 7 and 11 hours and used cylinder samples, temperature strain $\varepsilon_{(T)n}$ and shrinkage strain $\varepsilon_{(Shr)n}$ were ignored. The strain at timestep n for all stress increments r in the Kelvin model was given by the following equation:

$$\varepsilon_{(K)n} = \frac{\sigma_n}{9K} + \frac{\sigma_n}{3G} + \frac{1}{3G_k}\sum_{r=1}^{n-1}(\sigma_r - \sigma_{r-1})\cdot\left(1 - e^{-G_k(t_n - \tau_r)/\eta}\right) \qquad \textbf{Equation 28}$$

where t is the age of the sprayed concrete in hours,

σ_n is the stress at timestep n,

σ_r is the stress increment (r = 1, 2, 3,... n-1),

K is the elastic bulk modulus,

G is the elastic shear modulus,

$\eta = \dfrac{1.5\cdot 10^{11}\cdot e^{\left(\frac{-1.5}{t^{0.6}}\right)}}{2(1+\nu)} kPa.s$ is the Kelvin viscosity parameter and

$G_k = \dfrac{8.0\cdot 10^{6}\cdot e^{\left(\frac{-1.0}{t^{0.4}}\right)}}{2(1+\nu)} kPa$ is the Kelvin spring stiffness, and in both these last two equations t is the age in days.

This equation effectively adds another Kelvin element for each stress increment σ_r. The equation can be rearranged to find the stress due to elastic and delayed elastic strain at timestep n:

$$\sigma_{(K)n} = \frac{\varepsilon_n - \frac{1}{3G_k}\sum_{r=1}^{n-1}(\sigma_r - \sigma_{r-1})\cdot\left(1 - e^{-G_k(t_n - \tau_r)/\eta}\right)}{\left(\frac{1}{9K} + \frac{1}{3G}\right)} \qquad \textbf{Equation 29}$$

The flow rate at timestep n may be given by any of a number of different relationships. In this example the relationship between compliance rate and age given by Acker & Ulm (2001) was used:

$$\frac{dJ}{dt} = \frac{5.1}{t} \qquad \textbf{Equation 30}$$

where J is the compliance, which is the deformation per unit stress.

The stress due to flow strain at timestep n is given by:

$$\sigma_{(Flow)n} = \frac{\frac{dJ}{dt} \cdot (t_n - t_{n-1}) \cdot \sigma_{n-1}}{\left(\frac{1}{9K} + \frac{1}{3G}\right)}$$ **Equation 31**

This flow stress is simply subtracted from the calculated Kelvin stress $\sigma_{(K)n}$ to give the total stress σ_n. Similarly, stresses due to temperature or shrinkage could be subtracted.

4.3.2 Application to laboratory tests

The uniaxial compressive strength of the batch of sprayed concrete was found at four different ages by strength testing of cylinders. This allowed the target utilisation as a function of time to be set for the utilisation test, the aim of the utilisation test being to expose the sprayed concrete cylinder to a constant utilisation by varying the strain rate. It also meant that the strength development with age during the time period of the test was known. This was approximated to a linear relationship, which fitted the data well with an r^2 regression coefficient above 0.97 in each case.

A comparison of the back-calculated stress with the stress measured in the test by the load cell attached to the apparatus is shown in Figure 4-33. The only major discrepancy appears to occur in the first 2-3 readings when the strain rate was relatively high. This was probably due to bedding down of the contact at the ends of the sample. In Figure 4-34 the first readings where the strain rate was elevated were ignored and the agreement between the back-calculation and the measured stress was good. A comparison of the stress-strain behaviour measured in the test and back-calculated from the measured strain is shown in Figure 4-35 and again the agreement was good.

Figure 4-36 and Figure 4-37 show the comparison of measured stress with the back-calculated stress for utilisation tests 2 and 3 respectively. Again there was reasonable agreement, except during a period in utilisation test 2 when no readings were taken between 4 hours 45 minutes and 6 hours 40 minutes. This was because to some extent the back-calculation method can correct itself, but requires frequent and evenly spaced displacement data.

4.3.3 Application to the field data

An attempt was made to apply the back-calculation method to 3D optical surveying data from the SWOT frontshunt tunnel. At the monitoring section considered, the first reading of the monitoring points was 5.5 hours after the ring was sprayed. From then on, they were surveyed approximately 1-2 times per day. At each monitoring section, there were 5 monitoring points; Point 1 at the crown, Point 2 at the left shoulder, Point 3 at the right shoulder, Point 4 at the left knee and Point 5 at the right knee as shown in Figure 4-38.

The monitoring data was in 3-dimensional coordinate form with components of chainage along the tunnel centreline and horizontal and vertical offsets from the tunnel centreline. Firstly this data must be converted to displacements by subtracting the first reading, and then the horizontal and vertical displacements must be converted to radial and tangential displacements. For the radial displacements, convergence was taken as positive, and for the tangential displacements, clockwise displacements were taken to be positive. Several assumptions were made at this stage:

1. The longitudinal displacements along the tunnel centreline were ignored.
2. Thermal strains were not considered.
3. Shrinkage strains were not considered.
4. The effect of multiaxial stress states was ignored; a 1-dimensional constitutive law was applied in the back-calculation.

Problems arose when trying to apply the back-calculation to the data. The reason for this can be seen in a plot of radial displacement of the monitoring points against time, shown in Figure 4-39. Figure 4-39 shows that there was very little movement of the monitoring points, in general less than ± 3 mm. The repeatability of optical surveying techniques is typically ± 2-3 mm according to Bock (2003) and with best practice methods can only be as precise as ± 1 mm (Clayton *et al.*, 2000). In this case, the repeatability appears to have been approximately ± 3-4 mm for the most part and occasionally much worse. Apart from an initial movement of the crown downwards and the shoulders outwards, no pattern is perceptible. The fluctuations in the readings caused by this poor repeatability, coupled with the small magnitude of the displacements, caused

numerical instability in the back-calculation, which then oscillated from increasingly large positive stress increments to increasingly large negative stress increments.

4.4 Pressure cells at Heathrow Terminal 4

The arrangement of the pressure cells at Heathrow Terminal 4 is shown in Figure 3-5. 12 radial and 12 tangential pressure cells were placed at 12 locations in an array around the perimeter of the tunnel. At each location, 1 tangential and 1 radial cell were placed except at positions 4 and 5, where two tangential cells were placed, one towards the extrados and one towards the intrados, and at positions 10 and 11, where no tangential cells were placed. The pressure cells were installed before any of the sprayed concrete lining was sprayed. This meant that in general the quality of the installation was much better than at T5. Two arrays of pressure cells were installed in the Terminal 4 Concourse Tunnel at Main Monitoring Section I (MMS I) and at Main Monitoring Section VIII (MMS VIII).

The installation of the pressure cells was observed by Pierre van der Berg (van der Berg, 1999) and the initial and medium-term readings were taken by him and by Alun Thomas. The most recent readings in June 2004 and February 2005 were taken by the author with assistance from Alun Thomas and David Watson. Using the method of interpretation outlined in the previous sections the aim was to make a full interpretation of the data including the most recent readings that extend the range of the readings to 8 ½ years.

4.4.1 MMS I tangential pressure cells

The read pressure in the tangential pressure cells in Main Monitoring Section I (MMS I), already corrected for vibrating wire temperature sensitivity, is shown in Figure 4-40, Figure 4-41 and Figure 4-42 for the first 2 weeks after installation. Also marked on the figures are the timings of the top heading, bench and invert construction and the temperature measured by the thermistors attached to the pressure cells.

In all the tangential cells, a marked increase and subsequent decrease in read pressure as the temperature increased and decreased due to the effect of

hydration heat was observed. This was evidence that they all had a good contact with the sprayed concrete. The only exception was PCT4-IN, which instead measured negative stress during hydration. This must have been a malfunction of the vibrating wire reader, since after 4 negative readings the data suddenly returned to the positive domain. This has been known to occur and is usually due to the reader picking up a harmonic when the vibrating wire has been plucked badly. It was found in the laboratory and in the field that this could be mitigated by turning on the speaker on the reader and listening to the tone. Any dull or split notes could then be treated with caution. A misread frequency is always very far from the frequency expected. Alternatively, automatic dataloggers (Campbell Scientific CR10 or CR10X) were found to be more consistent than the handheld reader and less likely to misread.

The read pressure in the tangential cells over the first 3 months is shown in Figure 4-43, Figure 4-44 and Figure 4-45. Crimping was undertaken on 20th November 1996 for cells PCT5-IN, PCT5-OUT, PCT6, PCT7, PCT8, PCT9 and PCT12, and on 21st November 1996 for cells PCT4-IN and PCT4-OUT. PCT1, PCT2 and PCT3 were not crimped. Although the temperatures measured by all the other thermistors were stable during this period, the thermistor attached to PCT12 experienced a rise in temperature of approximately 10 °C followed by a return to normal some time before the 12th December 1996. This was due to the hydration of the *in situ* secondary lining concrete in the invert, which was poured on the 18th November 1996, 2 days before the crimping began. The thermistor attached to the radial cell PCR12 also measured an increase in temperature at this time. It should be expected that if the primary lining at the invert was heated, it should expand and hence increase the tangential stress in the primary lining. Due to the lack of readings, it is therefore difficult to separate the effect of crimping and underpassing on the tangential stresses from the effect of the invert concrete hydration heat on the primary lining.

The underpassing of the Down Line Vent tunnel can be seen in the difference between the readings taken on 3rd December and 9th December 1996 in Figure 4-43, Figure 4-44 and Figure 4-45. As shown in Figure 3-3, the 6.1 m diameter Down Line Vent tunnel's centreline was 3-4 m behind the MMS I cross-section and the vertical clearance from extrados to extrados was 5.12 m. This caused a

dramatic reduction in the stress measured by the bench and invert tangential cells in the Concourse tunnel in Figure 4-45. However, the elevated temperature in the invert due to the hydration of the invert secondary lining concrete also dropped towards ambient temperature at the same time. Therefore, it is difficult to separate the two effects on the invert tangential cells. PCT2 and PCT3 in the crown of the tunnel (Figure 4-43) ceased to function at this point as the crimping tubes were accidentally cut by operatives. PCT1, though, measured a rise in stress during underpassing, possibly caused by sagging of the Concourse tunnel as a whole as the Down Line Vent tunnel undermined it.

The lower top heading cells at positions 4 and 5 showed a more complex behaviour. The cells close to the intrados, PCT4-IN and PCT5-IN, measured a rise in stress of approximately 1 MPa, whereas the cells close to the extrados experienced a drop in stress of approximately 1-2 MPa to zero. Bearing in mind that pressure cells will still read zero in a negative stress field, the drop in stress may have been greater. This is evidence that the lining was put into bending. This mode of bending may have been induced by a drop in horizontal stress in the ground with little change in the vertical stress causing the Concourse tunnel to squat.

The read pressure over 9 years is shown in Figure 4-46, Figure 4-47 and Figure 4-48. PCT2, PCT3, PCT4-IN and PCT6 stopped functioning early in this period. Of the remaining cells, PCT5-IN shows a gradual decrease with time while PCT4-OUT shows a gradual increase with time. This was caused as the bending moment induced by underpassing of the Down Line Vent tunnel 'creeped out' with time. The bench cells PCT7, PCT8 and PCT9 dropped to zero and possibly lost contact during underpassing of the Down Line Vent tunnel and remained at around zero for the subsequent years. A possible exception was PCT8, which showed a small positive stress the last two times it was read, so it looks as though it has regained contact. The invert cell PCT12 measured a gradual increase of stress with time.

Since the underpassing of the Down Line Vent tunnel has affected the measured stress significantly, and most of the read pressures (with the exception of PCT1, PCT5-IN and PCT12) have at some stage dropped to zero, no attempts have been made to estimate the absolute values of stress from these data.

4.4.2 MMS I radial pressure cells

The read pressure in the MMS I radial pressure cells, already corrected for vibrating wire temperature sensitivity, is shown in Figure 4-49, Figure 4-50 and Figure 4-51 for the first 2 weeks after installation. Also marked on the graphs are the timings of the top heading, bench and invert construction and the temperature measured by the thermistors attached to the pressure cells. PCR4 fluctuated wildly for 3 days and then stopped reading altogether, and PCR5 also malfunctioned from the start, so the data have been left out of Figure 4-49.

For radial cells, ground reaction temperature sensitivity can only occur if the ring is closed, or if sufficient friction between the lining and the ground can act as restraint. In the top heading cells, there was no discernible decrease as the temperature dropped after the hydration peak, but in the bench and invert cells there was. This was especially pronounced in the bench cells (Figure 4-50) because the peak temperature of hydration coincided with the installation of the invert.

The read pressure in the MMS I radial cells over the first 3 months is shown in Figure 4-52, Figure 4-53 and Figure 4-54. PCR1 and PCR2 ceased functioning approximately 2 months after installation.

The bench cells, since they appeared to be more susceptible to ground reaction temperature sensitivity due to the timing of their installation, measured continually decreasing pressure as the temperature dropped from the hydration peak of approximately 35°C to the ambient temperature of approximately 14°C (Figure 4-53). This resulted in cells PCR6, PCR7 and PCR9 reading approximately zero pressure by the time of the underpassing of the Down Line Vent tunnel and so they could not measure the drop in pressure expected due to the underpassing. Although a small drop to zero from a small positive pressure is discernible in PCR6 and PCR7, this was not as large as the drop in pressure measured by PCR8. Although the invert radial cells PCR10, PCR11 and PCR12 in Figure 4-54 showed a drop in pressure at the time of underpassing, this coincided with a drop in temperature at this location that would also have caused a drop in pressure. The temperature rise between the 18th and the 22nd November 1996 and the subsequent fall around the time of the underpassing was probably caused by the invert construction at this time.

The read pressure over 9 years is shown in Figure 4-55, Figure 4-56 and Figure 4-57. PCR3 had ceased functioning by June 2004. Since the readings taken 6 months after construction in April 1997, in most of the cells the changes in pressure appear to be solely due to temperature changes. PCR9 continued to increase until November 1999, 3 years after construction. PCR6 recovered from reading zero pressure to reading a small positive pressure in the two most recent readings. PCR12 stabilised sometime between November 1998 and June 2004.

Since PCR1, PCR2 and PCR8 stopped functioning before 6 months, PCR3 stopped functioning after 3 years, PCR4 and PCR5 never functioned, and PCR6, PCR7 and PCR9 were zero at some point, the only cells for which reliable long-term data are available are the invert cells PCR10, PCR11 and PCR12. The long-term radial stresses for these cells are shown in Table 4-6.

Table 4-6: Radial stresses 8 ½ years after construction at MMS I

Cell	Radial stress	Percentage of hydrostatic overburden (348 kPa)	Temperature
PCR10	245 kPa	70 %	16.1 °C
PCR11	269 kPa	77 %	15.6 °C
PCR12	214 kPa	61 %	15.4 °C

The depth to the Concourse Tunnel axis was 17.4 m, and the bulk density of the Made Ground, Terrace Gravel and London Clay was 20 kN/m^3, with the water table at the surface (Powell *et al.*, 1997). Therefore, the hydrostatic full overburden pressure at tunnel axis level was 348 kPa. The radial stress around the invert was therefore between 61 and 77 % of hydrostatic full overburden pressure.

4.4.3 MMS VIII tangential pressure cells

The read pressure in the tangential pressure cells in Main Monitoring Section VIII (MMS VIII) already corrected for vibrating wire temperature sensitivity is shown in Figure 4-58, Figure 4-59 and Figure 4-60 for the first 2 weeks after installation. Also marked on the graphs are the timings of the top heading, bench

and invert construction and the temperature measured by the thermistors attached to the pressure cells.

In Figure 4-58, the pattern of behaviour before ring closure was very different to MMS I with less response to the rise and fall of temperature due to hydration heat generation. Very little tangential stress was measured in PCT1, PCT2 and PCT3, but higher stresses were measured in PCT4 and PCT5 near the footings of the top heading. This was what was expected structurally because the top heading has little structural rigidity, is predominantly loaded vertically by the ground and effectively is cantilevering off the rings behind. However, cell restraint temperature sensitivity should have caused an increase in pressure in all the cells as the temperature was rising, regardless of whether the arch was restrained or not.

At least partly, the difference may be explained by the smaller rise in temperature during hydration in MMS VIII. There followed a second peak 3 days after spraying in PCT2, PCT3 and PCT5. It is not known why this second peak occurred but may have been caused by the location of plant exhausts. Whereas all the top heading tangential cells in MMS I measured temperatures in excess of 40°C, the temperatures in MMS VIII only reached around 30°C, with the crown cell PCT1 reaching 36°C. This may have been because the as-built lining was thinner at MMS VIII and therefore less hydration heat was generated and stored, because there were less data points and the peak temperature was missed (there were 9 data points before ring closure at MMS I, but only 4 at MMS VIII), or because the dosage of accelerator was lower at MMS VIII. Once the invert was closed, an increase in tangential stress was measured by all the top heading cells except PCT3, which had a near-zero pressure reading until it was crimped on 15th November and therefore was not in good contact with the sprayed concrete until then.

The bench and invert tangential cells in Figure 4-59 and Figure 4-60 showed a marked change in pressure with temperature from the start. Again, the lack of data points compared to MMS I reduced the amount of detail available for interpretation. Nevertheless, the fact that they responded to temperature does prove that they had a good contact with the sprayed concrete.

The read pressure over the first 3 months is shown in Figure 4-61, Figure 4-62 and Figure 4-63. PCT1, PCT2 and PCT3 were crimped at 15:30 on 15th November 1996, and PCT4, PCT5, PCT6-OUT, PCT6-IN and PCT7-IN were crimped at 10:30 on 19th November 1996. PCT4 stopped functioning after crimping. This was not because the operating range was exceeded – the operating range was 10 MPa for this design of pressure cell – but was a coincidence.

Also marked on Figure 4-61, Figure 4-62 and Figure 4-63 is the period during which the crosspassages were being excavated between 7th November and 14th November 1996. During this period there was a gradual decrease in temperature with time of on average 4 °C, which will have caused a drop in read pressure of approximately 0.4 MPa at a cell restraint temperature sensitivity of 0.1 MPa/°C. This makes the sharp rises in tangential stress between 11:00 on the 7th November and 12:00 on 8th November 1996 seem smaller than they really were. An adjustment showing the change in stress solely due to crosspassage construction using a temperature sensitivity of 0.1 MPa/°C is shown in Figure 4-64. Figure 4-64 shows a significant rise in tangential stress of between approximately 0.2 and 1.4 MPa, particularly evident in the odd-numbered cells, which were on the right hand side of the tunnel. The stress measured by PCT7-IN increased much more than PCT7-OUT, indicating that the tunnel was bending in a squatting mode.

The read pressure over 9 years is shown in Figure 4-65, Figure 4-66 and Figure 4-67. Only PCT5, PCT7-IN, PCT7-OUT, PCT9 and PCT12 were still functioning and reading non-zero pressures up to the most recent readings. They all show sensitivity to temperature change. The long-term trend appears to be a gradual decrease in pressure, with the exception of PCT12 which shows a gradual increase.

4.4.4 MMS VIII radial pressure cells

The radial stresses in the radial pressure cells in Main Monitoring Section VIII (MMS VIII) already corrected for vibrating wire temperature sensitivity are shown in Figure 4-68, Figure 4-69 and Figure 4-70 for the first 2 weeks after installation. Also marked on the graphs are the timings of the top heading, bench and invert construction and the temperature measured by the thermistors attached

to the pressure cells. All of the radial cells were still functioning when the most recent readings were taken, and at no time since their installation did the read pressure descend to zero and the cells lose contact, so an absolute value of radial stress was obtained from all the radial cells at MMS VIII. This provides a valuable case study.

The radial stresses over the first 3 months are shown in Figure 4-71, Figure 4-72 and Figure 4-73. The period of adjacent crosspassage construction is marked on the figures, and caused a sudden increase in radial stress between 11:00 on 6th November and 12:00 on 8th November 1996 in PCR2, PCR3, PCR5, PCR9 and PCR11, as the ground pressure redistributed either side of the crosspassage. PCR7 measured a sudden drop in radial stress at this time followed by a net rise in radial stress between 12:00 on 8th November and 09:00 on 9th November. More gradual rises, against a backdrop of a gradual decrease in temperature of approximately 4°C, were measured over the whole period by PCR4, PCR6, PCR8, PCR10 and PCR12 on the other side of the tunnel.

The reason for the sudden change in radial and tangential stress on one side of the tunnel compared to the gradual change on the other side, when similar crosspassages were constructed on both sides equidistant from MMS VIII is not clear. On average, the increase in radial pressure between the 6th and 14th November was 37 kPa. If the ground reaction temperature sensitivity were assumed to be approximately 7 kPa/°C, then the increase of radial stress in MMS VIII due to crosspassage construction was on average 65 kPa, an increase of approximately 40 % on the radial stress prior to crosspassage construction.

The read pressure over 9 years is shown in Figure 4-74, Figure 4-75 and Figure 4-76. Most of the radial cells show only changes in radial stress due to temperature changes from about 6 months after construction, except for PCR6 and PCR12 which show a gradual increase over time. However, the last 2 readings of PCR6 and PCR12 in June 2004 and February 2005 show a decrease in radial stress with temperature, which indicates that the stress may have stabilised at these locations by this time. If it is assumed that this decrease in radial stress was solely due to ground reaction temperature sensitivity, then PCR6 would have a ground reaction temperature sensitivity of 9.1 kPa/°C and PCR12 would have a ground reaction temperature sensitivity of 4.9 kPa/°C.

These values are broadly within the range of values calculated for most of the T5 radial cells (Figure 4-9 and Figure 4-11) of 5.6-7.4 kPa/°C with 1 outlier at 14.9 kPa/°C, although PCR12 is just below this range. This suggests that ground pressure may still be increasing after 8 ½ years due to swelling of the clay, albeit at a very slow rate, at the location of PCR12 at the centre of the invert. Everywhere else around the tunnel lining the ground pressure had stabilised when nearby construction operations finished about 3 months after installation of the pressure cells.

Table 4-7 lists the radial stresses 8 ½ years after construction. It should be noted that due to the ground reaction temperature sensitivity, the values of stress are dependent on temperature at the time the reading is taken. Therefore, the temperatures measured by the thermistors attached to the cells are also listed.

Table 4-7 shows a general trend for radial stress to increase with depth. The condition of static equilibrium requires that the forces in opposite directions be equal, and so the difference between the pressure on the crown and the pressure on the invert must be approximately equal to the weight of the tunnel. If the radial stresses of PCR1, 2, 3, 4 and 5 were averaged and converted to a downwards force by multiplying by the width of the excavation (7.94 m), and the same were done to find an upwards force by averaging PCR10, 11 and 12, the difference would be a net upwards force of 850 kN/m. The 350 mm thick primary lining is estimated to weigh 209 kN/m, so it is feasible that the secondary lining, invert concrete and other installations could easily make up the difference.

Table 4-7: Radial stresses 8 ½ years after construction at MMS VIII

Cell	Radial stress	Percentage of hydrostatic overburden (348 kPa)	Temperature	Temperature sensitivity [+]
PCR1	85 kPa	25 %	14.3 °C	7.95 kPa/°C
PCR2	176 kPa	51 %	-	3.85 kPa/°C [‡]
PCR3	190 kPa	55 %	14.4 °C	5.93 kPa/°C
PCR4*	238 kPa	68 %	17.4 °C	-
PCR5	184 kPa	53 %	10.3 °C	3.76 kPa/°C
PCR6	186 kPa	54 %	14.9 °C	9.12 kPa/°C
PCR7	165 kPa	47 %	14.8 °C	7.34 kPa/°C
PCR8	230 kPa	66 %	15.2 °C	4.02 kPa/°C
PCR9	257 kPa	74 %	15.2 °C	4.95 kPa/°C
PCR10	316 kPa	91 %	15.3 °C	6.29 kPa/°C
PCR11	257 kPa	74 %	15.6 °C	9.03 kPa/°C
PCR12	272 kPa	78 %	-	5.04 kPa/°C [†]

* PCR4 was not functioning when the last reading was taken on 24/2/05, so the previous reading is listed here, taken on 25/6/04.

[+] Temperature sensitivity estimated from difference between last 2 readings.

[‡] Calculated using PCR1 temperature.

[†] Calculated using PCR11 temperature.

4.5 Discussion

Understanding of temperature sensitivity has been considerably improved. It may now be separated into 3 categories: temperature sensitivity of the vibrating wire and transducer, cell-restraint temperature sensitivity (tangential cells only) and ground reaction temperature sensitivity. The improved understanding of temperature sensitivity has led to an appreciation of the sensitivity of pressure cells to small changes in stress. It has also meant that the scatter observed in pressure cell measurements may now be accounted for by a known phenomenon

and not assigned to other variables or unreliability as it has been in the past (e.g. Bonapace, 1997).

Ground reaction temperature sensitivity has never before been identified in tunnel pressure cell data, but has been shown in this chapter to be important both for tangential cells and radial cells. For various reasons, including increased ridership and increased energy consumption of rolling stock, average and peak temperatures in the London Underground have been gradually increasing ever since it was opened (Kessell, 2005). It is possible that long-term increases in stress measured in London Underground tunnels over many years (Ward & Thomas, 1965; Barratt *et al.*, 1994) may at least in part be due to long-term increases in temperature. Another factor affecting some locations in London may be rising groundwater levels (Simpson *et al.*, 1989).

Strain sensitivity of tangential pressure cells has also been identified and investigated using a numerical model. Shrinkage of the T5 test panel resulted in a read pressure of between 3 to 4 MPa at 250 days (Figure 4-3), which is of the same order of magnitude as the stresses being measured. However, no long-term increase in pressure due to shrinkage was evident in the tangential pressure cell data from the tunnels. At T5 (Figure 4-21 and Figure 4-27), the primary lining was covered with a 50 mm thick finishing layer of sprayed concrete within 2 weeks of the end of the frontshunt tunnel excavation, which will have decreased the drying shrinkage of the primary lining. At T4 (Figure 4-46, Figure 4-47, Figure 4-48, Figure 4-65, Figure 4-66 and Figure 4-67), the secondary lining would have prevented drying shrinkage from occurring after it had been installed.

At early age, autogenous shrinkage may have increased the read pressure in the tunnel tangential cells, but this is difficult to quantify and separate from loading- and temperature-induced pressures.

The pressure cell data from T5 were compromised by various factors. Most of the tangential pressure cells were not crimped early enough to avoid zero readings and hence data was lost. The installation at Array 1 was poor, with most of the tangential and radial cells showing no sensitivity to temperature and reading zero stress. The installation at Array 2 was better, but crimping was

performed too late on 3 of the 5 tangential pressure cells. At T5, crimping was performed on the radial cells, but this was a mistake and should have been unnecessary if the cells had been well installed. Within 2 weeks, the rise in read pressure due to crimping dissipated.

Table 2-7 is reproduced below in Table 4-8 with the results from the radial pressure cells installed at T4 and T5 added for comparison. An estimate of volume loss is also provided where known. There is no correlation whatsoever between increasing volume loss and decreasing loads. In fact, the tunnels of Skempton (1943) and Ward & Thomas (1965) in all likelihood had the highest volume losses, and these tunnels also had the highest loads. The relatively low volume losses at the T4 concourse tunnel, T5 SWOT frontshunt tunnel and the Heathrow cargo tunnel (Muir Wood, 1969) did not result in higher loads acting on the linings. One could argue that the reasonably high loads at the Heathrow cargo tunnel were caused by not allowing sufficient deformation, but a more convincing argument is that the shallow cover of the tunnel did not allow a full ground arch to form. The balance of evidence therefore indicates that there is no benefit to be gained from allowing the ground to deform when tunnelling in London Clay.

The literature review categorised two types of tunnel behaviour according to Figure 2-39:

1. Tunnels which experience more than 80% of the maximum long-term radial pressure in fewer than 7 days (e.g. Muir Wood, 1969).
2. Tunnels which experience less than 60% of the maximum long-term radial pressure in the first 7 days, and subsequently pressures continue to increase at a gradual rate over a long period of several years (e.g. Ward & Thomas Site V, 1965; Barratt *et al.*, 1994).

Table 4-8: Comparison of T4 and T5 radial stress measurements with previous measurements in London Clay

Authors	Tunnel	Volume loss (%) ‡	Time period	Long-term load (% overburden)
-	T4 concourse MMS VIII	0.8 % *	8 ½ years	47-78 % †
-	T5 SWOT frontshunt Array 2	0.63 %	9 months	53-65 %
Bowers & Redgers 1996	Jubilee Line Extension, St. James's Park	3.3 % ¶	4 months	43-62 % (not stabilised)
Barratt *et al.* 1994	Jubilee Line, Regent's Park	1.5 % §	19 ½ years	40-64 %
Muir Wood, 1969	Heathrow Cargo Tunnel, Heathrow	0.2 % §	20 months	60-80 %
Ward & Thomas 1965	'Site V', Victoria Line, Netherton Rd., NE London	1.5 % §	3 ½ years	105 %
Ward & Thomas 1965	'Site O', Post Office Railway, London	None found	6 ½ years	71 % (not stabilised)
Cooling & Ward 1953	9' diameter water tunnel, London	None found	3 months	53-64 % (not stabilised)
Skempton 1943	Unknown tunnel, London.	None found	1 ½ months	102-108 %

‡ at the end of construction (short-term final settlement)

* Clayton *et al.* (2006)

† excluding 2 outlying points

¶ Standing & Burland (2006)

§ Mair (1992) or Mair & Taylor (1997)

The tunnels that appear in category 2 are also the tunnels with the higher volume losses in Table 4-8, whereas the tunnels that appear in category 1 have lower volume losses. One apparent exception to the rule is the Jubilee Line Extension at St.James's Park (Bowers & Redgers, 1996; Standing & Burland, 2006), which had an exceptionally high volume loss and yet a low long-term load. However, at

4 months after construction, the long-term load had not yet been reached, and inspection of Figure 2-37 suggests that this was the case and the load had yet to stabilise at a long-term value. If the long-term value were at a value greater than 80 % of full overburden pressure, then this tunnel would be in category 2 with less than 60 % of full overburden pressure in the first 7 days. Volume loss data for Cooling & Ward's (1953) water tunnel could not be found, but similarly when the last load measurement was taken at 3 months the load was still increasing.

Given the relatively low volume losses measured at the T4 concourse tunnel and the T5 SWOT frontshunt tunnel, the tunnels should be expected to be in category 1. The T5 SWOT frontshunt tunnel certainly fit into category 1, and even experienced higher radial pressures in the first 7 days than in the long-term, due to hydration heat expanding the completed ring against the ground (Table 4-5). As with the other category 1 tunnels such as the Heathrow cargo tunnel (Muir Wood, 1969), there was no gradual increase in pressure in the long-term.

A comparison of a top heading radial pressure cell, a bench radial pressure cell and an invert radial pressure cell with the category 1 tunnels (Ward & Thomas site V, 1965; Muir Wood, 1969) and the category 2 tunnels (Barratt *et al.*, 1994), is shown in Figure 4-77 for the first 50 days. The top heading and bench radial pressure behave as though they were category 1 tunnels, whereas the invert radial pressure behaves as though it were a category 2 tunnel, with a gradual increase in pressure over several years. As discussed in Section 2.6.2, this is because the ground around the invert experienced a greater degree of permanent unloading during construction, and this caused swelling of the clay as the negative excess pore pressures dissipated, in turn increasing the radial pressure over several years.

4.6 Conclusions

An understanding of the role of CAF, temperature sensitivity and strain sensitivity is important for the correct interpretation of pressure cell data. This research has improved this understanding and thereby improved confidence in the reliability of pressure cells by explaining many of the sources of what were previously thought of as random fluctuations in readings.

Radial pressure cells can be used to measure the radial stress acting on an SCL tunnel with an acceptable degree of accuracy and precision that is superior to the estimates of stress obtained by any other method. Identification of poorly performing radial cells can be achieved by estimating the sensitivity of the pressure cell to temperature changes.

Tangential pressure cells can be used to measure the tangential stress in a sprayed concrete lining. There are more steps in the interpretation; therefore they are less accurate than radial cells. Identification of poorly performing tangential cells can be achieved by inspection of the crimping response curve or by estimating the sensitivity of the pressure cell to temperature changes. With careful installation and crimping, and a high enough frequency of readings, the absolute values of stress may be found with an acceptable level of accuracy.

The radial pressure cell measurements at the Heathrow Terminal 5 (T5) Stormwater Outfall tunnel (SWOT) and Terminal 4 (T4) Concourse tunnel showed that SCL tunnels can be constructed in London Clay such that the radial stress stabilises as soon as construction activities have ended, at a value well below full overburden pressure. This is in contrast to older tunnels in London Clay with higher volume losses that have experienced a gradual increase over several years to a value close to full overburden pressure. This is due to the higher degree of unloading in the older tunnels generating greater, or more extensive, negative excess pore pressures. Other factors that may contribute to this phenomenon may be the rising groundwater levels in the deep aquifer of the London Basin, or in the case of London Underground tunnels, gradually increasing temperatures in the tunnels over many years.

A back-calculation method was developed that performed well when applied to laboratory tests. However, it did not perform well (as predicted by the literature review) when applied to tunnel lining displacement monitoring, since the accumulated errors were too large. The application of such back-calculation methods in soft ground should be robustly questioned.

The pressure cells at Heathrow Terminal 4 concourse tunnel also measured the effects of underpassing (MMS I), adjacent crosspassage construction (MMS

VIII) and pouring of the secondary concrete in the invert (MMS VIII). This illustrated not just their usefulness, but also their sensitivity.

Once installed, failure rates of pressure cells were low relative to other types of instrumentation, for example in-tunnel surveying targets (Clayton, 2006). Of the 48 pressure cells installed in the T4 concourse tunnel, only 2 were not functioning after installation, 9 were not functioning by 3 months, and after 8 years only 13 had failed. In other words, survivability was 73 % over 8 years. Of the 22 pressure cells installed in the T5 SWOT frontshunt tunnel and test panel, only 2 stopped functioning over the 9 months that readings were taken, although poor installation or crimping, particularly in Array 1, unnecessarily rendered several more useless.

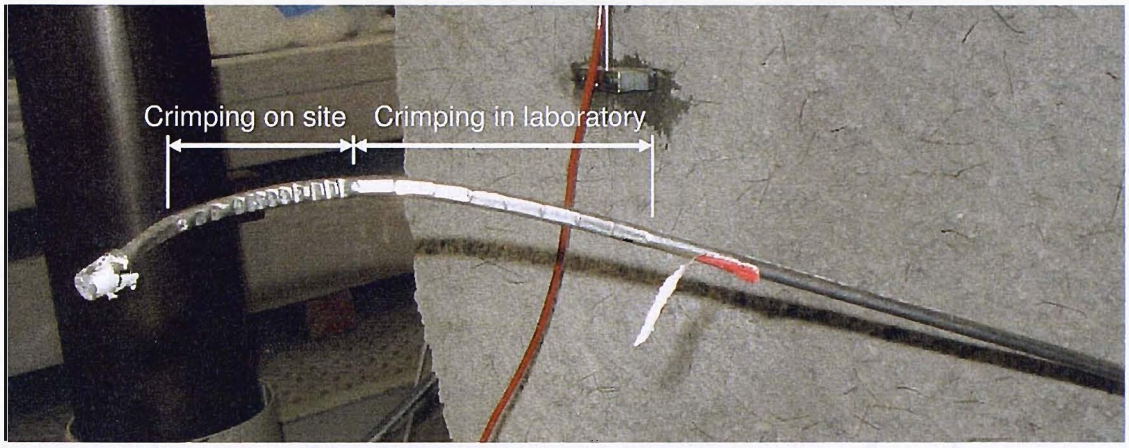

Figure 4-1: Crimping performed on site and in the laboratory

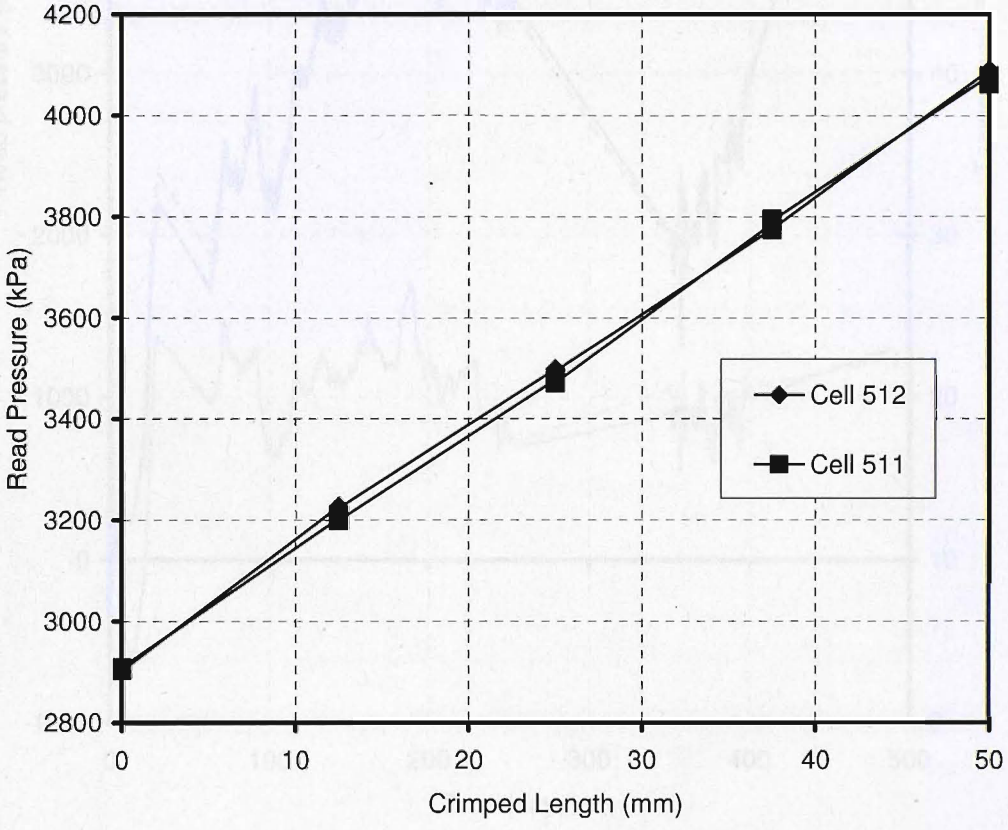

Figure 4-2: Crimping records from the test panel in the laboratory

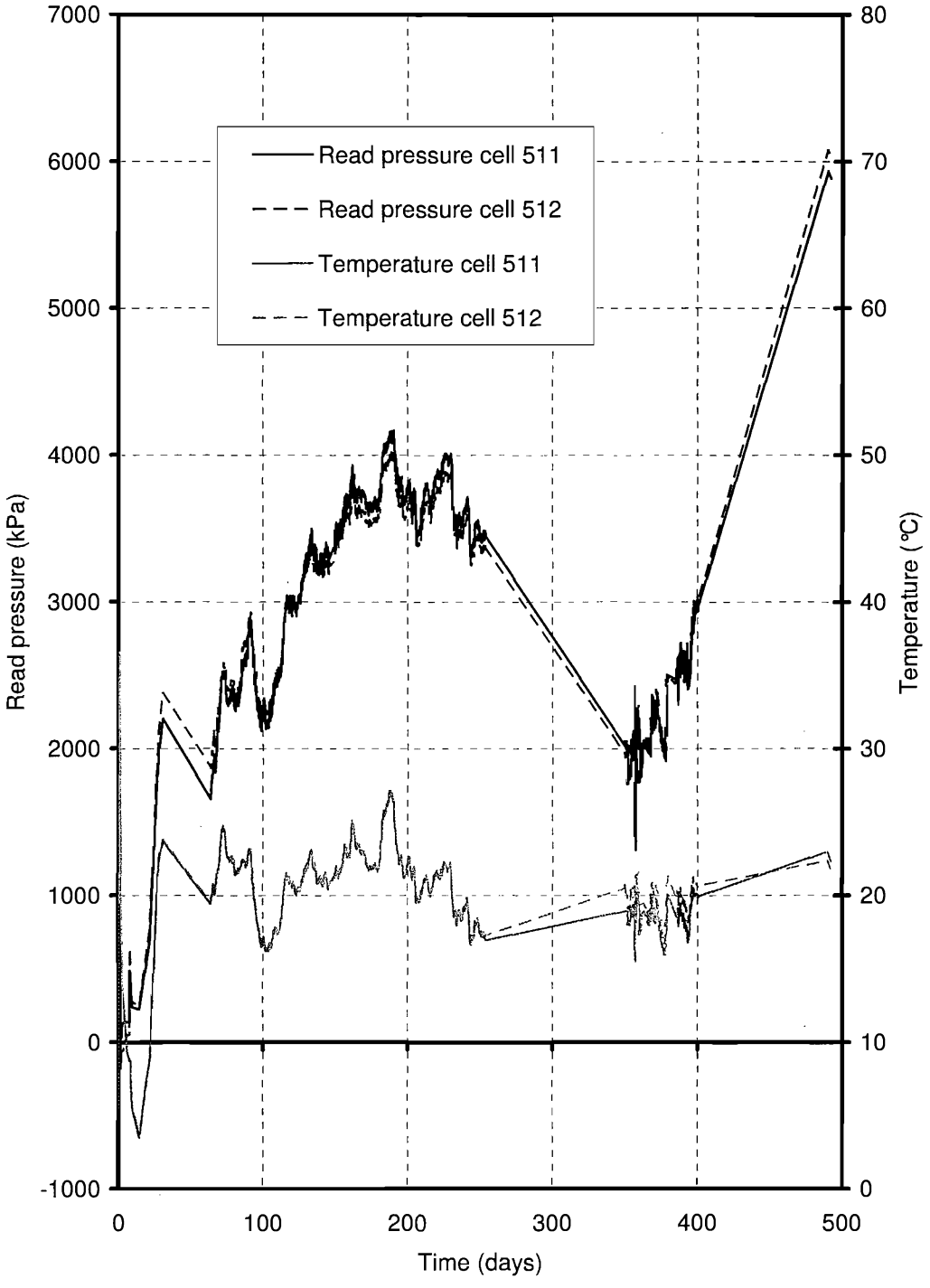

Figure 4-3: Read pressure and temperature in test panel tangential pressure cells 511 and 512

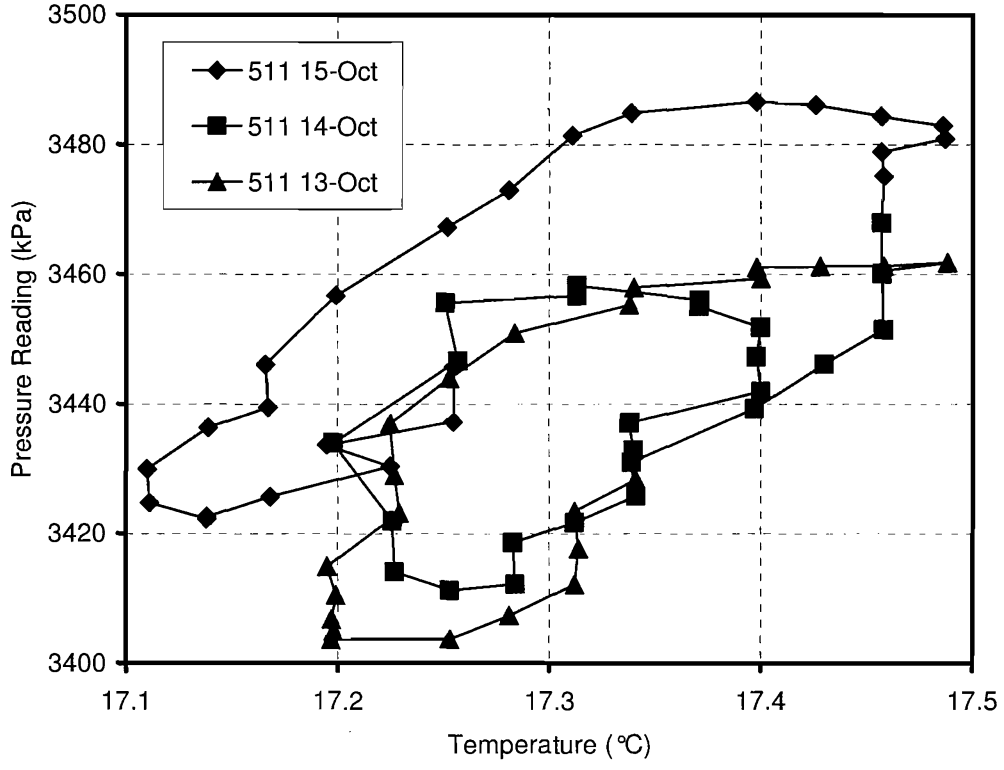

Figure 4-4: Variation of pressure due to temperature over 3 days in the test panel

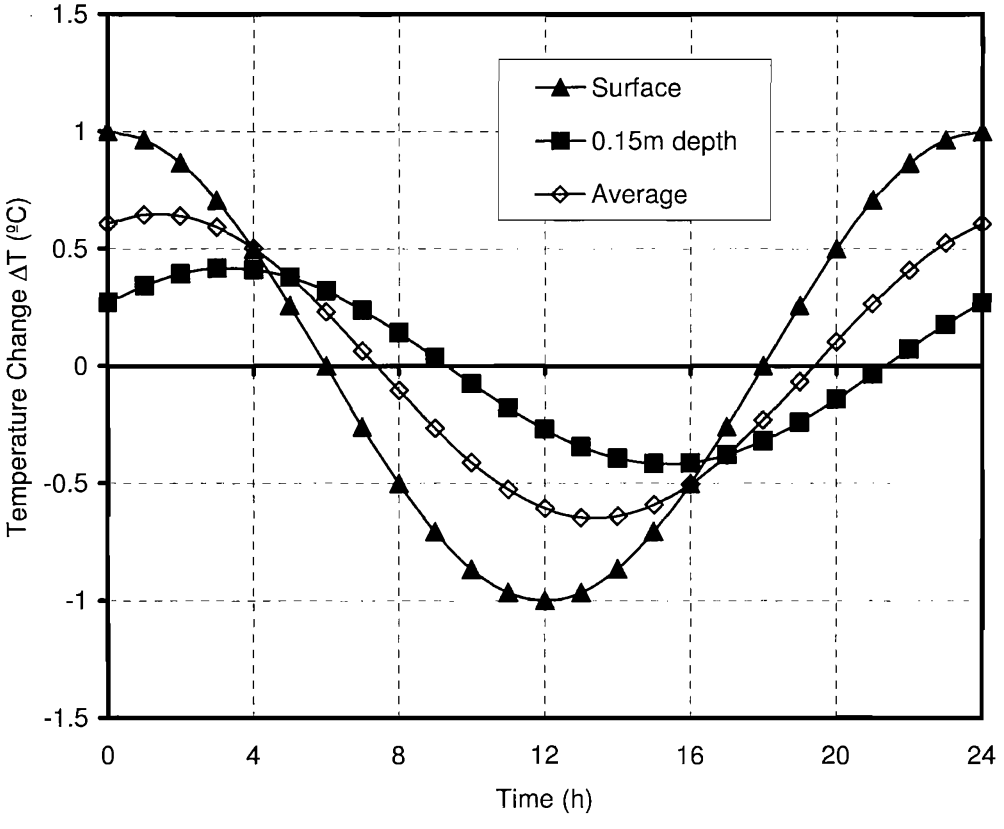

Figure 4-5: Variation of temperature with time due to diurnal surface temperature changes of ± 1 °C

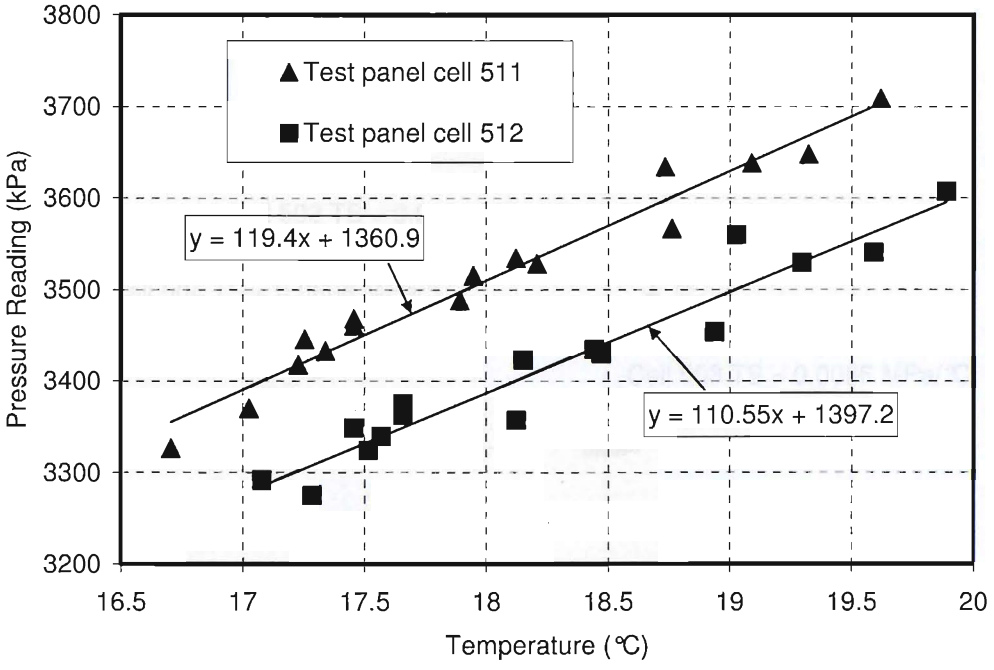

Figure 4-6: Temperature sensitivity estimation for test panel tangential pressure cells

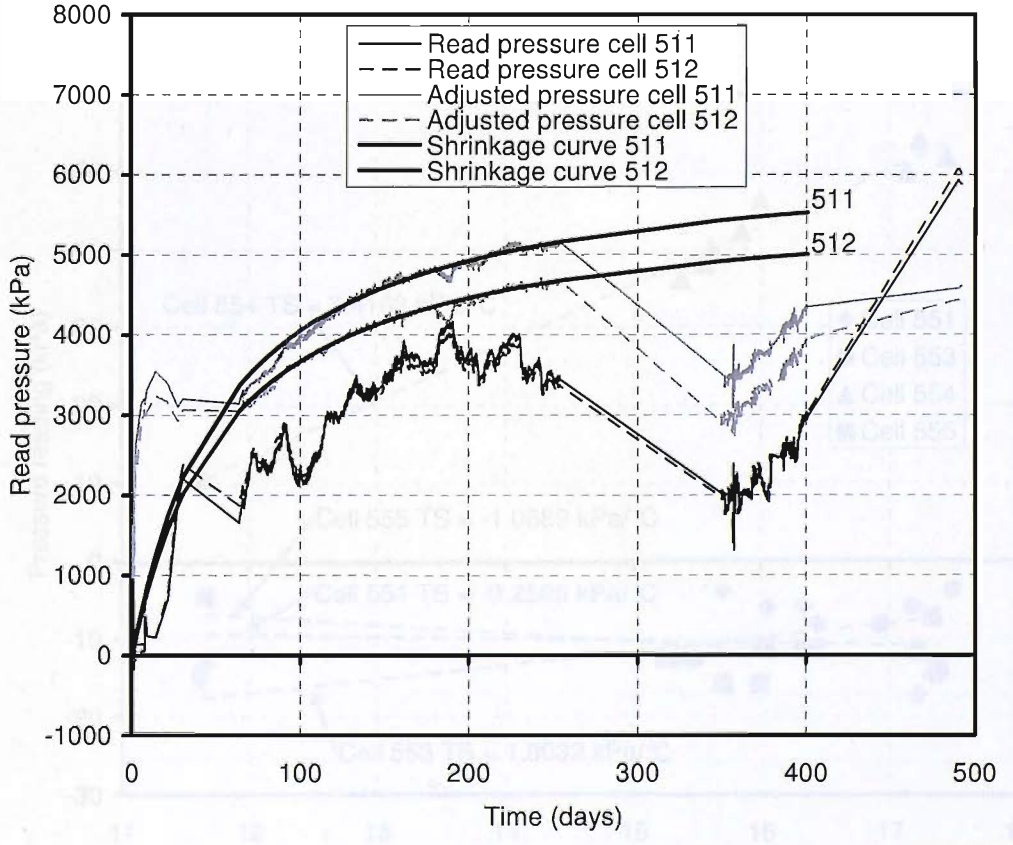

Figure 4-7: Read pressure and adjusted pressure in test panel tangential pressure cells 511 and 512

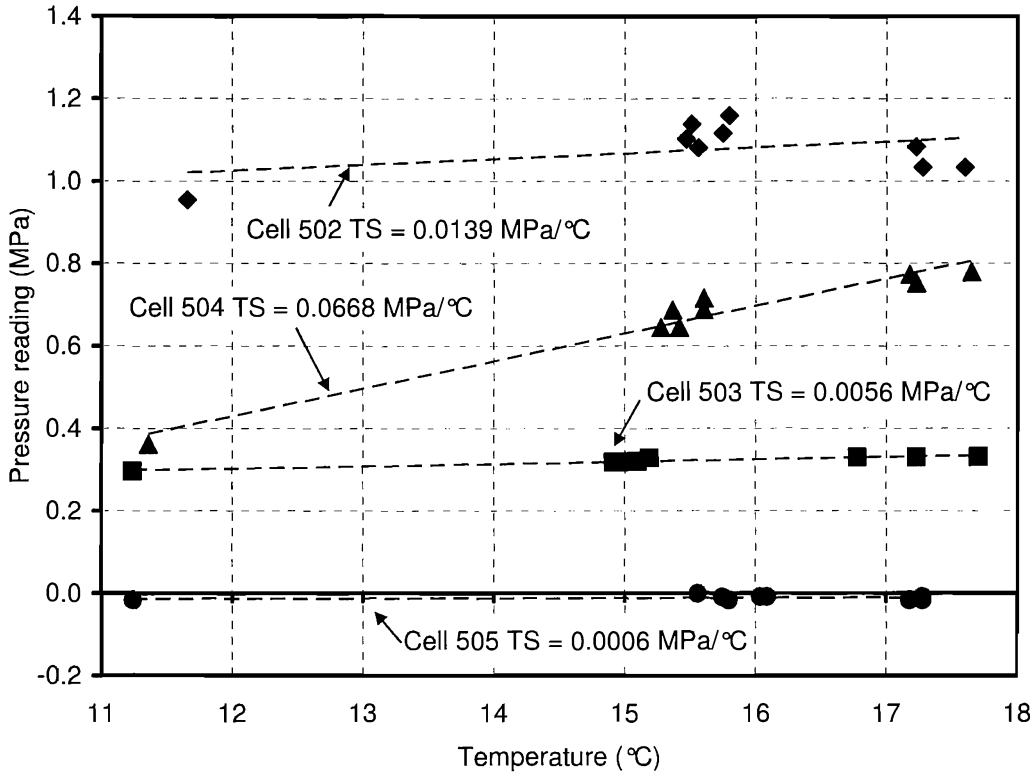

Figure 4-8: Temperature sensitivity estimation in T5 Array 1 tangential pressure cells

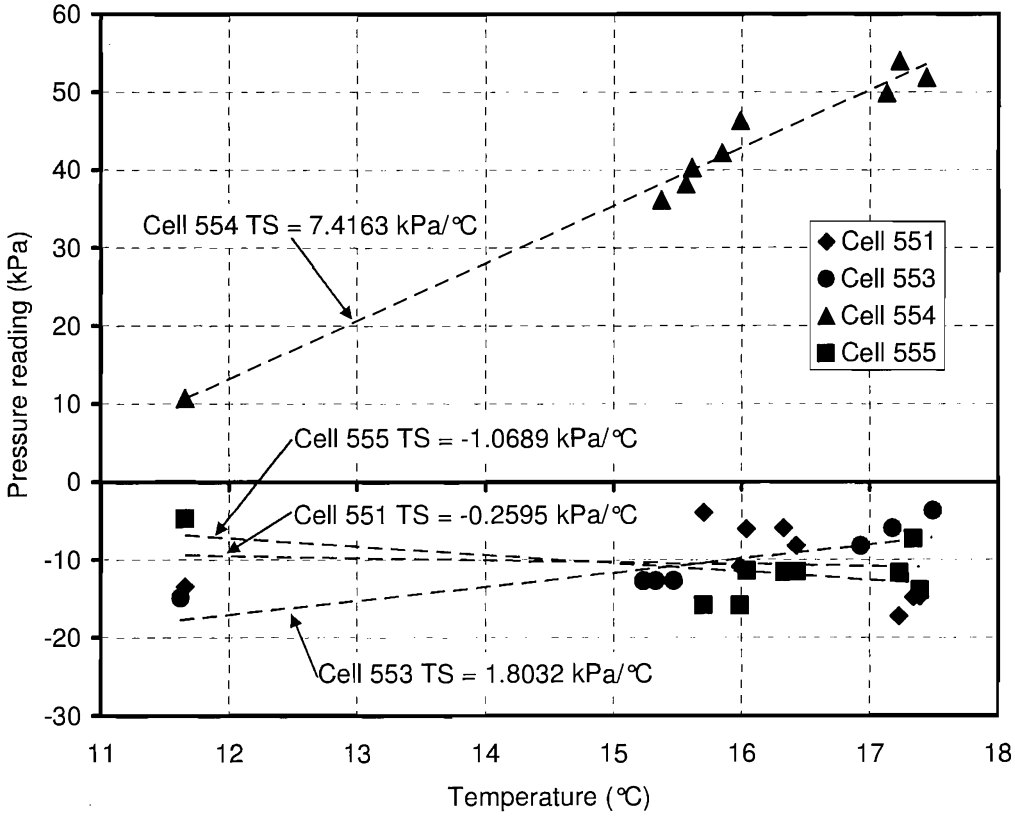

Figure 4-9: Temperature sensitivity estimation in T5 Array 1 radial pressure cells

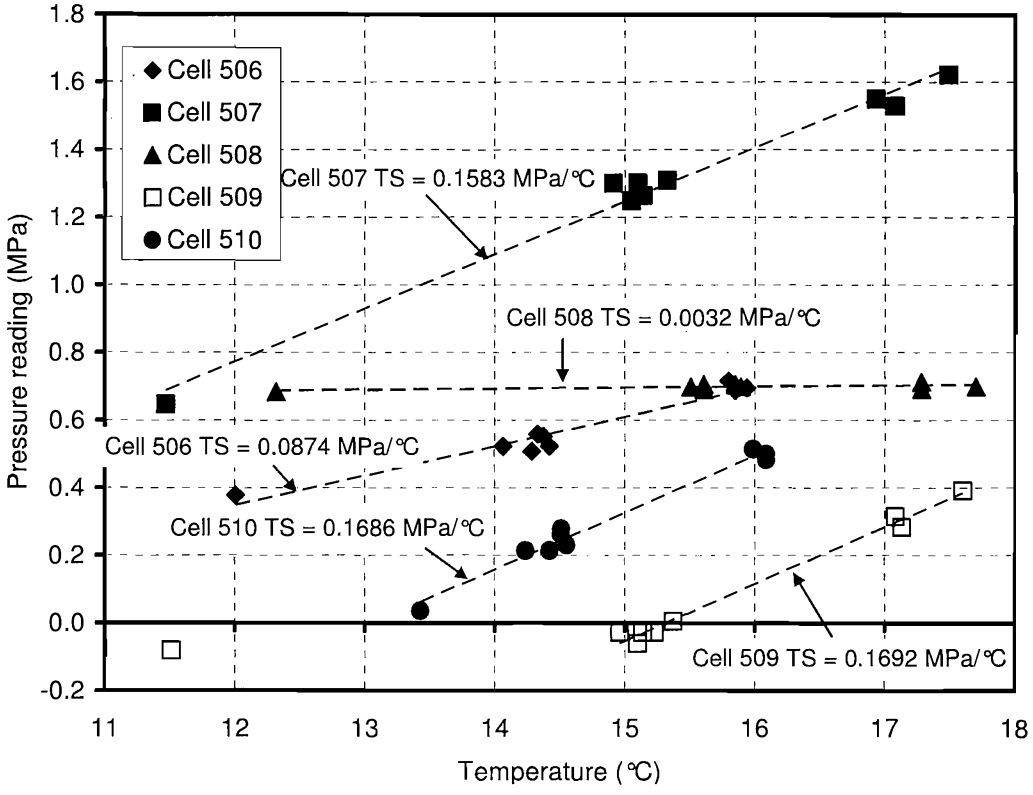

Figure 4-10: Temperature sensitivity estimation for T5 Array 2 tangential pressure cells

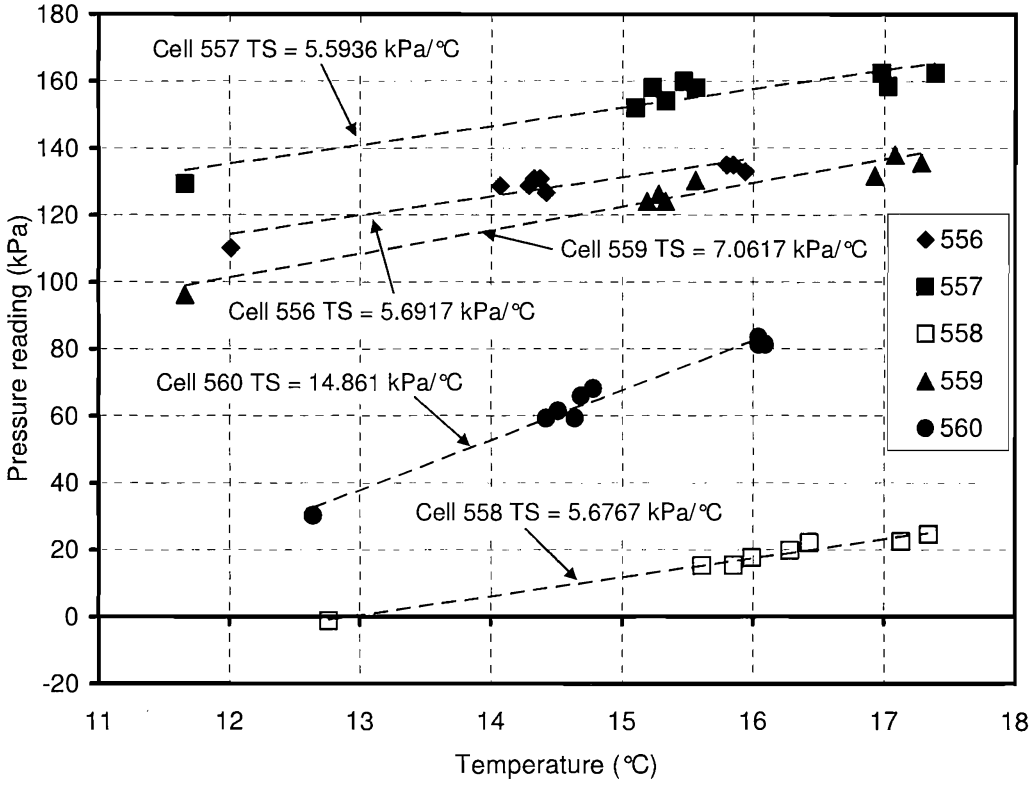

Figure 4-11: Temperature sensitivity estimation in T5 Array 2 radial pressure cells

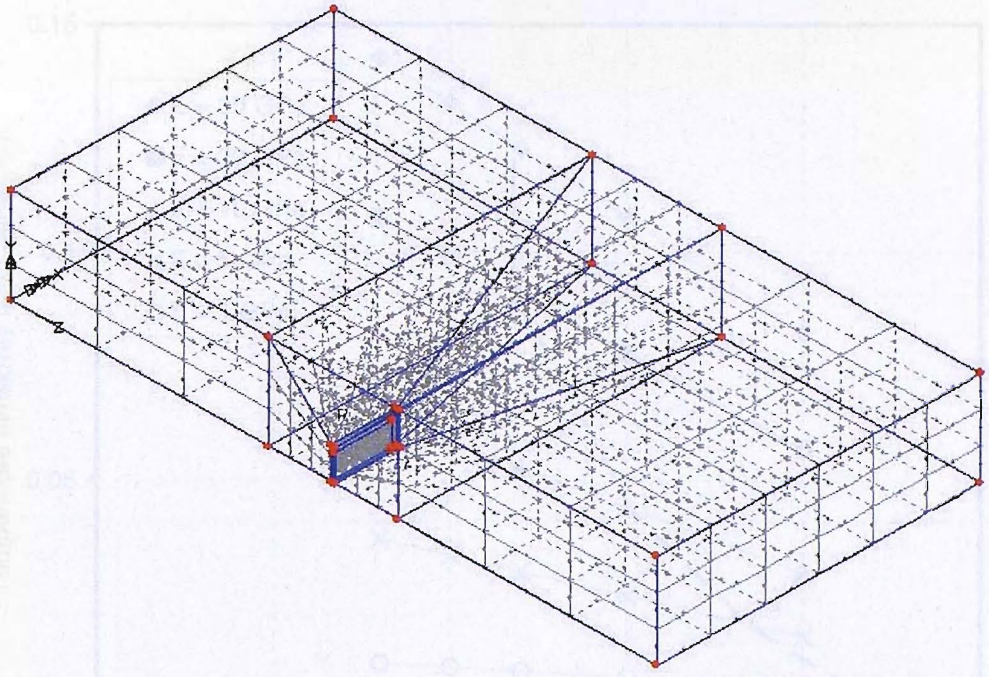

Figure 4-12: Finite element mesh of the test panel

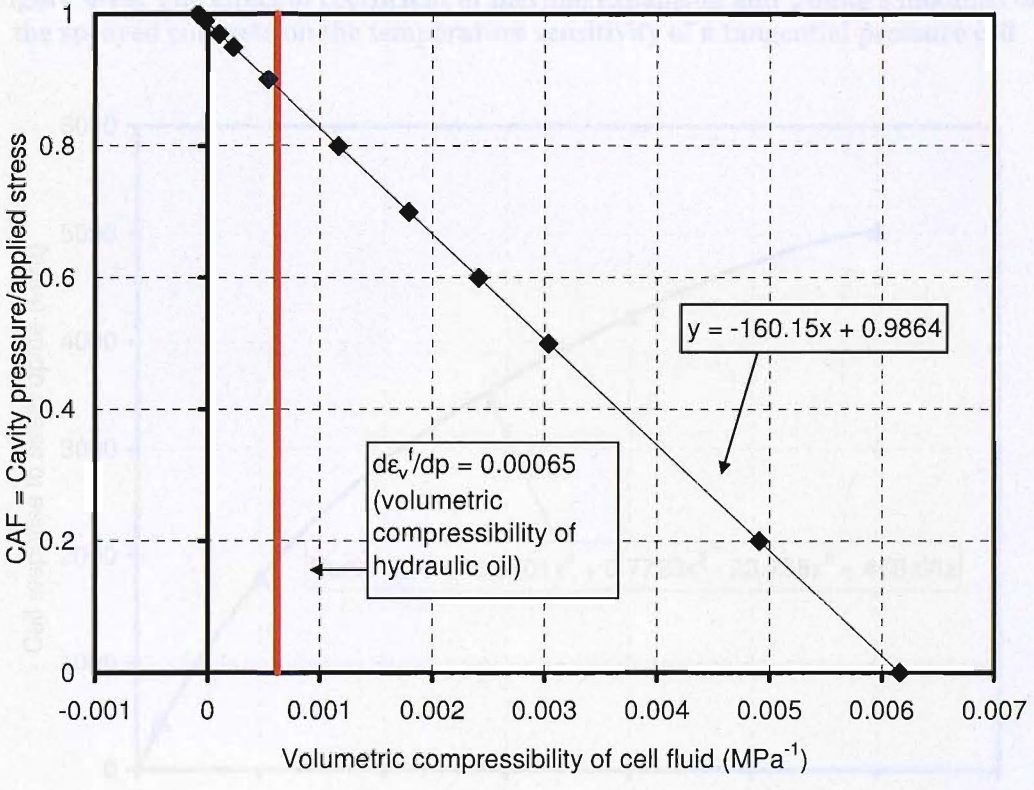

Figure 4-13: Variation of CAF with volumetric compressibility of cell fluid for material parameters in Table 4-2

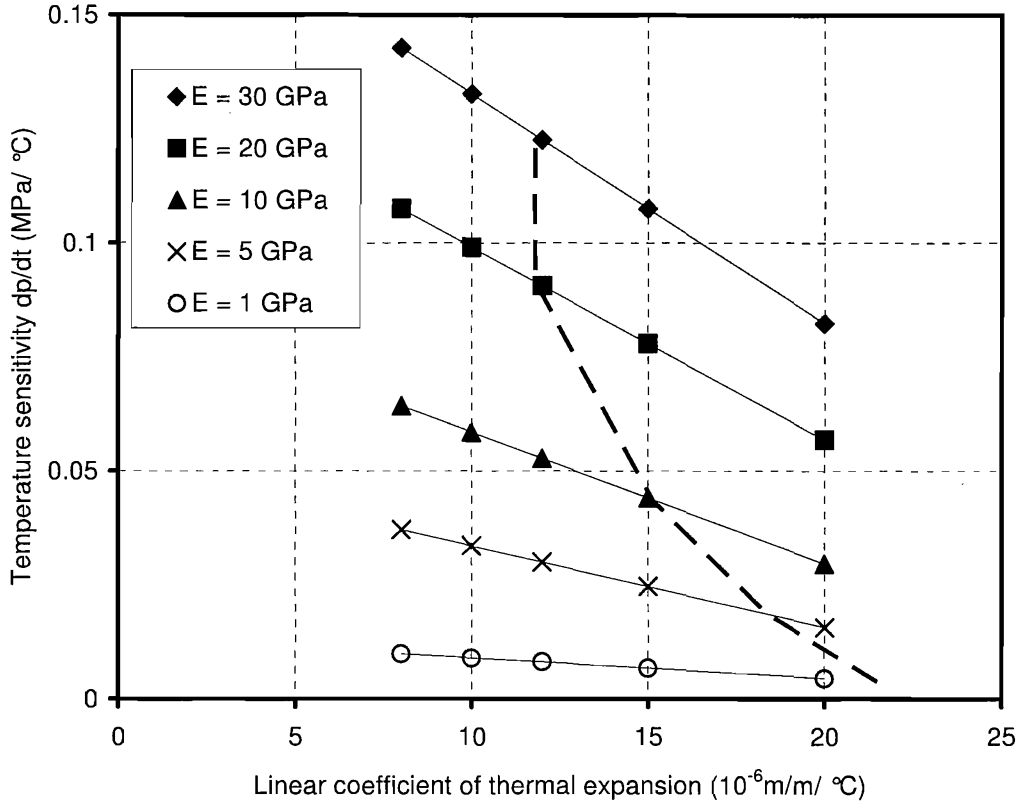

Figure 4-14: The effect of coefficient of thermal expansion and Young's modulus of the sprayed concrete on the temperature sensitivity of a tangential pressure cell

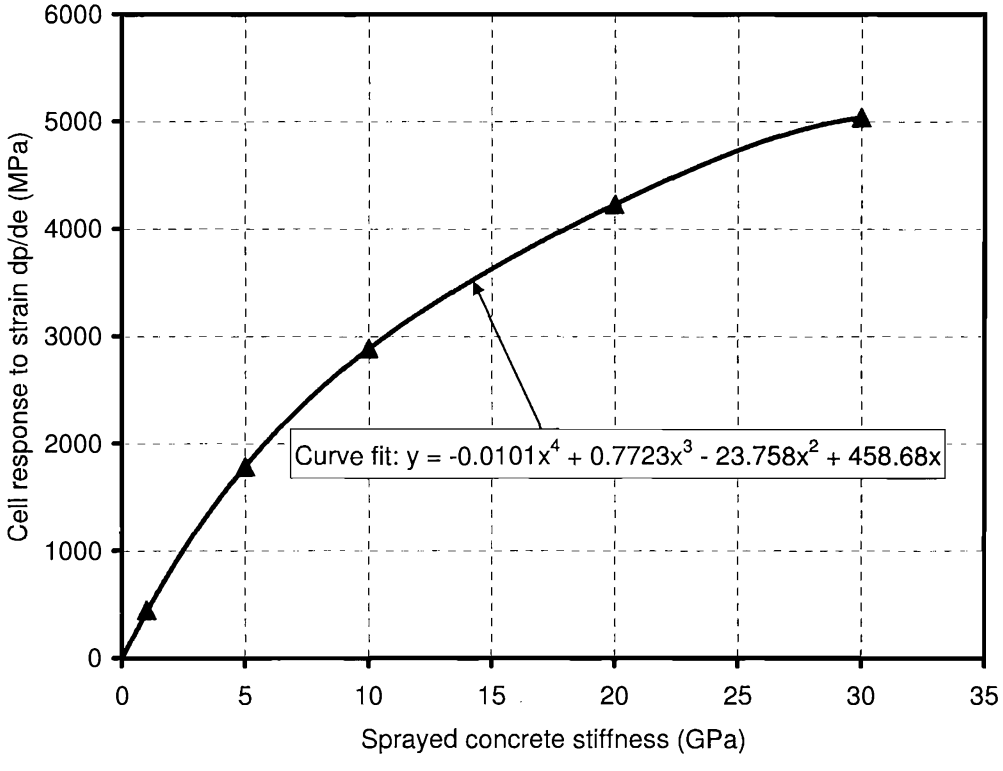

Figure 4-15: Variation of strain sensitivity with medium stiffness

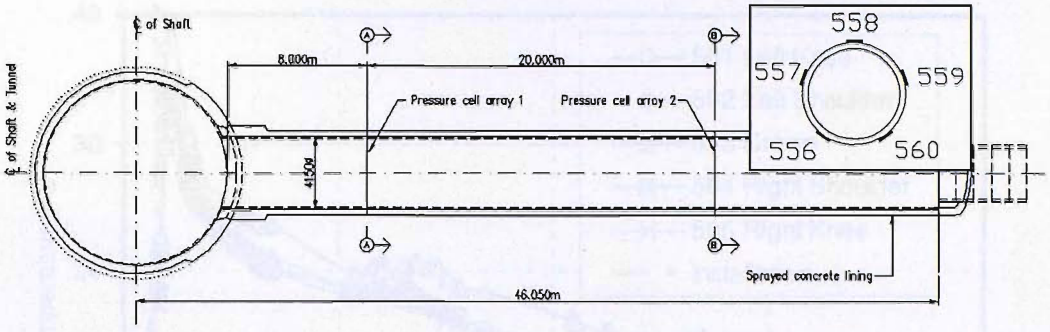

Figure 4-16: Location plan of pressure cell Array 1 and Array 2 in the Heathrow Terminal 5 SWOT frontshunt tunnel with indicative cross-section showing Array 2 radial cell positions

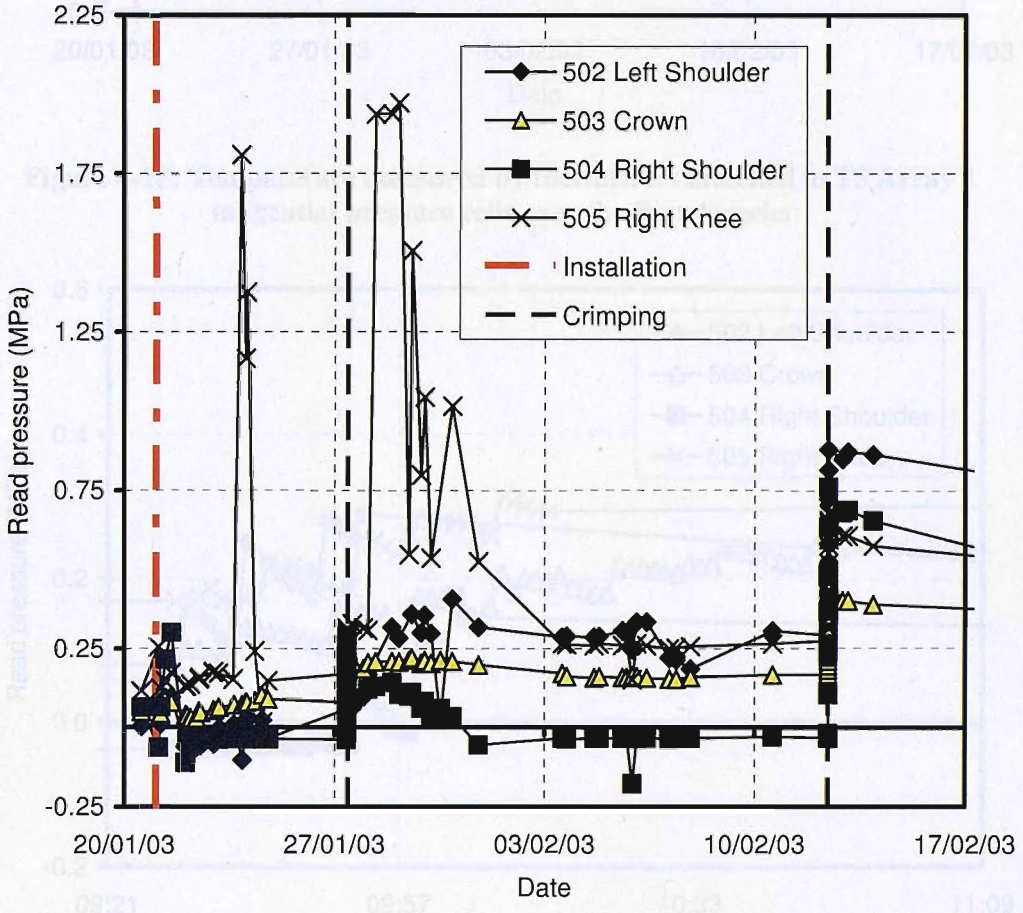

Figure 4-17: Read pressure in the T5 Array 1 tangential pressure cells over the first 4 weeks

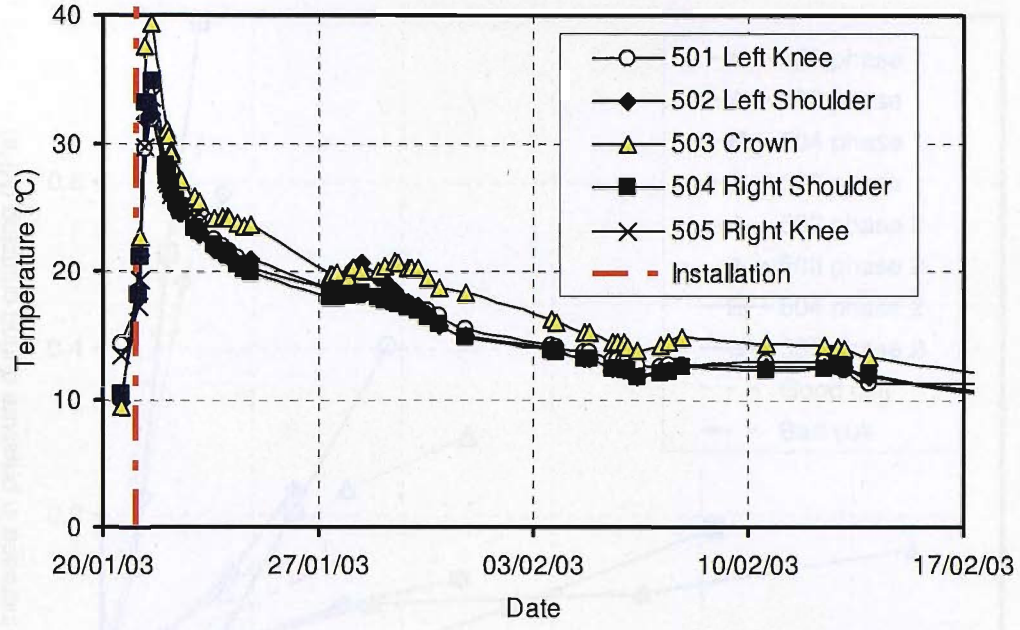

Figure 4-18: Temperature measured by thermistors attached to T5 Array 1 tangential pressure cells over the first 4 weeks

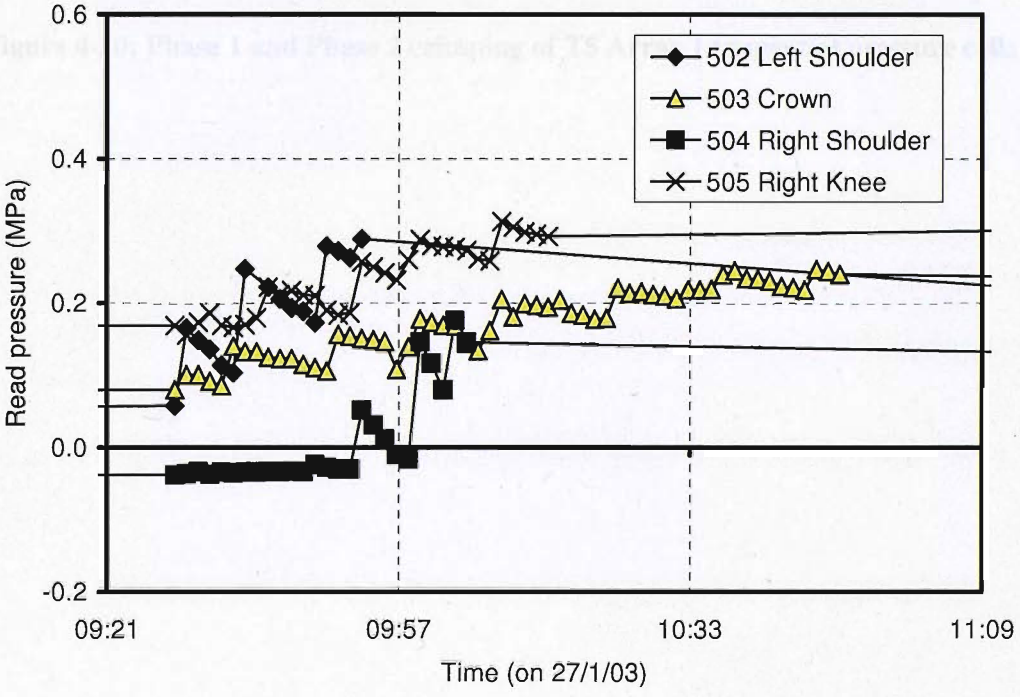

Figure 4-19: Phase 1 crimping of T5 Array 1 tangential pressure cells

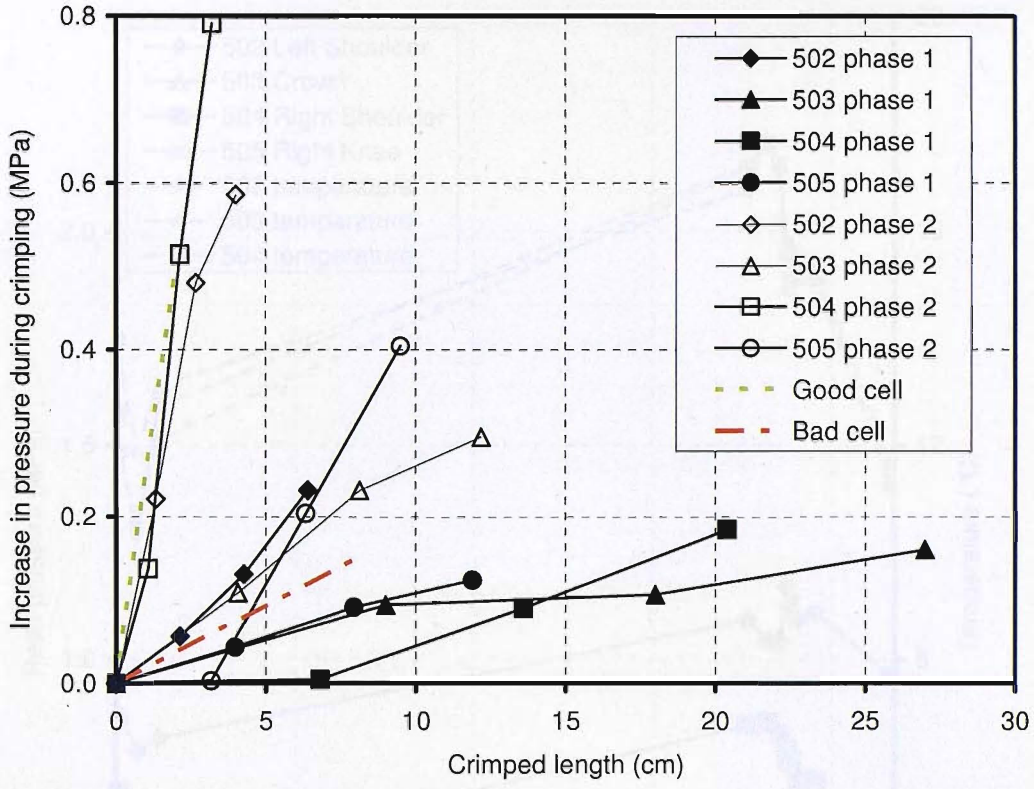

Figure 4-20: Phase 1 and Phase 2 crimping of T5 Array 1 tangential pressure cells

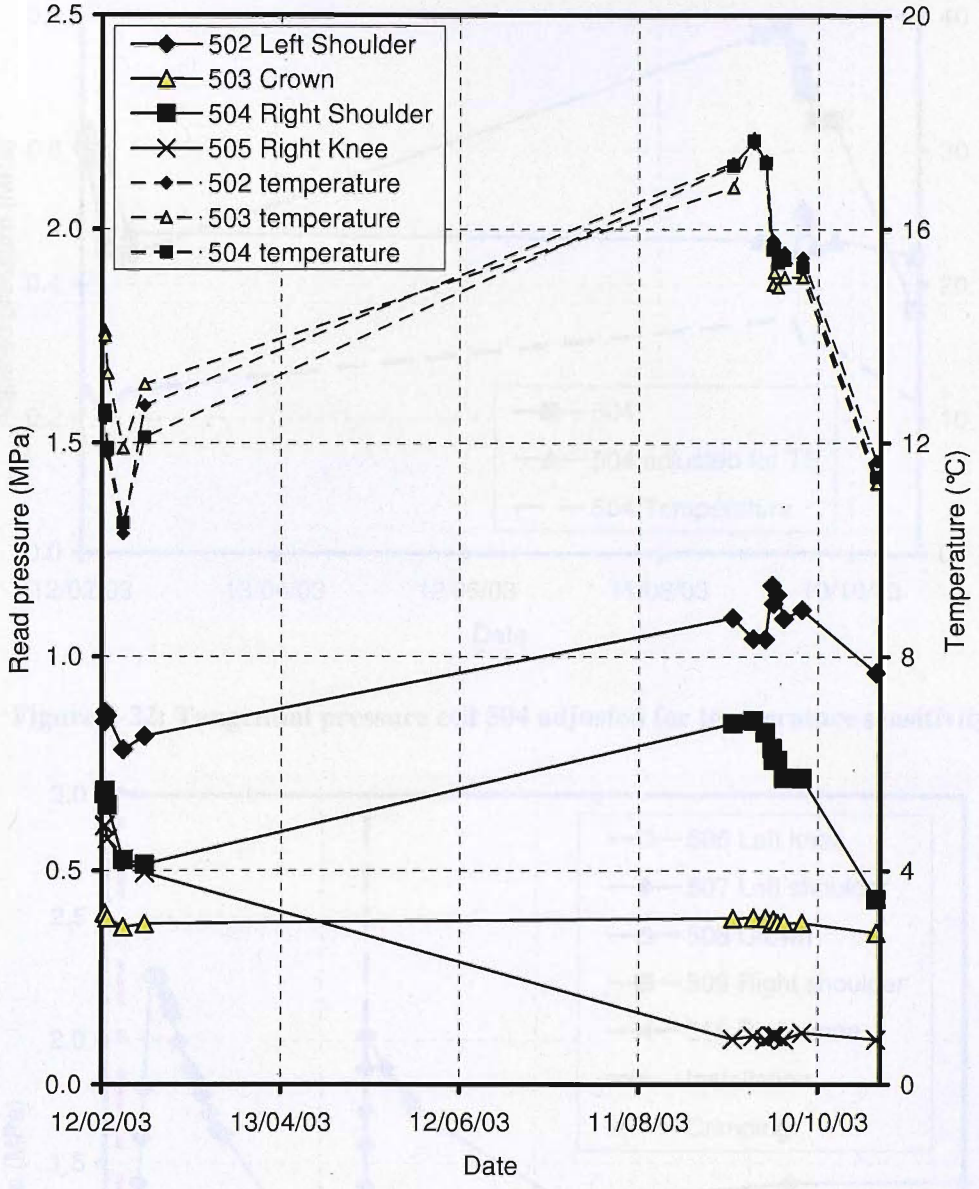

Figure 4-21: T5 Array 1 tangential pressure cells from Phase 2 crimping onwards

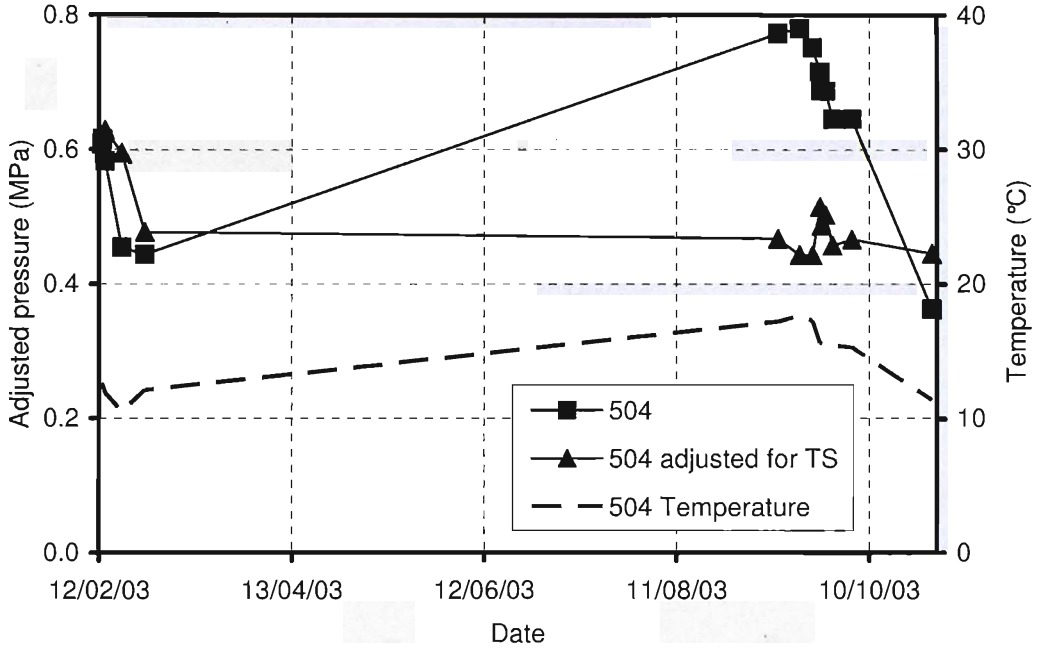

Figure 4-22: Tangential pressure cell 504 adjusted for temperature sensitivity

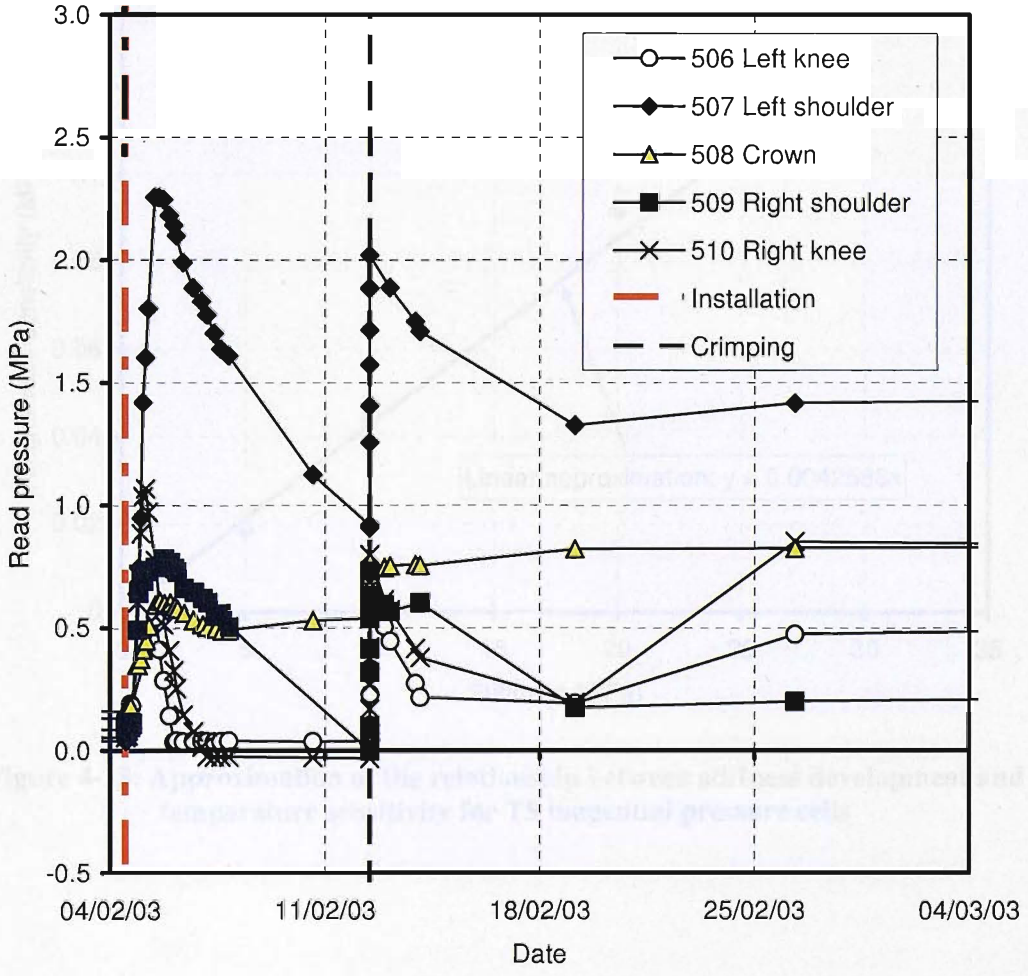

Figure 4-23: Read pressure in the T5 Array 2 tangential pressure cells over the first 4 weeks

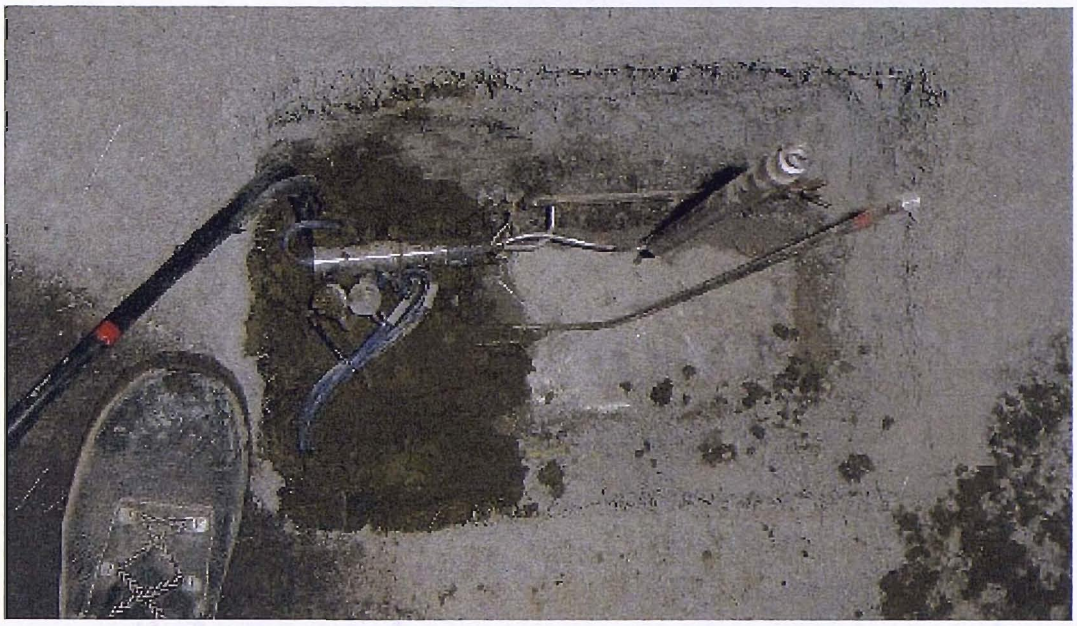

Figure 4-24: Installation of radial and tangential pressure cells within a box-out of the sealing layer at T5 Array 2

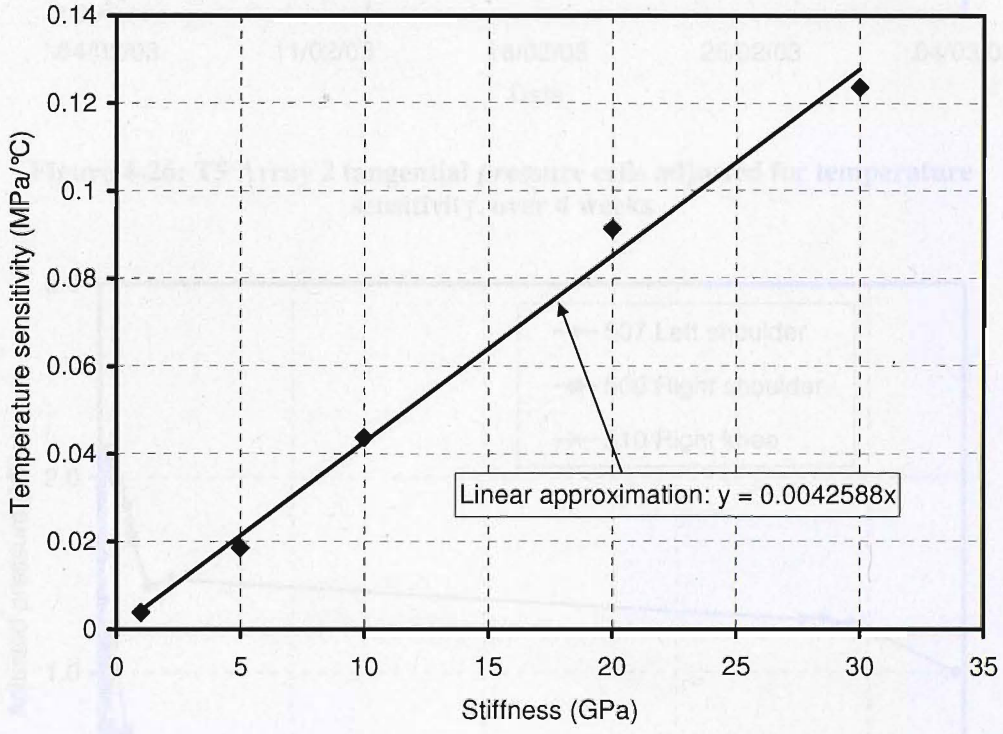

Figure 4-25: Approximation of the relationship between stiffness development and temperature sensitivity for T5 tangential pressure cells

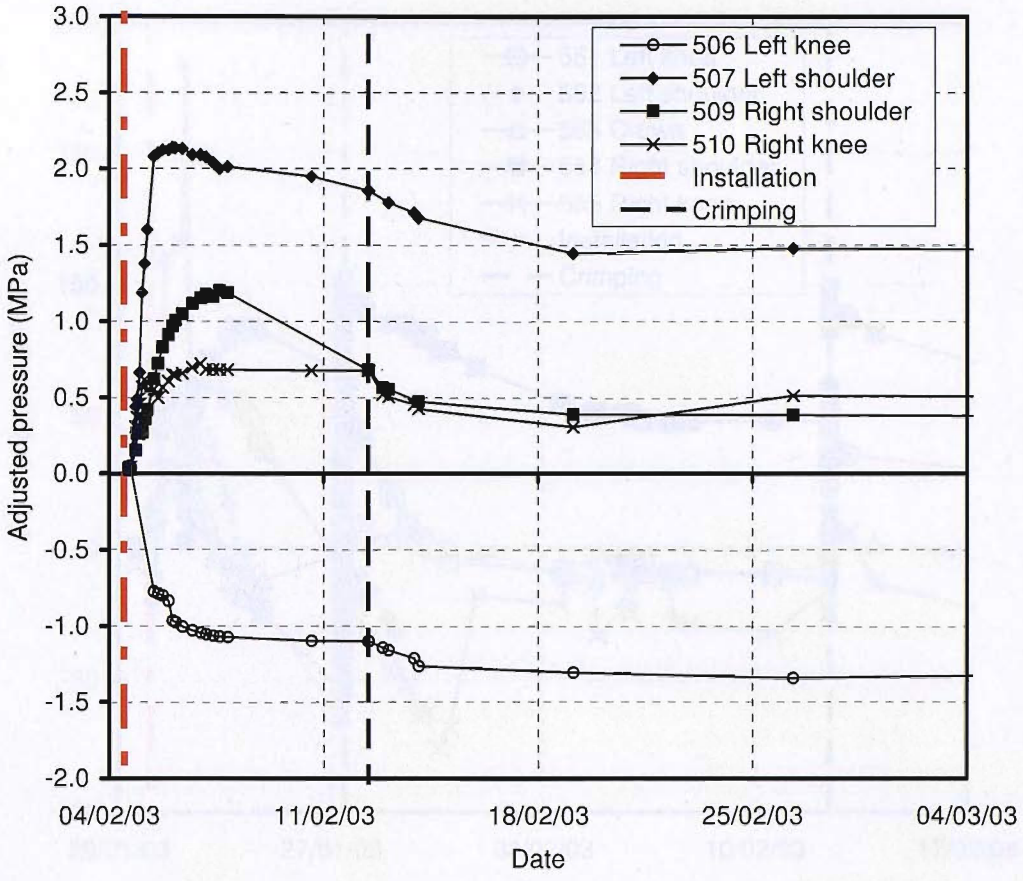

Figure 4-26: T5 Array 2 tangential pressure cells adjusted for temperature sensitivity, over 4 weeks

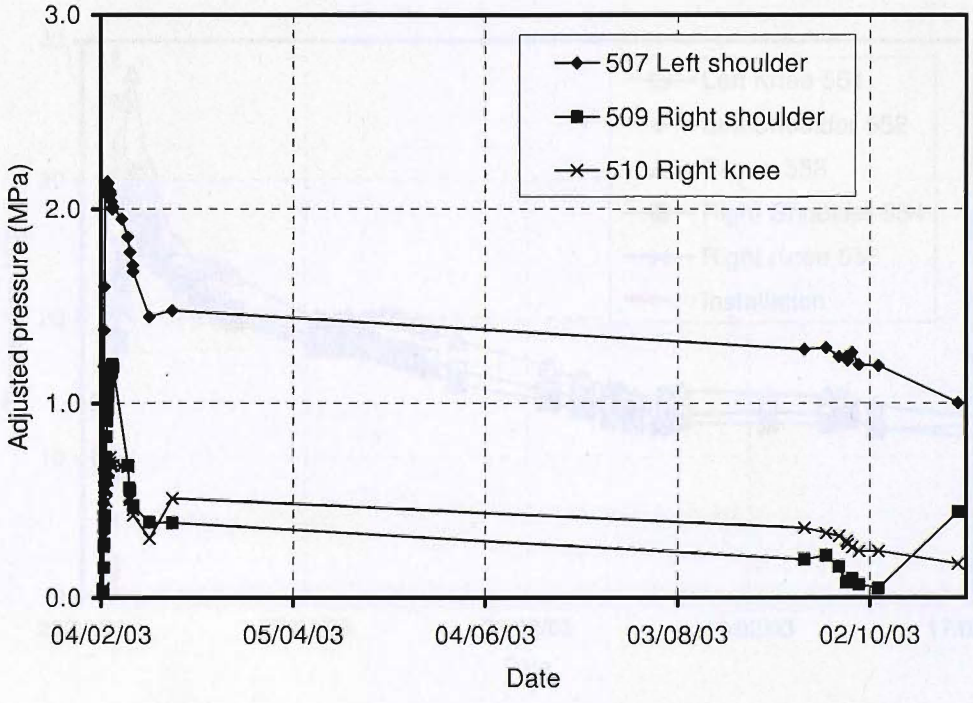

Figure 4-27: T5 Array 2 tangential pressure cells adjusted for temperature sensitivity, over 9 months

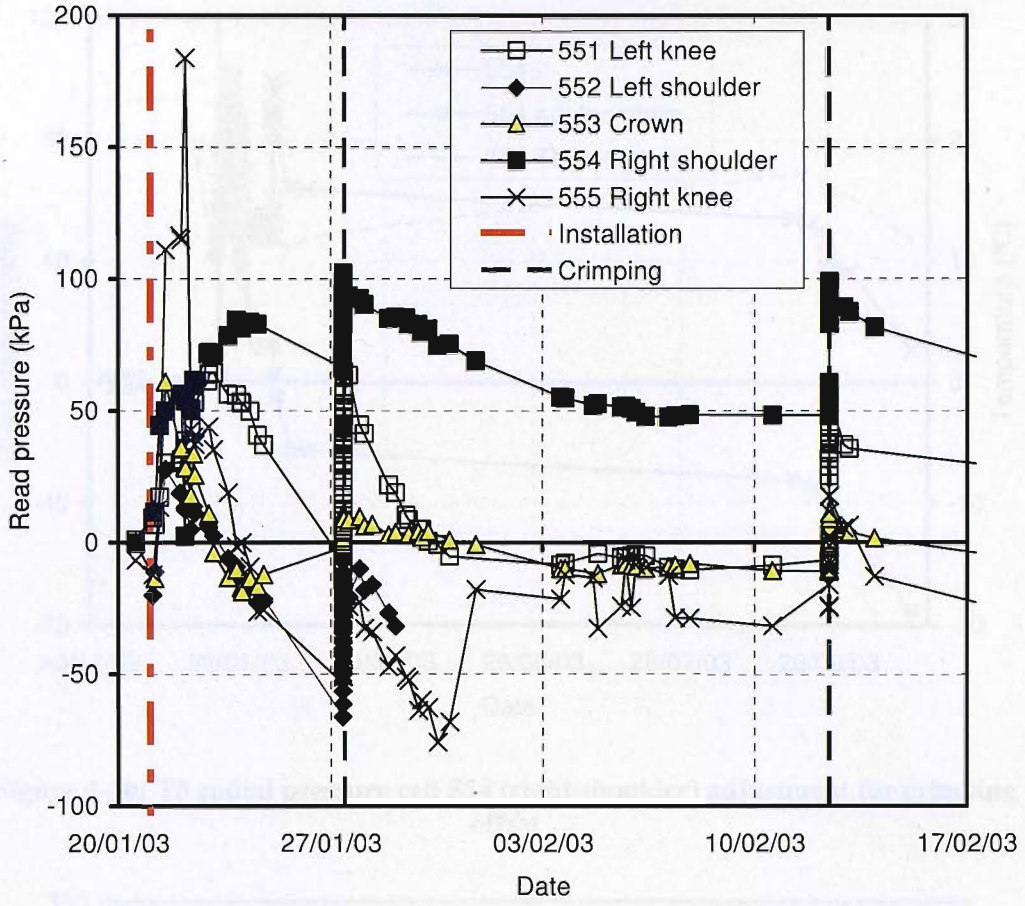

Figure 4-28: Read pressure in the T5 Array 1 radial pressure cells over the first 4 weeks

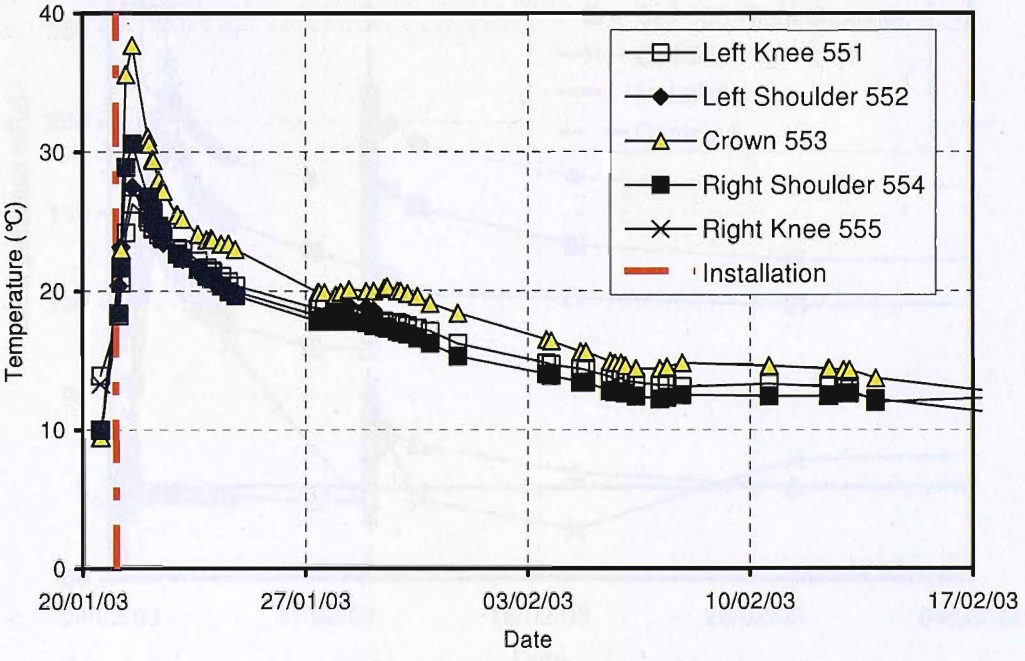

Figure 4-29: Temperature measured by thermistors attached to T5 Array 1 radial pressure cells over the first 4 weeks

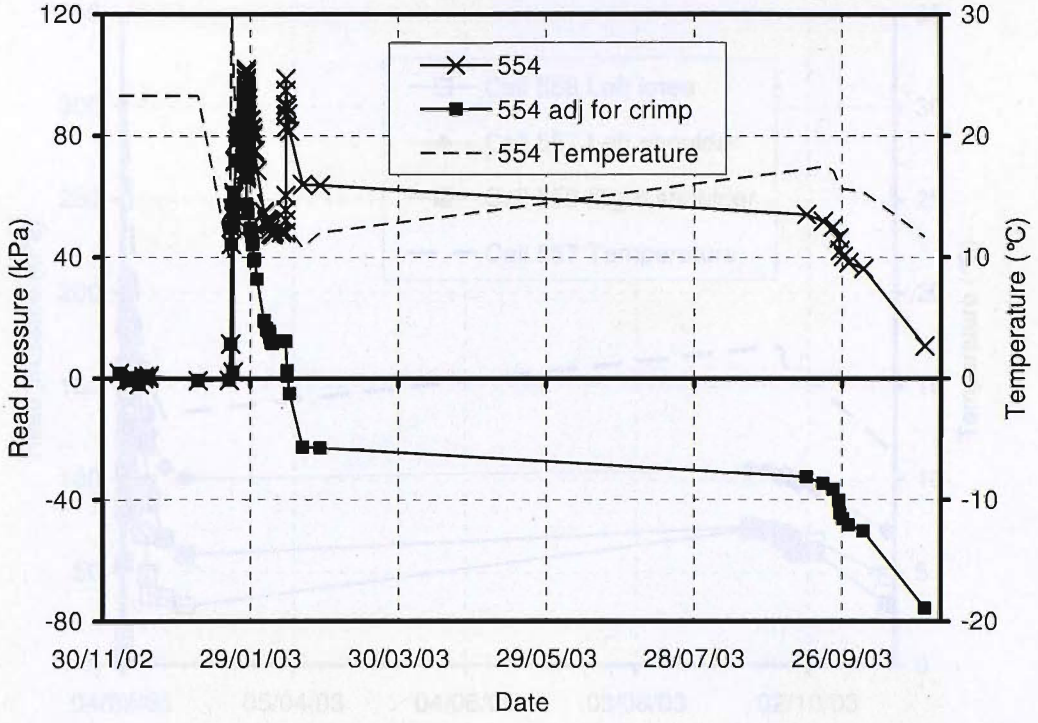

Figure 4-30: T5 radial pressure cell 554 (right shoulder) adjustment for crimping offset

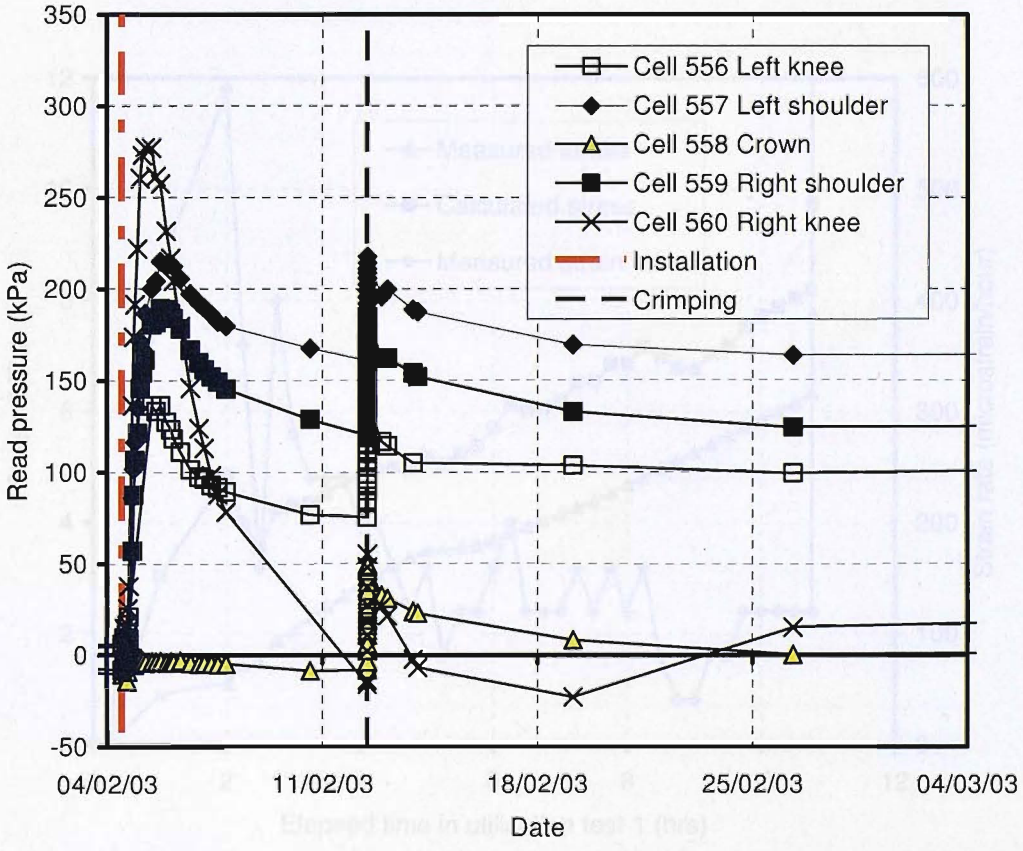

Figure 4-31: Read pressure in the T5 Array 2 radial pressure cells over the first 4 weeks

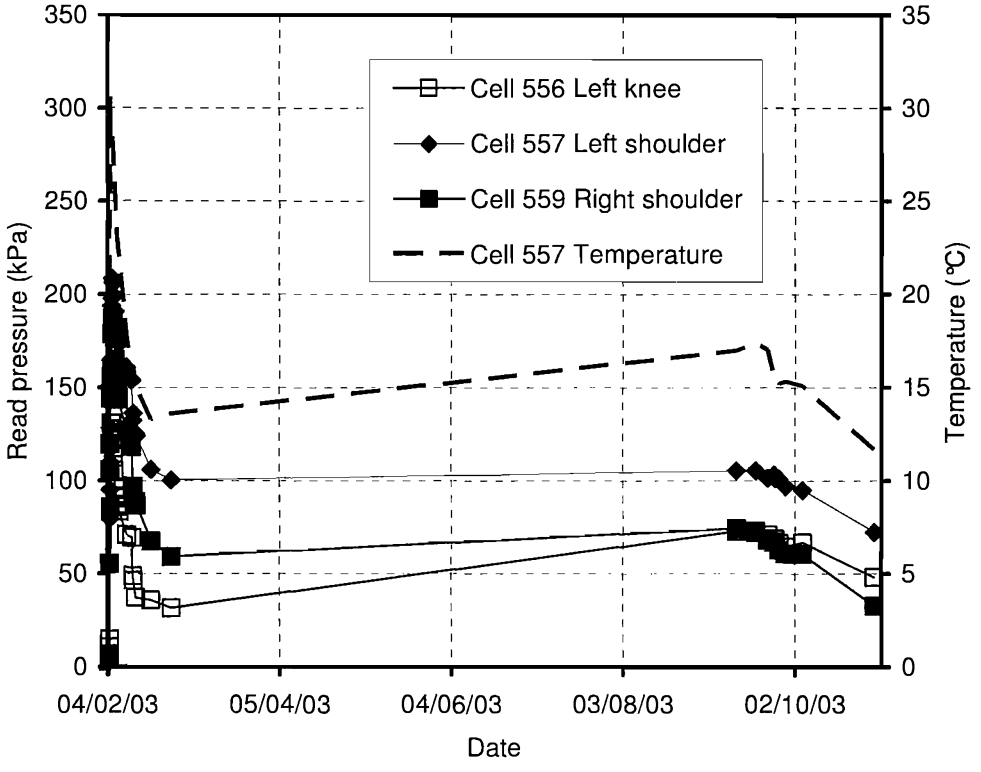

Figure 4-32: T5 Array 2 radial pressures over 9 months (not adjusted for crimping offset)

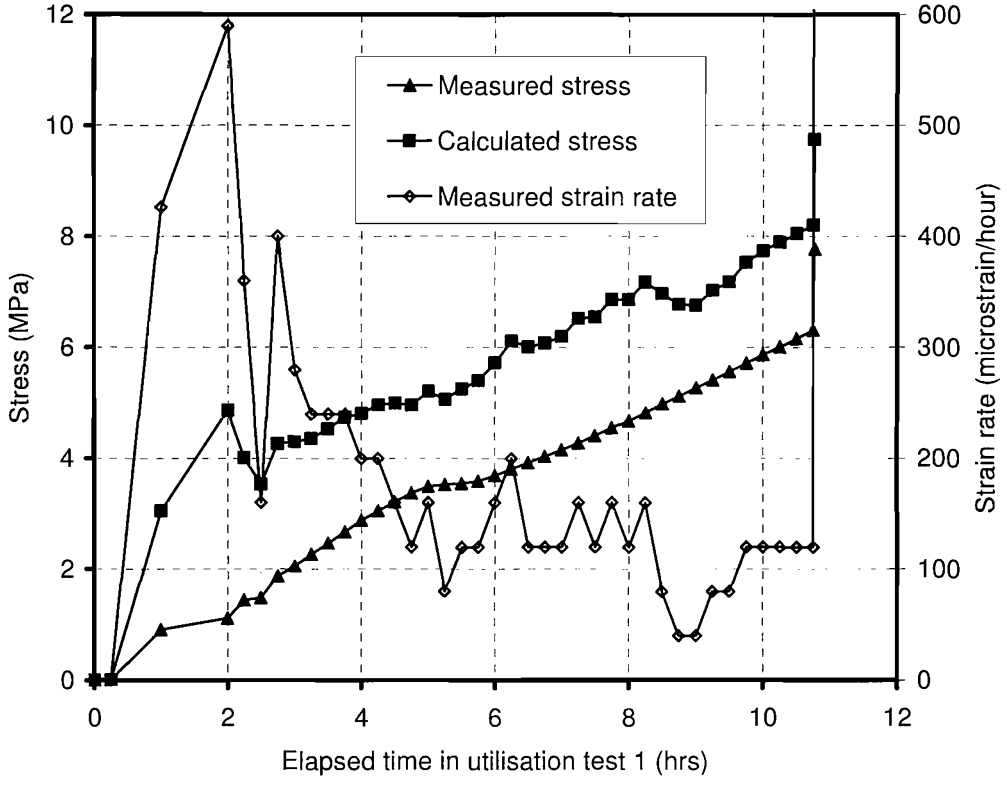

Figure 4-33: Comparison of measured stress in utilisation test 1 with stress back-calculated from measured strains

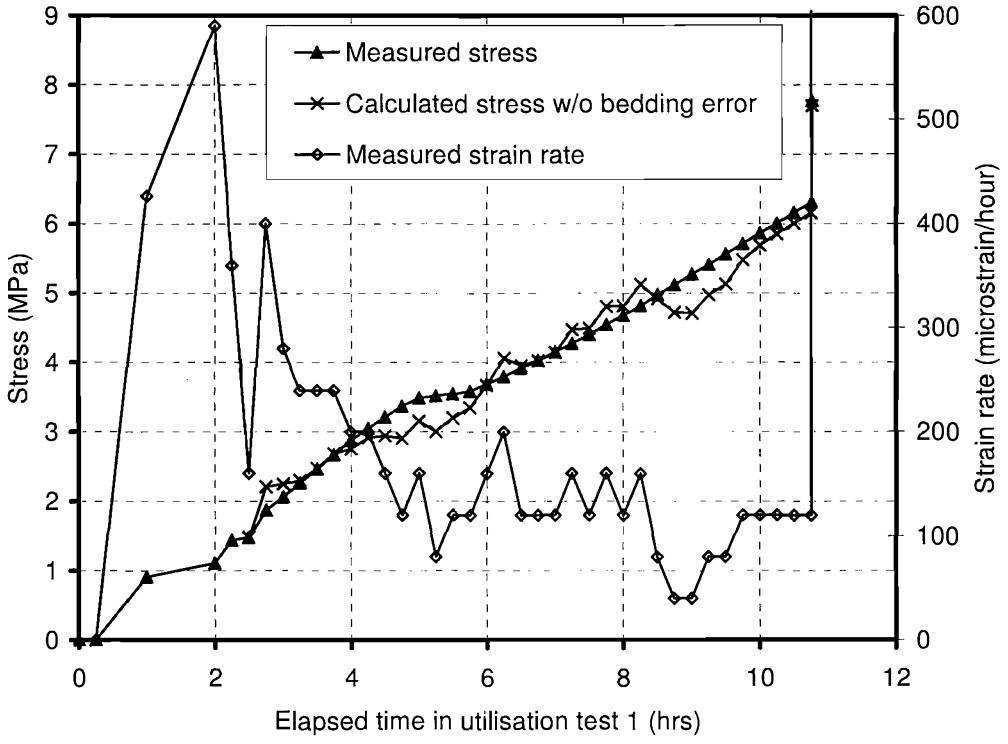

Figure 4-34: Comparison of measured stress in utilisation test 1 with stress back-calculated from measured strains with initial bedding error removed

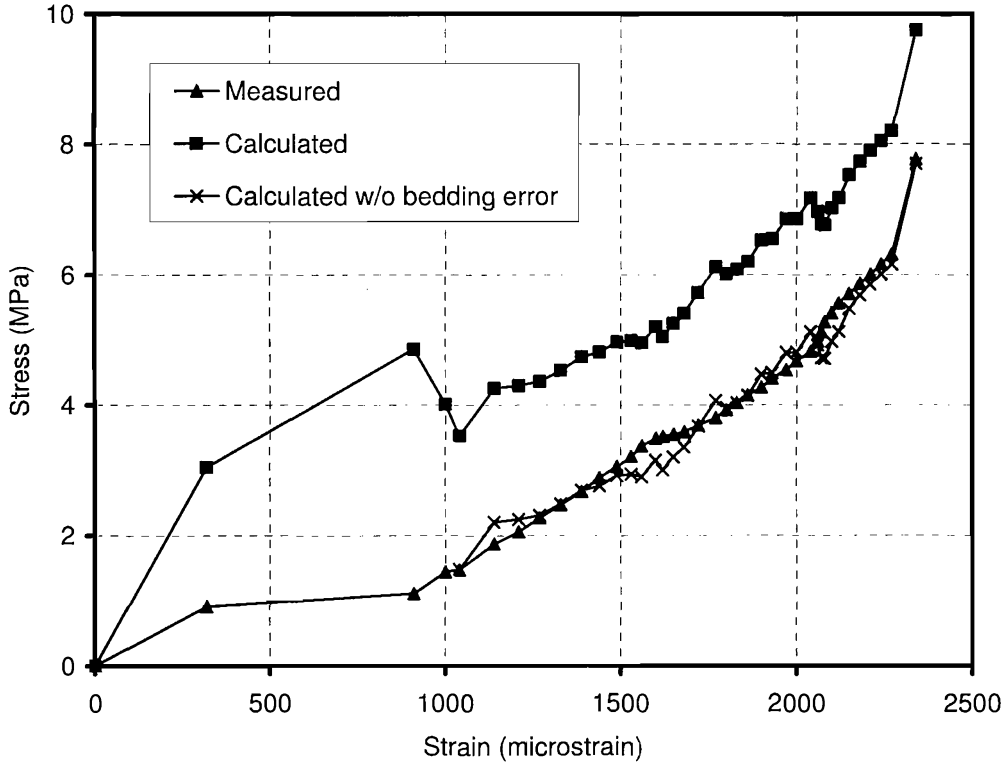

Figure 4-35: Comparison between measured and back-calculated stress-strain behaviour during utilisation test 1

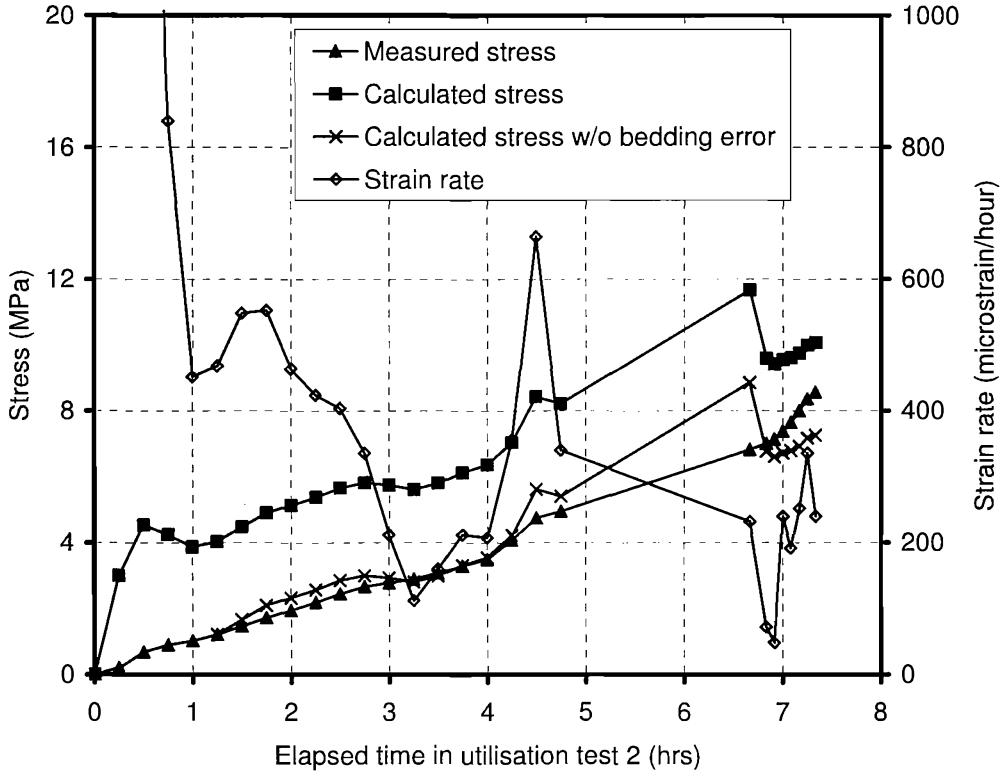

Figure 4-36: Comparison of measured stress in utilisation test 2 with stress back-calculated from measured strains

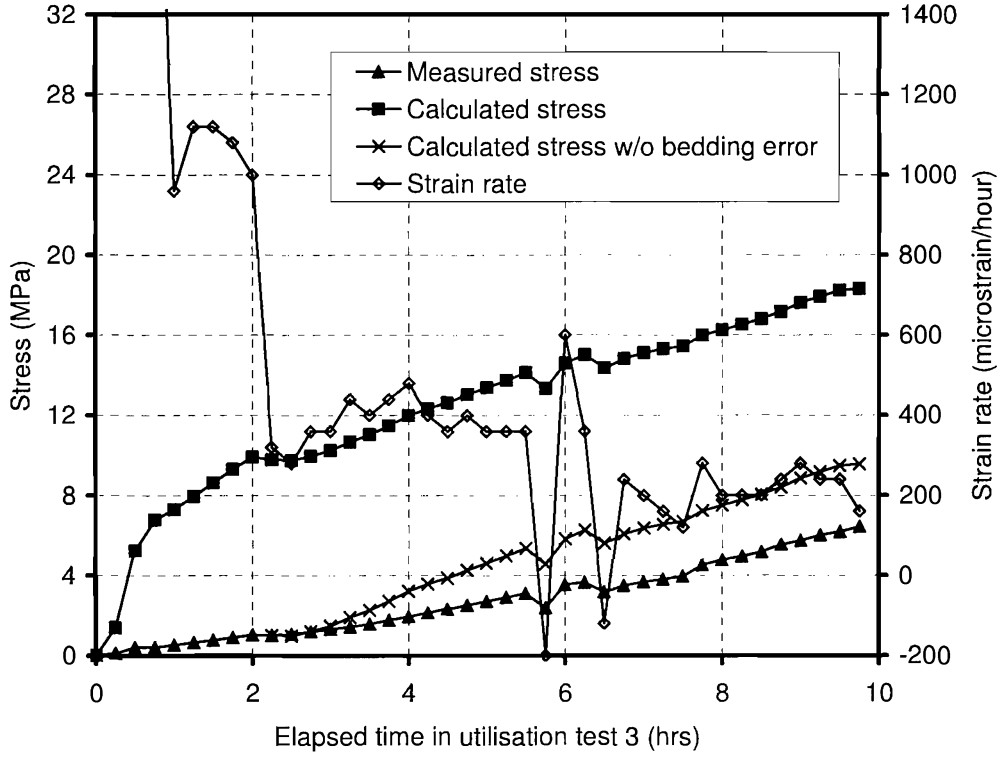

Figure 4-37: Comparison of measured stress in utilisation test 3 with stress back-calculated from measured strains

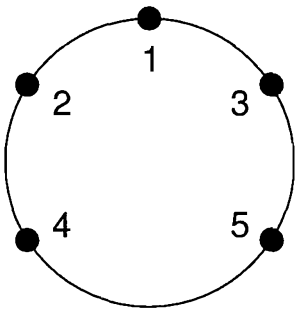

Figure 4-38: Position of monitoring points in the SWOT frontshunt tunnel

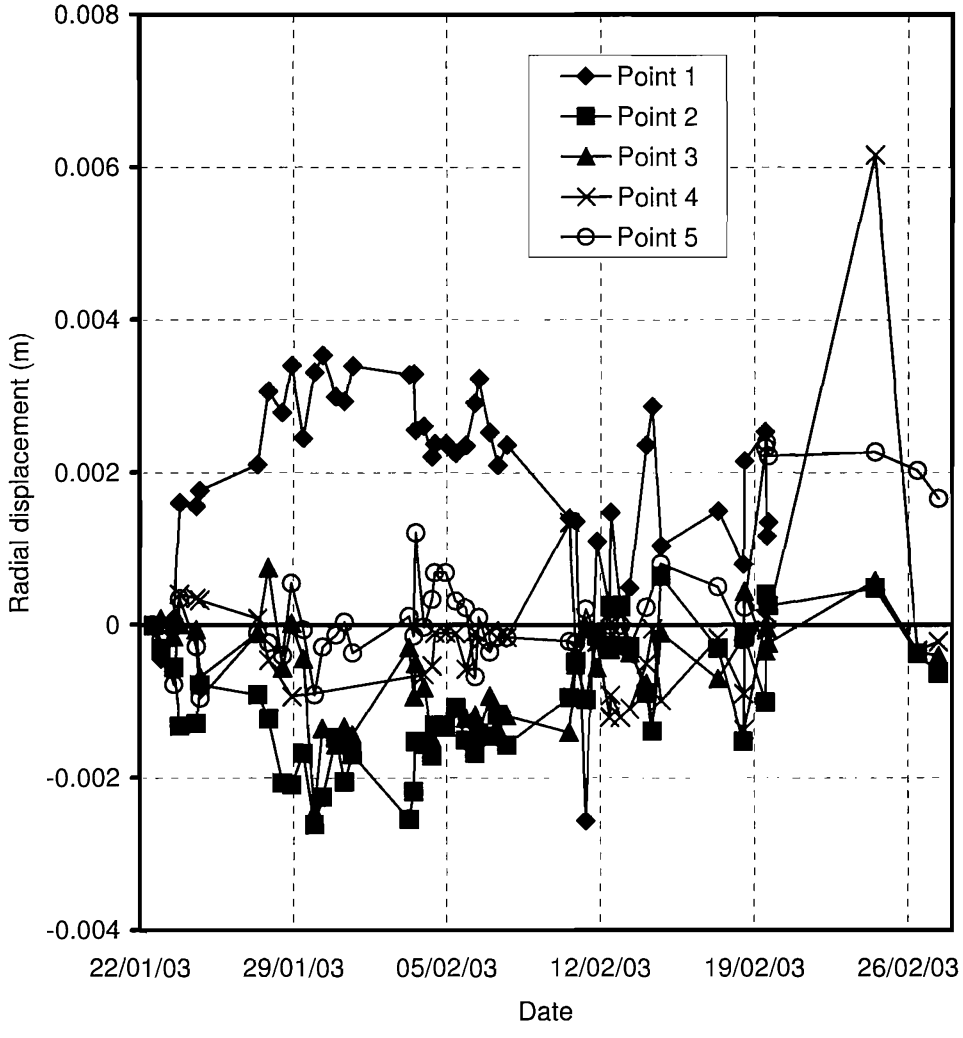

Figure 4-39: Radial displacements of the sprayed concrete lining measured by 3D optical surveying

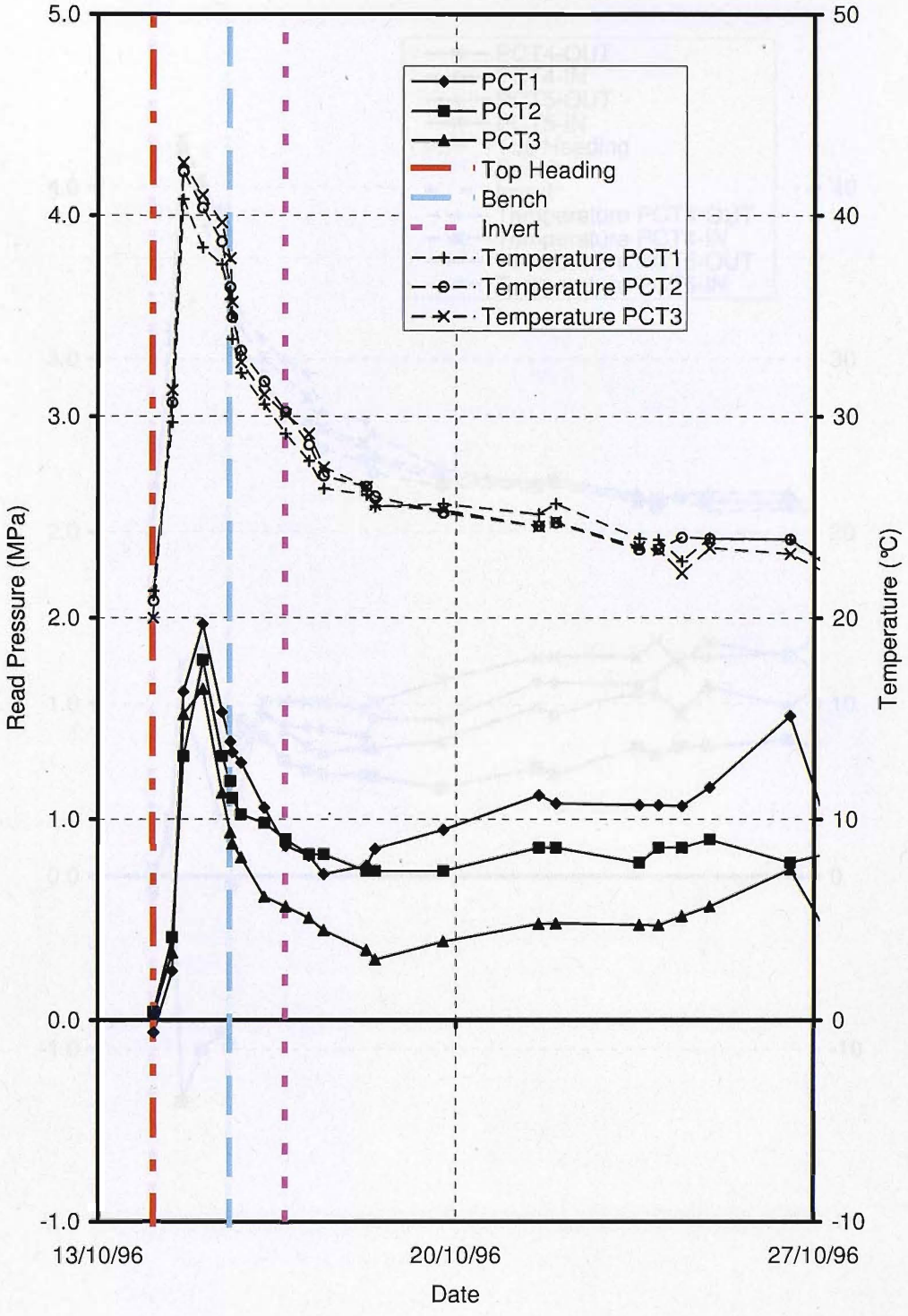

Figure 4-40: T4 concourse tunnel MMS I top heading upper tangential pressure cell readings PCT1, 2, 3 in first 2 weeks

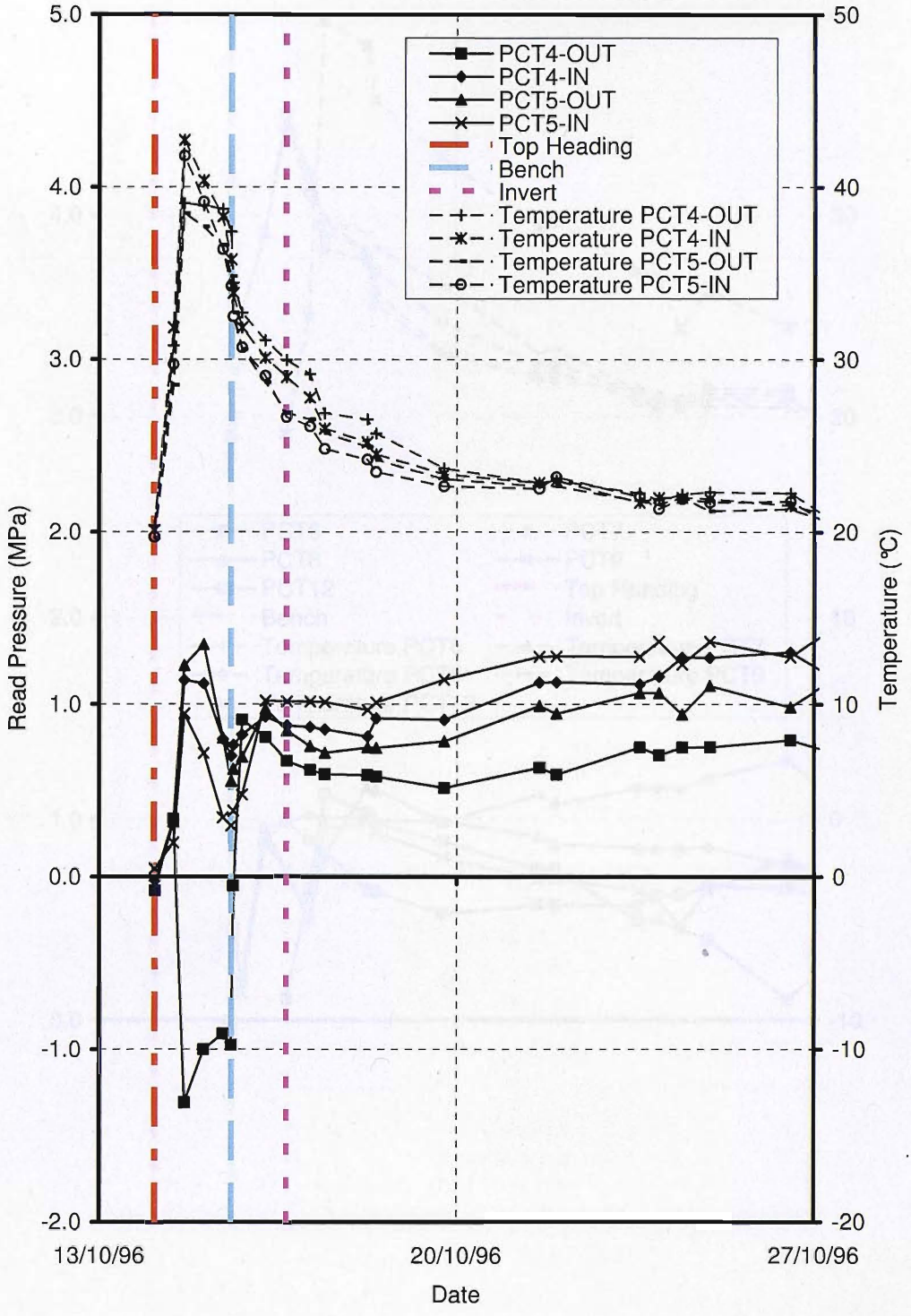

Figure 4-41: T4 concourse tunnel MMS I top heading lower tangential pressure cell readings PCT4-OUT, 4-IN, 5-OUT, 5-IN in first 2 weeks

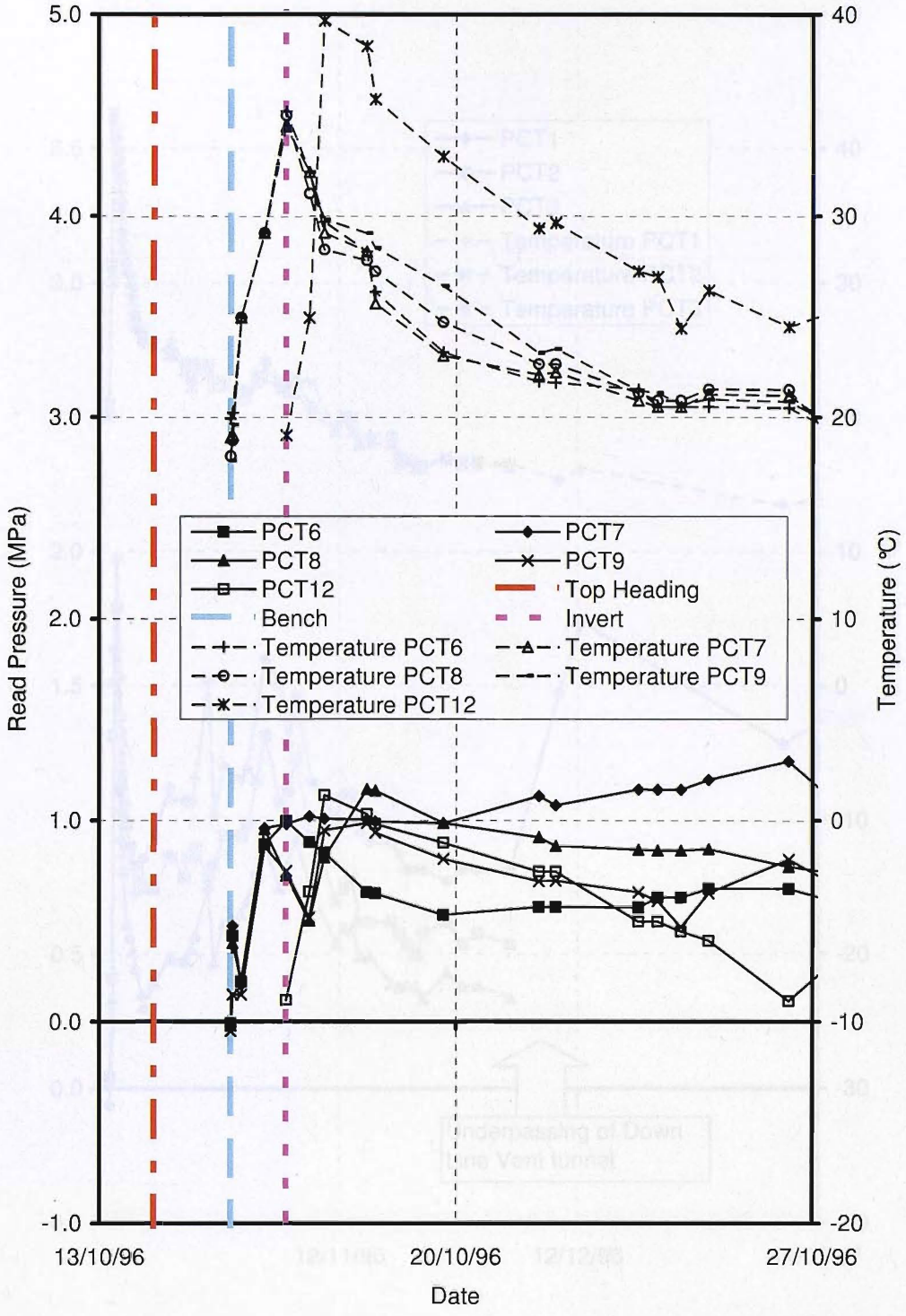

Figure 4-42: T4 concourse tunnel MMS I bench and invert tangential pressure cell readings PCT6, 7, 8, 9, 12 in first 2 weeks

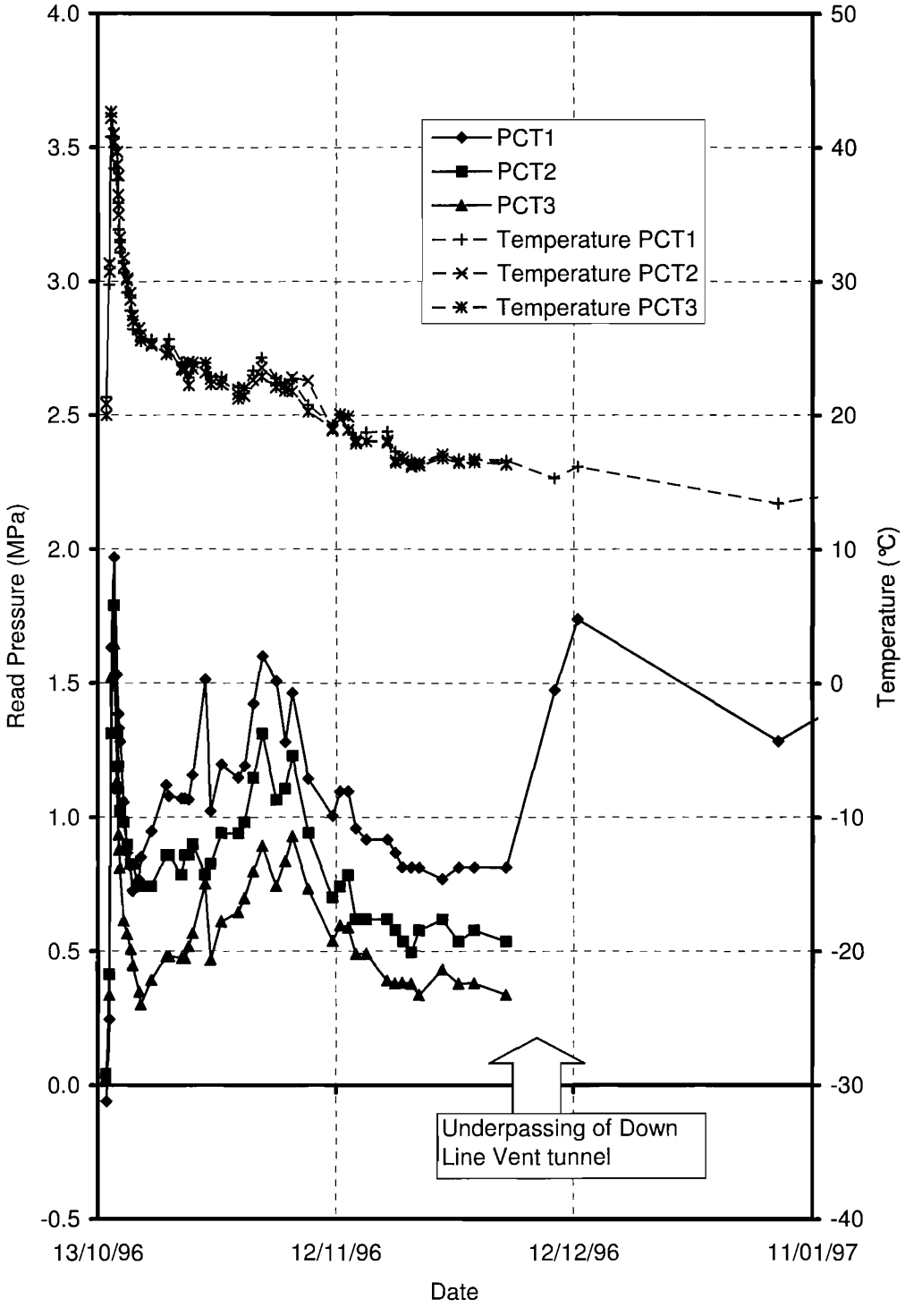

Figure 4-43: T4 concourse tunnel MMS I top heading upper tangential pressure cell readings PCT1, 2, 3 in first 3 months

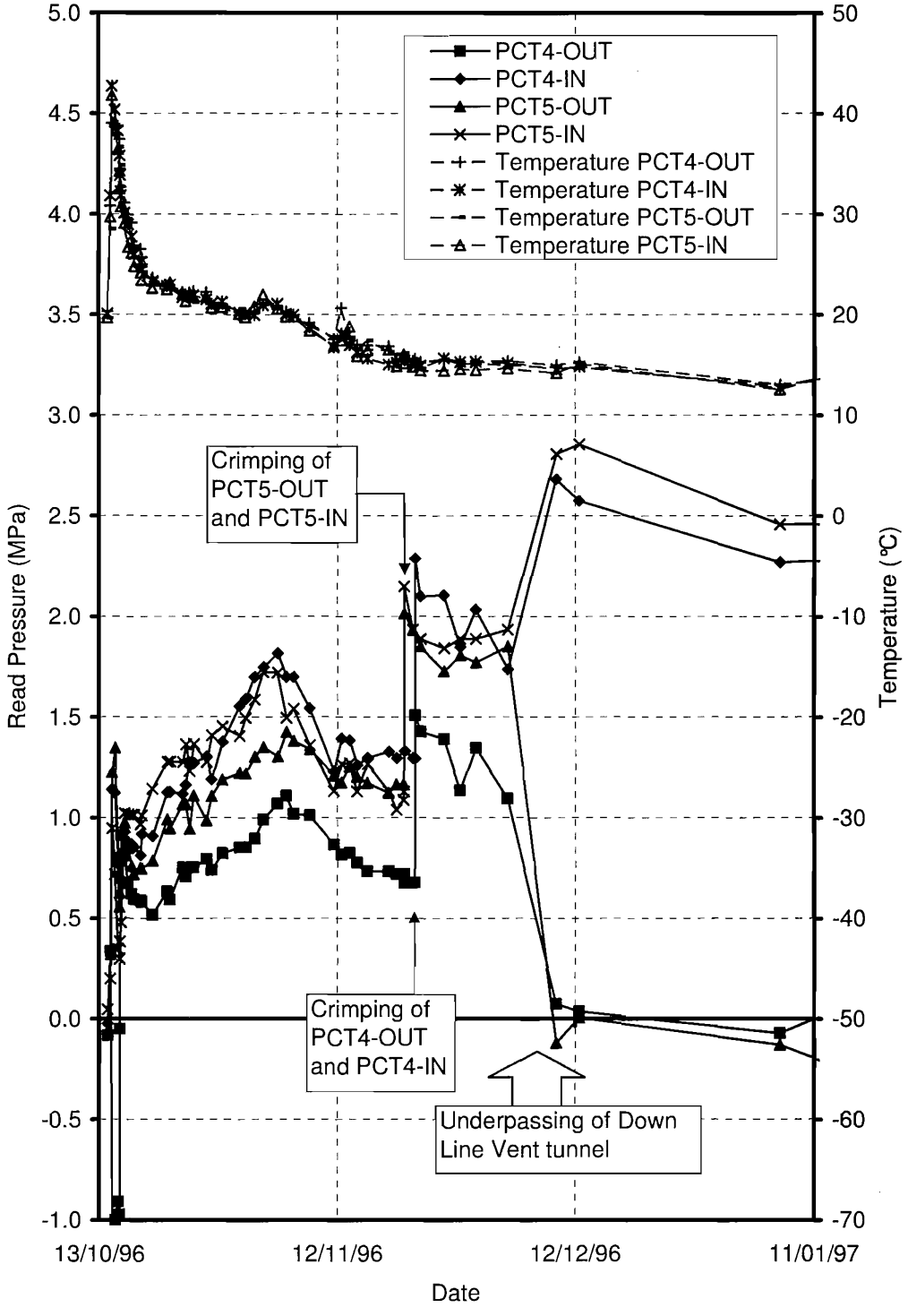

Figure 4-44: T4 concourse tunnel MMS I top heading lower tangential pressure cell readings PCT4-OUT, 4-IN, 5-OUT, 5-IN in first 3 months

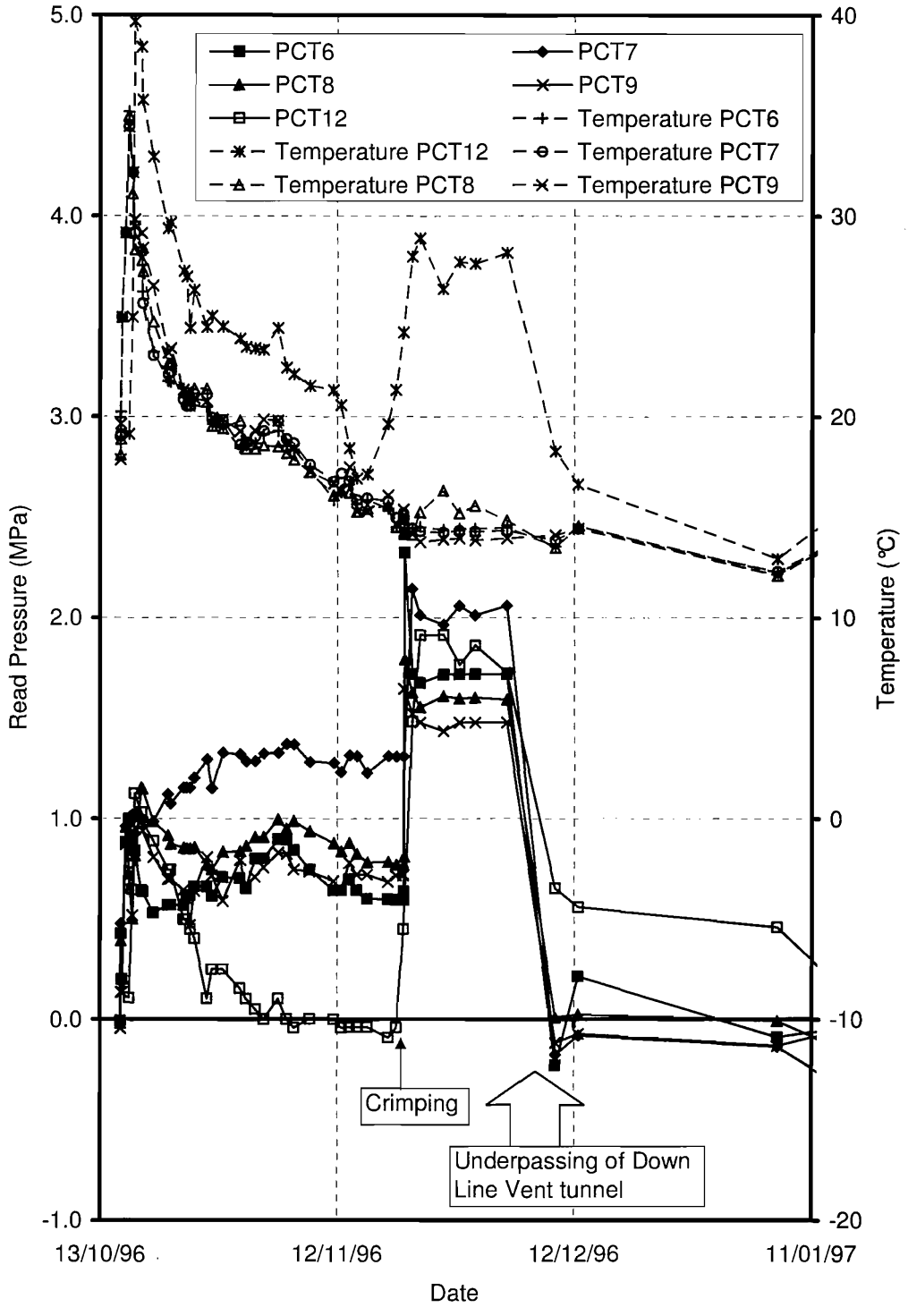

Figure 4-45: T4 concourse tunnel MMS I bench and invert tangential pressure cell readings PCT6, 7, 8, 9, 12 in first 3 months

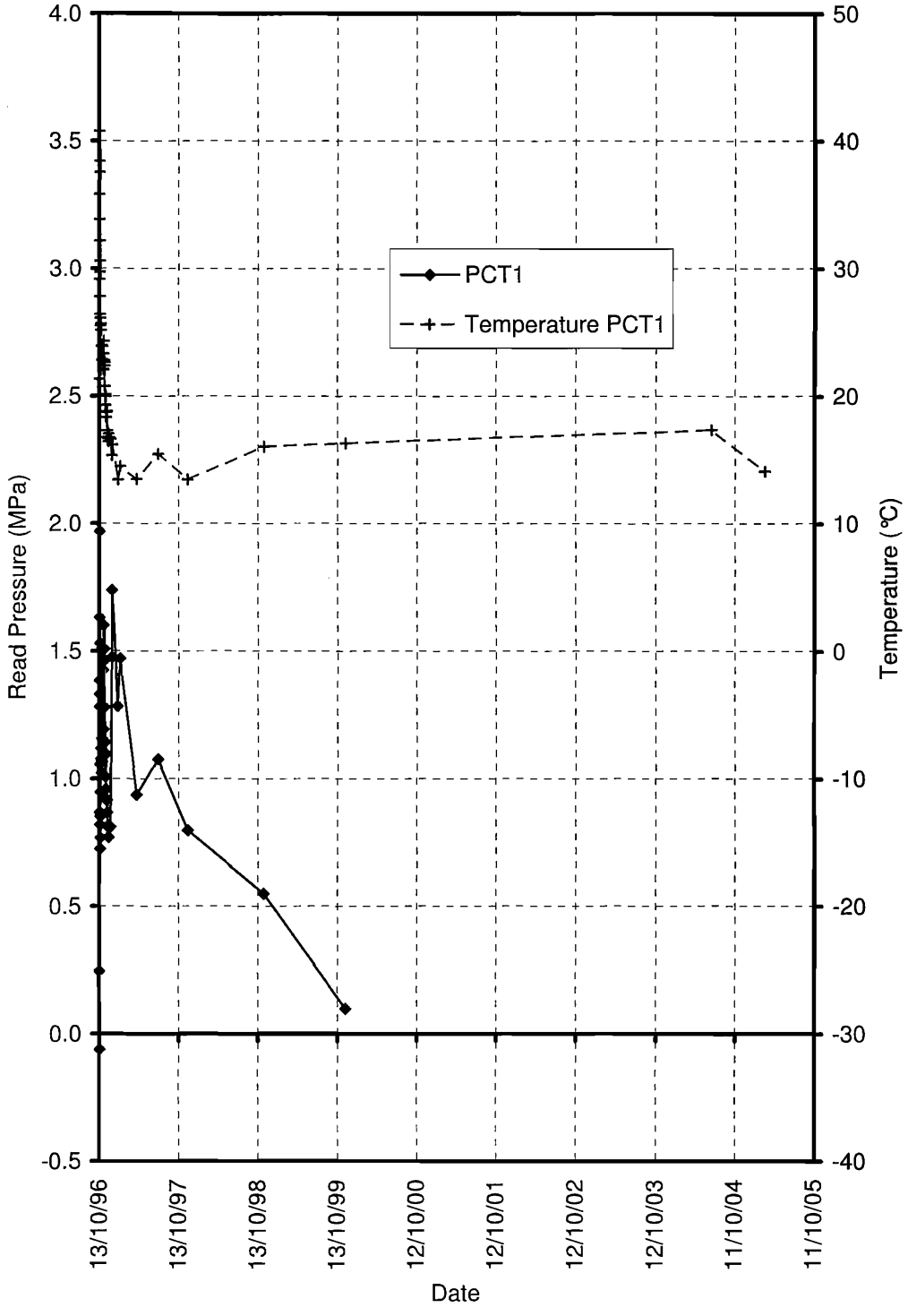

Figure 4-46: T4 concourse tunnel MMS I top heading tangential pressure cell readings for crown cell PCT1 over 9 years

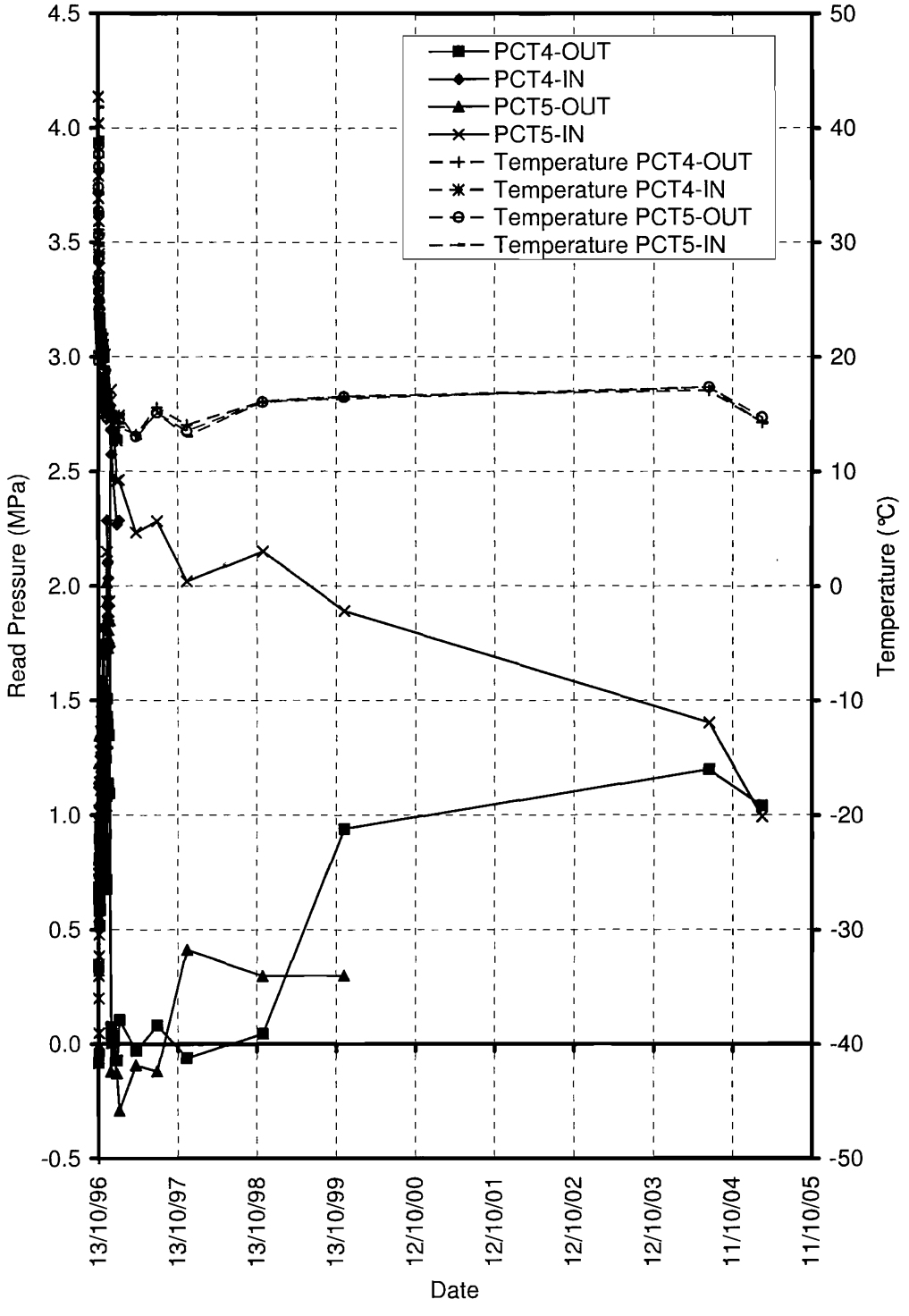

Figure 4-47: T4 concourse tunnel MMS I top heading lower tangential pressure cell readings PCT4-OUT, 4-IN, 5-OUT, 5-IN over 9 years

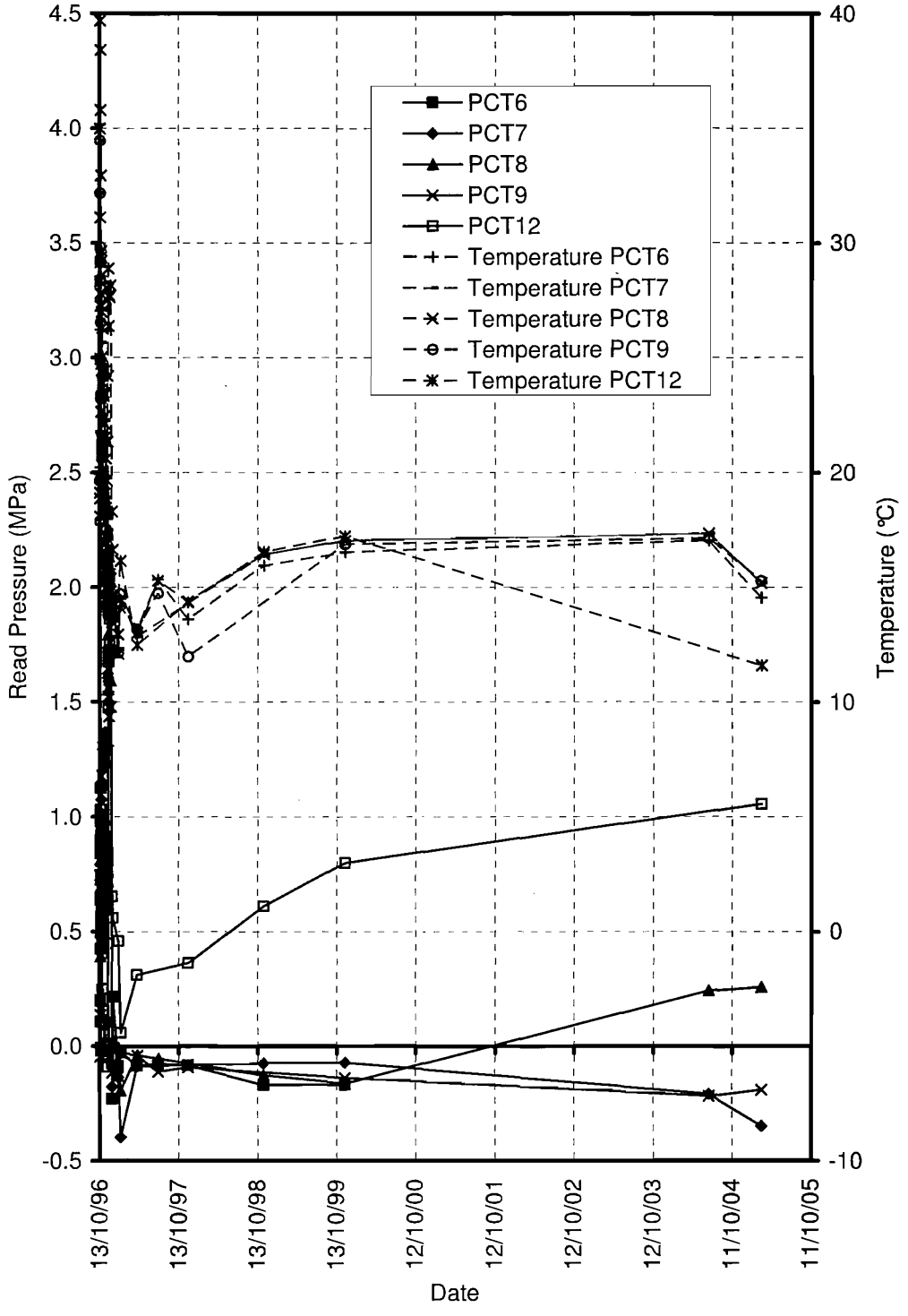

Figure 4-48: T4 concourse tunnel MMS I bench and invert tangential pressure cell readings PCT6, 7, 8, 9, 12 over 9 years

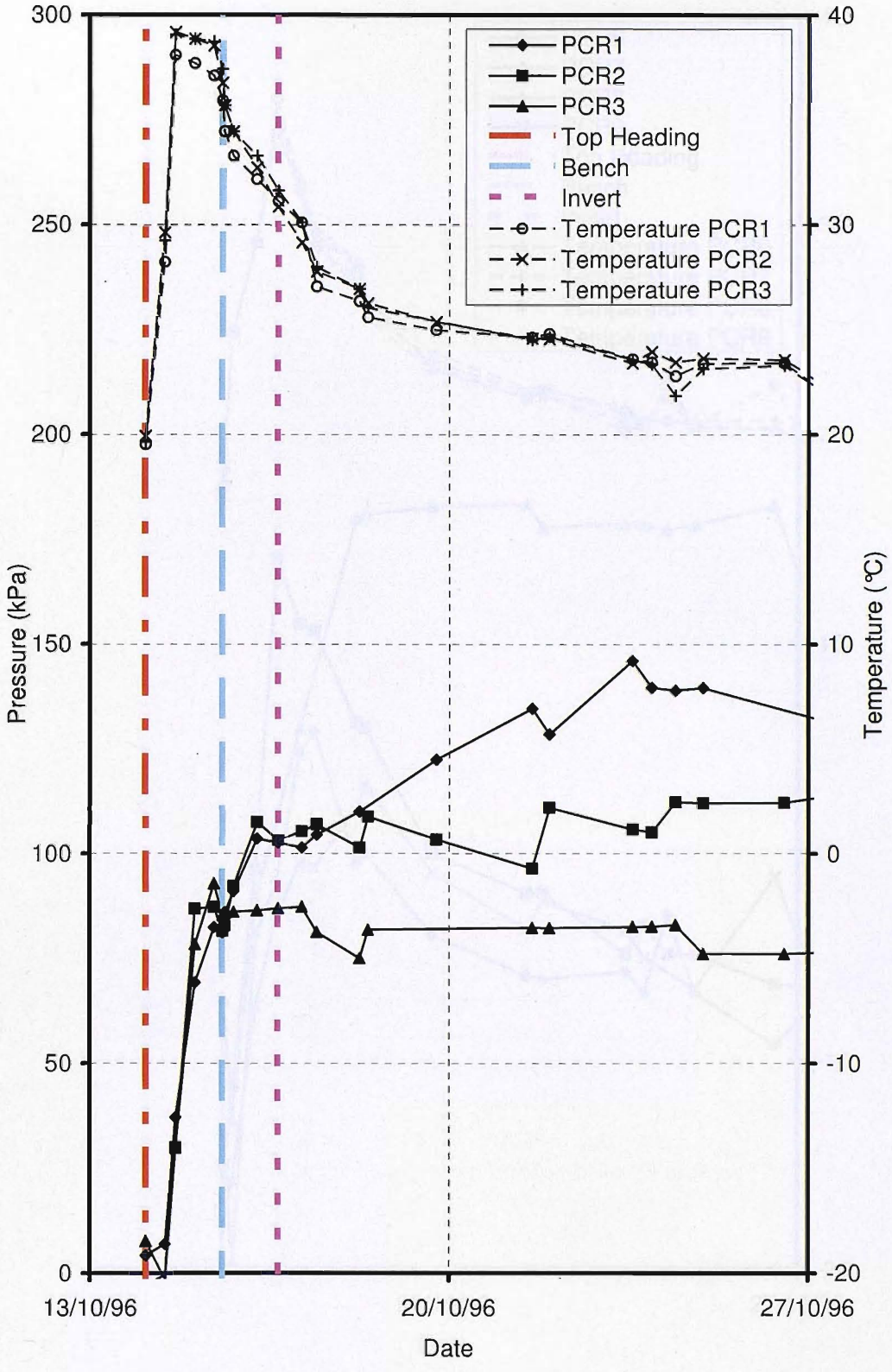

Figure 4-49: T4 concourse MMS I top heading radial pressure cell readings PCR1, 2, 3 in first 2 weeks (PCR4 & 5 not functioning)

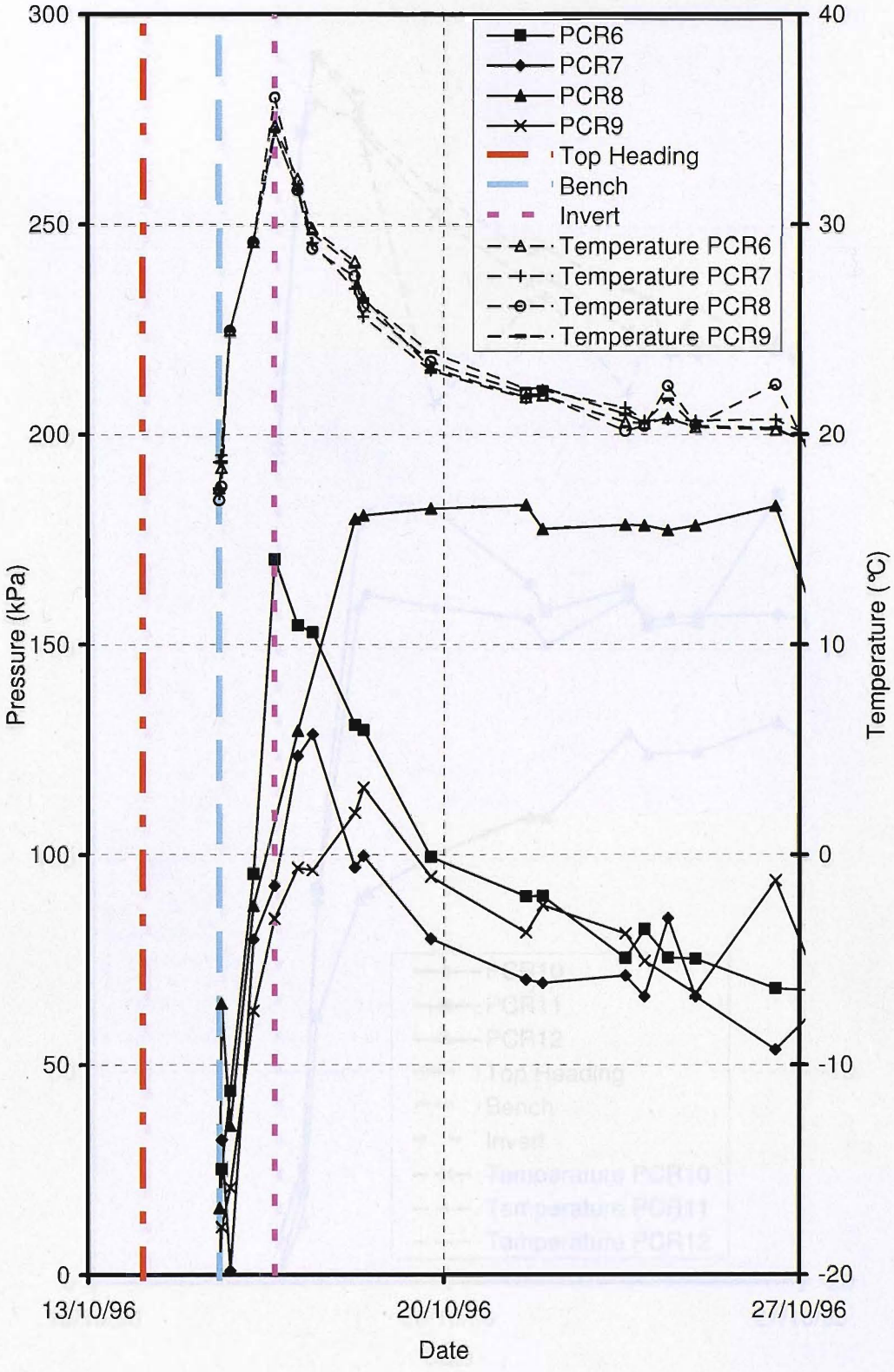

Figure 4-50: T4 concourse MMS I bench radial pressure cell readings PCR6, 7, 8, 9 in first 2 weeks

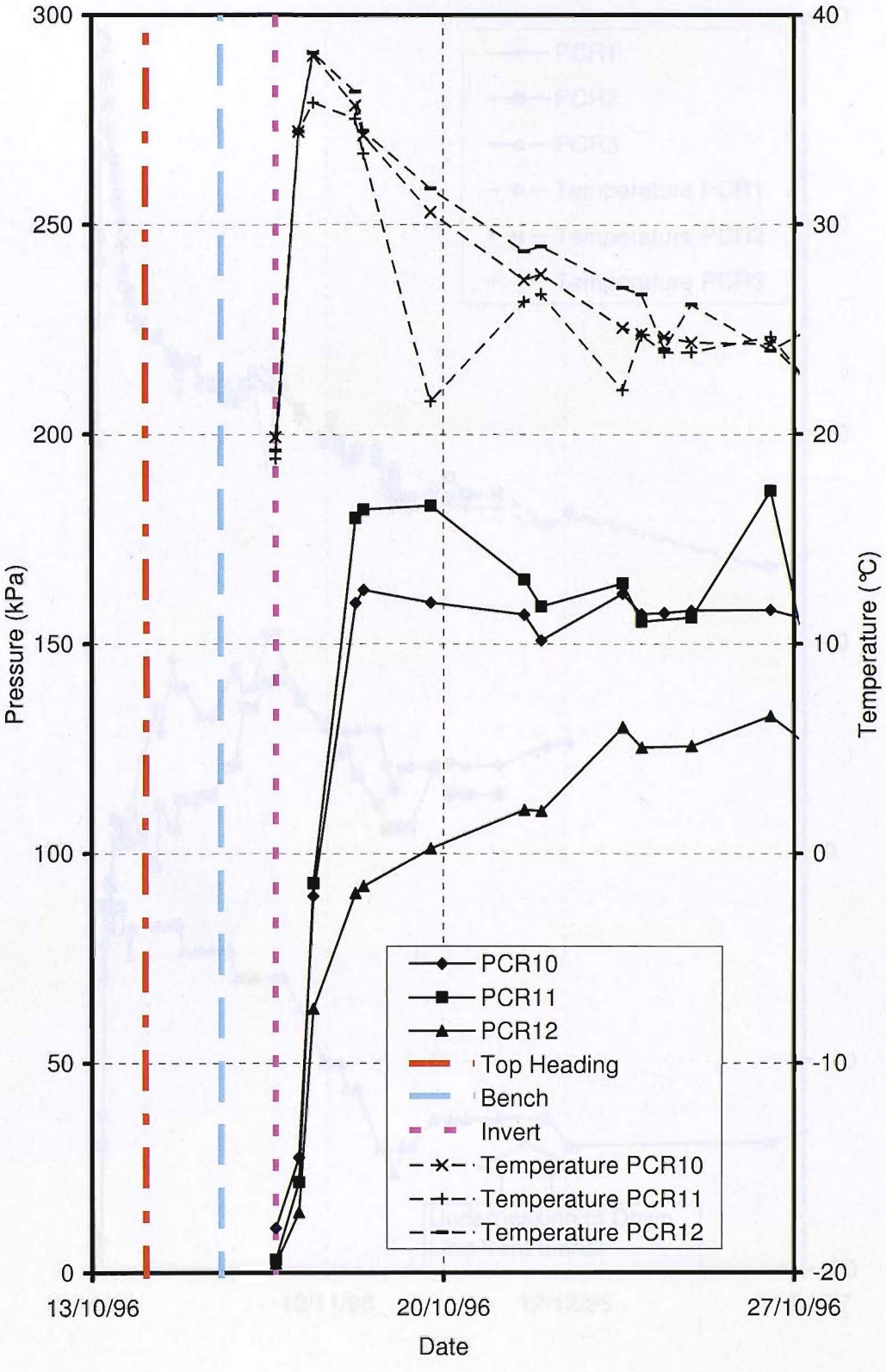

Figure 4-51: T4 concourse MMS I invert radial pressure cell readings PCR10, 11, 12 in first 2 weeks

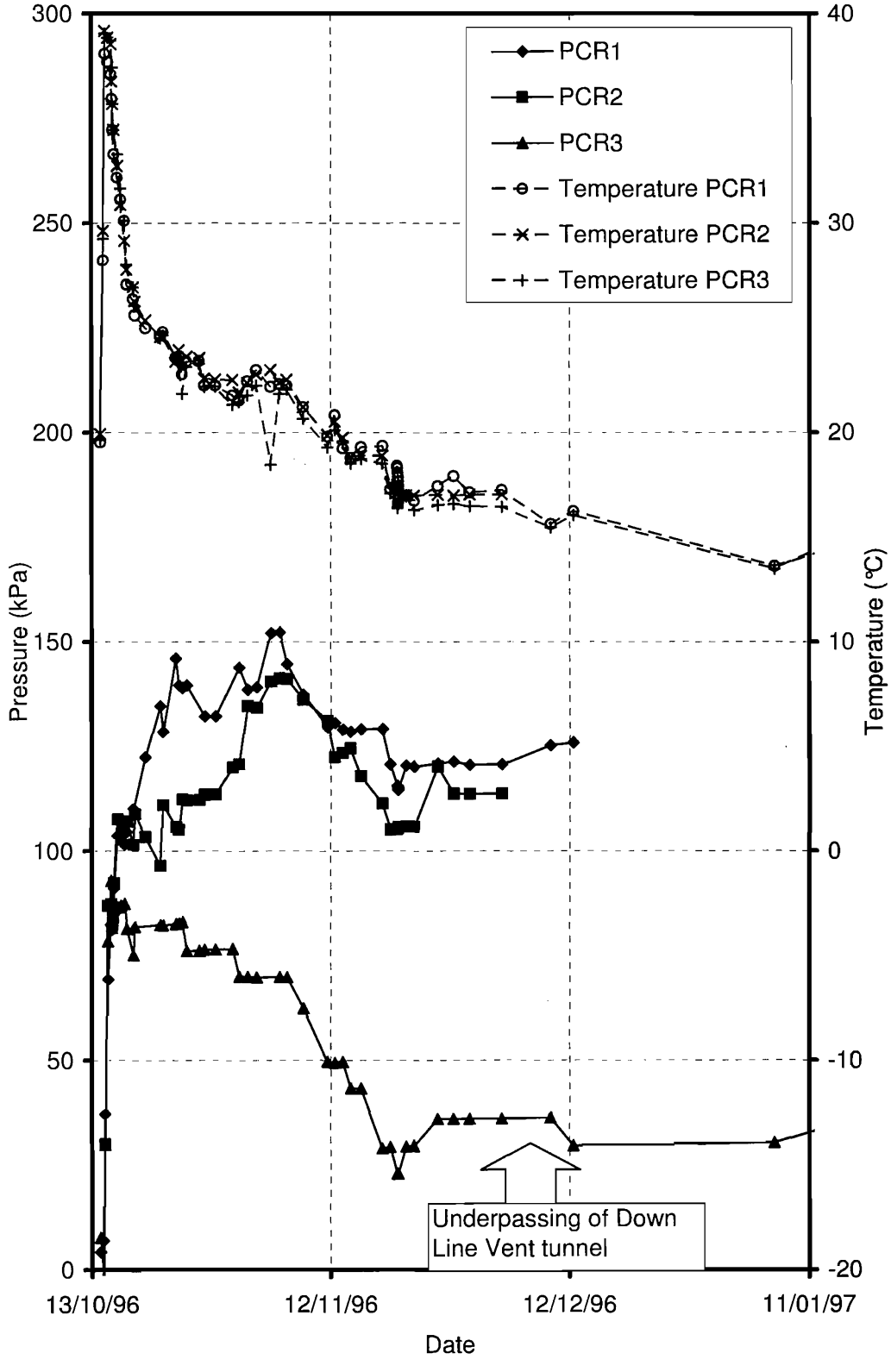

Figure 4-52: T4 concourse MMS I top heading radial pressure cell readings PCR1, 2, 3 in first 3 months (PCR4 & 5 not functioning)

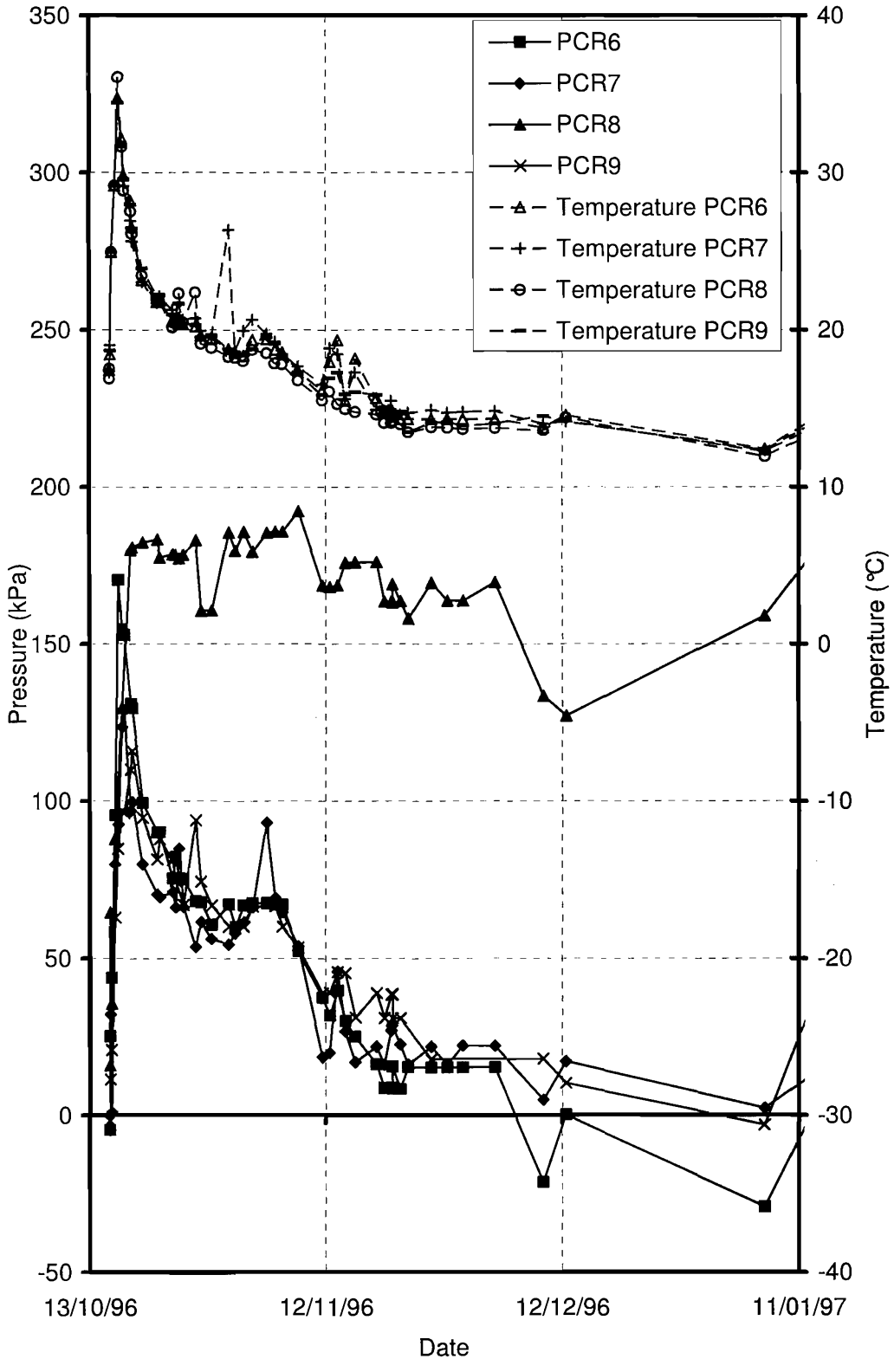

Figure 4-53: T4 concourse MMS I bench radial pressure cell readings PCR6, 7, 8, 9 in first 3 months

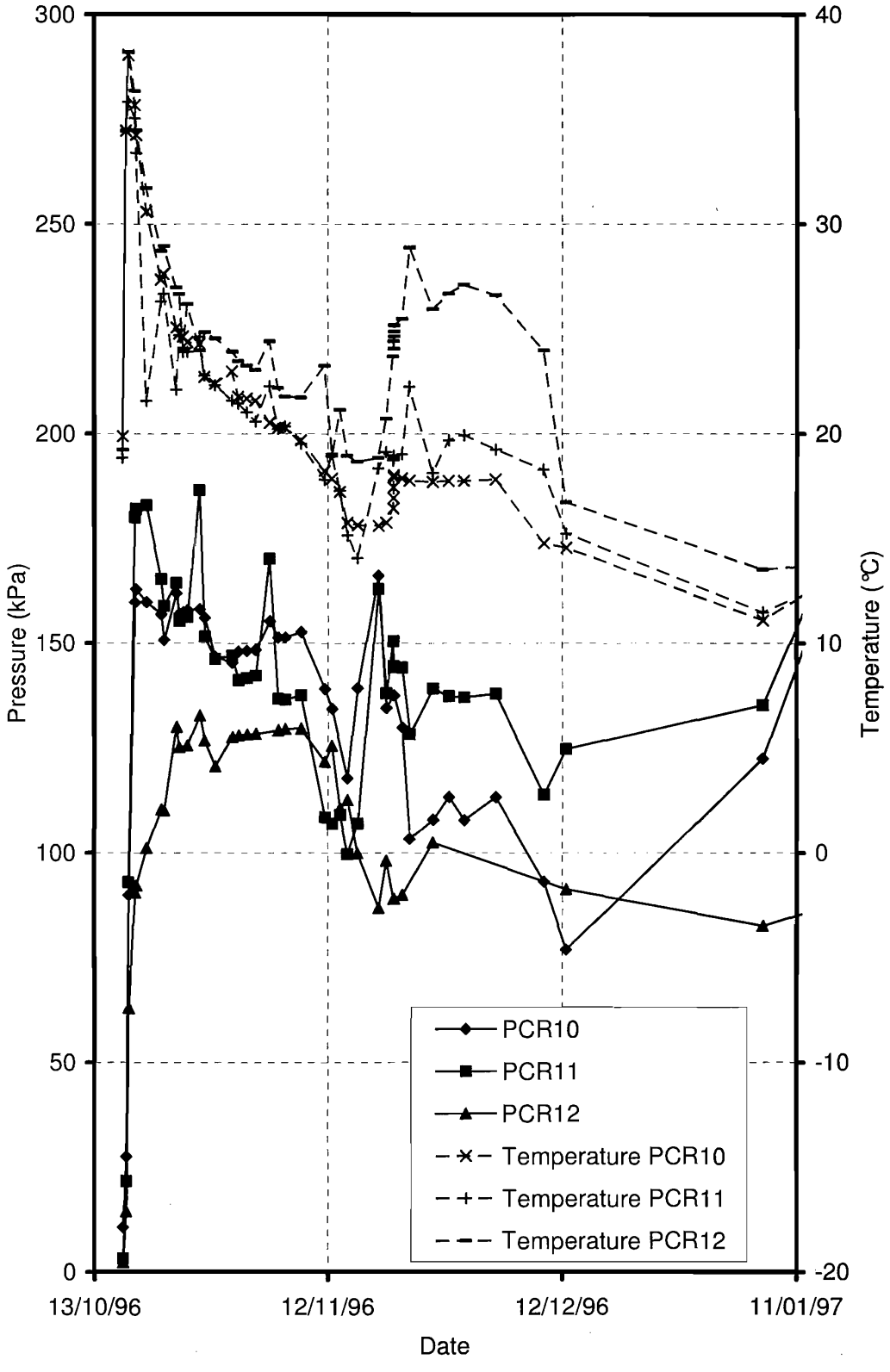

Figure 4-54: T4 concourse MMS I invert radial pressure cell readings PCR10, 11, 12 in first 3 months

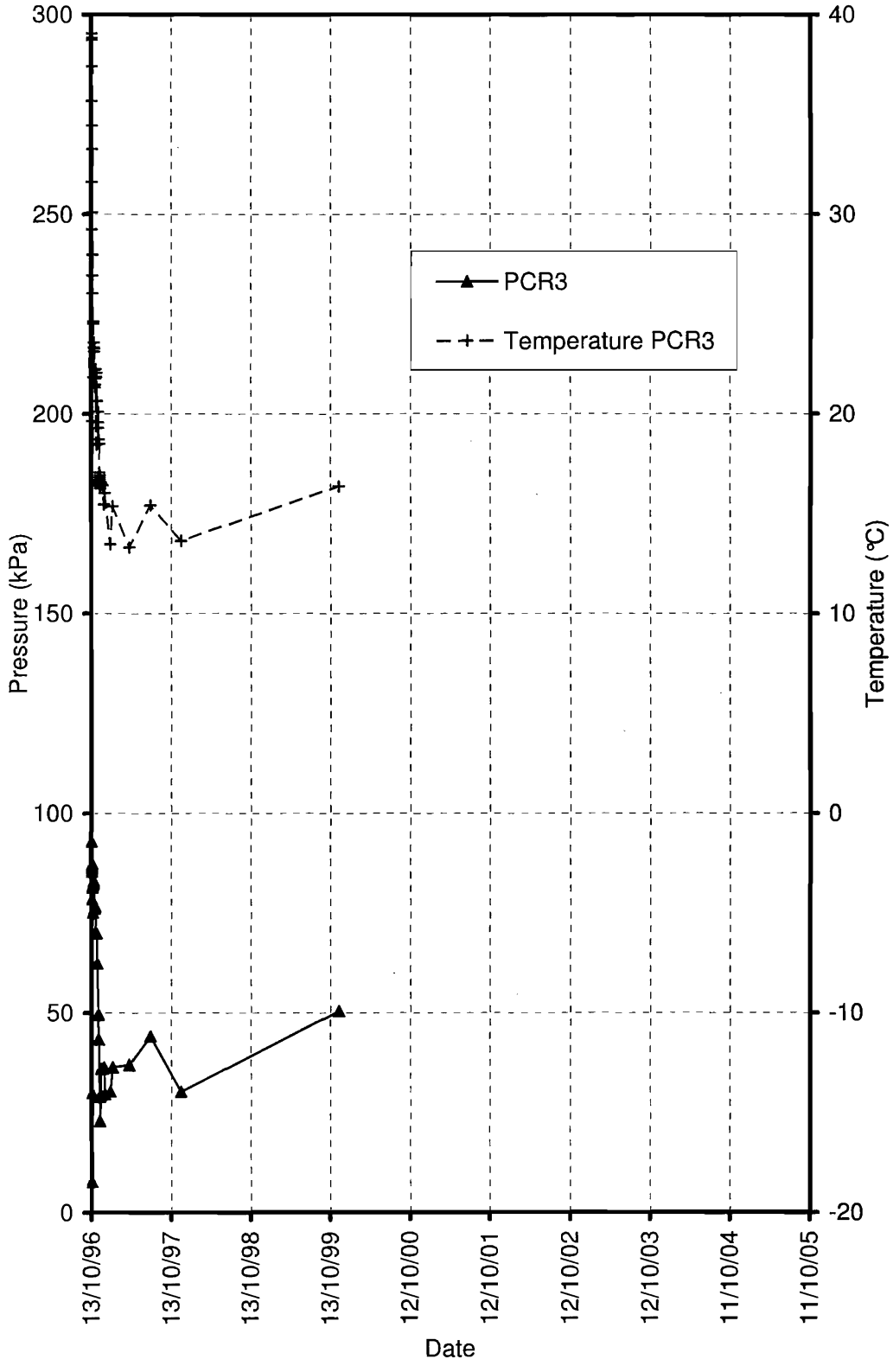

Figure 4-55: T4 concourse MMS I top heading radial pressure cell PCR3 over 9 years

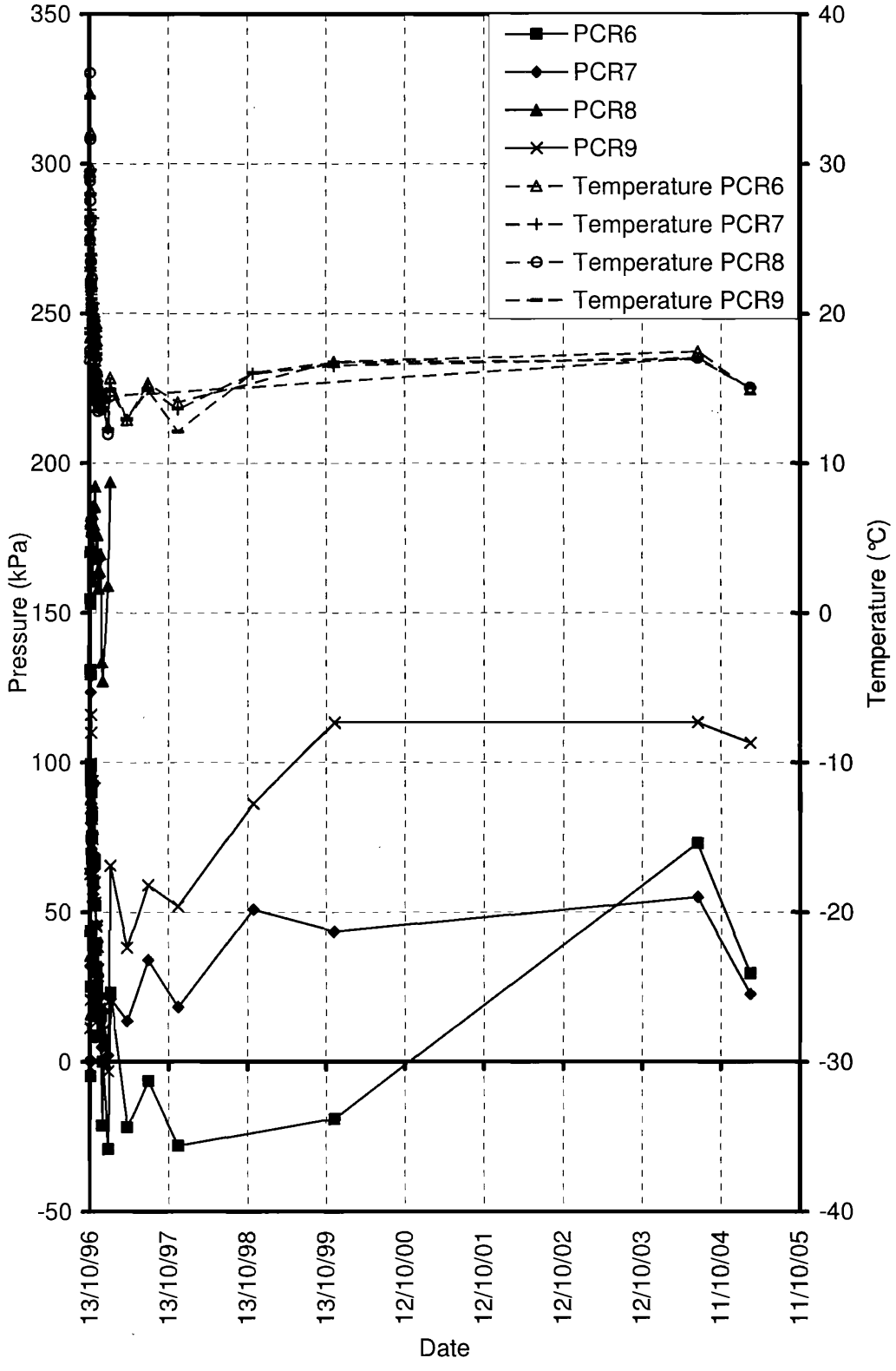

Figure 4-56: T4 concourse MMS I bench radial pressure cell readings PCR6, 7, 8, 9 over 9 years

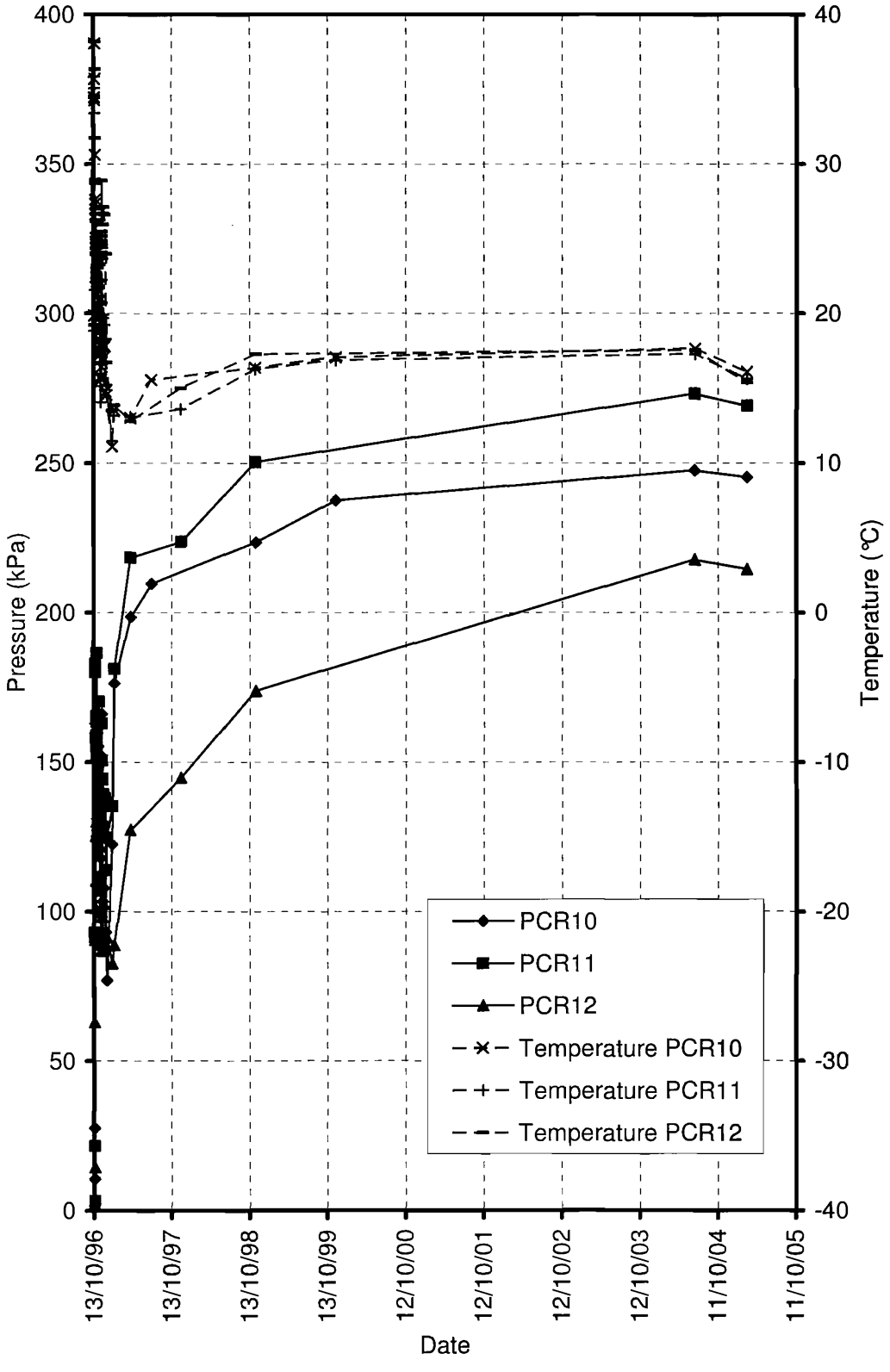

Figure 4-57: T4 concourse MMS I invert radial pressure cell readings PCR10, 11, 12 over 9 years

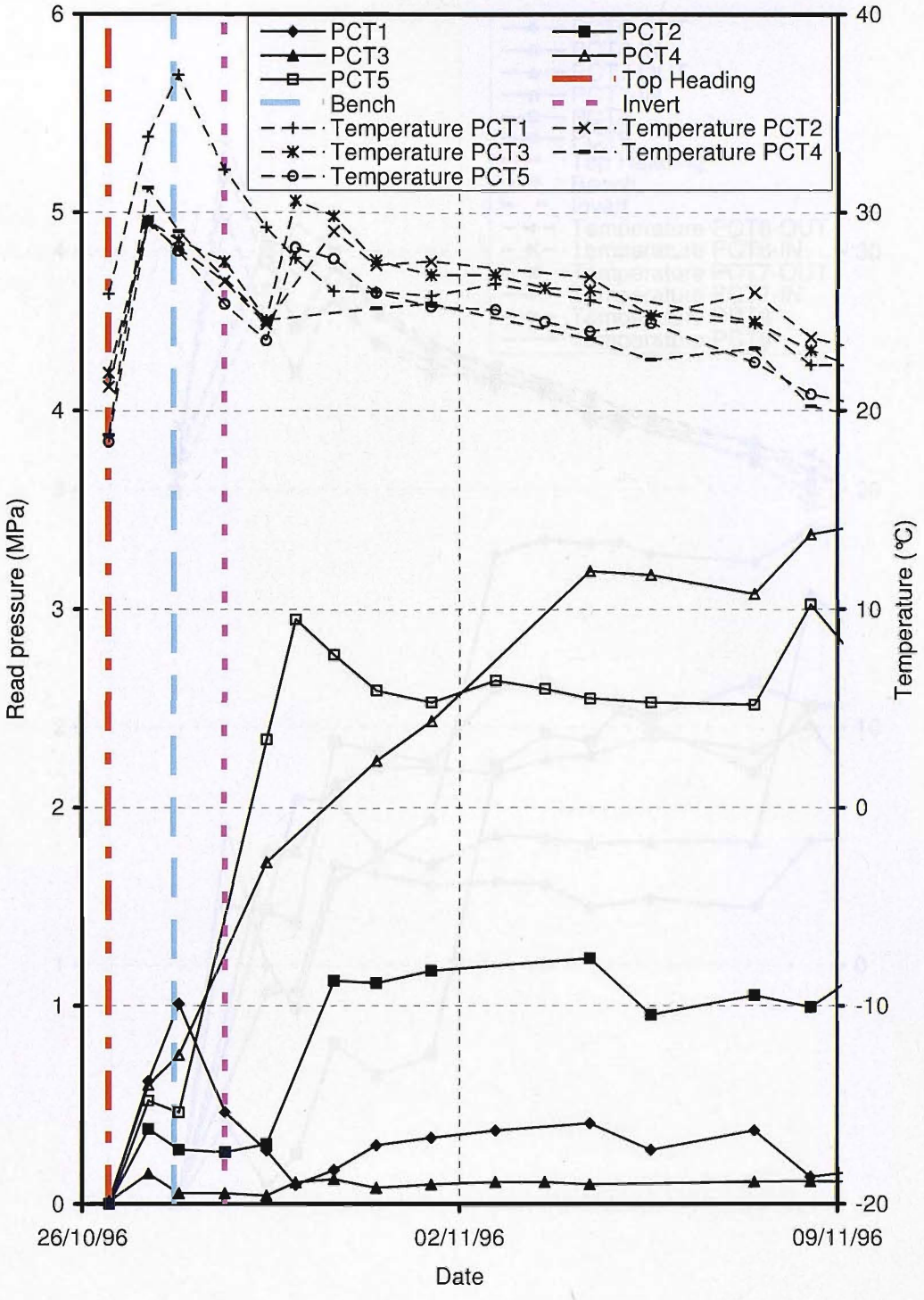

Figure 4-58: T4 concourse tunnel MMS VIII top heading tangential pressure cell readings PCT1, 2, 3, 4, 5 in first 2 weeks

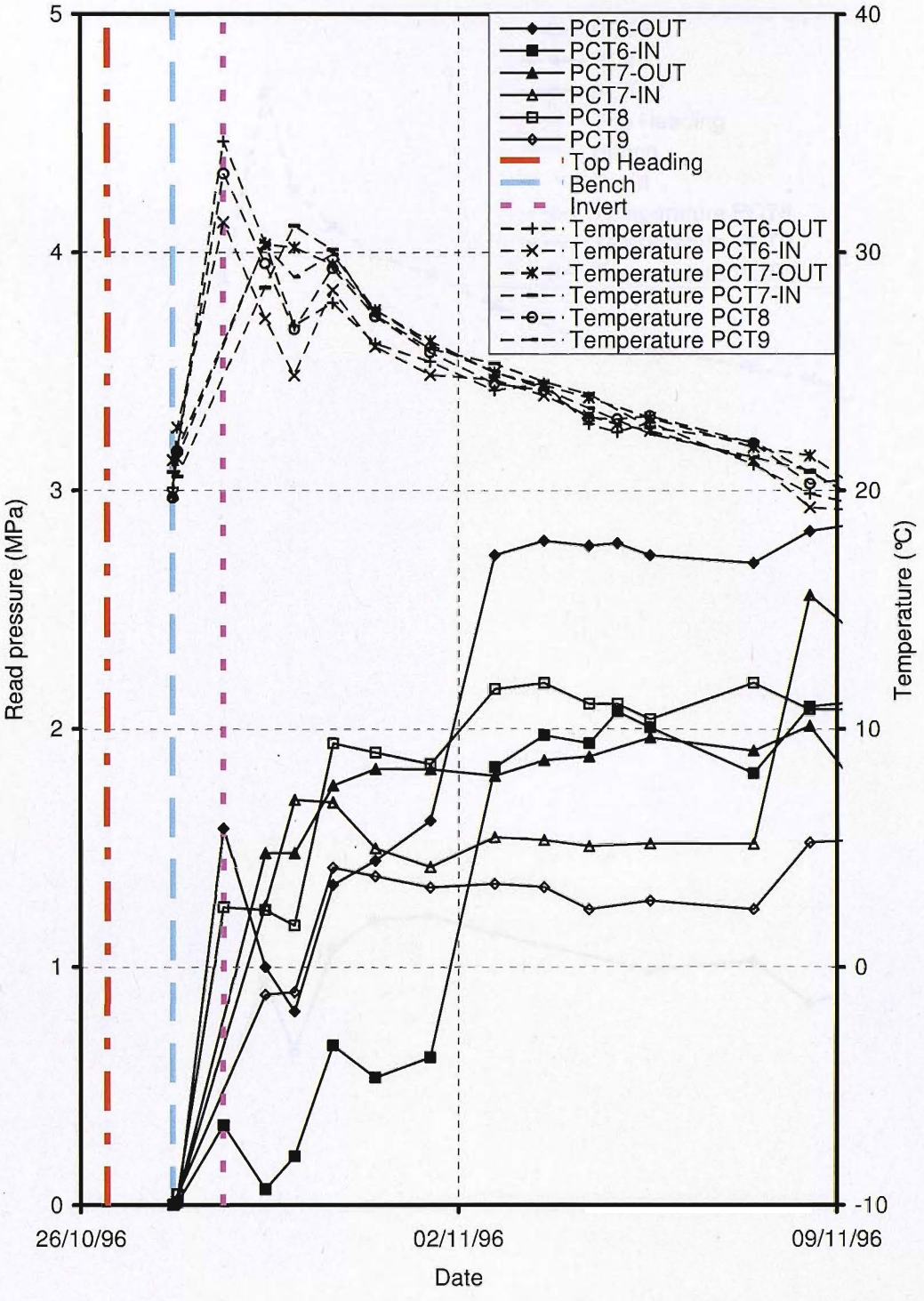

Figure 4-59: T4 concourse tunnel MMS VIII bench tangential pressure cell readings PCT6-OUT, 6-IN, 7-OUT, 7-IN, 8, 9 in first 2 weeks

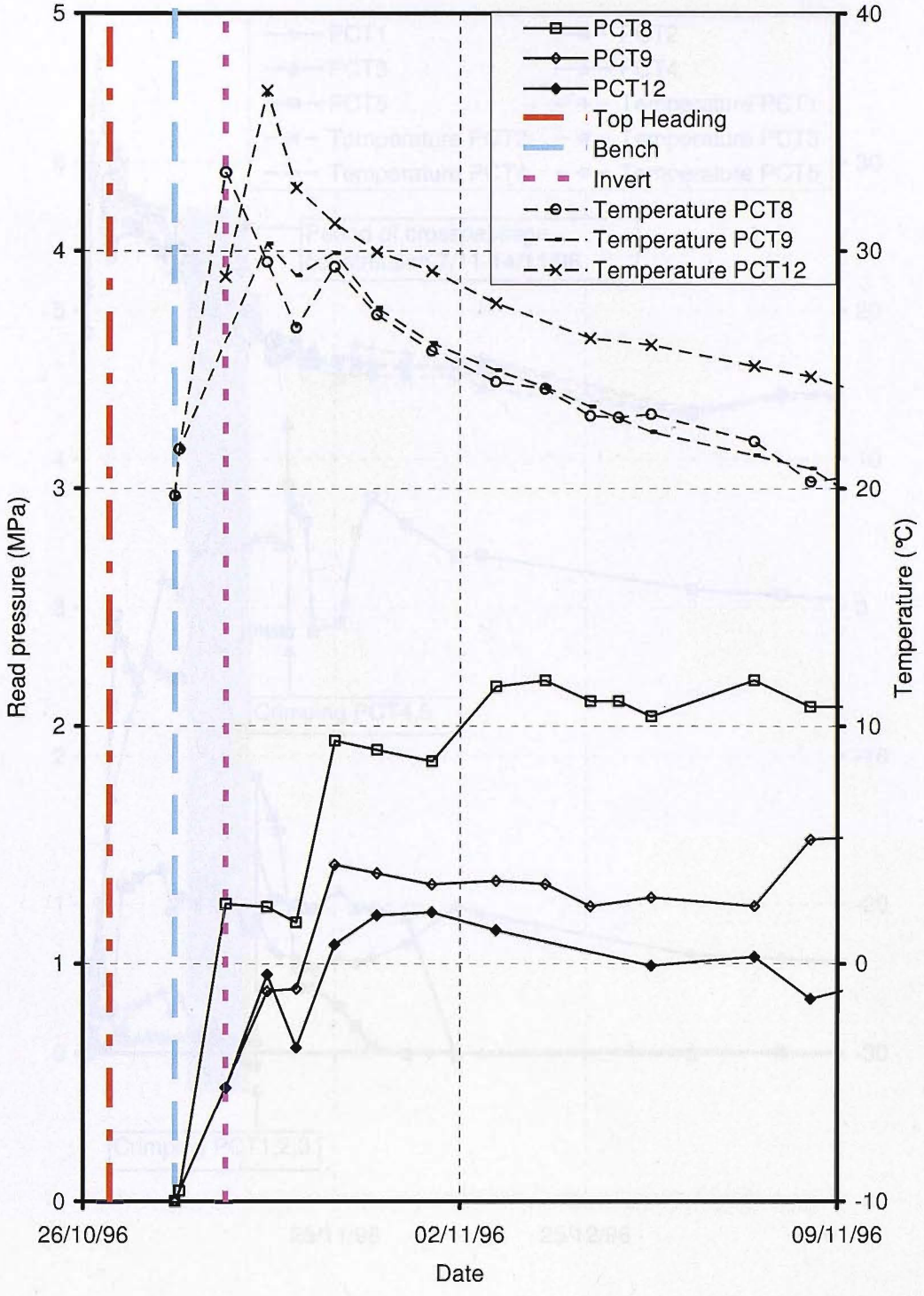

Figure 4-60: T4 concourse tunnel MMS VIII lower bench and invert tangential pressure cell readings PCT8, 9, 12 in first 2 weeks

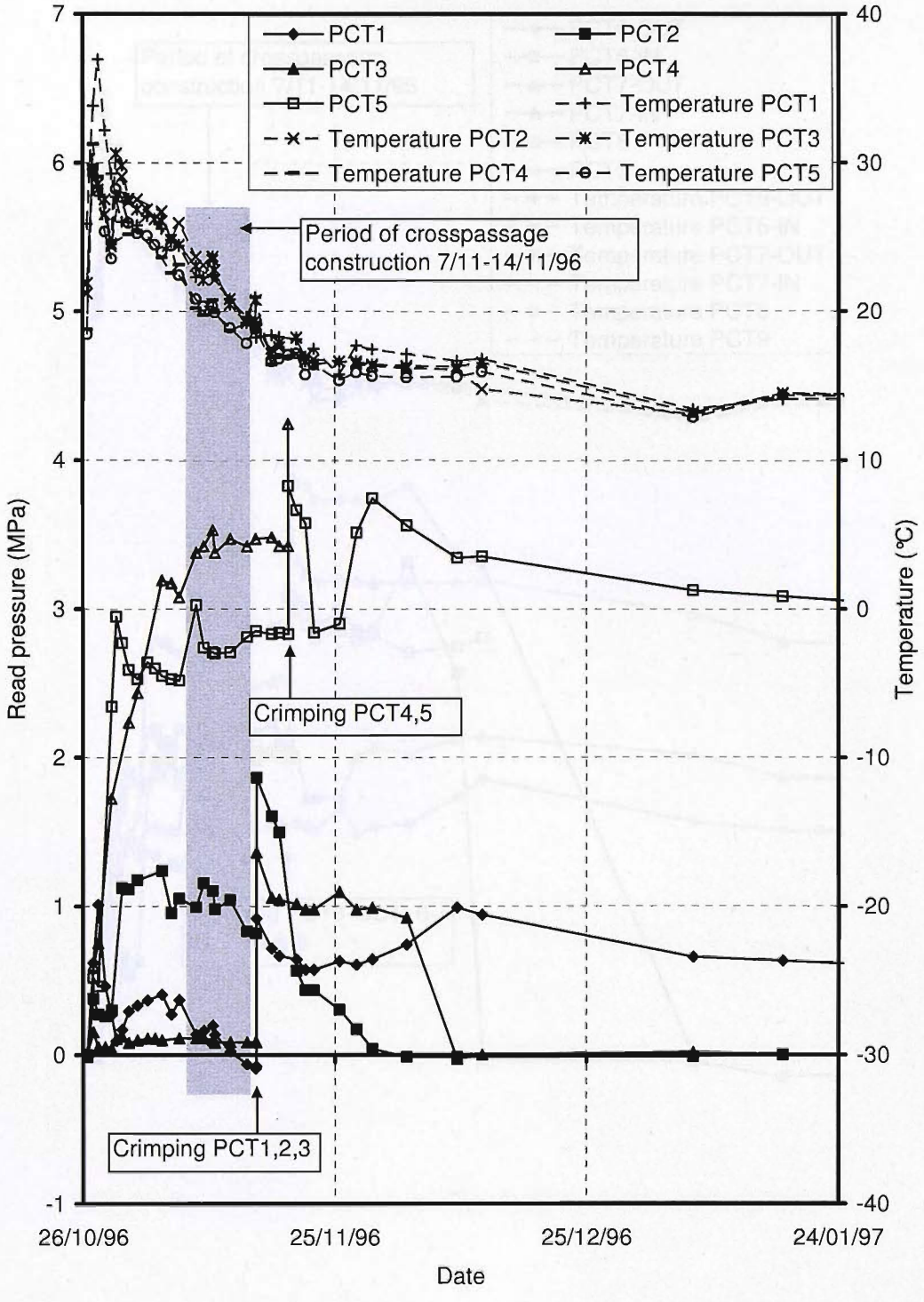

Figure 4-61: T4 concourse tunnel MMS VIII top heading tangential pressure cell readings PCT1, 2, 3, 4, 5 in first 3 months

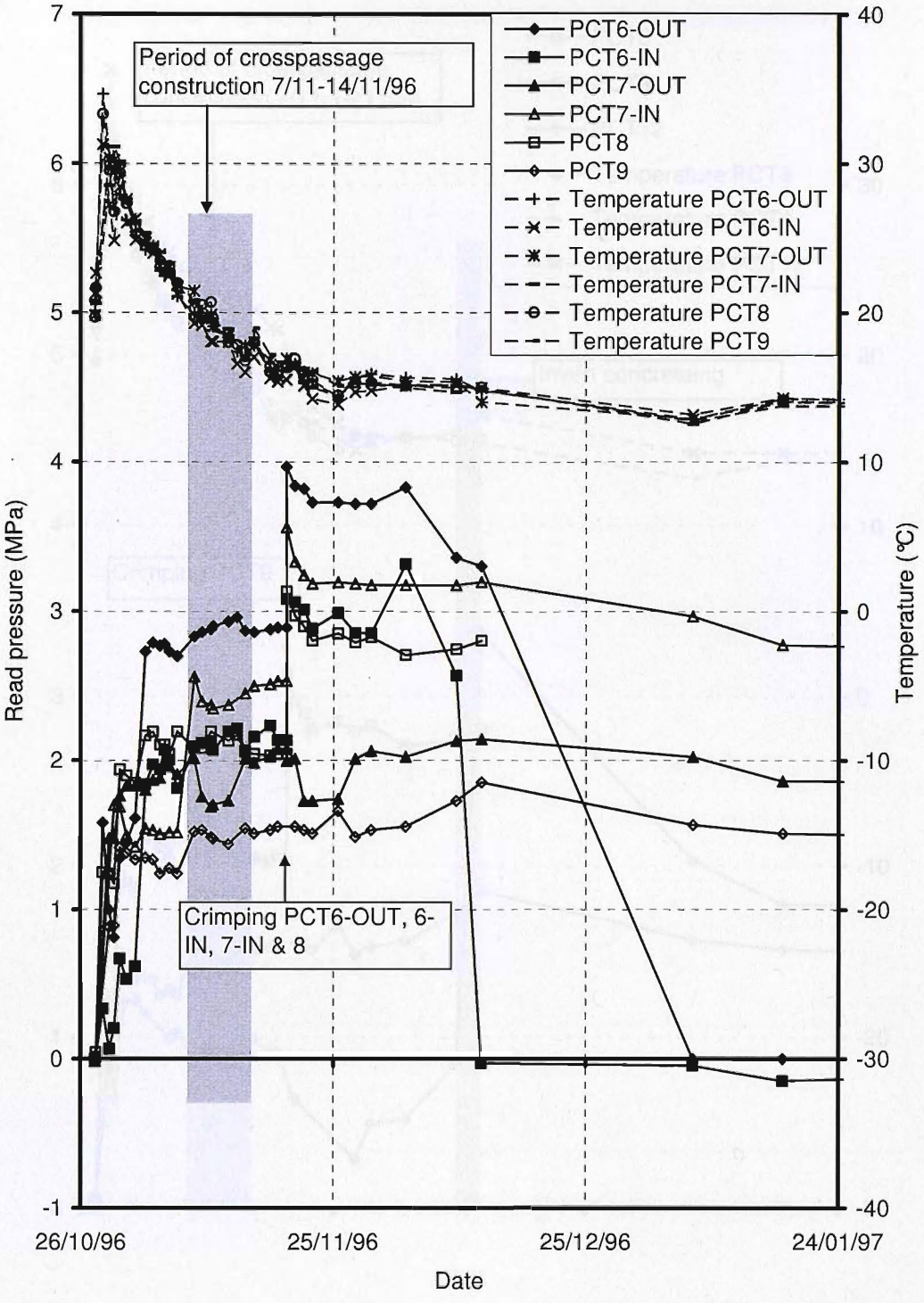

Figure 4-62: T4 concourse tunnel MMS VIII bench tangential pressure cell readings PCT6-OUT, 6-IN, 7-OUT, 7-IN, 8, 9 in first 3 months

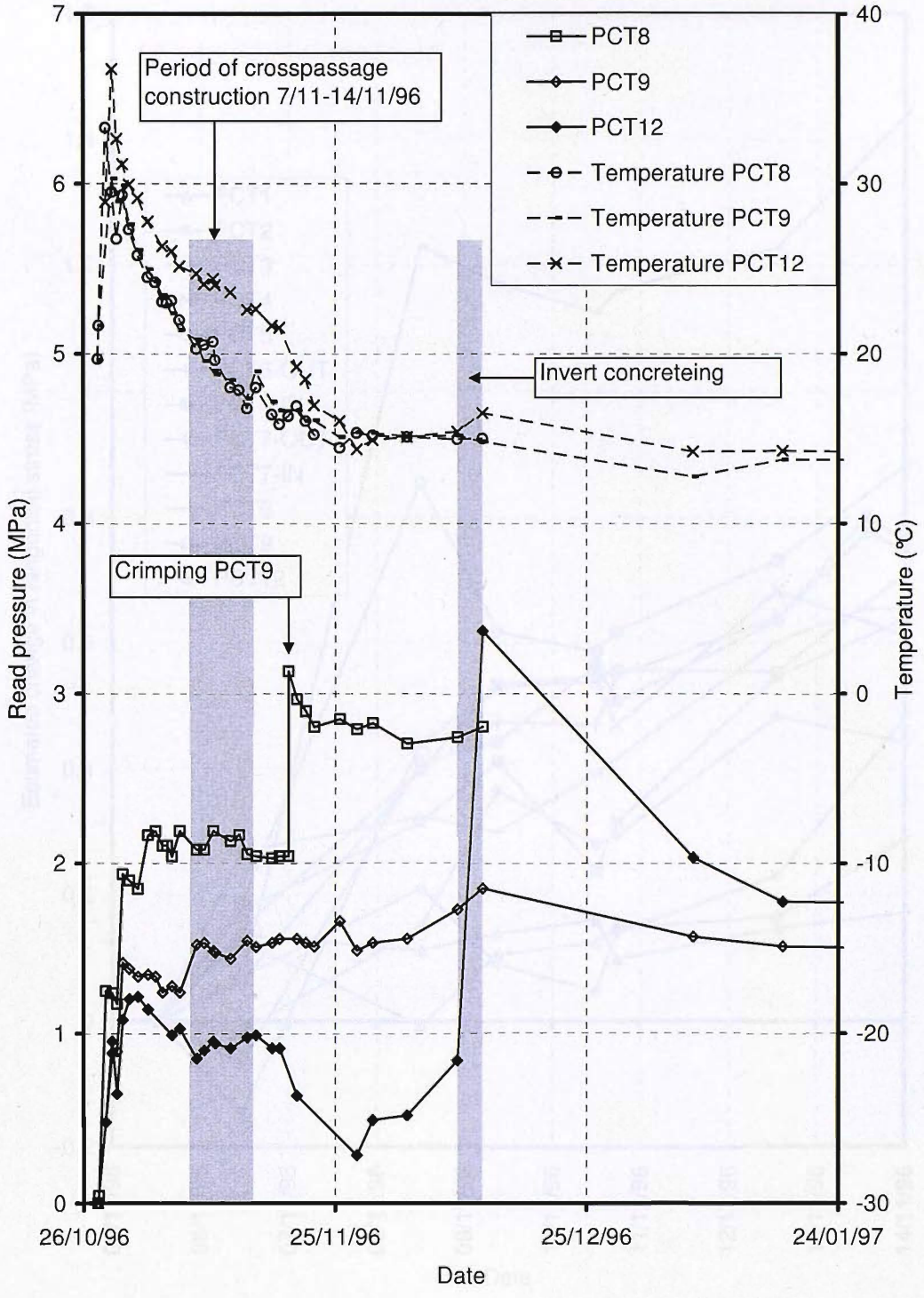

Figure 4-63: T4 concourse tunnel MMS VIII lower bench and invert tangential pressure cell readings PCT8, 9, 12 in first 3 months

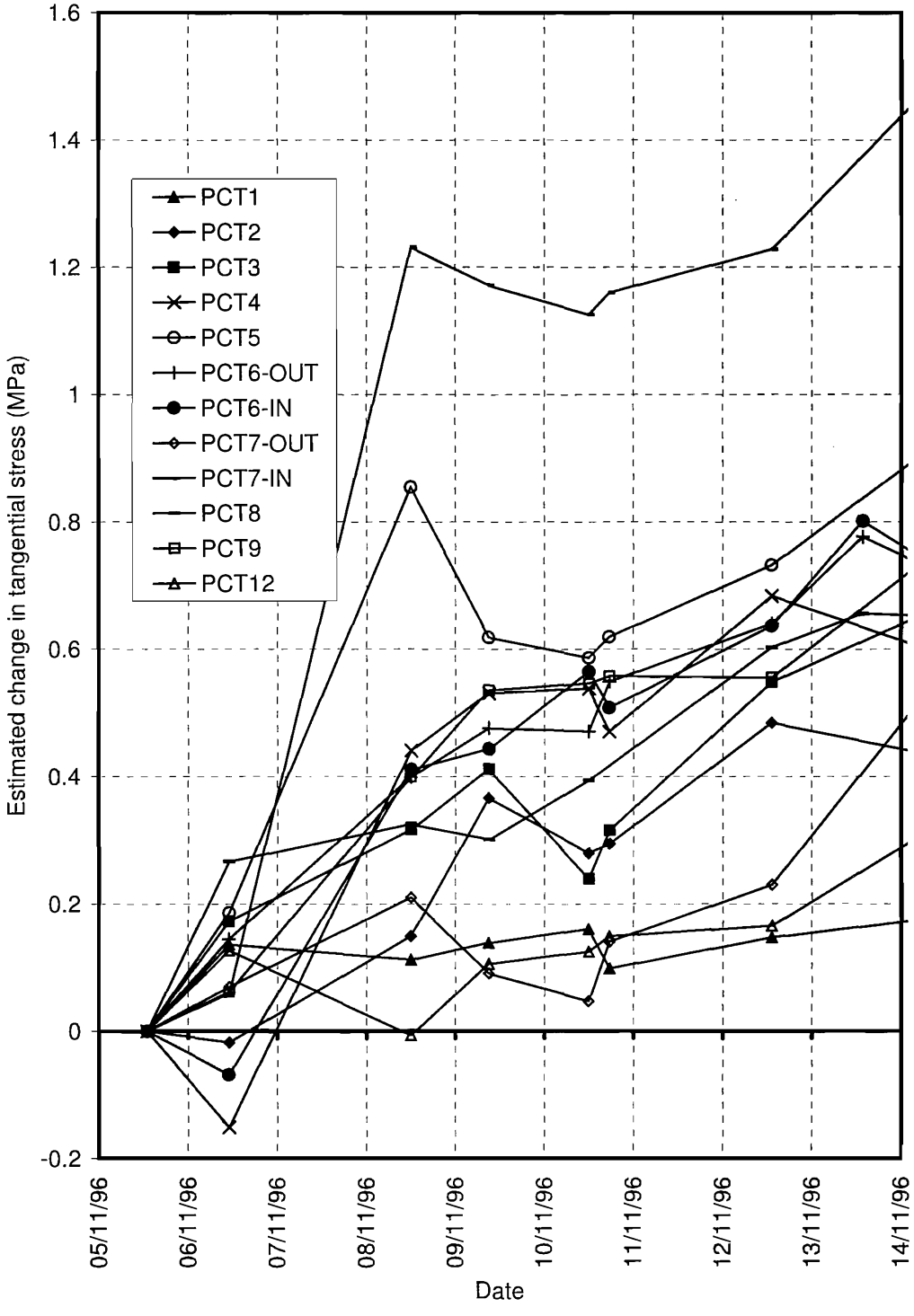

Figure 4-64: Estimated changes in tangential stress at MMS VIII due to adjacent crosspassage construction

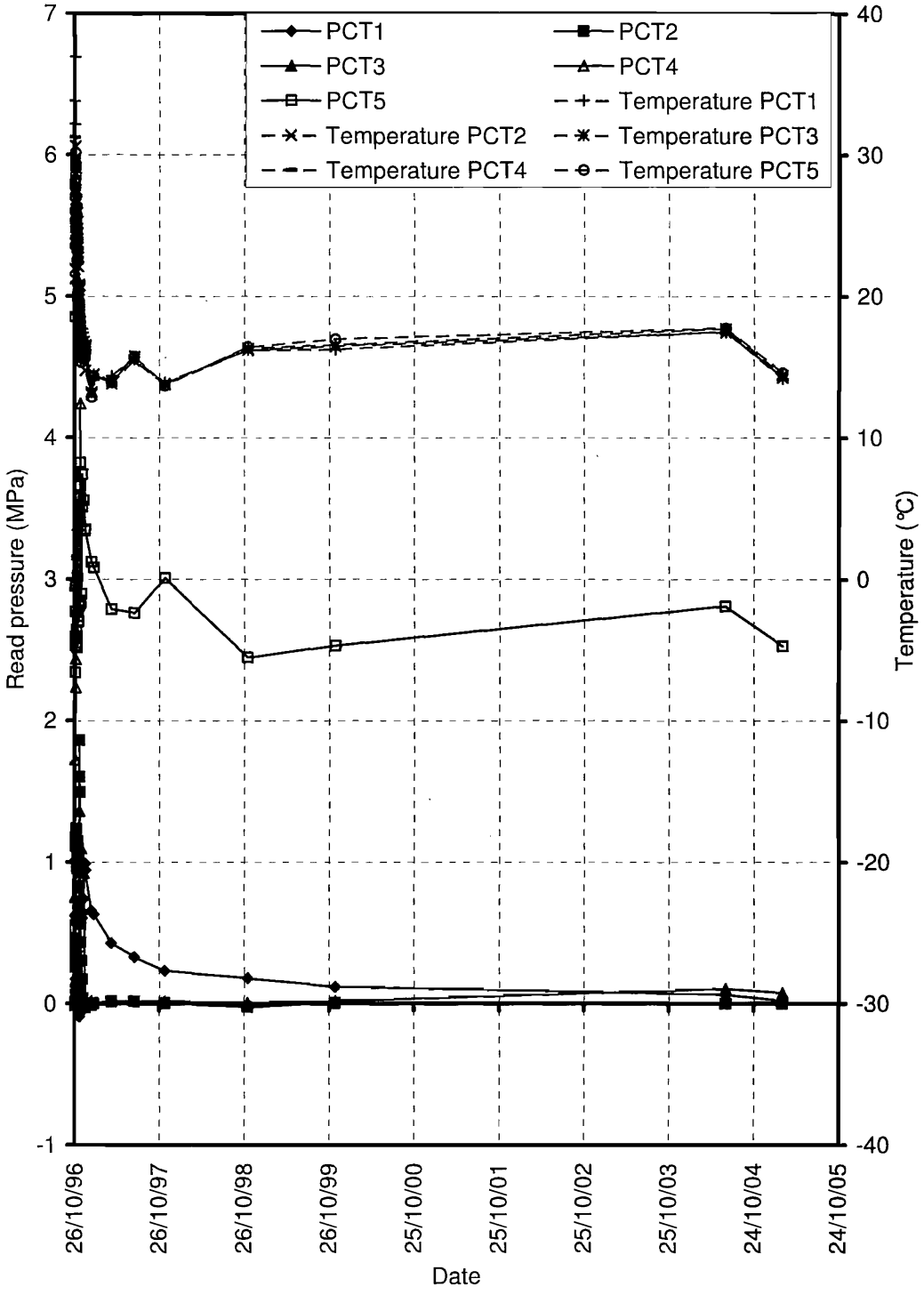

Figure 4-65: T4 concourse tunnel MMS VIII top heading tangential pressure cell readings PCT1, 2, 3, 4, 5 over 9 years

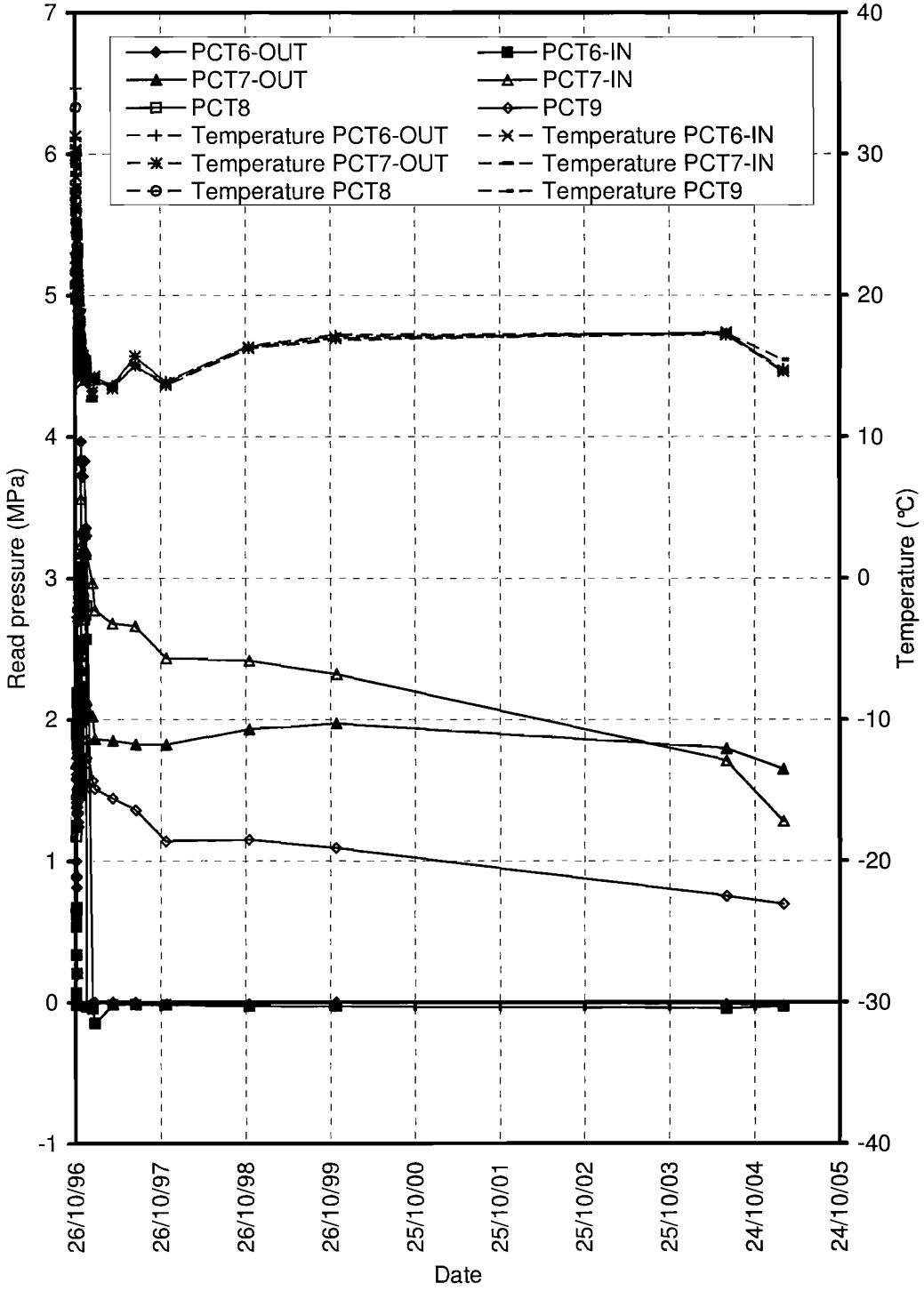

Figure 4-66: T4 concourse tunnel MMS VIII bench tangential pressure cell readings PCT6-OUT, 6-IN, 7-OUT, 7-IN, 8, 9 over 9 years

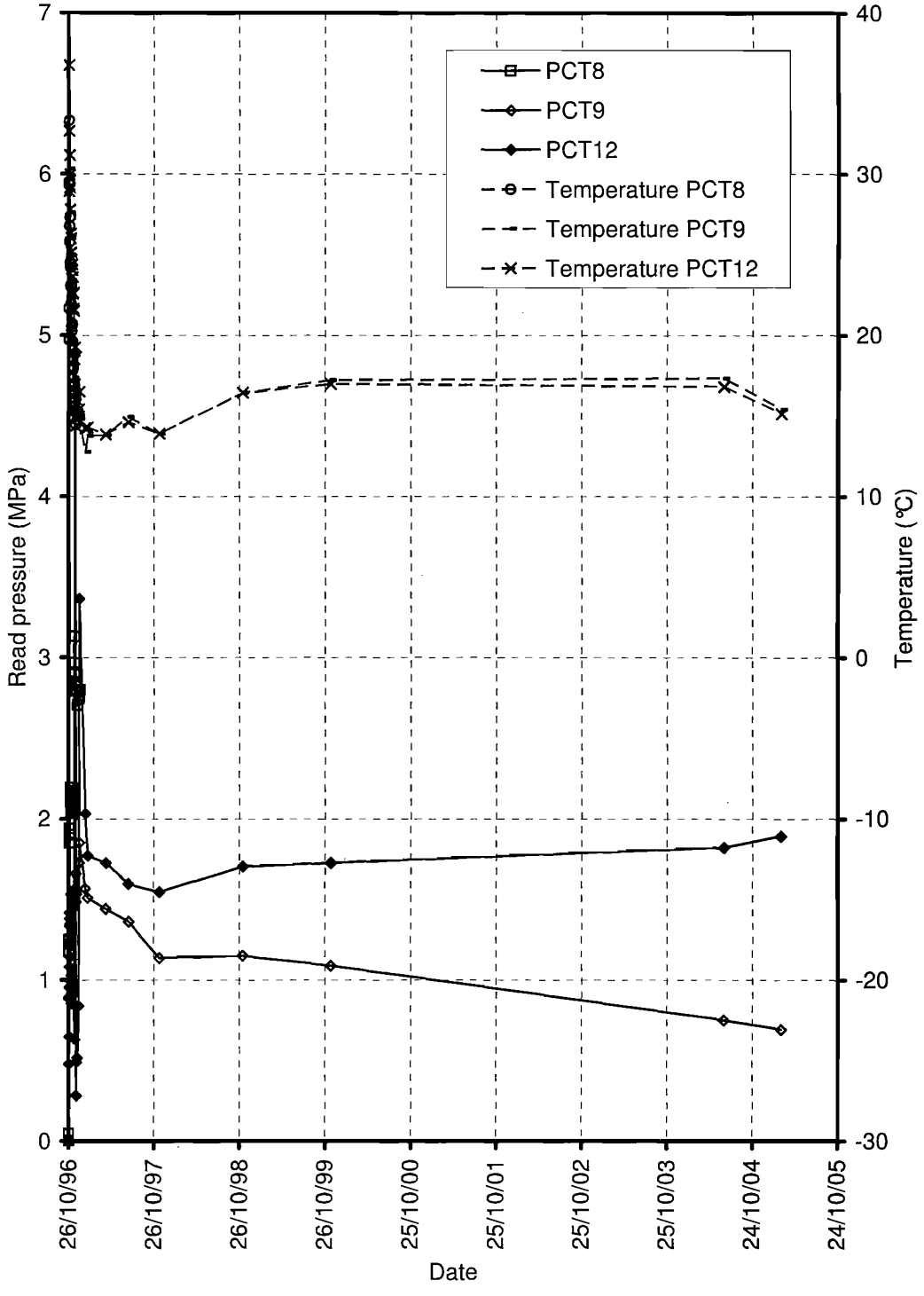

Figure 4-67: T4 concourse tunnel MMS VIII lower bench and invert tangential pressure cell readings PCT8, 9, 12 over 9 years

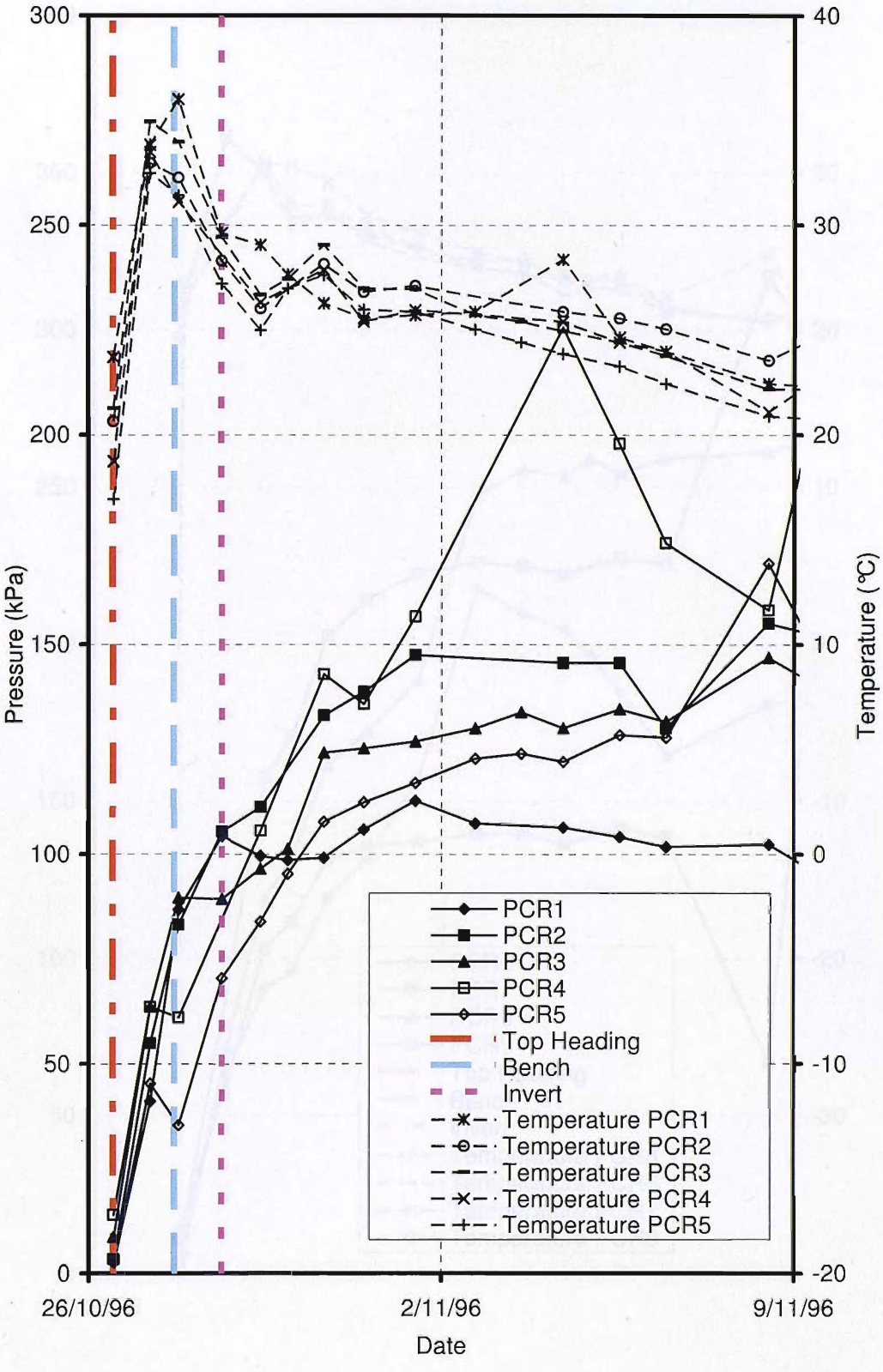

Figure 4-68: T4 concourse tunnel MMS VIII top heading radial pressure cell readings PCR1, 2, 3, 4, 5 in the first 2 weeks

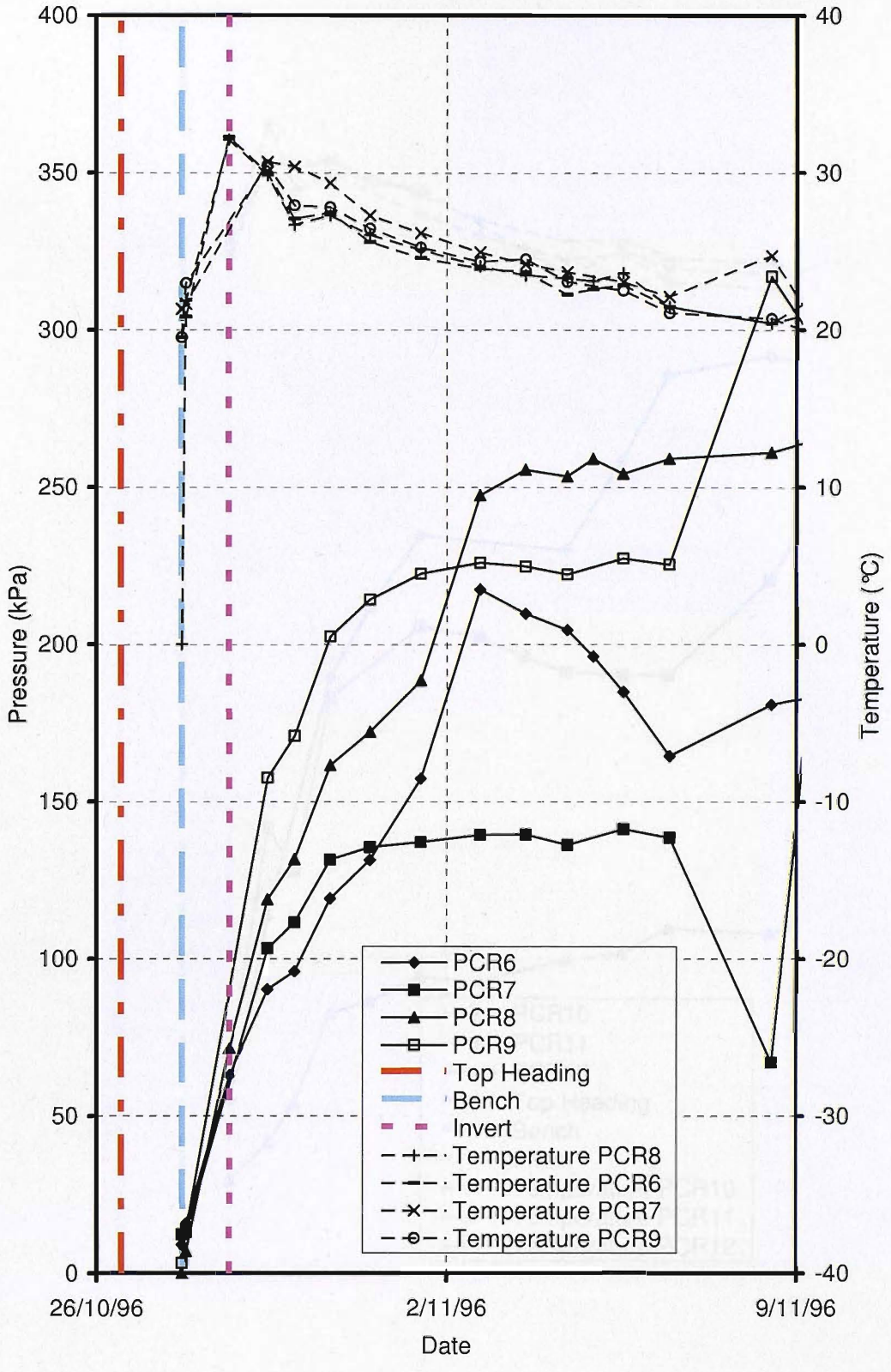

Figure 4-69: T4 concourse tunnel MMS VIII bench radial pressure cell readings PCR6, 7, 8, 9 in the first 2 weeks

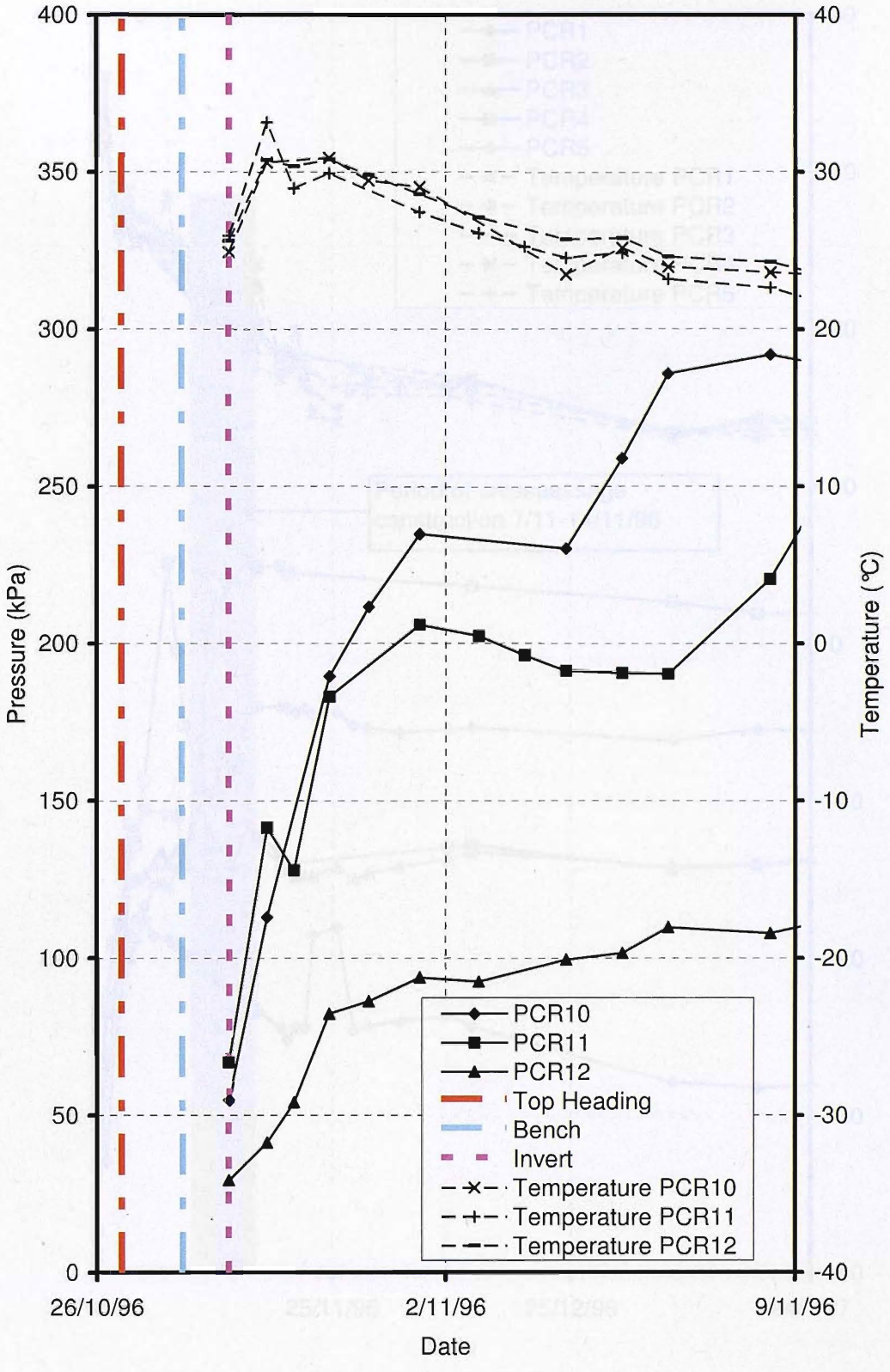

Figure 4-70: T4 concourse tunnel MMS VIII invert radial pressure cell readings PCR10, 11, 12 in the first 2 weeks

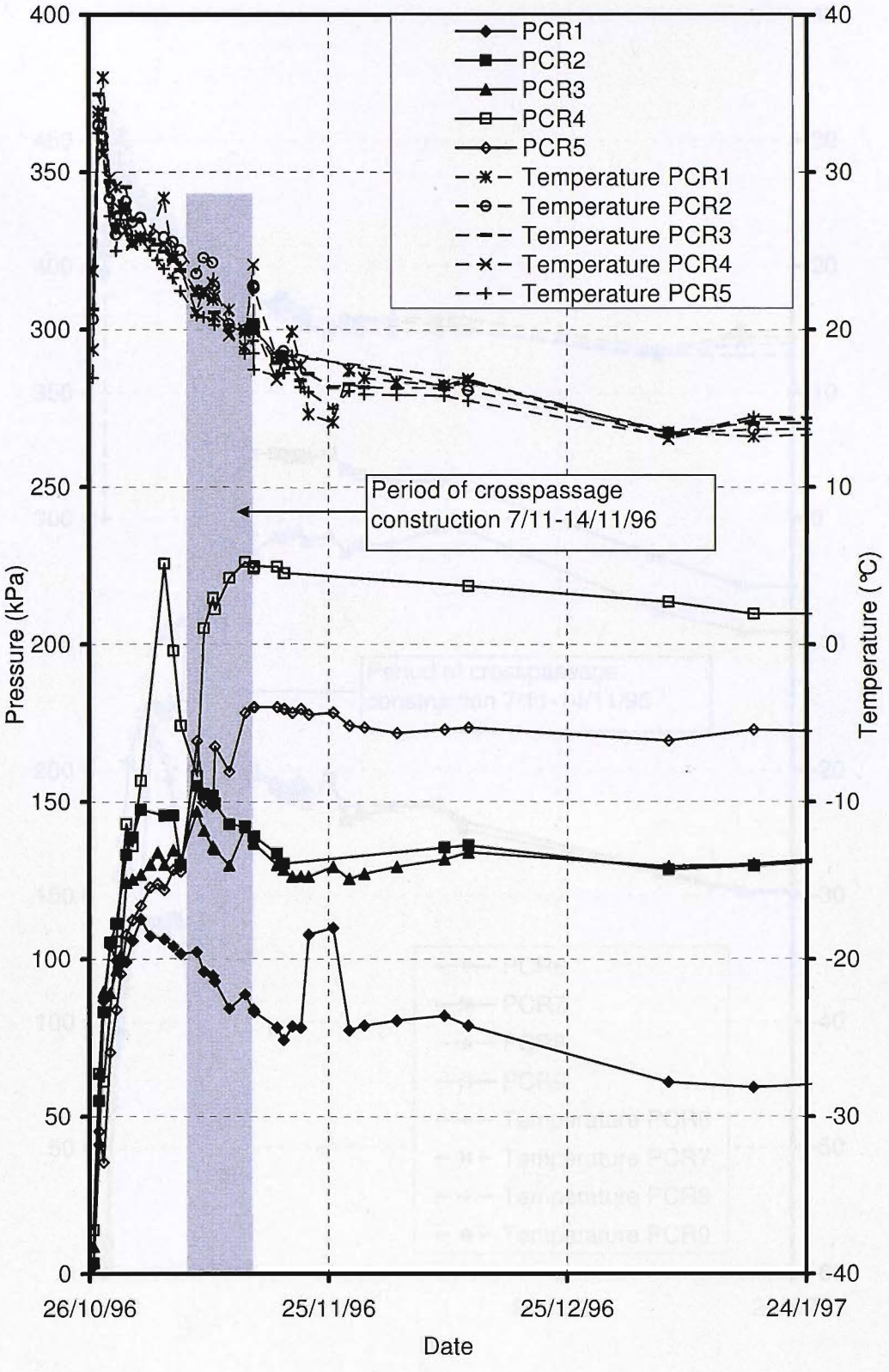

Figure 4-71: T4 concourse tunnel MMS VIII top heading radial pressure cell readings PCR1, 2, 3, 4, 5 in the first 3 months

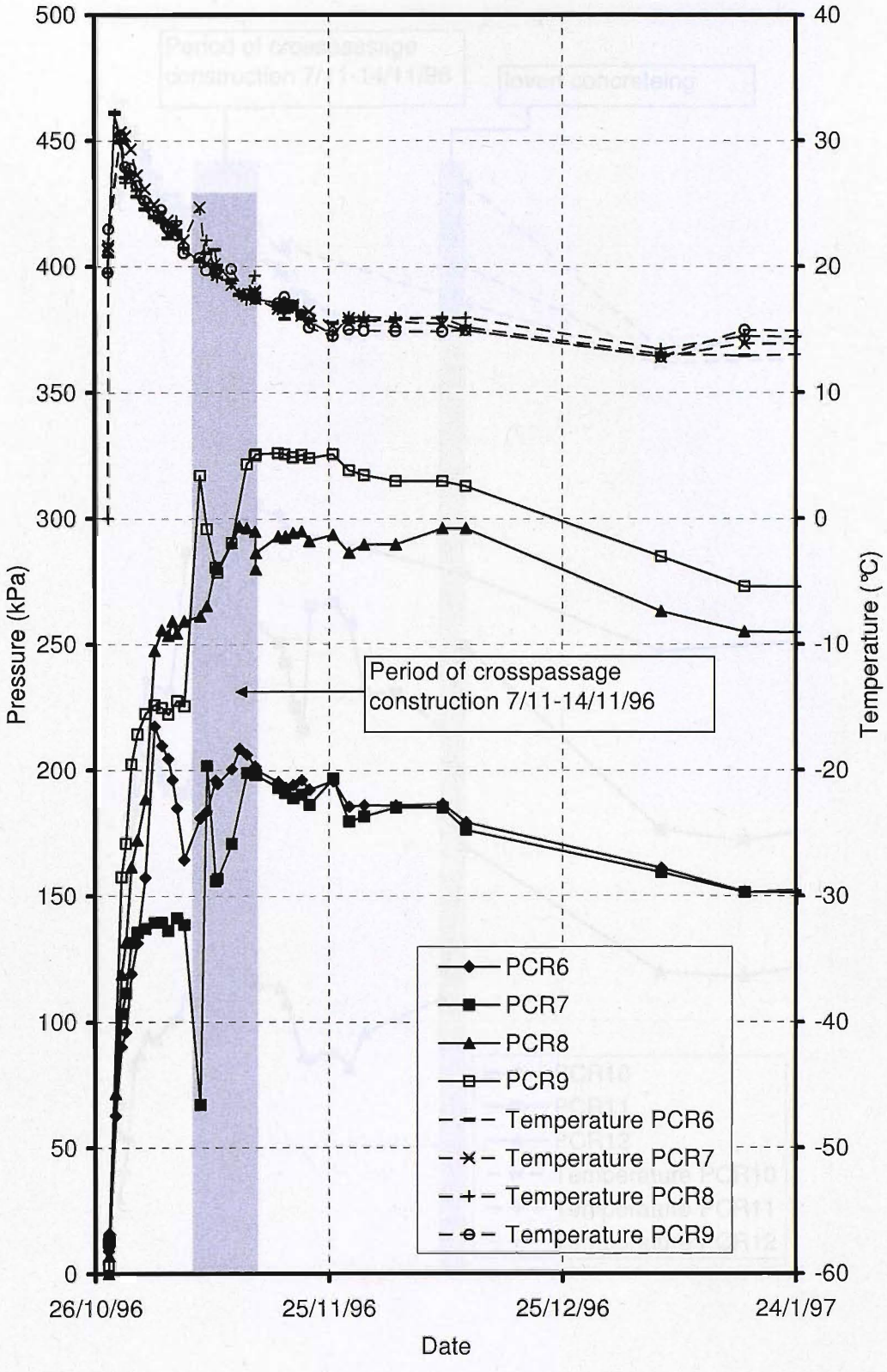

Figure 4-72: T4 concourse tunnel MMS VIII bench radial pressure cell readings PCR6, 7, 8, 9 in the first 3 months

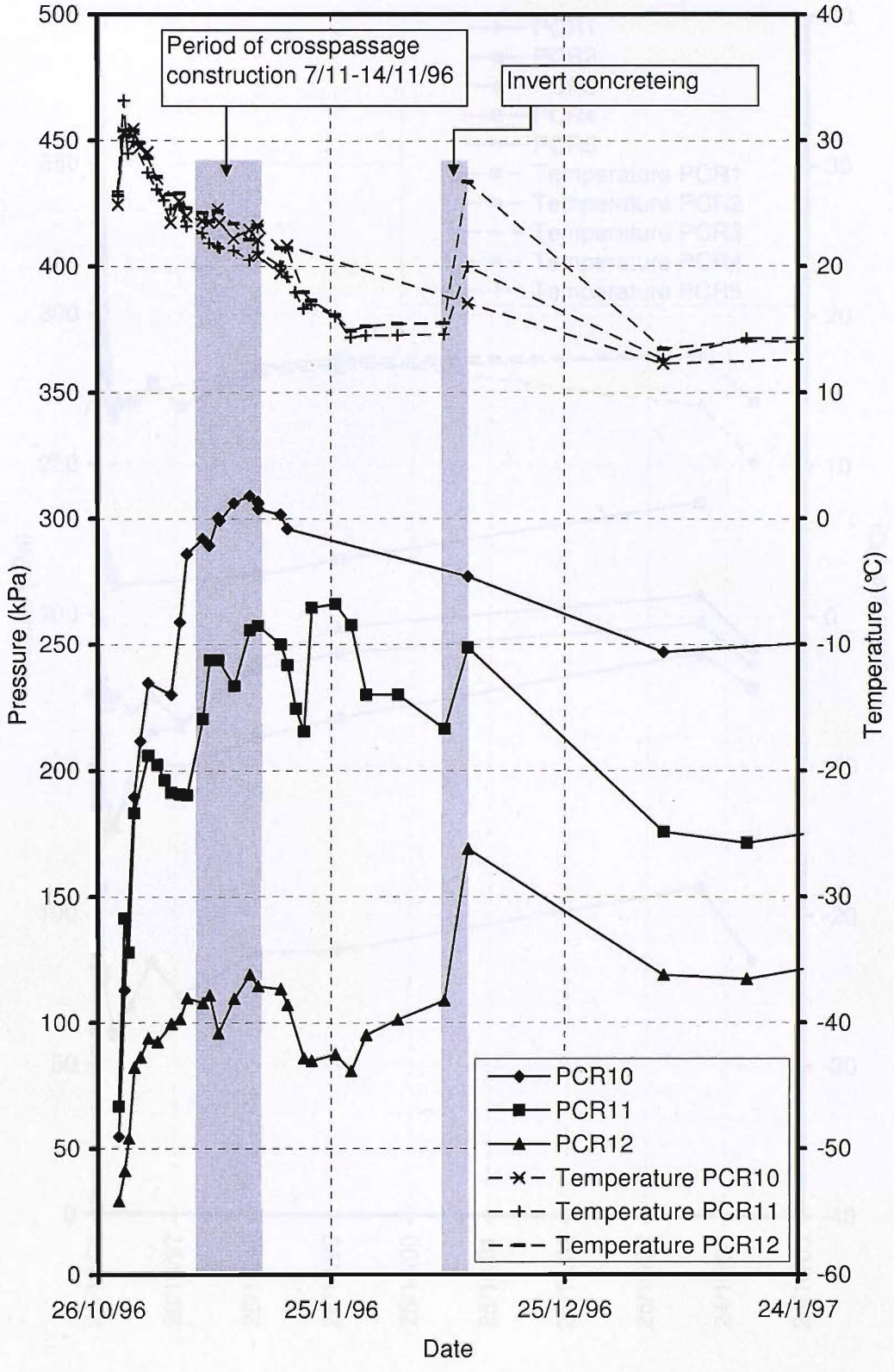

Figure 4-73: T4 concourse tunnel MMS VIII invert radial pressure cell readings PCR10, 11, 12 in the first 3 months

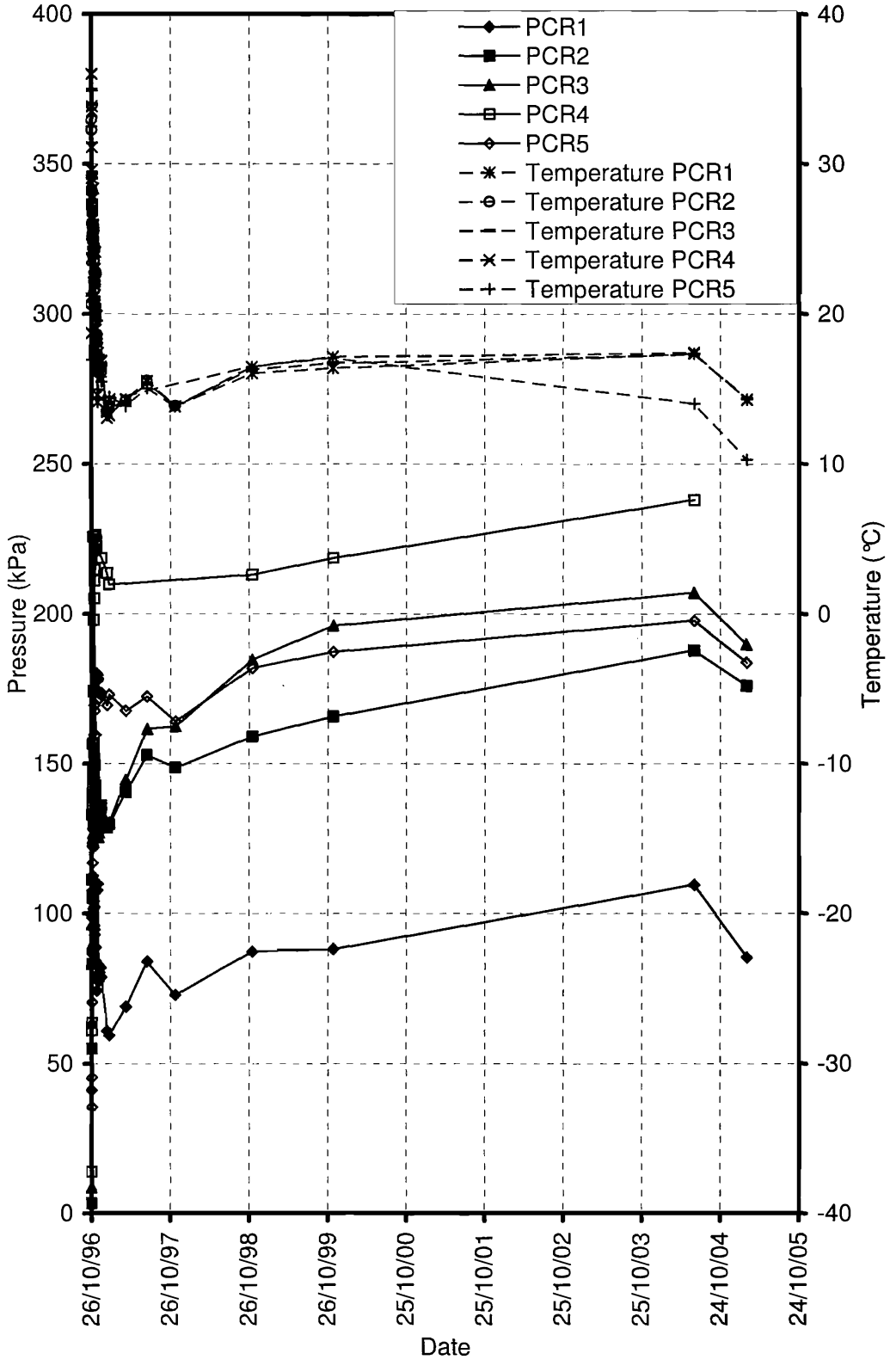

Figure 4-74: T4 Concourse tunnel MMS VIII top heading radial pressure cell readings PCR1, 2, 3, 4, 5 over 9 years

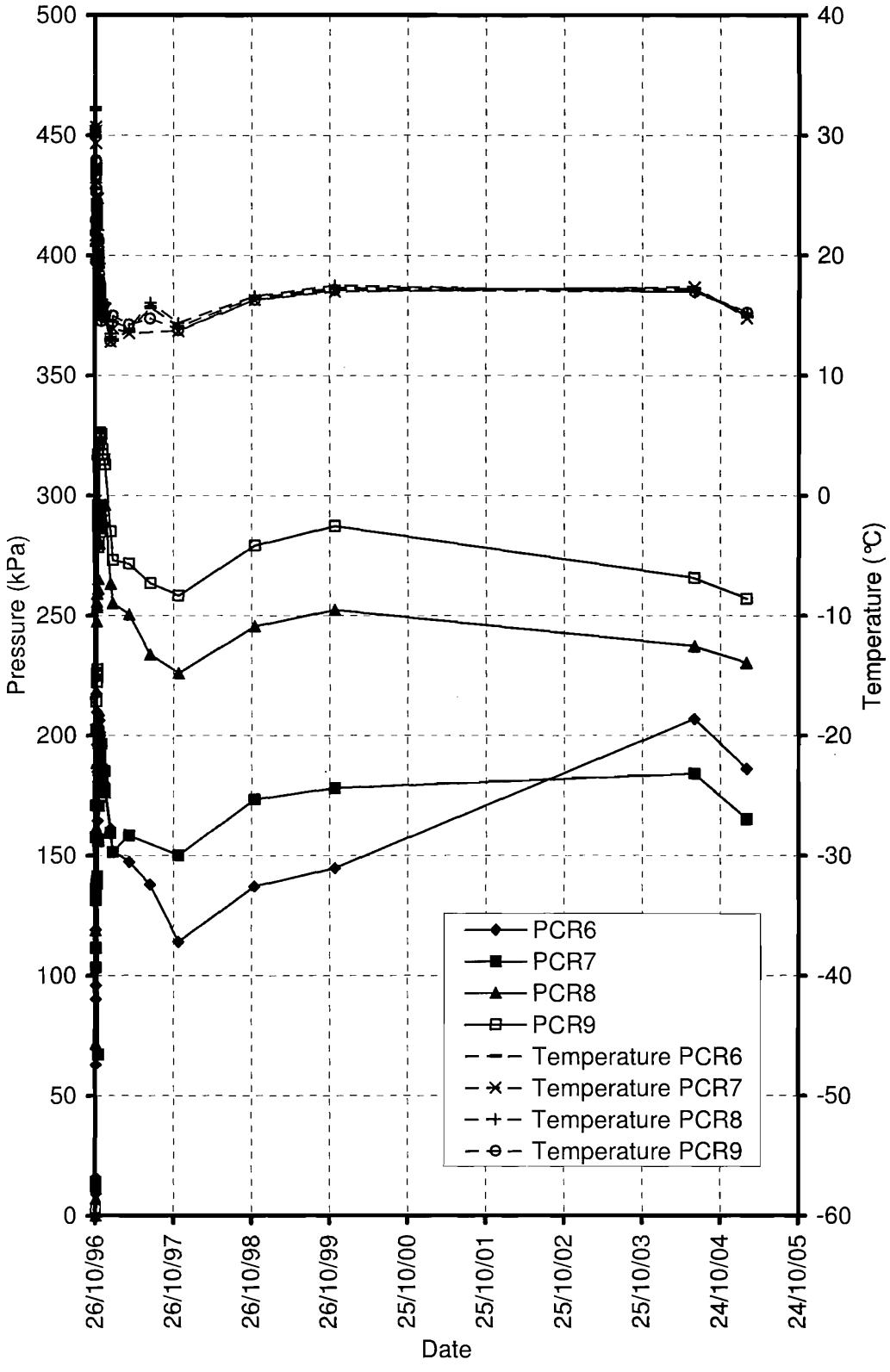

Figure 4-75: T4 Concourse tunnel MMS VIII bench radial pressure cell readings PCR6, 7, 8, 9 over 9 years

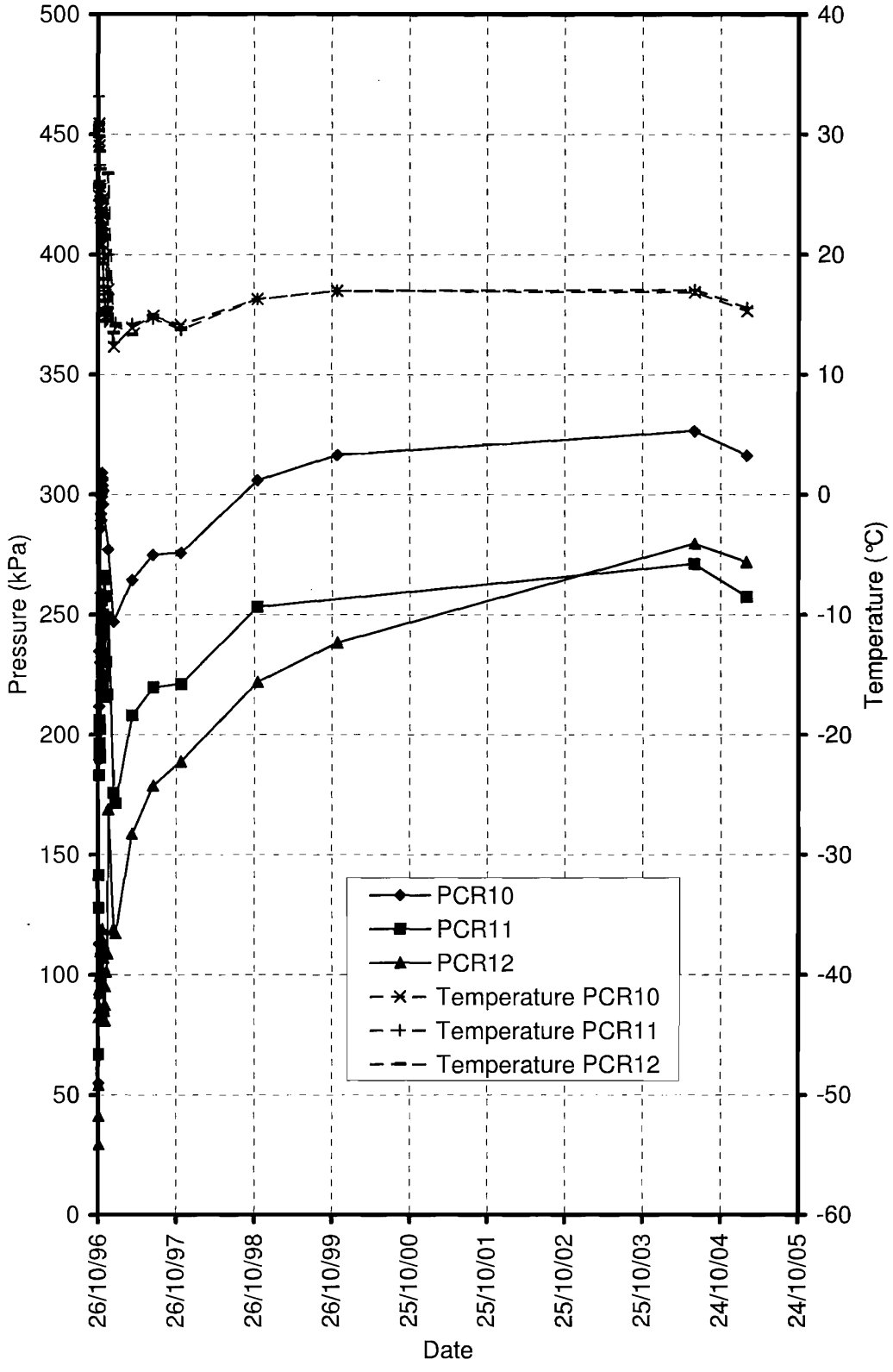

Figure 4-76: T4 Concourse tunnel MMS VIII invert radial pressure cell readings PCR10, 11, 12 over 9 years

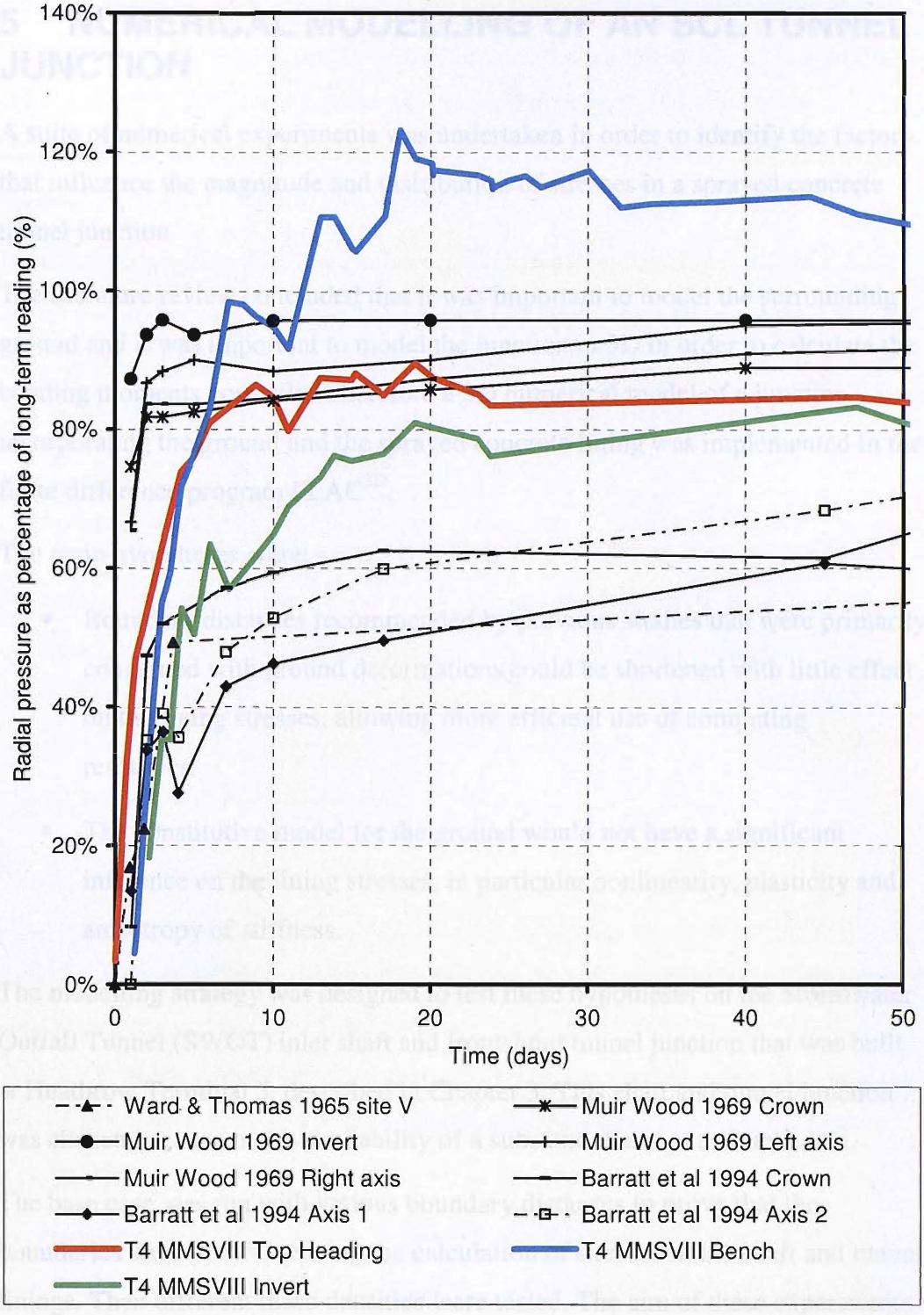

Figure 4-77: Comparison of development of radial pressure over 50 days

5 NUMERICAL MODELLING OF AN SCL TUNNEL JUNCTION

A suite of numerical experiments was undertaken in order to identify the factors that influence the magnitude and distribution of stresses in a sprayed concrete tunnel junction.

The literature review concluded that it was important to model the surrounding ground and it was important to model the junction in 3D in order to calculate the bending moments correctly. Therefore a 3D numerical model of a junction incorporating the ground and the sprayed concrete lining was implemented in the finite difference program FLAC^{3D}.

The main hypotheses were:

- Boundary distances recommended by previous studies that were primarily concerned with ground deformations could be shortened with little effect on the lining stresses, allowing more efficient use of computing resources.
- The constitutive model for the ground would not have a significant influence on the lining stresses, in particular nonlinearity, plasticity and anisotropy of stiffness.

The modelling strategy was designed to test these hypotheses on the Stormwater Outfall Tunnel (SWOT) inlet shaft and frontshunt tunnel junction that was built at Heathrow Terminal 5, described in Chapter 3. This shaft and tunnel junction was chosen because of the availability of a substantial amount of field data.

The base case was run with various boundary distances to prove that the boundaries were not influencing the calculation of stresses in the shaft and tunnel linings. Then different mesh densities were tested. The aim of these experiments was to minimise the size of the model and thus to minimise the calculation time while ensuring that acceptable results, in terms of detail and accuracy, were obtained. Once the base case had been validated in this way, it was then compared with the field data.

Since ground behaviour is complex and the methods of ascertaining parameters for use in analysis frequently result in high variability, sensitivity analyses will

always need to be undertaken in design. But 3D numerical modelling involves significant computation time, so it is desirable to limit the number of parameters that need to be taken into account in sensitivity analyses. Therefore, the importance of various aspects of ground behaviour to the calculation of lining stresses around the junction was investigated.

Increasing the lining thickness will result in lower stresses, but the stiffer structure will also attract more load; especially bending moments. Therefore, the effect of the lining thickness on the maximum and minimum stresses around the junction was investigated.

5.1 Base case

The base case was selected to represent current SCL design practice. Since the majority of research has in the past concentrated on the prediction of ground movements, a ground model was selected that was expected to replicate the general pattern of both the surface settlements and the ground deformations around the shaft and tunnel. As is common practice in design, a simple linear elastic sprayed concrete model was used.

5.1.1 Model geometry

The model was created using generic bricks, which are cuboidal (or, strictly speaking, parallelepiped) elements within which the number of zones along the 3 directions may be specified. The basic geometry is shown in Figure 5-1. The gridpoints of the generic bricks were then moved to create the inlet shaft and the frontshunt tunnel. A sketch of the model ready for analysis is shown in Figure 5-2 and Figure 5-3.

Indexing the gridpoints made the task of distorting the cuboidal bricks into the shape of the shaft and tunnel much easier. An example of the use of indexing is given in the FLAC^{3D} manual "Example Applications", Chapter 5: "Grid generation for intersecting tunnels" (Itasca, 2005). Indexing creates ordered arrays for each brick allowing the 'pointer address' of a gridpoint to be looked up using the ordinal position of the gridpoint in the brick. When the pointer address is known, the gridpoint may be interrogated or its properties altered. In this way, with extensive use of 'loop' statements to iterate through the gridpoints in a

brick, relatively simple functions could be written to adjust the positions of gridpoints in the model to create the mesh. Without indexing, the coordinate position of the gridpoint would be needed to 'find' the gridpoint, which would be straightforward for a regular mesh, but once the mesh has begun to be distorted this becomes difficult and tedious. In fact, even for a regular mesh, indexing results in more efficient programming that is much clearer and easier to understand.

First the peripheries of the inlet shaft and frontshunt tunnel were defined, and then the gridpoints inside the bricks could be moved to form an acceptable mesh by interpolating between the periphery gridpoints.

The basic dimensions from the SWOT frontshunt design are listed in Table 5-1.

Table 5-1: Basic dimensions from the SWOT frontshunt design

External radius of the inlet shaft (circular)	6.0 m
External radius of the frontshunt tunnel (circular)	2.4 m
Depth to frontshunt axis	11.8 m
Depth to base of shaft	18.7 m
Length of the frontshunt tunnel	40.0 m
Advance length in the shaft	1.2 m
Advance length in the frontshunt tunnel	1.0 m
Thickness of shaft lining	0.35 m
Thickness of tunnel lining	0.25 m

All the dimensions listed in Table 5-1 were used in the base case model sketched in Figure 5-2 except the length of the frontshunt tunnel (dimension 'd' in Figure 5-2), which was reduced to 20 m in the base case model to reduce calculation time.

The shell elements used to represent the sprayed concrete lining were placed at the extrados. This meant that the pressures at the interface of the ground and lining were in the correct position, but the centreline of the lining was effectively at the extrados. Because of this the lining behaved as though it had a radius half the lining thickness greater than in reality, with an effect on the bending moments and bending stiffness. The bending moments given in this chapter can be corrected using the following equation:

$$\frac{M^*}{M} = \frac{R^2}{R(R-t)} \qquad \textbf{Equation 32}$$

where M^* is the bending moment from the model,

M is the bending moment in the real situation,

R is the radius to the extrados and

t is the thickness of the (circular) sprayed concrete lining.

For the SWOT frontshunt tunnel dimensions, $M^*/M = 1.116$, meaning that the bending moment in the model is overestimated by 11.6 %. Using the same calculation, the bending moment in the shaft lining is overestimated by 6.2 %. In addition, the FLAC^{3D} manual indicates that the shell elements, because of their formulation, may underestimate bending stresses by up to 12 %, but this could only reduce the total error.

Since the purpose of the modelling was to investigate the stresses induced around the junction, it was envisaged that the full length of the frontshunt tunnel of 40 m would not need to be modelled, thus saving a considerable amount of computation time. Therefore, the strategy adopted was to run the base case with the full length of 40 m in order to compare the model results with the surface settlements above the tunnel and with the inclinometer movements. The base case was then run with the shorter tunnel length of 20 m, with the aim of demonstrating that the modelling of a longer tunnel had little effect on the stresses in the sprayed concrete lining around the junction.

The excavation stages in the inlet shaft and the frontshunt tunnel were modelled as a full-face excavation, where the face of the excavation was a plane normal to the longitudinal axis of the shaft or tunnel, as shown in Figure 5-4. In the shaft,

because the mesh was distorted to create the shaft and tunnel shapes, the advances were not quite regular and the face was not always perfectly normal to the longitudinal axis, as can be seen in Figure 5-5, which shows the shell elements representing the shaft and tunnel lining. The shaft advances therefore varied between 1.04 and 1.2 m. The tunnel advances were all 1 m long except the first 2 advances which were 0.5 m long. Figure 5-5 shows that the first 2 advances of the tunnel would have been non-cylindrical, and only the length of the advance along the longitudinal axis of the tunnel would have been exactly 0.5 m. The numbering of the inlet shaft and frontshunt tunnel advances is illustrated schematically in Figure 5-6.

For each excavation stage, one advance would be excavated by removing the zones representing the soil, the previous advance would be lined with shell elements (Figure 5-4), and then the model would be solved to equilibrium.

5.1.2 Ground model

The ground in the model was made up of two strata, one representing the Made Ground and Terrace Gravel and the second representing the London Clay. The Made Ground and Terrace Gravel extended from the surface to a depth of 5 m. The ground below 5 m was London Clay. The water table was set at a constant depth of 4 m. The ground types had the properties listed in Table 5-2.

Table 5-2: Ground properties used in FLAC^{3D} model

	Terrace Gravel	London Clay
Dry density (Mg/m^3)	1.6	1.5
Porosity n	0.35	0.5
Degree of saturation S	0.0 above water table, 1.0 below water table	
Undrained shear strength c_u (kPa)	N/A	$100 + 7.5z$ (*)
Coefficient of earth pressure at rest k_0	0.4	Variable (Figure 5-8)
Friction angle φ' (°)	N/A	0.0
Tangent shear modulus G	Variable	Variable
Tangent drained bulk modulus K'	Variable	Variable
Bulk modulus of the pore fluid K_f (GPa)	2.0 below water table	

*where z is the depth from the top of the London Clay (see Figure 5-7)

The London Clay was assumed to behave in an undrained manner during the timescale of the construction. There are two ways to model undrained behaviour:

1. Pore water can be ignored and the equivalent bulk modulus K_e set to a high value relative to the drained bulk modulus K', such that the Poisson's ratio is close to 0.5. With $K_e = 100K'$, the Poisson's ratio will be greater than 0.495, as recommended by Potts & Zdravković (1999). This is a total stress analysis.
2. Pore water can be modelled setting a fluid bulk modulus K_f (e.g. 2 GPa) and no flow allowed ('set fluid off' command in FLAC^{3D}). This allows the explicit use of effective stress parameters, but there is an increase in runtime of the model.

Option 2 was used for the base case because it allows effective stress parameters to be used, for which the site investigation data for stiffness moduli was better suited, and it also allowed the flow to be switched on to model long-term drained behaviour in the London Clay if required.

For option 2, Potts & Zdravković (1999) recommended setting the fluid bulk modulus K_f to a high value such that the equivalent bulk modulus K_e of the combination of solid soil particles and pore water acting together is between 100 and 1000 times the drained bulk modulus of the soil skeleton K'.

$$K_e = \beta K' \qquad \textbf{Equation 33}$$

where β is a constant between 100 and 1000.

In fact, to simplify matters further they recommend setting K_e equal to K_f, because, in their experience, the exact value is unimportant. If K_f were set to its maximum value, which is the value for pure water at room temperature (2 GPa), then this would mean K' was effectively being assumed to be 20 MPa for β equal to 100 and 2 MPa for β equal to 1000.

Skempton (1954) derived a pore pressure parameter B, given by:

$$B = \frac{\Delta u}{\Delta \sigma} \qquad \textbf{Equation 34}$$

where Δu is a change in pore pressure and

$\Delta \sigma$ is a change in total stress.

The parameter B therefore gives an indication of how close the behaviour of a porous material is to undrained constant volume behaviour. A value of B of unity represents constant volume behaviour with an undrained Poisson's ratio exactly equal to ½. B may also be given by:

$$B = \frac{1}{1 + n\left(\frac{K'}{K_f}\right)} \qquad \textbf{Equation 35}$$

B and the drained Poisson's ratio may be used to calculate the undrained Poisson's ratio using the following equation from Bishop & Hight (1977):

$$\nu_u = \frac{3\nu' + (1-2\nu')B}{3-(1-2\nu')B}$$ **Equation 36**

So if it is assumed that $K_e = K_f$, porosity $n = 0.5$ and drained Poisson's ratio ν' = 0.25, then the values in Table 5-3 are obtained:

Table 5-3: Values of undrained Poisson's ratio using Potts & Zdravković's (1999) method

$\beta = K_f/K'$	B	ν_u
100	0.995	0.498509
1000	0.9995	0.49985

Potts & Zdravković (1999) attempt to set the undrained Poisson's ratio, and hence B, to as high a value as possible without introducing numerical instability, with the aim of approaching constant volume behaviour where all the total stress changes are matched by an equal change in pore pressure.

However, in reality, undrained behaviour is not strictly constant volume and undrained volume change does depend on K' for most soils. Bishop & Hight (1977) found that the undrained Poisson's ratio approaches ½, and Skempton's parameter B approaches unity, *only* in the case where K' is very low (as for example in a normally consolidated soil under low effective stresses) and the soil is fully saturated. Bishop & Hight (1977) reported the undrained Poisson's ratio of several soils to be between 0.470 and 0.487 (Table 5-4).

Table 5-4: Values of undrained Poisson's ratio from laboratory tests (Bishop & Hight, 1977)

Material	Porosity n	Undrained Poisson's ratio v_u
Boise sandstone	0.25	0.27
Sands (marine sediment)	0.44	0.470
Clays (marine sediment)	0.86	0.487
Sand (after cyclic loading)	0.38	0.481

Therefore, it is simpler, and more consistent, to estimate the values of fluid bulk modulus K_f and drained bulk modulus of the soil K' and to use those in a model incorporating pore pressures rather than trying to input values that have no physical meaning.

The fluid bulk modulus of pure water at room temperature is 2 GPa (Itasca, 2002). This may be substantially reduced if there is dissolved air or air bubbles present in the pores. London Clay, however, is usually assumed to be fully saturated with little or no air content. Therefore, the value of 2 GPa has been used in the analyses.

The ground model used for the base case was isotropic nonlinear elastic - perfectly plastic. The tangent shear and bulk moduli vary with strain before failure using the relationship proposed by Jardine *et al.* (1986), adapted to work in 3D and normalised to mean effective stress p' rather than the undrained shear strength c_u. A derivation of the equations used is given in Appendix A.1. The values of the constants were taken from the back analysis of the nearby ART (Airside Road Tunnel) Eastern Portal contiguous piled walls by Scott *et al.* (2003), and these are also given in Appendix A.1.

The failure criterion used was a Tresca envelope, and the values of undrained shear strength c_u were based on a best fit of the site investigation data. This Tresca envelope was implemented in FLAC^{3D} by using the 'Mohr-Coulomb' material model and setting the angle of friction φ' to zero and the cohesion c' to the value of undrained shear strength. The relationship used was:

$$c_u = 100 + 7.5z \qquad \textbf{Equation 37}$$

where c_u is the undrained shear strength in kPa

and z is the depth from the top of the London Clay in m.

The site investigation data from unconsolidated undrained triaxial compression tests on 100 mm diameter samples is shown in Figure 5-7, along with the undrained shear strength profile used in the base case, the recommended design profile (GDBR, 2001) and a lower bound profile that will be used later. The site investigation data has a large scatter, and this is a good reason for using sensitivity analyses in design.

The *in situ* stress state used in the base case was based on the formula developed by Mayne & Kulhawy (1982). The site investigation data and the base case profile are shown in Figure 5-8. Again, the site investigation data has a large scatter. There seems to be a correlation between the value of K_0 and the sampling method used. For instance, the additional softening caused by the flush when rotary coring probably resulted in lower values of suction and hence lower values of horizontal stress. The disturbance from U100 sampling may have caused dilation, resulting in elevated values of suction compared to the thin-walled piston sampling. The influence of *in situ* stress on the lining stresses during junction formation will be investigated later by applying different profiles, including the recommended design profile from the T5 Geotechnical Design Basis Report (GDBR, 2001), which is also shown in Figure 5-8.

5.1.3 Sprayed concrete model

For the base case, isotropic linear elastic shell elements with a Young's modulus of 15 GPa and a Poisson's ratio of 0.25 were used to model the sprayed concrete lining. The shell 'thickness'[14] was 0.35 m in the shaft and 0.25 m in the tunnel lining.

5.1.4 Post-processing and results

The curvilinear shell elements representing the sprayed concrete lining produce results in the form of bending moments and axial forces in 2 directions, denoted

[14] Shells are 2D elements and hence have no thickness. However thickness is input as a parameter to enable calculation of the stiffness matrix.

by local axes X', Y' and Z'. X' is defined as the projection of the global X-axis onto the plane of the shell at the centroid[15], so in the shaft it represents the tangential direction and in the tunnel it represents the longitudinal direction. Z' is the direction normal to the shell at the centroid in the direction away from the zone to which it is attached, so it represents the radial direction towards the tunnel axis in both the shaft and the tunnel. Y' is defined such that X', Y' and Z' make up a right-hand set, so in the shaft it represents the vertical direction (the same as global Z) and in the tunnel it represents the tangential direction.

Since the design of sprayed concrete linings is primarily concerned with stresses, extreme fibre stresses at the intrados and extrados will be presented. These may be calculated from the bending moment and axial force since the shells are linear elastic. The notation of the bending moments follows the convention for shell, plate and beam elements adopted in most numerical analysis programs, although this is not the British or indeed European structural engineering convention. Thus, M_x is not the moment about the X'-axis, but the moment along it (in other words the moment about the Y'-axis). Similarly, M_y is the moment about the X'-axis. This means that when calculating the stresses, M_x and N_x are paired together and M_y and N_y are paired together (see Figure 5-9).

There are 6 'stress resultants' calculated by FLAC^{3D} of which only 4 have so far been mentioned. The other 2 are M_{xy} and N_{xy}, which result from the introduction of a 'drilling' degree of freedom (Figure 5-10). The 'drilling' degree of freedom allows the shell to represent in-plane bending while only using corner nodes (i.e. without using mid-side nodes), and prevents the absorption of strain energy through parasitic shear (e.g. Cook *et al.*, 2002). When calculating maximum stresses, the absolute value of M_{xy} must therefore be added to the M_x and M_y bending moments and when calculating minimum stresses, it must be subtracted from the M_x and M_y bending moments. An analogous calculation must be performed to take account of the N_{xy} force. In simple tunnel models, M_{xy} and N_{xy} may be negligible but around a junction they may reach significant levels. For example, Figure 5-11 shows high M_{xy} values reaching approximately ± 40 kNm

[15] This is the default setting, which may be changed by setting the 'SURFX' vector. The SURFX vector is projected onto the shell to define the local X' axis and its default setting is (1, 0, 0).

over large areas around the junction. This would affect the maximum and minimum stresses by + 2 MPa and – 2 MPa respectively.

The results may be more clearly presented by plotting graphs of stresses along a section. For example, the stresses in the shaft lining at tunnel axis level plotted against the distance around the perimeter of the shaft, or the stresses in the shaft lining on a vertical line above and below the tunnel opening plotted against depth, as shown on the location plan on Figure 5-12.

When recovering the 'stress resultants' from FLAC^{3D}, nodal averaging is used. Therefore, the stresses in the shaft and the tunnel shell elements must be recovered separately, or else the local coordinate axes at the nodes where the shaft and tunnel join will be at an average orientation and not in the plane of either the shaft or the tunnel. This was not an issue at the base of the shaft, since there was a pin joint connection there. This meant that there were 2 nodes in the same location where the shells connected – one for the shaft wall and one for the shaft base slab.

The extreme fibre hoop stress at the intrados and extrados around the perimeter of the shaft lining at tunnel axis level is shown in Figure 5-13 for 'adv17' (shaft completed – see Figure 5-6 for numbering) and 'advfs_1' and 'advfs_2' (the first 2 tunnel advances). Tension is positive. The average compressive hoop force at the tunnel axis level at the time of shaft completion ('adv17') was 1566 kN, which corresponds to 91 % of the *in situ* horizontal stress at this depth. This seems rather high, since with a sequential excavation one would expect more of the stress to be shared by the ground. The excavation of the first tunnel advance ('advfs_1') had the greatest effect on the stresses, with subsequent advances having a much smaller effect. However, the behaviour was not as expected, since the hoop stress changed to a high tensile stress only in the shell adjacent to the edge of the opening, and there was an increase in compressive stress further away. Mesh refinement in this area only served to accentuate this effect, with the tensile stress increasing and moving closer to the opening, and only affecting the closest shell.

The vertical stress at the intrados and extrados of the shaft lining at tunnel axis level is shown in Figure 5-14. The same phenomenon of a large stress change on

creating the opening ('advfs_1') only in the closest shell to the opening was evident. At shaft completion ('adv17'), the vertical stress was not constant, with a high tensile stress at the centreline of the tunnel, and a high compressive stress 2-3 m around the shaft, in the region of the edge of the future opening.

In addition, Figure 5-15 shows the distribution of stress along a vertical line in the shaft wall above and below the tunnel centreline. These large tensile stresses in the shaft lining cannot be explained by a real physical phenomenon. These stresses may have been an artefact of the modelling process, caused by the irregular shape of the advances in the shaft. These stresses that were locked into the shaft during the sequential excavation process would have affected the pattern of stress change when the tunnel opening was made.

The distorted mesh shown in Figure 5-5 that was necessary to form the correct junction shape without introducing illegal zone geometries may therefore have been causing problems. A new methodology was therefore required.

A relaxation method, where the entire shaft was excavated in a single stage and an internal pressure was applied to the interior prior to installation of the sprayed concrete lining shell elements, was used. This was performed in the following manner (after the initial conditions had been set):

1. The zones representing the soil within the shaft were removed (i.e. the shaft was excavated).
2. Displacement fixity was applied to all the gridpoints at the interior faces of the shaft.
3. A single calculation step was performed so that the unbalanced forces at the gridpoints would be calculated.
4. A force was applied to each gridpoint equal to the unbalanced force multiplied by a relaxation factor, in the opposite direction to the unbalanced force.
5. The model was then run to equilibrium.
6. The forces were removed and the shell elements representing the sprayed concrete lining were installed.
7. The model was again run to equilibrium.

8. Then the tunnel was advanced as before.

This had to be calibrated to a sequential excavation so that the correct relaxation factor was used. Since the mesh deformed to create the junction shape could not be used, the same generic mesh (Figure 5-1) with the same mesh density was used and deformed only to the shape of the shaft. This meant that the shaft advances were now perfectly parallel. The unexpected stresses calculated by the previous modelling method were no longer present, indicating that they were not realistic and were, after all, an artefact of the shape of the mesh.

Relaxation factors of 0.4, 0.6 and 0.8 were used to create a relationship between relaxation factor and hoop force at the tunnel axis level, shown in Figure 5-16. Figure 5-16 shows that the hoop force from the sequential excavation of the undistorted mesh could be simulated by a relaxation factor of 0.65. Since the relaxation method was to be applied to the distorted mesh so that the junction formation could be modelled, this is also shown on Figure 5-16, and the correct result was obtained. This provided a further check on the distorted mesh.

From this point on, all the runs presented will use the relaxation method in the shaft. When the ground model is changed, a new calibration will be performed and the relaxation factor recalculated. All references to the 'base case' will now mean the base case using the relaxation method in the shaft.

At this stage, an attempt was made to relax the equilibrium criterion and hence to reduce the calculation time required for each excavation stage. The FLAC^{3D} manual recommends using a 'mech. ratio' of 10^{-5}, and this is the default value in the program. The 'mech. ratio' is the ratio of the maximum unbalanced force of all the gridpoints in the model to the average applied gridpoint force. Alternatively, Thomas (2003) set a limit on the maximum unbalanced force at any gridpoint to 3 kN. Therefore the base case was also run with a 'mech. ratio' of 10^{-4} and a maximum unbalanced force of 3 kN. It was found that the differences between the two methods and the default criterion were similar, with a maximum difference of 0.2 MPa, or 8 % of the maximum stress. This was considered too large, since the maximum difference and the maximum stress did not coincide. As a percentage of the average stress, the maximum difference was

30 %. Therefore, the default 'mech. ratio' value of 10^{-5} was used. This resulted in a maximum unbalanced force at equilibrium of 0.6 kN.

The excavation of each advance of the tunnel should have an effect on the stresses in the shaft lining, but this effect should decrease and eventually become negligible as the tunnel face moves further away. This diminuation of influence with distance allows finite boundary distances to be used in geotechnical models. However, the effect of the tunnel on the shaft continued to cause changes in the stress distribution in the shaft lining that showed little inclination to decrease with distance. For instance, the hoop stress in the shaft lining at tunnel axis level is shown in Figure 5-17 and the vertical stress in the shaft above and below the tunnel centreline is shown in Figure 5-18. This continuing distortion of the shaft lining appeared to be caused by tensile stresses in the tunnel lining pulling the shaft at the connection between the shaft and tunnel. As the tunnel advanced, the ground moved towards the face of the tunnel from all directions. Thus around the tunnel lining, the movement of the ground was forwards towards the face and dragged the tunnel lining forward. Since more movement occurred close to the face, tensile longitudinal stresses were generated. This effect, peculiar to 3D modelling of advancing tunnels, was noted by Thomas (2003). It is not known whether this phenomenon occurs in reality, and would be dependent on the quality of the bond between the sprayed concrete and the ground, as well as other factors such as creep and shrinkage of the sprayed concrete, quality of the joints and the type and continuity of reinforcement. Therefore, it was considered unlikely that these tensile stresses really do occur.

In the case of the SWOT junction modelled, a circumferential crack-inducer was placed approximately 1 m into the tunnel to allow for differential settlements, and this would have precluded the transfer of tensile stresses in the tunnel to the shaft lining.

First of all, a pinned connection was used between the tunnel and shaft lining shell elements, instead of the fully fixed connection that was used previously. The hoop stress in the shaft lining at tunnel axis level is shown in Figure 5-19 and the vertical stress in the shaft lining above and below the tunnel centreline is shown in Figure 5-20. The pattern of stresses was different to the fully fixed connection shown in Figure 5-17 and Figure 5-18, and shows much smaller

bending moments. However, the stresses continued to increase and diverge, indicating that the bending moments in the shaft lining were continuing to increase even when the tunnel had advanced a considerable distance away. This meant that the tensile stress in the tunnel was still pulling on the shaft lining and distorting it. In effect, the tunnel was acting like a stiff dowel, transmitting forces from one location (the face of the tunnel) to another (the shaft).

In order to eliminate the influence of the tensile stresses in the tunnel on the shaft stresses, the connection between the shaft and tunnel shells was removed. The shaft would now only be affected by the ground movements caused by the tunnel construction, and not by any stress transfer from the tunnel lining shell elements to the shaft lining shell elements. The hoop stress in the shaft lining at tunnel axis level is shown in Figure 5-21, which should be compared to the fixed connection in Figure 5-17, and also with the pinned connection in Figure 5-19. The vertical stress in the shaft lining above and below the tunnel centreline is shown in Figure 5-22, which should be compared to the fixed connection in Figure 5-18 and the pinned connection in Figure 5-20. Even with a pinned connection, the change in stress in the shaft lining was mainly due to a gradual increase in bending stress. Although removing the connection where the shaft and tunnel lining shells joined reduced the magnitude of the stresses induced in the shaft by a factor of about ½, the bending stress continued to increase as the tunnel length increased, even between advfs_15 and advfs_21 (tunnel face 14 m and 20 m from the shaft wall respectively). It appeared that, after all, the continuing change in stress in the shaft lining as the tunnel length increased was due to the reduction in ground pressure acting on the tunnel side of the shaft, although it was exacerbated by the tensile pull of the tunnel lining. This reduction in ground pressure was caused by ground movements away from the shaft towards the face of the tunnel. This was magnified by the tunnel acting as a stiff dowel transferring shear stresses in the ground from the near the face of the tunnel to the ground adjacent to the shaft.

The hoop stresses in the 5th ring from the face of the tunnel at different locations along its length are shown in Figure 5-23 and Figure 5-24. From Ring 3 onwards, the stresses were virtually constant, indicating that the presence of the shaft no longer had an influence on the tunnel hoop stresses beyond this point. However,

as has been shown, this is no indication that the tunnel excavation will not continue to influence the stresses in the shaft beyond this point.

The ground movements during tunnel construction may have been overestimated because one would expect the delay between shaft and tunnel construction and the change in strain direction to restore the tangent stiffness of the London Clay to its initial small strain value. Therefore, a run was performed that zeroed displacements and initialised the function calculating the tangent stiffness after shaft construction. Only the magnitudes of the stresses in the shaft lining were affected, with a reduction of the order of 20 to 25 %. The increase in stress in the shaft lining with tunnel length still had not stabilised at advfs_21 (tunnel face 20 m from the shaft).

5.1.5 Boundary conditions

The boundary distances were limited by the maximum size of the model that could be held in the RAM of the computer, and the computation time which would be acceptable given the number of runs required. Another limitation was the size of the 'save file'. A 'save file' is the name FLAC^{3D} gives to the file that stores the state of the model. Therefore, the state of the model can be saved after various excavation stages and those states restored later to extract results. The maximum possible save file size was about 450 MB, since the RAM memory required by FLAC^{3D} was approximately double this figure and some memory was required for background operating system processes. Using a computer with 1.00 GB RAM and a CPU speed of 2.09 GHz the base case model with a 20 m long frontshunt tunnel was run in about 2.5 days and each save file was approximately 130 MB. If the number of zones in the model were doubled then the save file and the runtime would also be roughly doubled. If the RAM capacity were exceeded then virtual memory would need to be used (i.e. writing and reading from the hard disk), which would increase the runtime considerably.

Typically, the number of zones used in a tunnel analysis can be reduced by using a radial mesh and increasing the size of the zones with distance from the tunnel (e.g. Thomas, 2003). However, for a tunnel junction model a radial mesh will not work, and there is limited scope for increasing the zone sizes with distance from the tunnel. Therefore, the model size in terms of the number of zones tends to be

larger than for a single tunnel with the same model dimensions. In some instances of intersecting tunnels it may appear possible to use the existence of more than one plane of symmetry to reduce the size of the model, but if it is desirable to model sequential excavation, then it is generally only possible to use one plane of symmetry if at all. In the case of the SWOT frontshunt model, it was possible to benefit from the existence of one plane of symmetry, which may be uniquely defined by the axes of the shaft and tunnel, coincident with the X and Z axes in Figure 5-2.

For tunnelling problems, boundary positions for fixed boundaries are often set at locations where surface settlements are expected to be small (e.g. Franzius *et al.*, 2005). However, the main objective when designing tunnel junctions is to predict stresses in the lining, and it has been assumed in this study that the boundary positions have less impact on the lining stresses than they do on far-field surface settlements. Therefore, boundary distances smaller than those recommended in the past by Thomas (2003) and van der Berg (1999) have been used. Runs have also been performed with larger and smaller boundary distances than the base case to demonstrate the importance of this assumption to the lining stresses.

The distance to the boundary from the side of the inlet shaft (distance '(k)' in Figure 5-2) was increased from the original distance of 20 m in the base case to 40 m, and decreased in a subsequent run to 10 m. In a further run, the tunnel length (distance '(d)' in Figure 5-2) was increased from 20 m in the base case to 40 m. The mesh density was not changed.

Increasing the boundary distance to the side (k) did not have a significant effect on the stresses, as shown in Figure 5-25 and Figure 5-26. The largest stress difference of 0.38 MPa was very localised, and occurred at the location of the maximum hoop stress, which was 20.6 MPa. Expressed as a percentage of the average hoop stress prior to breakout of the opening (2.97 MPa), the maximum stress difference was 12.8 %. However, expressed as a percentage of the stress at this location, the maximum stress difference was less than 5 %.

Halving the boundary distance to the side (k) resulted in a maximum stress difference of 25 % of the average hoop stress in the shaft prior to breakout.

Increasing the boundary distance in the direction of the tunnel (d) had much less of an effect, with a maximum stress difference of 0.5 % of the average hoop stress.

5.1.6 Mesh refinement

The fineness of the mesh affects the accuracy and the detail of the results. A finer mesh can deal with high stress gradients better than a coarser one. At the same time, a finer mesh will also provide more detailed results. Therefore it was necessary to test the mesh to ensure that it was fine enough to predict stresses with sufficient precision. This was done by basing the original mesh on the advice of experienced numerical modellers at Mott MacDonald, within the limits of a manageable file size, and then making the mesh finer and coarser and comparing the results.

It was not possible to refine the mesh in all directions at once due to memory and runtime constraints, so 2 meshes refined in different areas were produced. A mesh was created with double the number of zones along the length, width and height of the frontshunt tunnel (dimensions (c), (d), (j) and (g) in Figure 5-2) compared to the base case (denoted 'fine mesh' in the figures). Then a mesh was created with double the number of zones around the side of the shaft in the X direction (dimension (b) in Figure 5-2) compared to the base case ('fine mesh2'). Finally a mesh that was coarser than the base case was created, with roughly half the number of zones in most directions ('coarse mesh'). This resulted in a save file size roughly one-sixth of the size of the base case save file, which shows how important mesh refinement is to the feasibility of 3D numerical modelling.

Figure 5-27 shows the effect of changing the mesh density on the hoop stresses in the shaft lining above and below the tunnel centreline. The data was taken from stage 'advfs_1', which was when the opening for the junction was created in the side of the shaft. With the exception of the 'coarse mesh' model, approximately the same pattern and magnitude of stresses was calculated by each of the finer meshes and the base case. It should be noted that only the coarse mesh had a different number of zones in the vertical direction.

The effect of mesh density on the hoop stress around the perimeter of the shaft lining at tunnel axis level, shown in Figure 5-28, was similar to the effect on the

hoop stress above and below the tunnel centreline. Again, the 'coarse mesh' model failed to match the pattern of behaviour of the finer meshes and the base case. It could be argued that the fact that the coarse mesh stresses didn't match the pattern of stresses of the finer meshes exactly, but was a fair approximation of them without introducing a new mechanism, should increase confidence in the robustness of the model. Although the finer meshes were almost colinear, the last data point before the opening showed a small variation in the case of 'fine mesh2'. 'Fine mesh2' had double the number of zones around the side of the shaft compared to the base case and 'fine mesh', and so it was better able to calculate the high stress gradients immediately adjacent to the opening. However, the difference was not great, with a maximum difference of 0.6 MPa when the stress gradient was approximately 5 MPa/m. Furthermore, it should be noted that at this point of maximum difference the stress is decreasing towards zero and is therefore not relevant in terms of design.

The effect of mesh density on the vertical stress around the perimeter of the shaft lining at tunnel axis level is shown in Figure 5-29. The differences between the base case and the finer meshes were negligible, but again with the exception of the last point at the edge of the opening for model 'fine mesh2'. However, the difference was small at less than 5 % of the stress at this location.

The base case mesh was therefore considered to give sufficiently accurate results when compared to meshes with a higher density. However, due to the relative nature of this kind of test, it was not considered an absolute guarantee that the model was producing reasonable results. In the next section, the mesh density required to accurately predict membrane stresses around an opening will be tested further by comparison with an analytical solution.

5.1.7 Comparison with the Kirsch analytical solution

In this section, a FLAC^{3D} model was set up to replicate the conditions of the Kirsch analytical solution (Hoek & Brown, 1980), described in Section 2.4.2. The aims of this section of work were threefold:

1. To show that the FLAC^{3D} shell elements were capable of accurately predicting membrane stresses in an area of high membrane stress gradients.

2. To verify the mesh refinement required to predict the high membrane stress gradients induced local to a hole in a plate.
3. To compare the base case results with the analytical solution.

Since the mesh in the T5 SWOT inlet shaft and frontshunt tunnel junction base case could only be refined so much before the model became too large, this gave an opportunity to verify that the mesh was reasonable, at least in terms of the calculation of membrane stresses.

The base case mesh density around the perimeter of the shaft lining was approximately 1.4 zones/m. Therefore a model was built in FLAC^{3D} of a plane stress plate with a hole in it, with mesh densities of 1.5, 2, 4 and 8 zones/m. The radius of the hole was 2.4 m, the same as the SWOT frontshunt tunnel. The boundary was set at 20 m from the edge of the hole. The agreement between the analytical solution and the models was very good, with the largest differences occurring within half a radius distance from the hole. The finer the mesh, the closer was the agreement with the analytical solution.

'Stress concentration factor', which is the ratio of the stress considered to the applied stress at the boundary of the model, is plotted in Figure 5-30 for the membrane force in the X-direction along a line parallel to the direction of applied stress (as indicated in the location key overlaid on Figure 5-30) up to a 1 radius distance (2.4 m) from the edge of the hole. Also plotted on the same figure is the stress concentration factor calculated using the Kirsch analytical solution. The stress concentration factor decreases to zero as it approaches the edge of the hole. The FLAC^{3D} models replicated this behaviour with varying degrees of accuracy, dependent on the fineness of the mesh. The stress at the edge of the hole was predicted by the model with a mesh density of 1.5 zones/m with less than 5 % error.

Figure 5-31 shows the stress concentration factor for the Y-component of the membrane force along a line parallel to the direction of applied stress. The Kirsch solution shows that the stress concentration factor should decrease from 0 to -1 as the edge of the hole is approached. Again the FLAC^{3D} models replicated this behaviour with varying degrees of accuracy, generally dependent on the

fineness of the mesh. The mesh density of 1.5 zones/m was actually the most accurate adjacent to the hole.

Figure 5-32 shows the stress concentration factor for the X-component of the membrane force along a line transverse to the direction of applied stress. The Kirsch solution shows that the maximum stress concentration factor of 3.0 occurs on this section, adjacent to the hole, and decreases with distance from the hole, eventually dropping towards 1.0. The FLAC^{3D} models replicated this behaviour with varying degrees of accuracy, generally dependent on the fineness of the mesh. The mesh density of 1.5 zones/m was actually the most accurate adjacent to the hole with an error of less than 0.5 %.

In conclusion, the mesh density of 1.5 zones/m, similar to the mesh density used in the SWOT junction model, predicted the maximum and minimum membrane stresses to within 5 % of the analytical solution. The generally good agreement between the FLAC^{3D} models and the Kirsch solution showed that the FLAC^{3D} shell elements could be used to predict membrane stresses in shell structures with high membrane stress gradients with reasonable accuracy.

If the results from the base case were plotted in the form of a stress concentration factor, the effect of modelling the ground-structure interaction and the curvature of the lining could be identified. The axial and bending stresses after creation of the opening were therefore normalised to the hoop axial stress at the end of shaft construction for the base case.

The hoop stresses in the shaft lining above and below the tunnel centreline are shown in Figure 5-33. The pattern of axial stress was similar to the Kirsch solution. However, the maximum axial stress adjacent to the opening was larger, with a stress concentration factor of 4.71 above the opening and 4.91 below the opening. But, as described in the literature review, Lew (1976) and Thareja *et al.* (1989) appeared to demonstrate that modelling ground-structure interaction should be beneficial at a junction and reduce stress concentrations to below the value predicted by simpler methods. However, this result was unique to the wished-in-place approach with the ground modelled by Winkler springs they adopted. In reality, the creation of the opening could cause the ground to arch

around the opening, exerting more load on the parent tunnel lining and thus producing higher stress concentrations than the Kirsch solution would predict.

To test the hypothesis that the high stress concentrations in the FLAC^{3D} model were caused by an increase in the total load applied to the shaft lining over and above a redistribution from the area of the opening to areas around it, the axial hoop forces in the shaft lining were integrated along the vertical boundary before and after the opening was created. The total load before breaking out the opening was -14041 kN, and after the opening had been made the total load was -17334 kN. This increase in ground load over the whole surface of the shaft lining by a factor of 1.2 was localised, and so the stress concentrations close to the opening could be expected to be more than the product of 1.2 and 3.0. This demonstrated the importance of using a 3D numerical model with the ground and excavation sequence modelled explicitly.

Figure 5-33 also shows the stress concentration factors for the bending stresses in the shaft lining. These were normalised to the hoop axial stress at the end of shaft construction and before the opening was created. The maximum stress concentration factors due to bending stress were 2.29 above the opening and 2.03 below it. The bending stress was calculated at the extreme fibre, so these stress concentration factors may be simply added or subtracted to the axial stress concentration factors to find the maximum and minimum stress concentrations. Therefore the maximum stress concentrations were 7.00 above the opening and 6.94 below it. These values are considerably higher than would be predicted using the Kirsch analytical solution or by the wished-in-place Winkler spring method of Lew (1976), which should not be used for the design of the construction of sprayed concrete tunnel junctions.

Figure 5-34 shows the hoop bending stress and hoop axial stress concentration factors around the perimeter of the shaft lining at tunnel axis level. Also shown on Figure 5-34 is the Kirsch solution, which shows the stress concentration factor at 1.0 in the far field and decreasing to zero adjacent to the opening, via a short curve into the negative domain 0.5 m from the opening. The axial stress concentration factor from the base case was similarly at 1.0 but then went past zero to -0.37 adjacent to the opening without the change in curvature. This was due to the number of shell elements being unable to cope with the detailed shape

of the stress variation. In order to model this accurately many more shell elements would be required, perhaps more than 8 zones/m, as shown in Figure 5-30 for the plane stress plate model. It was decided that accuracy could be sacrificed for simplicity in this case, because these stresses were not considered critical for design.

Another difference between the base case model and the Kirsch solution in Figure 5-34 was the zone of influence of the hole. The base case reached the far field value of 1.0 within 3.6 m of the hole, whereas the Kirsch solution approached 1.0 in a far more gradual manner. This may be caused by the curvature of the shaft lining and the different way in which it was loaded, which would serve to concentrate the effect of the opening more locally.

Finally, the vertical axial stress and the vertical bending stress concentration factors around the perimeter of the shaft lining at tunnel axis level are shown in Figure 5-35. The Kirsch solution shows the stress concentration factor at zero in the far field and increasing to -1.0 (tension) adjacent to the opening. In this case the behaviour of the shaft lining in the base case model was substantially different to the Kirsch solution. The stress concentration in the far field began at zero, but initially increased gradually around the shaft to a value of 0.33 at a distance of 2.15 m from the opening before decreasing quickly to a value of -1.70 adjacent to the opening. The Kirsch solution was replicated well by a similar mesh density (Figure 5-31) in the plane stress plate model, therefore the difference here must be due to the geometry of the shaft.

The effect of the shaft's cylindrical geometry can be seen in Figure 5-36. At tunnel axis level, the ring tried to close into the opening, causing an 'inverse squat' effect. This caused the shaft lining above and below the opening to get pushed outwards. These effects were localised close to the opening, and were the reason the stress concentrations were more localised for the 3D model compared to the prediction from the plane stress plate solution.

In conclusion, the base case model performed well, and differences between the results and the Kirsch solution could be assigned to differences of geometry and the presence of the ground in the numerical model. The Kirsch solution does not take into account the effect of the 3D geometry of the tunnels or the ground-

structure interaction, which may change the magnitude of the axial stresses and change their distribution. Nor can it predict the bending stresses associated with the 3D geometry of real tunnel junction problems. The combined effect of these phenomena resulted in a maximum stress concentration factor of 7.0, as compared to the maximum predicted by the Kirsch solution of 3.0.

In addition, the wished-in-place method of 3D numerical analysis with the ground modelled as Winkler springs should be restricted to specific applications only, for instance the application of a load to a secondary lining post-construction. It does not model the ground-structure interaction correctly and it does not model the sequence of construction, both of which were found to be important factors in the base case model.

5.1.8 Comparison with site data

There was a considerable amount of monitoring data available from the T5 SWOT frontshunt site. Therefore the ground displacements from the base case model were compared with field monitoring of surface settlements and inclinometer readings, the tunnel lining displacements were compared with the in-tunnel convergence monitoring and the radial stresses on the frontshunt tunnel were compared with the radial pressure cell readings.

The FLAC^{3D} model chosen for comparison was the base case with the full 40 m long frontshunt tunnel. The comparisons with the surface settlements due to shaft construction were made with the sequential shaft excavation. The comparisons with the frontshunt tunnel surface settlements were made with the base case model without any joints in the tunnel lining (i.e. with the high longitudinal stresses).

The surface settlements in front of and behind the shaft along the centreline of the frontshunt are shown in Figure 5-37 just before the start of SCL shaft construction, along with the settlements predicted by the base case model (with sequential excavation in the shaft, not the relaxation method). The first 7 m depth of the shaft were constructed using the caisson-sinking method with a segmental lining. However, in the model, these advances were modelled in the same way as the SCL advances. The surface settlements at the same locations at the end of shaft construction just before breakout of the frontshunt tunnel are shown in

Figure 5-38. There appeared to be a reasonably good agreement between the patterns of measured and predicted settlements, giving confidence that the shaft construction in the model was following a similar mode of behaviour. Unfortunately the first readings of the inclinometer adjacent to the shaft were not made until the shaft construction was already completed.

After shaft construction, the frontshunt tunnel construction could be compared at almost every advance with the surface settlement data, since the surface monitoring points were levelled twice a day, and the rate of advance of the frontshunt tunnel was less than 2 rings per day for the most part. A model with the frontshunt tunnel at its full length of 40 m was used for this purpose. This model took much longer to run, because there were more zones and also because there were 20 more tunnel advances than the base case model.

A comparison of the FLAC^{3D} and the indicative site surface settlements (c.f. Figure 3-13) are shown in Figure 5-39 for when the face was under the surface array. The indicative surface settlements observed when the face was under the array were approximately 45 % of the final value shown by the indicative Gaussian curve on Figure 3-13. FLAC^{3D} predicted these surface settlements reasonably well, with a maximum disparity of about 1 mm. However, the maximum FLAC^{3D} surface settlement occurred when the face was under the array, as indicated by the longitudinal settlement profile.

The longitudinal surface settlement above the tunnel centreline calculated by FLAC^{3D} is shown in Figure 5-40, along with the indicative longitudinal settlement profile observed in the field (c.f. Figure 3-12). The FLAC^{3D} model appears to show heave of the ground surface behind the face of the tunnel. This was probably related to the longitudinal stresses in the tunnel and its movement towards the face. Because of this, and the distortions to the shaft caused by the longitudinal stresses in the tunnel, only the creation of the opening will be considered in the rest of this chapter.

5.2 Impact of the ground model

The influence of various aspects of the constitutive model for the ground was tested by a sensitivity analysis. These aspects were:

- Ground stiffness – magnitude, nonlinearity and anisotropy.
- Plasticity.
- Initial *in situ* stress distribution.

The model runs were compared with each other using the following indicators:

- Stress concentration factors for hoop axial stress and hoop bending stress in the shaft lining along a vertical line above and below the tunnel centreline.
- Stress concentration factors for hoop axial stress and hoop bending stress in the shaft lining along a line of points around the perimeter of the shaft at tunnel axis level.
- Stress concentration factors for vertical axial stress and vertical bending stress in the shaft lining along a line of points around the perimeter of the shaft at tunnel axis level.

Different aspects of ground behaviour were investigated. These were:

- The magnitude of a constant (linear stress-strain) value of stiffness.
- Anisotropy.
- Small-strain stiffness behaviour (nonlinear stress-strain relationship).
- Failure criterion (in particular the value of undrained shear strength c_u)
- *In situ* stress distribution.

5.2.1 Stiffness and nonlinearity

First of all, the base case, which had a nonlinear stiffness, was compared with two linear stiffness models. The linear stiffness was set at a value corresponding to the secant stiffness at 0.1 % strain and 1 % strain. This resulted in a Young's modulus of 80 MPa for 0.1 % strain and 44 MPa for 1 % strain.

The different values of ground stiffness meant that the hoop stresses in the shaft lining after shaft construction were different in each case. Therefore the relaxation factor had to be calibrated for each model, and the values are listed in Table 5-5, along with the value of hoop stress at the tunnel axis level after shaft construction.

Table 5-5: Relaxation factors used in the analyses investigating the effect of ground stiffness, along with the corresponding hoop axial stress (compression is negative) at tunnel axis level at the end of shaft construction.

Model	Relaxation factor	Hoop stress at axis level
Base case (nonlinear stiffness)	65 %	-2.97 MPa
Linear stiffness E = 80 MPa	69 %	-3.07 MPa
Linear stiffness E = 44 MPa	73 %	-3.32 MPa

Table 5-5 shows that the ground in the base case model took a larger share of the load, which was reflected in both a lower relaxation factor and a lower hoop stress at the tunnel axis level. This indicated that the base case ground model provided a stiffer overall response to shaft construction than the two linear stiffness models.

In order to compare the effect of creating the opening on the different ground stiffness models, a stress concentration factor was introduced. This normalised the stresses to the hoop axial stress at the end of shaft construction and before the creation of the opening[16].

Figure 5-41 shows how the hoop stress concentration factor varies with distance from the opening above and below the tunnel centreline. The various stiffness models calculated maximum stress concentration factors for hoop axial stress between 3.38 and 3.96, with the 80 MPa linear stiffness model having the lowest value and the nonlinear stiffness base case having the highest. This indicated that the nonlinear model was now displaying the least stiff response. This may be because the effect of the opening was more local, hence the relatively high local strains resulted in a low tangent stiffness for the nonlinear model, as shown in Figure 5-42. The variation in maximum bending stress was much greater, at between 0.84 and 2.18, with the base case again having the highest stress concentration. Therefore it appeared that the bending stress concentration factor was much more sensitive to the ground stiffness than the axial stress concentration factor.

[16] This is the same as the stress concentration factor defined previously in Section 5.1.7.

Figure 5-43 shows the variation of stress concentration factor for the vertical stress with distance around the perimeter of the shaft at tunnel axis level. The effect was the same, with the base case having the highest stress concentration factors, and the 80 MPa linear stiffness model having the lowest. The maximum stress concentration factors for vertical bending stress were even larger than for the vertical axial stress, indicating once again the critical importance of calculating bending stresses.

In conclusion, soil stiffness can have a significant effect on the stress concentrations in the sprayed concrete lining of a tunnel junction. Within reasonable limits, soil stiffness has relatively little impact on the axial stress concentration factor, but a significant impact on the bending stress concentration factor.

The differences between the 2 linear stiffness models and the nonlinear stiffness model may have been subdued by the influence of plasticity close to the excavation, since all 3 models had the same failure criterion. Therefore, the linear model with 80 MPa stiffness and the nonlinear base case were run again, this time without a failure criterion.

A calibration exercise was performed and the relaxation factors used are listed in Table 5-6. Also included is the anisotropic model, which will be described in the next section. Removing the failure criterion decreased the relaxation factor, that is, it increased the amount of load being taken by the ground rather than the shaft lining, although for the linear stiffness runs, this difference was very small.

Table 5-6: Relaxation factors used in the analyses investigating the effect of ground stiffness without a failure criterion, along with the corresponding hoop axial stress (compression is negative) at tunnel axis level at the end of shaft construction

Model	Relaxation factor	Hoop stress at axis level
Base case (with failure criterion)	65 %	-2.97 MPa
Base case no failure criterion	61%	-2.80 MPa
Linear stiffness E = 80 MPa with failure criterion	69 %	-3.07 MPa
Linear stiffness E = 80 MPa no failure criterion	69 %	-3.07 MPa
Anisotropic stiffness no failure criterion	59 %	-2.49 MPa

The hoop stress concentration factor above and below the tunnel centreline is shown in Figure 5-44. The difference between the base case and the same model without a failure criterion was very small. Therefore the prior conclusions regarding the effect of stiffness were considered to hold true.

5.2.2 Stiffness anisotropy

Anisotropy of stiffness, with a higher stiffness in the horizontal plane than in the vertical direction was investigated. An anisotropic soil stiffness model with no failure criterion was compared to an isotropic soil stiffness model (as used in the base case) with no failure criterion. In both cases the stiffness was calculated using the nonlinear Jardine model. For the anisotropic model, the horizontal stiffness was set to 1.6 times the vertical stiffness.

As expected, the stiffer ground in the horizontal direction in the anisotropic model decreased the stresses in the shaft lining before the creation of the opening compared to the isotropic model (c.f. Table 5-6).

However, did the anisotropic model also decrease the stress concentration factor once the opening had been created? Figure 5-45 shows that for the hoop axial stress concentration factor, the difference was very small, but for the hoop

bending stress concentration factor, the difference was more significant. This confirmed the prior finding that stiffer ground will reduce bending stress concentrations. No signs of a different behaviour pattern were evident for the anisotropic case, only the effect of the higher stiffness was noticeable.

5.2.3 Plasticity

Plasticity was implemented using FLAC^{3D}'s 'Mohr-Coulomb' model. A lower-bound and a best-fit relationship between undrained shear strength and depth were fitted to the site investigation data. In addition, an estimate was made of the lowest value of undrained shear strength before failure would occur and this value was also used. In all cases, the friction angle and dilation angle were set to zero, so it was essentially a Tresca model with associative plasticity. The results from these three plasticity models were then compared to a model without a failure criterion. Since the base case included nonlinear stress-strain behaviour, a linear elastic model with a failure criterion was also compared to a linear elastic model without a failure criterion.

The lower-bound undrained shear strength was given by the following relationship:

$$c_u = 67 + 6z \qquad \textbf{Equation 38}$$

where c_u is the undrained shear strength in kPa and

z is the depth from the top of the London Clay stratum in m.

The best-fit undrained shear strength was given by the following relationship:

$$c_u = 100 + 7.5z \qquad \textbf{Equation 39}$$

and this was what was implemented in the base case model.

The lowest value of undrained shear strength before failure would occur was estimated using the relationships in Bjerrum & Eide (1956) for the shaft excavation and Mair (1998) for the tunnel face. For the tunnel face the limiting value of undrained shear strength was 27.4 kPa and for the shaft excavation it was 44.1 kPa. Therefore, a constant value of undrained shear strength of 50 kPa was adopted. The 3 undrained shear strength profiles used are shown in Figure 5-7.

The stress-strain behaviours of all of the models used to investigate soil plasticity are shown in the plot of deviator stress and axial strain in Figure 5-46.

A calibration was performed for each model, and a comparison is made in Table 5-7. The more plasticity that was occurring, the more the ground relaxed during sequential excavation and the lower the relaxation factor needed to be to simulate this. This was reflected in a lower hoop stress at tunnel axis level. It is perhaps counter-intuitive, given the evidence and arguments in the literature review and in Chapter 4, that the weaker ground ended up with a greater portion of the load. However, the possibility that some form of loosening would begin to occur above a certain strain level was not included in these models. Using similar elastic-plastic models, the same result was found by Panet & Guenot (1982) and is the basis of the widely-used 'convergence-confinement method' (AFTES, 2001).

Table 5-7: Relaxation factors used in the analyses investigating the effect of failure criterion, along with the corresponding hoop axial stress (compression is negative) at tunnel axis level at the end of shaft construction

Model	Relaxation factor	Hoop stress at axis level
Lowest value for stability $c_u = 50$ kPa	49 %	-2.35 MPa
Lower bound value $c_u = 67 + 6z$	61 %	-2.80 MPa
Base case ($c_u = 100 + 7.5z$)	65 %	-2.97 MPa

In design, Eurocode 7 (BS EN 1997) requires that 2 combinations are considered. For the first combination (DA1.1) the characteristic soil parameters are used, and the resulting actions from the calculation model are multiplied by a load factor. For the second combination (DA1.2) the undrained shear strength is divided by a factor of 1.4, and the resulting actions are not factored. Therefore, the effect of reducing the undrained shear strength by a factor of 1.4 is very pertinent to design. At tunnel axis level (z = 6.8 m), the base case undrained shear strength was exactly 1.40 times the lower bound undrained shear strength.

The hoop stress concentration factors in the shaft lining above and below the tunnel centreline are shown in Figure 5-47. Although the hoop stresses before creation of the opening were quite different for each failure criterion (Table 5-7), the stress concentration factors for the axial stress were similar, especially between the base case and the lower bound undrained shear strength profiles. This means that the axial stress in the DA1.2 model (lower bound undrained shear strength) is unlikely to be the worst case. Even with an undrained shear strength of 50 kPa, the axial stress concentration factor was only 1.15 times higher than the base case.

The bending stress concentration factors, however, showed a different response to the axial stresses. The model with an undrained shear strength of 50 kPa had the highest bending stress concentration factor, but the lower bound undrained shear strength model had the lowest bending stress concentration factor, although this was only about 10 % different from the base case. These differences were due to the different levels of stress before creation of the tunnel opening. The 50 kPa undrained shear strength model, for instance, which had the lowest hoop stress at the end of shaft construction, tended to catch up to the others when the opening was created, resulting in a higher stress concentration factor.

The stress concentration factors around the perimeter of the shaft lining at tunnel axis level showed a similar relationship between the failure criteria as that described for the hoop stress concentration factors in Figure 5-47, and so the diagrams have not been included here.

In conclusion it appears that within reasonable limits the failure criterion did not have a significant impact on the stress concentration factors due to creation of the tunnel opening. When the undrained shear strength was approaching a value that would cause instability (50 kPa), the stress concentration factors showed a noticeable increase. However, this would still not be a worst case for a design according to the Principles of Eurocode 7.

5.2.4 *In situ* stress distribution

The *in situ* vertical stress distribution was calculated from the unit weights of the soils and the position of the groundwater table, with the groundwater pressure distribution assumed hydrostatic. The *in situ* horizontal stress distribution was

difficult to ascertain from the results of site investigation and laboratory testing, with different methods of testing resulting in wide scatter in the results, as described in Section 5.1.2 and Figure 5-8. It was therefore deemed necessary to test the importance of the *in situ* stress by varying the value of the coefficient of earth pressure at rest K_0. K_0 in the 5m depth of overlying Terrace Gravels was assumed to be 0.4 as recommended by the T5 Geotechnical Design Basis Report (2001). The K_0 profile with depth in the London Clay was set by the following methods:

- K_0 set to 1.0 in the London Clay.
- K_0 set according to Mayne & Kulhawy (1982); this was approximately the average of the site investigation data. This was the base case. Averaged over the tunnel section K_0 was approximately 1.45.
- K_0 according to the recommendation of the T5 GDBR (2001). This was close to representing an upper bound to the site investigation data. Averaged over the tunnel section K_0 was approximately 1.95.

These profiles are also shown on Figure 5-8.

The relaxation factors from the calibration exercise are listed in Table 5-8.

Table 5-8: Relaxation factors used in the analyses investigating the effect of *in situ* stress, along with the corresponding hoop axial stress (compression is negative) at tunnel axis level at the end of shaft construction

Model	Relaxation factor	Hoop stress at axis level
Base case	65 %	-2.97 MPa
$K_0 = 1.0$	65 %	-2.28 MPa
T5 recommended values of K_0	57 %	-3.36 MPa

The hoop stress in the shaft lining before creation of the opening was different for each model, with a higher horizontal *in situ* stress resulting in a higher hoop stress in the shaft lining after shaft excavation. The ratios between the different models were exactly equal to the ratios of *in situ* total stress. For instance, the base case hoop stress after shaft construction was 1.30 times the hoop stress in

the run with K_0 set to 1.0, and the *in situ* total stress ratio at tunnel axis level was 1.30 in the base case.

Similarly, the effect of creating the tunnel opening was almost exactly proportional to the *in situ* total stress ratio, as evidenced by the similarity of the values of stress concentration factors in Figure 5-48. The higher values of bending stress concentration factor for the T5 recommended profile may have been caused by the rapid decrease in K_0 with depth at this location (c.f. Figure 5-8), compared to the relatively constant values of the base case and the run with K_0 set to 1.0.

In conclusion, the *in situ* stress was not found to have an effect on the stress concentration factors due to junction construction. However, this conclusion may only be applicable to a shaft-tunnel junction and not a tunnel-tunnel junction where existing bending stresses due to $K_0 \neq 1.0$, or a non-circular parent tunnel may play a role in the stress concentration factors after junction construction.

5.3 Impact of lining thickness

The thickness of the shaft lining was varied to find the effect on the stresses due to junction construction. The base case had a lining thickness of 0.35 m, and so two more runs were performed with a thickness of 0.2 m and 0.8 m.

Again, a calibration to find the shaft relaxation factor was performed and the results are shown in Table 5-9.

Table 5-9: Relaxation factors used in the analyses investigating the effect of lining thickness, along with the corresponding hoop axial force (compression is negative) at tunnel axis level at the end of shaft construction

Model	Relaxation factor	Hoop force at axis level
Base case, t = 0.35 m	65 %	-1040 kN/m
Thin lining, t = 0.2 m	64 %	-986 kN/m
Thick lining, t = 0.8 m	67 %	-1127 kN/m

The thin lining required a lower relaxation factor to simulate the shaft construction because more deformation occurred after installation of the lining.

The converse was true for the thick lining. The hoop *force* at axis level is shown in Table 5-9, rather than the hoop *stress* shown in previous tables and figures, to allow an easy comparison between the different lining thicknesses.

The hoop axial stress concentration factors above and below the tunnel opening are shown in Figure 5-49. There was a general trend showing that the thinner the lining, the lower the axial stress concentration factor, but the variation between the 0.2 and 0.8 m thick linings was within 15 %.

The hoop bending stress concentration factors, also shown in Figure 5-49, varied much more with lining thickness, and displayed more complex behaviour. The rate of change of bending stress concentration factor was lower for the thick lining, and this meant that the base case had a higher bending stress concentration factor adjacent to the opening.

In design, it is likely that the lining thickness used in the calculation model would only be changed by relatively small amounts once the stresses have been calculated. Given the low variability of the maximum total stress concentration factor (axial and bending combined) of 4.59, 5.66 and 5.11 for a 0.2, 0.35 and 0.8 m thick lining respectively, it is considered unlikely that the design would need to iterate more than once to find an optimal solution.

The sectional capacities of these lining thicknesses would of course depend on the steel reinforcement. However, it is unlikely that a 0.2 m thick lining with a typical characteristic compressive strength for sprayed concrete of 40 MPa would be sufficient in this case, given that the maximum stress was 27.4 MPa and the combined factor of safety required by Eurocode 7 DA1.1 would be 2.1 (material factor 1.5, load factor 1.4). A rough calculation of this kind indicates that a lining thickness of approximately 0.4 m would have been sufficient for the stresses due to creation of the tunnel opening.

5.4 Comparison with pressure cell data

The T4 concourse tunnel pressure cell array MMS VIII was close to where 2 crosspassages were constructed, one on either side of the concourse tunnel for passenger access to the platform tunnels (c.f. Figure 3-1, Figure 3-2 and Figure 3-3). The crosspassages were 5.04 m diameter, and MMS VIII was located in an advance that was 3 to 4 m from the crosspassages' centreline. Therefore the

pressure cells were approximately 1 m from the edge of the crosspassage excavation.

The effect of the period of crosspassage construction on the pressure cell readings described in Sections 4.4.3 and 4.4.4 could be characterised by a general increase in axial tangential stress of between 0.6 and 1.5 MPa, and a squatting of the concourse tunnel inducing bending stresses. The increase of radial stress in MMS VIII due to crosspassage construction was on average 65 kPa, an increase of approximately 40 % on the radial stress prior to crosspassage construction. The increase of radial stress and the increase of tangential stress were broadly consistent with each other.

The Kirsch solution predicts a maximum hoop stress concentration factor of 3.0 at the edge of the opening, but this decreases to 1.65 a distance of 1 m from the edge of the opening.

The modelling presented so far in Chapter 5 was based on a shaft-tunnel junction from the Heathrow T5 SWOT project. The inlet shaft was 12.0 m diameter and the frontshunt tunnel was 4.8 m diameter. So, although the shaft was quite a lot larger than the T4 concourse tunnel, the T5 frontshunt tunnel was almost the same size as the T4 crosspassages. Therefore, data from the MMS VIII tangential pressure cells have been added to Figure 5-33 to compare with the results of the numerical modelling and the Kirsch analytical solution. Before this can be done, however, the values of the tangential stress concentration factors must be calculated from the MMS VIII readings. This is shown in Table 5-10 below. The crown cells PCT1, 2 and 3 and the invert cell PCT12 were omitted because the comparison was meant to be approximately at axis level.

Table 5-10: Stress concentration factors at MMS VIII due to crosspassage construction

Pressure cell	Tangential stress before crosspassage construction (MPa)	Change in tangential stress due to crosspassage construction (MPa)	Stress concentration factor
PCT4	3.17	0.59	1.19
PCT5	2.53	0.94	1.37
PCT6-OUT	2.73	0.71	1.26
PCT6-IN	2.00	0.72	1.36
PCT7-OUT	1.96	0.57	1.29
PCT7-IN	1.52	1.51	1.99
PCT8	2.04	0.65	1.32
PCT9	1.28	0.77	1.6

The values of stress concentration factor in Table 5-10 were plotted on the same graph as the numerical modelling results and the Kirsch solution in Figure 5-50. The highest field measurement of stress concentration factor, from cell PCT7-IN, illustrates the effect of bending stress to increase the magnitude of the stress concentration. This would not have been predicted by the analytical solution. However, the combined effect of the axial and bending stress concentration factors from the numerical model was higher. The reason the numerical modelling prediction was so much higher was because the bending stress concentration factor was calculated at the extreme fibre, and the tangential pressure cells, even when placed side-by-side were a minimum of 60 mm from the extrados and 70 mm from the intrados. Therefore, the average eccentricity of the tangential cell centroid from the centreline of the lining section was never more than 65 mm, compared to the distance to the extreme fibre, which was 175 mm.

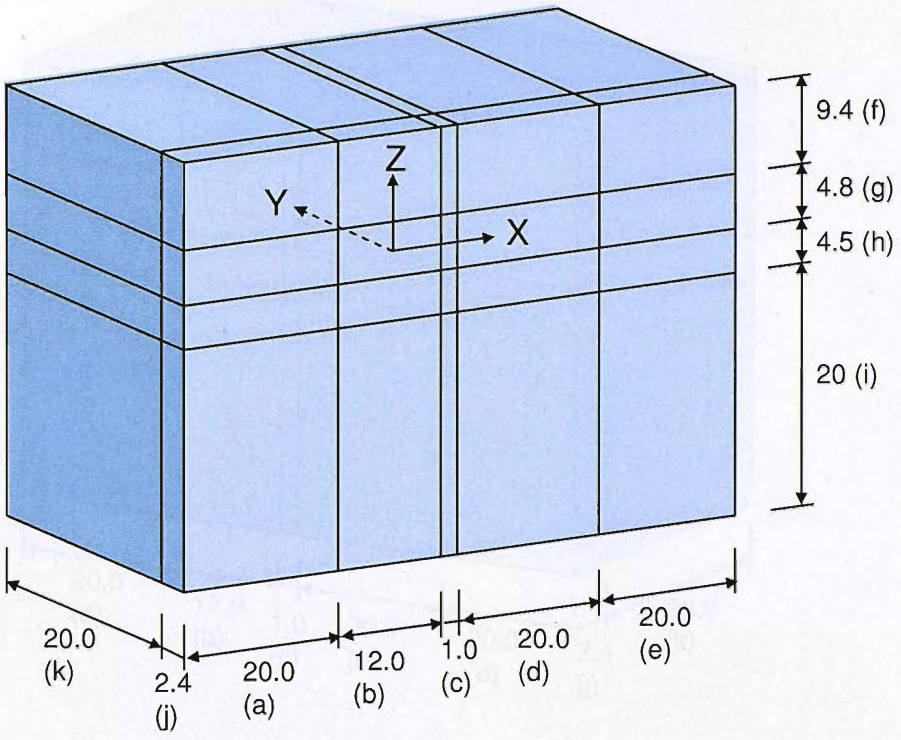

Figure 5-1: Isometric view of generic bricks for FLAC^{3D} model creation (dimensions in metres)

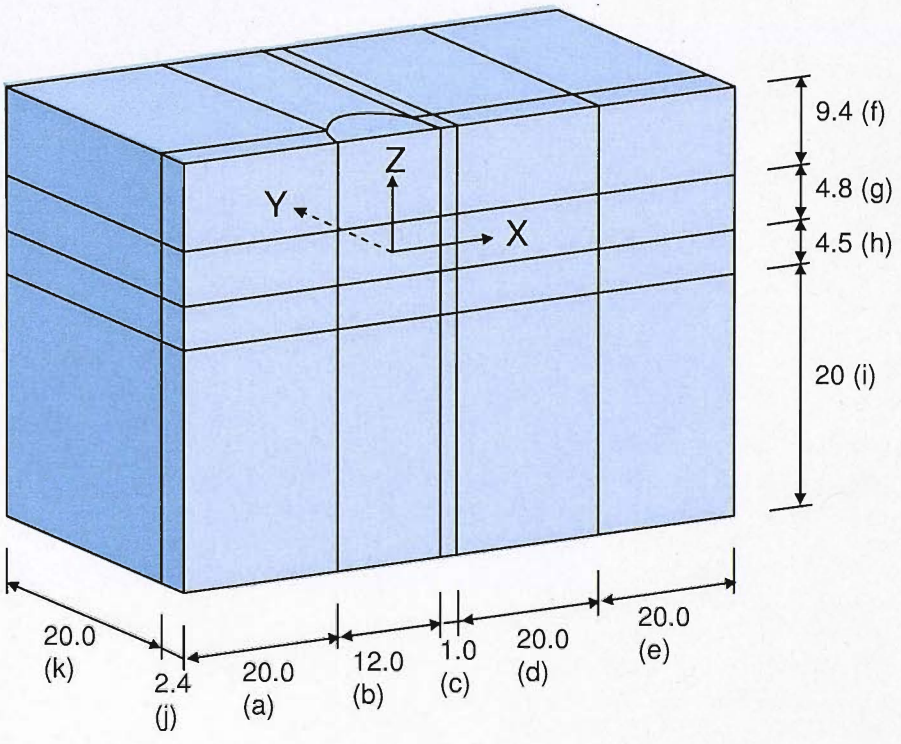

Figure 5-2: Isometric view of deformed generic bricks ready for analysis

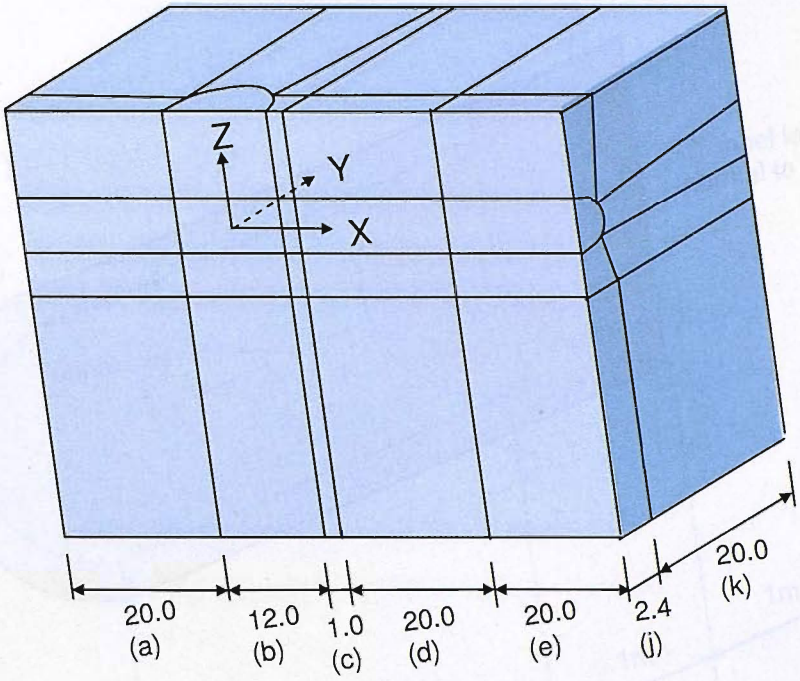

Figure 5-3: Rotated view of Figure 5-2

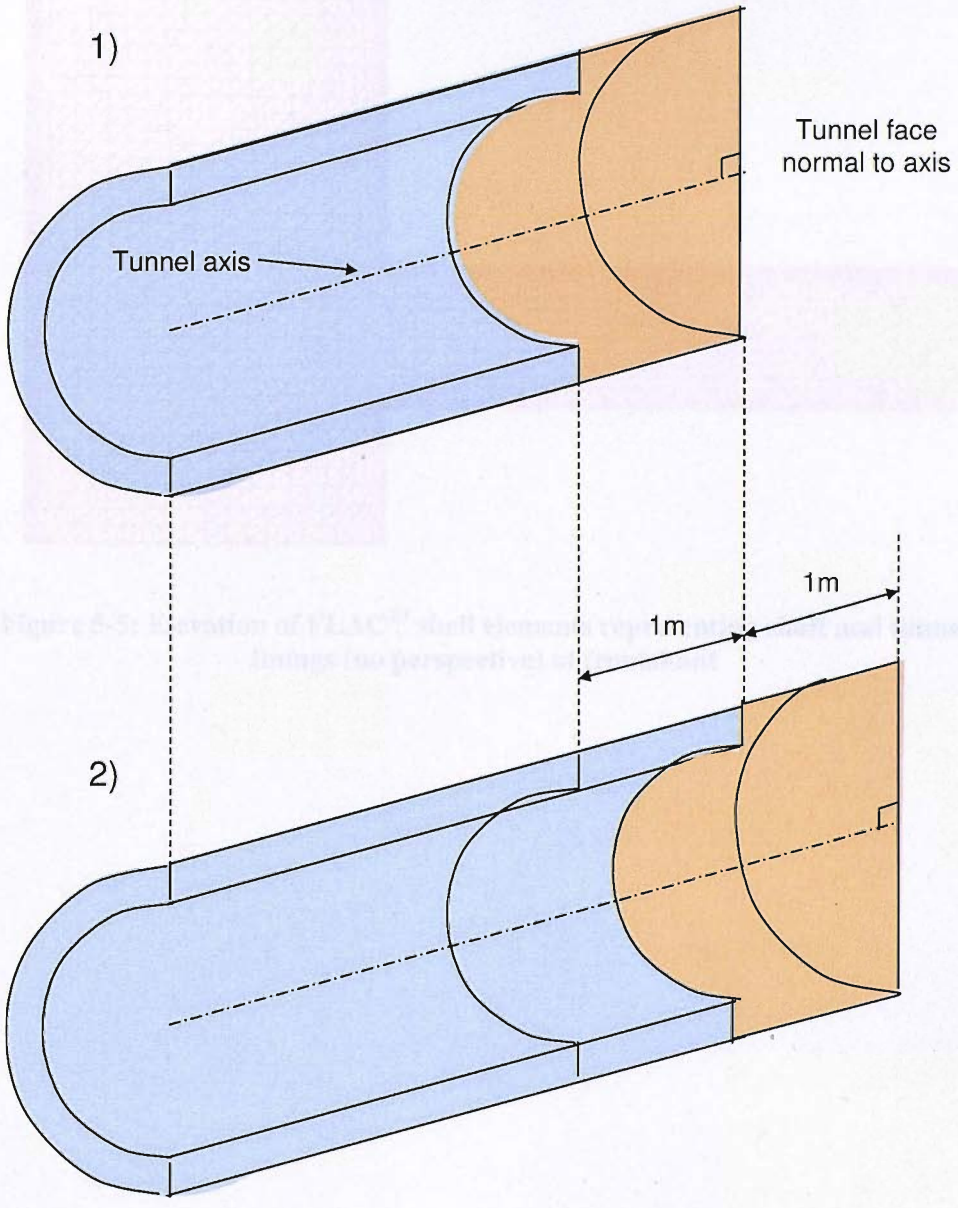

Figure 5-4: 3D view of a full-face advancing tunnel with a face normal to the longitudinal axis of the tunnel. 1) Before excavation of advance 2)Excavation of advance and installation of lining in previous advance.

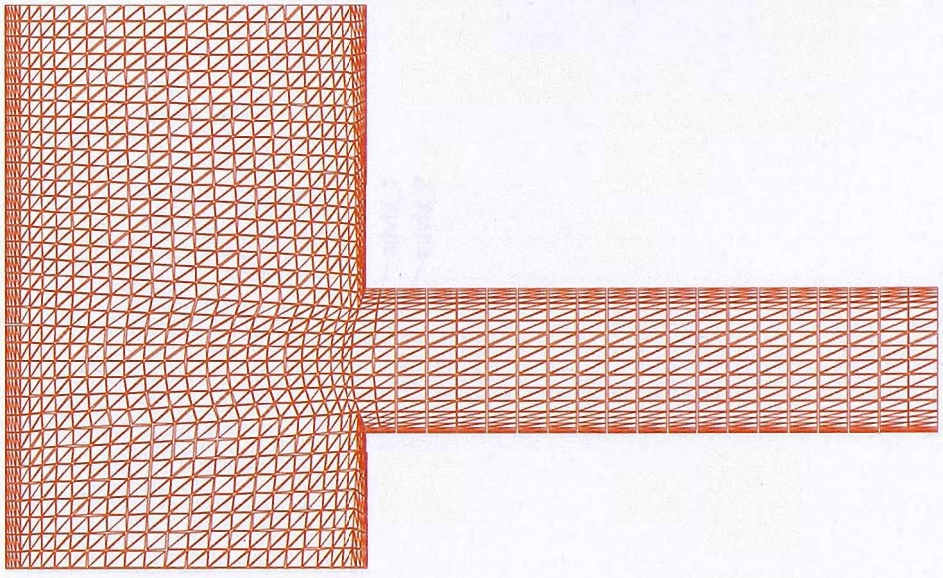

Figure 5-5: Elevation of FLAC^{3D} shell elements representing shaft and tunnel linings (no perspective) at frontshunt

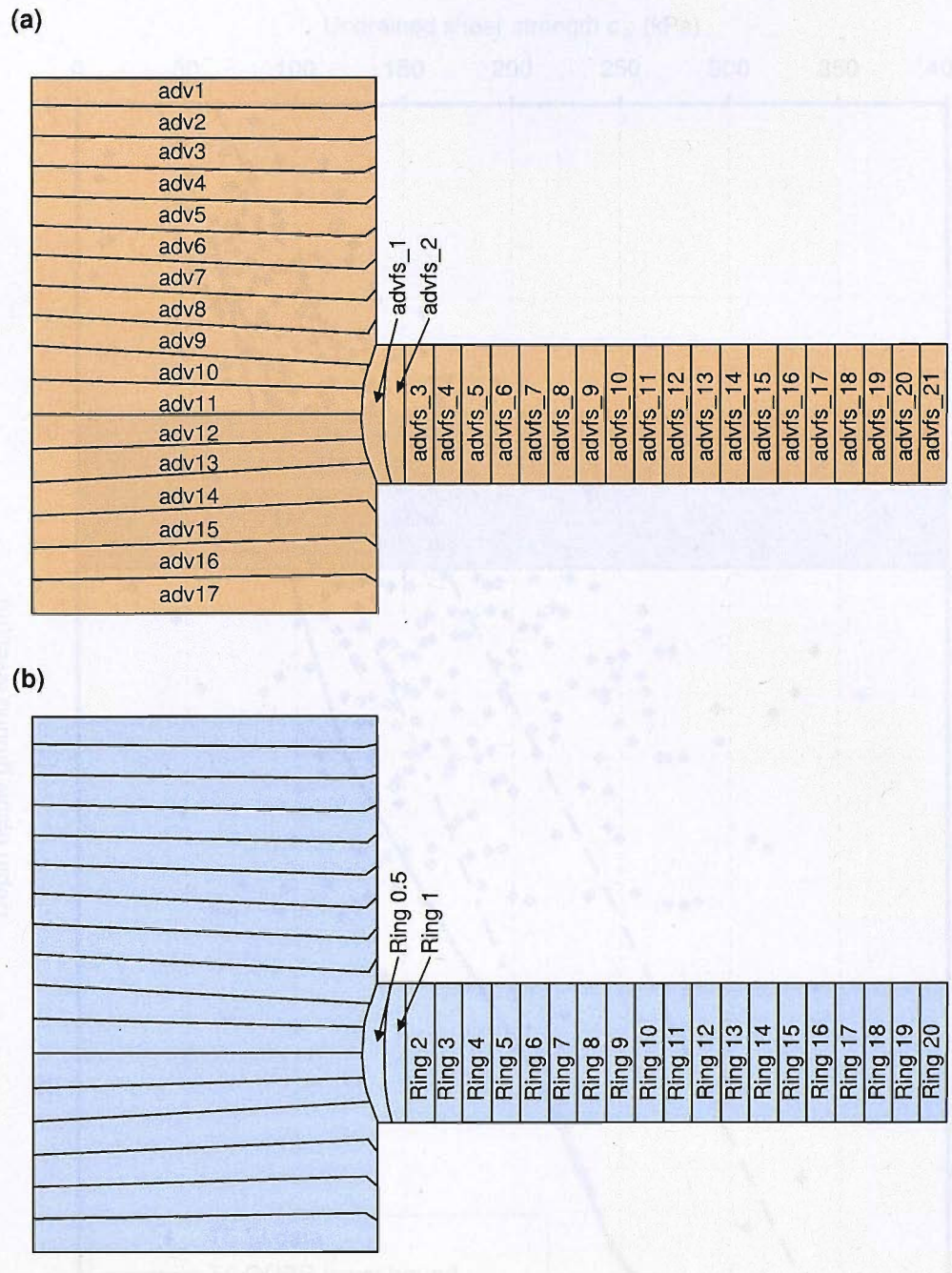

Figure 5-6: Sketch showing numbering system for (a) inlet shaft and frontshunt tunnel advance numbers (b) frontshunt tunnel ring numbers

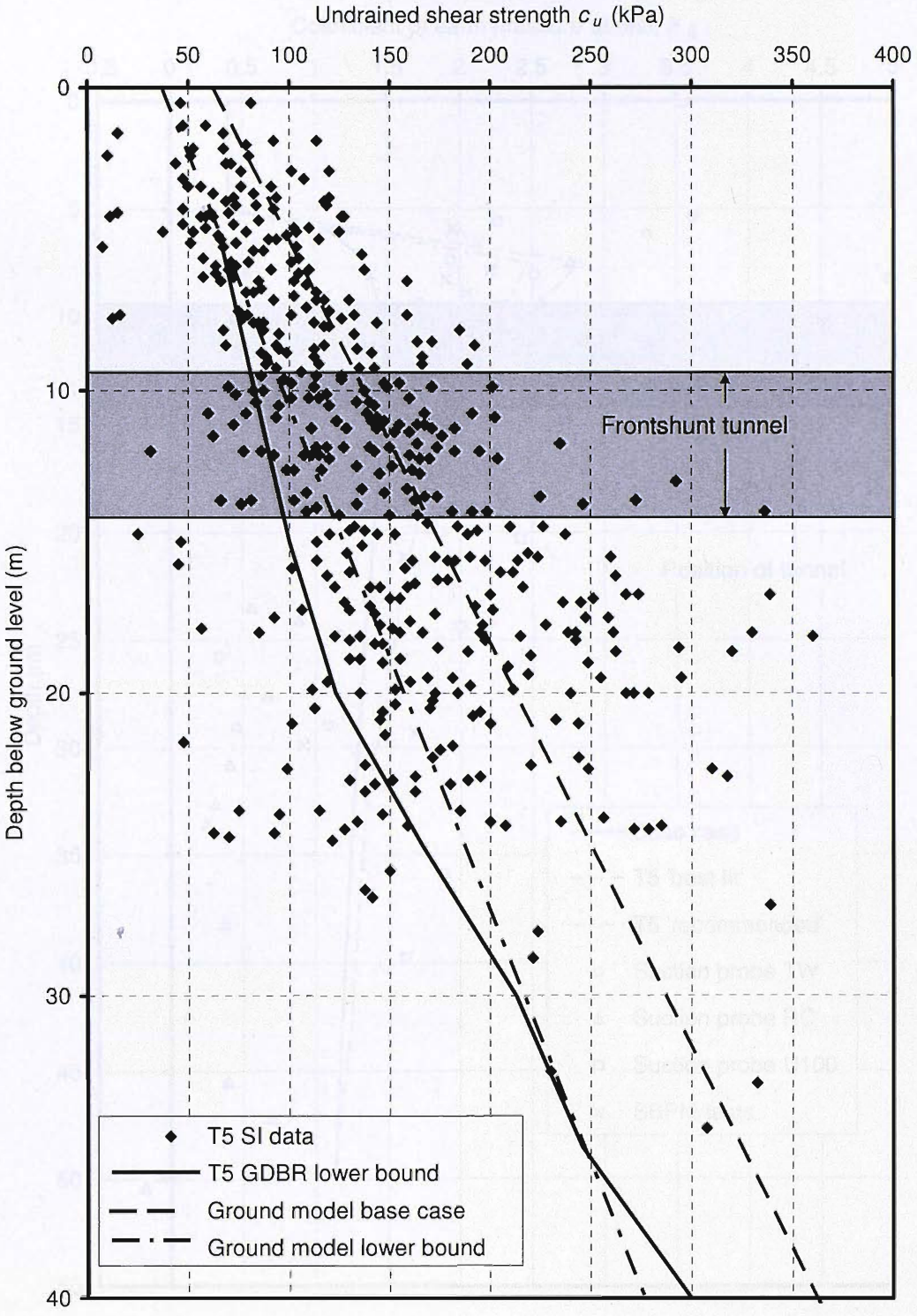

Figure 5-7: Undrained shear strength vs. depth from UU triaxial compression tests on 100 mm diameter samples at T5

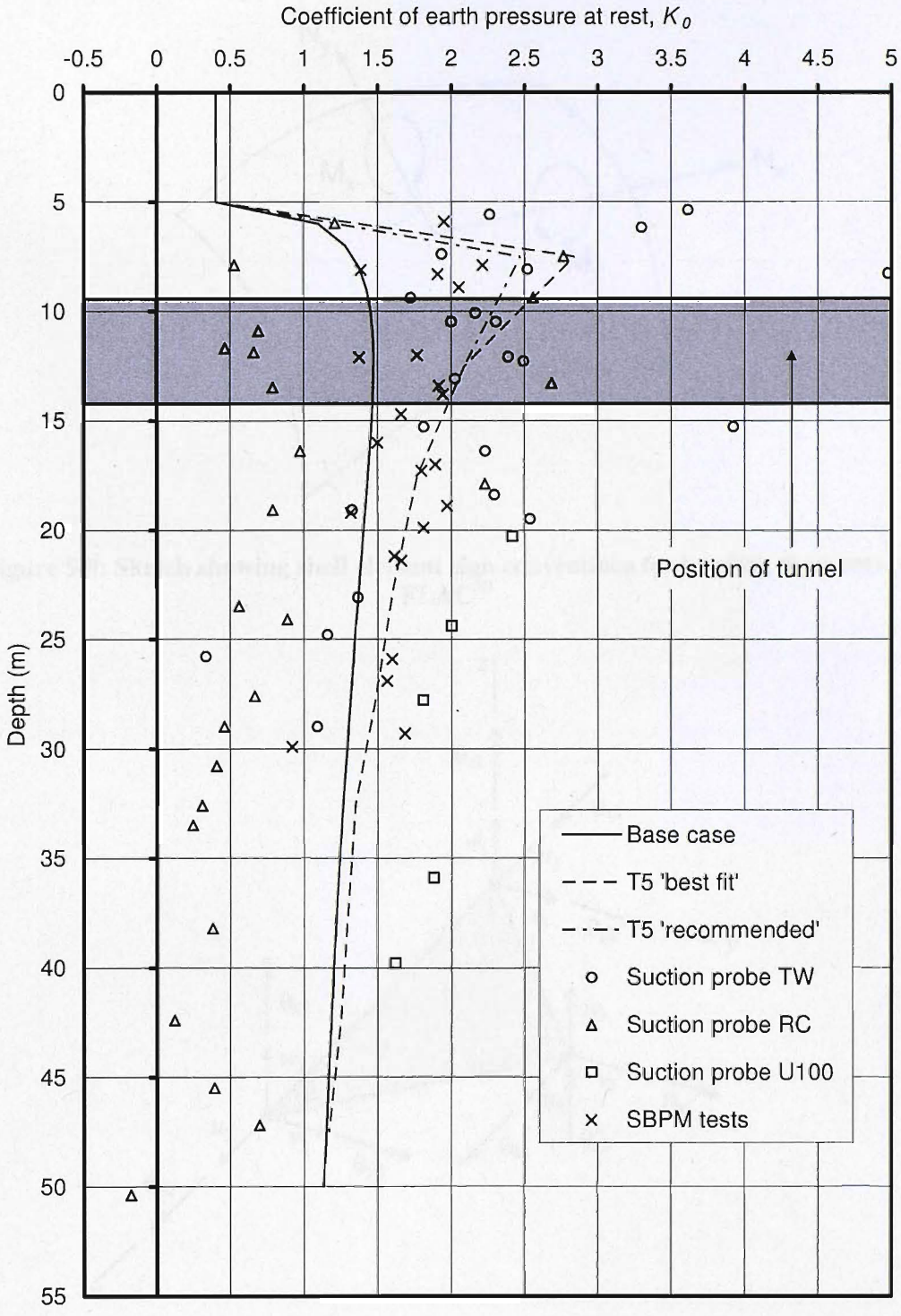

Figure 5-8: K_0 site investigation data and design profiles with depth; TW = thin-walled sampler, RC = rotary core, U100 = 'Undisturbed' 100mm sampler, SBPM = self-boring pressuremeter

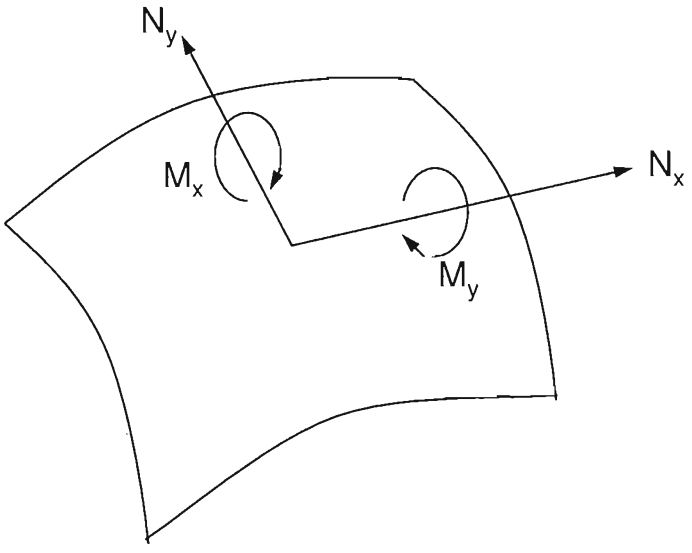

Figure 5-9: Sketch showing shell element sign conventions for bending moments in FLAC^{3D}

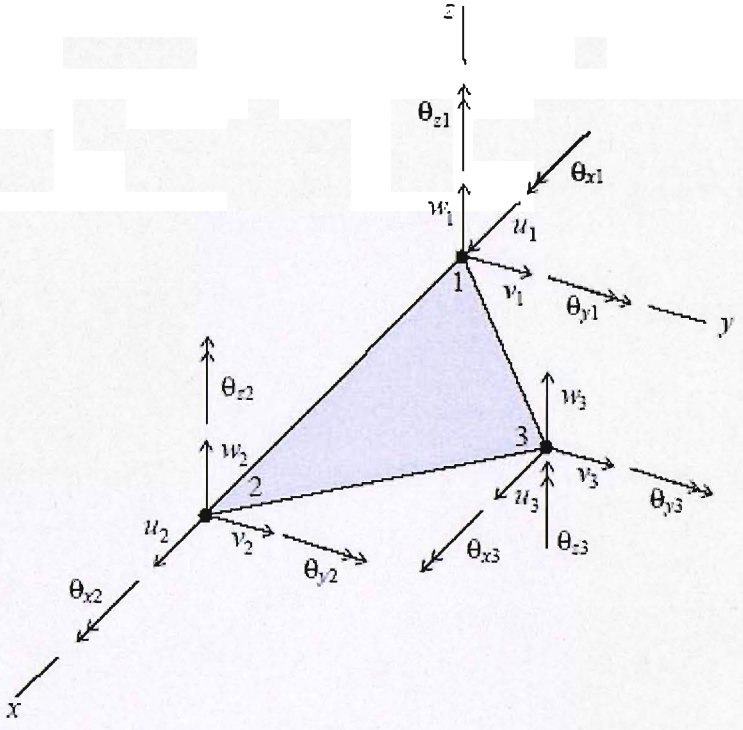

Figure 5-10: Shell-type SEL coordinate system and 18 degrees of freedom available to the shell finite elements (from Itasca, 2002)

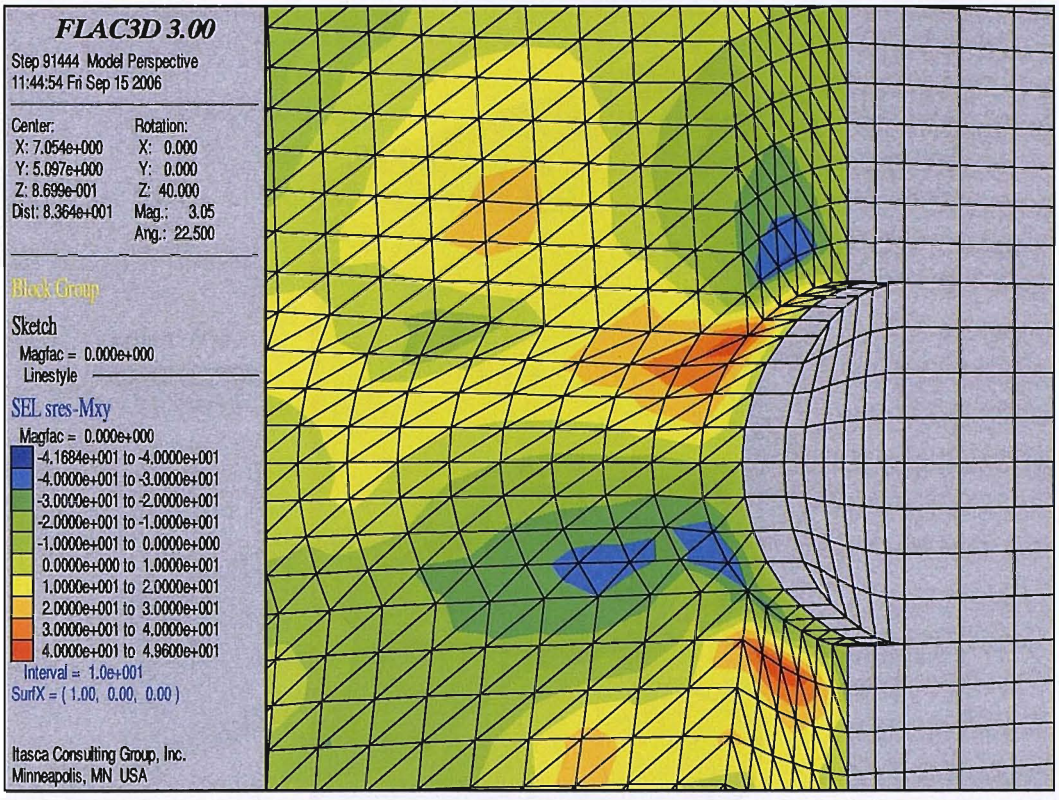

Figure 5-11: Contours of M_{xy} moment around junction at advance advfs_2

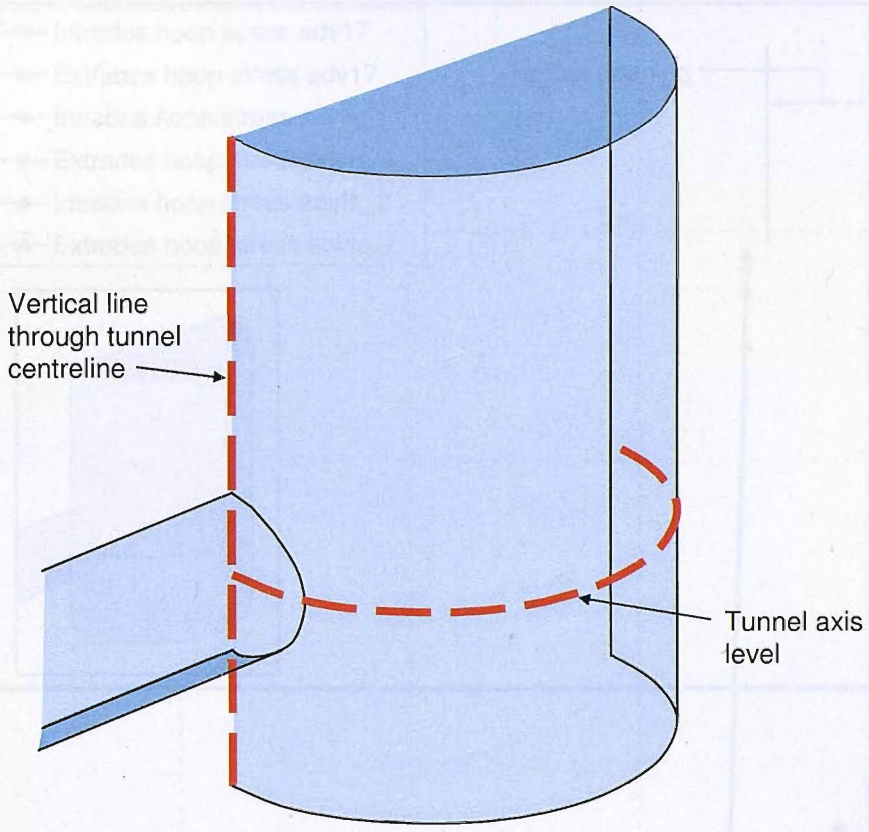

Figure 5-12: Sketch showing location of lines along which results graphs from the numerical modelling are plotted

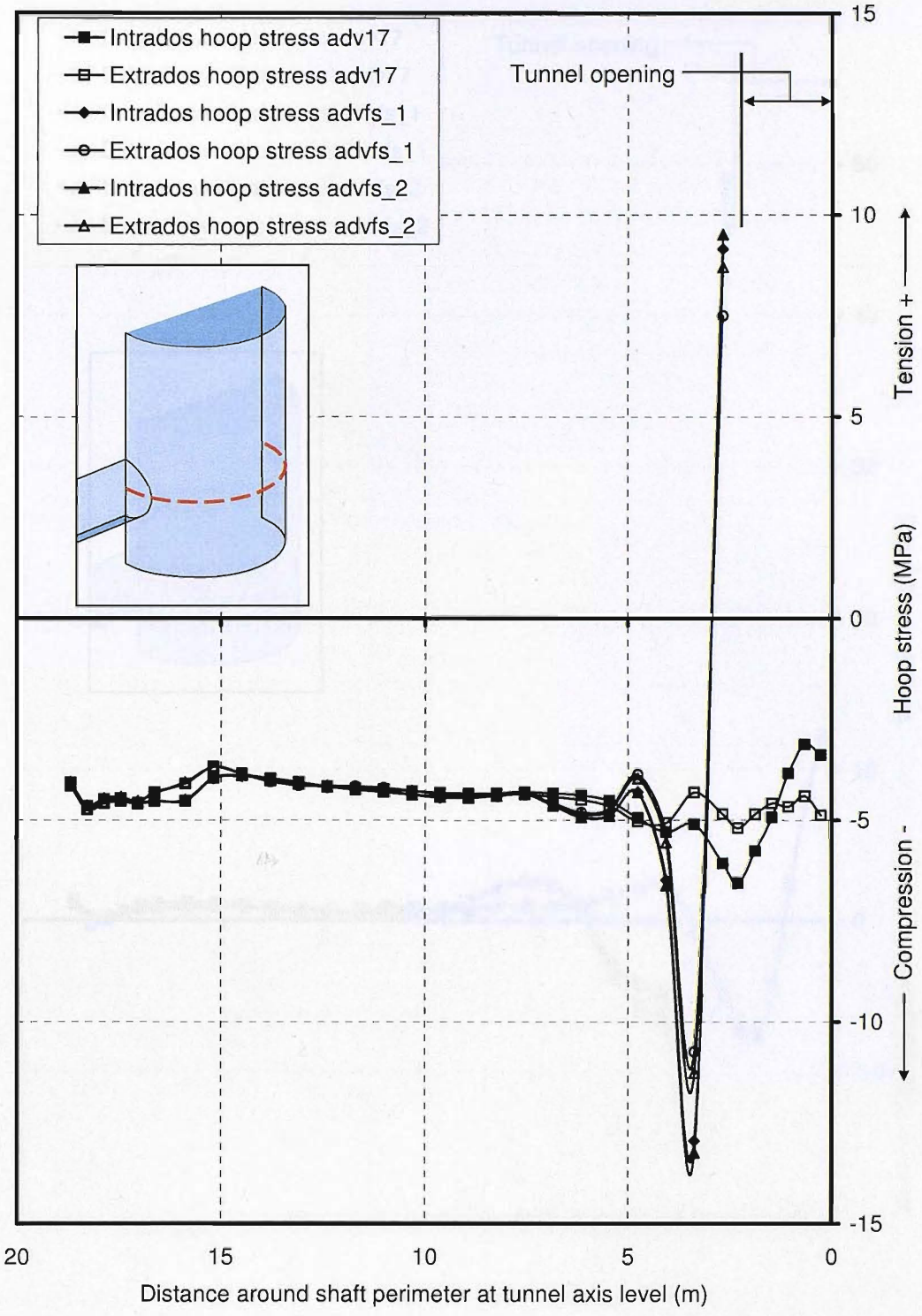

Figure 5-13: Hoop stress around the shaft perimeter at tunnel axis level (base case)

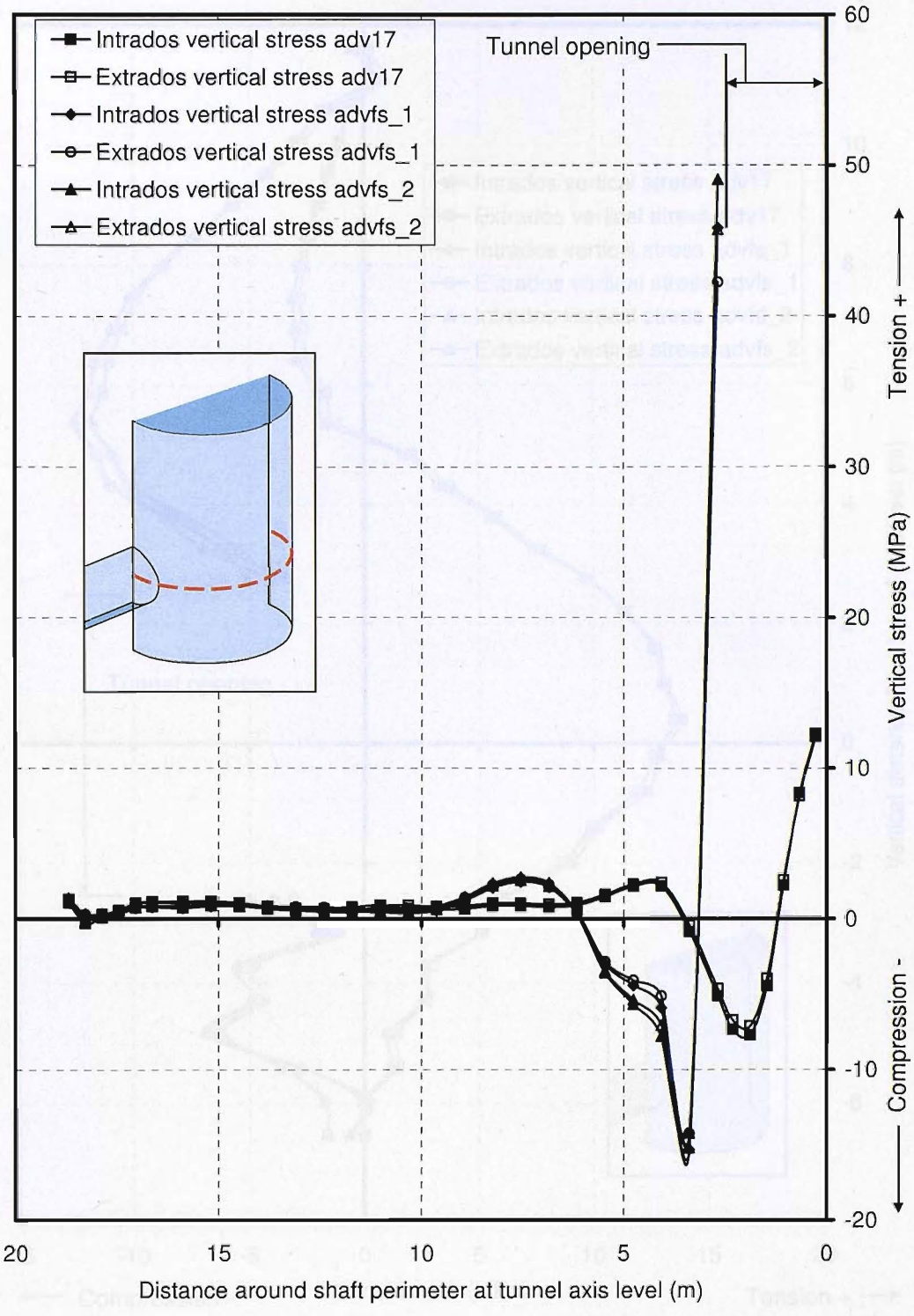

Figure 5-14: Vertical stress around the shaft perimeter at tunnel axis level (base case)

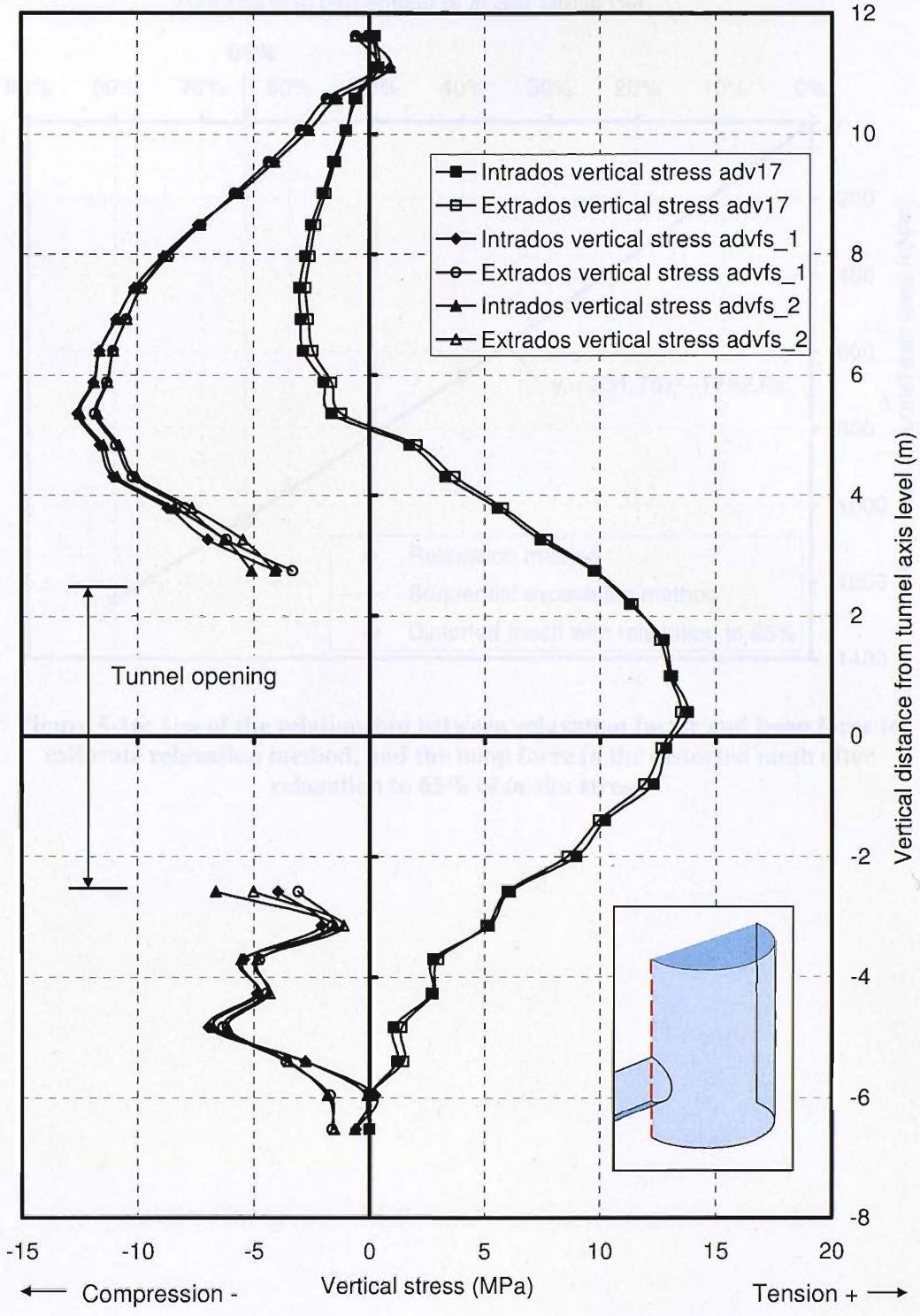

Figure 5-15: Vertical stress in the shaft lining above and below the tunnel centreline (base case)

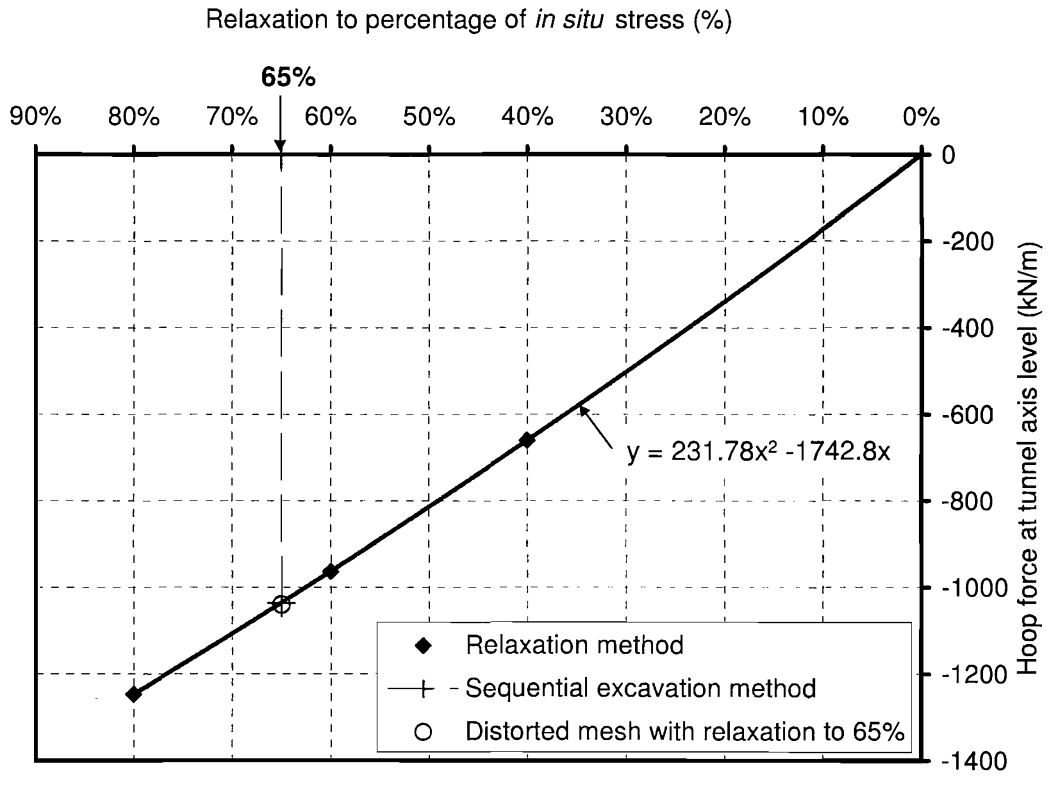

Figure 5-16: Use of the relationship between relaxation factor and hoop force to calibrate relaxation method, and the hoop force in the distorted mesh after relaxation to 65% of *in situ* stress.

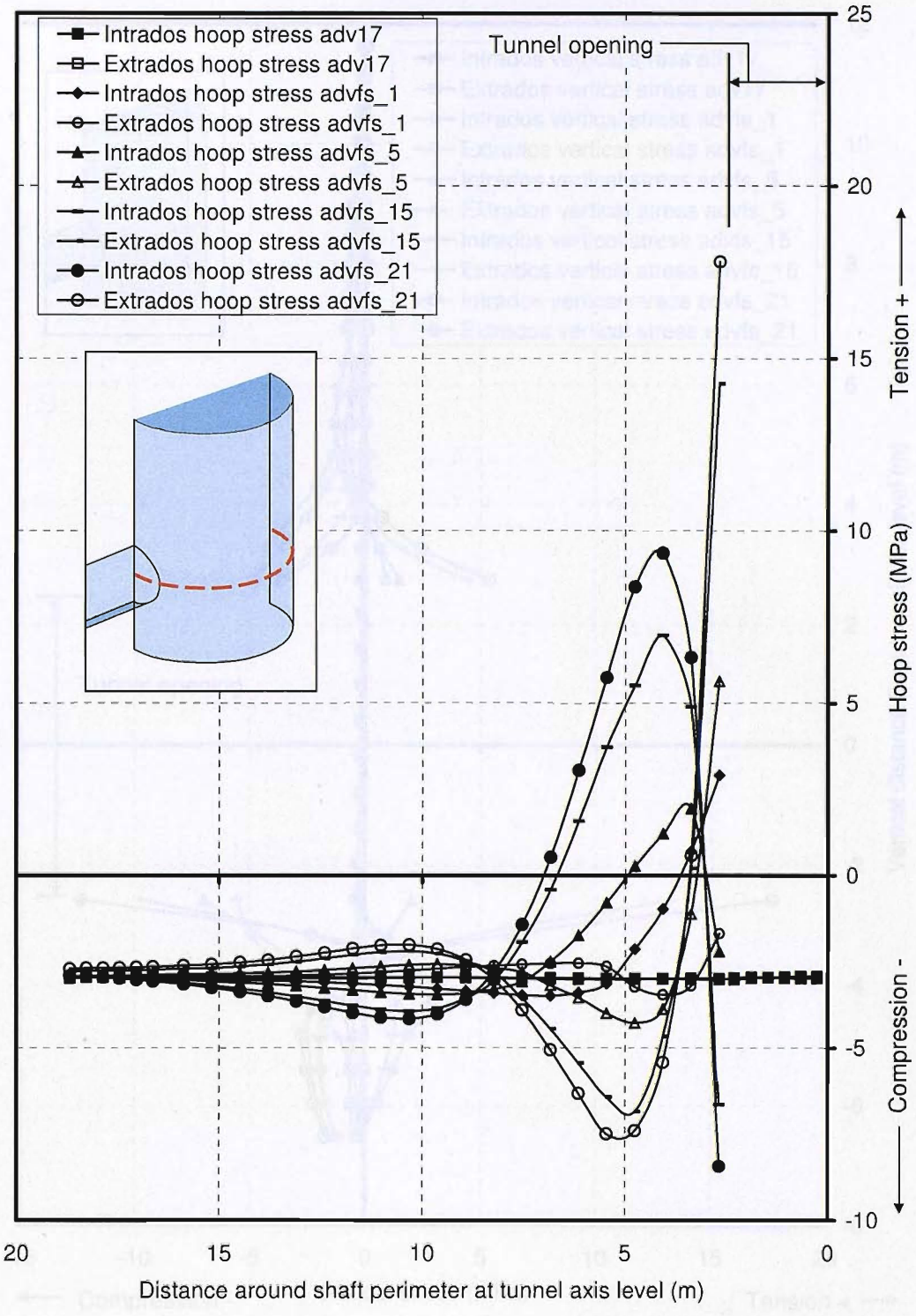

Figure 5-17: Hoop stress in the shaft lining at tunnel axis level as the tunnel length increases

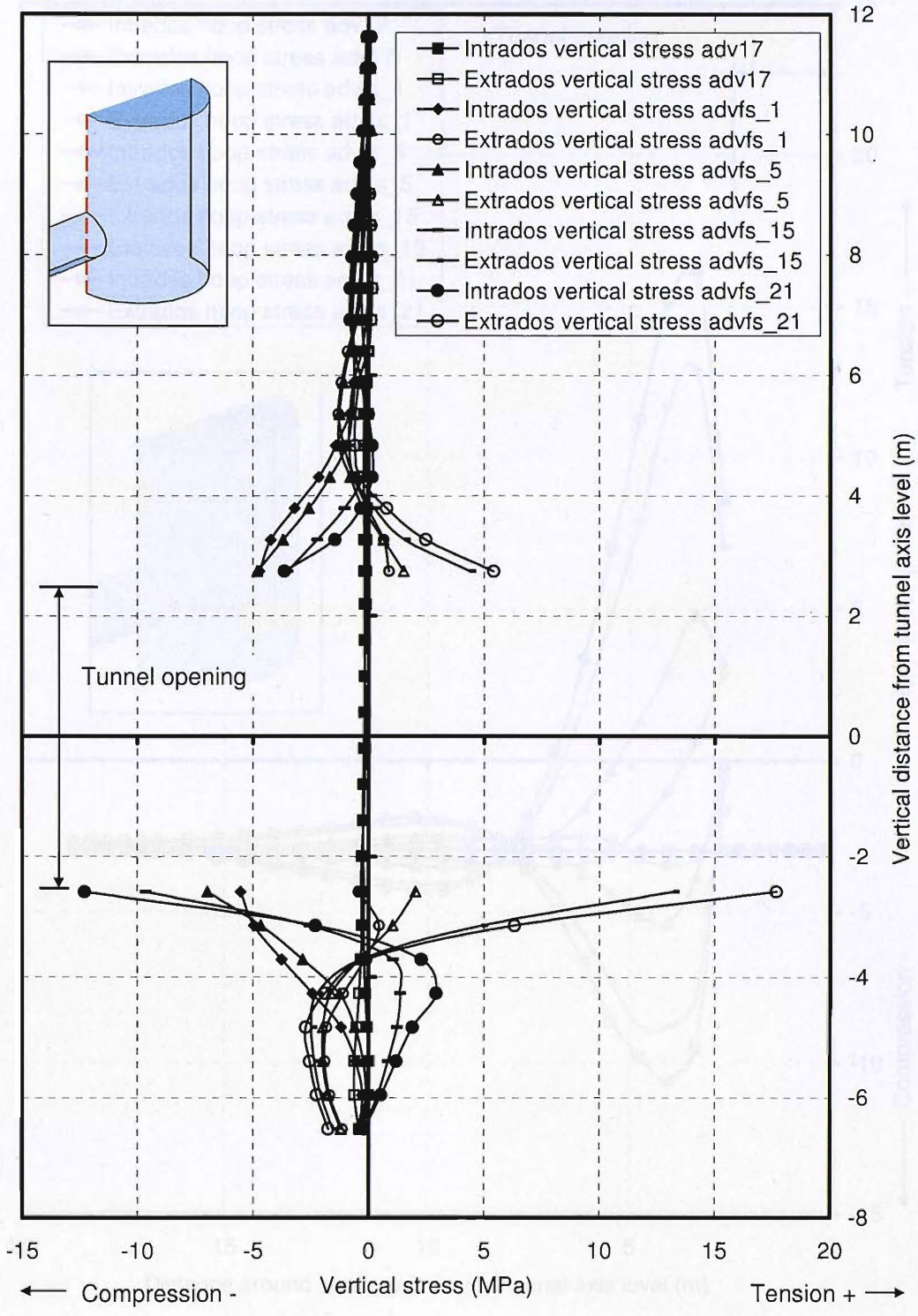

Figure 5-18: Vertical stress in the shaft lining above and below the tunnel centreline as the tunnel length increases

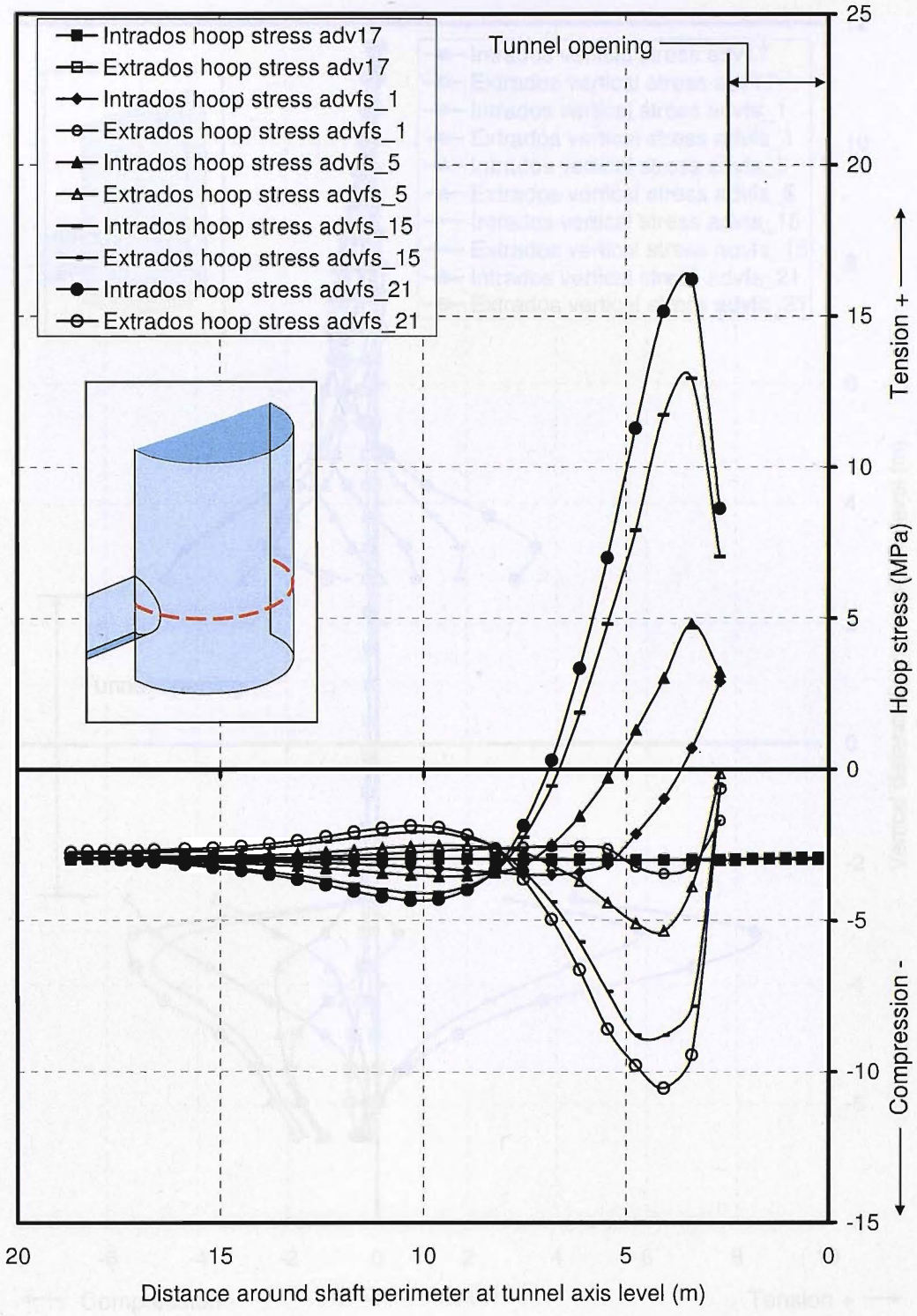

Figure 5-19: Hoop stress in the shaft lining at tunnel axis level as tunnel length increases for model with a pinned connection between the shaft and tunnel lining

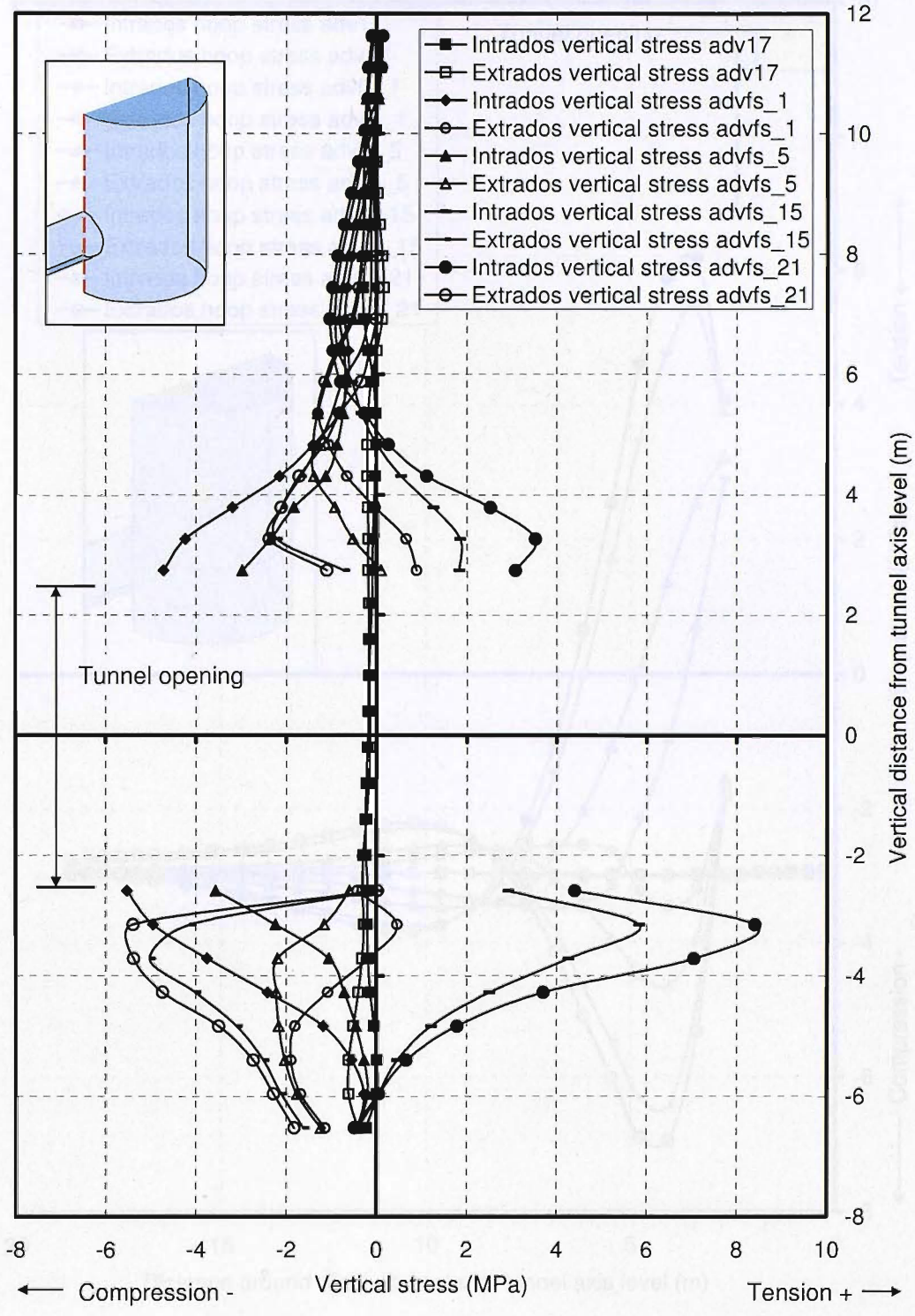

Figure 5-20: Vertical stress in the shaft lining above and below the tunnel centreline as the tunnel length increases for model with a pinned connection between the shaft and tunnel lining

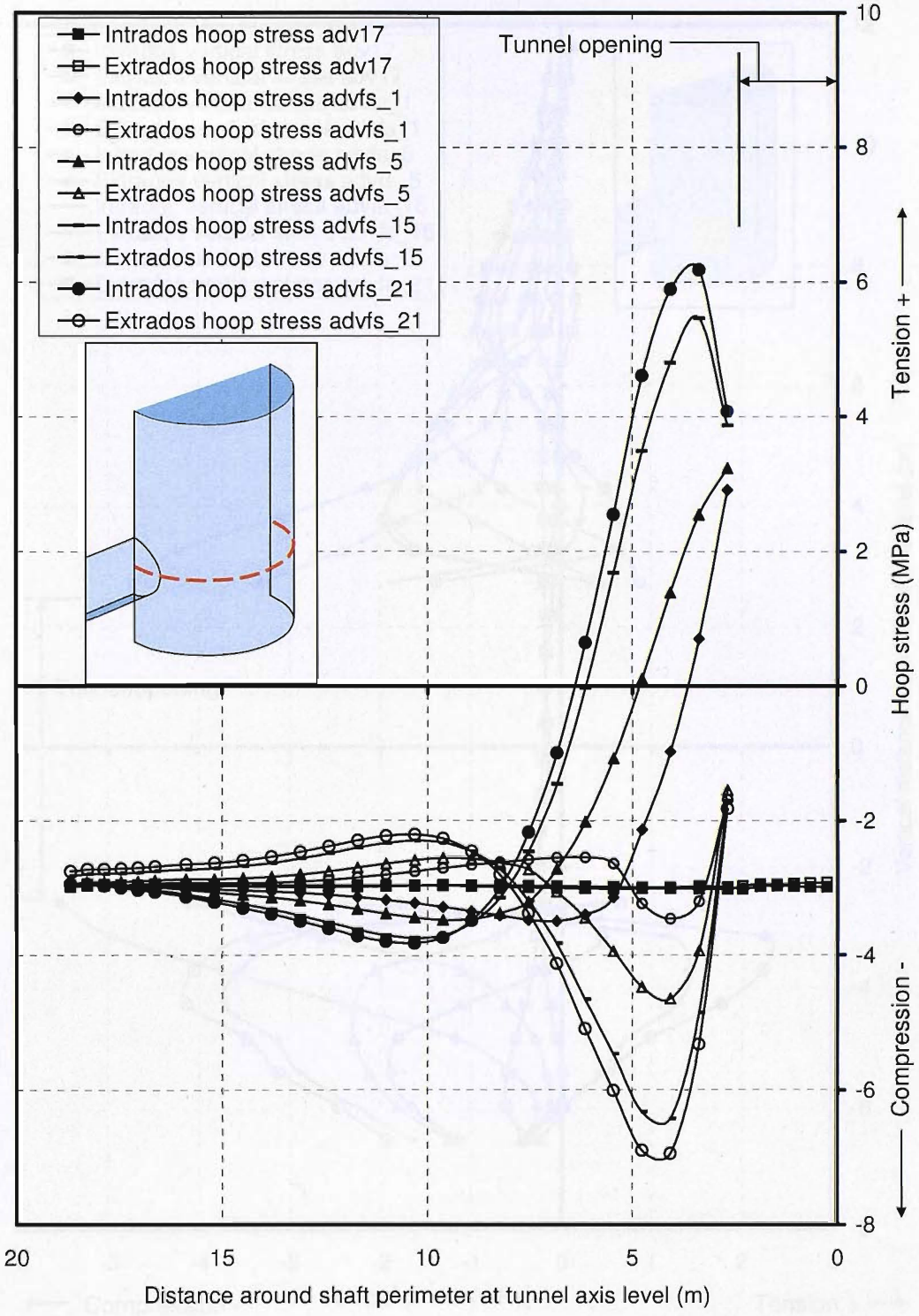

Figure 5-21: Hoop stress in the shaft lining at tunnel axis level as tunnel length increases for model with no connection between shaft and tunnel lining shells

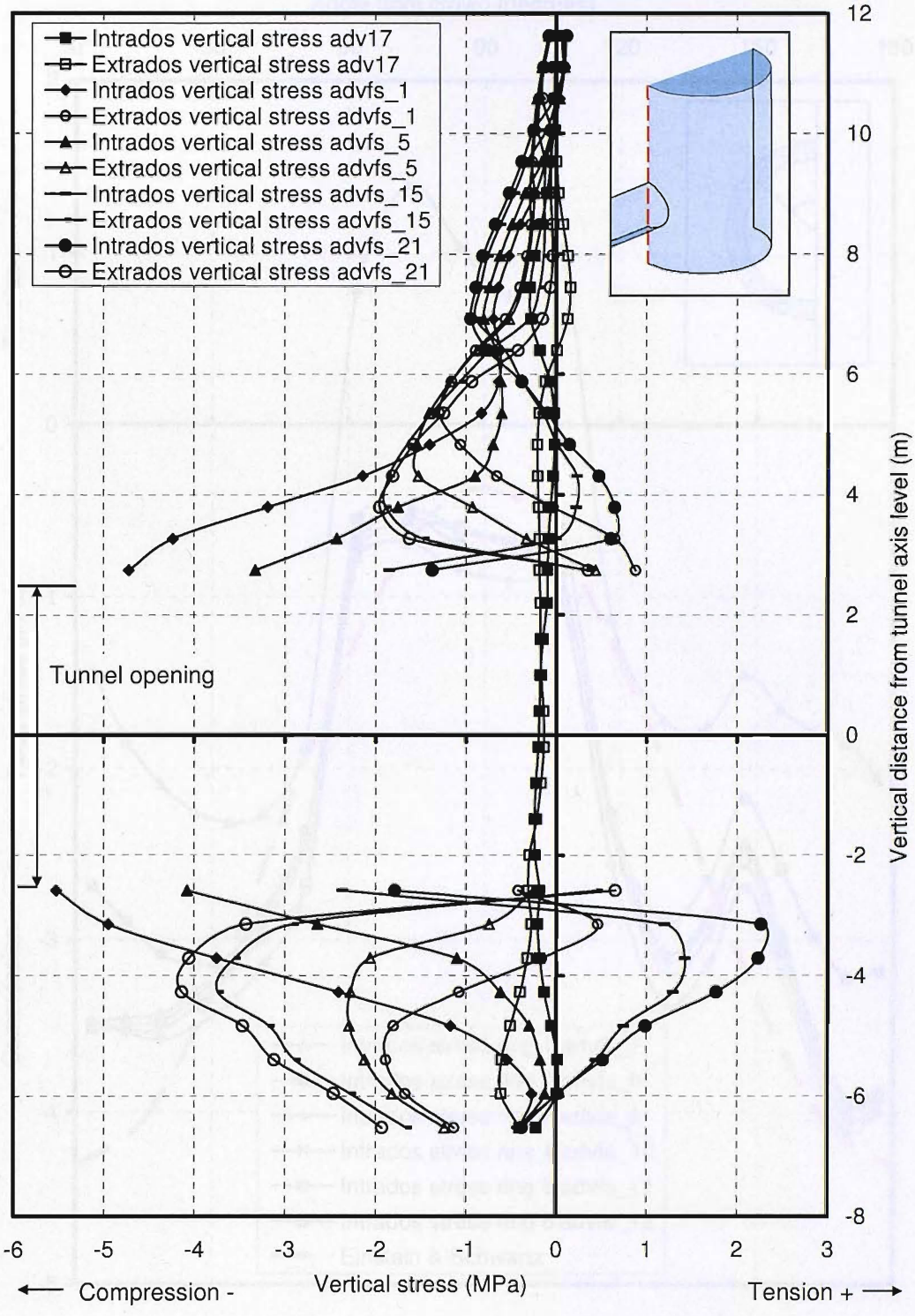

Figure 5-22: Vertical stress in the shaft lining above and below the tunnel centreline as the tunnel length increases for model with no connection between shaft and tunnel lining shells

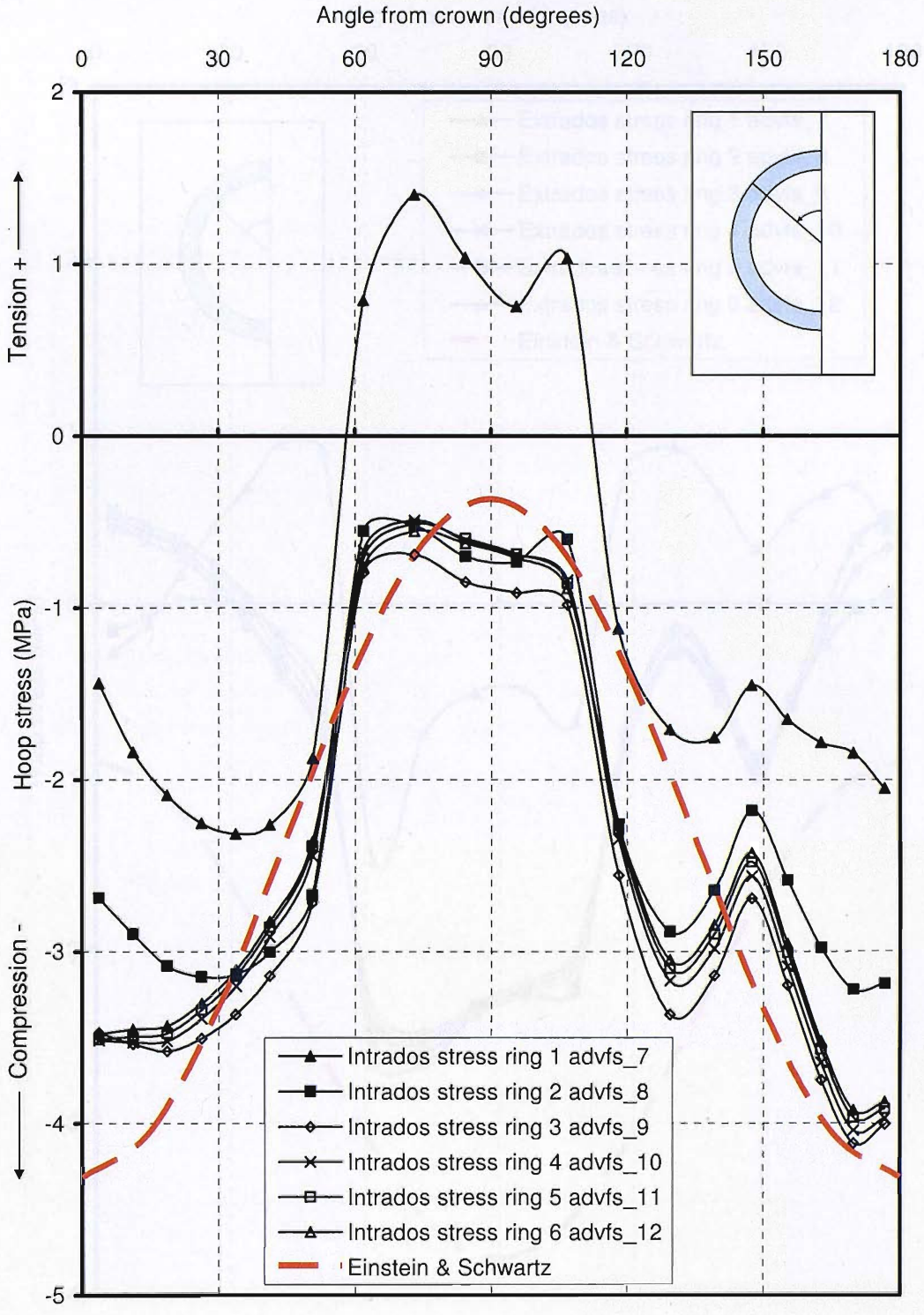

Figure 5-23: Intrados hoop stress 5th ring from face, various locations – tunnel and shaft not connected

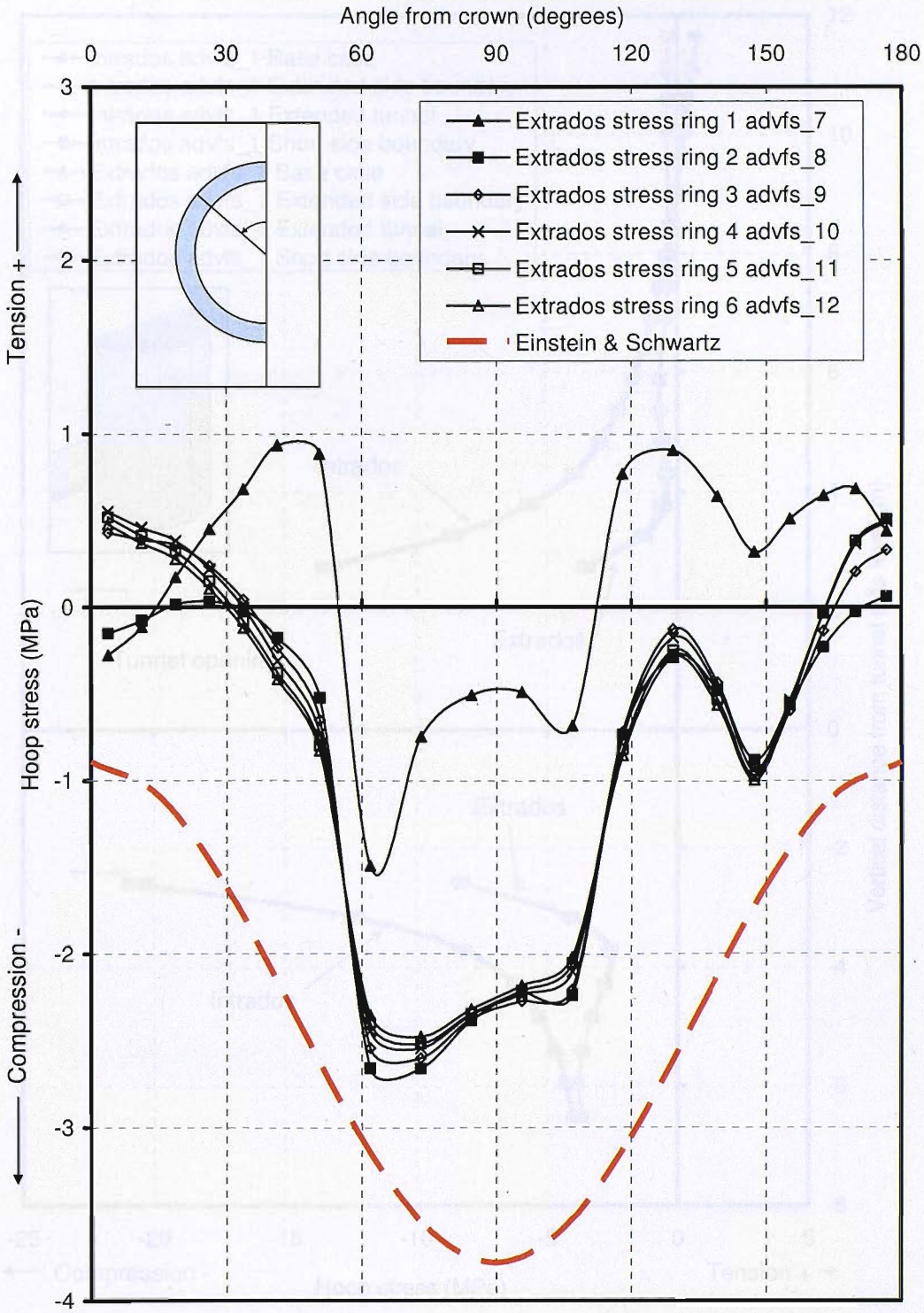

Figure 5-24: Extrados hoop stress for the 5th ring from the face, various locations – tunnel and shaft not connected

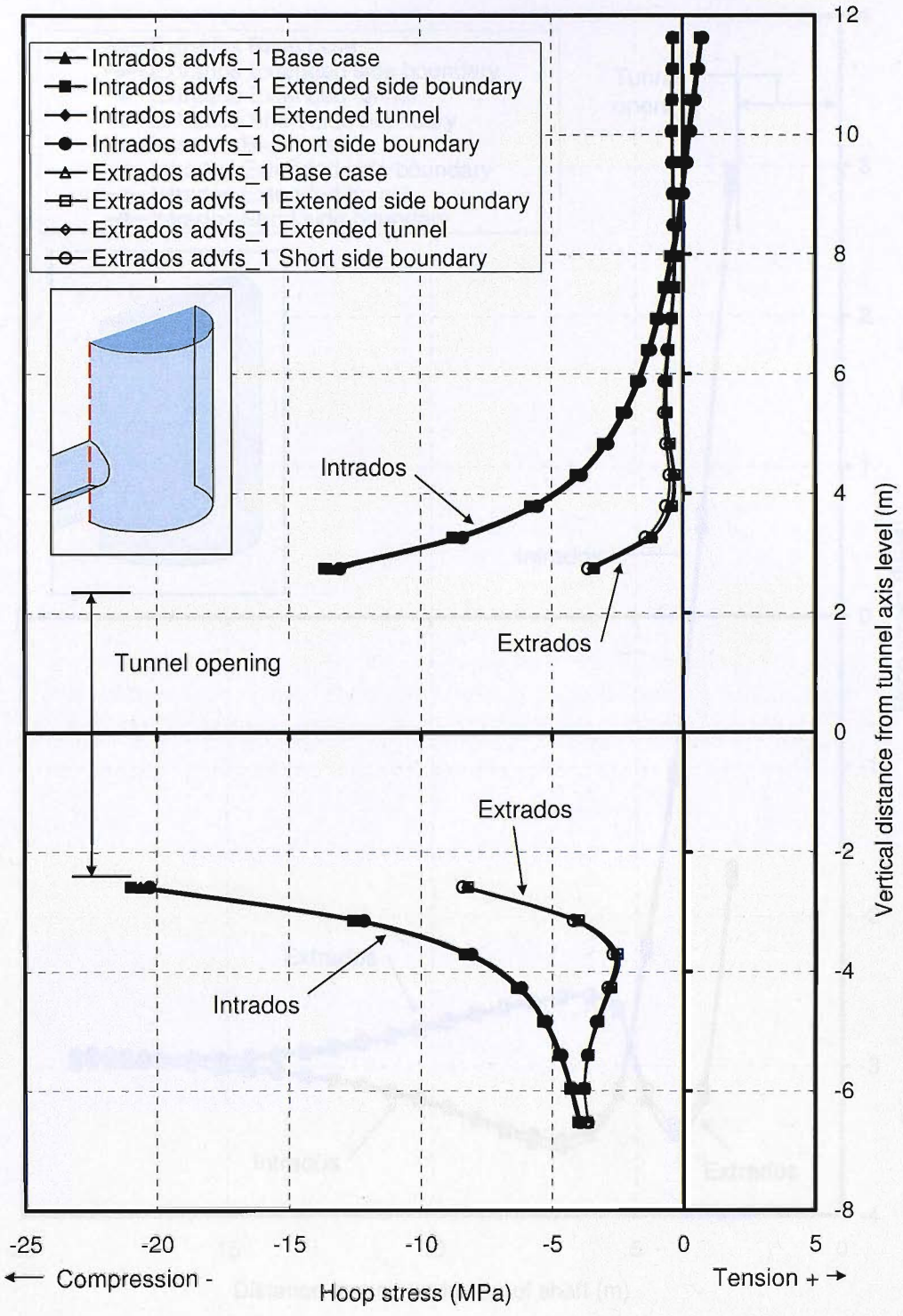

Figure 5-25: Effect of boundary distances on the shaft lining hoop stresses at stage advfs_1 (creation of opening) above and below the tunnel centreline

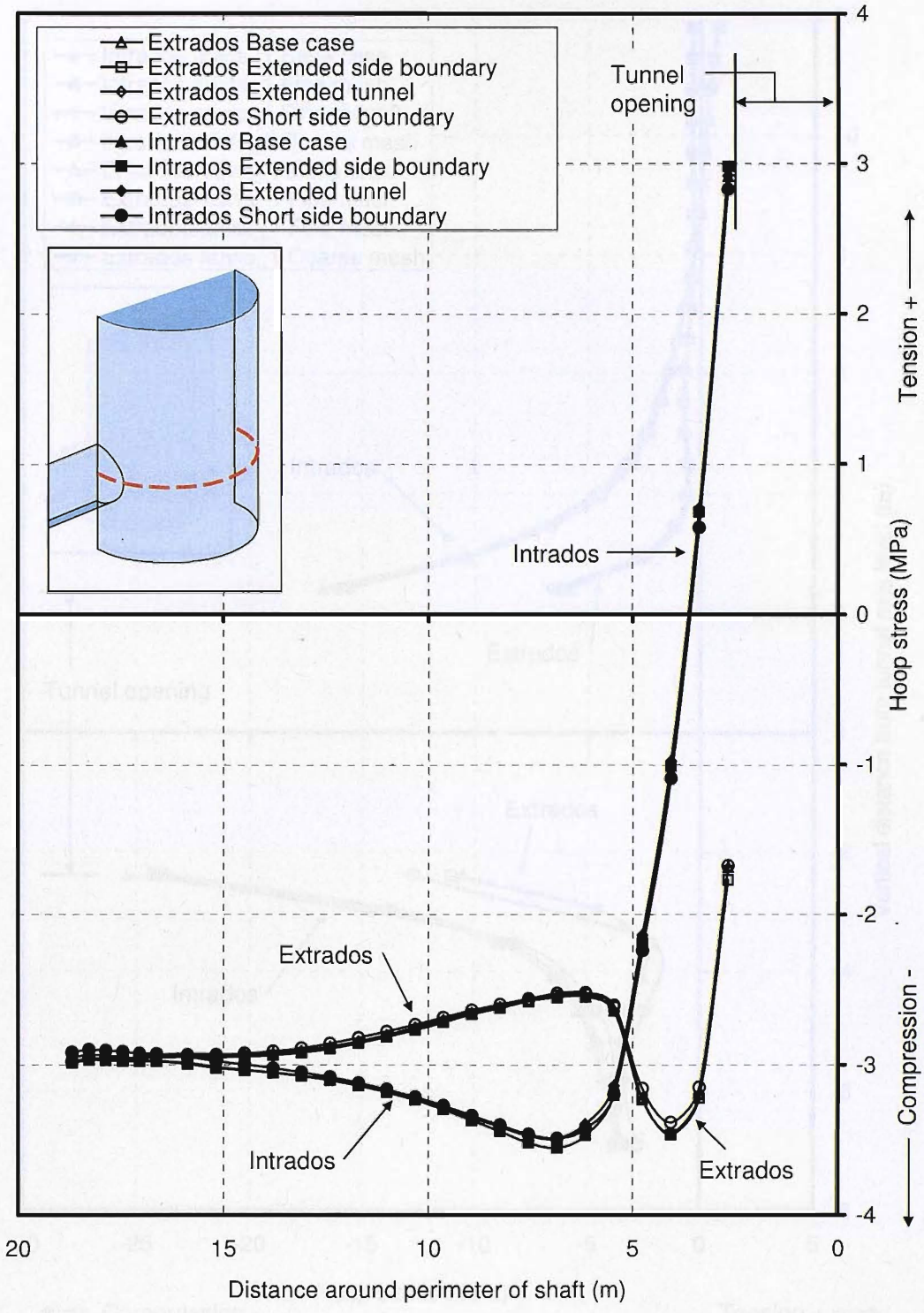

Figure 5-26: Effect of boundary distances on the shaft lining hoop stresses at stage advfs_1 at tunnel axis level

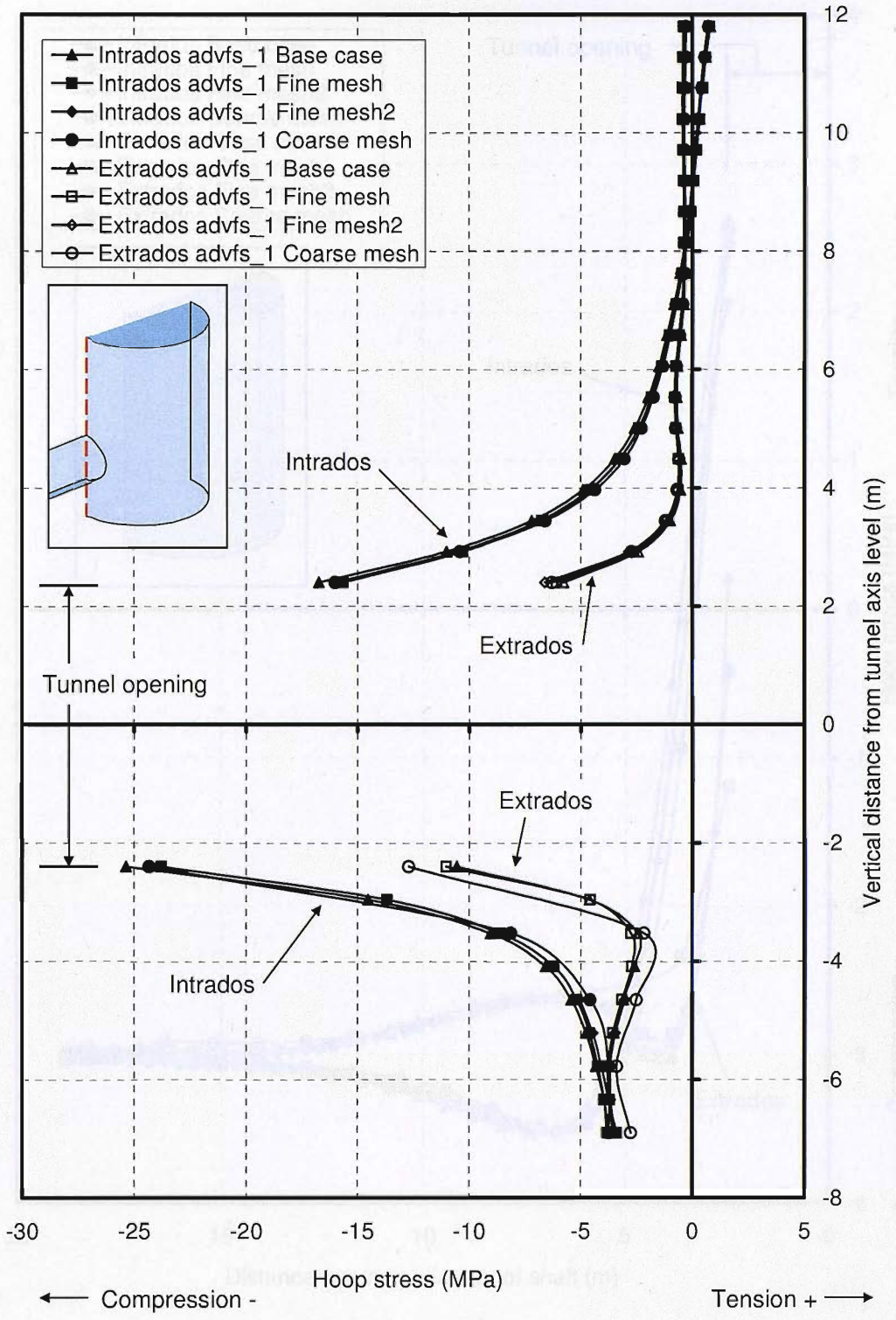

Figure 5-27: Effect of mesh refinement on the shaft lining hoop stresses at stage advfs_1 above and below the tunnel centreline

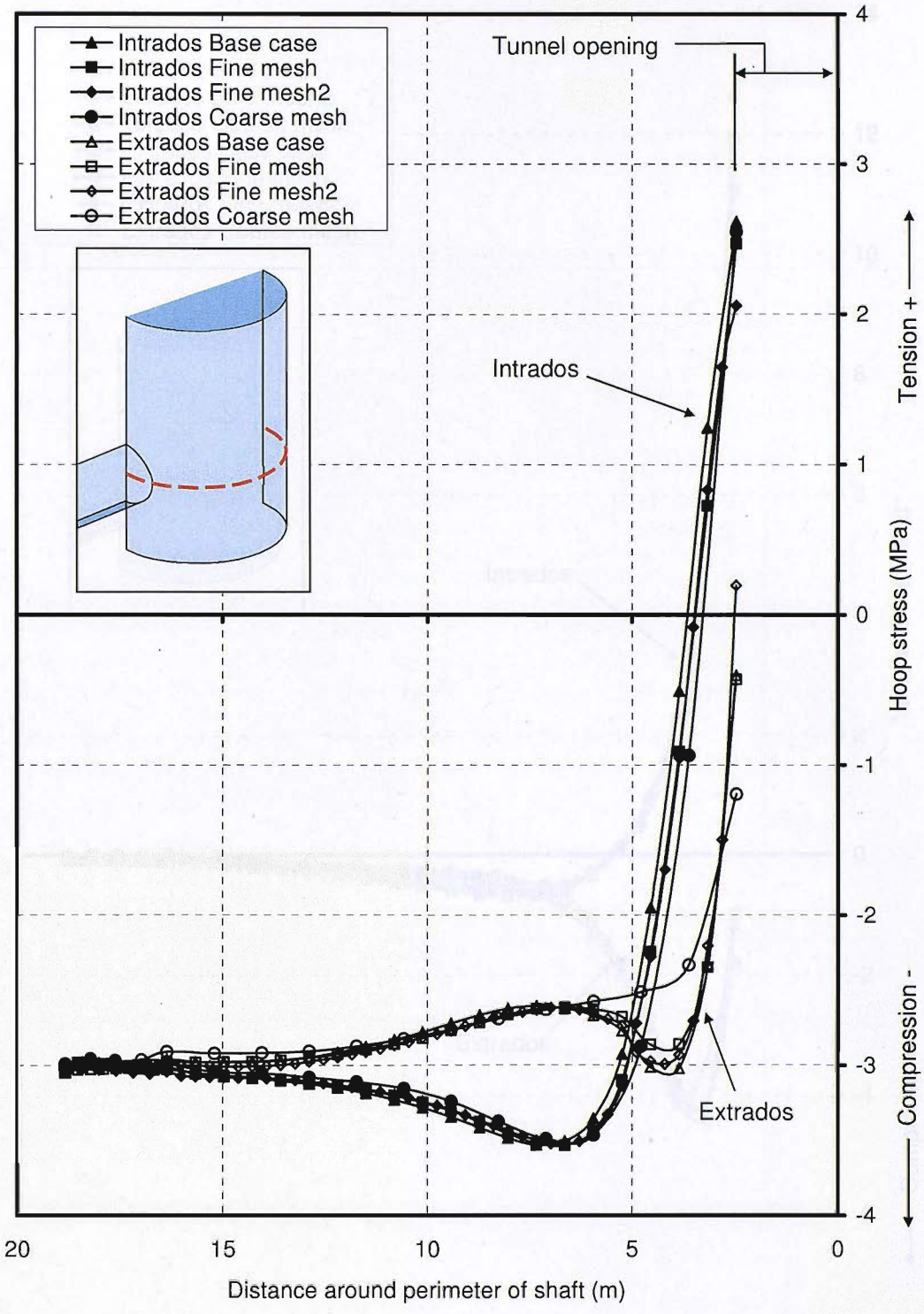

Figure 5-28: Effect of mesh refinement on the shaft lining hoop stresses at stage advfs_1 at tunnel axis level

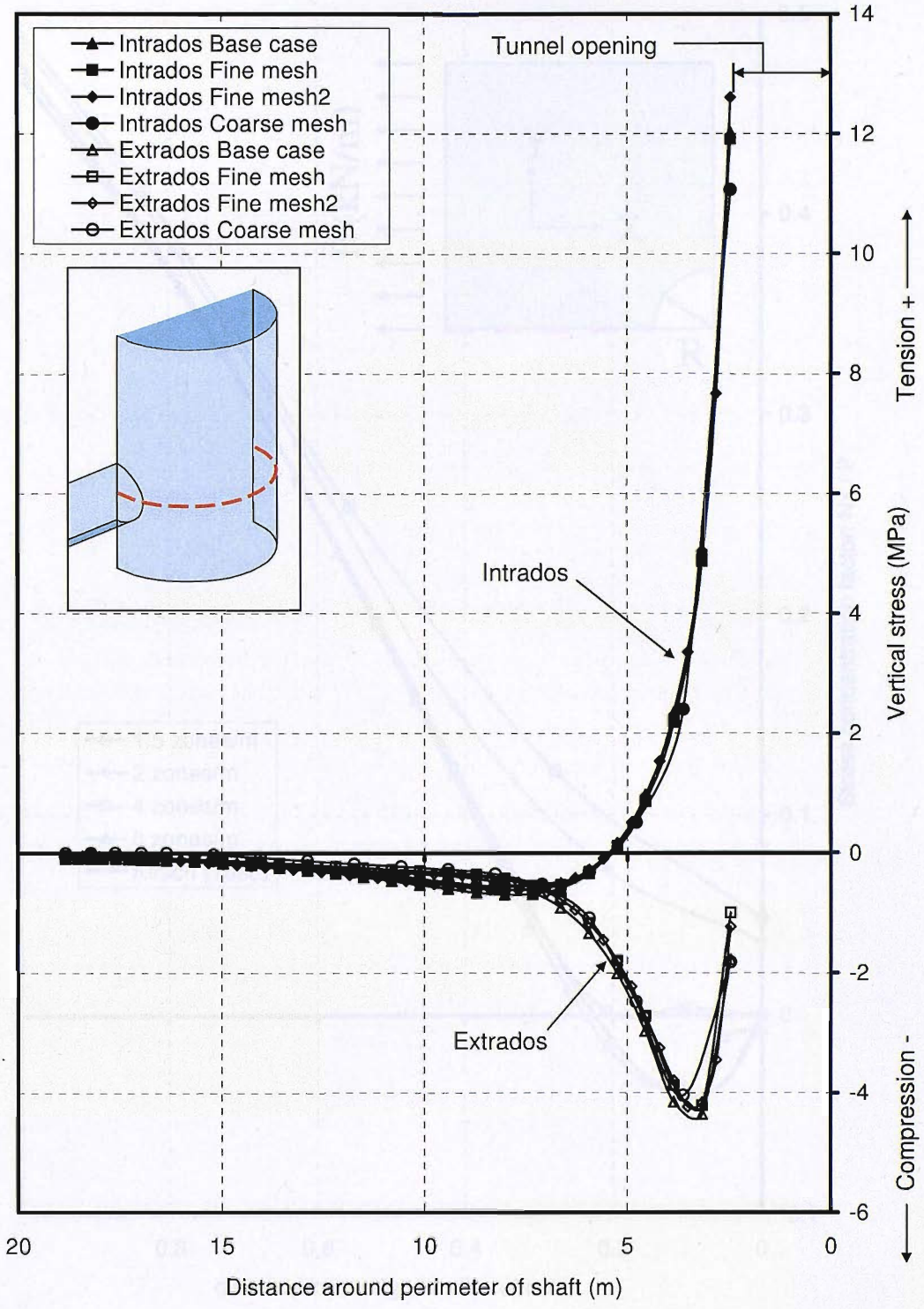

Figure 5-29: Effect of mesh refinement on the shaft lining vertical stresses at stage advfs_1 at tunnel axis level

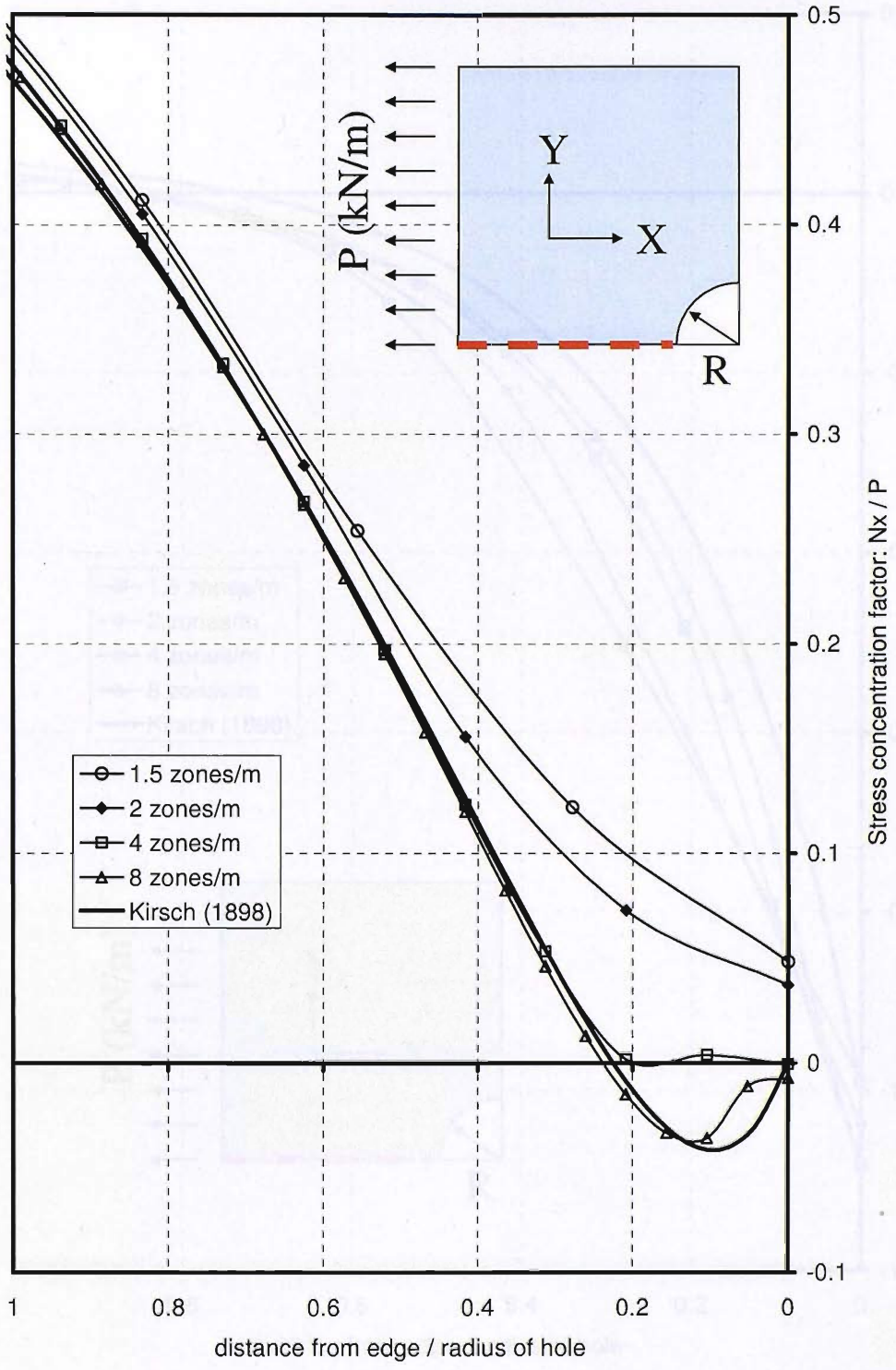

Figure 5-30: Stress concentration factor for a plane stress plate with a hole in the direction of the applied stress (Nx/P) along a line parallel to the direction of the applied stress.

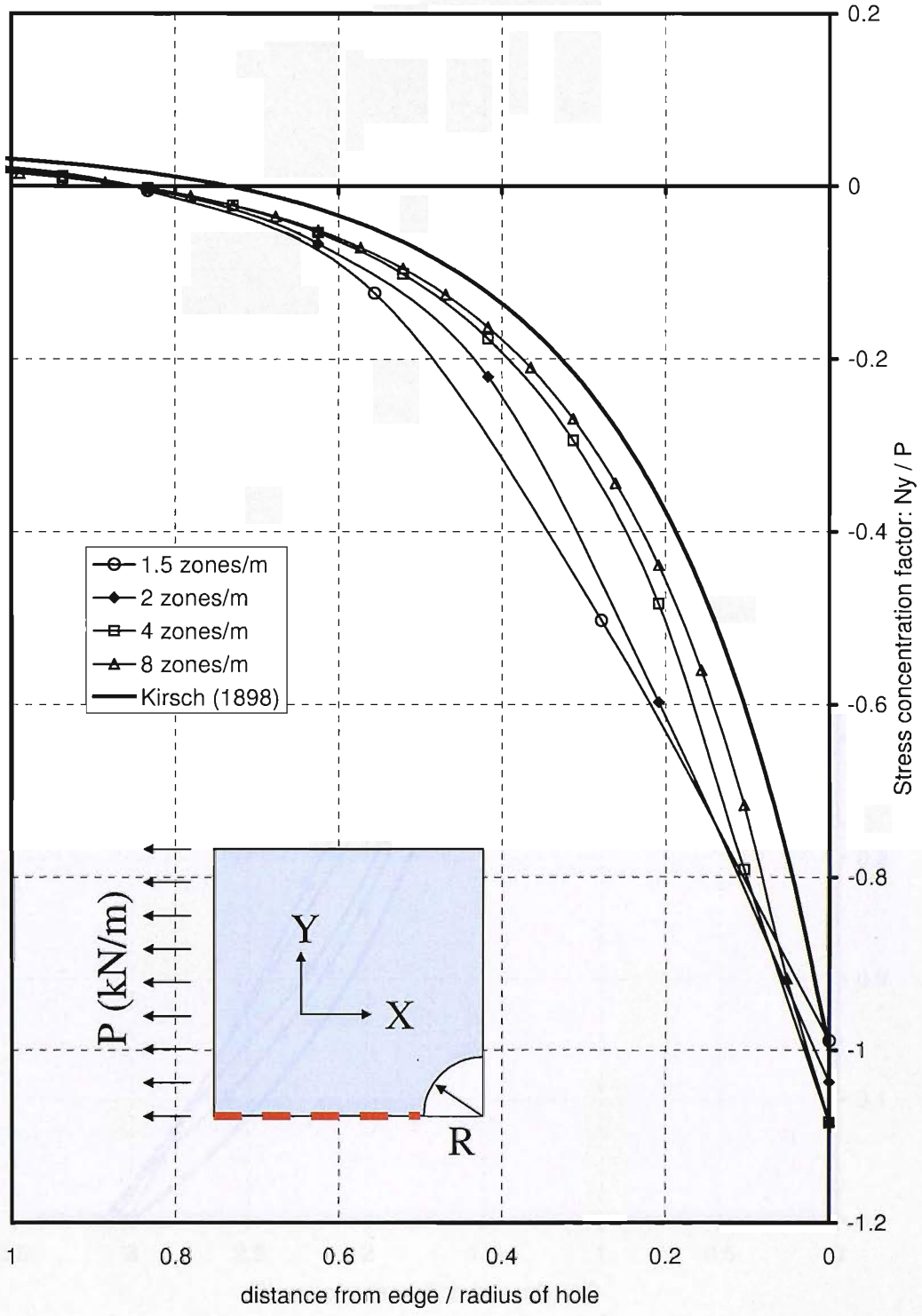

Figure 5-31: Stress concentration factor for a plane stress plate with a hole in the direction transverse to the applied stress (Ny/P) along a line parallel to the direction of the applied stress.

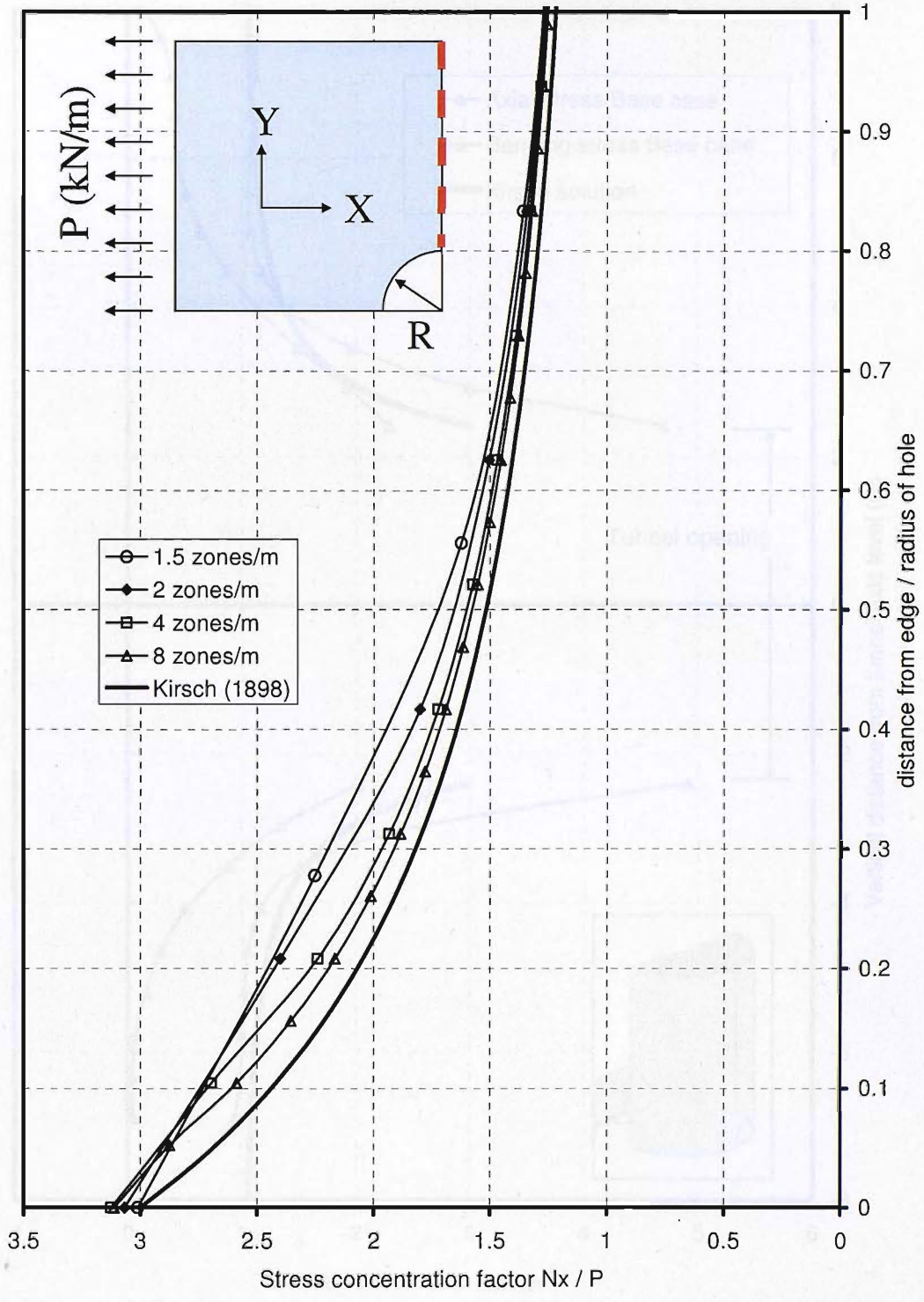

Figure 5-32: Stress concentration factor for a plane stress plate with a hole in the direction parallel to the applied stress (Nx/P) along a line transverse to the direction of the applied stress.

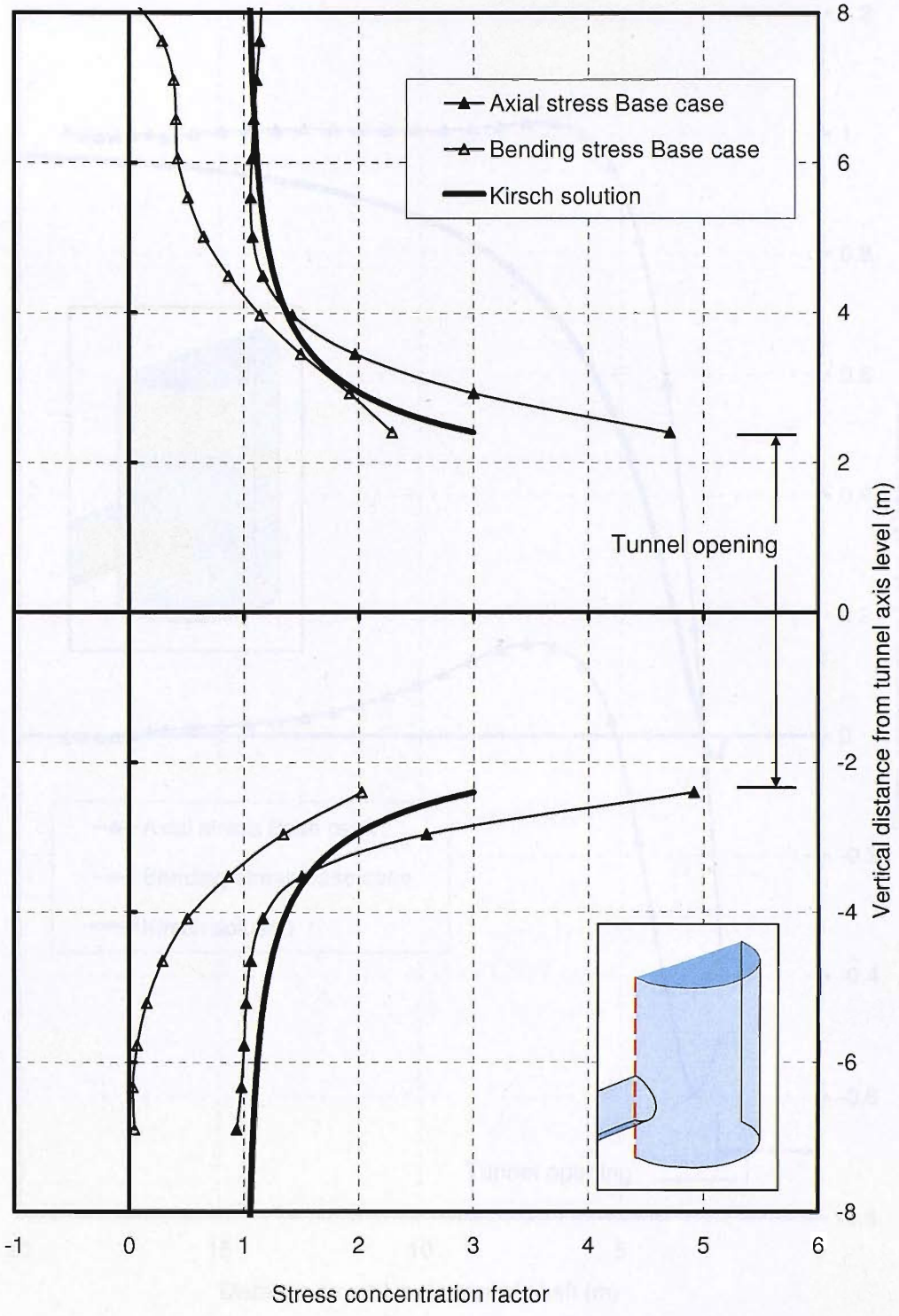

Figure 5-33: Comparison of stress concentration factor for hoop stress in the shaft lining above and below the tunnel centreline with Kirsch analytical solution.

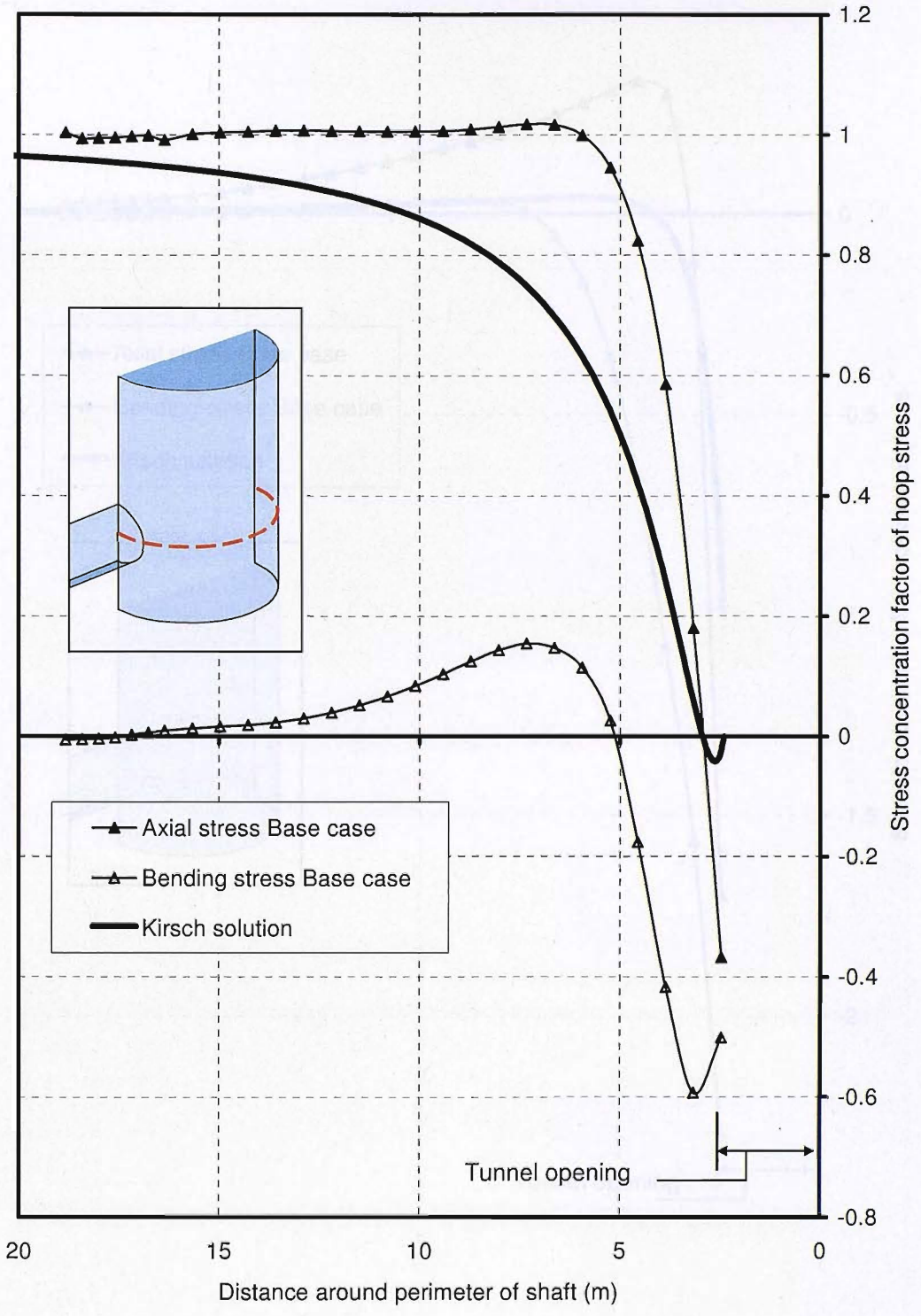

Figure 5-34: Comparison of stress concentration factor for hoop stress in the shaft lining at tunnel axis level with Kirsch analytical solution.

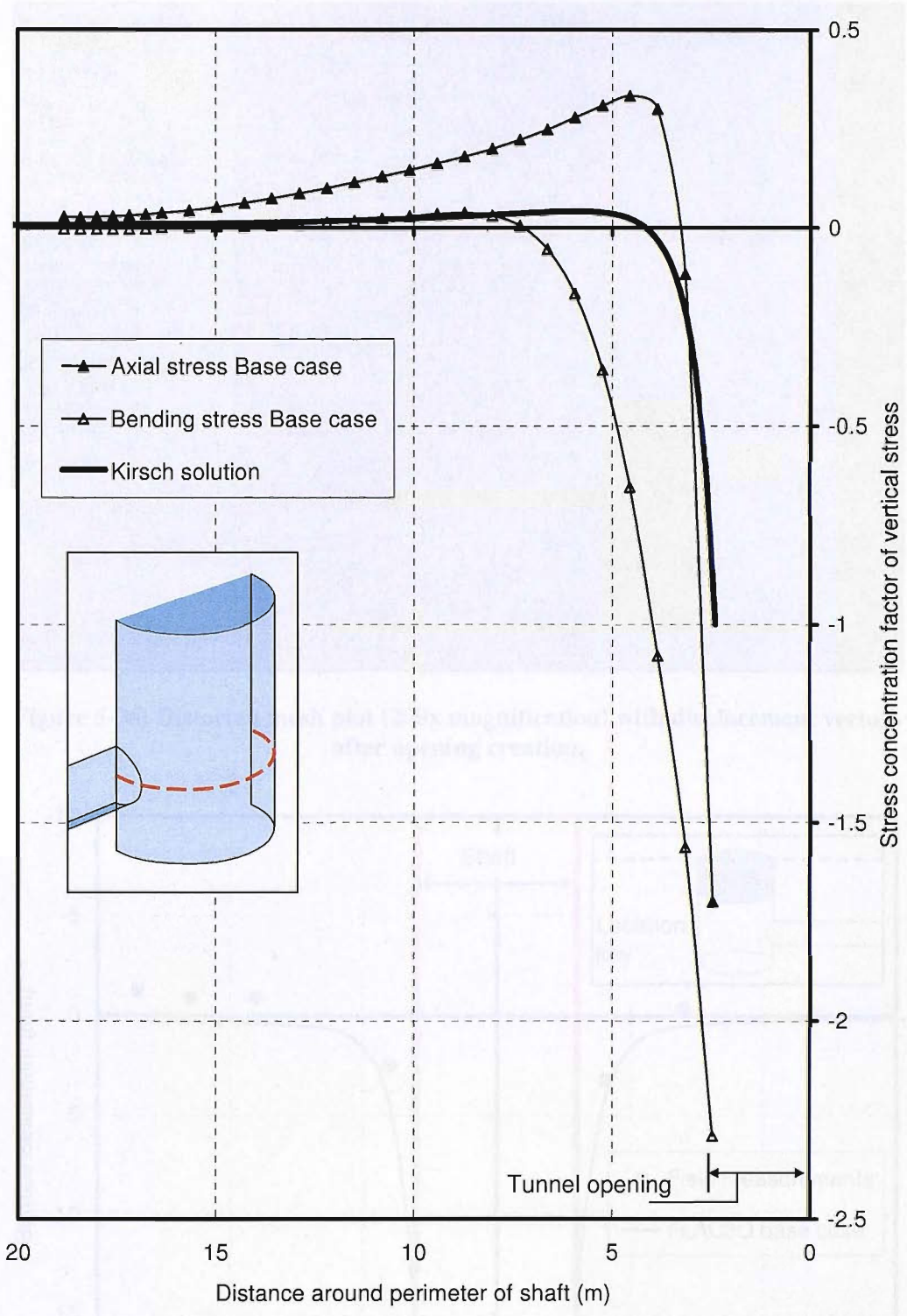

Figure 5-35: Comparison of stress concentration factor for vertical stress in the shaft lining at tunnel axis level with Kirsch analytical solution.

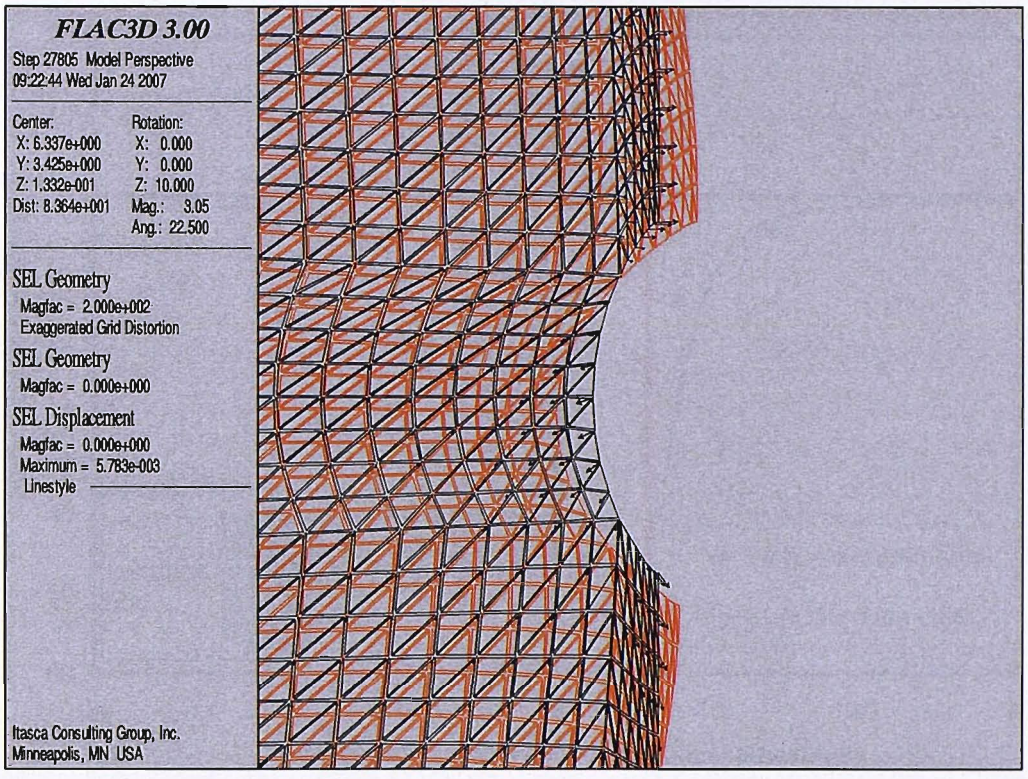

Figure 5-36: Distorted mesh plot (200x magnification) with displacement vectors after opening creation.

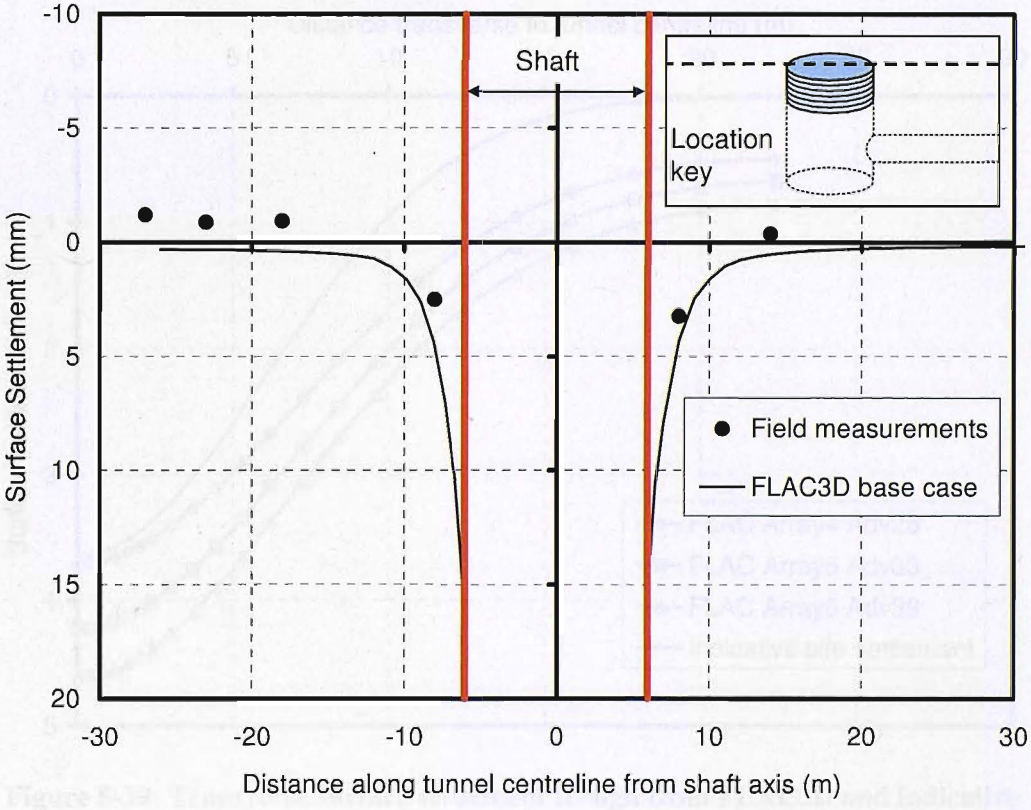

Figure 5-37: Comparison of base case predicted surface settlements and field measurements at the start of SCL shaft construction (first 7 m depth was constructed using the caisson-sinking method with precast concrete segments)

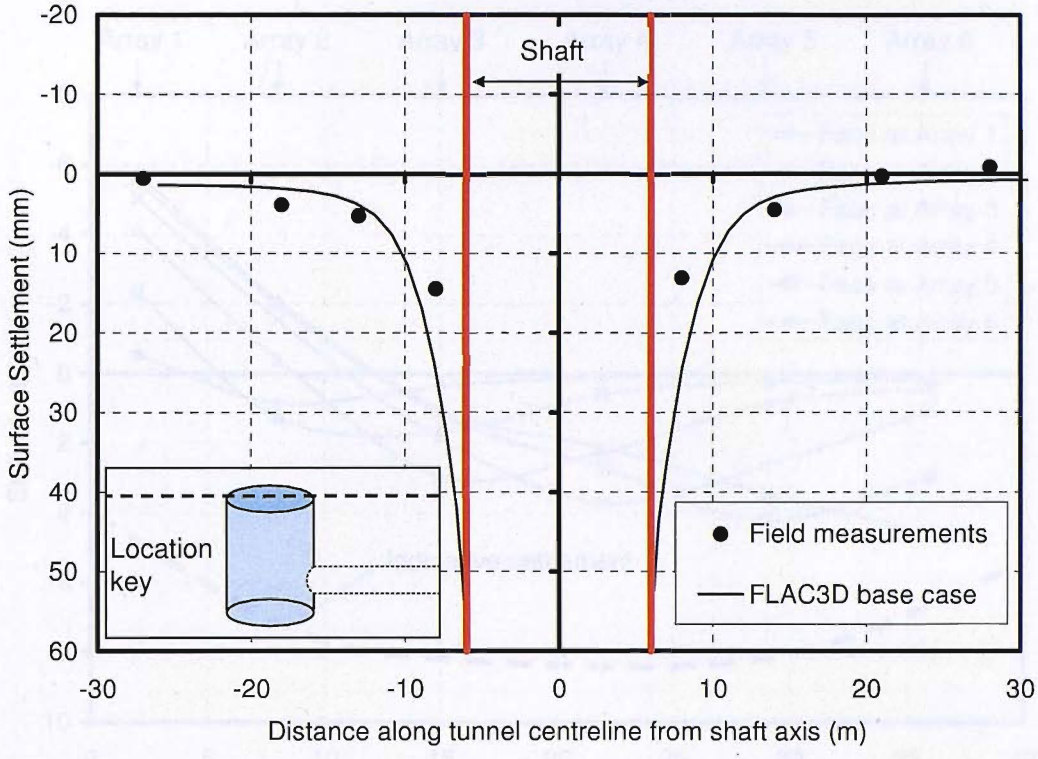

Figure 5-38: Comparison of base case predicted surface settlements and field measurements on completion of shaft construction

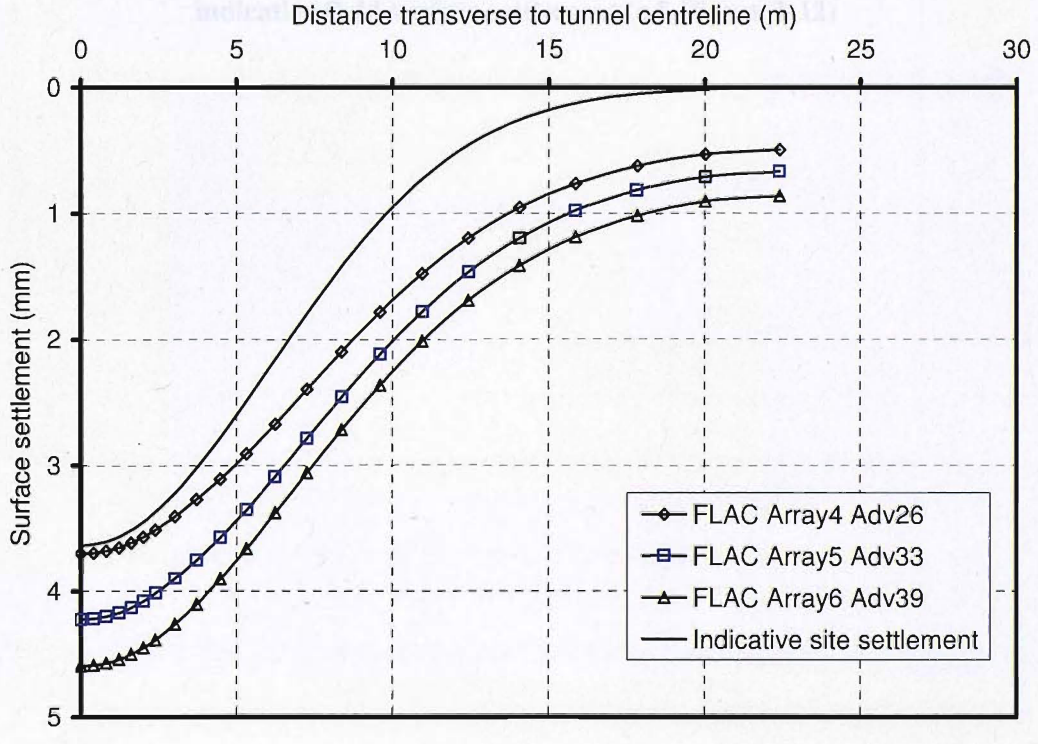

Figure 5-39: Transverse surface settlement trough from FLAC3D and indicative site settlement profile when the face is under the transverse array (c.f. Figure 3-10)

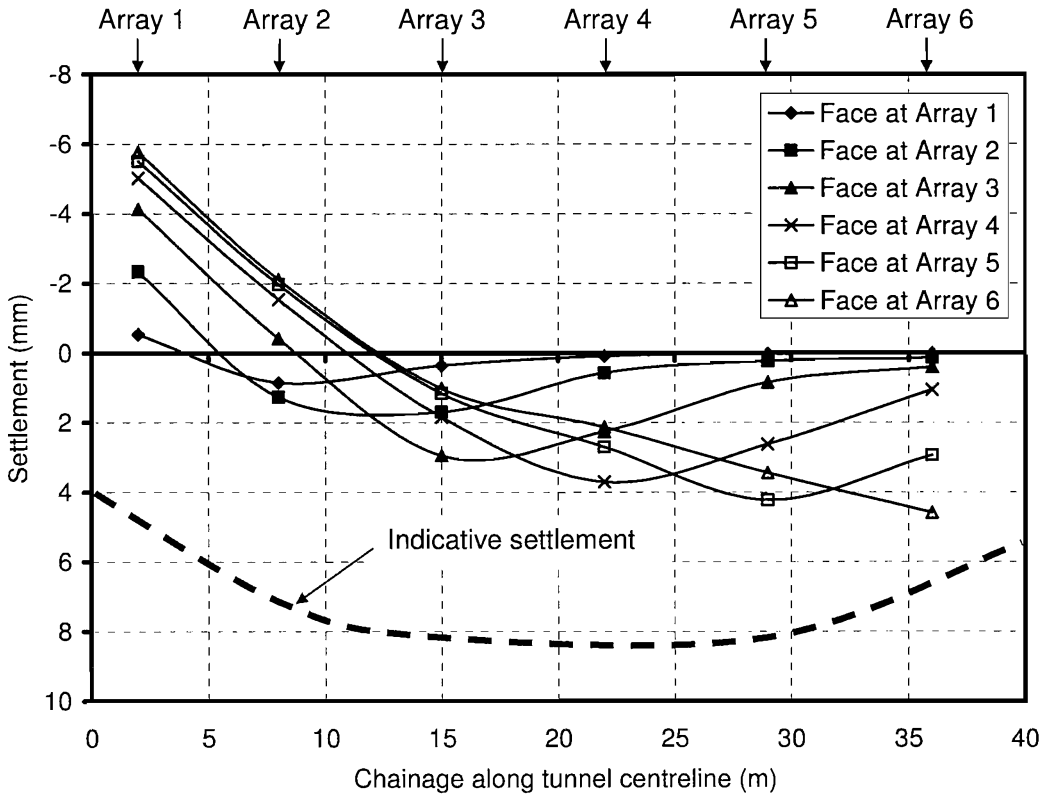

Figure 5-40: Longitudinal surface settlement profile calculated by FLAC^{3D} and indicative field surface settlement (c.f. Figure 3-12)

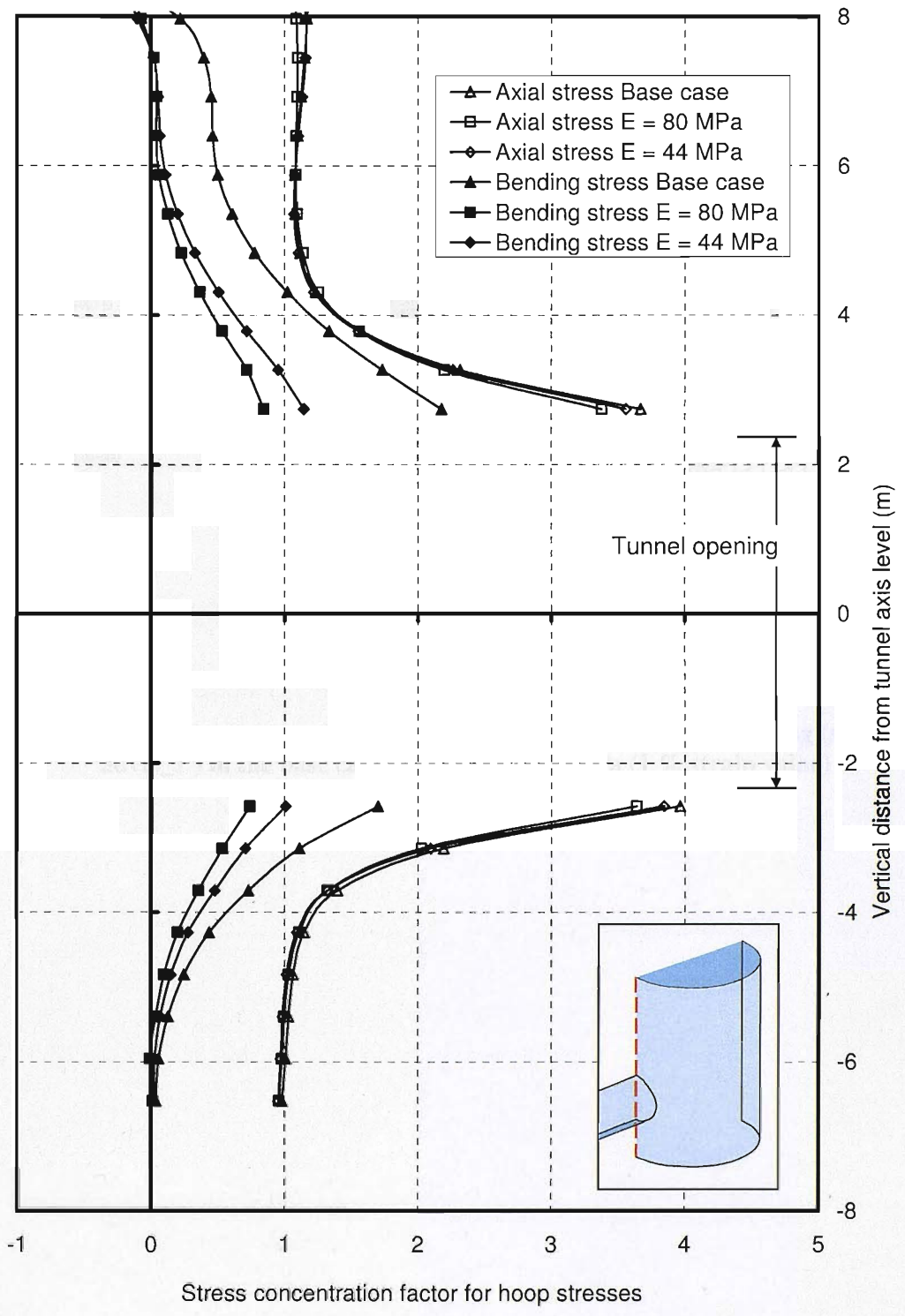

Figure 5-41: Effect of ground stiffness on hoop stress concentration factor above and below the tunnel centreline

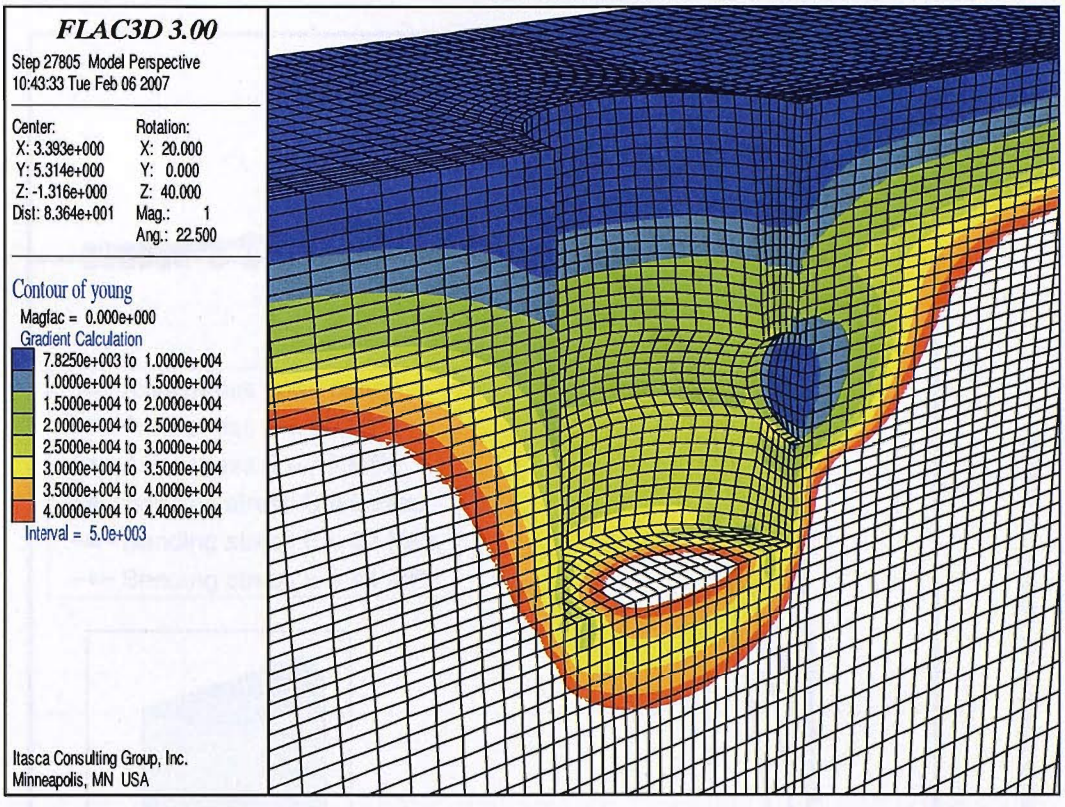

Figure 5-42: Young's modulus of the soil after creation of the opening (stage 'advfs_1') in the base case; values up to 44 MPa (1 % strain value)

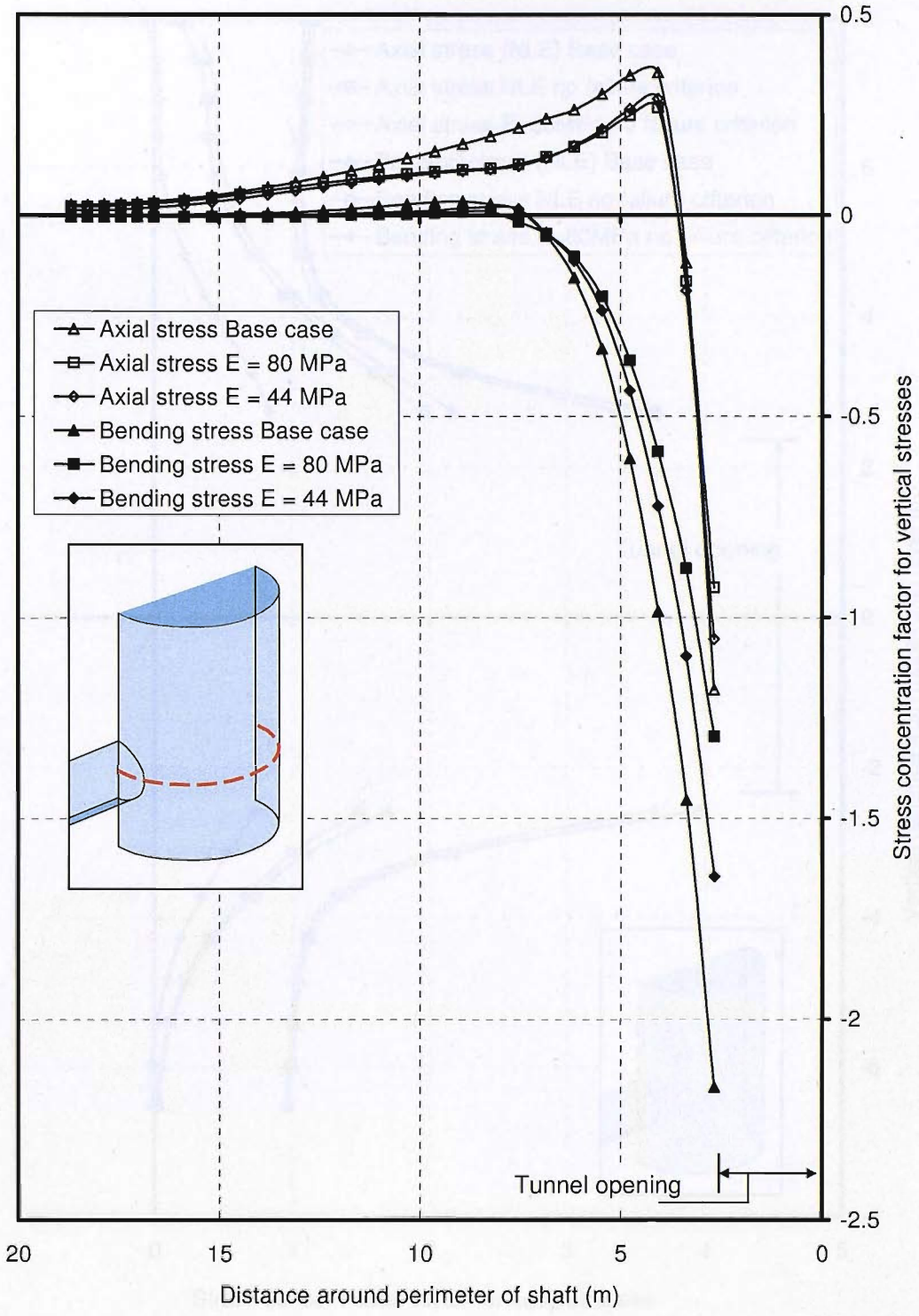

Figure 5-43: Effect of ground stiffness on vertical stress concentration factor at tunnel axis level

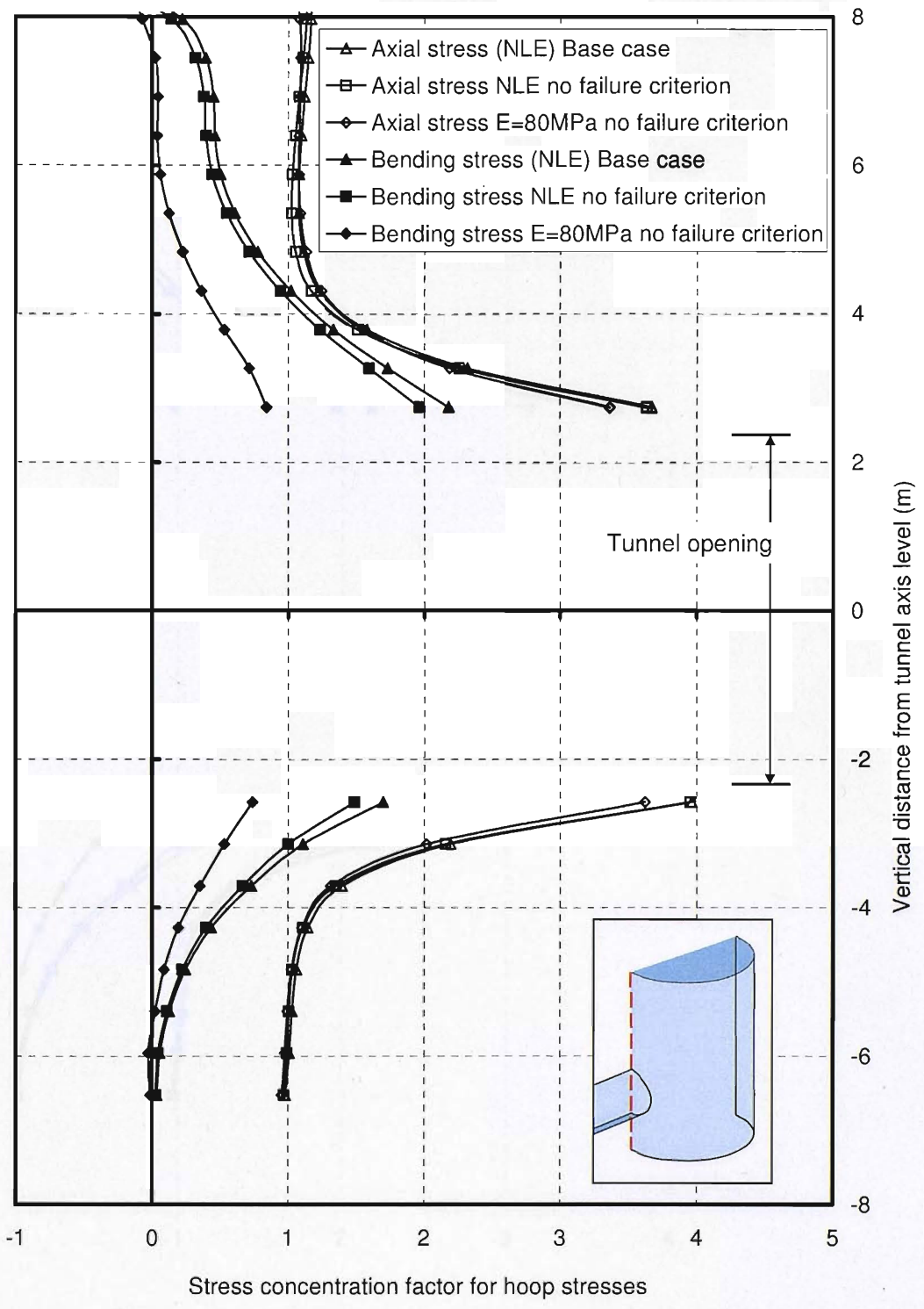

Figure 5-44: Effect of ground stiffness without a failure criterion on hoop stress concentration factor above and below the tunnel centreline (NLE = nonlinear elastic)

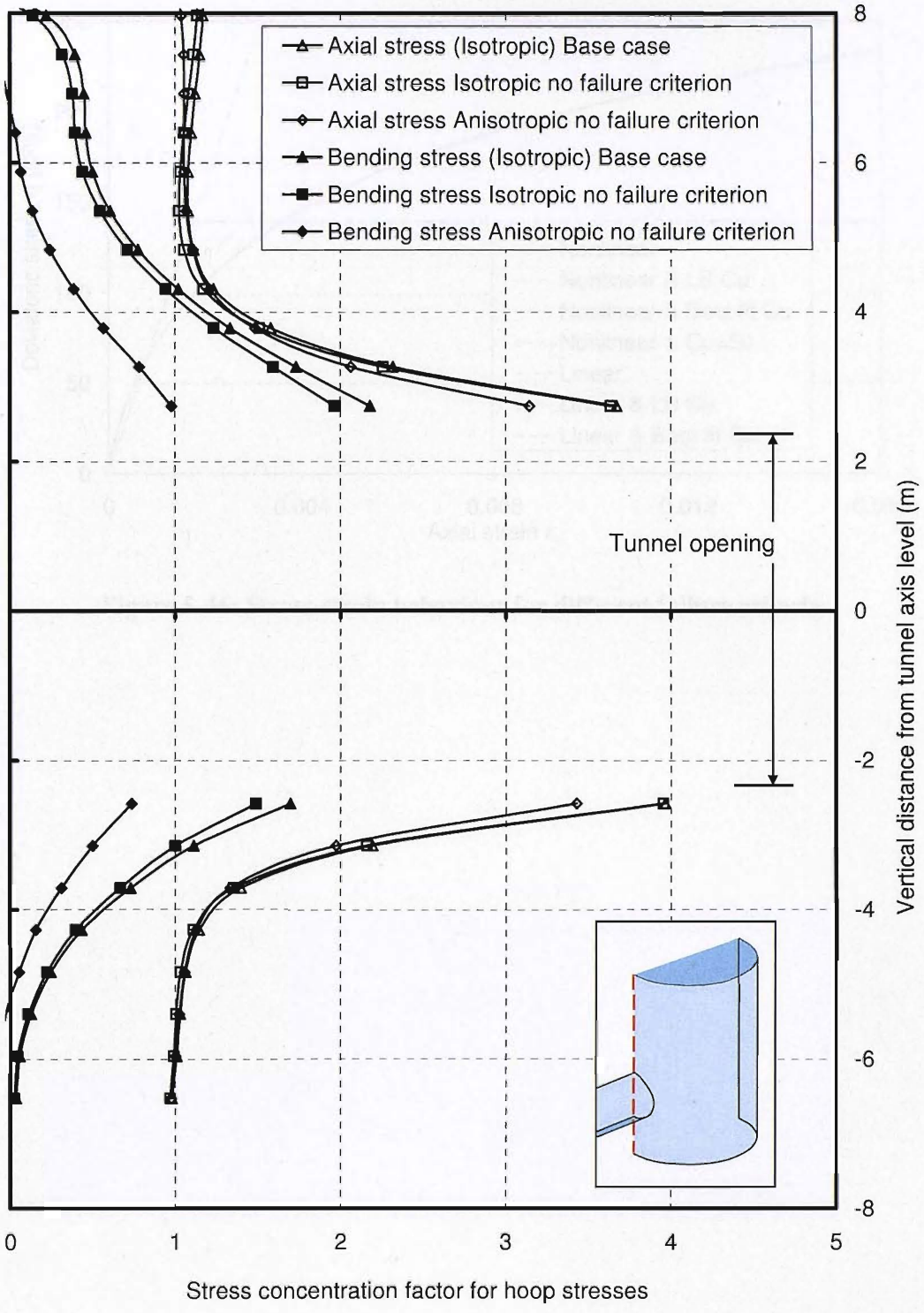

Figure 5-45: Effect of ground stiffness anisotropy on hoop stress concentration factor above and below the tunnel centreline

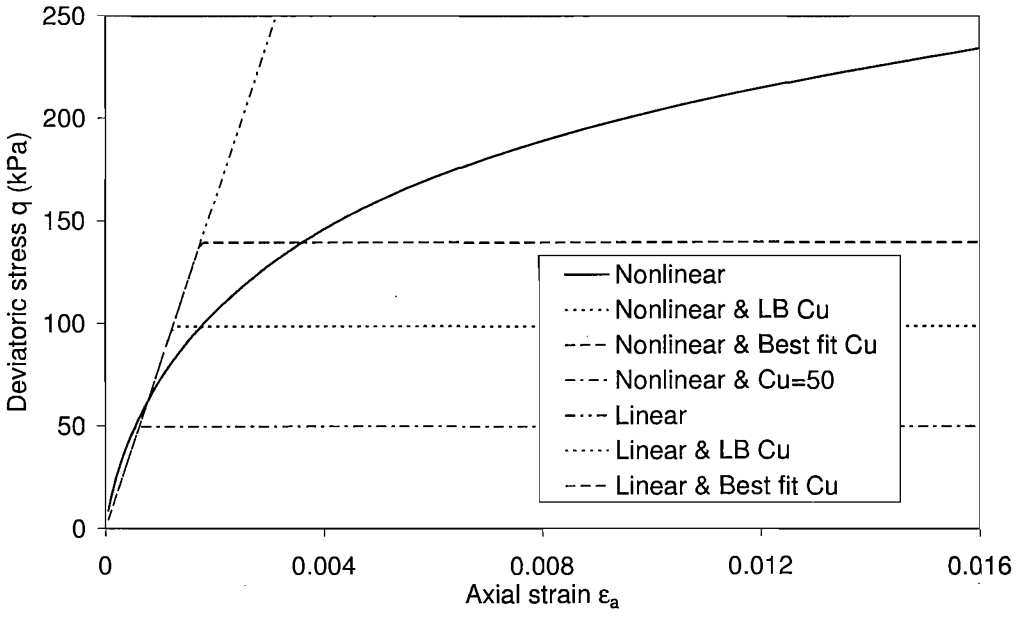

Figure 5-46: Stress-strain behaviour for different failure criteria

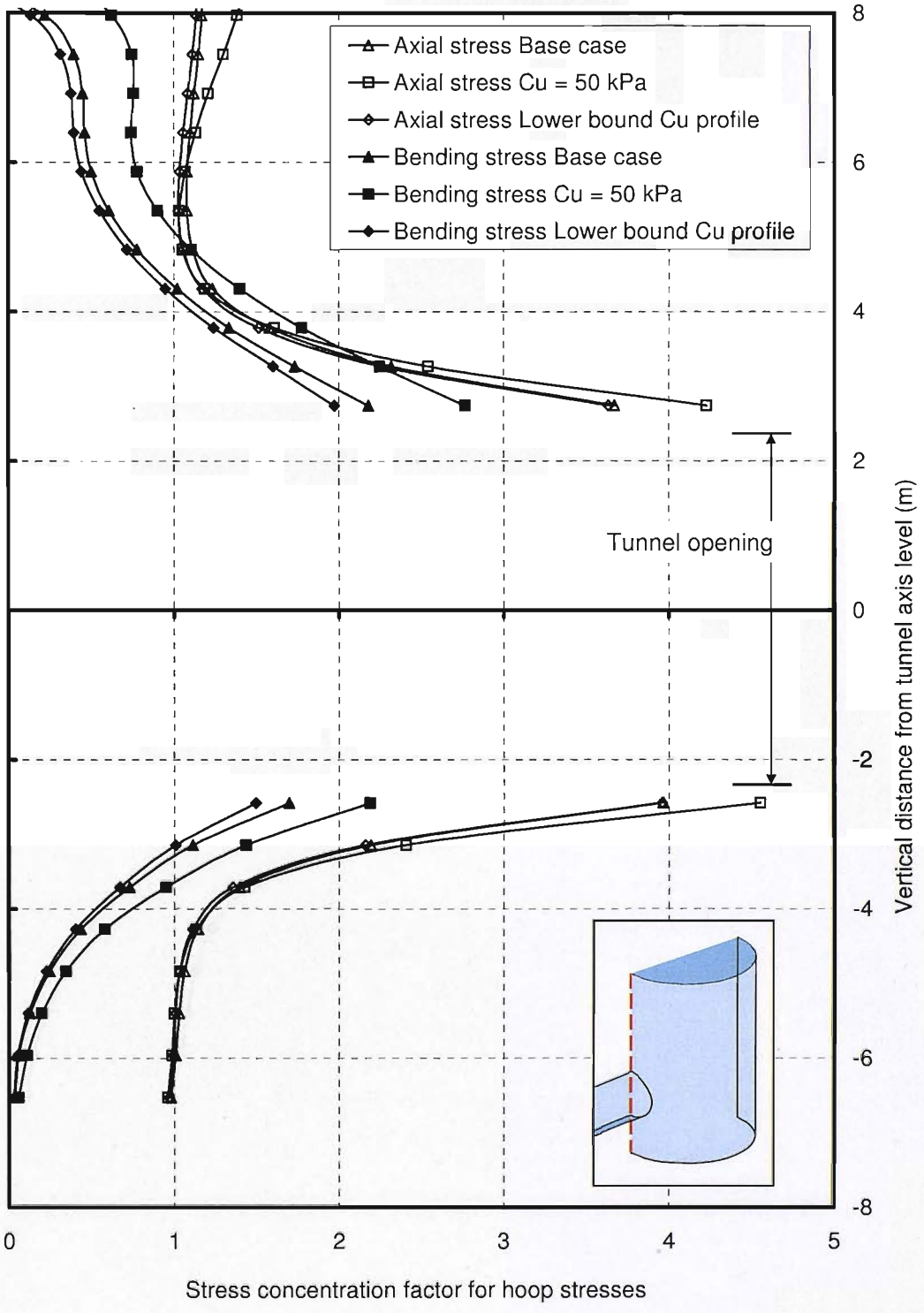

Figure 5-47: Effect of failure criterion on hoop stress concentration factor above and below the tunnel centreline

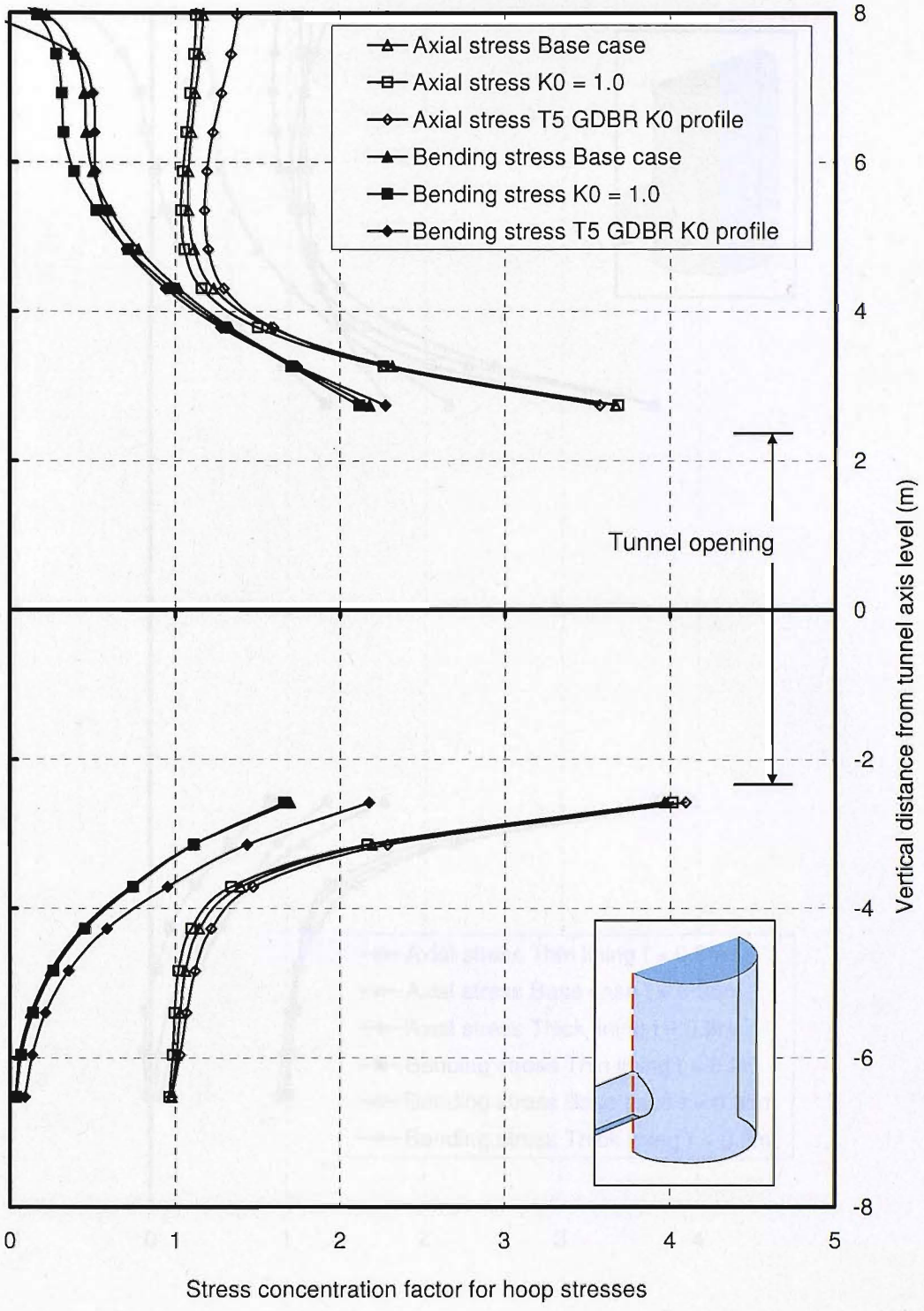

Figure 5-48: Effect of K_0 profile on hoop stress concentration factor above and below the tunnel centreline

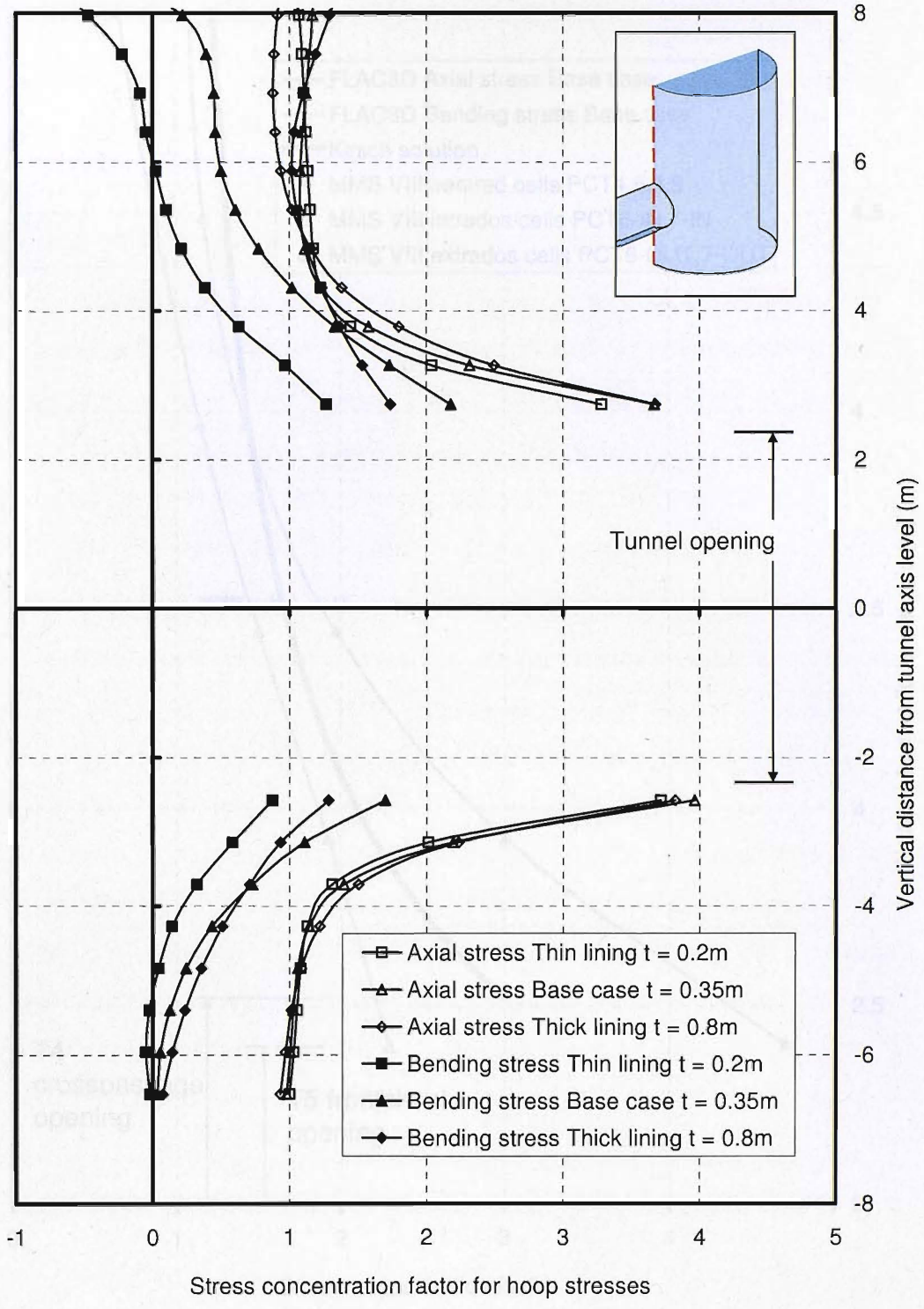

Figure 5-49: Effect of lining thickness on hoop stress concentration factor above and below the tunnel centreline

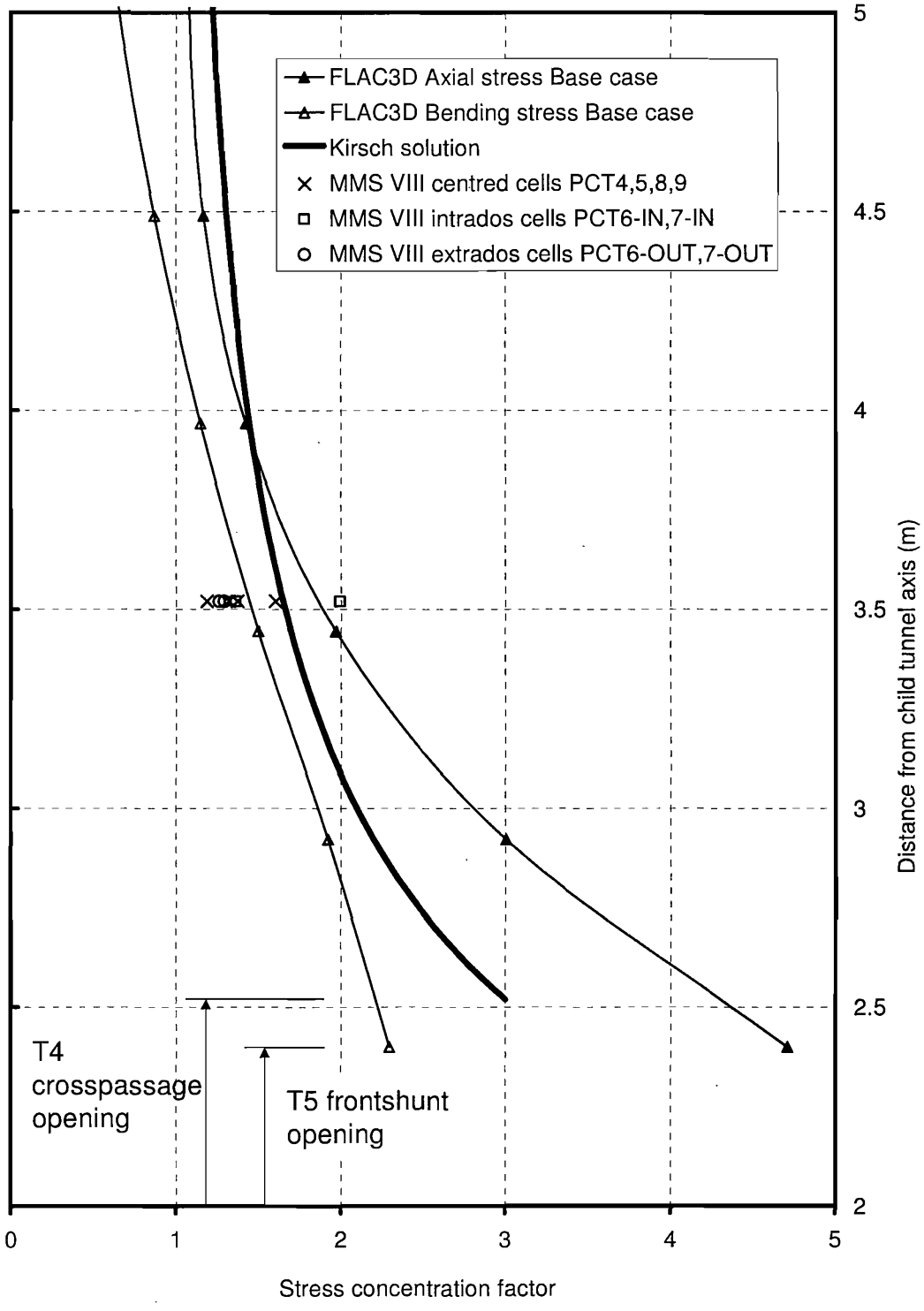

Figure 5-50: Stress concentration factors from MMS VIII compared to the Kirsch analytical solution and the results of 3D modelling

6 CONCLUSIONS

The objectives of the research were to improve the methods of stress prediction and stress measurement in sprayed concrete linings.

The literature review concluded that stress measurement is required for design verification as part of a holistic risk management process for SCL tunnels.

Measurements of stress may be obtained using a variety of methods. However, slot-cutting, overcoring and undercoring only provide a one-off measurement in mature concrete and back-calculation of stresses from measured displacements was found to introduce too many errors to provide meaningful results. Pressure cells provide continuous measurement, and in Chapter 4 it was demonstrated that if they are interpreted carefully they can provide reasonably accurate measurements of radial and tangential stress in an SCL tunnel.

In Chapter 4, three different types of temperature sensitivity were identified; the temperature sensitivity of the vibrating wire and transducer, the cell restraint temperature sensitivity and the ground reaction temperature sensitivity. Each must be treated in a different way. Cell restraint temperature sensitivity was found to only occur in tangential cells and can give an indication of the quality of the installation. Ground reaction temperature sensitivity of pressure cells has never before been identified, but was found to account for long-term fluctuations in radial pressure cell data that may have previously been ascribed to unreliability. Strain sensitivity of pressure cells was also identified in Chapter 4 and investigated using a finite element model.

The interpretation of tangential pressure cell data should follow the following steps:

1. Make adjustment for temperature sensitivity of the vibrating wire and vibrating wire transducer (using manufacturer's calibration).
2. Remove any zero offset.
3. Remove any crimping offset.
4. Check for lost pressures, i.e. check if the pressure cell has at any time lost contact with the sprayed concrete (the read pressure is zero).

5. Estimate cell restraint temperature sensitivity from test panel data and estimate its variation with time during early age. Apply correction.
6. Estimate shrinkage pressure development with time from the test panel data and subtract from readings.

The interpretation of radial pressure cells should follow the following steps:

1. Make adjustment for temperature sensitivity of the vibrating wire and vibrating wire transducer (using manufacturer's calibration).
2. Remove any zero offset.
3. Remove any crimping offset.
4. Check for lost pressures if the pressure cell has at any time lost contact with the sprayed concrete or ground. This is unlikely in the case of radial cells.

Radial cells are therefore more reliable because there are fewer steps required in their interpretation. Furthermore, while steps 1-4 are fairly straightforward, steps 5 and 6 in the interpretation of tangential cells (not required for the interpretation of radial cells) are also the steps that introduce the largest errors. Even accounting for these errors, it was shown that tangential cells will still provide useful measurements of stress.

By following the recommendations set out in this thesis, it should now be possible to make a reasonably accurate estimate of *absolute* values of radial and tangential stress using pressure cells.

A review of previous stress measurements in shallow tunnels in London Clay indicated that behaviour may be characterised by one of the following two categories:

1. Tunnels which experience more than 80 % of the maximum long-term radial pressure in fewer than 7 days.
2. Tunnels which experience less than 60 % of the maximum long-term radial pressure in the first 7 days, and subsequently pressures continue to increase at a gradual rate for a long period.

It was shown that tunnels with low volume losses tended to fall into category 1, and tunnels with large volume losses tended to fall into category 2. This was explained by the degree of permanent unloading that the ground around the tunnel experienced during construction. The T5 SWOT frontshunt tunnel was in category 1 and had a volume loss of 0.63 %. The T4 concourse tunnel top heading and bench were in category 1, while the invert was in category 2. The T4 concourse tunnel had a volume loss of 0.8 %.

The majority of the load came onto the lining soon after the ring was closed at T4 and T5. In the case of the T5 SWOT frontshunt tunnel, the excavation was full-face with the ring closed immediately, so the heat of hydration caused the ring to expand against the ground resulting in a maximum load at the peak temperature of hydration of up to approximately 100 % of hydrostatic full overburden pressure. This also demonstrated the importance of ground reaction temperature sensitivity. At T4 and T5 the maximum long-term ground pressure stabilised at a value well below full overburden pressure.

Sprayed concrete linings (SCL) are frequently the preferred choice of support for short lengths of tunnel and for complex geometries and arrangements of tunnels. This means that junctions are not exceptions, but commonplace SCL structures. Despite this fact, the majority of research effort has in the past concentrated on straight lengths of SCL tunnel.

The literature review of previous work on tunnel junctions came to the conclusion that a 3D numerical model with ground and excavation sequences modelled explicitly must be used if a reasonable prediction of stress concentrations is to be obtained. This was borne out by the modelling described in Chapter 5, where it was found that bending stresses, construction sequence and explicit modelling of the ground-structure interaction had a significant and usually unfavourable effect on the stress concentrations around a junction. The maximum axial stress concentration factor was about 5 and the maximum bending stress concentration factor was just over 2 for the base case model, resulting in a maximum stress concentration of approximately 7. Compared to Kirsch's analytical solution (Hoek & Brown, 1980), which predicted a maximum stress concentration factor of 3, or the simple 3D models of Lew (1976) or Hocking (1978), which predicted even smaller stress concentrations of less than

2, the values found in Chapter 5 were much higher. Therefore, the simpler methods should be avoided and 3D numerical modelling used whenever possible.

A modelling methodology for design of SCL tunnel junctions was developed that was feasible to implement on a standard PC, and was shown to provide reasonable results. A mesh density of 1.4 zones/m was used around the shaft and tunnel and the minimum boundary distance used was 20 m (equal to 1.7 times the diameter of the shaft, or 4.2 times the diameter of the tunnel). The shaft construction was approximated by a relaxation method, and the tunnel was excavated in stages. Each model, including calibration of the relaxation method, took approximately 2.5 days to run on a 2.9 GHz Pentium 4 PC.

The tunnel was consistently found to have lower stresses than it would have experienced if the shaft were not present, i.e. the junction was beneficial to the child tunnel. This was contrary to the predictions of the wished-in-place models described in the literature review.

There were problems with the sequential excavation of the tunnel, with ground movements around the tunnel towards the face inducing longitudinal stresses in the tunnel, which pulled at the junction with the shaft. This meant that the effect of the tunnel construction did not diminish with distance from the shaft. Disconnecting the shaft and tunnel reduced the magnitude of this effect, but the tunnel still acted as a stiff dowel in the ground, transferring shear stresses from the face of the tunnel to the shaft.

Axial stress concentration factor was unaffected by stiffness, nonlinearity, anisotropy and plasticity of the ground, or its *in situ* stress distribution.

Bending stress concentration factor was affected by the stiffness of the ground and to a lesser extent the undrained shear strength of the ground. *In situ* stress distribution did not have a significant effect on bending stress concentration factor, but this conclusion may not hold true for a tunnel-tunnel junction or for a non-circular parent tunnel.

The lining thickness had very little effect on axial stress concentration factor, but a significant and complex effect on bending stress concentration factor. In spite of this, the lining thickness had a relatively small overall effect on the combined

stress concentration factor. Therefore it was considered unlikely that a design would need to iterate more than once to arrive at the optimal lining thickness.

The tangential stresses measured at MMS VIII in the Terminal 4 concourse tunnel, 1 m from the edge of the crosspassage openings, showed good agreement with the predictions from the numerical modelling. A high stress concentration due to bending stress demonstrated that the Kirsch analytical solution was unconservative.

Further work is required to investigate the effect of child tunnel longitudinal stresses and ground movements on the parent tunnel of an SCL junction. This is important because designers need to know how much of the child tunnel construction needs to be modelled. This work may need to include field measurements as well as numerical analyses.

This thesis has clarified the requirements for successful prediction of stress concentrations around SCL tunnel junctions. Mesh refinement, boundary distances and the influence of soil parameters and lining thickness have been investigated. Further parametric studies to investigate the influence of geometry are recommended to include in the first instance varying the ratio of the diameters of the parent and child tunnels, and investigation of tunnel-tunnel junctions as well as shaft-tunnel junctions.

Using more complex constitutive models for the sprayed concrete lining would not be possible in FLAC^{3D} without the use of zones (solid elements). The large number of zones required to produce sufficiently accurate results, according to the recommendations of Pound (2006), precludes this approach at the present time. It may be possible in the near future, either by using a different analysis program, by optimising the number of zones required, or by using more powerful computing resources, to achieve this.

Field measurements of stresses and deformations in and around SCL tunnel junctions are required to increase confidence in the ability of 3D numerical analysis to make reasonable predictions of behaviour. SCL junctions are, after all, commonplace, not atypical SCL structures.

REFERENCES

Acker, P. & Ulm, F. -J. (2001). Creep and shrinkage of concrete: physical origins and practical measurements. *Nuclear Engineering and Design* **203**, 143-158.

ACI 209R-92 (1992). *Prediction of creep, shrinkage and temperature effects in concrete structures*, ACI Committee 209, American Concrete Institute. Michigan, USA: ACI.

ACI 318-89 (1989). *Building code requirements for structural concrete.* ACI Committee 318, American Concrete Institute. Michigan, USA: ACI.

ACI 363R-92 (1992). State-of-the-art report on high-strength concrete (reapproved 1997). *2004 ACI Manual of Concrete Practice*, Part 5, American Concrete Institute. Michigan, USA: ACI.

Addenbrooke, T. I., Potts, D. M. & Puzrin, A. M. (1997). The influence of pre-failure soil stiffness on the numerical analysis of tunnel construction. *Géotechnique* **47**, No.3, 693-712.

AFTES (1992a). *Working group no.6 recommendations on sprayed concrete*, prepared by M. Legrand. Paris: AFTES.

AFTES (1992b). *Working group no.7 temporary and permanent support*, prepared by P. Gesta. Paris: AFTES.

AFTES (2001). *Recommendations on the convergence-confinement method*, prepared by M. Panet. Paris: AFTES.

Aldrian, W. & Kattinger, A. (1997). Monitoring of performance of primary support of NATM station at Heathrow Terminal 4. *Proc. of Tunnels for People* (eds. J. Golser, W. J. Hinkel and W. Schubert), pp.71-77. Rotterdam:Balkema.

Annett, M. F., Earnshaw, G. & Leggett, M. (1997). Permanent sprayed concrete tunnel linings at Heathrow Airport. *Proc. of Tunnelling '97, London*, pp.517-534. London: IMM Books.

ASTM C469-94 (1994). *Standard Test Method for Static Modulus of Elasticity and Poisson's Ratio of Concrete in Compression.* Philadelphia, USA: ASTM.

ASTM C1018-97 (1997). *Standard Test Method for Flexural Toughness and First-Crack Strength of Fiber-Reinforced Concrete (Using Beam with Third-Point Loading).* Philadelphia, USA: ASTM.

Atkinson, J. H. & Mair, R. J. (1983). Loads on leaking and watertight tunnel linings, sewers and buried pipes due to groundwater. *Géotechnique* **33**, No.3, 341-344.

Atkinson, J. H., Richardson, D. & Stallebrass, S. E. (1990). Effect of recent stress history on the stiffness of overconsolidated soil. *Géotechnique* **47**, No.2, 235-253.

Aydan, Ö., Sezaki, M. & Kawamoto, T. (1992). Mechanical and numerical modelling of shotcrete. In *Numerical Models in Geomechanics* (eds. G. N. Pande and S. Pietruszczak), pp.757-764. Rotterdam: Balkema.

Barla, G. & Rossi, P. P. (1983). Stress measurements in tunnel linings. *Proc. Int. Symp. on Field Measurements in Geomechanics* (ed. Kovári, K.), pp.987-998. Rotterdam: Balkema.

Barratt, D. A., O'Reilly, M. P. & Temporal, J. (1994). Long-term measurements of loads on tunnel linings in overconsolidated clay. *Proc. Tunnelling '94*, pp.469-481. London: IMM.

Bažant, Z. P. (2001). Prediction of concrete creep and shrinkage: past present and future. *Nuclear Engineering and Design* **203**, 27-38.

Bažant, Z. P. & Baweja, S. (2000). Creep and shrinkage prediction model for analysis and design of concrete structures (Model B3). In *Creep and Shrinkage of Concrete* (ed. A. Al-Manasseer), ACI Special Publication 194. Michigan, USA: ACI.

Beer, G., Sigl, O. & Brandl, J. (1997). Recent developments and application of the boundary element method. *Proc. of Numerical Models in Geomechanics* (eds. S. Pietruszczak and G. N. Pande), pp.461-467. Rotterdam: Balkema.

Belshaw, D. J. & Palmer, J. H. L. (1978). Results of a program of instrumentation involving a precast segmented concrete-lined tunnel in clay. *Can. Geotech. J.* **15**, 573-583.

Biliris, C. & Purwodihardjo, A. (2005). Numerical analysis of an opening in a bolted cast iron tunnel lining. *Proc. of Underground Construction 2005* (on CD-ROM). Brintex: London.

Binda, L., Saisi, A. & Zanzi, L. (2003). Sonic tomography and flat jack tests as complementary investigation procedures for the stone pillars of the temple of S. Nicolò l'Arena (Italy). *NDT & E International*, **36**, No.4, June, 215-227.

Bishop, A. W. & Hight, D. W. (1977). The value of Poisson's ratio in saturated soils and rocks stressed under undrained conditions. *Géotechnique* **27**, No.3, 369-384.

Bissonnette, B. & Pigeon, M. (1995). Tensile creep at early ages of ordinary, silica fume and fiber reinforced concretes. *Cement and Concrete Research* **25**, No.5, 1075-1085.

Bjerrum, L. & Eide, O. (1956). Stability of strutted excavations in clay. *Géotechnique* **6**, no.1, 32-47.

Bock, H. (2003). Geotechnical instrumentation of tunnels. In *Summerschool on Rational Tunnelling* (ed. D. Kolymbas), Innsbruck, Austria, pp.187-224. Berlin: Logos Verlag.

Bolton, M. D. (1991). *A Guide to Soil Mechanics*, 439pp. Cambridge: M D & K Bolton.

Bonapace, P. (1997). Evaluation of stress measurements in NATM tunnels at the Jubilee Line Extension Project. *Proc. of Tunnels for People* (eds. J. Golser, W. J. Hinkel & W. Schubert), pp.325-330. Rotterdam:Balkema.

Bowers, K. H. & Redgers, J. D. (1996). Discussion: Observations of lining load in a London Clay tunnel. *Proc. Int. Symp. on Geotechnical Aspects of Underground Construction in Soft Ground* (eds. Mair & Taylor), London, UK. Rotterdam: Balkema.

BRE (1995). *BRE Digest 409*, Building Research Establishment, September 1995, 8pp. Garston, UK: Building Research Establishment.

Brierley, G. S. & Cording, E. J. (1976). The behaviour during construction of the Dupont Circle subway station lining. In *Shotcrete for Ground Support, Proc. of the Engineering Foundation Conference*, Easton, Maryland, USA, pp.675-712. New York and Detroit: ASCE and ACI SP-54.

Broch, E., Grøv, E. & Davik, K. I. (2002). The inner lining system in Norwegian traffic tunnels. *Tunnelling and Underground Space Technology* **17,** 305-314.

Brooks, J. J. (1989). Influence of mix proportions, plasticizers and superplasticizers on creep and drying shrinkage of concrete. *Magazine of Concrete Research* **41**, No.148, 145-153.

Brooks, J. (1999). Shotcrete for ground support as used in the Asia Pacific region. In *RETC Proceedings 1999*, pp.473-524. Colorado, USA: SME.

Brown, D. A. (2004). Hull wastewater flow transfer tunnel: recovery of tunnel collapse by ground freezing. *Proc. Inst. Civ. Engrs Geotech. Engng* **157**, No.2, 77-83.

Brown, E. T. & Hocking, G. (1976). The use of the three dimensional boundary integral equation method for determining stresses at tunnel intersections. In *Design and Construction of Tunnels and Shafts, Proc. of the 2nd Australian Conference on Tunnelling*, pp.55-64. Victoria: Australasian Institute of Mining and Metallurgy.

Brown, E. T. (1981). Putting the NATM into perspective. *Tunnels and Tunnelling*, November, 13-17.

Bruzzi, D., Zattoni, A. & Pezzetti, G. (1999). Pressure cells: How to obtain better results. *Proc. 5th Int. Symp. on Field Measurements in Geomechanics* (eds. C. F. Leung, S. A. Tan and K. K. Phoon), Singapore, pp.61-65. Rotterdam: Balkema.

BS1881 Part 101 (1983). *Testing concrete – part 101: Method of sampling fresh concrete on site*. London: British Standards Institution.

BS1881 Part 105 (1984). *Testing concrete – part 105: Method for determination of flow*. London: British Standards Institution.

BS1881 Part 121 (1983). *Testing concrete – part 121: Method for determination of static modulus of elasticity in compression.* London: British Standards Institution.

BS8110 Part 1 (1997). *Structural use of concrete – Part 1: Code of practice for design and construction.* London: British Standards Institution.

BTS (2004). *Tunnel lining design guide*, 184pp. London: Thomas Telford.

Bürge, T. A. (2001). Mode of action of alkali-free sprayed shotcrete accelerators. In *Shotcrete: Engineering Developments, Proc. Int. Conf. Engineering Developments in Shotcrete*, Hobart, Tasmania, Australia (ed. E.S. Bernard), pp.79-85. Rotterdam: Balkema.

Burlion, N., Skoczylas, F. & Dubois, T. (2003). Induced anisotropic permeability due to drying of concrete. *Cement and Concrete Research* **33**, 679-687.

Burnett, A. D. & Fookes, P. G. (1974). A regional engineering geological study of the London Clay in the London and Hampshire basins. *Q. Jl. Engng. Geol.* **7**, 257-295.

Byfors, J. (1980). *Plain concrete at early ages,* CBI Forskning Fo 3:80, 464 pp. Stockholm: Swedish Cement and Concrete Research Institute.

Callister Jr., W. D. (1997). *Materials science and engineering an introduction,* 4th Edition, 852pp. New York: John Wiley & Sons.

Carslaw, H. S. & Jaeger, J. C. (1959). *Conduction of Heat in Solids*, Second Edition, 510 pp. Oxford: Oxford Science Publications.

CDM Regulations (2000). The construction (design and management) (amendment) regulations. London: HMSO.

CEB-FIP (1993). *Model code for concrete structures*, 437pp. Paris: Comité Euro-International du Béton – Fédération Internationale de la Précontrainte/London: Thomas Telford.

Celestino, T. B., De Mariano, M., Ferreira, A. A. & Guimaraes, M. C. A. B. (1997). Undercoring technique for stress measurements in shotcrete lining. *Proc. Tunnels for People* (eds. J. Golser, W. J. Hinkel and W. Schubert), pp.59-64. Rotterdam: Balkema.

Cerulli, T., Dal Negro, E., Hansen, R., Maltese, C., Pistolesi, C. & Wilberg, J. (2002). Physical mechanical analysis of concrete sprayed with two different alkali free accelerators: morphological and chemical implications. *Proc. 4th Int. Symp. Sprayed Concrete – Modern use of wet mix sprayed concrete for underground support*, Davos, Switzerland (eds. K. R. Berg, K. I. Davik and K. Garshol), pp.58-72. Oslo: Norwegian Concrete Association.

Chang, J., Scott, J. M. & Pound, C. (2001). Numerical study of Heathrow cofferdam. *Proc. 2nd Int. Symp. FLAC and Numerical Modeling in Geomechanics*, Lyon, France (eds. D. Billaux, X. Rachez, C. Detournay, and R. Hart), pp.163-169. Lisse: Swets & Zeitlinger.

Chang, Y. & Stille, H. (1993). Influence of early age properties of shotcrete on tunnel construction sequences. *Proc. Shotcrete for Underground Support VI* (eds. D. F. Wood and D. R. Morgan), Niagara-on-the-lake, Canada, pp.110-117. USA: ASCE.

Chen, W. -F. (1982). *Plasticity in reinforced concrete*, 474pp. New York: McGraw-Hill.

CIRIA (1992). *Early age thermal crack control in concrete,* CIRIA Report 91, prepared by T.A. Harrison. London: CIRIA.

Clayton, C. R. I., Bica, A. V. D., Hope, V. S. & Heymann, G. (1995). *Methods of measuring stresses on and in sprayed concrete linings*, University of Surrey Report no. CB/GE/12/01, prepared for Heathrow Express, British Airports Authority.

Clayton, C. R. I., Hope, V. S., Bica, A. V. D. & Heymann, G. (1998). The use of mercury-filled pressure cells for measuring stresses on and in shotcrete linings. In *Tunnels and Metropolises, Proc. World Tunnel Congress* (eds. A. Negro Jr. & A. A. Ferreira), São Paulo, Brazil, pp.355-359. Rotterdam: Balkema.

Clayton, C. R. I., Hope, V. S., Heymann, G., van der Berg, J. P. & Bica, A. V. D. (2000). Instrumentation for monitoring sprayed concrete lined soft ground tunnels. *Proc. Inst. Civ. Engrs Geotech. Engng* **143**, 119-130.

Clayton, C. R. I. & Heymann, G. (2001). Stiffness of geomaterials at very small strains. *Géotechnique* **51**, No.3, 245-255.

Clayton, C. R. I., van der Berg, J. P., Heymann, G., Bica, A. V. D. & Hope, V. S. (2002). The performance of pressure cells for sprayed concrete tunnel linings. *Géotechique* **52**, No.2, 107-115.

Clayton, C. R. I, Thomas, A. H. & van der Berg, J. P. (2003). SCL tunnel design in soft ground – insights from monitoring and numerical modelling. In *Summerschool on Rational Tunnelling* (ed. D. Kolymbas), Innsbruck, Austria, pp.61-92. Berlin: Logos Verlag.

Clayton, C. R. I., van der Berg, J. P. & Thomas, A. H. (2006). Monitoring and displacements at Heathrow Express Terminal 4 station tunnels. *Géotechnique* **56**, No.5, 323-334.

Cook, R. D., Malkus, D. S., Plesha, M. E. & Witt, R. J. (2002). *Concepts and applications of finite element analysis*, 4th edition, 719pp. New York, USA: John Wiley & Sons.

Cooley, P. (1982). Wedge-block tunnels in water supply. *J. Instn Water Engrs and Scientists* **36**, February, 8-26.

Cooling, L. F. & Ward, W. H. (1953). Measurements of loads and strains in earth supporting structures. *Proc. 3rd ICSMFE*, Session 7/3, Vol.2, pp.162-166.

Coussy, O. (1995). *Mechanics of Porous Continua*, 455pp. Chichester: John Wiley & Sons.

Coutinho, A. (1953). Discussion: Development of a device for the direct measurement of compressive stresses. *Journal of the American Concrete Institute* **25**, 216/3-216/6.

Curtis, D. J. (1974). Visco-elastic tunnel analysis. *Tunnels & Tunnelling*, November, 38-39.

Curtis, D. J. (1975). Discussion: The circular tunnel in elastic ground. *Géotechnique* **25**, No.1, 115-127.

Damtoft, J. S., Herfort, D. & Yde, E. (1999). Concrete binders, mineral additions and chemical admixtures: state of the art and challenges for the 21st century. In *Creating with Concrete, Opening and Leader Papers of the Proc. of the Int. Cong.*, Dundee, Scotland (eds. R. K. Dhir, P. C. Hewlett and M. R. Jones), pp.153-168. London: Thomas Telford.

DD ENV 1992-1-1 (1992). *Eurocode 2: Design of Concrete Structures. General Rules for Buildings* (Together with United Kingdom National Application Document). London: British Standards Institution.

Deane, A. P. & Bassett, R. H. (1995). The Heathrow Express trial tunnel. *Proc. Instn. Civ. Engrs. Geotech. Engrg.* **113**, July, 144-156.

de Farias, M. M., Moraes Júnior, A. H. & Pacheco de Assis, A. (2004). Displacement control in tunnels excavated by the NATM: 3D numerical simulations. *Tunnelling and Underground Space Technology* **19**, 283-293.

de Mello Franco, J. A., Armelin, J. L., Santiago, J. A. F., Telles, J. C. F. & Mansur, W. J. (2002). Determination of the natural stress state in a Brazilian rock mass by back analysing excavation measurements: a case study. *Int. J. Rock Mech. & Min. Sci.* **39**, 1005-1032.

Descoeudres, F. & Egger, P. (1977). Monitoring system for large underground openings – experiences from the Grimsel-Oberaar scheme. *Proc. Int. Symp. Field Measurements in Rock Mechanics* (ed. K. Kovári), Zurich, Switzerland, pp.535-549. Rotterdam: Balkema.

Dimmock, R. & Lackner, J. (1997). A unique NATM solution for the London Underground. *Proc. Int. Conf. and seminar on Tunnelling under difficult conditions and rock mass classification*, 27-29 October 1997, Basel, Switzerland. Bedford: International Technical Conferences Ltd.

Ding, Y. & Kusterle, W. (1999). Comparative study of steel fibre-reinforced concrete and steel mesh-reinforced concrete at early ages in panel tests. *Cement and Concrete Research* **29**, 1827-1834.

Ding, Y. & Kusterle, W. (2000). Compressive stress-strain relationship of steel fibre-reinforced concrete at early age. *Cement and Concrete Research* **30**, 1573-1579.

Duddeck, H. & Erdmann, J. (1985). On structural design models for tunnels in soft soil. *Underground Space* **9**, 246-259.

EFNARC (1996). *European specification for sprayed concrete*, 35pp. Paris: European Federation for Producers and Applicators of Specialist Products for Structures (EFNARC).

EFNARC (1999a). *European specification for sprayed concrete - execution of spraying (revised version of section 8)*, 8pp. Paris: European Federation for Producers and Applicators of Specialist Products for Structures (EFNARC).

EFNARC (1999b). *European specification for sprayed concrete – guidelines for specifiers and contractors*, 36pp. Paris: European Federation for Producers and Applicators of Specialist Products for Structures (EFNARC).

Einstein, H. H. & Schwartz, C. W. (1979). Simplified analysis for tunnel supports. *J. Geotech. Engng Div. ASCE*, April, 499-518.

Eisenstein, Z., Kuwajima, F. M. & Heinz, H. K. (1991). Behaviour of shotcrete tunnel linings. In *RETC Proceedings 1999*, Chapter 4, pp.47-57. Colorado, USA: SME.

Emanuel, J. H. & Hulsey, J. L. (1977). Prediction of the thermal coefficient of expansion of concrete. *ACI Journal*, April 1977, 149-155.

England, G. L. & Illston, J. M. (1965). Methods of computing stress in concrete from a history of measured strain – part 2: the rate of flow method. *Civil Engineering and Public Works Review*, May 1965, 692-694.

Franzen, T., Garshol, K. F. & Tomisawa, N. (2001). Sprayed concrete for final linings: ITA working group report. *Tunnelling and Underground Space Technology* **16**, 295-309.

Franzius, J. N., Potts, D. M. & Burland, J. B. (2005). The influence of soil anisotropy and K_0 on ground surface movements resulting from tunnel excavation. *Géotechnique* **55**, No.3, 189-199.

Fricker, S. O. & Alder, A. J. (2001). The use of 3-dimensional numerical analysis in tunnel design. *Proc. Underground Construction 2001*, pp.449-461. London: IMM.

Garshol, K. F. (2002). Admixtures and other factors influencing durability of sprayed concrete. *Proc. 4th Int. Symp. Sprayed Concrete – Modern use of wet mix sprayed concrete for underground support*, Davos, Switzerland, (eds. K. R. Berg, K. I. Davik and K. Garshol), pp.123-129. Oslo: Norwegian Concrete Association.

GDBR (2001). *T5 Geotechnical Design Basis Report*, 4th draft, prepared for BAA plc by TPS Consult, February 2001.

Geisler, H., Wagner, H., Zieger, O., Mertz, W. & Swoboda, G. (1985). Practical and theoretical aspects of the three-dimensional analysis of finally lined intersections. *Proc. 5th Int. Conf. Numerical Methods in Geomechanics* (eds. T. Kawamoto & Y. Ichikawa), Nagoya, Japan, pp.1175-1183. Rotterdam: Balkema.

Geokon (1995). *Instruction manual model 4850, NATM style VW concrete stress cells*, Doc Rev B, 6/97, 17pp.

Glötzl, R. (1996). Measuring stresses in shotcrete. *World Tunnelling*, April 1996, 109-110.

Godfrey, P. S. (1996). *A guide to the systematic management of risk from construction*, CIRIA special publication 125. London: CIRIA.

Golser, J. (1976). The New Austrian Tunnelling Method (NATM) (theoretical background – practical experiences). In *Shotcrete for Ground Support,*

Proc. of the Engineering Foundation Conference, Easton, Maryland, USA, pp.675-712. New York and Detroit: ASCE and ACI SP-54.

Golser, J. (1978). History and development of the New Austrian Tunnelling Method. *Proc. Engineering Foundation Conference Shotcrete for Underground Support III*, St. Anton am Arlberg, Austria, pp.1-13. New York: ASCE.

Golser, J. (1999). Behaviour of early-age shotcrete. *Proc. Shotcrete for Underground Support VII*, São Paulo, Brazil.

Golser, J. & Brandl, J. (1996). Die neue Österreichische Tunnelbaumethode als einschalige Bauweise. *Proc. 5th Int. Conf. Spritzbeton-Technologie '96*, Innsbruck, Austria, pp.65-69.

Golser, J. & Kienberger, G. (1997). Permanent sprayed concrete tunnel lining – loading and safety issues. *Felsbau* **6**, 416-421.

Golser, J., Schubert, P. & Rabensteiner, K. (1989). *Proc. Int. Cong. Progress and Innovation in Tunnelling* (ed. K. Y. Lo), Toronto, pp.79-85. Toronto: Tunnelling Association of Canada / National Research Council of Canada / International Tunnelling Association.

Goudie, A. S. & Brunsden, D. (1994). *The environment of the British Isles.* Oxford: Clarendon Press.

Gourvenec, S. M., Mair, R. J., Bolton, M. D. & Soga, K. (2005). Ground conditions around an old tunnel in London Clay. *Proc. Instn. Civ. Engrs Geotech. Engng)* **158**, 25-33.

Graham, J., Crooks, J. H. A. & Bell, A. L. (1983). Time effects on the stress-strain behaviour of natural soft clays. *Géotechnique* **33**, No.3, 327-340.

Graham, J. & Houlsby, G. T. (1983). Anisotropic elasticity of a natural clay. *Géotechnique* **33**, No.2, 165-180.

Grant, R. J., Stallebrass, S. E. & Taylor, R. N. (1999). Modelling soil deformations at a tunnel heading using physical and numerical techniques. In *Geotechnical Engineering for Transportation Infrastructure* (eds. Barends *et al.*), pp.2045-2051. Rotterdam: Balkema.

Grose, W. J. & Eddie, C. M. (1996). Geotechnical aspects of the construction of the Heathrow Transfer Baggage System tunnel. *Proc. Int. Symp. Geotechnical Aspects of Underground Construction in Soft Ground* (eds. R. J. Mair and R. N. Taylor), London, UK, pp.269-276. Rotterdam: Balkema.

Grose B., Macklin S. & Yeow H. C. (2005). Numerical tunnel design – how far have we come? *Tunnels & Tunnelling International*, May 2005, pp.40-43.

Grøv, E. (2001). Active design in civil tunnelling with sprayed concrete as a permanent lining. *Shotcrete: Engineering Developments, Proc. Int. Conf. Engineering Developments in Shotcrete*, Hobart, Tasmania, Australia (ed. E.S. Bernard), pp.123-133. Rotterdam: Balkema.

Grove, D. M. & Davis, T. P. (1992). *Engineering quality and experimental design*, 361pp. Longman Scientific and Technical.

Groves, P. N. & Morgan, S. R. (1997). Engineering consequences of ground conditions on NATM works at London Bridge Station, Jubilee Line Extension. *Proc. Tunnelling '97*, London, 1997, pp.677-692. London: IMM Books.

Guedes de Melo, P. F. M. & Santos Perreira, C. (1999). The role of the soil k_0 value in numerical analysis of shallow tunnels. *Proc. Int. Symp. Geotechnical Aspects of Underground Construction in Soft Ground* (eds.

O. Kusakabe, K. Fujita and Y. Miyazaki), Tokyo, Japan, pp.379-384. Rotterdam: Balkema.

Gunn, M. J. & Taylor, R. N. (1983). Discussion: Loads on leaking and watertight tunnel linings, sewers and buried pipes due to groundwater. *Géotechnique* **33**, 73-77.

Hafez, N. M. (1995). *Post-failure modelling of three-dimensional shotcrete lining for tunnelling*. PhD thesis, University of Innsbruck.

Hagedorn, H. & Wei, Z. Q. (2001). Monocoque lining design for the Gotthard Base Tunnel. In *Shotcrete: Engineering Developments, Proc. Int. Conf. Engineering Developments in Shotcrete*, Hobart, Tasmania, Australia (ed. E.S. Bernard), pp.123-133. Rotterdam: Balkema.

Hellmich, C., Ulm, F. -J. & Mang, H. A. (1999a). Multisurface chemoplasticity. I: Material model for shotcrete. *J. Eng. Mech.*, June, 692-701.

Hellmich, C., Ulm, F. -J. & Mang, H. A. (1999b). Multisurface chemoplasticity. II: Numerical studies on NATM tunnelling. *J. Eng. Mech.*, June, 702-713.

Hellmich, C., Macht, J., Lackner, R., Mang, H. A. & Ulm, F. -J. (2001a). Phase transitions in shotcrete: from material modelling to structural safety assessment. In *Shotcrete: Engineering Developments, Proc. Int. Conf. Engineering Developments in Shotcrete*, Hobart, Tasmania, Australia (ed. E.S. Bernard), pp.173-184. Rotterdam: Balkema.

Hellmich, C., Mang, H. A. & Ulm, F. -J. (2001b). Hybrid method for quantification of stress states in tunnel shells: combination of 3D in situ displacement measurements and thermochemoplastic material law. *Computers and Structures* **79**, 2103-2115.

Hellmich, C., Lackner, R. & Mang, H. A. (2003). Thermochemomechanical material model for shotcrete. *Numerical simulation in tunnelling* (ed. G. Beer), pp. 61-81. Vienna: Springer-Verlag.

Henderson, T. O. & Pickles, A. R. (2004). Geotechnical management on major infrastructure projects. *Proc. Instn Civ. Engrs Geotech. Engng* **157**, No. GE4, 165-171.

Hocking, G. (1978). Stresses around tunnel intersections. In *Computer Methods in Tunnel Design*, pp.41-60. London: ICE.

Hoek, E. & Brown, E. T. (1980). *Underground Excavations in Rock*, 527pp. London: IMM.

Holzleitner, W. (2004). Personal communication, 9th October 2004.

HSE (1996). *Safety of New Austrian Tunnelling Method (NATM) tunnels*, Health and Safety Executive, 86pp. London: HSE Books, HMSO.

Hudson, J. A., Cornet, F. H. & Christiansson, R. (2003). ISRM Suggested Methods for rock stress estimation – Part 1: Strategy for rock stress estimation. *Int. J. Rock Mech. & Min. Sci.* **40**, 991-998.

Hughes, T. G. (1997). *Flat jack investigation of Heathrow Terminal 4 concourse tunnel 13-19th November 1996*. Report by Cardiff School of Engineering, University of Wales for the University of Surrey, 22pp.

Hughes, T. G. & Pritchard, R. (1997). *In situ* measurement of dead and live load stresses in a masonry arch. *Engineering Structures* **20**, nos.1-2, 5-13.

ICE (1996). *Sprayed concrete linings (NATM) for tunnels in soft ground*, ICE design and practice guide, 88pp. London: Thomas Telford Publishing.

Illston, J. M. (1978). Creep of concrete. Chapter 4 of *Creep of engineering materials* (ed. C.D. Pomeroy), pp.47-66. London: Mechanical Engineering Publications Ltd. (IMechE).

Itasca (2002). *FLAC^{3D} version 2.1 manual.* Minneapolis: Itasca Consulting Group Inc.

Itasca (2005). *FLAC^{3D} version 3.0 manual.* Minneapolis: Itasca Consulting Group Inc.

Jäger, J. (2002). Tunnel junction at shallow cover: a case study. *Proc. 3rd Int. Conf. Engineering Computational Technology* (eds. B. H. V. Topping & Z. Bittnar), Stirling, Scotland. Stirling, Scotland: Civil-Comp Press.

Jaeger, J. C. & Cook, N. G. W. (1979). *Fundamentals of Rock Mechanics*, 3rd edition, 593pp. London: Chapman and Hall.

Jardine, R. J., Potts, D. M., Fourie, A. B. & Burland, J. B. (1986). Studies of the influence of non-linear stress-strain characteristics in soil-structure interaction. *Géotechnique* **36**, No.3, 377-396.

Jeng, F., Lin, M. -L. & Yuan, S. -C. (2002). Performance of toughness indices for steel fiber reinforced concrete. *Tunnelling and Underground Space Technology* **17**, 69-82.

Jones, B. D. (2003). *Rail Tunnels – T5C Shotcrete Usage Study.* BAA/T5 internal report T5-RI-AS-51-292-RX-00001, version 1.3, 27pp.

Jones, B. D., Thomas, A. H. & Clayton, C. R. I. (2004). Interpretation of pressure cells in sprayed concrete tunnel linings. In *Rock Engineering Theory and Practice, Proc. ISRM Regional Symp. Eurock 2004 & 53rd Geomechanics Colloquy* (ed. W. Schubert), Salzburg, Austria, pp.233-236. Essen: Verlag Glückauf GmbH.

Kessell, C. (2005). Cooling the tube seminar. *Railway Engineers Forum*, October 21st 2005. London: IEE, IMechE.

Khoury, G. A. (2000). Effect of fire on concrete and concrete structures. *Prog. Struct. Engrg. Mater.* **2**, 429-447.

Kim, K. & Franklin, J. A. (1987). ISRM Commission on Testing Methods: Suggested methods for rock stress determination. *Int. J. Rock Mech. Min. Sci. & Geomech. Abstr.*, **24**, No.1, 53-73.

Kimmance, J. P. & Allen, R. (1996). The NATM and Compensation Grouting Trial at Redcross Way. *Proc. Int. Symp. Geotechnical Aspects of Underground Construction in Soft Ground* (eds. R. J. Mair & R. N. Taylor), London, UK, pp.385-390. Rotterdam: Balkema.

Kondepudi, D. & Prigogine, I. (1998). *Modern thermodynamics*. Chichester: John Wiley & Sons.

Kovári, K. (2003a). History of the sprayed concrete lining method – part I: milestones up to the 1960s. *Tunnelling and Underground Space Technology* **18**, 57-69.

Kovári, K. (2003b). History of the sprayed concrete lining method – part II: milestones up to the 1960s. *Tunnelling and Underground Space Technology* **18**, 71-83.

Kusterle, W. A. (1993). Regulating the strength development of shotcrete. *Proc. Int. Symp. Sprayed Concrete* (eds. R. Kompen, O. A. Opsahl and K. R. Berg), Fagernes, Norway, pp.221-232. Oslo: Norwegian Concrete Institute.

Kusterle, W. & Pfeuffer, M. (2001). Reduction of rebound and dust for the dry-mix shotcrete process. In *Shotcrete: Engineering Developments, Proceedings of the International Conference on Engineering Developments in Shotcrete*, Hobart, Tasmania, Australia (ed. E.S. Bernard), pp.167-172. Rotterdam: Balkema.

Kuwajima, F. M. (1999). Early age properties of the shotcrete. *Proc. Shotcrete for Underground Support VIII* (eds. T. B. Celestino and H. W. Parker), São Paulo, Brazil. Reston, Virginia, USA: ASCE.

Kuwajima, F. M., Negro Jr., A., Celestino, T. B. & Ferreira, A. A. (1991). Mini flat jack test for assessment of tunnel lining stresses. *Proc. 9th Panamerican Conf. on Soil Mechanics and Foundation Engineering*, Viña del Mar, Chile, Vol.3, pp.1377-1390.

Laplante, P. & Boulay, C. (1994). Evolution du coefficient de dilatation thermique du béton en fonction de sa maturité aux tout premiers ages. *Materials and Structures* **27**, 596-605.

Lee, K.M. & Rowe, R. K. (1989). Deformations caused by surface loading and tunnelling: the role of elastic anisotropy. *Géotechnique* **39**, No.1, 125-140.

Lew, T. K. (1976). *Three-dimensional static finite element analysis of lined, right-angle cross, circular tunnel intersections in rock*, Civil Engineering Laboratory (CEL) report, Navy, Port Hueneme, California.

Li, L. & Cornet, F. H. (2004). Three dimensional consideration of flat jack tests. *SinoRock 2004 Symp., Int. J. Rock Mech. & Min. Sci.* **41**, No.3, Paper 1B 10, CD-ROM, 6pp.

Londe, P. (1977). Field measurements in tunnels. *Proc. Int. Symp. Field Measurements in Rock Mechanics* (ed. K. Kovári), Zurich, Switzerland, Vol.1, pp.619-638.

Londe, P. (1982). Concepts and instruments for improved monitoring. *J. Geotech. Engng Div. ASCE*, **108**, No.GT6, 820-834.

Macht, J., Lackner, R., Hellmich, C. & Mang, H. A. (2003). Quantification of stress states in shotcrete shells. In *Numerical simulation in tunnelling* (ed. G. Beer), pp.225-248. Vienna: Springer-Verlag.

Mair, R. J. & Wood, D. M. (1987). *Pressuremeter Testing: Methods and Interpretation*, 160pp, Construction Industry Research and Information Association Book B3. London: Butterworths.

Mair, R. J. (1992). Unwin Memorial Lecture 1992 – Developments in geotechnical engineering research: application to tunnels and deep excavations. *Proc. Instn Civ. Engrs Civ. Engng* **93**, February, 27-41.

Mair, R. J. & Taylor, R. N. (1997). Bored tunnelling in the urban environment. Theme Lecture, Plenary Session 4. *Proc. 14th Int. Conf. Soil Mechanics and Foundation Engineering*, Hamburg, Vol.4.

Mair, R. J. (1998). Geotechnical aspects of design criteria for bored tunnelling in soft ground. In *Tunnels and Metropolises, Proc. World Tunnel Cong.* (eds. A. Negro Jr. and A. A. Ferreira), São Paulo, Brazil, pp.183-199. Rotterdam: Balkema.

Maltese, C., Cerulli, T., Pistolesi, C., Salvioni, D., Dal Negro, E. & Hansen, R. (2002). *Proc. 4th Int. Symp. Sprayed Concrete – Modern use of wet mix sprayed concrete for underground support* (eds. K. R. Berg, K. I. Davik and K. Garshol), Davos, Switzerland, pp.238-252. Oslo: Norwegian Concrete Association.

Marshall, M. A., Milligan, G. W. E. & Mair, R. J. (1996). Movements and stress changes in London Clay due to the construction of a pipe jack. *Proc. Int. Symp. Geotechnical Aspects of Underground Construction in Soft Ground* (eds. R. J. Mair and R. N. Taylor), London, UK, pp.719-724. Rotterdam: Balkema.

Mayne, P. W. & Kulhawy, F. H. (1982). K_0-OCR relationships in soil. *Proc. Amer. Soc. Civ. Engrs. Geotech. Engng* **GT6**, June, 851-872.

McDonald, D. B. & Roper, H. (1991). Discussion: Factors influencing relative humidity in concrete, by L. J. Parrott. *Magazine of Concrete Research* **43**, No.157, 305-307.

Melbye, T. A. & Dimmock, R. H. (2001). Modern advances and applications of sprayed concrete. In *Shotcrete: Engineering Developments, Proc. Int. Conf. Engineering Developments in Shotcrete*, Hobart, Tasmania, Australia (ed. E. S. Bernard), pp.7-29. Rotterdam: Balkema.

Metje, N., Chapman, D. N., Rogers, C. D. F., Kukureka, S. N., Miao, P. & Henderson, P. J. (2005). Optical fibre sensors for remote tunnel displacement monitoring. *Proc. Underground Construction 2005*, London, UK. London: Brintex.

Morgan, H. D. (1961). A contribution to the analysis of stress in a circular tunnel. *Géotechnique* **11**, No.1, 37-46.

Morgan=Tunnelling (2002). *Early age evaluation of MF24 permanent sprayed concrete*. Report for T5 project no.6376/Report/005, 31pp. Rugby: Morgan=Tunnelling Research and Development.

Muir Wood, A. (2004). *The early age effects of shrinkage and temperature change on a reinforced concrete pile*. Master of Engineering Science individual project report, University of Southampton, 28pp.

Muir Wood, A. M. (1969). Written contribution, plenary session 4. *Proc. 7th Int. Conf. Soil Mechanics and Foundation Engineering*, Vol.3, Mexico, pp.363-365.

Muir Wood, A. M. (1975). The circular tunnel in elastic ground. *Géotechnique* **25**, No.1, 115-117.

Muir Wood, A. M. (2003). What tends to go wrong in tunnelling. *Summerschool on Rational Tunnelling* (ed. D. Kolymbas), Innsbruck, Austria, pp.237-254. Berlin: Logos Verlag.

Muir Wood, D. (1990). *Soil Behaviour and Critical State Soil Mechanics*, 462pp. Cambridge: Cambridge University Press.

Müller-Salzburg, L. (1977). The use of deformation measurements in dimensioning the lining of subway tunnels. *Proc. Int. Symp. Field Measurements in Rock Mechanics* (ed. K. Kovári), Zurich, Switzerland, Vol.1, pp.451-471.

Navaneethan, T., Sivakumar, V., Wheeler, S. J. & Doran, I. G. (2004). Assessment of suction measurements in saturated clays. *Proc. Instn Civ. Engrs Geotech. Engng* **158**, 15-24.

Negro, A., Sozio, L. E. & Ferreira, A. A. (1996). Tunnelling in São Paulo, Brazil. *Proc. Int. Symp. Geotechnical Aspects of Underground Construction in Soft Ground* (eds. R. J. Mair and R. N. Taylor), London, UK, pp.295-300. Rotterdam: Balkema.

Negro, A., Kochen, R., Goncalves, G., Martins, R. M. & Pinto, G. M. P. (1998). Prediction and measurement of stresses in sprayed concrete lining (Brasilia South Wing tunnels). *Proc. Tunnels and Metropolises* (eds. A. Negro Jr. and A. A. Ferreira), pp.405-410. Rotterdam: Balkema.

Negro, A. & de Queiroz, P. I. B. (2000). Prediction and performance: a review of numerical analyses for tunnels. *Proc. Int. Symp. Geotechnical Aspects of Underground Construction in Soft Ground* (eds. O. Kusakabe, K. Fujita and Y. Miyazaki), Tokyo, Japan, pp.409-418. Rotterdam: Balkema.

Neville, A. M. (1995). *Properties of Concrete*, 4th Edition. Longman Group Limited.

Neville, A. M., Dilger, W. H. & Brooks, J. J. (1983). *Creep of plain and structural concrete*, 361pp. Construction Press, Longman Group Limited.

New, B. M. & Bowers, K. H. (1994). Ground movement model validation at the Heathrow Express trial tunnel. In *Tunnelling '94, Proc. 7th Int. Symp. IMM and BTS*, London, UK, pp.310-329. London: Chapman and Hall.

Niu, J. X., Wong, I. H. & Makino, M. (2005). Temperature effects on strut loads and ground movements for a 31m deep excavation in Singapore. *Proc. Underground Singapore 2005*, pp.129-135. Singapore: Tunnelling and Underground Construction Society (Singapore).

Novotný, M. & Mařík, L. (2004). World of underground construction: Strenger tunnel. *Tunel* **1/2004** (Czech tunnel magazine), 43-48.

O'Reilly, M. P., Mair, R. J. & Alderman, G. H. (1991). Long-term settlements over tunnels; an eleven year study at Grimsby. *Proc. Tunnelling '91*, pp.55-64. London: IMM.

Oreste, P. P. (2002). The importance of longitudinal stress effects on the static conditions of the final lining of a tunnel. *Tunnelling and Underground Space Technology* **17**, 21-32.

Oreste, P. P. & Peila, D. (1997). Modelling progressive hardening of shotcrete in convergence-confinement approach to tunnel design. *Tunnelling and Underground Space Technology* **12**, No.3, 425-431.

Ortigao, J. A. R., Davidovitch, A., Moraes, A. & Vallejos, D. (1998). Fibre reinforced shotcrete lining at the Covanca Tunnel. In *Tunnels and Metropolises, Proc. of World Tunnel Congress* (eds. A. Negro Jr. And A. A. Ferreira), São Paulo, Brazil, pp.335-341. Rotterdam: Balkema.

Österreichischer Betonverein (1999). *Sprayed Concrete Guideline*, 83pp., Austrian Concrete Society. Vienna: ÖBV.

Pacovský, J., Barták, J. & Bucek, M. (1991). Measuring of contact stress between soil and rock mass and engineering structure. *Proc. Int. Symp. Field Measurements in Geomechanics* (ed. G. Sørum), Oslo, pp.61-70. Rotterdam: Balkema.

Paglia, C., Wombacher, F. & Böhni, H. (2003). The influence of alkali-free and alkaline shotcrete accelerators within cement systems. Influence of the temperature on the sulphate attack mechanisms and damage. *Cement and Concrete Research* **33**, 387-395.

Palermo, G. & do Lago Helene, P. R. (1998). Shotcrete as final lining for tunnels. In *Tunnels and Metropolises, Proc. of World Tunnel Congress* (eds. A. Negro Jr. and A. A. Ferreira), São Paulo, Brazil, pp.349-354. Rotterdam: Balkema.

Panet, M. & Guenot, A. (1982). Analysis of convergence behind the face of a tunnel. *Proc. Tunnelling '82*, Brighton, pp.197-204. London: IMM.

Pantazopoulou, S. J. & Zanganeh, M. (2001). Triaxial tests of fiber-reinforced concrete. *Journal of Materials in Civil Engineering* **13**, No.5, 340-348.

Parrott, L. J. (1991). Factors influencing relative humidity in concrete. *Magazine of Concrete Research* **43**, No.154, 45-52.

Peck, R. B. (1969a). Ninth Rankine Lecture: Advantages and limitations of the observational method in applied soil mechanics. *Géotechnique* **19**, No.2, 169-187.

Peck, R. B. (1969b). Deep excavations and tunnelling in soft ground. *Proc. 7th Int. Conf. Soil Mechanics and Foundation Engrg (7th ICSMFE)*, Mexico, State-of-the-art report, pp.225-290.

Picha, J. (1991). A contribution to measurements of rock pressure on concrete constructions using hydraulic pressure cells. *Proc. Int. Symp. Field Measurements in Geomechanics* (ed. G. Sørum), Oslo, pp.71-75. Rotterdam: Balkema.

Potts, D. M. & Zdravković, L. (1999). *Finite element analysis in geotechnical engineering, Vol.1: Theory*. London: Thomas Telford.

Pöttler, R. (1990). Time-dependent rock-shotcrete interaction, a numerical shortcut. *Computers and Geotechnics* **9**, 149-169.

Pöttler, R. (1993). To the limits of shotcrete linings. *Proc. Shotcrete for Underground Support V* (eds. J. Sharp & T. Franzen), Uppsala, Sweden, pp.83-90. USA: ASCE.

Pound, C. (2002a). *Investigation of the Lasershell tunnel method.* Report for T5 by Mott MacDonald, document no. T5-RY-CR-C1-29X-RX-00003.

Pound, C. (2002b). *Further investigation of the Lasershell tunnel method.* Report for T5 by Mott MacDonald, document no. T5-RY-CR-C1-29X-RX-00004.

Pound, C. (2006). The performance of FLAC zones in bending. *Proc. 4th Int. FLAC symp. FLAC and Numerical Modeling in Geomechnics 2006* (eds. P. Varona and R. Hart), Madrid, Spain, pp.351-357. Minneapolis: Itasca Consulting Group, Inc.

Powderham, A. J. (1994). An overview of the observational method: development in cut and cover bored tunnelling projects. *Géotechnique* **44**, No.4, 619-636.

Powell, D. B. & Beveridge, J. P. (1998). Understanding NATM as a design process in construction. In *Big Digs Around the World, Proc. Sessions of Geo-Congress 98*, Boston, Massachusetts, Geo-Institute, ASCE, October 1998 (eds. J. R. Lambrechts, R. Hwang and A. Urzua), pp.380-397. Virginia: ASCE.

Powell, D. B., Sigl, O. & Beveridge, J. P. (1997). Heathrow Express – design and performance of platform tunnels at Terminal 4. *Proc. Tunnelling '97*, London, pp.565-593. London: IMM.

Powell, D. B., Thomas, A. H. & Hilar, M. (2004). The role of numerical modelling in tunnel design. *Tunel* **1/2004** (Czech tunnel magazine), 25-28.

Powrie, W. (1997). *Soil Mechanics: Concepts and Applications*, 420pp. London: E & FN Spon.

Prudêncio Jr., L. R. (1998). Accelerating admixtures for shotcrete. *Cement and Concrete Composites* **20**, 213-219.

Rabcewicz, L. v. (1954a). Bolted support for tunnels – part one. *Water Power*, April, 150-155.

Rabcewicz, L. v. (1954b). Bolted support for tunnels – part two. *Water Power*, May, 171-175.

Rabcewicz, L. v. (1964a). The New Austrian Tunnelling Method – part one. *Water Power*, November, 453-457.

Rabcewicz, L. v. (1964b). The New Austrian Tunnelling Method – part two. *Water Power*, December, 511-515.

Rabcewicz, L. v. (1965). The New Austrian Tunnelling Method – part three. *Water Power*, January, 19-24.
Rabcewicz, L. v. (1969a). Stability of tunnels under rock load – part one. *Water Power*, June, 225-229.
Rabcewicz, L. v. (1969b). Stability of tunnels under rock load – part two. *Water Power*, July, 266-273.
Rabcewicz, L. v. (1969c). Stability of tunnels under rock load – part three. *Water Power*, August, 297-302.
Rabcewicz, L. v. & Golser, J. (1973). Principles of dimensioning the supporting system for the "New Austrian tunnelling method". *Water Power*, March, 88-93.
Rabcewicz, L. v. & Golser, J. (1974a). Application of the NATM to the underground works at Tarbela – part one. *Water Power* **26**, No.9, September, 314-321.
Rabcewicz, L. v. & Golser, J. (1974b). Application of the NATM to the underground works at Tarbela – part two. *Water Power* **26**, No.10, October, 330-335.
Rammah, K. I., Val, D. V. & Puzrin, A. M. (2004). Effects of ageing on small-strain stiffness of overconsolidated clays. *Géotechnique* **54**, No.5, 319-322.
Rastrup, E. (1956). The temperature function for heat of hydration in concrete. *Proc. of RILEM Symp. – Winter Concreting Theory and Practice*, Copenhagen, session BII. Paris: RILEM.
Robins, P. J., Austin, S. A. & Jones, P. A. (2003). Spatial distribution of steel fibres in sprayed and cast concrete. *Magazine of Concrete Research* **55**, No.3, 225-235.
Rocha, M. (1966). Rock mechanics in Portugal. *Proc. 1st Int. Cong. on Rock Mechanics*, ISRM, Lisbon, Portugal, Vol.3, pp.121-132. Lisbon: ISRM.
Rocha, M., Baptista Lopes, J. J. & Neves da Silva, J. (1966). A new technique for applying the method of the flat jack in the determination of stresses inside rock masses. *Proc. 1st Int. Cong. on Rock Mechanics*, ISRM, Lisbon, Portugal, Vol.3, pp.57-65. Lisbon: ISRM.
Rokahr, R. B. (1995). Wie sicher ist die NÖT? *Felsbau* **13**, No.6, 334-340.
Rokahr, R. B. & Lux, K. H. (1987). Einfluβ des rheologischen Verhaltens des Spritzbetons auf den Ausbauwiderstand. *Felsbau* **5**, No.1, 11-18.
Rokahr, R. B., Stärk, A. & Zachow, R. (2002). On the art of interpreting measurement results. *Felsbau* **20**, No.2, pp.16-21.
Rokahr, R. B. & Zachow, R. (1997). Ein neues Verfahren zur täglichen Kontrolle der Auslastung einer Spritzbetonschale. *Felsbau* **15**, No.6, 430-434.
Rokahr, R. B. & Zachow, R. (1999). *Betonspannungsermittlung in der Spritzbetonaußenschale mit dem Programm STRESS am Beispiel Eggetunnel.* Internal report, University of Hannover, 6pp.
Romero, V. (2002). NATM in soft-ground: a contradiction of terms? *World Tunnelling*, September, 338-343.
Sauer, G. & Sharma, B. (1977). A system for stress measurement in constructions in rock. *Proc. Int. Symp. Field Measurements in Rock Mechanics* (ed. K. Kovári), Vol.1, pp.317-329.
Schubert, P. (1988). Beitrag zum rheologischen Verhalten von Spritzbeton. *Felsbau* **6**, No.3, 150-153.

Schuller, M. P. (2003). Nondestructive testing and damage assessment of masonry structures. *Prog. Struct. Engrg Mater.* **5**, 239-251.

Scott, J. M., Pound, C. & Shanghavi, H. B. (2003). Heathrow Airside Road Tunnel – wall design and observed performance. *Proc. Int. Conf. Underground Construction 2003*, pp.281-292. London: Brintex Ltd.

Simpson, B., Blower, T., Craig, R. N. & Wilkinson, W. B. (1989). *The engineering implications of rising groundwater levels in the deep aquifer beneath London*, CIRIA Special Publication 69, 116pp. London: CIRIA.

Simpson, B., Atkinson, J. H. & Jovičić, V. (1996). The influence of anisotropy on calculations of ground settlements above tunnels. *Proc. Int. Symp. Geotechnical Aspects of Underground Construction in Soft Ground* (eds. R. J. Mair and R. N. Taylor), London, UK, pp.591-594. Rotterdam: Balkema.

Simpson, B., O'Riordan, N. J. & Croft, D. D. (1979). A computer model for the analysis of ground movements in London Clay. *Géotechnique* **29**, No.2, 149-175.

Sjöberg, J., Christiansson, R. & Hudson, J. A. (2003). ISRM Suggested Methods for rock stress determination – Part 2: Overcoring methods. *Int. J. Rock Mech. & Min. Sci.* **40**, 999-1010.

Skempton, A. W. (1943). Discussion: Tunnel linings with special reference to a new form of reinforced concrete lining, by G. L. Groves. *J. Instn Civ. Engrs* **20**, No.5, March, 53-56.

Skempton, A. W. (1954). The pore pressure coefficients *A* and *B*. *Géotechnique* **4**, No.4, 143-147.

Standing, J. R., Farina, M. & Potts, D. M. (1998). The prediction of tunnelling induced building settlements – A case study. In *Tunnels and Metropolises, Proc. World Tunnel Congress* (eds. A. Negro Jr. & A. A. Ferreira), São Paulo, Brazil, pp.1053-1058. Rotterdam: Balkema.

Standing, J. R. & Burland, J. B. (2006). Unexpected tunnelling volume losses in the Westminster area, London. *Géotechnique* **56**, No.1, 11-26.

Stärk, A. (2004). Personal communication, 7th October 2004.

Stärk, A., Rokahr, R. B. & Zachow, R. (2001). A new method for a daily monitoring of the stress intensity of a sprayed concrete lining. In *Progress in Tunnelling after 2000, Proc. of the World Tunnel Congress* (eds. P. Teuscher and A. Colombo), Milan, Italy, June 2001, Vol.1, pp.699-705. Bologna: Patron Editore.

Stärk, A., Rokahr, R. B. & Zachow, R. (2002). What do we measure: displacements or safety? In *Mining and Tunnelling Innovation and Opportunity, Proc. 5th North American Rock Mechanics Symp. and17th Tunnelling Association of Canada Conf.: NARMS-TAC 2002*, pp.1629-1638. Toronto: University of Toronto Press.

Swedish Cement and Concrete Research Institute (1956). Hardening of concrete as influenced by temperature, session BII general report. *Proc. RILEM Symp. – Winter Concreting Theory and Practice*, Copenhagen, session BII. Paris: RILEM.

Swoboda, G. & Hafez, N. M. (1995). Structural analysis of shotcrete in tunnelling. *Proc. Engrg Foundation Conf. Shotcrete for Underground Support VII* (eds. H. Klapperrich, R. Pöttler and J. Willocq), Telfs, Austria, pp.170-179. USA: ASCE.

Swoboda, G., Moussa, A., Lukas, W. & Kusterle, W. (1993). On constitutive modelling of shotcrete. *Proc. Int. Symp. Sprayed Concrete*, Fagernes, Norway, pp.133-141. Oslo: Norwegian Concrete Association.

Takino, K., Kimura, H., Takeda, N. & Ito, F. (1985). Three-dimensional behaviour of tunnel intersection. *Proc. 5th Int. Conf. Numerical Methods in Geomechanics* (eds. T. Kawamoto and Y. Ichikawa), Nagoya, Japan, pp.1185-1192. Rotterdam: Balkema.

Thareja, D. V., Madhavan, K., Sharma, K. G. & Natarajan, R. (1985). Three dimensional finite element analysis of branching tunnels. *Proc. 5th Int. Conf. Numerical Methods in Geomechanics* (eds. T. Kawamoto and Y. Ichikawa), Nagoya, Japan, pp.1193-1199. Rotterdam: Balkema.

The Engineering Council (1993). *Guidelines on risk issues*, 48pp. London: The Engineering Council.

Thomas, A. H., Powell, D. B. & Savill, M. (1998). Controlling deformations during the construction of NATM tunnels in urban areas. *Proc. Int. Conf. Underground Construction in Modern Infrastructure, Stockholm, Sweden* (eds. T. Franzen, S. –G. Bergdahl and A. Nordmark), pp.207-212. Rotterdam: Balkema.

Thomas, A. H., Clayton, C. R. I. & Norris, P. (2001). The role of constitutive models in the analysis of shotcrete-based ground support systems. In *Shotcrete: Engineering Developments, Proc. Int. Conf. Engineering Developments in Shotcrete*, Hobart, Tasmania, Australia (ed. E. S. Bernard), pp.237-244. Rotterdam: Balkema.

Thomas, A. H. (2003). *Numerical modelling of sprayed concrete lined (SCL) tunnels*. Ph.D. thesis, University of Southampton.

Thomas, A. H., Casson, E. & Powell, D. B. (2003). Common ground – the integration of the design and construction of a sprayed concrete lined (SCL) tunnel in San Diego, USA. In *Underground Construction 2003*, Excel, Docklands, UK, pp.71-82.

Thomas, A. H., Legge, N. B. & Powell, D. B. (2004). The development of sprayed concrete lined (SCL) tunnelling in the UK. In *Rock Engineering Theory and Practice, Proc. ISRM Regional Symposium Eurock 2004 & 53rd Geomechanics Colloquy*, Salzburg, Austria (ed. W. Schubert), pp.25-30. Essen: Verlag Glückauf.

Tomlinson, M. J. (1995). *Foundation Design and Construction*, 6th edition, 536pp. Harlow: Addison Wesley Longman.

Ulm, F. -J. & Coussy, O. (1995). Modeling of thermochemomechanical couplings of concrete at early ages. *J. Engng Mech. ASCE* **121**, No.7, pp.785-794.

Vandewalle, M.A. (1998). Design of steel fiber reinforced concrete and shotcrete for tunnel linings. In *Tunnels and Metropolises, Proc. World Tunnel Congress* (eds. A. Negro Jr. and A. A. Ferreira), São Paulo, Brazil, pp.329-334. Rotterdam: Balkema.

van der Berg, J. P., Clayton, C. R. I., Powell, D. B. & Savill, M. (1998a). Monitoring of the Concourse Tunnel at Heathrow Express Terminal 4 station constructed using the NATM. In *Tunnels and Metropolises, Proc. World Tunnel Congress* (eds. A. Negro Jr. and A. A. Ferreira), São Paulo, Brazil, pp.1163-1168. Rotterdam: Balkema.

van der Berg, J. P., Clayton, C. R. I. & Hope, V. S. (1998b). An evaluation of the role of monitoring during the construction of shallow NATM tunnels in

urban areas. *Proc. North American Tunnelling '98* (ed. L. Ozdemir), Newport Beach, California, USA, pp.251-257.

van der Berg, J. P. (1999). *Measurement and prediction of ground movements around three NATM tunnels*. PhD thesis, University of Surrey, UK.

van der Berg, J. P., Clayton, C. R. I. & Powell, D. B. (2003). Displacements ahead of an advancing NATM tunnel in the London clay. *Géotechnique* **53**, No.9, 767-784.

Vogler, U. W., Deffur, R. D. & Bieniawski, Z. T. (1976). CSIR large flat jack equipment for determining rock mass deformability. *Proc. Symp. Exploration for Rock Engineering*, Johannesburg, South Africa (ed. Z. T. Bieniawski), pp.105-111. Rotterdam: Balkema.

Ward, W. H. & Pender, M. J. (1981). Tunnelling in soft ground: general report. *Proc. 10th Int. Conf. Soil Mechanics and Foundation Engineering*, Stockholm, Vol.4, pp.261-275.

Ward, W. H. & Thomas, H. S. H. (1965). The development of earth loading and deformation in tunnel linings in London Clay. *Proc. 6th ICSMFE*, Vol.2, Divisions 3-6, Montreal, Canada, 8th-15th September, pp.432-436.

Weiler, W. A. & Kulhawy, F. H. (1982). Factors affecting stress cell measurements in soil. *J. Geotech. Engng Div. ASCE*, **108**, No.GT12, 1529-1548.

Wetzig, V. (2003). Fire protection in tunnelling. In *Summerschool on Rational Tunnelling* (ed. D. Kolymbas), Innsbruck, Austria, pp.409-427. Berlin: Logos Verlag.

Williams, F. T. (1974). The behaviour of stress measuring devices in rocks of various properties. *Proc. Int. Conf. Field Instrumentation in Geotechnical Engineering*, BGS, London, pp.462-474. London: Butterworths.

Williams, I., Neumann, C., Jäger, J. & Falkner, L. (2004). Innovativer Spritzbeton-Tunnelbau für den neuen Flughafenterminal T5 in London (Innovative Shotcrete Tunnelling for London Heathrow's new Terminal 5). *Proc. Österreichischer Tunneltag 2004*, Salzburg, Austria, pp.41-61. Salzburg: Die SIGN Factory.

Woodford, C. & Skipp, B. O. (1976). *Experimental and numerical studies on the action factor of Gloetzl earth pressure cells*. CIRIA Report No. 6153, Research Project RP/185. London: Construction Industry Research and Information Association.

Yamashita, Y. & Fujiwara, T. (1988). An example of measurements on the behaviour of oblate and large section tunnel in unconsolidated ground. *Proc. 2nd Int. Symp. Field Measurements in Geomechanics* (ed. S. Sakurai), Kobe, Japan, pp.871-880. Rotterdam: Balkema.

Yazdchi, M., Macklin, S. R. & Yeow, H. –C. (2006). 3D modelling of sprayed-concrete-lined tunnels in clay. *Proc. Instn Civ. Engrs Geotech. Engrg* **159**, issue GE4, 243-250.

Young, W. C. (1989). *Roark's formulas for stress and strain*, 6th edition, 763pp. New York: McGraw-Hill.

Appendix A

A.1 Derivation of Jardine equations for use in 3D.

The Jardine equations were originally applied to a triaxial test, therefore they needed to be adapted to work in 3 dimensions for application in FLAC^{3D}. A validation of the Jardine nonlinear model is also presented.

A.1.1 Jardine model equations

$$G_{\tan} = \frac{p'}{3}\left[A + B\cos\left(\alpha X^{\gamma}\right) - \frac{B\gamma\alpha X^{\gamma-1}}{\ln 10}\cdot\sin\left(\alpha X^{\gamma}\right)\right] \qquad \textbf{Equation 40}$$

where $X = \log_{10}\left(\frac{\varepsilon_a}{3}\right)$

$$K_{\tan} = p'\left[R + S\cos\left(\lambda Y^{\mu}\right) - \frac{S\lambda\mu Y^{\mu-1}}{\ln 10}\cdot\sin\left(\lambda Y^{\mu}\right)\right] \qquad \textbf{Equation 41}$$

where $Y = \log_{10}\left(\frac{\varepsilon_v}{T}\right)$

Constants from the T5 GDBR and also from the back-analysis by Scott *et al.* (2003) on the ART Eastern Portal contiguous pile retaining walls, a recent Mott MacDonald project (Camden station redevelopment) and from Standing *et al.* (1998), which was used by Chang *et al.* (2001) for back-analysis of the Heathrow Cofferdam are shown in Table_Apx A-1 and Table_Apx A-2 below:

Table_Apx A-1: Values of Jardine stiffness parameters for London Clay

London Clay	**A**	**B**	**C**	**α**	**γ**	**ε_{smin}**	**ε_{smax}**
T5 GDBR	770	730	7.0e-6	1.338	0.684	7.0e-6	1.5e-3
Scott *et al.*	1020	980	4.20e-6	1.35	0.59	4.20e-6	2.00e-2
Camden	980	870	8.9e-6	1.41	0.75	8.90e-6	3.0e-3
Standing *et al.*	1260	1143	1.00e-6	1.335	0.617	1.40e-5	2.00e-3
London Clay	**R**	**S**	**T**	**λ**	**μ**	**ε_{vmin}**	**ε_{vmax}**
T5 GDBR	150	100	4.9e-5	2.0	1.0	5.0e-5	8.01e-4
Scott *et al.*	150	100	4.9e-5	2.0	1.0	5.0e-5	8.01e-4
Camden	175	125	5.6e-5	1.85	0.69	5.60e-5	3.0e-3
Standing *et al.*	618	570	1.00e-5	2.069	0.42	1.00e-4	2.00e-3

Table_Apx A-2: Values of Jardine stiffness parameters for Terrace Gravel

Terrace Gravel	**A**	**B**	**C**	**α**	**γ**	**ε_{smin}**	**ε_{smax}**
T5 GDBR	1100	1050	9.0e-6	1.22	0.75	9.0e-6	2.0e-3
Scott *et al.*	1100	1050	9.0e-6	1.22	0.75	9.01e-6	2.00e-3
Standing *et al.*	1104	1035	5.00e-6	0.974	0.94	8.80e-6	3.50e-3
Terrace Gravel	**R**	**S**	**T**	**λ**	**μ**	**ε_{vmin}**	**ε_{vmax}**
T5 GDBR	275	225	2.8e-5	1.1	1.0	3.0e-5	7.0e-3
Scott *et al.*	275	225	2.80e-5	1.1	1.0	3.00e-5	7.00e-3
Standing *et al.*	275	225	2.00e-5	1.044	0.98	2.10e-5	2.00e-3

Since the Jardine relationship between strain and stiffness is based on axial strain in an undrained triaxial test, it is necessary to find how this relates to 3D stresses. So in an undrained triaxial test:

$$\varepsilon_1 = \varepsilon_a \qquad \textbf{Equation 42}$$

and

$$\varepsilon_2 = \varepsilon_3 = -0.5\varepsilon_a \qquad \textbf{Equation 43}$$

Now,

$$\gamma_{oct} = \frac{2}{3}\left[(\varepsilon_1 - \varepsilon_2)^2 + (\varepsilon_2 - \varepsilon_3)^2 + (\varepsilon_3 - \varepsilon_1)^2\right]^{1/2} \qquad \textbf{Equation 44}$$

Substituting Equation 42 and Equation 43 into Equation 44:

$$\gamma_{oct} = \frac{2}{3}\left[(\varepsilon_a + 0.5\varepsilon_a)^2 + (-0.5\varepsilon_a + 0.5\varepsilon_a)^2 + (-0.5\varepsilon_a - \varepsilon_a)^2\right]^{1/2} \qquad \textbf{Equation 45}$$

$$\therefore \gamma_{oct} = \sqrt{2} \cdot \varepsilon_a \qquad \textbf{Equation 46}$$

The tensorial octahedral shear strain ε_{soct} is required, not the engineering octahedral shear strain γ_{oct}. Therefore,

$$\varepsilon_{soct} = \frac{\gamma_{oct}}{2} = \frac{1}{\sqrt{2}}\varepsilon_a \qquad \Rightarrow \varepsilon_a = \sqrt{2} \cdot \varepsilon_{soct} \qquad \textbf{Equation 47}$$

Now in a Cartesian coordinate system formulation of Equation 44:

$$\varepsilon_{soct} = \frac{1}{3}\left[(\varepsilon_x - \varepsilon_y)^2 + (\varepsilon_y - \varepsilon_z)^2 + (\varepsilon_z - \varepsilon_x)^2 + 6(\varepsilon_{xy}^2 + \varepsilon_{yz}^2 + \varepsilon_{zx}^2)\right]^{1/2} \qquad \textbf{Equation 48}$$

Using the relationship Equation 47 in Equation 48:

$$\varepsilon_a = \frac{\sqrt{2}}{3}\left[(\varepsilon_x - \varepsilon_y)^2 + (\varepsilon_y - \varepsilon_z)^2 + (\varepsilon_z - \varepsilon_x)^2 + 6(\varepsilon_{xy}^2 + \varepsilon_{yz}^2 + \varepsilon_{zx}^2)\right]^{1/2} \qquad \textbf{Equation 49}$$

The 'full strain increment vector' (fsi vector) of a zone, available in FLAC^{3D} as z_fsi(pnt,array), contains all the required strain components for Equation 49 above. Equation 49 is the one used in the FISH (FLAC^{3D}'s programming language) function that applies Jardine nonlinearity to the model. Every 10 steps, the fsi vector and the mean effective stress *p'* is found for each zone and the stiffness is updated. Standing *et al.* (1998) did a similar calculation, although without knowing the value of 'E' – the "stress invariant used in ICFEP", it is not possible to say if it was exactly the same.

A.1.2 Validation

A model of a triaxial test was created in FLAC^{3D}. A single-element model could have been used, but Simpson *et al.* (1979) found that this did not work well because a triaxial specimen does not fail in either a plane strain or axisymmetric manner. For a single 3D solid element, this means it is unlikely to model a shear failure appropriately. The plan was to also test the failure criterion with the triaxial test, and since there was no significant increase in runtime compared to a single element the triaxial cylinder mesh was used for this study also.

The analysis type was total stress undrained with no pore pressures. Initial stresses were set at 200 kPa, and an external pressure of 200 kPa was applied on all sides. This was then solved to ensure equilibrium. Then the deviator stress was increased incrementally. The purposes of the study were:

1. To show that the constitutive model was working.
2. To ensure that the stress increment size was not important (i.e. the stress path was always the same).
3. To optimise the solution control method, such as varying the number of steps between stiffness updates, or varying the convergence criterion (the 'mech. ratio').

The results are shown in Figure_Apx A-1 below. There was an error involved by stepping immediately to the maximum stress rather than by increments. However, it was very small. It seems that due to the way FLAC^{3D} approaches a solution by using the velocity of gridpoints, the nonlinear stress path was followed almost perfectly. Also, there was virtually no error involved in using a convergence criterion of 1e-5 rather than 1e-7 at typical values of stress and strain.

It was necessary to show that FLAC^{3D} would use the right value of shear modulus at any level of shear. This was done by extracting the axial strain and the value of the shear modulus of a zone near the centre of the model and comparing them to the theoretical curve.

The relationship between axial strain and tensorial octahedral shear strain was given by Equation 47 as:

$$\varepsilon_{soct} = \frac{1}{\sqrt{2}}\varepsilon_a \qquad \textbf{Equation 50}$$

The results in Figure_Apx A-1 show that the model seems to be applying the right stiffness values. The final value of stiffness at high strains above $\varepsilon_{s\max}$ is limited in FLAC^{3D} by an algorithm which sets $3G_{\tan}/p'$ to 50, whereas the theoretical limit is about 54 for this value of p'.

The next step was to plot the deviatoric stress vs. the axial strain. The simplest way of arriving at the theoretical solution was to calculate the undrained Young's modulus as follows:

$$E_{u\tan} = 3G_{\tan} \qquad \textbf{Equation 51}$$

Increments of axial strain were then used to calculate the tangent stiffness using the Jardine model equations and hence calculate the deviatoric stress:

$$q = E_u \cdot \varepsilon_a \qquad \textbf{Equation 52}$$

The results are shown in Figure_Apx A-2. The difference in the final value of stiffness mentioned previously is evident in the divergence of the two curves at large strains.

Each time the stiffness is updated, the program must cycle through all the zones in the model calculating the stiffness from the strain increment vector. Although this only takes 2-3 seconds, if it must be done every step it will have a significant impact on the total runtime when each step takes approximately 1 second. Therefore the number of steps between updates has been varied with the aim of optimising the process. This is shown in Figure_Apx A-3. The number of steps between updates chosen for the analyses of the tunnel junction was 10, which results in an error of approximately 5 %.

In order to check the effect of the stress increment size on the nonlinearity of the stress path, a deviator stress of 160 kPa was approached in various increments of stress. This is shown in Figure_Apx A-4. The difference between the value of strain at 160 kPa using 4 kPa increments and 40 kPa increments is very small. There is a slight difference between these values and the strain calculated in one increment of 160 kPa, but this error is still very small, less than 5 %.

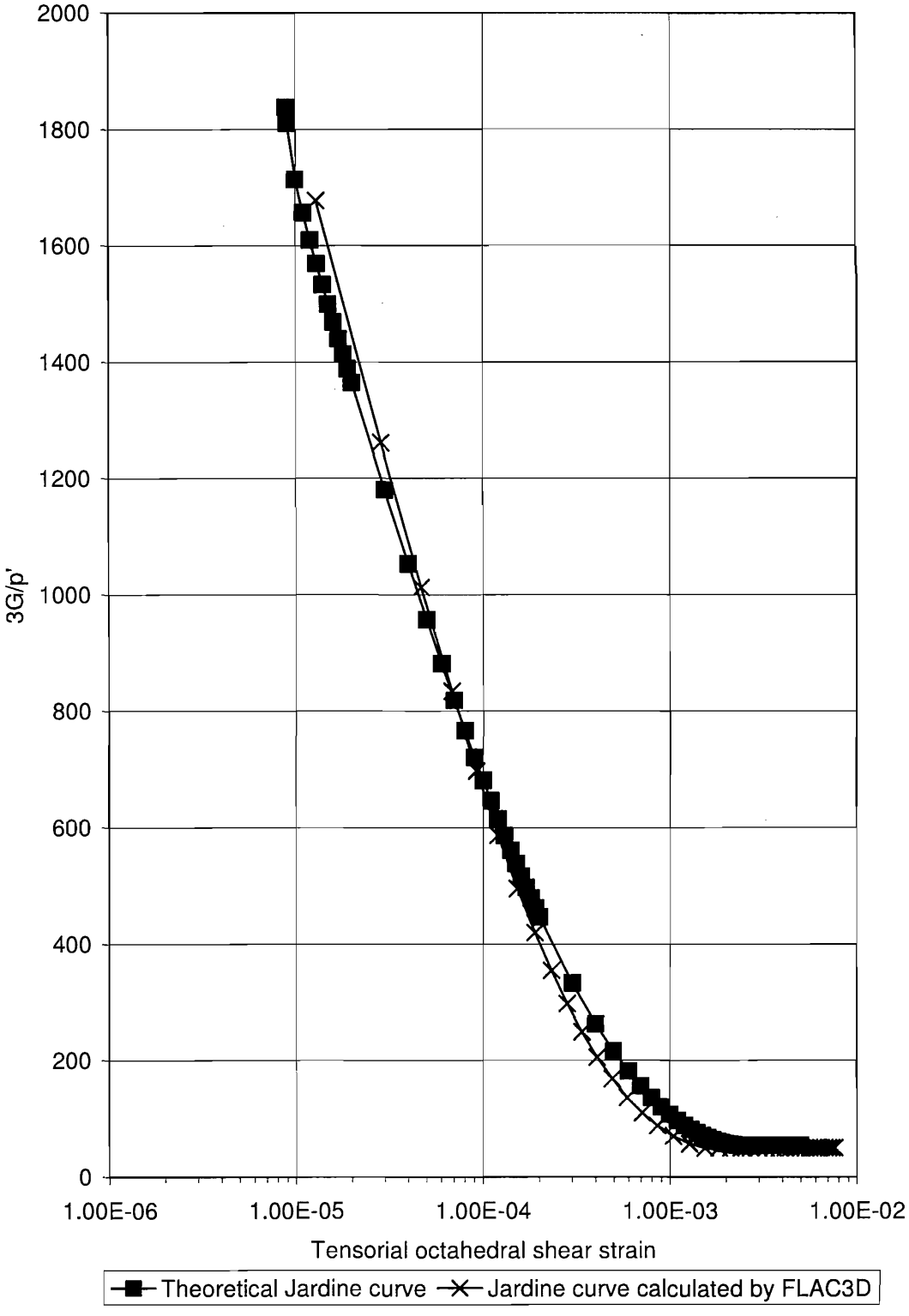

Figure_Apx A-1: Comparison of theoretical and calculated Jardine curves

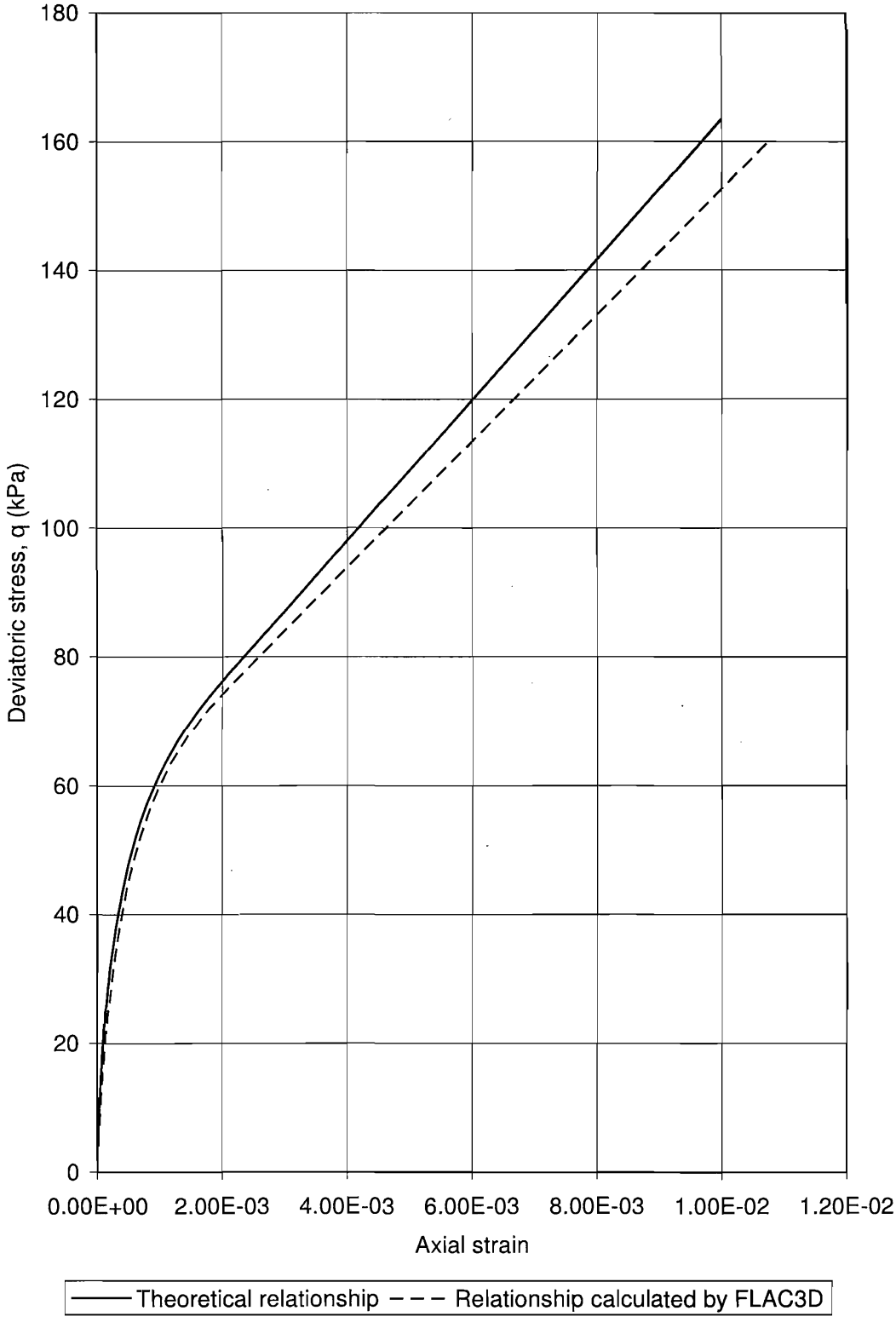

Figure_Apx A-2: Comparison of theoretical and FLAC3D stress-strain relationship

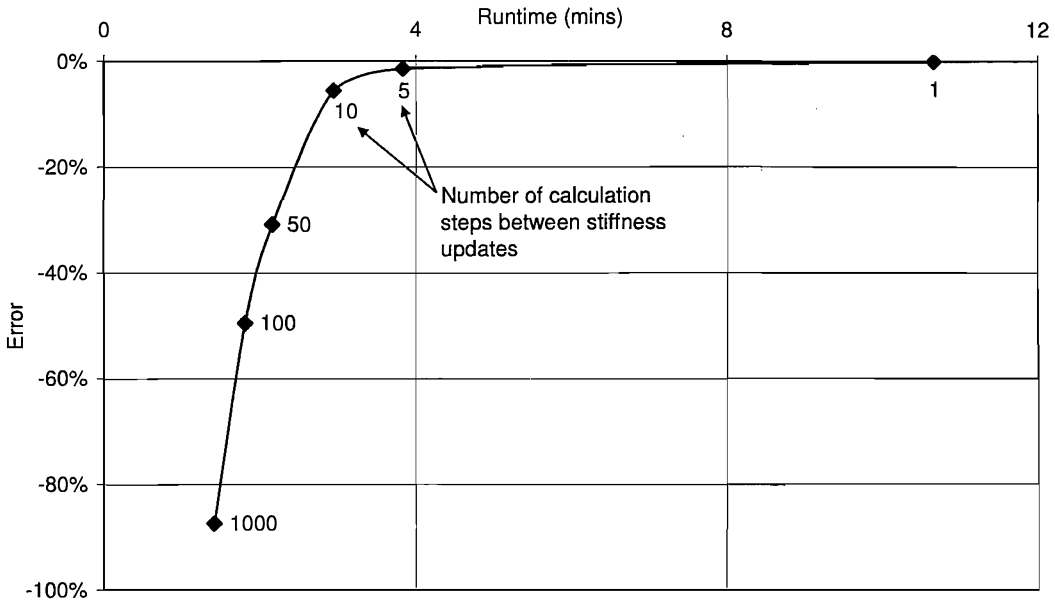

Figure_Apx A-3: Optimisation of number of steps between updating soil stiffness

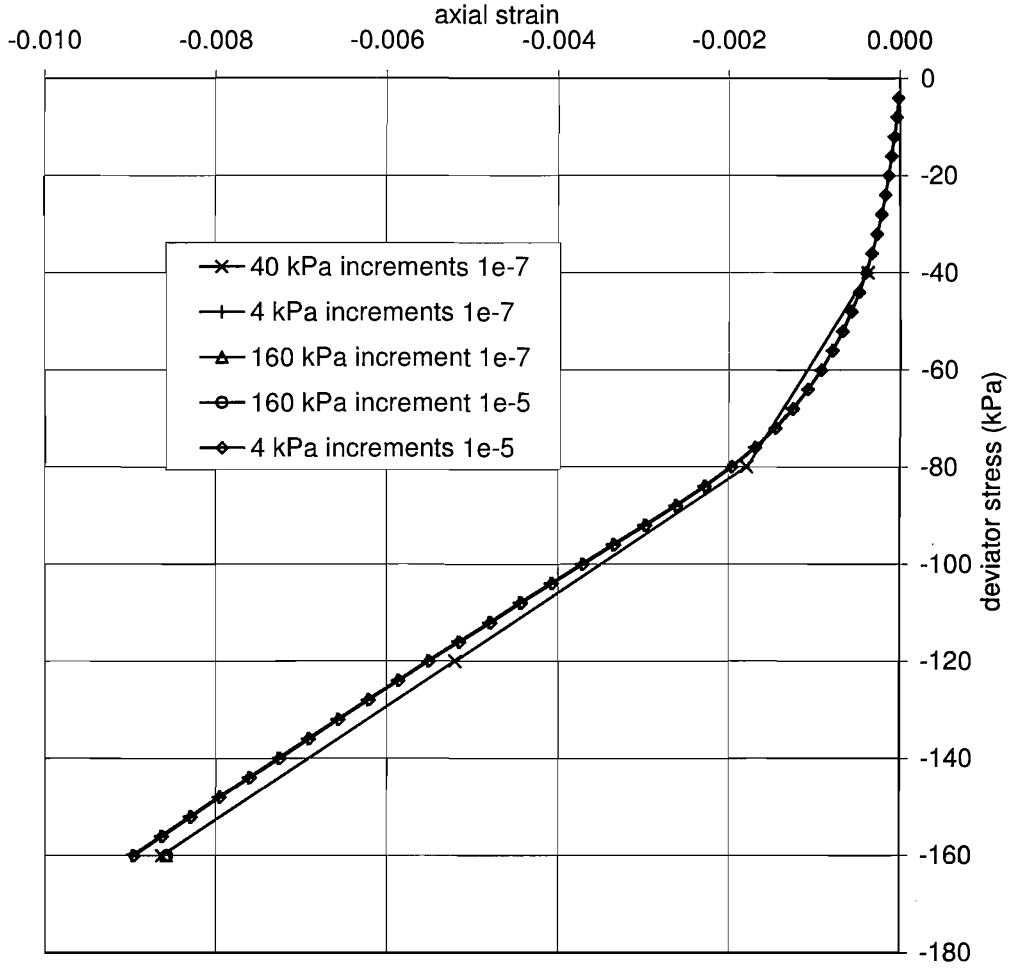

Figure_Apx A-4: Error due to stress increment size and mech. ratio